Mesures précises de sections efficaces $e^+e^- \longrightarrow$ Hadrons : tests du Modèle Standard et applications en QCD

B. Malaescu

n° d'ordre : **LAL 10-113**
ORSAY **Juillet 2010**

Université Paris-Sud 11
Ecole Doctorale de Physique de la Région Parisienne - ED 107

THÈSE

présentée pour obtenir le grade de

Docteur en Sciences de l'Université Paris-Sud 11

Spécialité : Physique de Particules

par

Bogdan Malaescu

Mesures précises de sections efficaces $e^+e^- \to \mathrm{Hadrons}$: tests du Modèle Standard et applications en QCD

Soutenue le 19 Juillet 2010 devant le Jury composé de :

MM.	G. Wormser	Président
	P. Aurenche	Rapporteur
	M. Davier	Directeur de thèse
	S. Descotes-Genon	Directeur de thèse
	G. Hamel de Monchenault	Rapporteur
	A. Pich	Examinateur
	D. Bernard	Invité

Résumé

Le Modèle Standard (MS) de la physique de particules avec les théories de jauge pour les interactions forte et électrofaible n'a pas encore été mis en défaut par les données expérimentales. Dans les recherches de nouvelle physique, au delà du MS, deux approches sont en général suivies : les recherches exploratoires à la frontière de haute énergie et des tests de précision à des énergies plus basses. Le but de cette thèse est dans le cadre de la deuxième approche, d'obtenir et utiliser des données précises des annihilations e^+e^- en hadrons, à des énergies de l'ordre 1 GeV. Ces données représentent un ingrédient important pour les tests du MS impliquant la polarisation du vide, comme par exemple la comparaison du moment magnétique du muon avec la théorie, ainsi que pour des tests de QCD et applications. Les différentes parties de cette thèse décrivent quatre aspects de mon travail dans ce contexte.

(1) Les mesures de sections efficaces en fonction de l'énergie nécessitent la déconvolution des spectres de données des effets de détecteur. Je propose une nouvelle méthode itérative de déconvolution des données expérimentales, qui présente des améliorations par rapport aux outils existants. On peut déconvoluer, d'une manière dynamiquement stable, des spectres de données qui peuvent être fortement affectées par des fluctuations dans la soustraction du bruit de fond, et simultanément reconstruire des structures qui n'étaient pas initialement simulées.

(2) Le coeur expérimental de cette thèse est constitué par l'étude du processus $e^+e^- \to K^+K^-$, du seuil jusqu'à 5 GeV, utilisant la méthode de rayonnement dans l'état initial (ISR), par la mesure de $e^+e^- \to K^+K^-\gamma$ avec le détecteur BABAR. Toutes les efficacités utiles sont mesurées utilisant les données expérimentales, et la normalisation absolue est fournie par la mesure simultanée du processus $\mu\mu\gamma$. J'ai effectué l'analyse complète où une incertitude systématique de 0.7% a été obtenue sur la résonance dominante, ϕ. Le facteur de forme du kaon chargé a été mesuré. Il présente une décroissance rapide au delà du ϕ et des structures distinctes dans la région $1.7 - 2.5$ GeV, où on connaît l'existence de résonances de type vecteur. La dépendance en énergie, à haute masse, est comparée à la prédiction de QCD.

On présente aussi les résultats du canal $e^+e^- \to \pi^+\pi^-$, du seuil jusqu'à 3 GeV, pour lequel j'ai effectué la déconvolution des effets de détecteur et j'ai obtenu les résultats finals qui sont comparés avec les données existantes.

(3) La prédiction pour le moment magnétique du muon (exprimée par l'intermédiaire de son 'anomalie', i.e. la déviation par rapport à la valeur de Dirac pour le rapport gyro-

magnétique égale à 2) est calculée dans le cadre su MS. Notre travail concerne seulement la contribution de polarisation hadronique du vide, obtenue à partir des données e^+e^- par une intégrale de dispersion. Comme la même information peut en principe être obtenue avec des données sur les désintégrations hadroniques du τ, on fait d'abord la mise à jour de la comparaison entre les utilisations des deux sources de données, et on trouve une différence réduite entre les évaluations correspondantes. Le nouveau résultat basé sur les données τ s'écarte de 1.9 déviations standard de la mesure directe. En suite, les nouvelles données précises de BABAR sont inclues dans une analyse combinée utilisant des outils (avec une procédure d'interpolation et moyennage de données améliorée, une propagation des incertitudes plus rigoureuse et une validation systématique) que j'ai développés. Avec les nouvelles données, le désaccord entre les résultats basés sur des données e^+e^- et τ pour le mode dominant 2π est réduit davantage, du 2.4σ précédent à 1.5σ, dans l'intégrale de dispersion, bien que des différences locales significatives entre les spectre persistent encore. Nous obtenons l'évaluation basée sur des données e^+e^- $a_\mu^{\rm had,LO} = (695.5 \pm 4.1) \cdot 10^{-10}$, où l'incertitude prend en compte toutes les sources. L'incertitude la plus grande pour la prédiction du MS est encore due à la polarisation hadronique du vide, mais elle est maintenant plus petite que l'erreur expérimentale. La comparaison actuelle entre la mesure directe et notre prédiction (basée sur les données e^+e^-) montre une indication intéressante de nouvelle physique (un effet à 3.2σ).

(4) Les règles de somme de QCD sont des outils puissants pour obtenir des informations précises sur les paramètres de QCD, comme la constante de couplage fort α_s. Cette étude devrait faire usage de la mesure complète de $e^+e^- \to$ hadrons jusqu'à environ 2 GeV. Comme BABAR n'a pas encore mesuré complètement tous les processus hadroniques, j'ai travaillé sur une situation similaire utilisant les fonctions spectrales des désintégrations hadroniques du τ, mesurées par ALEPH.

Je discute en détail la prédiction de QCD perturbatif, obtenue avec deux méthodes différentes : la théorie de perturbations à ordre fixe (FOPT) et la théorie de perturbations avec intégration de contour améliorée (CIPT). Les incertitudes théoriques correspondantes sont étudiées aux échelles de masse du τ et respectivement du Z. On trouve que la méthode CIPT est plus stable par rapport aux contributions manquantes d'ordre supérieur et par rapport à des changements de l'échelle de renormalisation. Il est également montré que FOPT souffre à cause de problèmes de convergence le long du contour d'intégration. La fiabilité d'une classe de modèles pour la fonction d'Adler, basée sur des renormalons, est étudiée dans le contexte de la comparaison entre CIPT et FOPT. On trouve que ces modèles ne sont pas suffisamment contraints pour qu'ils puissent identifier la meilleure méthode à utiliser pour la détermination de $\alpha_s(m_\tau^2)$.

La détermination de α_s est mise à jour et une valeur très précise pour $\alpha_s(m_\tau^2)$ est obtenue en utilisant CIPT ($0.344 \pm 0.005_{\rm exp} \pm 0.007_{\rm th}$). Une fois évoluée à la masse du Z, cette valeur est en accord avec $\alpha_s(M_Z^2)$ mesurée directement à partir de la largeur du Z. Ce résultat représente le test le plus précis du running de α_s en QCD.

Abstract

The Standard Model (SM) of particle physics with gauge theories for strong and electroweak interactions is still unchallenged by experimental data. Looking for new physics beyond the SM, two approaches are traditionally followed: exploratory searches at the high energy frontier and precision tests at lower energies. The scope of this thesis is within the second approach, obtaining and using accurate data on e^+e^- annihilation into hadrons at energies of the order 1 GeV. These data represent a very valuable input for SM tests involving vacuum polarization, such as the comparison of the muon magnetic moment to theory, and for QCD tests and applications. The different parts of this thesis describe four aspects of my work in this context.

(1) Measurements of cross sections as a function of energy necessitate the unfolding of data spectra from detector effects. I propose a new iterative unfolding method for experimental data, with improved capabilities compared to existing tools. We are able to unfold, in a dynamically stable way, data spectra which can be strongly affected by fluctuations in the background subtraction and simultaneously reconstruct structures which were not initially simulated.

(2) The experimental core of this thesis is a study of the process $e^+e^- \to K^+K^-$ from threshold to 5 GeV using the initial state radiation (ISR) method (through the measurement of $e^+e^- \to K^+K^-\gamma$) with the BABAR detector. All relevant efficiencies are measured with experimental data and the absolute normalization comes from the simultaneously measured $\mu\mu\gamma$ process. I have performed the full analysis which achieves a systematic uncertainty of 0.7% on the dominant ϕ resonance. The charged kaon form factor is obtained showing a fast decrease beyond the ϕ and some distinct structures in the $1.7 - 2.5$ GeV region where vector resonances are known to exist. The energy behaviour at large energies is compared to QCD predictions.

Also presented are results on $e^+e^- \to \pi^+\pi^-$ from threshold to 3 GeV for which I performed the unfolding and obtained the final results which are compared to existing data.

(3) The prediction of the muon magnetic moment (expressed through its 'anomaly', i.e. the deviation from the Dirac value of the gyromagnetic ratio equal to 2) is done using the SM. Our work concerns only the hadronic vacuum polarization contribution obtained from e^+e^- data through a dispersion integral. As the same information can in principle be obtained for data on hadronic τ decays, we first update the comparative use of the two sources of input data and find a reduced difference between the corresponding evaluations.

At the same time, the new tau-based estimate of the muon magnetic anomaly is found to be 1.9 standard deviations lower than the direct measurement. Then the new precise BABAR data are included in a combined analysis using tools (featuring improved data interpolation and averaging, more accurate error propagation and systematic validation) I developed. With the new data, the discrepancy between the e^+e^- and τ-based results for the dominant two-pion mode is further reduced, from previously 2.4σ to 1.5σ, in the dispersion integral, though significant local discrepancies in the spectra persist. We obtain for the e^+e^--based evaluation $a_\mu^{\rm had,LO} = (695.5 \pm 4.1) \cdot 10^{-10}$, where the error accounts for all sources. The largest uncertainty for the SM prediction is still from hadronic vacuum polarization, but it is now below the experimental error. The present comparison between the direct measurement and our (e^+e^--based) prediction shows an interesting hint for new physics (3.2σ effect).

(4) QCD sum rules are powerful tools for obtaining precise information on QCD parameters, such as the strong coupling α_s. This study should involve the complete measurement of $e^+e^- \to$ hadrons up to about 2 GeV. Since BABAR has not yet completely measured all hadronic processes, I worked on a similar situation using the spectral functions from τ decays measured by ALEPH.

I discuss to some detail the perturbative QCD prediction obtained with two different methods: fixed-order perturbation theory (FOPT) and contour-improved perturbative theory (CIPT). The corresponding theoretical uncertainties are studied at the τ and Z mass scales. The CIPT method is found to be more stable with respect to the missing higher order contributions and to renormalisation scale variations. It is also shown that FOPT suffers from convergence problems along the complex integration contour. The reliability of a class of renormalon-based models for the Adler function is studied, in the context of the CIPT vs. FOPT comparison. It is found that these models are not enough constrained to be able to distinguish the best perturbative method to be used for the determination of $\alpha_s(m_\tau^2)$.

The α_s determination is revisited and a very precise result on $\alpha_s(m_\tau^2)$ is obtained using CIPT ($0.344 \pm 0.005_{\rm exp} \pm 0.007_{\rm th}$). When evolved to the Z mass, this value agrees with $\alpha_s(M_Z^2)$ directly measured from the Z width. This result is the most precise test of the α_s running in QCD.

Contents

Introduction

The Standard Model of particle physics (SM) explains the electromagnetic, strong and weak interactions between elementary particles, leaving aside gravitation. Even within the SM, the origin of its parameters is not explained. These remarks, together with some other unexplained problems like the hierarchy of fundamental interactions or yet the existence of dark matter, point out that the SM does not provide the fundamental Lagrangian of Nature. Nowadays, many efforts are done, trying to find evidence of Physics beyond the SM in laboratories, where these effects could eventually be well understood.

Tests of the SM can be performed through precision measurements of the cross sections of e^+e^- annihilation to hadrons. They embed similar information to the spectral functions determined from the invariant mass distributions of hadronic τ decays. These are fundamental quantities describing the production of hadrons from the non-trivial vacuum of strong interactions, expressed in the form of spectral functions. Both kinds of spectral functions are especially useful at low energies where perturbative QCD fails to locally describe the data, and where the theoretical understanding of the strong interactions remains at a qualitative level. Due to these limitations on the theoretical side, spectral functions play a crucial role in calculations (through dispersion relations) of hadronic vacuum polarization contributions to observables such as the muon anomalous magnetic moment and the effective electromagnetic coupling ($\alpha(s)$) at the Z mass. Furthermore, a precise assessment of the fundamental parameters of the Standard Model is mandatory to test the consistency of the theory and to exploit its full predictive potential, with the aim of identifying discrepancies indicating loopholes in our understanding of its dynamics or providing signs of New Physics. The coupling constant α_s is the central ingredient of the strong sector of the theory, which can be determined at different scales using a large range of processes. At low energies, a precise value of α_s can be extracted from the spectral functions mentioned before. The renormalisation group equation allows one to evolve α_s up to the Z mass, and the comparison with the direct measurement at that scale provides a direct test of the running of QCD.

Traditionally, the measurement of the cross sections of e^+e^- annihilation to hadrons is done through energy scans, where data are gathered for different collision energies. However, several problems are seen when this method is used. As colliders perform well only in a limited energy range, data from different experiments must be combined in order to cover the full range of interest for the previously mentioned applications. The data on the exclusive low energy cross sections were obtained mainly at e^+e^- colliders in Novosibirsk and Orsay. Above ~ 2.5 GeV exclusive measurements are not practicable due

to the high hadron multiplicity, and the experiments at high energy colliders ADONE, SPEAR, DORIS, PETRA, PEP, VEPP-4, CESR and BEPC have measured the total inclusive cross section ratio R. Even within the data set of a given experiment, the change of the beam energy can modify the machine environment and this leads to 'point-to-point systematics' for data taken at different energy values.

Long time ago, a proposal was made to study events where hard Initial State Radiation (ISR) is emitted. Indeed, this allows the study of the e^+e^- annihilation to be performed on a large range of effective energies, below the nominal collision energy. The full cross section can hence be measured with identical collider and detector conditions. However, as the diagrams for the production of these events are one order higher in α compared to e^+e^- annihilation into hadrons, the statistics is supressed. In fact, the use of this method became possible thanks to the high luminosity of the ϕ and B factories, which largely compensates the previously mentioned loss of statistics.

On the experimental side, the main goal of this thesis is to provide a precise measurement of the cross section $e^+e^- \to K^+K^-(\gamma)$, using ISR data obtained with the BABAR detector. This provides us with an important contribution for the running of the electromagnetic coupling constant and also for the muon $g-2$. Although I did not participate in most of the studies (those similar to the K^+K^- analysis) aiming at obtaining the cross section $e^+e^- \to \pi^+\pi^-(\gamma)$, I brought my contribution in the final stages of this analysis and I will present the results. This channel provides the largest hadronic contribution to $g-2$, below 1 GeV, and is important for $\alpha(s)$ too. These two measurements employ the effective ISR luminosity obtained from a similar analysis of $\mu^+\mu^-$ events. The achieved precision for the two hadronic cross sections is better than 1%, as required for precise tests of the SM.

All the experimental data are altered by detector resolution effects, which must be unfolded in order to obtain the final cross section. I present a newly developped, general unfolding method which shows several advantages with respect to the previous ones. I apply and test a simplified version of this method for the BABAR K^+K^-, $\pi^+\pi^-$ and $\mu^+\mu^-$ mass spectra.

Several consistency checks have been performed on our data. In addition, I compare them to those obtained by previous experiments and use them to perform a series of phemomenological studies. In view of further phenomenological applications, I developped a new software package (HVPTools) for a consistent statistical treatment of all the data sets. It allows one to combine cross section data (but also mass spectra etc.) from several experiments into a single average spectral function, taking into account all the correlations between the points of a given experiment, as well as between different experiments. We use the combined spectral function to update the hadronic contribution to $g-2$. We compare this result with the one we obtain using the similarly combined τ spectral functions.

Spectral functions from e^+e^- annihilation will also be exploited for QCD studies. Before the completion of the full R measurement with BABAR data up to 2 GeV, I made some studies using the ALEPH τ spectral functions to determine the value of $\alpha_s(m_\tau^2)$. At that occasion, I performed several tests of the perturbative methods employed therein.

Since the publication of our results, a series of papers were written arguing on the best perturbative method to be used in these studies. We discuss some of the arguments, paying a special attention to the relevance of renormalon-based models for such a study.

Chapter 1

An Iterative, Dynamically Stabilized Method of Data Unfolding

1.1 Introduction

Experimental distributions of specific variables in high-energy physics are altered by detector effects. This can be due to limited acceptance, finite resolution, or other systematic effects producing a transfer of events between different regions of the spectra. Provided that they are well controlled experimentally, all these effects can be included in the Monte Carlo simulation (MC) of the detector response, which can be used to correct the data. The detector response is encoded in a transfer matrix connecting the measured and true variables under study. Several deconvolution methods for data affected by detector effects were described in the past (see for example [1–6]).

The aim of this chapter is to illustrate a new unfolding method allowing one to obtain a data distribution as close as possible to the "real" one for rather difficult, yet realistic, examples. This method is based on the idea that if two conditions are satisfied, namely the MC simulation provides a relatively good description of the data and of the detector response, one can use the transfer matrix to compute a matrix of unfolding probabilities. If the first condition is not fulfilled one can iteratively improve the transfer matrix. Our method is using a first step, providing a good result if the difference between data and normalized reconstructed MC is relatively small, on the entire spectrum. If this is not the case, one should proceed with a series of iterations.

The author learned the existence of the iterative methods present in the above list, when this study was close to completion. Two of these methods [3, 4] use a direct comparison of data and reconstructed MC events to compute normalization coefficients for the true MC events. However, it has been shown [7, 8] that in this approach iterations converge rather slowly. Further on, Ref. [5, 6] present methods based on the comparison of the true MC with the unfolding result at a given iteration. This comparison allows the computation of the probability matrix to be used at the next step. For the parts of our procedure which are similar to the ones in these last two papers, we will emphasize which

are the differences that make our method more general and better behaved.

In Section 1.2 we present a series of considerations taken into account in our newly developed unfolding method. We introduce the ingredients of the method in Sections 1.3 - 1.6. In Section 1.7 we assemble all these elements into an unfolding strategy. We provide two examples of applications of the method, with some possible tests, in Sections 1.8 and 1.9. We introduce the notations systematically and we also recall them in Appendix .1.

I have also decribed the unfolding method presented here in Ref. [10].

1.2 Important considerations for the design of the procedure

In the unfolding procedure we will not concentrate on the correction of acceptance effects. It is straightforward to perform it on the distribution corrected for the effects resulting in a transfer of events between different bins of the spectrum. Actually, these transfers have a physical meaning only for events which are in the acceptance of the detector and which passed all the cuts [1]. However, as the transfer matrix used in the unfolding is obtained from simulation, one must perform data/MC corrections for acceptance effects before the unfolding.

A first, rather tricky point is the way how the unfolding deals with new structures, not considered in the MC generator, but which can be present in the data. These structures are affected by the detector effects, and hence they need to be corrected. It seems that the Singular Values Decomposition (SVD) [1] and the iterative [2,3,5,6] methods provide a natural way of performing this correction. However, if the new structures in the data contain a relatively important number of events, they could also affect the normalization of MC spectra with respect to the data. For the unfolding procedure described here, we introduce a comparison method between data and MC spectra which is able to distinguish significant shape differences when computing the relative normalization factor. It is especially useful when the differences between the two spectra consist of relatively narrow structures. Our normalization method allows a meaningful comparison of data and MC spectra and improves the convergence of the algorithm in this case. If the differences are widely distributed, they have smaller impact on the normalization factor, and the sensitivity of our method is weaker too.

Since experimental spectra are generally obtained after background subtraction, this operation (performed before the unfolding) results in an increase of errors for the corresponding data points. Due to bin-to-bin or correlated fluctuations of the subtracted

[1] The method described in [5] computes at each iteration the spectrum corrected for the acceptance. This result is then used to improve the folding matrix (i.e. the probabilities of the causes, as they are called in this reference). Furthermore, the folding probabilities for each bin are normalized to the corresponding acceptance. It is straightforward to prove analytically that this method is completely equivalent to the one used in [6], where the acceptance is ignored in the unfolding and the corresponding correction is done at the end.

background, these points can fluctuate within their errors, possibly hiding systematic effects as large as the uncertainty due to background subtraction. These fluctuations can be important especially on distribution tails or dips, where the signal is weak and the background subtraction relatively large. Actually, it is only when the background subtraction produces a large increase of the uncertainties of the data points (well beyond their original statistical errors), that these fluctuations become a potential problem [2]. The problematic regions of the spectrum can be identified even before going to the unfolding. When computing the central values of the corrected distribution, the unfolding procedure has to take into account the size of the experimental errors, including those from background subtraction. Not doing so could result in too large a transfer of events between different regions of the spectrum. Depending on the shape of the distribution, this would affect the regions of important background subtraction, but could also bias the central values in the more precisely known regions. Such a systematic effect of the procedure is to be avoided, and we treat this problem carefully. To our knowledge, none of the previous methods aim at dealing with this second type of problem, and at distinguishing it from the previous one [3].

The method method presented here is able to deal with the potential problems described above. The induced fluctuations are dynamically reduced, in the sense that the way in which bin-by-bin corrections are performed avoids this problem. Therefore, no additional smoothing by a model-dependent fitting of the unfolding result at each iteration step (as proposed in [5]), is required.

The transfer of events performed by the unfolding introduces bin-to-bin correlations for the final spectrum. For further use of the data, these correlations are to be reduced as much as possible, if this can be done without introducing significant systematic biases of the result. Actually, the correction of systematic effects can generally be obtained without performing on each data point the maximal transfer of events (predicted by the transfer matrix), but only part of it. The method described in this chapter allows one to control the amount of these correlations and an optimization can be done with respect to the potential systematic bias of the final result.

This method is to be applied on binned, one dimensional data and the label of the physical quantities will be provided by the bin numbers. It can be directly generalized to multidimensional problems. For the sake of simplicity, we will consider only examples where the number of bins of the data and reconstructed MC is the same as the one for the unfolded distribution and true MC. However, it is rather easy to generalize the method to include a change of binning in the unfolding operation. All the formulae in the following will be given for this general case. We suppose the statistics of the data and of the simulation high enough to allow a "reasonable" separation into a series of bins . If this is not the case, the size of the bins must be adapted to the available statistics.

[2]The statistical fluctuations of the data, not including the ones from background subtraction, are not potential sources of bias at this level.

[3]In [5] a proposal was made to deal with the background subtraction in the unfolding procedure itself, by introducing an additional "cause responsible for the observables". This would indeed perform the subtraction, but would not solve the problem of the systematic effects by itself.

1.3 Folding and unfolding

In the MC simulation of the detector one can directly determine the number of events which were generated in the bin j and reconstructed in the bin i (A_{ij}). Provided that the transfer matrix A gives a good description of the detector effects, it is straightforward to compute the corresponding folding and unfolding matrix:

$$P_{ij} = \frac{A_{ij}}{\sum_{k=1}^{n_d} A_{kj}}, \tag{1.1}$$

$$\tilde{P}_{ij} = \frac{A_{ij}}{\sum_{k=1}^{n_u} A_{ik}}. \tag{1.2}$$

The folding probability matrix, as estimated from the MC simulation, P_{ij} gives the probability for an event generated in the bin j to be reconstructed in the bin i. The unfolding probability matrix $\tilde{P}_{ij}$ corresponds to the probability for the "source" of an event reconstructed in the bin i to be situated in the bin j. These matrix elements are well defined if the true MC bin j, and respectively the reconstructed MC bin i, are not empty. If that is not the case, one can set these values to zero and a special treatment must be provided for these bins in the unfolding algorithm.

The folding matrix describes the detector effects, and one can only rely on the simulation in order to compute it. The quality of this simulation must be the subject of dedicated studies within the analysis, and generally the transfer matrix can be improved before the unfolding. Systematic errors can be estimated to it and they are propagated to the unfolding result. We will assume in the following that the transfer matrix has been improved in this way, and in particular the folding matrix [4], so that it can be directly used in the data unfolding. Actually, no change of the folding matrix is produced in the unfolding procedure because there is no additional information becoming available on it at that point.

The unfolding matrix depends not only on the description of detector effects but also on the quality of the model which was used for the true MC distribution. It is actually this model which can (and will) be iteratively improved, using the comparison of the true MC and unfolded distributions.

The reconstructed (r) and true (t) MC distributions are related through:

$$r_i = \sum_{k=1}^{n_u} P_{ik}\, t_k, \tag{1.3}$$

$$t_j = \sum_{k=1}^{n_d} \tilde{P}_{kj}\, r_k. \tag{1.4}$$

Provided that the detector effects are well simulated, the folding equation (1.3) will also stand for data, relating the measured spectrum to the true one in the real world. The unfolding equation (1.4) can be written for data only in an approximate way, due to the

[4] This hypothesis is implicit for all the unfolding methods.

differences between the model used for the true MC distribution and the real physical signal [5]. However, the true MC distribution (and hence the unfolding matrix) can be iteratively improved and therefore it is an improved version of (1.4) that will be used to compute the unfolding result from data. Other effects will also be taken into account in a more elaborated unfolding equation, as we shall see in the next sections.

1.4 The regularization function

In order to dynamically reduce fluctuations and to prevent the transfer of events which could be due to fluctuations, in particular from the subtracted background, one can use a regularization function $f(\Delta x, \sigma, \lambda)$. This function provides an information on the significance of the absolute deviation Δx between data and simulation in a given bin, with respect to the corresponding error σ. It is a smooth monotonous function going from 0, when $\Delta x = 0$, to 1, when $\Delta x >> \sigma$. λ is a scaling factor, used as a regularization parameter. As we will see in the following, changing the regularization function used in our method will change the way we discriminate between real deviations and statistical fluctuations. It can be seen as the complementary of a generalized (by the use of λ) "p-value" of a given deviation between two variables affected by errors, if one considers the hypothesis that the MC describes well the data in the given bin. Actually, for $\lambda = 1$ this function is the complementary of the p-value defined in [9], computed for a given PDF. If the correlations between the errors of the values entering the computation of Δx are not negligible, only the uncorrelated part must be kept when computing σ.

For the unfolding procedure, we can consider several functions of the relevant variable $\Delta x/(\lambda\sigma)$:

$$f_1 = Erf\left(\frac{\Delta x}{\sqrt{2}\lambda\sigma}\right), \tag{1.5}$$

$$f_{1+n} = 1 - e^{-\left(\frac{\Delta x}{\lambda\sigma}\right)^n}, \text{with } n \in \{1; 2; 3; 4\}, \tag{1.6}$$

$$f_{5+n} = 1 - \frac{1}{1 + \left(\frac{\Delta x}{\lambda\sigma}\right)^n}, \text{with } n \in \{1; 2; 3\}. \tag{1.7}$$

Their dependence on the relevant ratio is shown in Fig. 1.1 . In general, we will use different λ parameters for the regularization function for each componenent of the unfolding procedure. We will see however that some of these parameters can be unified (i.e. assigned identical values) or even dropped (when a trivial value is assigned to them).

1.5 Monte Carlo normalization procedure

In the unfolding procedure we need to perform a comparison of data and reconstructed MC, as well as true MC and intermediate unfolded spectra. We keep in mind that the

[5] One can see these differences as an uncertainty on the initial unfolding matrix.

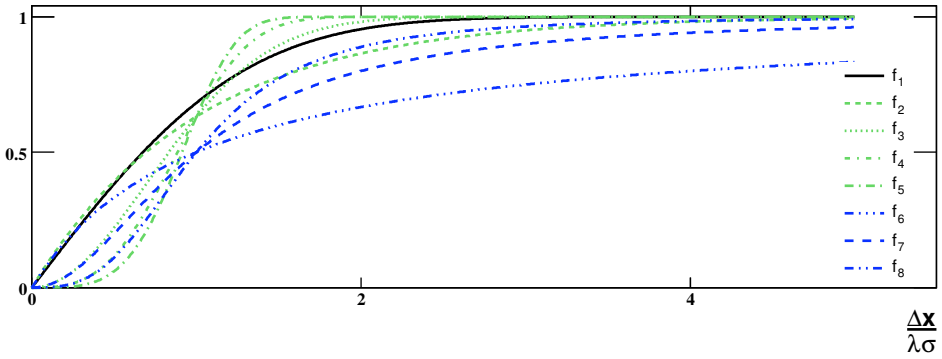

Figure 1.1: Behaviour of the functions $f_{1..8}$ (see text) with respect to $\Delta x/(\lambda\sigma)$.

data may contain structures, which were not (well) simulated in the MC. If the number of events corresponding to them is not negligible with respect to the total number of events in the data, the normalization of the MC spectra should be determined with care. One must actually ignore the events in these structures (and not included in simulation) when computing the normalization factor. Not doing so (a standard normalization procedure would use the total number of events in the two spectra) could result in generating fake differences between the two spectra, in regions where the data are well described by the simulation.

For a good normalization, one needs to get an estimation of the number of events in the data/intermediate unfolding spectrum which corresponds to features that were simulated in the reconstructed/true MC (N_d^{MC}). Dividing N_d^{MC} by the number of events in the true and reconstructed MC spectra (N_{MC}) one gets the normalization factor to be used for the MC. This is done as follows:
1) A first estimation of this number is provided by the total number of events in the data and in the intermediate unfolding distribution (N_d), minus those which are assigned to a fluctuation in the background subtraction: $N_d^{MC} = \sum_{k=1}^{n_d} \left(d_k - B_k^d\right) = \sum_{k=1}^{n_u} \left(u_k - B_k^u\right)$. Here n_d is the number of bins in the data and in the reconstructed MC distribution, n_u is the number of bins in the unfolding result and in the true MC distribution, d_k stands for the number of reconstructed and background subtracted data events in the bin k, u_j stands for the number of unfolded events in the bin j and $B^d(B^u)$ is the (estimated) vector of the number of events in the data (unfolded) distribution [6] which are associated to a

[6] At this level we made a distinction between B_k^d and B_k^u only to keep the method as general as possible. Indeed, if the binning of the initial (data) and final (unfolded) distributions are not the same, one must build a prescription to convert one vector into another, by a rebinning (in any case, no transfer by unfolding will be done for these events). Using a rebinning transformation R to pass from data to unfolding bins and another one (R') to pass from unfolding to data bins, one can convert one vector into the other, through:

$$B^u \xrightarrow{R} B^d,$$
$$B^d \xrightarrow{R'} B^u(').$$

These two transformations, if valid for all the sets of possible spectra in the two binnings (as defined

fluctuation in the background subtraction [7]. We will explain in the next section how $B^d(B^u)$ are obtained.
One can then improve the estimation of N_d^{MC} by an iterative procedure:
2) A better estimation is provided by

$$(N_d^{MC})' = N_d^{MC} + \sum_{k=1}^{n_{d/u}} (1 - f\left(|\Delta(d/u)_k|, \tilde{\sigma}(d/u)_k, \lambda_N\right)) \cdot \Delta(d/u)_k, \tag{1.8}$$

with $\Delta(d/u)_k = (d/u)_k - (B^d/B^u)_k - \frac{N_d^{MC}}{N_{MC}} \cdot (r/t)_k$. Here, for a given bin (k), r_k is the number of reconstructed MC events, t_k is the number of true MC events, and $\tilde{\sigma}(d/u)_k$ is the uncertainty to be used for the comparison of the two spectra [8].
Using Eq. (1.8), one adds to the previous estimate other events which have a low probability to belong to initially unknown (not included in the MC generator) structures. On the contrary, due to the factor in front of $\Delta(d/u)_k$, there is only a relatively small contribution from events likely to come from them.
In the special cases when $(d/u)_k - (B^d/B^u)_k < 0$ or $(r/t)_k = 0$, the content of the corresponding bins will be neglected when computing the number of events for the data and MC. This kind of situation will also receive a special treatment in the unfolding procedure, the estimation of the fluctuations in background subtraction and the improvement of the transfer matrix.
3) Replace N_d^{MC} by $(N_d^{MC})'$ and iterate until the change in N_d^{MC} between two consecutive iterations gets very small.
In the examples presented in this chapter we stop the normalization iterations when the relative improvement of two consecutive steps was less than 10^{-6}.

It should be emphasized that a better estimation of N_d^{MC} improves the separation between "known" and "unknown" structures, which then improves the next estimation. At the same time, the values of the parameter λ_N (for normalization), providing a good convergence of the normalization procedure, need to be studied, as described in Section 1.8.2. The convergence properties of the normalization procedure also depends on the amount of fluctuations in background subtraction which are not yet identified when the normalization is performed. In the normalization procedure, these fluctuations, corresponding to data points with larger error bars, would more likely not be identified as new

before), must be non-linear and/or one must allow for small local differences (not amplifying with iterations) between a vector and the one obtained by applying $R \times R'$. Actually, if they were linear, as their two matrix would contain only positive elements, even if $n_d = n_u$, their product could not be equal to the identity matrix. If the binning of the data and unfolding result are the same, the two vectors will always be identical (i.e. $R = R' = I$).

[7] This estimate could also contain statistical data fluctuations but, as their absolute size reduces with the amplitude of the spectrum, they are less "dangerous" for the unfolding result.

[8] $\tilde{\sigma}(d/u)_k = \sqrt{\sigma^2((d/u)_k) + (\frac{N_d^{MC}}{N_{MC}})^2 \cdot \sigma^2((r/t)_k)}$ if the uncertainties of d_k or u_k ($\sigma((d/u)_k)$) are not correlated with the uncertainties of r_k or respectively t_k ($\sigma((r/t)_k)$). This hypothesis is indeed true for the first-step comparison of data and reconstructed MC. The situation is different at further iteration steps and for the comparison of true MC and intermediate unfolding spectra. There, only their uncorrelated parts must be added quadratically to get $\tilde{\sigma}_k$. In practice, however, as the MC errors are generally negligible, considering only the data/unfolding errors at this level may be sufficient.

structures. As the estimation of the remaining fluctuations from background subtraction gets improved, the normalization follows.

1.6 Ingredients for the iterative unfolding procedure

In this section we describe the three main components of the iterative method: the general one-step unfolding procedure, the estimation of remaining fluctuations from background subtraction and the improvement of the unfolding probability matrix. They all make use of the normalization procedure described in section 1.5.

1.6.1 The general one-step unfolding procedure

Equation (1.4) can be seen as a "basis for the unfolding", in the sense that it describes this operation performed on the MC. If the differences between data and reconstructed MC are relatively small, then those between the unfolding result and true MC will be small too. In any case, one can start with an unfolded distribution equal to the true MC, and add to it the unfolded data events which are not present in the reconstructed MC. For the initial true MC one can use either a previously measured spectrum (if available) or one inspired by the data (and the folding matrix).

In order to perform the unfolding, one must first use the iterative procedure described in Section 1.5 to determine the MC normalization coefficient (N_d^{MC}/N_{MC}). At this level, it is the comparison of the reconstructed MC with the data that is used in the normalization procedure.

One can then proceed to the unfolding, where, in the case of identical initial and final binnings, the result for $j \in [1; n_u]$ is given by:

$$\begin{aligned} u_j &= t_j \cdot \frac{N_d^{MC}}{N_{MC}} + B_j^u \\ &+ \sum_{k=1}^{n_d} \begin{cases} f\left(|\Delta d_k|, \tilde{\sigma} d_k, \lambda\right) \Delta d_k \tilde{P}_{kj} + \left(1 - f\left(|\Delta d_k|, \tilde{\sigma} d_k, \lambda\right)\right) \Delta d_k \delta_{kj}, \text{ if } r_k \neq 0 \\ \qquad\qquad\qquad\qquad\qquad\qquad\qquad\qquad\qquad\qquad \text{and } d_k - B_k^d > 0, \\ \Delta d_k \delta_{kj}, \text{ if } r_k = 0 \text{ or } d_k - B_k^d \leq 0, \end{cases} \end{aligned} \tag{1.9}$$

where the same notation as in (1.8) is used. In the case of different binnings for the data and the unfolding, the Kroneker symbol δ must be replaced by a rebinning transformation R.

The first two contributions to the unfolded spectrum are given by the normalized true MC and the events potentially due to a fluctuation in background subtraction, which we do not transfer from one bin to another. Then one adds the number of events in the data minus the estimated effect from background fluctuations, minus the normalized reconstructed MC. A fraction f of these events are unfolded using the estimate of the unfolding probability matrix $\tilde{P}$, and for the rest only a rebinning is done (if necessary).

With the description of the regularization functions given in Section 1.4, it is clear that reducing λ would result in increasing the fraction of unfolded events, and reducing the fraction for which only a rebinning is done. This unfolding step benefits from two regularizations: one through the use of the previously described functions, and a second (implicit) one, through the mixing of events in different bins, by transfer of events. Changing λ can reduce one regularization and enhance the other. Choosing an appropriate value for this coefficient provides one with a dynamical attenuation of spurious fluctuations, without reducing the efficiency of the unfolding itself. This is possible due to the fact that the fraction of unfolded events is larger when the deviations between the spectra are larger with respect to the corresponding errors.

Some precautions need to be taken if $d_k - B_k^d \leq 0$ or $r_k = 0$. The first situation can typically occur if the background subtraction that was made for data, in the given bin, is too large, or if the binning is not well adapted to the data statistics. The second one indicates that the given data bin size is too small even for the MC statistics and the corresponding unfolding elements can not be computed. In these two situations, the events which are present in the data minus the estimated fluctuations from background subtraction and minus the normalized reconstructed MC will be simply rebinned (or kept in their original bin if the data and unfolding binnings are identical).

1.6.2 The estimation of remaining fluctuations from background subtraction

After having performed one unfolding procedure yielding a result u, as described before, we directly compare it with the true MC. Doing this, we can estimate the fluctuations from the subtracted background events. As these fluctuations must stay identical between the reconstructed data and the unfolding result, it is important that the first unfolding as well as the following iterations do not affect them (hence a constraint on the parameter of this estimation procedure, λ_S (for subtraction)).

Just as for the general one-step unfolding procedure, one must first use the iterative method described in Section 1.5 to determine the MC normalization coefficient (N_d^{MC}/N_{MC}), looking this time for structures present in the unfolding result, but not simulated in the true MC.

Then one can (re-)estimate the fluctuations from background subtraction

$$\left(B_j^u\right)' = \left(1 - f\left(\left|\Delta' u_j\right|, \tilde{\sigma} u_j, \lambda_S\right)\right) \Delta' u_j, \tag{1.10}$$

where $\Delta' u_k = u_k - \frac{N_d^{MC}}{N_{MC}} t_k$.

Here, increasing λ_S would increase the fraction of not-simulated events, which will be assigned to the estimate of the remaining fluctuations from the background subtraction. In principle one could perform this estimation using Δ, with the right side of (1.10) increased by the previous estimate $\left(B_j^u\right)$, but here we rather use Δ' so that we avoid an artificial increase of $(B^u)'$ in regions where the spectra differ only due to a normalization

effect. This allows one to use sufficiently large values of λ_S, to efficiently isolate remaining background fluctuations. The use of large values of λ_S will also prevent the propagation and potential amplification of the fluctuations in the unfolding result.

Once this estimate is obtained, one can use it to get a better normalization and then reestimate the fluctuations from background subtraction. This new information is however exploited very fast, one or two iterations being enough at this level.

One can perform the (re-)estimation (1.10) only in the usual case, when $u_j - B_j^u > 0$ and $t_j \neq 0$. Otherwise, the estimation of the fluctuations from background subtraction is trivially modified

$$\left(B_j^u\right)' = \Delta' u_j,$$

implying a fixation of the corresponding "pathological" events at the next unfolding step. This solution seems natural if the unfolding result minus the estimated fluctuation from background subtraction has a negative number of events in the given bin. Such a situation can occur due to an overestimation (possibly due to a statistical fluctuation) of the background that was subtracted to get the data spectrum to be unfolded. If the origin of the problem is the low MC statistics in the neighbourhood of the given bin, a more suitable solution could be the choice of an adapted binning. We feel that this problem should be dealt within unfolding methods.

1.6.3 The improvement of the unfolding probability matrix

As explained in the introduction, if the initial true MC distribution does not contain or badly describes some structures which are present in the data, one can iteratively improve it, and hence the transfer matrix. This can be done by using a better (weighted) true MC distribution, with the same folding matrix describing the physics of the detector, which will yield an improved unfolding matrix.

Just as in the previous section, one must determine the MC normalization coefficient, looking for structures present in the unfolding result, but not simulated in the true MC. As the description of the new structures by the MC will get improved, the task of the normalization procedure will be easier.

The improvement is performed for one bin j at the time. If however $u_j - B_j^u < 0$ or $t_j = 0$, one does not modify the transfer matrix in the corresponding true bin. Generally, this is not the case, and one can get an improved determination of all the elements of the column j of the transfer matrix

$$A'_{ij} = A_{ij} + f\left(\left|\Delta u_j\right|, \tilde{\sigma} u_j, \lambda_M\right) \Delta u_j \, P_{ij} \, \frac{N_{MC}}{N_d^{MC}}, \text{ for } i \in \{1; N_d\} \; . \tag{1.11}$$

Here, λ_M (for modification) stands for the regularization parameter used when modifying the matrix. Increasing λ_M would reduce the fraction of events in Δu_j used to improve the transfer matrix.

This method allows an efficient improvement of the folding matrix, without introducing spurious fluctuations. This is due to the fact that the larger the difference between the spectra, with respect to the corresponding errors, the larger the fraction of events used for the improvement of the matrix will be. The amplification of small fluctuations can be prevented at this step of the procedure too.

1.7 The iterative unfolding strategy

In this section we describe a quite general unfolding strategy, based on the elements presented before. It works for situations presenting all the difficulties listed before, even in a simplified form, where some parameters are dropped and the corresponding steps get trivial. The strategy can be simplified even more, for less complex problems.

One will start with a null estimate of the fluctuations from background subtraction. A first unfolding, as described in Section 1.6.1, is performed, with a relatively large value of $\lambda = \lambda_L$. This step will not produce any important transfer of events from the regions with potential remaining background fluctuations (provided that λ_L is large enough). Actually, it is the condition that this transfer must be very small that will impose a minimal value for λ_L. The first unfolding will perform the correction equal to the difference between the normalized true and reconstructed MC. This is generally the main correction that the unfolding has to provide. Concerning the new structures in the data, depending on their relative size, on the size of the transfer corrections and on λ_L, the corresponding corrections at this level can be more or less important.

One can even drop λ_L, by taking its value very large, which amounts to performing only the main correction discussed in the previous paragraph. This obviously guarantees the stability of the fluctuations in background subtraction, for this step.

At this level one can start the iterations:
1) Estimation of the fluctuations in background subtraction
An estimate of the fluctuations in background subtraction can be obtained using the procedure described in Section 1.6.2. The parameter λ_S used here must be large enough, in order not to underestimate them. As explained before, this can also prevent unfolding fluctuations from propagating. λ_S can however not be arbitrary large, as this operation must not bias initially unknown structures, by not allowing their unfolding. The ability of the method to simultaneously satisfy to these conditions depends on the properties of the function f_n, as it defines the degree of significance of deviations between spectra.
2) Improvement of the unfolding probability matrix
Using the method described in Section 1.6.3, one can improve the folding matrix A and get a better estimate of the remaining fluctuations from background subtraction. A parameter λ_M, small enough for an efficient improvement of the matrix, yet large enough not to propagate spurious fluctuations (if not eliminated at another step), must be used at this step.
3) An improved unfolding
A parameter $\lambda = \lambda_U$ will then be used to perform an unfolding following Section 1.6.1,

exploiting the improvements done at the previous step. It must be small enough to provide an efficient unfolding, but yet large enough to avoid spurious fluctuations (if not eliminated elsewhere).
These three steps will be repeated until one gets a good agreement between data and reconstructed MC plus the estimate of fluctuations in background subtraction. Another way of proceeding could consist in stopping the iterations when the improvement brought by the last one on the intermediate result is relatively small. If the parameters of the unfolding are well chosen, the two conditions yield similar results. Provided that one has a good model for the data spectrum, one can even use a toy simulation to estimate the needed number of steps.

The values of the λ parameters are to be obtained from toy simulations, as will be shown in the following. As one does not have a prior lower limit for λ_M and λ_U, other than the one related to the regularization, one can discard them by taking their values to zero (i.e. using all the data - reconstructed MC difference in the unfolding, and all the difference between the true MC and the intermediate unfolding, to improve the transfer matrix). This can be done if the higher limit on λ_S provides enough regularization at the level of the subtraction procedure.

In principle, one could also perform an estimation of the fluctuations in background subtraction, when comparing the data with the reconstructed MC. This could be done as a straightforward adaptation of the method explained in Section 1.6.2, or by computing this estimate as an improvement of the previous one (i.e. with $\Delta' d$ replaced by Δd in Eq. (1.10)). However, when doing the estimation of the fluctuations in background subtraction at the data - reconstructed MC level, one would benefit less (due to resolution effects) from the iterative improvement of the MC spectra. This improvement is useful in the method of Section 1.6.2 (especially when the number of events in the new structures as well as the resolution effects are large), as it directly facilitates the separation between real new structures and fluctuations (and also indirectly, through the normalization procedure).

1.8 A complex example for the use of the unfolding procedure

In the following we describe a rather complicated, yet realistic test, proving the robustness of the method. It exhibits all the features discussed previously, which are simultaneously taken into account by the unfolding. For the clarity of the presentation, the structures and dips of the spectrum are however separated. The true and reconstructed spectra for this test have 200 identical bins.

1.8.1 Building the data spectra and transfer matrix

The first step consists in building a model for the transfer matrix $\bar{A}$. The matrix

$$T_{ij} = \frac{N_T}{2\pi\sigma_s\sigma}\left(1 + 0.2\,e^{-\frac{(j-130)^2}{2\sigma_r^2}} - e^{-\frac{(j-40)^2}{2\sigma_d^2}}\right) e^{-\frac{(j-100)^2}{2\sigma_s^2} - \frac{(i-j)^2}{2\sigma^2}}, \tag{1.12}$$

with $N_T = 10^6$, $\sigma_s = 40$, $\sigma = 3$, $\sigma_r = 1$ and $\sigma_d = 4$ exhibits resolution effects and corresponds to a true spectrum which is mainly Gaussian. In addition, this spectrum includes a Gaussian resonance (more narrow than resolution) centred on the bin 130 and a dip around the bin 40 (larger than resolution). One then includes a systematic transfer of events from high to lower bins, getting the final model matrix:

$$\bar{A}_{kj} = \sum_{i=k}^{N} T_{ij}\, c_1 \left(\frac{k+1}{i+1}\right)^4 e^{-(i-k)/c_2}, \tag{1.13}$$

with $c_1 = 2$ and $c_2 = 8$. For example, such a transfer of events, occurs in measurements of the cross section $e^+e^- \to hadrons(n\gamma)$ with the radiative return method (see for example [60]). Indeed, not detecting a final state photon will result in an underestimation of the hadronic mass of the given event.

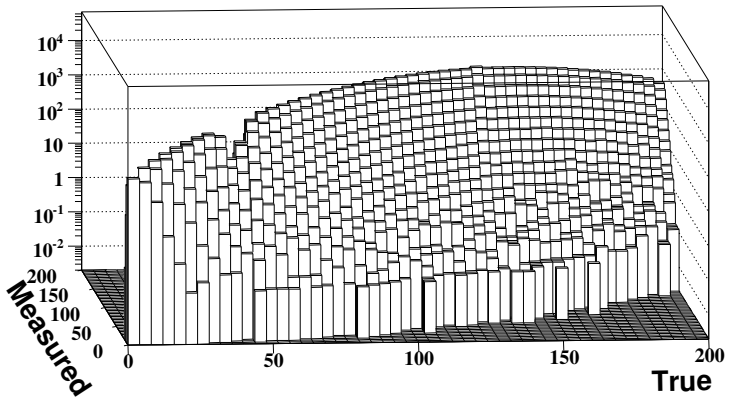

Figure 1.2: Transfer matrix A. Here, for display reasons, the bins are four times larger than the real ones (an average was computed inside squares of $4X4$ initial bins).

The model itself provides the "real" detector matrix ($\bar{A}$) which is crucial for building and folding the true distribution. The MC transfer matrix A (see Fig. 1.2) used as input of the unfolding procedure is a statistical realisation [9] of $\bar{A}$.

The folding probability matrix is computed from $\bar{A}$. One must then fix a normalisation ratio between data and MC simulation (usually of the order of 1/10). The normalised true distribution corresponding to $\bar{A}$ represents the true MC model ($\bar{t}$). At this point, one can

[9] The statistical fluctuations of the transfer matrix (accounting for the finite MC statistics) follow a Poisson law, preserving positivity.

compute the reconstructed MC in the model ($\bar{r}$), by folding $\bar{t}$. The $\bar{r}$ and $\bar{t}$ distributions are different from the reconstructed and respectivelly true MC in the unfolding, only by the fluctuations introduced between A and $\bar{A}$. Indeed, r and t are correlated random realisations of $\bar{r}$ and $\bar{t}$. The data model (at the true level) will be given by $\bar{t}$, completed with structures unknown to the MC (a "bias"):

$$bias_j = \frac{2 \cdot 10^4}{3\sqrt{2\pi}} \left[e^{-\frac{(j-90)^2}{2\sigma_1^2}} + e^{-\frac{(j-170)^2}{2\sigma_2^2}} \right], \tag{1.14}$$

with $\sigma_1 = \sqrt{6}$ and $\sigma_2 = 4$. The two resonances have widths comparable to resolution, one being more narrow (and therefore hard to correct) and one larger. The folding of the data model yields the reconstructed spectrum (after adding Gaussian fluctuations within statistical errors). The final data spectrum in our toy model (filled circles in Fig. 1.6) is obtained after adding a component simulating the effect of a background subtraction (there where it can typically be large in practice, i.e. in the dip of the spectrum), with the average per bin:

$$B_i^d = \frac{7 \cdot 10^3}{3\sqrt{2\pi}} e^{-\frac{(i-40)^2}{2\sigma_b^2}}, \tag{1.15}$$

with $\sigma_b = \sigma_d$. For the simulated effect of background subtraction, we attribute an error equal to its average value in each bin. The subtracted background can come with fluctuations corresponding to its errors, which are statistical or systematic (i.e. correlated or not between neighbour bins). In order to simultaneously simulate these two situations (statistical fluctuations and bias in the background subtraction), we fluctuate the contribution (1.15) within its errors for $i \leq 40$ only, and we add it to the data fluctuated within their statistical errors. The final errors of the data, which will enter the unfolding algorithm, are given by the quadratic sum of the errors of the subtracted background plus the statistical ones from the data without background.

The unfolding result is to be compared with the data model plus the remaining fluctuations from background subtraction. This represents a test over a very large dynamic scale. The results that will be presented for this test were obtained using the function (1.6), for $n = 2$, but similar results were obtained with the other functions. We will come back to this point later.

1.8.2 Optimization of the parameters

The parameters to be used in the unfolding procedure were studied with different toy simulations, with various parameters for the simulated fluctuations in background subtraction and for the bias. In practice, one needs approximate values of the parameters for the spectrum and the potentially dangerous background fluctuations, in order to perform the further study, to determine the parameters of the unfolding. One can get a very preliminary estimate for the parametrization of the spectrum from the data, together with the folding matrix, and from the procedure of background subtraction. Once the

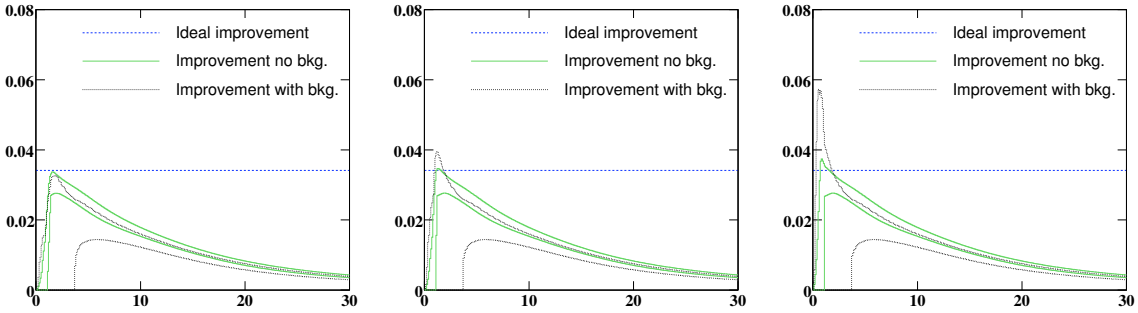

Figure 1.3: Normalization relative improvement limits as a function of λ_N, without fluctuations from background subtraction (green continuous lines) or with their usual amplitude (1.15) (dotted black lines), obtained after, at most, from left to right, 30, 50 and respectively 200 steps. The dashed blue line shows the expected "ideal improvement".

unfolding is performed, the determination of the spectrum parameters is also drastically improved. In principle, at that point, one could try to re-estimate the optimal parameters of the unfolding and try to improve them with more accurate toy simulations. In practice however, except for very extreme situations, this new estimate will be consistent with the first one.

The optimization of the parameter λ_N used in the normalization procedure, was studied for the comparison between data and reconstructed MC, with a null estimate of the fluctuations from background subtraction. As explained before, at this level, one does not take advantage of the corrections of the resolution effects on new resonances. Actually, these corrections make easier the separation of new structures and fluctuations. A procedure that works properly at the data/reconstructed MC level, would work even better when comparing an intermediate unfolding result and the true MC. Furthermore, the normalizations at these two levels are improved by a better estimation of the fluctuations in background subtraction and by the improvement of the transfer matrix through the true MC.

The first part of this study was performed with toys of data and reconstructed MC spectra, obtained as described in Section 1.8.1, with or without the remaining fluctuations from background subtraction given by Eq. (1.15). In both cases, the first estimate of N_d^{MC} is given by the number events in the data N_d. For 100 toys, we plot the minimal and maximal improvement brought by the procedure $((N_d - N_d^{MC})/N_d)$, for a large interval of λ_N values (see Fig. 1.3). We stop iterating when the relative improvement of two consecutive steps gets less than 10^{-6}, or after a fixed number of steps (if the first condition was not fulfilled before). The improvement brought by the procedure is to be compared with the "ideal improvement" computed from the ratio of the number of events in the new structures and the total number of events in the data.

Fast convergence and good stability (with respect to the background fluctuation problem) are exhibited for large values of the parameter of normalization. The procedure

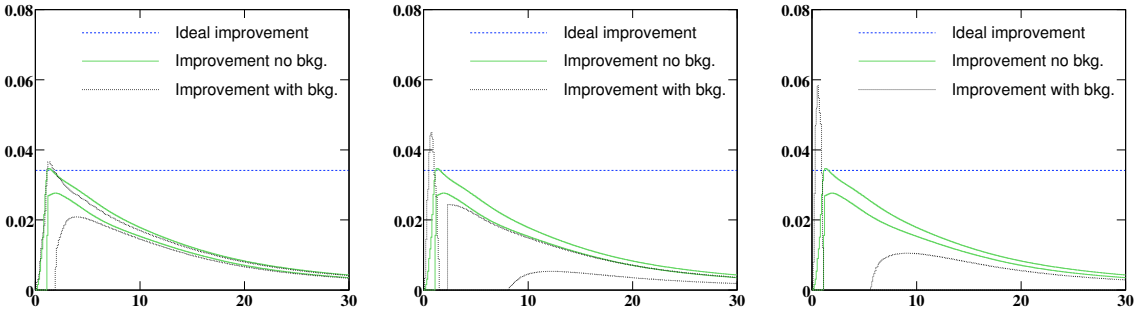

Figure 1.4: Normalization relative improvement limits as a function of λ_N, without fluctuations from background subtraction (green continuous lines) or with them having a value twice less (left), twice larger (middle) and four times larger (right) than usual (dotted black lines). In the right figure, only the upper limit of the normalization improvement, obtained when fluctuations from background subtraction are present, is visible. These improvement values were obtained after, at most, 50 steps. The dashed blue line shows the expected "ideal improvement".

is clearly sensitive to the presence of fluctuations in background subtraction, which are treated more like real structures, for small values of λ_N. It is only in this region of values of λ_N that the limit on the number of steps plays a role. Too small a value of λ_N could be identified, even when running on fluctuating data, by the presence of instabilities in the sign and size of the correction (their size could not converge for a reasonable number of iterations). One can conclude from these plots that a value of $\lambda_N \approx 5$ would provide a relatively good and stable normalization improvement at the first steps of the unfolding, as well as when one gets an estimate of the fluctuations in background subtraction. In this second case, a smaller value of λ_N could bring an even better improvement. Other amplitudes of fluctuations in background subtraction (see Fig. 1.4) could yield different conclusions. If these fluctuations are larger, one could prefer to use a large value of the parameter (which could even be equivalent to performing the standard normalization) before the first estimation of fluctuations in background subtraction, and a smaller one afterwards. It has been tested that a change of the centre of the distribution of fluctuations in background subtraction (Eq. (1.15)) by $\pm\sigma_b$ does not change the conclusions related to the normalization parameter.

In practice, one can perform the previous study on a model similar to the data or directly using the data and reconstructed MC distributions. In this second case, only the black limits in Fig. 1.3 would be available.

The plots in the rest of this subsection were obtained for slightly changed parameters of the data-MC bias and background subtraction fluctuations (as it would be the case if the model was built to reproduce the caracteristics of some data):

- an amplitude of the resonance initially centred on the bin 90 (moved to the bin 87, with a width $\sigma_1 = \sqrt{5}$ for this scan), reduced by 25% with respect to Eq. (1.14);
- the amplitude of the resonance initially centred on the bin 170 (centred on the bin

173, with a width $\sigma_2 = 5$ for this scan), increased by 25%;

- the effect of the fluctuations in background subtraction reduced by 25% with respect to the one in Eq. (1.15), and centred on the bin 37, with $\sigma_b = 5$.

The resulting optimal parameters are stable with respect to various changes of this type (compatible with the precision one could achieve in practice).

The choice of the value λ_L (to be used for the first unfolding step) is made such that, the fluctuations in background subtraction are not unfolded, and hence do not bias other regions of the spectrum. We have observed that the value $\lambda_L \approx 7$, would be large enough, to prevent unfolding fluctuations in background subtraction for different relative values of their amplitude. Actually, the method is stable for λ_L values in the range of 7 to infinity. However, in order to show that this parameter can be dropped and the procedure simplified, we choose a very large value for it, such that the correction done by the first unfolding is given only by the difference between the true and reconstructed MC.

The two other parameters to be used and the number of necessary iterations, are analysed using a scan of their values, for test spectra with different amplitudes of the initially unknown resonances. For every set (λ_M, λ_U), we compute a χ^2 estimator between the final reconstructed MC and the data minus the events to be subtracted, as well as between the unfolding result and the true spectrum plus background fluctuations, for a number of steps minimizing this last χ^2 (see Fig. 1.5). These χ^2 estimators are computed using simply the statistical errors of the data, plus the small ones from MC for the first estimator. The anomalous values (once divided by the number of degrees of freedom), obtained sometimes for the optimal parameters, can be explained by the fact that we ignore the change in the errors of the spectrum and they correlations due to the unfolding. However, as we are not interested in the absolute values of these χ^2 estimators, but only on the optimal parameters, this way to proceed is good enough. Actually it is even to be preferred due to its inherent sensitivity to some potential instabilities of the iterations (for inappropriate values of the parameters), generating large fluctuations. This sensitivity would be lost if one would compute the χ^2 using for example the errors resulting from a toy simulation.

Asking for small values of the two χ^2 estimators (at the unfolded/true MC and data/reconstructed MC level respectively), one can clearly discriminate the best region of values for λ_M and for λ_U. They are valid, not only for the parameters of the spectra used in this scan, but also for different ones used in the test of the method, as we'll see in the following. The corresponding plots indicate here small χ^2 values for λ_U and λ_M close to zero (or even null), indicating that the use of these parameters is not absolutely necessary. These plots also give even more information about potentially problematic parameterizations yielding for example badly unfolded (not enough corrected) new structures if λ_M is too large, or to fluctuations if one performs only small unfolding corrections in the iterations (using a too large λ_U value) and the other parameters preventing their propagation are not appropriate. This kind of study has some sensitivity to λ_S (to be used in the subtraction procedure) too, through the χ^2 at the unfolded/true MC level. Actually, if its value is too large, the subtraction is too strong preventing the good reconstruction of

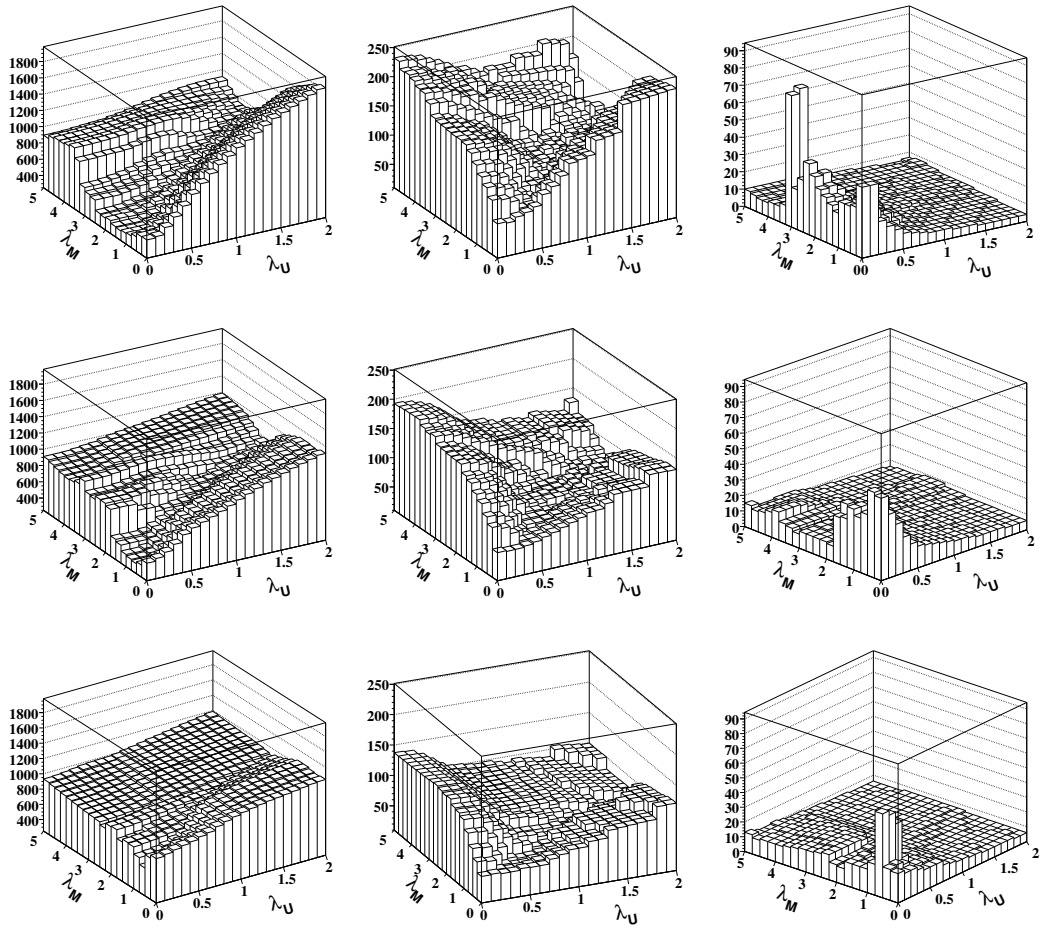

Figure 1.5: χ^2 between the unfolding result and the data model plus fluctuations in background subtraction (left column), χ^2 between the final reconstructed MC and the data minus the events estimated as being due to fluctuations in background subtraction (middle column), and the optimal number of steps (right column). These plots were obtained for $\lambda_S = 3$ (top line), $\lambda_S = 5$ (middle line) and $\lambda_S = 7$ (bottom line).

new structures. As we saw before, this χ^2 is also enhanced if fluctuations propagate (for example because of a too small λ_S). These χ^2 estimators provide however only global comparisons of the spectra. Therefore, for complex situations like in this example, a more precise determination of the parameters is provided by local comparisons of the spectra within toy simulations (i.e. local contributions to the previous χ^2 estimators). This kind of comparison performed for the spectra used in the previous scans, or other similar variations, indicates that a value $\lambda_S \approx 5$ allows one to fix the fluctuations in background subtraction and to prevent the ones of the procedure, without a bias of the reconstruction of new structures. As we will see, the choice of this value, as well as the other parameters, can be tested directly when unfolding the data.

The plot of the optimal number of iterations provides a relatively good estimation

of the number of steps which are needed in practice, when the corresponding unfolding parameters are used. The confidence one can have in this number depends however on the precision with which one knows the widths of the new resonances. One should keep in mind that this is just an estimation and, once the unfolding parameters are determined, a better suited strategy could be to stop the algorithm when the iterations start having a small impact on the result or yet when one gets a good agreement between data and reconstructed MC.

1.8.3 Unfolding the spectrum, possible tests of the result and systematic errors

Here we present the way the unfolding behaves for the distributions described in Section 1.8.1. This tests the reliability of the unfolding method as well as the one of the procedure used to optimize the parameters.

As explained in the previous subsection for the various test distributions, here also a parameter $\lambda_L \approx 7$ would be large enough to leave the contribution of fluctuations in background subtraction at its initial position. The first unfolding step was however performed with a very large value for this parameter (see Fig. 1.6 and 1.7) and it corrects all the elements of the spectrum which are simulated in the MC, for both kinds of transfer effects (in spite of the fact that they are relatively important).

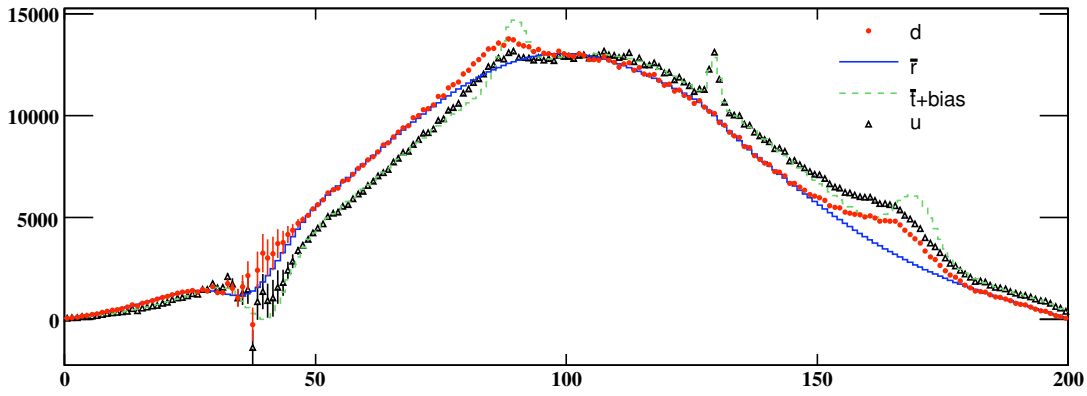

Figure 1.6: The unfolding result after the first step (triangles), compared to the data distribution (filled circles), the the reconstructed MC in the model (solid line) and the true MC model plus the bias (dashed line).

This first step could also perform part of the needed corrections for the new structures, but we postpone these corrections to further unfolding steps, by taking a very large λ_L. This is actually what one can see in Fig. 1.8, where we show the result of the first step of an unfolding performed with $\lambda_L = 0$. Such a strategy partially corrects the shape of the new structures in data. However, it also propagates fluctuations originally introduced

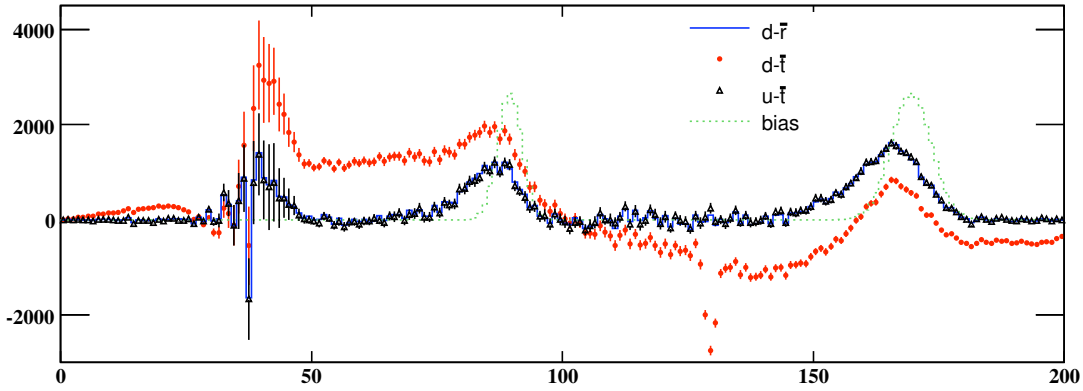

Figure 1.7: Unfolding result after the first step minus the true MC model (triangles), data minus the true MC model (circles), data minus the reconstructed MC in the model (solid line), and bias (dotted line).

by background subtraction to regions of the spectrum which were initially known more preciselly, biasing them. This bias will not be removed by the following iterations and therefore one must really avoid to introduce it at the first step. It is here that we see one of the advantages of this new unfolding method, which, if propertly parametrised, prevents the apparition of this type of bias.

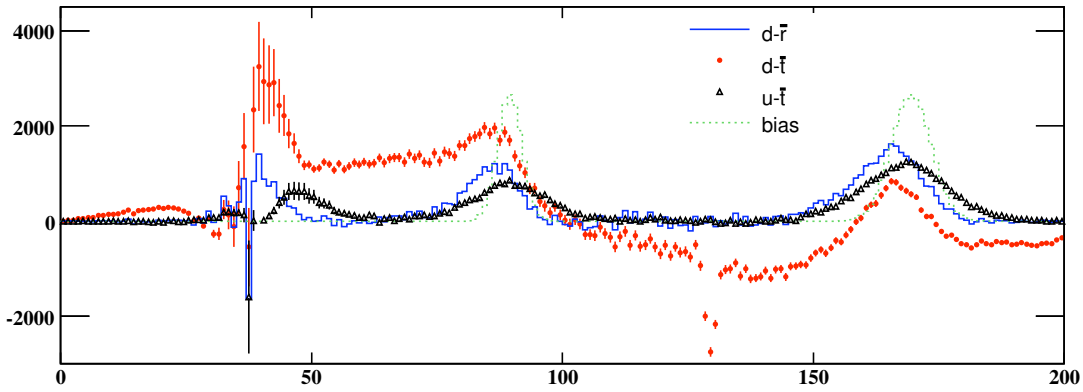

Figure 1.8: Result after the first step of an unfolding with $\lambda_L = 0$ minus the true MC model (triangles), data minus the true MC model (circles), data minus the reconstructed MC in the model (solid line), and bias (dotted line).

A series of 65 iterations was then performed, with complete unfolding and matrix modification (i.e. taking the parameters $\lambda_U \to 0$ and $\lambda_M \to 0$). Actually, in this case the regularization is provided by the use of $\lambda_S = 5$, and the use of λ_U and λ_M can be dropped. A very good estimation of the fluctuations in background subtraction is obtained at the

first iteration, and the further improvements are relatively small. However, for the sake of generality, it has been tested that good results can be obtained, with non-zero values of λ_U and λ_M.

The main effect of these iterations is to correct the folding matrix, by introducing in the true MC distribution (and implicitly in the reconstructed one), the structures which were not present in the initial simulation (see Fig. 1.9). A first reason for which such a high number of iterations was needed in this test are the large resolution effects which must be corrected for the initially unknown structures, even for the narrow one. It has been tested that between 15 and 20 iterations are generally enough to reconstruct well the new structure centred on the bin 170, which is slightly larger than the detector resolution (being however strongly affected by its effects too).

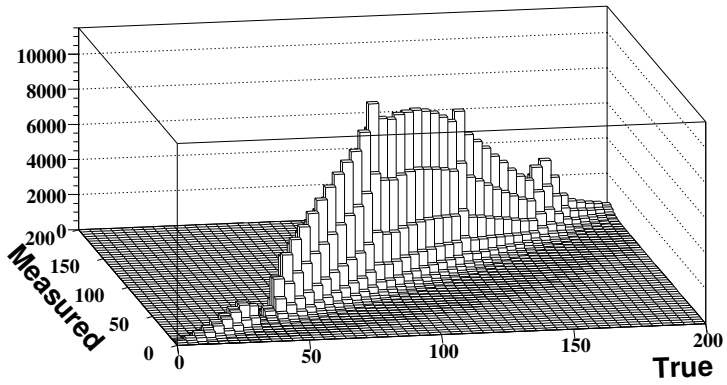

Figure 1.9: Transfer matrix after 65 iterations.

The final estimation (see Fig. 1.10) reproduces well the fluctuations from background subtraction added in the region of the dip, for the bins where it was statistically fluctuating as well as for the ones where it was stable. The need to distinguish between potentially fluctuations in background subtraction and new structures, especially when having an important transfer of events in the unfolding, imposes important constraints on the parameter values that can be employed. This can be a the second reason which can increase the number of needed iterations. The difference between the data and the improved reconstructed MC is basically equal to the estimate of fluctuations from background subtraction, which is not used when modifying the transfer matrix.

The final unfolding result reconstructs well all the structures in the data model, without introducing important systematic effects due to the fluctuations in background subtraction (see Fig. 1.11 and Fig. 1.12). The errors of the unfolding result(s) were estimated using 100 MC toys, with fluctuated data and transfer matrix for the unfolding procedure. The corrected structures are affected by fluctuations coming from all the data bins contributing to them, which is particularly important for large folding/unfolding effects like the ones in this example. As expected, new structures are more affected than the ones initially included in the MC, because the corresponding data fluctuations can locally affect the improved MC transfer matrix.

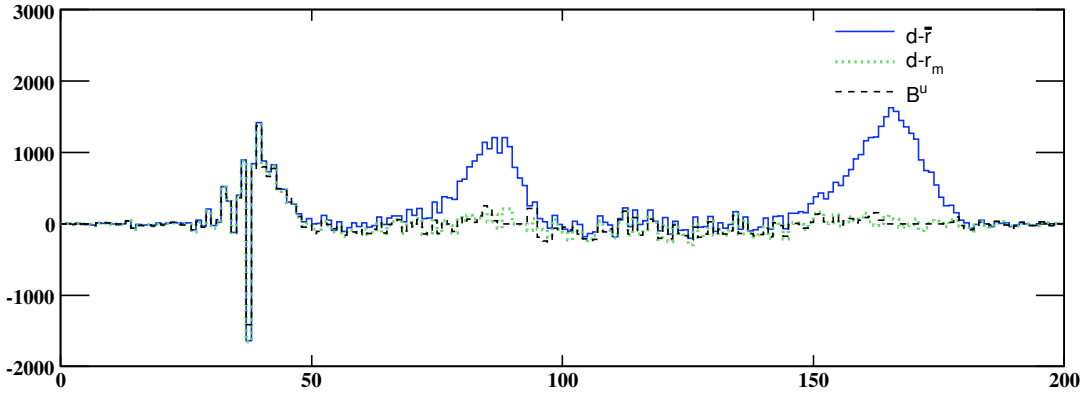

Figure 1.10: Estimate of fluctuations in background subtraction (dashed line), data minus the modified (improved) reconstructed MC (dotted line) after 65 iterations, and data minus the reconstructed MC in the model (solid line).

At this point one could perform a test of the parameterization of the procedure, directly on the data. Actually one could perform a series of toy simulations of the unfolding, and compare the average of the unfolding results with the result found previously. A significant difference between the two, in any region of the spectrum, would indicate a problem in the parameterization, which should be reconsidered. An increase of the fluctuation of the unfolding result in the toys with respect to the ones of the data, comparable or larger than the correction performed on new structures (i.e. by iterations if the first step is trivialized as before), would indicate the same kind of troubles. No such problems were observed in the previous example.

If the study described in the previous subsection, using global χ^2 comparison between the spectra, is not enough sensitive to the values of the unfolding parameters, one can always build toy models for the data (following 1.8.1) and perform the unfolding as explained before, in order to tune the method. One can use in the folding the matrix given by the MC, while a statistically fluctuated one will be used in this unfolding. The bias, used to get the data model, and the fluctuations in background subtraction, will be choosen such that the folded toy data are qualitatively close to the real ones. The local comparison of the unfolding result with the toy data model provides an excellent sensitivity to the parameters of the method. Once the method is tuned, the possible (small) remaining difference between the unfolding result and the data model can be used to estimate the systematic error of the method.

Among the functions listed in Eq. (1.5), (1.6) and (1.7), the ones with a null derivative at the origin seem to provide a better separation of fluctuations and real deviations. The small differences between the results obtained with the several (well suited) functions, as well as the ones related to some reasonable changes in the regularization parameter(s), can be used to estimate the corresponding systematic errors of the procedure. There is however at least a partial overlap between this estimation of the systematic error and the

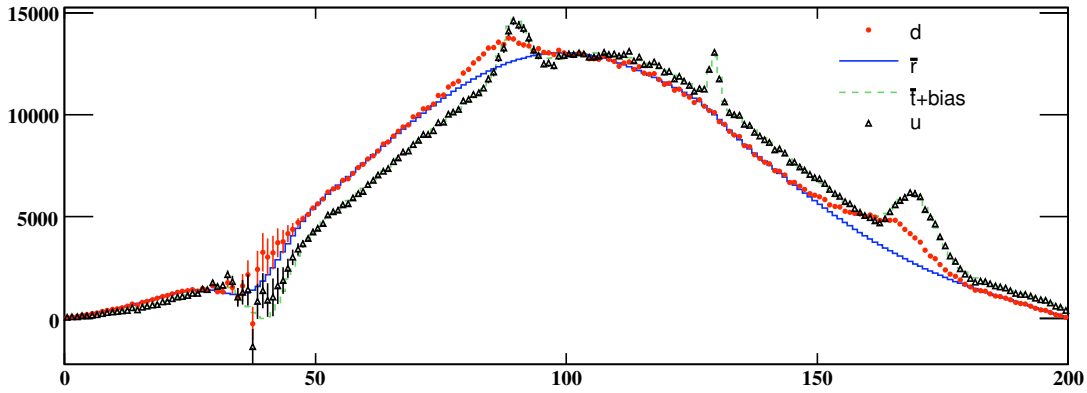

Figure 1.11: The unfolding result after 65 iterations (triangles), compared to the data distribution (filled circles), the reconstructed MC in the model (solid line) and the true MC model plus the bias (dashed line).

one proposed in the previous paragraph.

The systematic errors related to the unfolding are not only due to the procedure, but also to the knowledge of the folding matrix. The difference between data and MC at this level can be estimated in practice by detailed studies of events affected by effects that the unfolding procedure must correct. If the amount of some of these events is different in data and in the simulation, one can even correct the last one. This could also reduce the correction the unfolding has to bring at the level of the spectra. One can estimate the uncertainty on the transfer matrix coming from this (or yet another) kind of effects/corrections. Performing the unfolding with the transfer matrix modified within these uncertainties allows one to compute the systematic error associated to the final spectrum. There can indeed also be an overlap between this estimation of the systematic error due to the transfer matrix and the ones previously associated to the unfolding procedure.

We have seen that this unfolding method allows one to unfold structures having a width smaller than the detector resolution. However, these reconstructed structures are for sure affected by the fluctuations of the data bins where their events were initially situated, and by the precision of the knowledge of the transfer matrix. These two effects put a limit on the quality of the reconstructed structures.

The use of the regularization functions in this method imply non-linear effects in the passage from data to the unfolded spectrum. This is actually a general feature of the regularization methods used in the unfolding procedures. It can slightly affect the shape of the error distribution of the unfolded spectrum. In this example, this type of effect was observed mainly at the edges of the new structures introduced in data, where it is more difficult to distinguish between statistical fluctuations and real significant deviations.

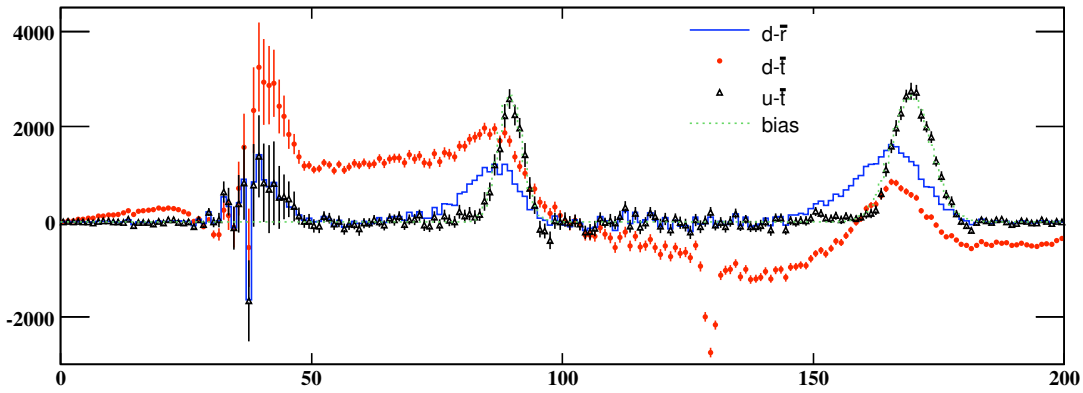

Figure 1.12: Unfolding result after 65 iterations minus the true MC model (triangles), data minus the true MC model (circles), data minus the reconstructed MC in the model (solid line), and bias (dotted line).

1.9 A simpler example

In this section we provide an example that could be closer to most applications of this method, namely when the effects of the folding and the data-MC differences are relatively small. We indicate how the method can be considerably simplified for this kind of application and how one can easily build a test (or a procedure to set the remaining parameter(s)) of the method.

1.9.1 Building the data spectra and transfer matrix

To build this second example we use the same procedure as the one described in subsection 1.8.1, but we bring important changes in the spectra and transfer matrix. In order to provide a rather low statistics test of the method, we reduce the global statistics of MC and data by a factor of about 20 (their relative ratio is equal to 10, like in the previous example).

Concerning the transfer matrix, besides this change, we remove the dip around the bin 40 in Eq. (1.12) and we reduce resolution effects by taking $\sigma = 1$. The effect of systematic transfers of events from high index bins to the lower ones is also reduced by putting $c_1 = 8$ and $c_2 = 2$, in Eq. (1.13).

The "bias" of the data model with respect to the true MC model is changed to a smaller and a smoother one:

$$bias_j = \frac{75}{\sqrt{2\pi}} \left[-e^{-\frac{(j-50)^2}{2\cdot 20^2}} + e^{-\frac{(j-140)^2}{2\cdot 20^2}} \right], \tag{1.16}$$

and we do not introduce any important fluctuations in background subtraction. The errors associated to the data points are simply the statistical ones.

1.9.2 A simplified version of the unfolding procedure

Given the fact that the complexity of this test is considerably reduced, with respect to the previous one, a simplified (next to trivial) version of the unfolding procedure allows one to perform the needed corrections.

First of all, as in this example there are no significant new structures in the data, the normalization procedure looses its sensitivity and does not indicate any possible improvement at this level. Indeed, one can see this by making a scan of the possible λ_N values with fluctuating data, as it was shown in the previous example. In the present case, the improvement limits interval contains the null value, for any value of the λ_N parameter. One can therefore drop this procedure here, for example by setting $\lambda_N = 0$ (i.e. by using the standard normalization).

The possibility of fixating fluctuations in background subtraction is also dropped here. In practice one can take this decision by comparing the size of the data point errors with respect to the available statistics, or equivalently using the errors introduced by the background subtraction itself. The possible effect of this simplification in the unfolding strategy can also be tested directly on data, as explained in the previous example.

We will finally use a simplified unfolding procedure using a first step with the initial transfer matrix and a parameter λ_L, and an iteration where the transfer matrix is improved and a new unfolding is performed. In this example, one iteration modifying the matrix is enough to correct the systematic data-reconstructed MC differences. The figure 1.13

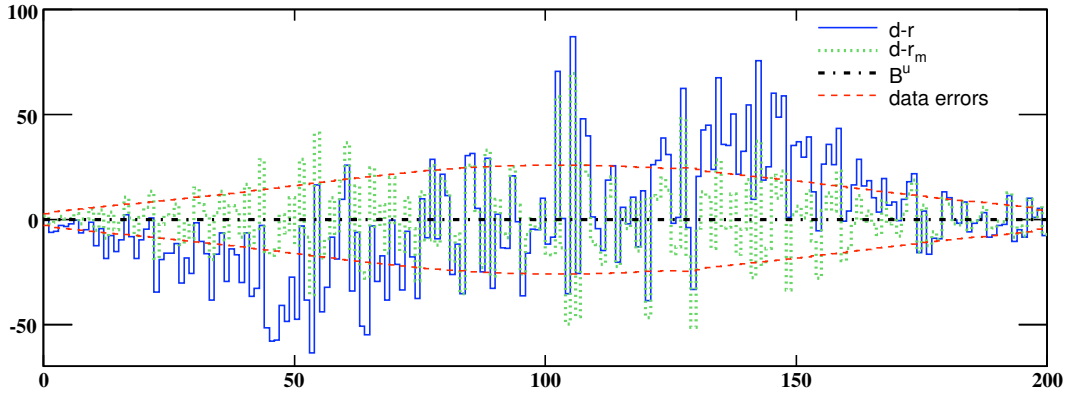

Figure 1.13: Data minus the original reconstructed MC (solid line), data minus the modified reconstructed MC (dotted line), estimate of the fluctuations from background subtraction (dashed-dotted line), null in this example and the data errors (dashed line).

indicates this difference before the unfolding, and after one iteration. For the example shown here we chosed $\lambda_L = 1.5$. Although this choice is not crucial for the effect shown in this figure, its motivation will become clear after the following studies. In order to measure the full potential systematic effect of this iteration, we set the corresponding

parameters: $\lambda_U = 0$ and $\lambda_M = 0$ (i.e. we perform the maximal change of the transfer matrix and the maximal unfolding correction afterwards).

1.9.3 Building a simple toy test of the unfolding procedure and its parameterization

We propose a direct test of the unfolding procedure and its parameterization, searching for potential systematic biases that could be introduced at this level. For this test we build a toy data model and toy reconstructed data, inspired directly by the original data spectrum and the MC simulation (which can be directly used in practice). The toy reconstructed data are then unfolded with a transfer matrix (A') obtained after a fluctuation of the initial one available in practice (A). Therefore, the MC for this test is identical to the one in the "real" unfolding, up to statistical fluctuations. We compare the result to the toy data model.

We define the true MC model ($\bar{t}$) as the normalized initial true MC (obtained from the matrix A, without any additional statistical fluctuations). Just as in the first example the reconstructed MC in the model ($\bar{r}$), is the result of the folding of the $\bar{t}$, using the transfer matrix A. It is identical to the reconstructed MC in the first unfolding step, up to statistical fluctuations between A and A'. As usual, we add a bias to the true MC model, in order to get the toy data model. In order to build a test as close as possible to the real situation, the bias is obtained from the difference between data and the normalized initial reconstructed MC, multiplied by a constant factor. The toy data model is then folded using the transfer matrix A. We define the toy reconstructed data as the result of this folding, with or without final statistical fluctuations. It is interesting to consider here these two variations of the test. The first one, where the data are fluctuated statistically, is closer to the real unfolding operation and tests the existence of potentially spurious effects due to the limited statistics in data (and MC). The second test, allows an easier search for potential systematic effects of the method, which one can look for in the difference between the unfolding result and the toy data model.

If the multiplicative factor, used to obtain the bias, equals one, the difference between data and reconstructed MC in the model in this test, is very close to the data - reconstructed MC difference in the real unfolding procedure (up to final statistical fluctuations (if any), transfer matrix fluctuations and smoothing folding effects) (see Fig. 1.14). We consider this factor equal to one in the following test (if not stated otherwise). Just as in the "real unfolding" (see Fig. 1.13) all the systematic effects in the data - reconstructed MC difference are corrected after the first iteration. A test as the one build here is well suited, provided the data-MC difference and the unfolding corrections are relatively small.

We measure the bias of the unfolding result with respect to the toy data model, after the first step and after one iteration. At this level one cannot observe any systematic bias after the first unfolding step, and the impact of the iteration is very small.

This study was performed for several sets of independently generated data. In practice, one could build several models starting from statistically fluctuated data samples. In order

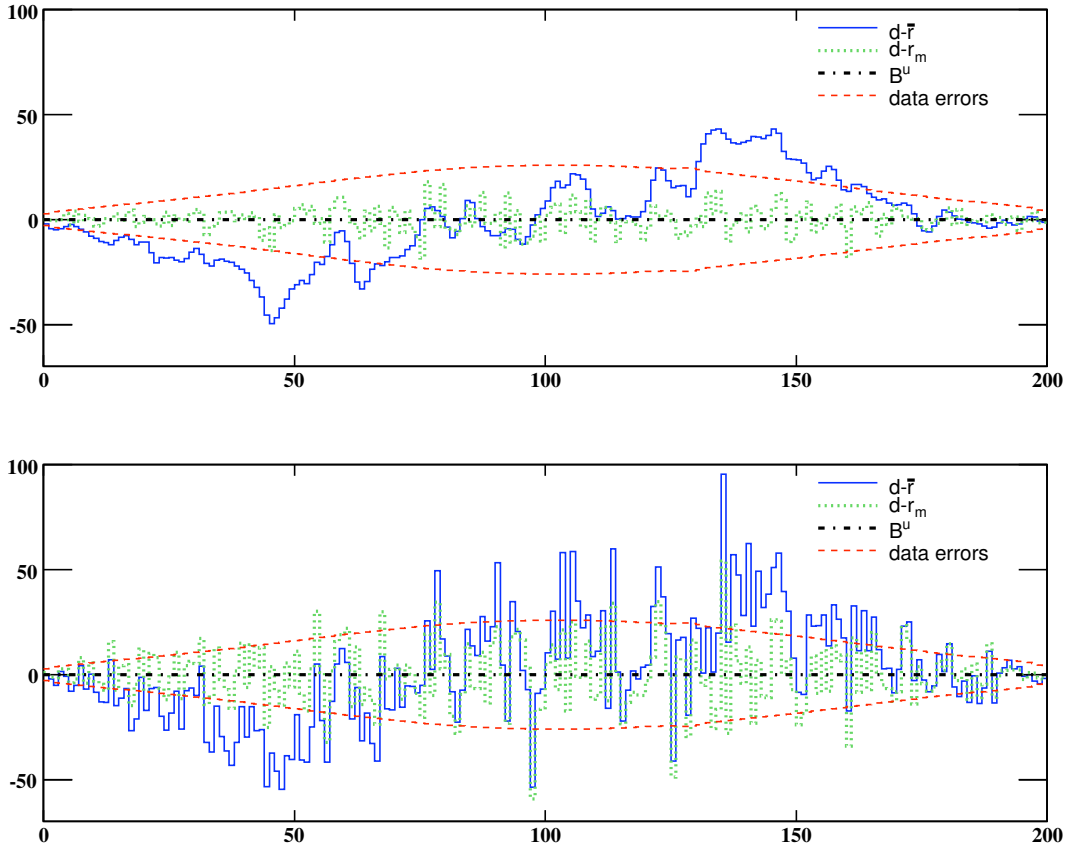

Figure 1.14: Data minus the reconstructed MC in the model (solid line), data minus the modified reconstructed MC (dotted line), estimate of the fluctuations from background subtraction (dashed-dotted line), null in this example and the data errors (dashed line). The upper plot corresponds to the case where no additional statistical fluctuations were added to the test data, while the data were fluctuated statistically for the example shown in the lower plot.

to measure the potential bias, we compute it in larger bins (each of which contains 40 initial bins). For λ_L values up to at least 1.5 we find maximal relative biases in the interval $[0.1; 0.5]\%$. This interval becomes $[0.2; 0.8]\%$ for $\lambda_L = 2$, $[0.3; 0.9]\%$ for $\lambda_L = 3$ and $[0.8; 1.6]\%$ for very large λ_L values (i.e. when no unfolding correction is done on the data-reconstructed MC difference).

This study shows that from the point of view of the potential bias remaining after the first unfolding step, the λ_L values up to 1.5 provide very comparable results. However, the larger the λ_L value, the less smoothing is done on the data, as the fraction of their fluctuations kept in their initial bin for the final spectrum is larger, and the bins of the final spectrum are less correlated.

This type of test could also be used to identify situations where the detector transfer matrix is (almost)singular. Such a situation would be encountered for example in the rather pathological situation of a detector with very bad resolution, in which case the data

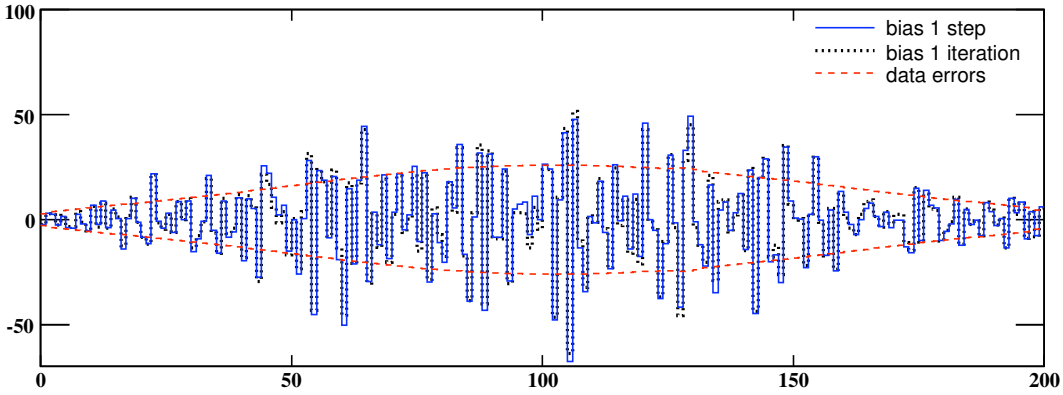

Figure 1.15: Remaining bias after the first unfolding step (solid line), after one iteration (dotted line), and the data errors (dashed line). This plot corresponds to the case where no additional statistical fluctuations were added to the test data, and the first unfolding was performed with $\lambda_L = 1.5$.

would be compatible with the reconstructed MC no matter what true MC distribution was used. Therefore, the unfolding result would also be compatible with any other true MC that is used to build the transfer matrix. It is at this point that the test described in this subsection comes into play. Using various toy data models for this test, one would assign a very large systematic error to the unfolding result, making it compatible with any spectrum preserving the number of events. This would of course indicate that the solution of the unfolding is not well defined.

1.9.4 Unfolding the data

Just as in the case of the previous test, for the "real" unfolding, the first step provides the main systematic correction, while the effect of the iteration is very small (see Fig. 1.16). The impact of the first iteration on the unfolding result can be seen as another measurement of the systematic error of the method. Just as in the case of the toy test, we measured this effect in larger bins (each of which contains 40 initial bins). We perform this study for several sets of independently generated data and transfer matrix. For λ_L values up to at least 1.5 we find an averaged maximal (over 5 large bins) improvement of the order of 0.1% with however important relative fluctuations between different data sets. When increassing λ_L, the potential improvement gets larger and more significant with respect to fluctuations. Its value is approximatively 0.2% for $\lambda_L = 2$, 0.5% for $\lambda_L = 3$, and 1.1% for very large λ_L values. This confirms the previous conclusion concerning this test, namely that for $\lambda_L \lessapprox 1.5$ the first unfolding step provides already a good result, while the iteration(s) could be useful for larger λ_L values.

As explained before, using a larger λ_L prevents the unfolding and smoothing of the data fluctuations, keeping the bins less correlated. This effect can be observed at the level

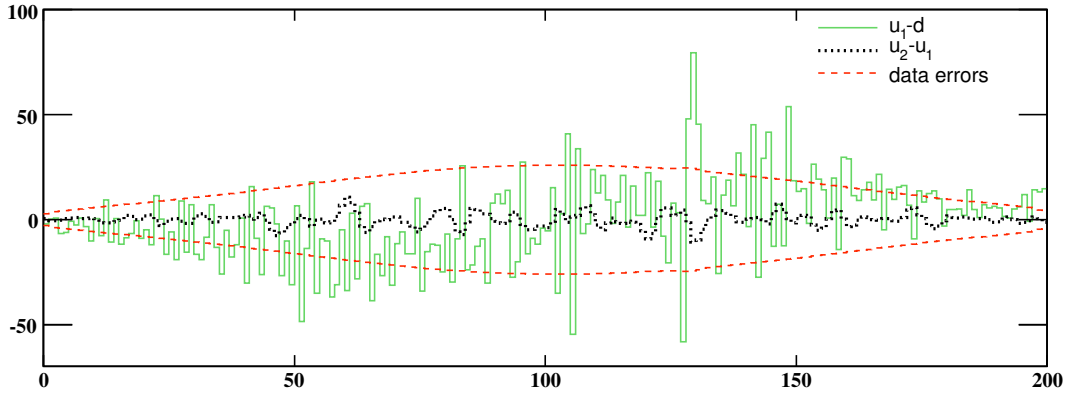

Figure 1.16: Correction bringed by the first unfolding step (solid line), correction bringed by one iteration (dotted line), and the data errors (dashed line). This plot corresponds to the case where the first unfolding was performed with $\lambda_L = 1.5$.

of the diagonal errors of the unfolding result, after one step (see Fig. 1.17). Indeed, the

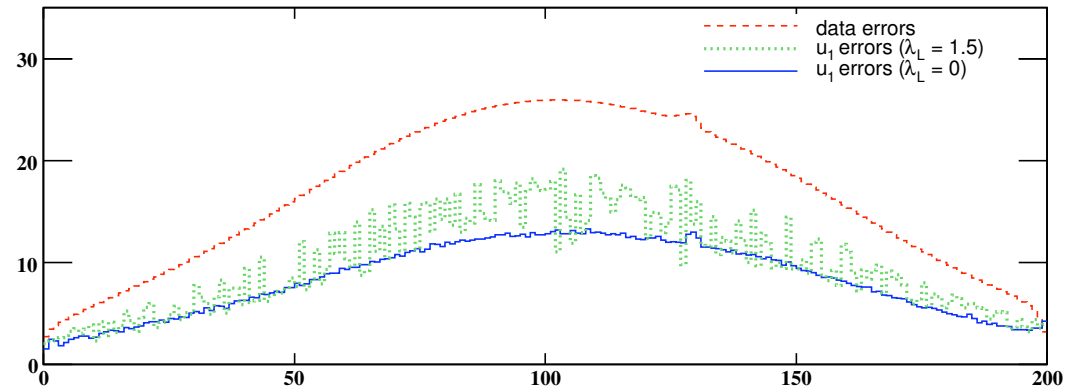

Figure 1.17: Diagonal errors after the first unfolding step for $\lambda_L = 1.5$ (dotted line), for $\lambda_L = 0$ (solid line), and the data errors (dashed line).

diagonal errors after the first unfolding step for $\lambda_L = 1.5$ are larger than the ones obtained for $\lambda_L = 0$, the two being smaller than the ones of the data, due to correlations.

If, after the unfolding, the bin-to-bin correlations enhanced by the transfers of events are too large for the further use of the spectrum, one could decide to compute this spectrum in less correlated, larger bins (if this would not imply a too large lost of information on the shape of the spectrum). This could be achieved through the use of a different (smaller) number of bins for the tMC distribution or by a rebinning operation after the unfolding.

All the functions listed in Eq. (1.5), (1.6) and (1.7) yield very similar results for the

unfolding in this example, although the suitable regularization parameters can be different for them.

1.10 Conclusions

In this chapter we introduced an unfolding procedure allowing one to deal with a series of problems that one can meet in practice, and which were not considered by the previous methods. Using a regularization function, one can consistently compare MC with data spectra, even when the last one contain structures which were not initially simulated. It is the same regularization function that allows one to unfold spectra containing important fluctuations from the background subtraction, without generating biases by the transfer of these events in other regions of the spectrum. Further more, one can dynamically avoid spurious fluctuations of the method when performing iterations to reconstruct structures that were not initially simulated. This method also allows the user to keep under control the bin-to-bin correlations of the final spectrum, while the needed systematic corrections are performed.

We have described a general unfolding strategy that can be used for rather complicated situations, where all the problems discussed before are present. A simplified strategy has been studied and it can be applied for more common problems. We have described the way one can build reliable toy tests inspired by data, which can provide a good parameterization of the procedure. We also propose some tests for the intermediate or final results of the procedure, to be performed directly when unfolding the data.

Statistical errors can be directly propagated in this method. We have proposed several ways of estimating the systematic effects associated to the method, as well as the ones dues to the poor knowledge of transfer matrix.

The C++ source code (relying on ROOT functionality) for the unfolding procedure (and the various described tests) can be obtained upon request from the author.

Several variations of the unfolding strategy and/or intermediate steps, besides the ones mentioned in the text, are possible. In the general strategy, one could for example simultaneously compute the estimate of the remaining fluctuations from background subtraction and improve the transfer matrix. This could be achieved by a straight-forward merging of the formulas 1.10 and 1.11, with the use of the same $\lambda_S = \lambda_M$ parameter. One could even place the events from the estimate of fluctuations from background subtraction on the diagonal of the transfer matrix. In this case, the corresponding events are not moved by the unfolding, just because they are "predicted" to be kept in place by the transfer matrix. Further on, at the different steps of the general unfolding strategy described in this chapter (or of its possible variations), one could use different functions or parameters, which would yield an even more general method.

Chapter 2

Measurement of the cross section for $e^+e^- \to K^+K^-(\gamma)$ with the ISR Method

2.1 Introduction

This study takes place in the context of a precision measurement of $R = \sigma(e^+e^- \to \text{hadrons})/\sigma(e^+e^- \to \mu^+\mu^-)$ at low energy using the ISR method, where an important hadronic channel above 1 GeV is K^+K^-. The precision required on the integrals involving R needed in the vacuum polarization calculations should be better than 1%, so that systematic uncertainties on R which are correlated over the relevant mass range have to be kept well below this level.

In this note we present a precision measurement of the $e^+e^- \to K^+K^-(\gamma)$ cross section, taking advantage of the previous detailed studies on triggers and filters [20], tracking [21], particle ID [22, 26, 27]. In these the studies the relevant efficiencies are measured on pure data samples using 2-body ISR processes, *i.e.* using the same environment as the physics samples and the correct data sampling. The ISR luminosity has been determined with a systematic uncertainty of 0.4%, essentially independent of mass, representing a gain of a factor 5 compared to the previous multihadron ISR analyses.

The R ratio is obtained in fact from the ratio of the measured $e^+e^- \to K^+K^-\gamma(\gamma)$ and $e^+e^- \to \mu^+\mu^-\gamma(\gamma)$ ISR cross sections. In this way several systematic uncertainties cancel. The measurement of the latter process has been presented in Ref. [28].

Alternatively, and this is the way we are going to proceed, one can view the $\mu\mu$ analysis as giving the effective ISR luminosity needed to obtain the KK cross section, while retaining all the advantages of measuring their ratio.

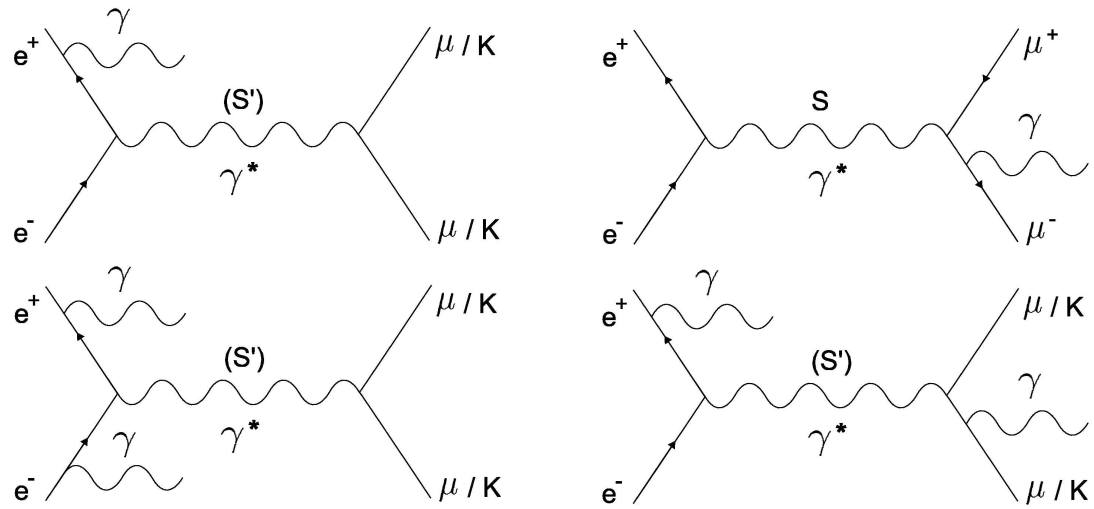

Figure 2.1: Feynman diagrams for the lowest order ISR processes $e^+e^- \to \gamma\gamma^* \to \gamma\mu^+\mu^-$ (γK^+K^-) (top left), lowest order FSR process $e^+e^- \to \gamma\mu^+\mu^-$ (top right), additional ISR processes (bottom left) and additional ISR processes (bottom right).

2.2 Principle of the Measurement: the ISR method

Previous measurements of the cross section $e^+e^- \to K^+K^-(\gamma)$ were done by energy scans, the collider energy (and hence the background conditions) being different for every measured point on the spectrum. The energy range was rather limited, for a given collider, and the results obtained with this method have 'point-to-point systematics' for data taken at different energy values.

During the last decade, the use of the Initial State Radiation (ISR) method [11] became possible, allowing the measurement of the $\sqrt{s'}$ spectrum, from relatively high masses, down to the threshold. Exploited in our annalysis, the ISR method is based on the measurement of the KK mass spectrum of the process $e^+e^- \to K^+K^-\gamma$ which proceeds in general through ISR and FSR lowest-order (LO) diagrams (see Fig. 2.1). However, unlike for the pointlike muon case, we expect the FSR K contribution to be very small because of the kaon structure and the subsequent smallness of the kaon form factor at $\sqrt{s} = 10.58$ GeV. Thus the $|FSR|^2$ contribution is negligible, while the interference between ISR and FSR amplitudes vanishes for a charge-symmetric acceptance. The spectrum statistics obtained by the ISR method is reduced by a factor α requiring hence a high luminosity, achieved at meson factories (ex.: B).

In order to control the overall efficiency to high precision, it was found necessary to include higher-order radiation in the event sample. In practice the next-to-leading-order is sufficient to reach accuracies of 10^{-3}, so the selection keeps $KK\gamma$ as well as $KK\gamma\gamma$ final states, where the additional photon can be either ISR or FSR. It should be noted that, since we are interested in the process $KK(\gamma)$ produced by ISR, the relevant final state mass is m_{KK} when there is no additional radiation or additional ISR, or $m_{KK\gamma_{FSR}}$ in the case of additional FSR. In all cases the main ISR photon is assumed to be the photon

with the highest energy in the e^+e^- center-of-mass.

From the observed m_{KK} distribution we obtain through unfolding the $\sqrt{s'} = m_{KK(\gamma)}$ (this mass does not include the ISR photon) spectrum of $KK\gamma(\gamma)$ events which is related to the physics quantities through

$$\frac{dN_{KK\gamma(\gamma)}}{d\sqrt{s'}} = \frac{dL^{eff}_{ISR}}{d\sqrt{s'}}\ \varepsilon_{KK\gamma}(\sqrt{s'})\ \sigma^0_{KK(\gamma)}(\sqrt{s'})\ , \tag{2.1}$$

where $\varepsilon_{KK\gamma}$ is the full acceptance for the event sample, determined by MC with corrections obtained from data, and $\sigma^0_{KK(\gamma)}$ is the bare cross section (excluding vacuum polarization) for the process $e^+e^- \to K^+K^-(\gamma)$ (including additional FSR photons).

The effective ISR luminosity function,

$$\frac{dL^{eff}_{ISR}}{d\sqrt{s'}} = L_{ee}\ \frac{dW}{d\sqrt{s'}}\ \left(\frac{\alpha(s')}{\alpha(0)}\right)^2\ \frac{\varepsilon_{ISR\gamma}(\sqrt{s'})}{\varepsilon^{MC}_{ISR\gamma}(\sqrt{s'})}\ , \tag{2.2}$$

takes into account the e^+e^- luminosity (L_{ee}), the probability to radiate an ISR photon (with possibly additional ISR photons) ($\frac{dW}{d\sqrt{s'}}$) so that the produced final state (excluding ISR photons) has a mass $\sqrt{s'}$, and the ratio of $\varepsilon_{ISR\gamma}$, the efficiency to detect the main ISR photon, to the same quantity, $\varepsilon^{MC}_{ISR\gamma}$, in simulation. The effective ISR luminosity function is measured from the obtained mass spectrum of $\mu\mu\gamma(\gamma)$ events following a relation analogous to Eq. (2.1), inserting for $\sigma^0_{\mu\mu(\gamma)}(\sqrt{s'})$ the cross section computed with QED. The results of this measurement are given in Ref. [28]. The radiator probability $\frac{dW}{d\sqrt{s'}}$ depends on the energy in the ee center-of-mass $\sqrt{s}$, $\sqrt{s'}$, and the angular range (θ^*_{min},θ^*_{max}) of the ISR photon in the ee center-of-mass. For convenience we use $\theta^*_{min} = 20^0$ and $\theta^*_{max} = 160^0$, comfortably bracketing the photon detection range. The term $(\alpha(s')/\alpha(0))^2$ is the vacuum polarization correction.

This way of proceeding amounts to taking the ratio $R_{exp}(\sqrt{s'})$ of the produced $KK\gamma(\gamma)$ and $\mu\mu\gamma(\gamma)$ events as a function of $\sqrt{s'}$:

$$R_{exp}(\sqrt{s'}) = \frac{\frac{dN^{prod}_{KK\gamma(\gamma)}}{d\sqrt{s'}}}{\frac{dN^{prod}_{\mu\mu\gamma(\gamma)}}{d\sqrt{s'}}} \tag{2.3}$$

$$= \frac{\sigma^0_{KK(\gamma)}(\sqrt{s'})}{(1+\delta^{\mu\mu}_{FSR})\sigma^0_{\mu\mu(\gamma)}(\sqrt{s'})} \tag{2.4}$$

$$= \frac{R^0(\sqrt{s'})}{(1+\delta^{\mu\mu}_{FSR})(1+\delta^{\mu\mu}_{add\ FSR})} \tag{2.5}$$

The bare (no vacuum polarization, but additional FSR included) R^0 follows the usual definition

$$R^0(\sqrt{s'}) = \frac{\sigma^0_{KK(\gamma)(\sqrt{s'})}}{\sigma_{pt}(\sqrt{s'})} \tag{2.6}$$

with $\sigma_{pt} = 4\pi\alpha^2/3s'$ is the cross section for pointlike charged fermions. The factors $(1+\delta^{\mu\mu}_{FSR})$ and $(1+\delta^{\mu\mu}_{add\ FSR})$ correct for the lowest-order $|FSR|^2$ contribution (including the possibility of additional ISR photons) in $ee \to \mu\mu\gamma$ and additional FSR in $ee \to \mu\mu$ processes. Since the lowest-order process for muons should be well described by QED calculations (even including additional ISR and FSR radiation), one can use the MC generator (AfkQed) to predict the relative amount of the remaining $|FSR|^2$ contribution (after integrating over the (almost) charge-symmetric acceptance) as a function of mass:

$$\delta^{\mu\mu}_{FSR} = \frac{|FSR|^2}{|ISR|^2} \ . \tag{2.7}$$

Many advantages follow from taking this ratio:

- the result is independent of the BABAR luminosity L_{ee};
- the ISR photon efficiency cancels out;
- the result is independent of the presence of additional ISR photons;
- vacuum polarization also cancels out;
- Monte Carlo simulation is used to compute the acceptance of the studied $X\gamma$ processes, with $X = KK(\gamma), \mu\mu(\gamma)$, and several systematic effects cancel in the ratio;
- the overall systematic uncertainty on the KK cross section is reduced, as some individual uncertainties cancels between the kaons and muons.

2.3 The BaBar Experiment

The BABAR detector collected data on events produced at the PEP-II storage ring, located at SLAC. Due to its high luminosity, and hence the large amount of produced B mesons, the PEP-II collider is also called B-factory. In this section we give a brief description of PEP-II and the BABAR detector. More details on these topics can be found in Ref. [12, 13].

2.3.1 The PEP-II Asymmetric Collider

The main components of the PEP-II facility are the linear accelerator (linac) and the e^+e^- storage rings (see Fig. 2.2). The electron beam is produced in the electron gun, accelerated by the electric field and injected into the linac, where they are accelerated with synchronized radio-frequency (RF) electromagnetic pulses. After reaching an energy of about 1 GeV, the electron beam is directed to a damping ring where its spatial and momentum spread are reduced, and then re-directed to the linac and accelerated to 8.9 GeV. Half of the generated electron bunches are accelerated to about 30 GeV, extracted from the linac and used to generate the positron beam by colision with a tungsten target. The

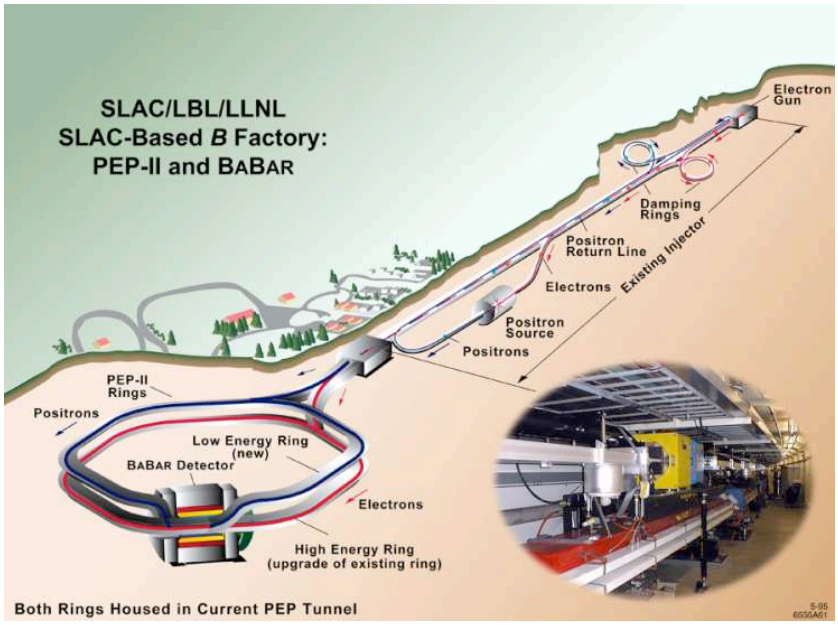

Figure 2.2: A schematic view of the B factory accelerator complex at SLAC.

positron bunches are sent to the source end of the linac, and then they are accelerated and shaped like the electron beam. Before the injection into the PEP-II storage rings, the positron beam reaches an energy of 3.1 GeV.

The beams circle in opposite directions in the two storage rings (the high energy ring for the electron beam and the low energy beam for the positron beam). They are further focused by a complex of magnets and accelerated by RF cavities to compensate the synchrotron-radiation losses. The beams collide head-on, at the interaction point, where the BABAR detector is located. The asymmetric collision occurs at a center-of-mass energy of 10.56 GeV, corresponding to the mass of the $\Upsilon(4S)$ resonance. The Lorentz boost of the final states with respect to the BABAR detector is $\beta\gamma = 0.56$. This boost was designed to make possible the experimental separation of the decay vertices of B mesons (which are very close in the CM frame, at the $\Upsilon(4S)$ mass), from which one can determine their relative decay length, and thus extract the time dependence of their decay rates.

The design luminosity of $3 \times 10^{33}\text{cm}^{-2}\text{s}^{-1}$ has been improved by a factor of four, a peak-luminosity record being achieved in August 2006. During the running period, from October 1999 to April 2008, PEP-II has delivered an integrated luminosity of 553.48 fb^{-1} and BABAR recorded 531.43 fb^{-1} (see Fig. 2.3), part of which has been used for this analysis.

2.3.2 The BABAR Detector

BABAR is a compact, multi-purpose detector. Its various components are shown in Fig. 2.4. We use a right-handed coordinate system which for the BABAR detector is

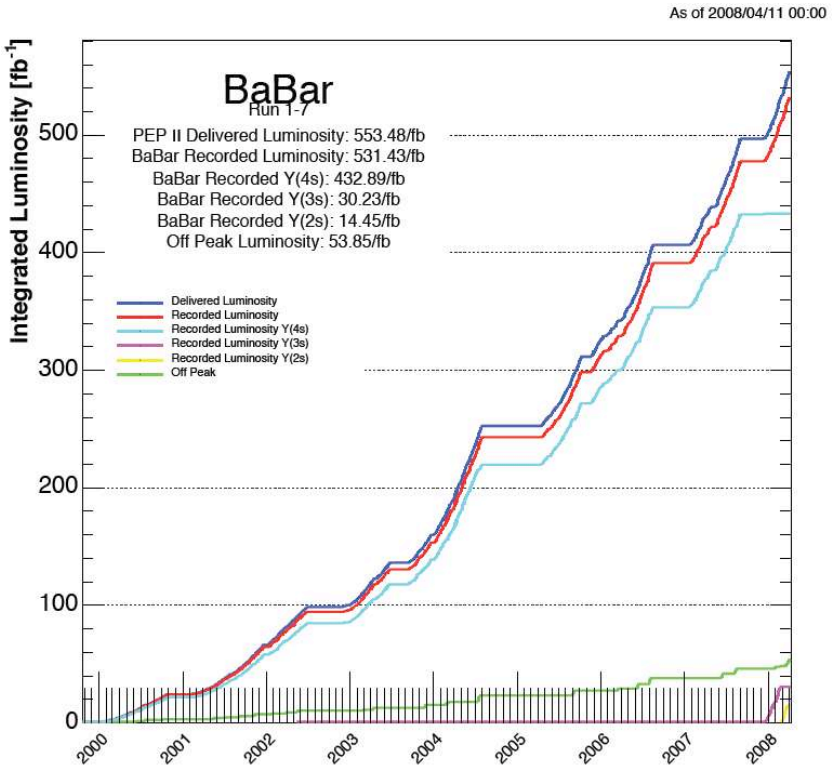

Figure 2.3: Integrated luminosities delivered by PEP-II and recorded by BABAR.

defined with its z-axis pointing in the running direction of the higher energy (electron) beam (with a small offset of about 20 mrad in the horizontal plane). This direction is also called "forward direction". The positive y-axis points upwards vertically, while the positive x-axis is horizontal, pointing away from the center of the PEP-II storage rings. The geometric center of the detector is offset with respect to the beam-beam interaction point (IP) by 37 cm in the running direction of the lower energy beam. This maximizes the geometric acceptance for the boosted $\Upsilon(4S)$ decays.

The inner detector consists of a silicon vertex tracker (SVT), a drift chamber (DCH), a ring-imaging Cherenkov detector (DIRC), and a CsI calorimeter (EMC). The principal axis of the drift chamber coincides with the z-axis of the coordinate system. These detector systems are surrounded by a superconducting solenoid, designed for a field of 1.5 T. The steel flux return is instrumented for muon and neutral hadron detection. The polar angle coverage extends to 350 mrad in the forward direction and 400 mrad in the backward direction.

In order to reduce the effects of multiple Coulomb scattering on tracks, special care has been taken to keep the material in the active volume of the detector to a minimum. The distribution of material "in front of" each detector system is shown in Fig. 2.5. Each curve indicates, in units of radiation lengths, the material that a high energy particle traverses before it reaches the first active element of a specific detector system. The next sections are dedicated to the description of each subsystem.

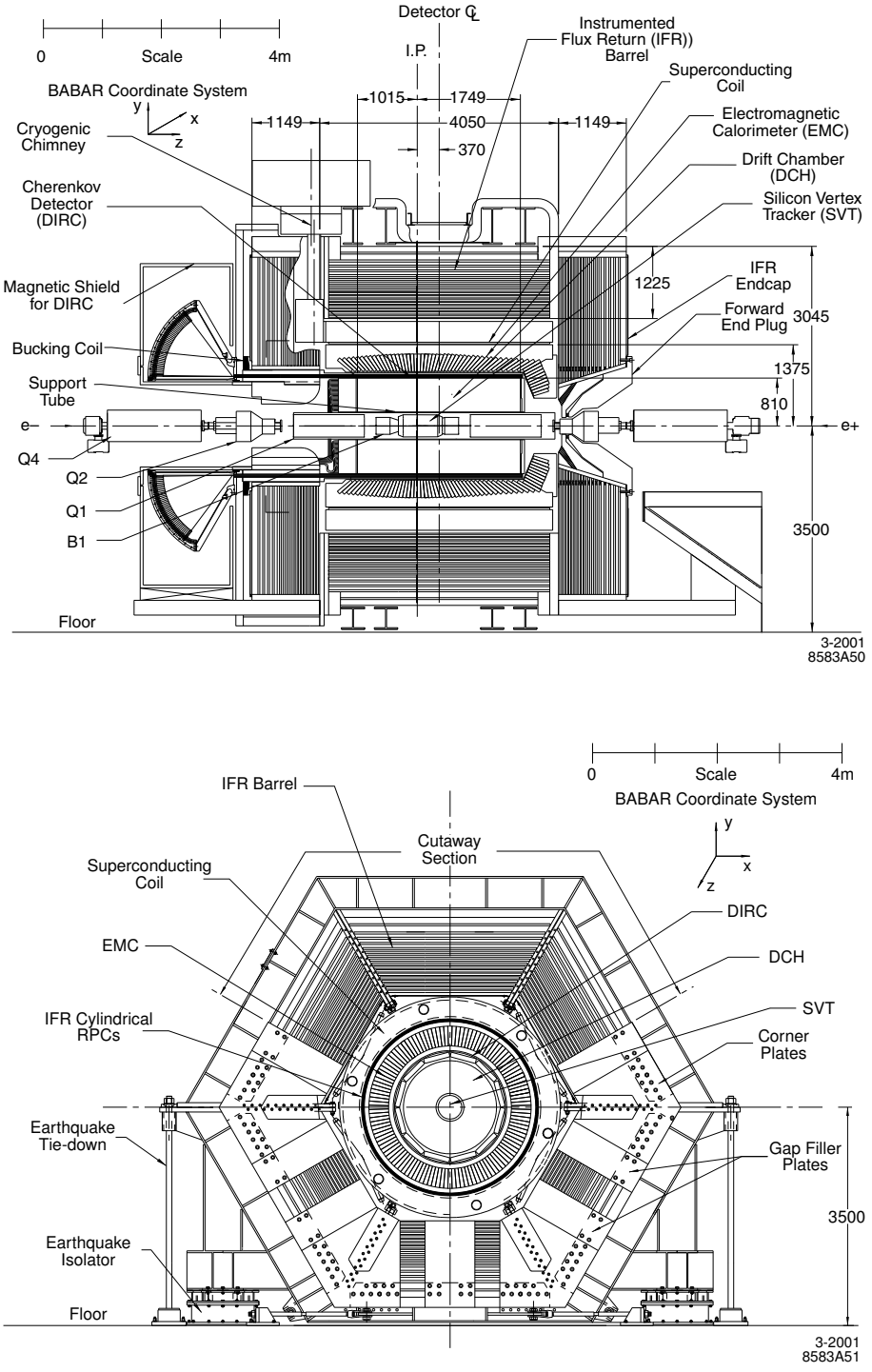

Figure 2.4: Longitudinal (top) and transverse (bottom) views of the BABAR detector.

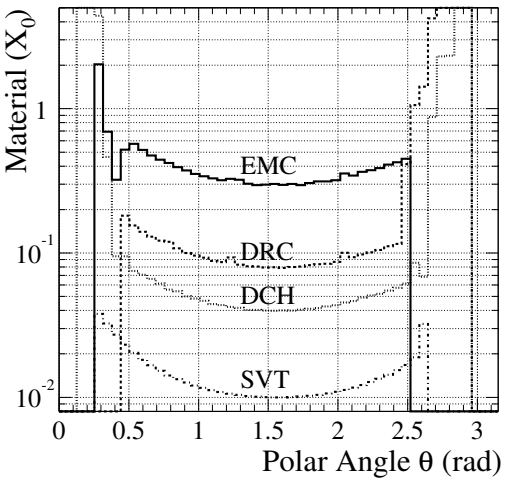

Figure 2.5: Amount of material (in units of interaction lengths) which a high energy particle, originating from the center of the coordinate system at a polar angle θ, traverses before it reaches the first active element of a specific detector system.

The Silicon Vertex Tracker

The silicon vertex tracker, together with the drift chamber, constitute the tracking system of the BABAR detector. They are designed to detect charged tracks and measure their vertices, momenta and dE/dx (used for charged particle identification) with high precision.

Fig. 2.6 shows a longitudinal and a transverse section of the SVT, which is optimized for the reconstruction of the primary and secondary vertices. It consists of five layers of double-sided silicon strip sensors, organized in 6, 6, 6, 16, and 18 modules respectively, covering 90% of the solid angle in the c.m. system. The strips on opposite sides of the sensors are oriented orthogonally to each other, allowing a simultaneous measurement of ϕ and z: the ϕ measuring strips run parallel to the beam, while the z measuring ones are oriented transversely to the beam axis. The modules of the inner three layers are straight, and the overlap between neighbour modules gives a full azimuthal coverage. They were placed as close as possible to the beam pipe, in order to minimize the influence from multiple scattering. The modules of layers 4 and 5 are arch-shaped, minimizing the amount of silicon used to satisfy the coverage angle and increasing the crossing angle for tracks near acceptance edges. Each of them has two sub-layers placed at slightly different radii, to avoid gaps and provide suitable overlaps in ϕ. They are mainly used to match tracks reconstructed by the SVT with the ones in the DCH.

The hit reconstruction efficiency for the SVT is about 97% and the spatial resolution of the hits is between 10 and 50 μm, depending on the orientation of the strip (ϕ or z) and the layer. The dE/dx resolution from ten measurements per track is about 14% .

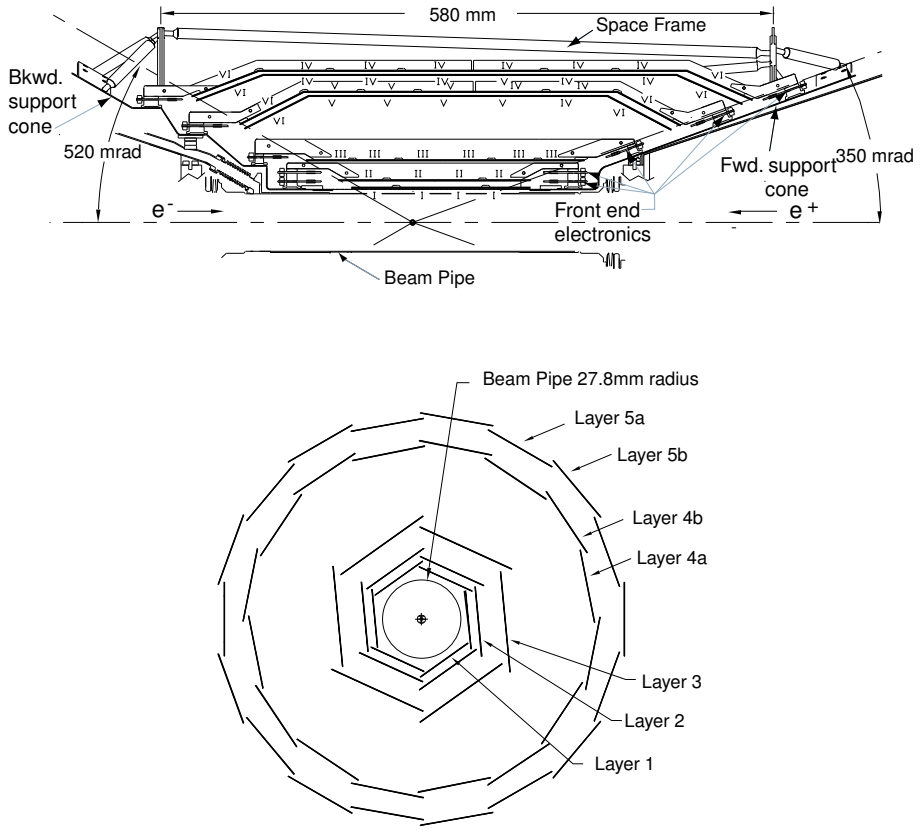

Figure 2.6: Longitudinal (top) and transverse (bottom) views of the SVT.

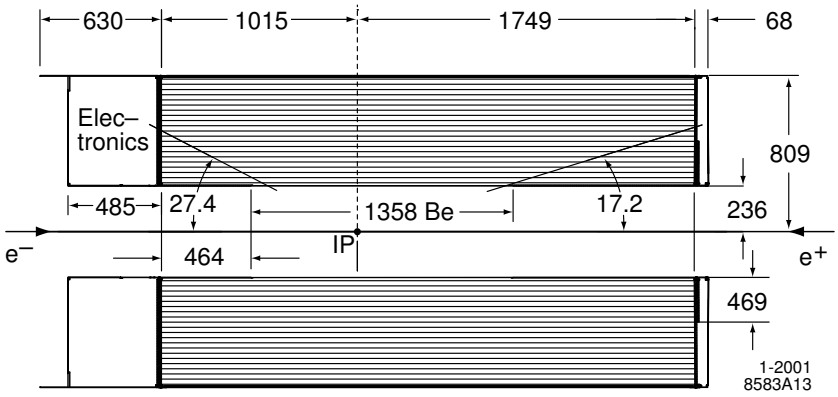

Figure 2.7: Longitudinal view of the DCH, with main dimensions.

The Drift Chamber

As we saw before, the multi-wire DCH is the second sub-detector of the tracking system. It is designed to measure momenta (from the curvature of the tracks in the 1.5 T solenoidal magnetic field) and dE/dx for the charged particles. It also allows the reconstruction of secondary vertices located outside the SVT.

The DCH is cylindrical, with a length of about 2.8 m, an inner radius of 23.6 cm and an outer radius of 80.9 cm (see Fig. 2.7). It consists of 7104 hexagonal cells, approximatelly 1.8 cm wide per 1.2 cm high, making 10 superlayers of 4 layers each (thus providing up to 40 position and ionization loss measurements per trajectory). In order to allow for position measurement in the z direction, six super layers are stereo layers with alternating tilts of $\pm(45 \approx 76)$ mrad. The other four super-layers are axial. Each cell consists of one sense wire (20 μm in diameter and operating typically at a voltage of 1960 V) surrounded by six field wires (120 μm in diameter and operating at ground potential). The DCH is filled with a 80 : 20 helium:isobutane gas mixture, providing an avalanche gain of about 5×10^4 at a typical operating voltage of 1960 V.

At the design voltage, the DCH tracking efficiency is about $98 \pm 1\%$ for tracks with momenta above 200 MeV/c and polar angles $\theta > 500$mrad (29°). While position and angle measurements near the IP are dominated by the SVT, the DCH contributes primarily to the p_T measurement with a relative resolution:

$$\frac{\sigma_{p_T}}{p_T} = (0.13 \pm 0.01)\% \cdot p_T + (0.45 \pm 0.03)\%, \tag{2.8}$$

where p_T is expressed in GeV/c. The first contribution, dominating at high momenta, comes from the curvature error due to finite spatial measurement resolution. The second one, dominating at low momenta, is due to multiple Coulomb scattering.

The angular resolution on the track direction can be parametrized as $\sigma_\phi = 0.43$ mrad and $\sigma_{\mathrm{cotan}\theta} = 0.53 \cdot 10^{-3}$.

The achieved resolution on the measurement of dE/dx is typically 7.5% (measured with Bhabha events). It is close to the expected resolution of 7%, and allows a 3σ K/π

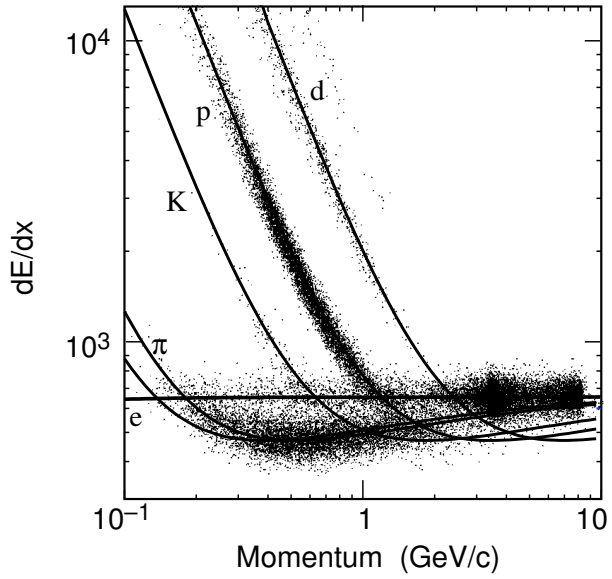

Figure 2.8: The specific energy loss, dE/dx, for charged particles, as a function of track momenta. The superimposed curves show the Bethe-Bloch predictions.

separation for momenta up to about 700 MeV/c. The measured dE/dx as a function of track momentum, for different charged particles, is shown in Fig. 2.8. For the tracks of high momenta, in the barrel region, the DIRC complements the PID capability, as we'll see in the next section.

The Cherenkov Detector

The Detector of Internally Reflected Cherenkov radiation (DIRC) is employed mainly for the separation of pions and kaons, from the pion Cherenkov threshold, up to about 4.2 GeV/c. As it was shown in Fig. 2.4, the DIRC radiator bars are placed in front of the EMC. In order to minimize the impact on the EMC measurements, the 144 DIRC bars are long, but thin and light. They are made of synthetic, fused silica, and arranged in a 12-sided polygonal barrel with 12 bars per side (see Fig. 2.9(a)). The radiator bars cover about 94% of the azimuthal angle and 83% of the polar angle in the CM frame. The DIRC photon detectors are placed at the backward end to minimize interference with other sub-detectors in the forward region. Mirrors are placed at the forward end of the radiator bars, to reflect incident photons to the backward end.

When a charged particle passes through the radiator, moving faster than light in the same medium, Cherenkow radiation is emitted at an angle θ_C with respect to the direction of the particle (see Fig. 2.9(b)). This angle is given by

$$\cos\theta_{\rm C} = \frac{1}{{\rm n}\beta}, \tag{2.9}$$

where n represents the mean refraction index of fused silica ($n = 1.473$), $\beta = v/c$, with v = velocity of the particle and c = speed of light in vacuum. The produced photons reflect

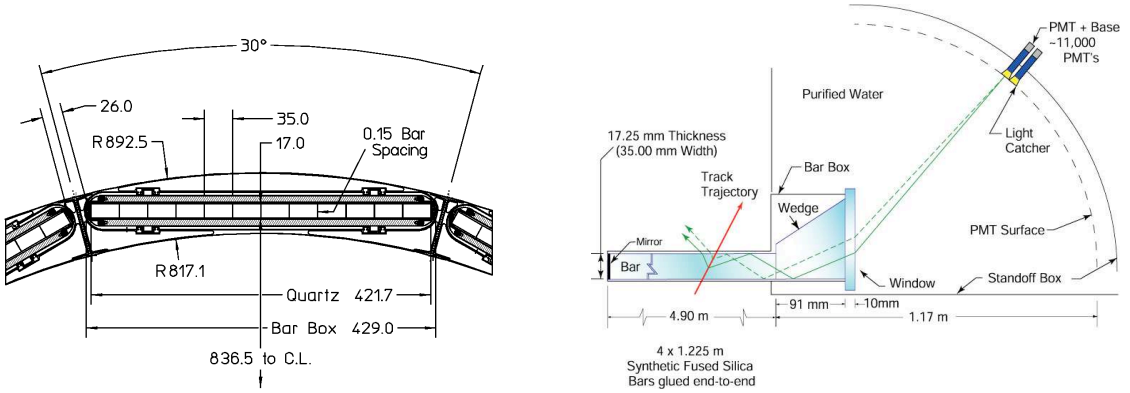

(a) Transverse section of the DIRC bar box, with main dimensions (mm).

(b) Schematic view of the DIRC fused silica radiator bar and imaging region.

Figure 2.9: The DIRC detector.

in the radiator bars being transported to their backward end, where they enter a standoff box filled with purified water (with $n = 1.346$ and are finally detected by the photo multiplier tubes (PMTs). The PMTs are arranged in 12 sectors of 896 phototubes each, placed at a distance of about 1.2 m from the bar end. They have a diameter of 29 mm and are surrounded by reflecting "light catcher" cones to capture light which would otherwise miss the PMT active area. The expected Cherenkov light pattern, at the surface where the PMTs are located, is essentially a conic section. The opening angle of the cone is the Cherenkov production angle, modified by refraction at the surface between water and the fused silica window. Knowing the location of the PMT that observes a Cherenkov photon and the charged particle direction from the traking system, the Cherenkov angle can be determined. The value of θ_C allows one to compute the speed of the particle. Knowing the momentum of the associated track (from the SVT and DCH), one computes the mass of the particle which is thus identified.

The time taken for the Cherenkov photons to travel from the place where they are emittend to the PMT is used to effectively supress hits from beam-generated background and from other tracks in the event. It also allows to resolve some ambiguities in the association between PMT hits and the charged track (for example, the forward-backward ambiguity between photons that have or have not been reflected by the mirror at the forward end of the bars).

The measured Cherenkov angles as a function of the track momenta, for different types of particles, are shown in Fig. 2.10(a). From Fig. 2.10(b) we see that the DIRC has a very good π/K separation: about 8σ at 2 GeV/c, more than 4σ at 3 GeV/c and about 2.5σ at 4.1 GeV/c.

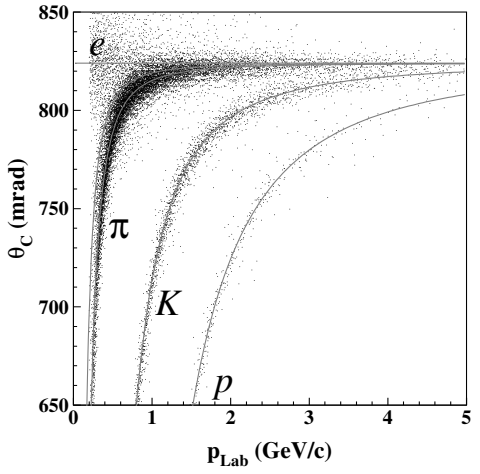

(a) The measured Cherenkov angle θ_C vs track momentum p_{Lab} for different charged particles.

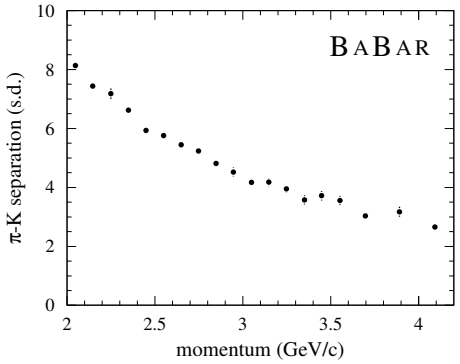

(b) The π/K separation in units of standard deviations.

Figure 2.10: The PID performance of the DIRC.

The Electromagnetic Calorimeter

The BABAR EMC was designed as an hermetic, total absorption calorimeter, in order to measure electromagnetic showers from photons and electrons (positrons) with excellent efficiency, and energy and angular resolution, over an energy range from 20 MeV to 9 GeV. It is composed of a finely segmented array of thallium-doped cesium iodide (CsI(Tl)) crystals (see Fig. 2.11(a)). They are read out with silicon photodiodes matched to the spectrum of scintillation light. The EMC consists of a cylindrical barrel of 48 rings with 120 identical crystals each, and a conical forward endcap of 8 rings with a total number of 820 crystals. It has a full coverage in azimuth, and a coverage from 15.8° to 141.8° in polar angle (see Fig. 2.11(b)). This corresponds to a solid angle coverage of 90% in the center-of-mass reference frame.

Typical electromagnetic showers spread over many adjacent crystals, forming a cluster of energy deposit. The energy deposit clusters are identified by the reconstruction algorithm. If they have a lateral shape consistent with the expected pattern from an electromagneric shower, they are identified as photons when they are not associated to any charged track extrapolated from the SVT and DCH. They are identified as electrons when they match to a charged track and the ratio between the measured energy E in the EMC and the momentum p measured by the tracking system is close to one ($E/p \approx 1$). The ratio E/p is actually the main variable for discriminating hadrons from electrons.

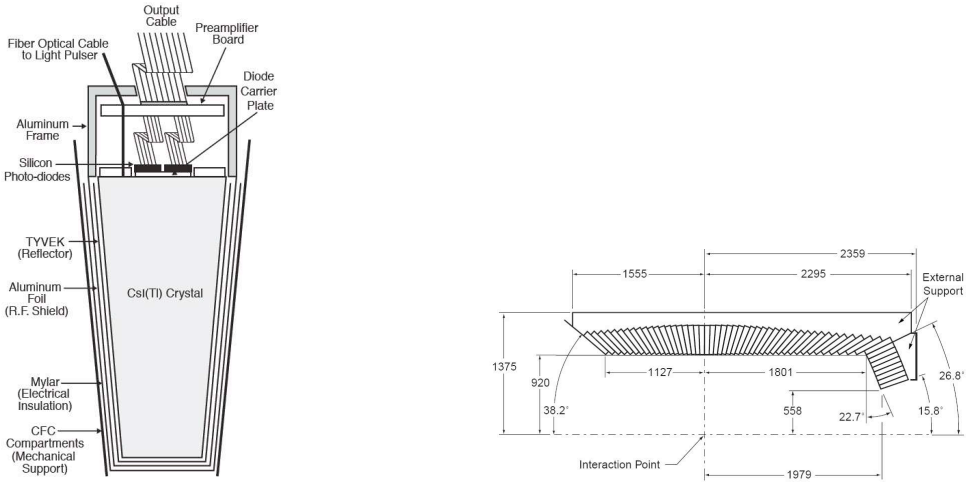

(a) A schematic view of an EMC crystal.

(b) Longitudinal section of the EMC.

Figure 2.11: The EMC detector.

The achieved energy and angular resolutions are given by

$$\frac{\sigma_E}{E} = \frac{2.32 \pm 0.30\%}{\sqrt[4]{E(GeV)}} \oplus (1.85 \pm 0.12)\%, \tag{2.10}$$

$$\sigma_{\theta,\phi} = \left(\frac{3.87 \pm 0.07}{\sqrt{E(GeV)}} \oplus 0.00 \pm 0.04 \right) \text{mrad}. \tag{2.11}$$

In both cases, the energy dependent term, dominant at low energy, arises mainly from fluctuations in the number of photons, but also from electronic noise of the photon detector and electronics. The constant term, dominant at high energies, is due to non-uniformity of light collection, leakage and or absorption in the material between and in front of the crystals, and calibration uncertainties.

The Instrumented Flux Return

The Instrumented Flux Return (IFR) is designed to identify muons with high efficiency and good purity, over a large solid angle, and to detect neutral hadrons (primarily K_L^0 and neutrons) over a wide range of momenta and angles with good resolution. The IFR uses the steel flux return of the magnet as muon filter and hadron absorber. Single gap resistive plate chambers (RPCs) are used as detectors.

A planar RPC consists of two 2 mm thick bakelite (phenolic polymer) sheets (see Fig. 2.12(a)), which have a large resistivity ($10^{11} - 10^{12} \Omega$ cm). The 2 mm gap between the two sheets is closed at the edge by a 7 mm wide frame and filled with a non-flammable gas mixture of 56.7% argon, 38.8% freon and 4.5% isobutane. The inside surfaces of the bakelite sheets are smoothed with a linseed-oil coating in order to obtain an uniform

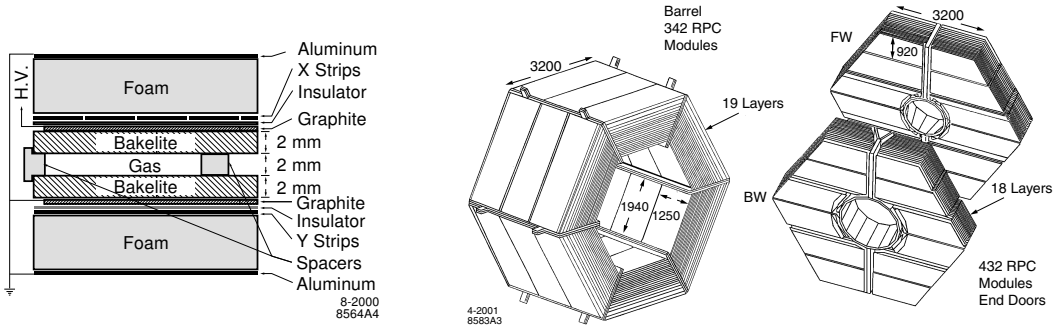

(a) A schematic view of an RPC.

(b) Overview of the IFR: barrel sectors and forward (FW) and backward (BW) end doors of the flux return.

Figure 2.12: The IFR detector.

electric field, thus preventing discharges in the gas and large dark currents. Their external surfaces are coated with graphite, connected to high voltage ($\sim$ 8 kV) and respectively to the ground, and protected by an insulating mylar film. Ionizing particles which cross the gap create streamers of ions and electrons in the gas, which in turn create signals via capacitive readout aluminium strips mounted on each side of the RPCs. The read out is done in two orthogonal directions.

The RPCs are installed in the finely segmented steel of the barrel and the end doors of the flux return (see Fig. 2.12(b)). There are 19 RPCs layers in the barrel, and 18 in the endcaps. Two extra layers of cylindrical RPCs are installed between the EMC and the magnet cryostat to detect particles exiting the EMC. The total active area covered by the IFR detectors is of about 2000 m^2.

Among the active RPC modules, 75% have a detection efficiency which exceeds 90%. If the clusters detected by the RPCs are within a predefined distance with respect to the predicted intersection of a charged track (extrapolated from the tracking system to the IFR) and the RPCs, then the cluster is associated to the track. The cluster not associated with a charged track are regarded as being due to neutral hadrons. The direction of neutral hadrons is determined from the event vertex and the centroid of the neutral cluster in the IFR.

The information from the IFR is almost the only one to identify muon tracks. A muon identification efficiency close to 90% has been achieved in the momentum range $1.5 < p < 3.0$ GeV/c, with a fake rate of pions of $6 \sim 8\%$ (see Fig. 2.13).

Soon after the beginning of the data taking with BABAR, some problems came out regarding the RPCs (more precisely with the linseed-oil used in their fabrication). This led a continuous significant reduction of the detection efficiency. The lost of muon ID capability was avoided by replacing the forward endcap with new improved RPCs (in 2002) and the replacement of the barrel with Limited Streamer Tubes (LSTs). The data used for the studies presented in the following were recorded before the installation of the

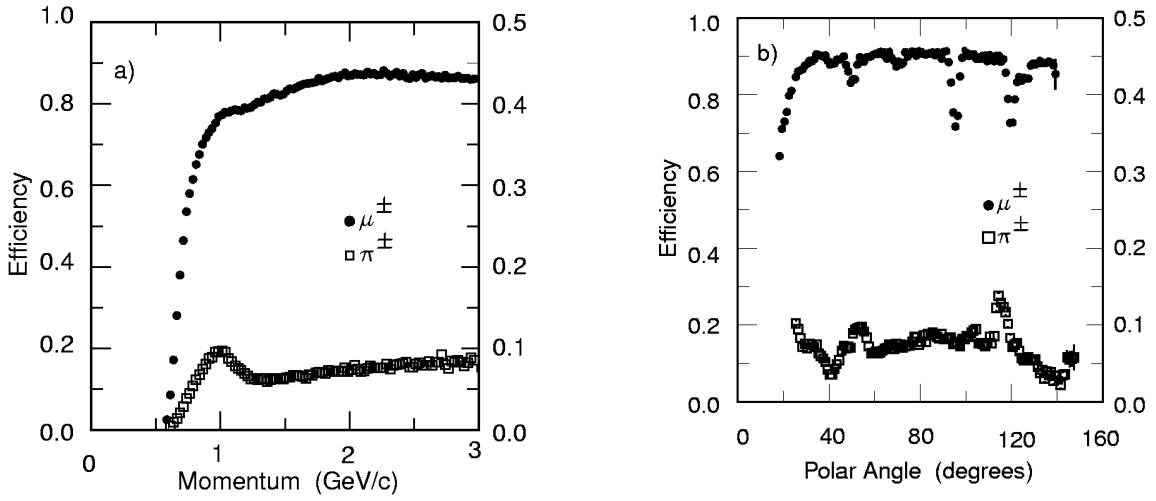

(a) (b)

Figure 2.13: Muon identification efficiency (left scale) and pion misidentification probability (right) as a function of (a) the laboratory track momentum, and (b) the polar angle (for $1.5 < p < 3.0$) GeV/c, obtained with loose selection criteria (defined in table 2.3).

LSTs.

2.3.3 The Trigger System

The trigger system is designed to select a large variety of physics processes, with a high, stable and well-understood efficiency, while keeping the output rate below 400 Hz to satisfy computing limitations of the offline processing farms. It is implemented in a two level hierarchy: the hardware Level 1 (L1) followed by the software Level 3 (L3).

The L1 trigger involves the OR of several conditions based on charged tracks in the DCH above a preset transverse momentum, showers in the EMC, and tracks detected in the IFR. These data are processed by three specialized hardware processors: the DCH trigger (DCT), the EMC trigger (EMT), and the IFR trigger (IFT). The resulting summary data on the position and energy of the particle are then processed by the global trigger (GLT), specific triggers are formed and sent to the Fast Control and Timing System (FCTS). If the FCTS gives a valid trigger, a L1 Accept is issued to initiate the event readout. The L1 trigger has an output rate of the order of 1 to 3 kHz, depending on luminosity and background conditions.

Based on both the complete event and the L1 trigger information, the L3 software algorithm refines the selection of events of interest, allowing them to be transfered to mass storage data for further analysis. It uses an algorithm based on the drift chamber tracking, which rejects beam-induced charged particles background produced in the material close to the IP, and a second algorithm based on calorimeter clustering. Based on the L3 tracks

and clusters, a variety of filters (BGFilters) perform events classification and background reduction. The data rate after the L3 is reduced to about 200 Hz.

2.4 Samples and Event Selection

2.4.1 Data and Monte Carlo samples

The analysis is based on the data collected by the BABAR detector, in runs 1 through 4. Run 2 is split into 3 parts (a, b, c), reflecting different operating performances of the IFR detector. Data in run 2c are actually removed from this analysis and the determination of R, because of the very poor IFR condition in this period. Measurements are performed separately for all runs, but are generally regrouped into runs 1-2 and runs 3-4 because of important differences in muon ID performances in these two periods. The data actually used correspond to a total integrated luminosity of 230.8 fb^{-1} (Table 2.1), known with an accuracy of 0.94% ([24], [25]).

Corresponding samples of fully simulated events have been generated with the AfkQED generator (based on Ref. [14]), with a statistics ~ 5 times larger than data for $\mu\mu\gamma(\gamma)$ and ~ 30 times for $KK\gamma(\gamma)$. AfkQed uses the LO QED matrix element, requiring the ISR photon polar angle in the center-of-mass to be in the range $20^\circ - 160^\circ$ (larger than the detector acceptance), and the energy in the e^+e^- center-of-mass (E^*_γ) to be larger than 3 GeV. Thus only $\mu\mu$ and KK masses less than about 7 GeV are available in the simulation, which however covers well the low mass region (below 5 GeV) we want to study. Additional radiation from the initial state is generated with the structure function method in the collinear approximation (there is no large angle additional ISR in AfkQed), while additional final state photons are generated with the PHOTOS package [16]. Another cut $m_{x^+x^-\gamma_{ISR}(\gamma_{addFSR})} > 8$ GeV was applied at the generation level, producing a lack of second hard photon radiation, unlike data.

Large samples of MC events at the quadrivector level were produced using the nearly exact NLO generator Phokhara [17,18]. Phokhara uses the NLO QED matrix element, but events with two final state photons are not generated. This should not be a limitation at energies O(1 GeV) since LO FSR is only at the 1 % level in the $\mu\mu$ cross section. It could be a more significant issue at 3-5 GeV energies where FSR becomes more important. The same cuts as for AfkQED are applied on the ISR photon, but there is no cut on $m_{x^+x^-\gamma_{ISR}(\gamma_{addFSR})}$.

2.4.2 ISR event selection

In the final state of $e^+e^- \to K^+K^-\gamma(\gamma)$, there are two charged tracks and one hard photon. One can also have additional ISR or FSR photons. The following event selection criteria are used to filter events with a hard photon detected at large angle (which will allow the measurement of the cross section on the full range of interest, from threshold to

Table 2.1: Summary of luminosities (fb^{-1}) for all data sets. The splitting of run 2 into (a, b, c) parts is made necessary because of different IFR conditions. Data from run 2c are not used in this analysis.

	On peak	Off peak	Total
run 1 (9932-17106)	20.46	2.62	23.07
run 2a (18184-25797)	36.65	4.67	41.32
run 2b (26222-29435)	20.31	2.22	22.52
run 2c (25804-26080)	1.32	0.0	1.32
run 3 (32955-39320)	31.09	2.40	33.49
run 4 (40055-50635)	100.34	10.06	110.41
Sum			232.14

high masses) and to reduce backgrounds dominated by radiative Bhabha events:

- any L1 and L3 trigger fired and BGFilter satisfied;
- 2 and only 2 'good' tracks identified as kaons, and in the DIRC active areas;
- ISR photon within the angular range [0.35;2.40] rad and with a CM energy higher than 3 GeV.

'Good' tracks must satisfy the following requirements:

- within the angular range [0.40;2.45] rad;
- $doca_{xy}$ <0.5 cm, where $doca_{xy}$ is the distance of closest approach to the beam axis in the xy plane;
- distance to the center of the beam spot along the z axis smaller than 6 cm;
- momentum of the track higher than 1GeV/c (in order to have a good μ-ID);
- number of drift chamber hits used in the track reconstruction ≥15;
- electron veto $((E_{cal}/p - 1)/0.15)^2 + ((dE/dx_{DCH} - 690)/150)^2 < 1$, where E_{cal} is the energy deposit in the calorimeter, associated to the track.

A pre-selection of ISR candidates was done in order to make relevant analyses more efficient. In pre-selection, a track definition ('standard' track) with more relaxed criteria is used: $doca_{xy}$ <2.5 cm, no cut on the number of DCH hits and momentum only limited by $p_T > 0.1$GeV/c.

All types of ISR events are pre-selected requiring an OR of four conditions:

- even number of standard tracks (with zero total charge) and angle between the missing momentum vector (excluding the highest energy photon in the e^+e^- center-of-mass, called ISR photon, as well as the extra detected photons) and the ISR photon less than 0.3 rad (in the lab frame);

- even number of standard tracks (with zero total charge) and angle between the missing momentum vector (excluding the highest energy photon in the e^+e^- center-of-mass, called ISR photon; but including the extra detected photons) and the ISR photon less than 0.3 rad (in the lab frame);

- any odd number of standard tracks (for efficiency purposes);

- number of K^0_S candidates (2 tracks with a secondary vertex and mass in a window around K^0_S mass) larger than 1.

2.4.3 Establishing the best kaon identification for this analysis

A complete and mutually-exclusive set of ID classes of charged particles (as they were used in [29]) was initially defined in view of this study (see Table 2.2). They included muons, pions, kaons and electrons. Protons (antiprotons) are not considered in the particle hypotheses since the $p\overline{p}\gamma$ final state occurs only at a very small rate, requiring a dedicated analysis already performed in BABAR [30], and is subtracted statistically. Apart from the identification of physical particle types, the $'0'$ ID type is assigned when the number of photons in the DIRC is not sufficient to define a Cherenkov ring, thus preventing π-K separation.

The completeness is necessary for $\pi\pi/\mu\mu$ analysis: since no positive identification can be established for pions, the cut-based μ-ID selection (Table 2.3) is the primary tool. For KK the situation is different as kaons can be positively identified in the DIRC. Thus μ background is less severe as for pions and the muon veto can be consequently relaxed. This is the object of the study below.

In addition to the E_{cal}, the following variables are used in muon identification [23] :
1. The number of IFR hit layers in a cluster (N_L).
2. The number of interaction lengths traversed by the track in the IFR (λ). It is estimated with the use of the track extrapolation into the IFR until the last hit layer.
3. The number of interaction lengths which the track is expected to traverse in the IFR in the muon hypothesis (λ_{exp}). It is estimated with the use of the track extrapolation into the IFR until the last active layer.
4. The $\chi^2/d.o.f.$ of the IFR hit strips in the cluster with respect to the track extrapolation (χ^2_{trk}).
5. The $\chi^2/d.o.f.$ of the IFR hit strips with respect to a 3-rd order polynomial fit of the cluster (χ^2_{fit}).
6. The average multiplicity of hit strips per layer (m) and its standard deviation (σ_m).
7. A variable T_c, which reflects the distribution of IFR hits along the track.

Using the previously introduced variables, we define: $\delta\lambda = \lambda_{exp} - \lambda$. The cuts corresponding to the various muon definitions can be found in Table 2.3.

The kaon identification relies in particular on a likelihood-based selector (K_{selector}). A Likelihood is computed for each particle hypothesis. It is defined as the product of the corresponding Likelihoods for dE/dx in the driftchamber (DCH) and the silicon vertex tracker (SVT), and Cherenkov angle in the DIRC. The DCH and SVT Likelihoods are computed comparing the measured dE/dx to the prediction from the Bethe-Bloch parametrisation. Gaussian PDFs are used to compute these two Likelihoods, the errors being bifurcated for the SVT. For the DIRC, a binned Likelihood is used. It is designed to treat well the tails in the DIRC response, especially at particle thresholds. This binned Likelihood is multiplied by a Gaussian DIRC angle Likelihood for momentum larger than 1.5GeV/c. This is meant to improve the DIRC angle bands separation.
Finally, the Likelihood selectors consist of different cuts on the relevant Likelihood ratios. In particular, for the "kaon tight" selector, which is used here, we have: $(L_K/(L_K + L_\pi) > 0.9)$ AND $(L_K/(L_K + L_P) > 0.2)$.

Five possible kaon identifications are tested for this analysis, an optimization being done for the signal and the amount of background from muons. We abandon the completeness of particle ID classes, in order to increase efficiency. The difference between the five definitions comes essentially from the muon ID, used in the veto of the corresponding background. In the five kaon identifications studied here, in addition to the common selection criteria listed in the previous section, we apply for the two tracks the cuts on E_{cal}/p and N_{DIRC} in Table 2.2, we ask a kaon tight Likelihood, plus the cuts in Table 2.4. Actually, the first kaon definition in this table ($K - ID = 1$) corresponds to the one that was given in Table 2.2.

For the tests of the possible choice of the K-definition, we consider events with a very tight cut on the χ^2 of the kinematic fits ($(\chi^2_{addISR})^2 + (\chi^2_{addFSR})^2 < 30^2$, as they will be defined in Sec. 2.8) and also events with no additional photon detected. Actually, it is from this region of the χ^2 plane that we get most of our signal, as well as most of the background from $\mu\mu$ events. This background can be important essentially in the high mass region, where the kaon form factor drops.

As expected, with the $K - ID = 2$ we get higher statistics than with the first one, but there is also more background from muons (see Fig. 2.14). For the 4^{th} and 5^{th} definitions we get statistics which are very similar to the one we had with the 2^{nd} definition, but the background from muons is much smaller. The 3^{rd} definition has still too small statistics to be acceptable. The same hierarchy of statistics is observed on the data. However, we should emphasize that, as the χ^2 cut will be different in the final analysis, the absolute number of events in these plots is not final. Only their relative values for different possible definitions matter here in order to choose the best K-ID.

After a comparison of the amounts of muon noise we get for the 4^{th} and 5^{th} definitions (slightly larger in the latter), we decided to keep the kaon definition number 4, for the analysis. By doing this, we strongly improve statistics with respect to what we would get using the kaon definition in Table 2.2.

Table 2.2: Generic definition of particle ID types (first column) using combinations of experimental conditions (first row): "+" means "condition satisfied", "−" means "condition not satisfied", an empty box means "condition not applied". The conditions μ_{selector} and K_{selector} correspond to the cut-based "muon loose" and likelihood-based "kaon tight" flags, respectively (see text). This K_{selector} identification is included in all the kaon definitions studied in the folowing (see text). The variable E_{cal} corresponds to the energy deposit in the EMC associated to the track. Two cuts requiring the track to extrapolate to an IFR active area and to a DIRC active area (excluding cracks between modules and bad efficiency areas) are implicitly applied in all the definitions.

	μ_{selector}	$E_{cal}/p > 0.8$	$N_{DIRC} \leq 2$	K_{selector}
'μ'	+			
'e'	−	+		
'0'	−	−	+	
'K'	−	−	−	+
'π'	−	−	−	−

Table 2.3: Definition of μ ID classes according to Ref. [23].

	Loose	Tight	Very Tight
Ecal (GeV)	< 0.5	$(0.05, 0.4)$	$(0.05, 0.4)$
N_L	≥ 2	≥ 2	≥ 2
$\delta\lambda$	< 2.0	< 1	< 0.8
λ	> 2	> 2.2	> 2.2
T_C	> 0.2	> 0.3	> 0.34
m	< 10	< 8	< 8
σ_m	< 6	< 4	< 4
χ^2_{trk}	< 7	< 5	< 5
χ^2_{fit}	< 4	< 3	< 3

Table 2.4: Possible kaon ID definitions for this analysis. In the first row, "−" means "condition not applied". The IFR active area cut excludes cracks between modules and bad efficiency areas. In the second row, "+" means "condition satisfied", "−" means "condition not satisfied". A similar cut for the DIRC active areas is applied in all the definitions.

K-ID	μ-ID veto	IFR active area cut
1	loose	+
2	−	−
3	loose	−
4	tight	−
5	very tight	−

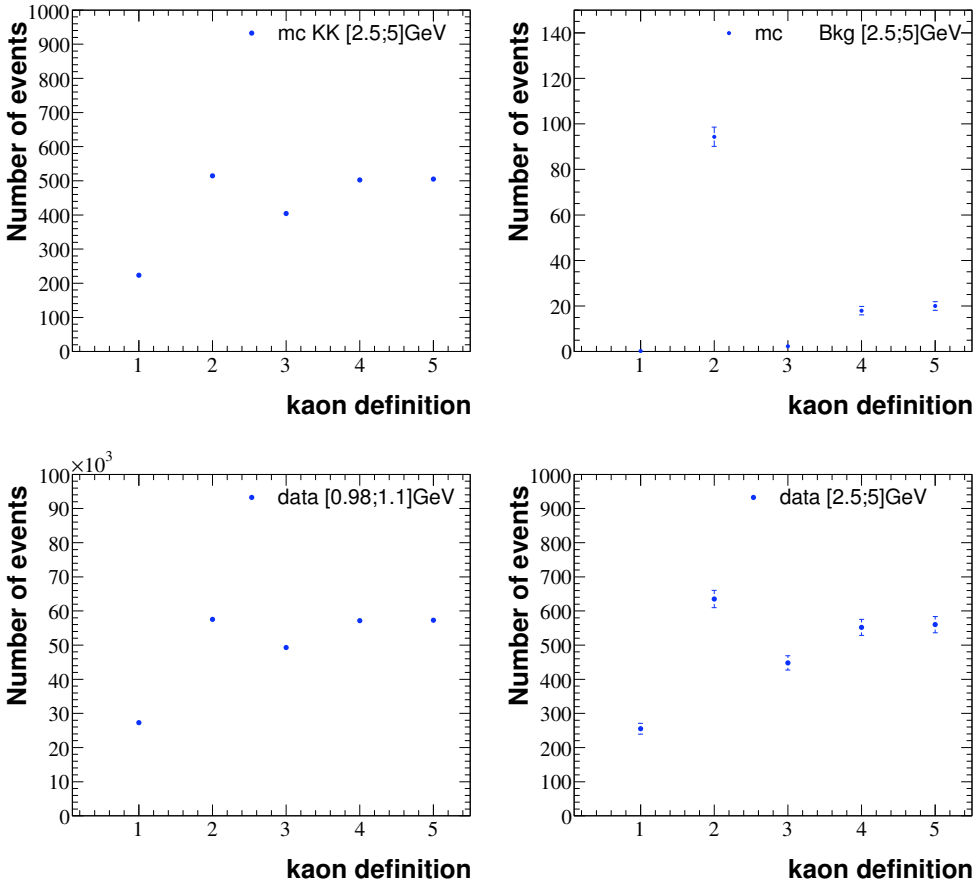

Figure 2.14: Top: number of events in the MC signal (left), and μ background (right) normalized to the luminosity, in the [2.5;5] GeV mass interval, for the five possible kaon definitions. Bottom: number of events in the data, in the [0.98;1](left) and [2.5;5](right) GeV mass intervals, for the five possible kaon definitions.

2.4.4 Data-MC corrections for detector simulation

The analysis uses as a starting point the Monte Carlo simulation for acceptance, χ^2 cut efficiency of the kinematic fit, trigger, tracking and particle ID. Through specific studies we have determined the ratios of efficiencies obtained in data and simulation, and apply them as corrections to the Monte Carlo global efficiency. Thus, the corrected acceptance is

$$\varepsilon = \varepsilon_{\rm MC} \left(\frac{\varepsilon^{\rm data}_{trigger}}{\varepsilon^{\rm MC}_{trigger}}\right) \left(\frac{\varepsilon^{\rm data}_{tracking}}{\varepsilon^{\rm MC}_{tracking}}\right) \left(\frac{\varepsilon^{\rm data}_{PID}}{\varepsilon^{\rm MC}_{PID}}\right) \left(\frac{\varepsilon^{\rm data}_{\chi^2}}{\varepsilon^{\rm MC}_{\chi^2}}\right) . \tag{2.12}$$

These corrections are reviewed in turn in the next sections. More data/MC corrections are needed for the geometrical acceptance, due to approximations made at the level of MC generators. Actually, most of the work for this analysis went into the computation of these corrections. Care was taken to avoid correlations between efficiency determinations and corrections. This is especially important for trigger and tracking, where the efficiency loss has the same physical origin, as we will see in the following. It is for this reason that the trigger efficiency is measured on a sample with no cut on the number of tracks, and tracking efficiency is measured for events which passed the trigger cuts.

2.5 Trigger and Filter Efficiencies

2.5.1 General method

No specific trigger configuration is required at analysis level, except that the OR of all lines at a given trigger level is set. Since individual trigger and filter line responses are stored for every event, efficiencies are computed by crossing the response of trigger lines, after choosing lines as orthogonal and as efficient as possible. Trigger efficiencies are determined on data and simulation samples, after applying identical event selections and measurement methods, and data/MC corrections are computed from the comparison of measured efficiencies.

The method has been applied to the measurement of L1, L3, and BGFilter efficiencies. The difficulty in this study is that trigger efficiencies have to be determined for a sample unbiased with respect to the number of tracks actually reconstructed. In practice, one and two-track samples are sufficient.

Because of the loose requirement with respect to tracking, the samples contain a large non-$KK\gamma$ background. In addition, backgrounds have different trigger efficiencies than the signal, hence have to be carefully studied and subtracted out. Background is subtracted from data using MC, after proper normalization, and if necessary, data-MC correction of the efficiencies in an iterative procedure.

The measurement bias has been controlled directly on data using the downscaled

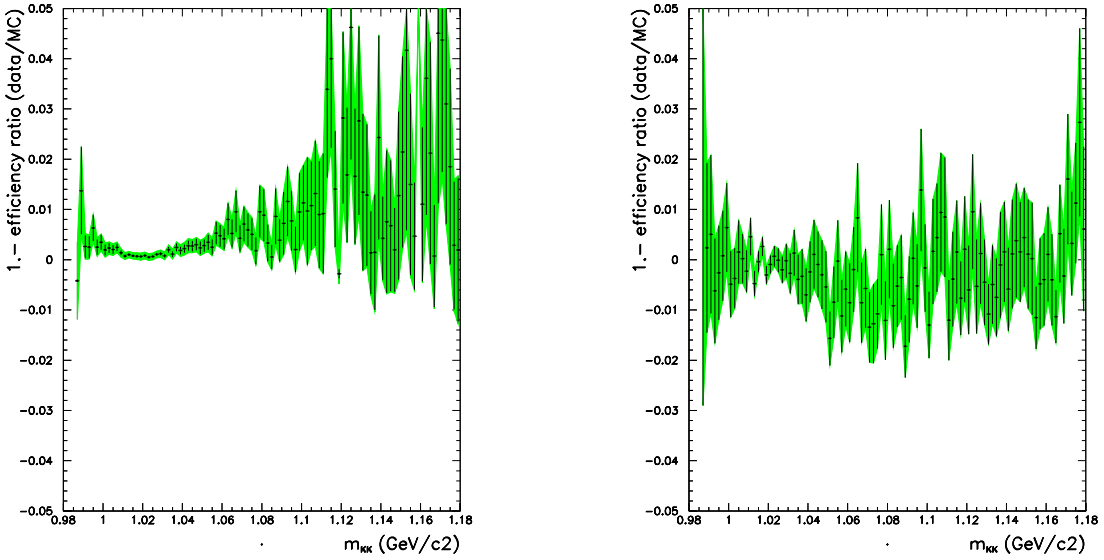

Figure 2.15: $1 - \frac{\epsilon^{trig}_{data}}{\epsilon^{trig}_{MC}}$ corrections for the BGFilter (left) and L3 (right) efficiencies.

events, and on simulation by comparison of the measured efficiencies to the true ones. Correlations between line responses have indeed been found, that induce biases in the measured efficiencies. The physics origin of the correlations has been carefully studied to ascertain that they do not induce data-MC discrepancies beyond the differences observed between the measured efficiencies. Once the origin of the bias has been identified, an indirect assesment of the data/MC consistency is performed. It was demonstrated that most trigger inefficiencies are directly related to track overlap in the DCH and/or EMC and/or IFR (see Fig. 2.16). We will come back to the DCH overlap problem in the tracking studies. For all details, see Ref. [20].

2.5.2 Trigger efficiency corrections to the cross section

L1 data/MC corrections for the $KK\gamma$ cross section through the R ratio are found conservatively below 5 10^{-4}.

The data/MC corrections for the L3 and BGFilter are shown as a function of the fitted KK mass, in Fig. 2.15. For the BGFilter it is below the per mil level at the ϕ mass, and slightly larger at higher masses. The L3 correction of the order of 5 10^{-4} at the ϕ peak, and consistent with ϕ over the full mass range.

2.6 Tracking Efficiency

Even if ratios such as $R = K^+K^-\gamma$ / $\mu^+\mu^-\gamma$ are measured, cancelling many factors, the fact that kaons and muons have different tracking efficiencies, mostly due to kaon decays and interactions with the detector material, must be dealt with.

2.6.1 Principle of measurement

A 1C kinematic fit is used to select $K^+K^-\gamma$ events for trigger and tracking efficiency studies. The fit is performed using as input only one kaon track (called 'primary') and the ISR photon, and the momentum vector of the second kaon is predicted. Testing whether the predicted track has been actually reconstructed in the tracking system, with a charge opposite to that of the primary track, yields the tracking efficiency when averaged over the sample of predicted tracks.

Conditions must be satisfied to ensure the validity of the measurement:

- the event must be triggered on and selected without specific requirements on the second track,
- a pure $KK\gamma$ sample is selected with additional cuts to enhance the purity, in addition to the kinematic fit,
- attention is given to the angular and momentum resolution of the predicted track since it must fulfill the tracking acceptance.

The determination of the tracking efficiency is based on the assumption that the efficiencies of the two tracks are uncorrelated. However, a very sharp increase of the tracking inefficiency is observed for overlapping tracks in the DCH (see Fig. 2.16), justifying the use of the signed angle difference between tracks in the transverse plane $\delta\phi \equiv \phi^+ - \phi^-$, as the main variable for these studies. The same type of inefficiency increase was also observed for muons and pions (Fig. 2.17 and 2.18 respectively.). Not only the individual track efficiency is locally reduced, but a correlated loss of the 2 kaon tracks occurs. These effects have been studied in details [21].

It should be emphasized that the method determines the efficiency to reconstruct a given track in the SVT+DCH system somewhere in a specified geometrical acceptance, no matter how close or distant this track is with respect to the real one. However, the possible mismatch in momentum and/or angles will affect the full kinematic reconstruction of the event and its effect will be included in the efficiency of the corresponding χ^2 cuts used for the physics sample.

The final physics sample is required to have 2 and only 2 good tracks with opposite charges, so that the understanding of the tracking involves not only track losses, but also the probability to reconstruct extra tracks as a result of secondary interactions with the detector material or the presence of beam-background tracks.

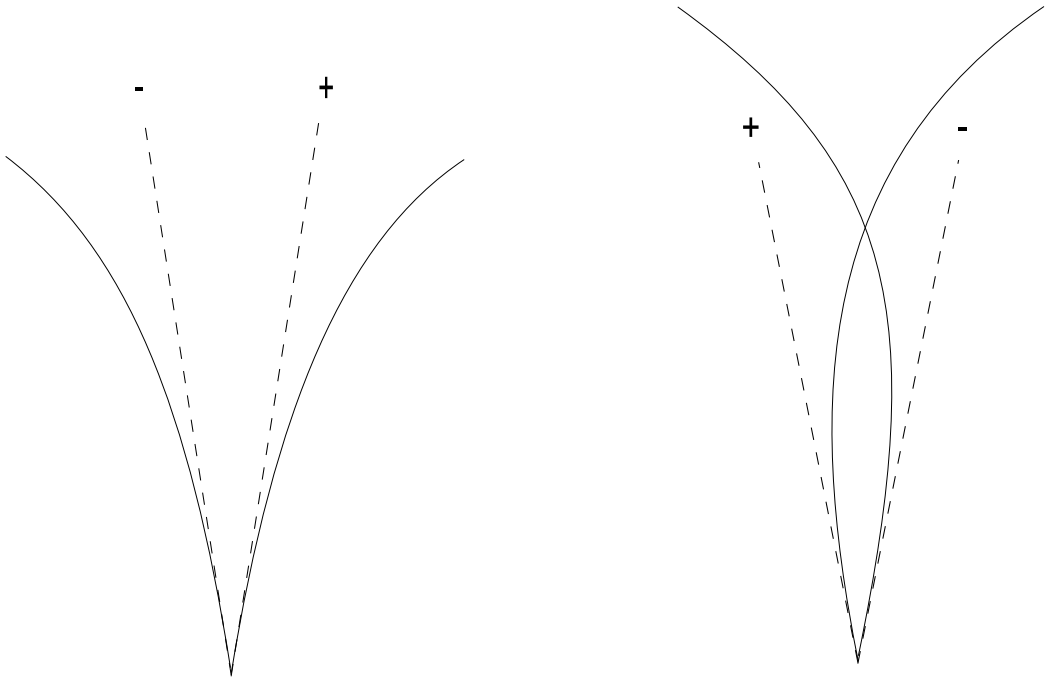

Figure 2.16: Tracks configurations with $\delta\phi < 0$ (left) and $\delta\phi > 0$ (right). An overlap between the two tracks in the DCH is produced in the second case.

A lot of attention has been paid to biases affecting the tracking efficiency measurement as a result of the selection of the primary track and of the event-level background cuts. All components are evaluated and included in the results.

Because of backgrounds, the kaon tracking efficiency can be obtained directly for data only in the ϕ peak region, between 1 and 1.05 GeV. Below and above this region, the results are too sensitive to the background subtraction. However the main sources of track loss have been identified —the kaon in-flight decay, the track overlap in the DCH and the secondary interactions. Despite these restrictive mass interval conditions, it is possible to investigate both the $\delta\phi$ overlap region and the behaviour of isolated tracks, whose inefficiency is controled by decays (which dominate the isolated track loss) and secondary interactions.

For all details, see Ref. [21].

2.6.2 Tracking efficiency correction to the cross section

A clear asymmetry is observed in the data/MC correction for tracking efficiency, coming from the track overlap. This correction is measured in a relatively small angular interval due to the lack of statistics at high masses (large angles). The measurement is actually done on the ϕ resonance, which is close to the threshold (small angles between the tracks), still covering quite well the region of "maximum overlap", for $\delta\phi \approx 0.1$rad. Actually, for

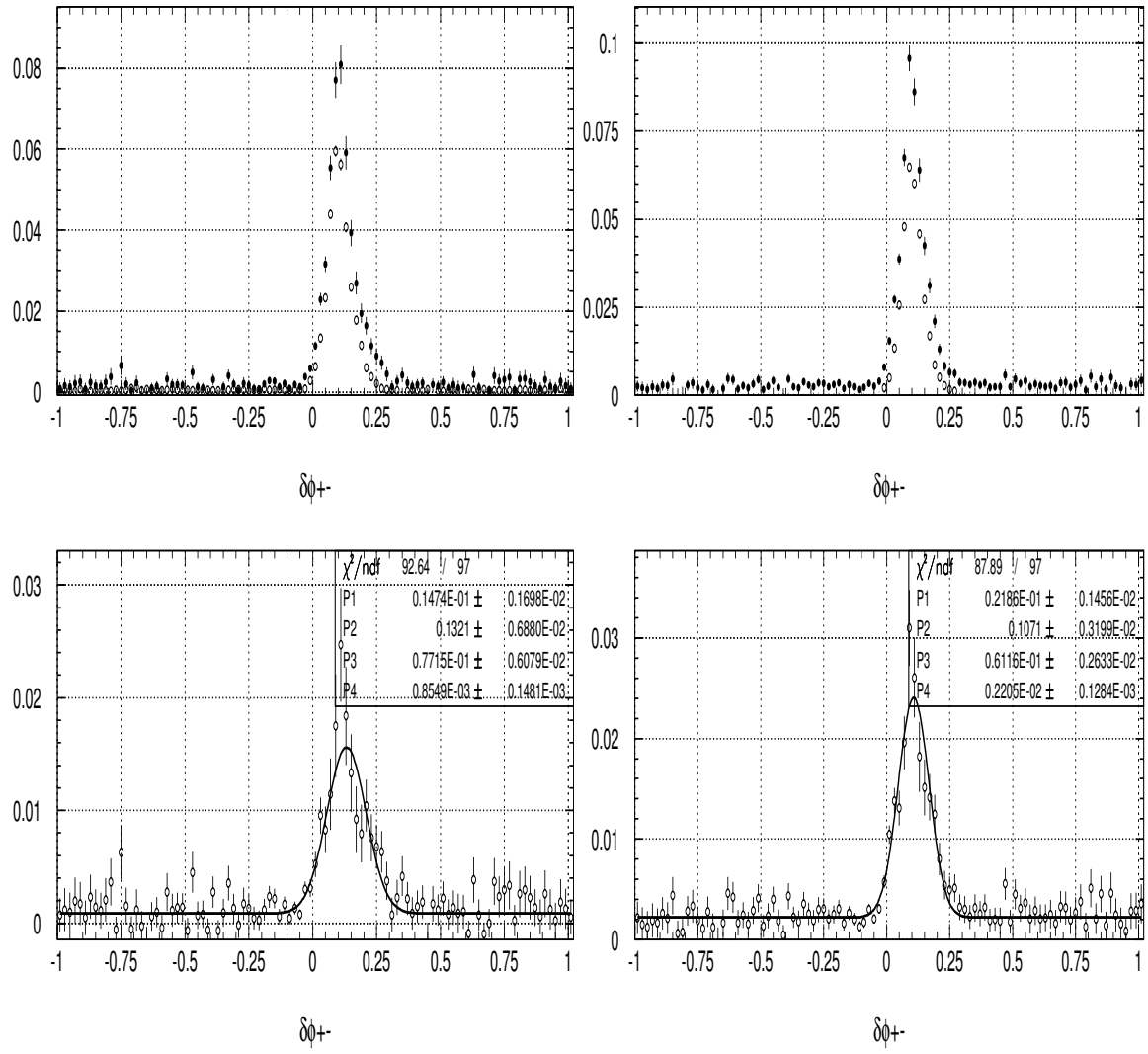

Figure 2.17: The muon tracking inefficiencies (top) for data (black points) and MC (open circles) and their difference (bottom) as a function of $\delta\phi$: runs 1-2 (left) and 3-4 (right).

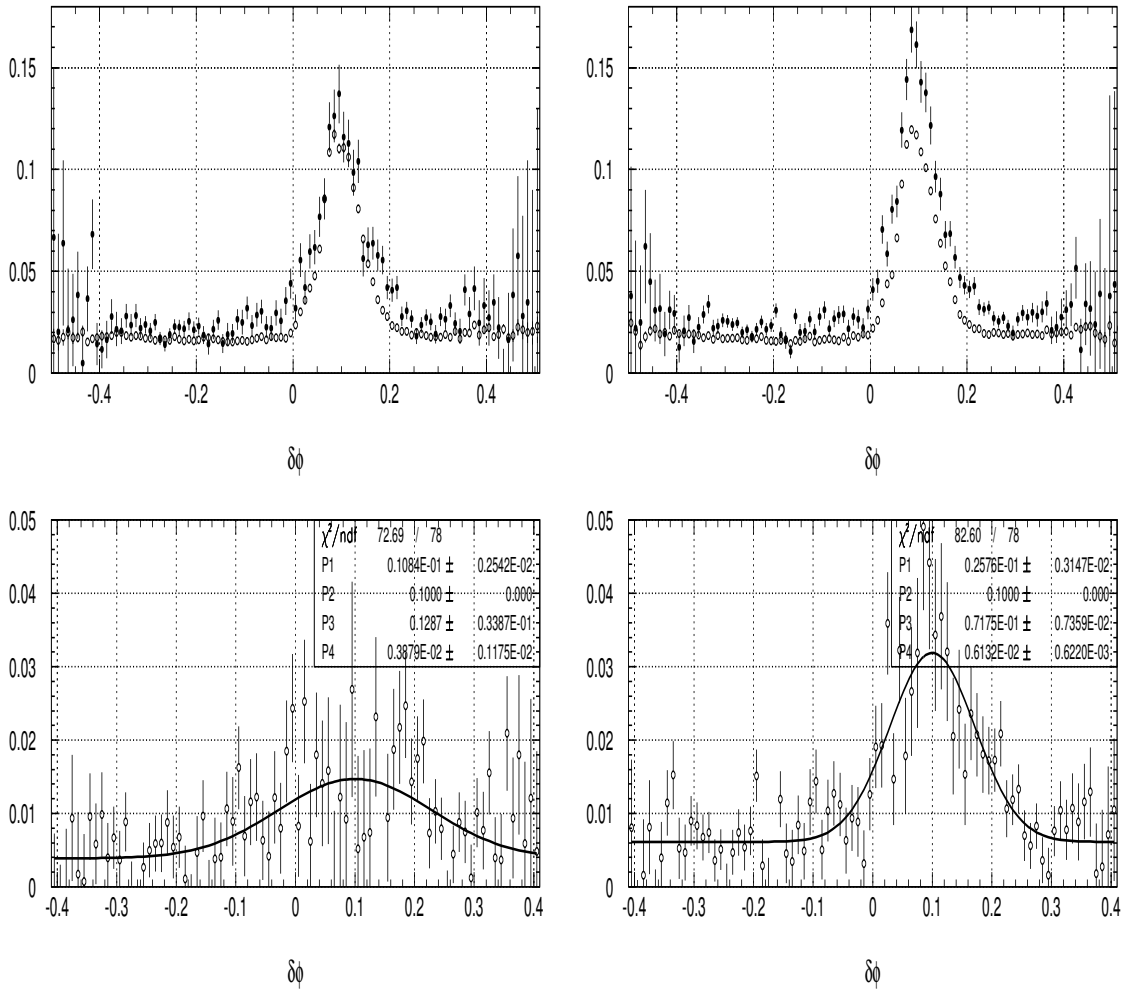

Figure 2.18: The pion tracking inefficiencies (top) for data (black points) and MC (open circles) and their difference (bottom) as a function of $\delta\phi$: runs 1-2 (left) and 3-4 (right).

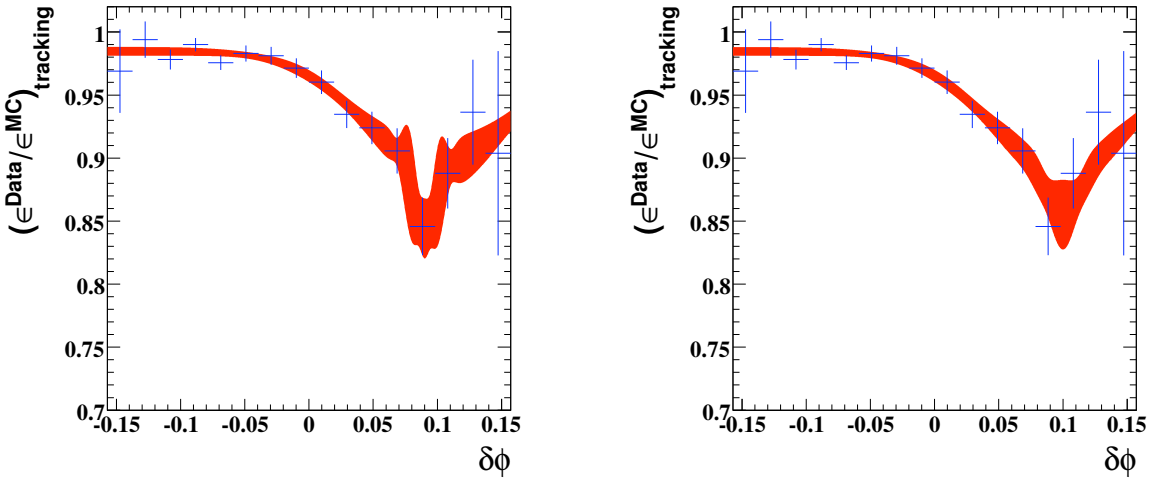

Figure 2.19: Fits of the data/MC correction for the tracking-efficiency (per event, i.e. for the two tracks) as a function of $\delta\phi$. The function for the fits is a constant plus two Gaussians. The central values of the Gaussians are fixed at 0.1 rad in the right plot and at 0.1 and 0.09 rad in the left plot for a slightly better fit. The red band indicates the errors computed from the covariance matrix of the fit parameters.

kinematic reasons, the ϕ sample covers only half of the overlap peak. Having identified and characterized the track efficiency losses, it is possible to extrapolate the correction outside this narrow $\delta\phi$ interval, using a phenomenological fit with a constant plus two Gaussians (see Fig. 2.19). This model is justified by the fact that the corrections for pions and muons have a symmetric behaviour on the two sides of the "maximum overlap" (see Fig. 2.17 and 2.18). A variation of this fit is used to estimate a systematic error of the extrapolation method.

A sampling of the correction is performed using the KK MC simulation, in order to determine the correction as a function of the KK invariant mass. It increases from 3.5% at the threshold to about 4.5% in the ϕ region and a little beyond (this mass range corresponds to low absolute values of the angle in Fig. 2.19), and it reduces to around 1.5% at high masses (corresponding to large absolute values of the angle in Fig. 2.19). The errors on the parameters of the fit, as well as their correlations, are propagated through this sampling procedure into the final correction. They dominate the final error and are strongly correlated between the different mass bins. The (diagonal) statistical error from the sampling is also computed and added to the covariance matrix of the correction. The total error accounts for about 0.3% on the whole mass range. The corrections obtained with the sampling on MC events are shown in Fig. 2.20 (top). The small (at a level smaller than one per mil) systematic effect coming from different fit parametrizations is shown on the bottom of the same figure.

In principle, this ratio should be corrected for data/MC differences in the probability of loosing the two tracks in a correlated way, and in the probability for having an extra reconstructed track. These two corrections are found to be small for kaons and their potential effect is included in the systematic error.

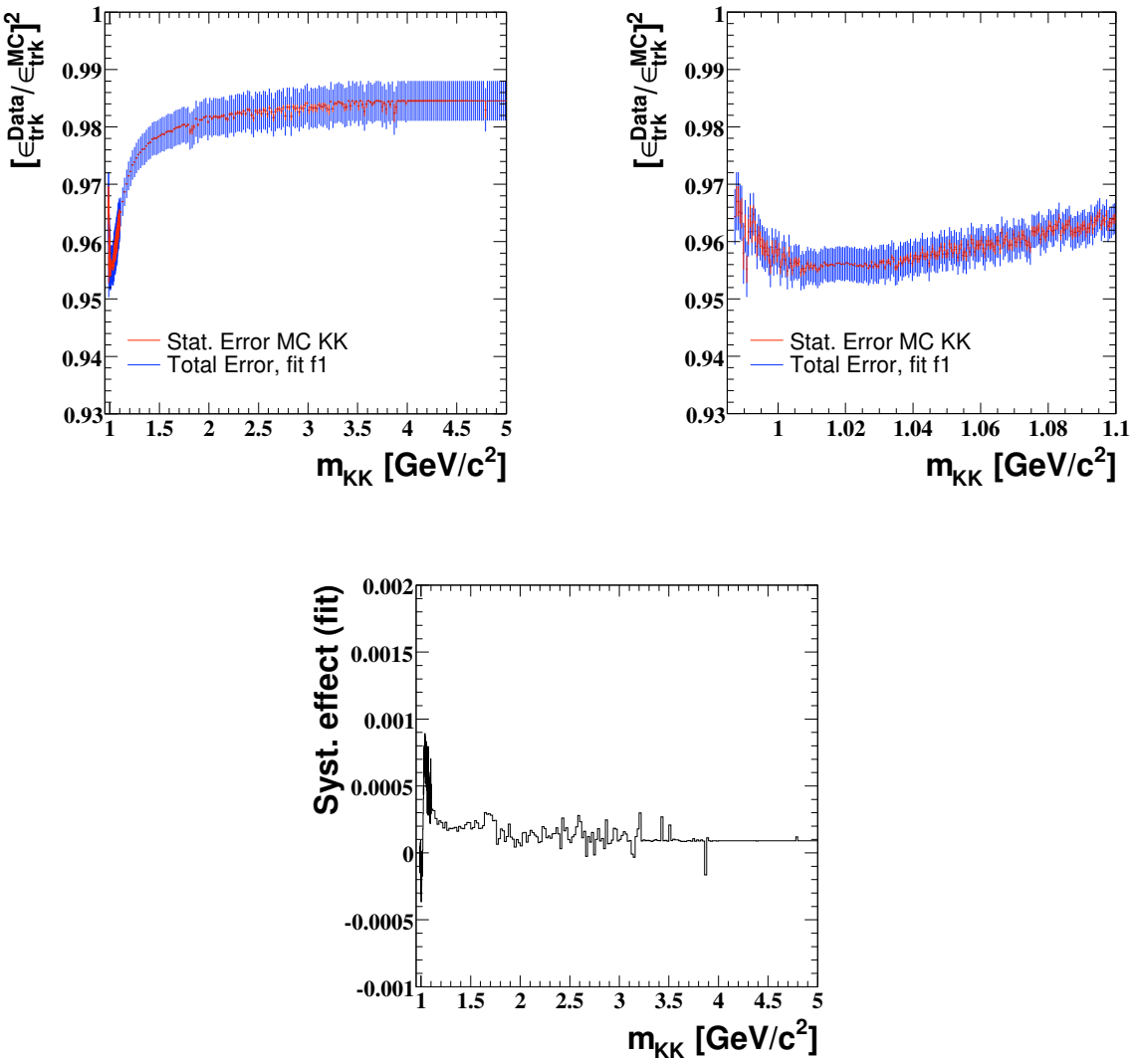

Figure 2.20: Top: the data/MC correction for the tracking-efficiency as a function of the KK invariant mass. The red error bars show the (small) statistical errors from the sampling, whereas the blue ones show the total errors (including the errors from the fit). Bottom: the systematic effect on the efficiency correction, estimated from the difference between the various fits.

The total systematic error for the data/MC corrections for the tracking efficiency is of about 0.13% below 1.05 GeV and 0.62% above. In this second mass region, the error is dominated by the difference between the true MC efficiency and the measured one (which gives the systematic bias of the measurement method). This is certainly an overestimate of the effect for the data/MC efficiency correction (100% of the MC bias).

2.7 Particle ID Efficiencies

One must also correct the mass spectrum for the identification inefficiency of the kaons. Since in this analysis the separation of kaon, muon and pion processes depends exclusively on particle identification (ID), it is of utmost importance to control the ID efficiencies. Thus, specific studies were done for the mis-identification efficiencies yielding the $\mu\mu$ and $\pi\pi$ backgrounds. In practice, we use simulation to get particle (mis-)ID efficiencies and we perform data/MC corrections (see Eq. 2.12).

2.7.1 K-ID

The method to determine the kaon ID efficiencies makes use of the $KK\gamma$ sample itself, where one of the produced charged particles is tagged as kaon and the identification of the second one is tested. A 1C kinematic fit is performed using only the two charged tracks. A cut $\chi^2_{KK} < 15$ is applied to strongly reduce multihadronic background, while a cut $\chi^2_{KK} < \chi^2_{\pi\pi}$ reduces the pion contamination. The background from photon conversions in the process $e^+e^- \to \gamma\gamma$ is eliminated by a cut on the distance (in the transverse plane) between the vertex of the two tracks and the interaction point. The purity of the kaon sample is further enhanced by a cut on the fitted KK mass, which must be in the window $1.01 - 1.04$ GeV. A slightly larger window is used to constrain the background.

This method relies on the independence between the measurements of the efficiencies of the two kaons in the event. In fact, one could think of two mechanisms breaking this assumption:

- When the two tracks are close to each other when crossing the DIRC, the pattern of Cherenkov photons can generate some confusion in the reconstruction software, leading to a correlation between the two measured efficiencies (overlap correlation).

- Since the ID efficiency is expected to depend on the kaon momentum and direction, the selection of the primary kaon track induces a restriction in the phase space of the kaon candidate (for example if the mass of the pair is constrained), hence producing a sampling bias for the measurement of its efficiency (kinematic correlation).

These correlation sources were studied and they are included in the systematic uncertainties.

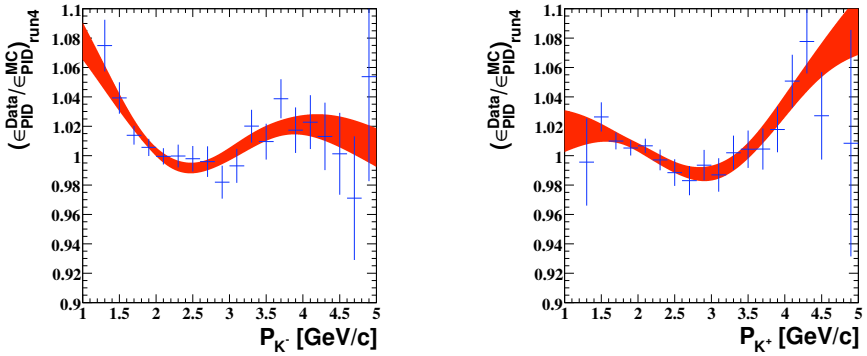

Figure 2.21: Fits of the data/MC correction for the particle ID efficiency, as a function of momentum, for the run 4 data. The function for the fits is a first order polynomial plus a Gaussian. The red band indicates the errors computed from the covariance matrix of the fit parameters. The fits are done separately for negative (left) and positive (right) tracks.

The K-ID efficiency is studied separately for positive and negative tracks and the MC is found not to accurately describe the K^+ data (e.g. a much larger fraction of kaons is misidentified as muons). The data/MC corrections for the K-ID efficiency are obtained as a function of the momentum of the charged particle, separately for each of the four runs. Due to the lack of statistics at high momenta, the correction is measured in the $[1;5]$GeV/c momentum interval. An extrapolation must be done for higher momenta, and this is achieved through a fit (see Fig. 2.21).

Just as for the tracking, a sampling of this correction is performed using the KK MC simulation, in order to determine the correction as a function of the KK invariant mass. Run 1 data are combined with run 2, and run 3 with run 4, at the level of the mass spectra, i.e. before computing the average. The errors on the parameters of the fits, as well as their correlations, are propagated through the sampling procedure into the final correction and its covariance matrix. The (diagonal) statistical error from the sampling is also computed and added to the covariance matrix of the correction. The corrections as a function of the KK invariant mass are shown in Fig. 2.22.

The systematic uncertainties on this correction account for 0.26% from correlated loss of KK ID and 0.10% from the purity of the kaon candidate sample.

2.7.2 $\mu \to K$ and $\pi \to K$ mis-ID

The $\mu \to K$ and $\pi \to K$ mis-ID efficiencies are measured on MC and on data. This is done by selecting a tag (a track identified as muon, respectively pion) to define the total sample, and testing the second track for K-ID. The purity of the sample is provided by the cuts $m_{\mu\mu} \in [2.5;5]$ GeV and $0.6 \leq m_{\pi\pi} \leq 0.9$ GeV, as well as by the use of the tight χ^2-cut (see Sec. 2.8). These cuts are chosen to be close to the mass intervals of muon/pion background for kaons, and as such they cover similar angular regions of the detector. The data and MC mis-ID efficiencies as well as the data/MC corrections are shown in Fig. 2.23 as a function of the track momentum. The corrections have a rather flat behaviour, with

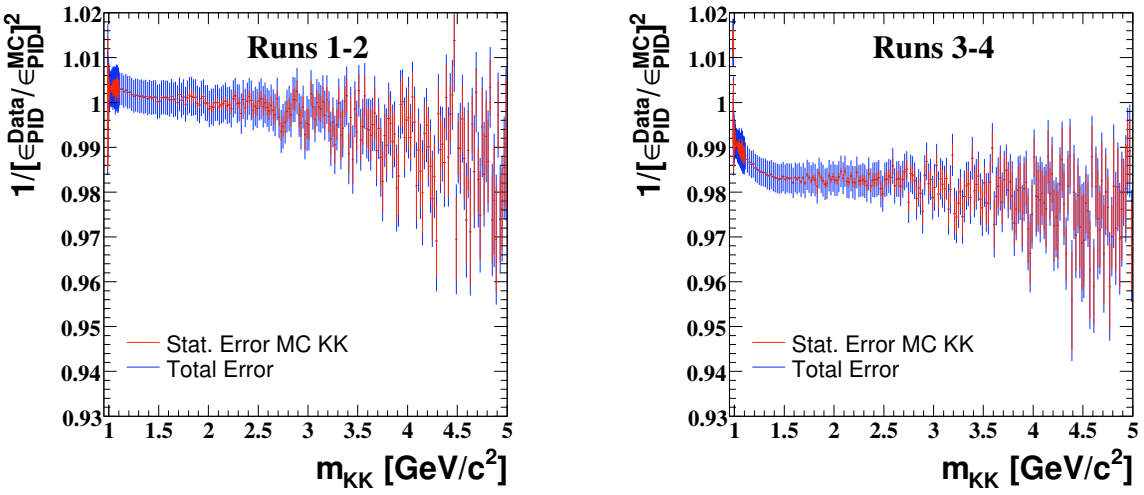

Figure 2.22: The inverse data/MC correction for K-ID efficiency as a function of the KK invariant mass, for runs 1 and 2 (left) and 3 and 4 (right). The red error bars show the statistical errors from the sampling, whereas the blue ones show the total errors (including the errors from the fit). The plots correspond to a sampling with MC events in the tight χ^2 region.

some structures due to shape differences in data and MC. They account for about $0-50\%$ for muons and $0-15\%$ for pions.

The sensitivity of the data/MC correction to the muon sample purity is estimated for the muons, using events that satisfy to a looser mass cut: $m_{\mu\mu} \in [1.5; 5]$ GeV, and a systematic error determined. The mass cut is less critical for pions, where we select exactly the ρ mass region which contributes the most to the kaon background.

In order to obtain the data/MC mis-ID corrections for $\mu\mu \rightarrow {}'KK'$ and $\pi\pi \rightarrow {}'KK'$, as a function of the KK invariant mass, a sampling is performed on the $\mu\mu$ and $\pi\pi$ MC, using events mis-identified KK (see Fig. 2.24). The errors of the fit parameters (and their correlations) are fully propagated to this correction. The correction for $\mu\mu \rightarrow {}'KK'$ is rather flat, while the one for $\pi\pi \rightarrow {}'KK'$ shows a rather important mass dependence. The systematic error for $\mu\mu \rightarrow {}'KK'$ data/MC mis-ID correction, is estimated to be of about 30%. It accounts for possible sampling biases, effects due to the fits as well as a small KK background in the data sample with a loose mass cut.

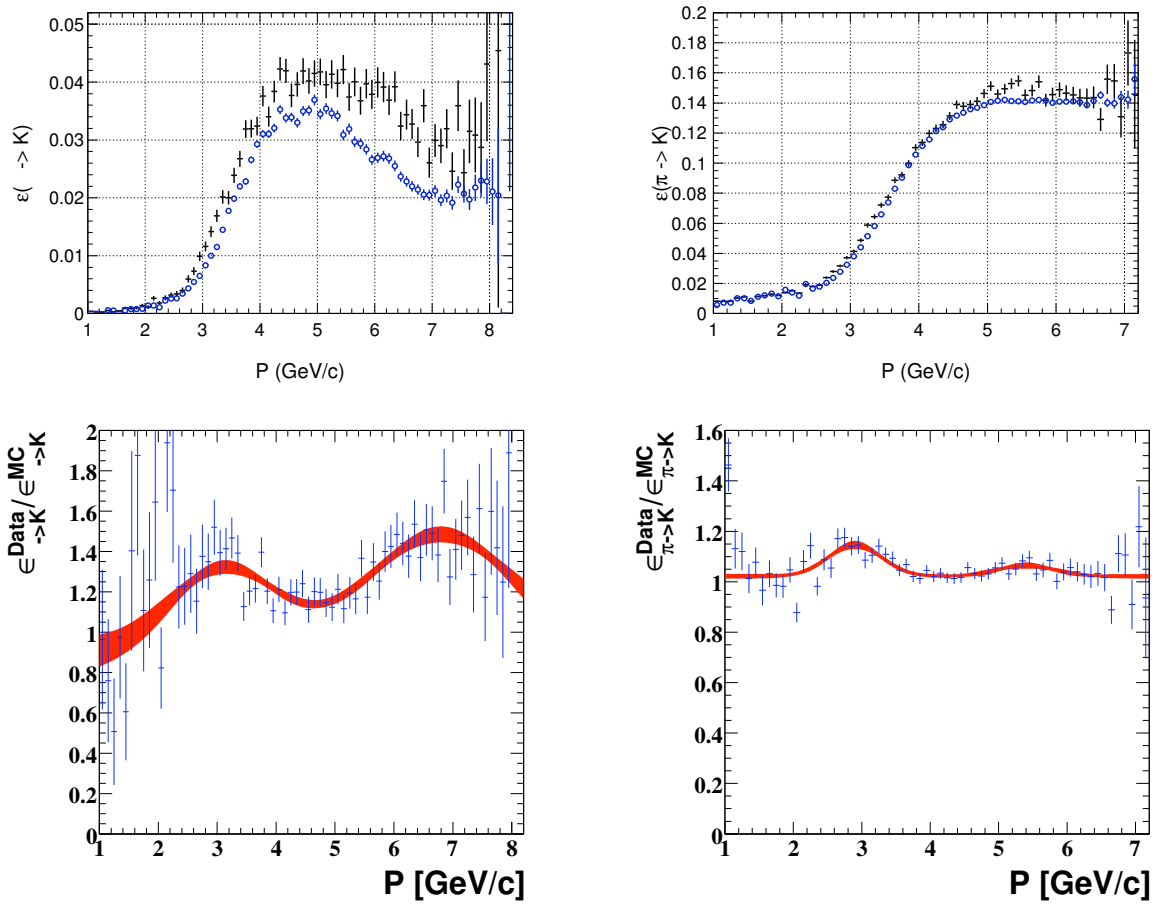

Figure 2.23: Top: data (black points) and MC (blue circles) efficiencies for the mis-ID as a function of the track momentum. Bottom: data/MC correction for the mis-ID as a function of the track momentum. The red band corresponds to a fit by a constant plus two gaussians, where the error is propagated from the covariance matrix of the fit parameters. The plots correspond to $\mu \to K$ (left) and $\pi \to K$ (right), with a cut $m_{\mu\mu} \in [2.5; 5]$ GeV and respectively $m_{\pi\pi} \in [0.6; 0.9]$ GeV.

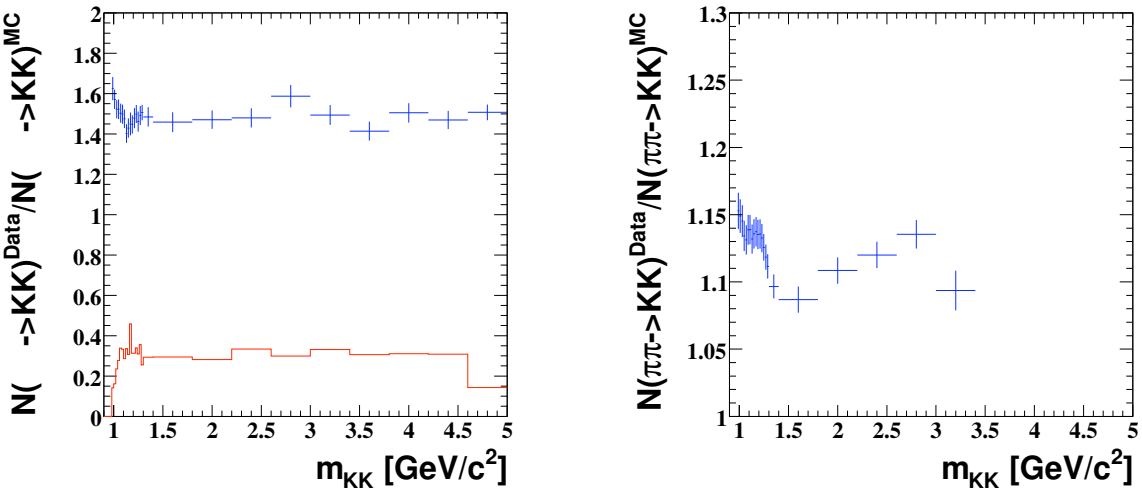

Figure 2.24: Data/MC correction for the $\mu\mu \rightarrow {}'KK'$ (left) and $\pi\pi \rightarrow {}'KK'$ (right) mis-ID as a function of the invariant KK mass. In the left plot the blue points corresponds to the sampling of the mis-ID fit obtained for tracks of events with $m_{\mu\mu} \in [2.5; 5]$ GeV, while the red histogram is the absolute difference with respect to the sampling for the fit with $m_{\mu\mu} \in [1.5; 5]$ GeV taken as a systematic error. The errors of the points are obtained from the diagonal of the covariance matrix of the correction, propagated from the covariance matrix of the fit parameters. The statistical errors of the sampling MC events are not included here, as they were already included in the uncorrected spectra.

2.8 Kinematic Fits and Background Study

2.8.1 Kinematic fits with possibly one additional photon

As for the analysis of the $\mu\mu\gamma$ and $\pi\pi\gamma$ processes, the event definition is enlarged to include the radiation of one photon in addition to the already required ISR photon. Two types of fits are considered, according to the following situations:

- The additional photon is detected in the EMC, in which case its energy and angles can be readily used in the fit: we call this a 3C FSR fit, although the extra photon can be either from FSR or from ISR at large angle. The energy of the primary ISR photon is not used in the fit, as it brings little information for the relatively low masses involved. The threshold for the additional photon is kept low (20 MeV). This can introduce some background, but with little effect as the fit in that case would not be different in practice from a standard fit to the $KK\gamma$ hypothesis.

- The additional photon is assumed to be from ISR at small angle with respect to the beams. Since no more information [1] is available it is postulated that the extra photon is perfectly aligned with either the e^+ or the e^- beams. The corresponding so-called 2C ISR fit ignores additional photons measured in the EMC and returns the energy of the fitted collinear ISR photon.

In both cases the constrained fit procedure uses the measured momenta and angles of the two kaons and their covariance matrix in order to solve the four energy-momentum conservation equations. The kaon mass is assumed for the two charged particles. Each event is characterized by the χ^2 values, χ^2_{addFSR} and χ^2_{addISR} from the two fits which can be reported on a 2D plot. In practice the quantities $\ln(\chi^2+1)$ are used so that the long tails can be properly visualized. Events without any extra measured photons have only the χ^2_{addISR} value and they are plotted separately on a line above the χ^2_{addFSR} overflow. In the case of several extra detected photons, FSR fits are performed using each photon in turn and the fit with the best χ^2_{addFSR} is retained.

It is easy to visualize the different interesting regions in the 2D χ^2 plane (see Fig. 2.25). Most of the events peak at small values of both χ^2, but the tails along both axes clearly indicate events with additional radiation: small-angle ISR along the χ^2_{addFSR} axis (with large ISR energies at large values of χ^2_{addFSR}), FSR or large-angle ISR along the χ^2_{addISR} axis (with large FSR energies at large values of χ^2_{addISR}). Events along the diagonal do not satisfy either hypotheses and result from resolution effects for the kaon tracks or the direction of the primary ISR photon, or possibly additional radiation of more than one photon. Events affected by secondary interactions are also in this region. Multibody background is expected to populate the region where both χ^2 are large and consequently

[1] This is not strictly true as the missing photon could be completely reconstructed if the ISR photon energy was used in the kinematic fit. However tests have shown that the relative quality of this new information does not permit a significant improvement for the fitted direction of the additional ISR photon over the collinear assumption.

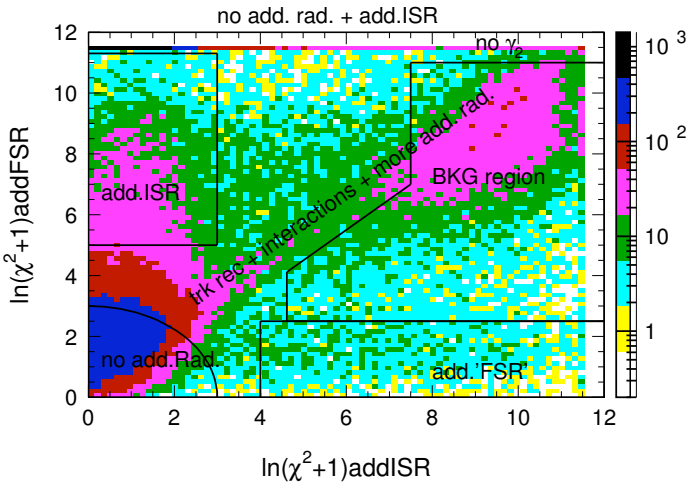

Figure 2.25: The 2D-χ^2 distribution for the $KK\gamma(\gamma)$ data sample in the [0.98;5] GeV fitted KK mass interval, where different interesting regions are defined.

a background region is defined in the 2D χ^2 plane. This region has to be optimized as a compromise between efficiency and background contamination in the signal region. More practically, the optimization is rather on the control of the corresponding systematic uncertainties.

Finally, the KK mass is obtained using the fitted parameters of the two kaons from the ISR fit if $\chi^2_{addISR} < \chi^2_{addFSR}$ and from the FSR fit in the reverse case.

2.8.2 MC χ^2 distributions for signal and backgrounds

An important source of background for $K^+K^-\gamma(\gamma)$ comes from other ISR events: $\pi^+\pi^-\gamma$, $\mu^+\mu^-\gamma$, $K^+K^-\eta\gamma$, $K^+K^-\pi^0\gamma$, $\pi^+\pi^-\pi^0\gamma$, $\pi^+\pi^-2\pi^0\gamma$, $p\bar{p}\gamma$ and $K_SK_L\gamma$. Actually, these types of events are included in our physical sample if a (double) mis-ID occurs and/or the photons from a π^0 or η decay are not reconstructed. Non-ISR $q\bar{q}$ and $\tau^+\tau^-(\gamma)$ events represent other sources of background. In this case, it is an energetic photon from a π^0 decay that is misidentified as ISR.

Scale factors are computed for the various MC samples, using the number of expected events (from the integrated luminosity and the measured cross sections) and the number of events at the generator level (before any cuts). The shapes and normalizations of the $K^+K^-\eta\gamma$, $\pi^+\pi^-\gamma$, $K^+K^-\pi^0\gamma$ and $p\bar{p}\gamma$ spectra in MC are corrected (reweighted) using the cross-sections measured by BABAR, and errors are propagated accordingly. Thus the rescaled MC spectra can be directly compared to the data. This is not true for the $q\bar{q}$ MC background that requires a special normalization procedure (Section 2.8.3).

In the following we will analyse the signal and background in three different K^+K^- fitted invariant mass regions: [0.95;1.1], [1.1;3] and [3;5] GeV. The separation of the last two intervals will be motivated in the study of the $q\bar{q}$ MC.

We plot the number of events in the plane $\ln(\chi^2_{addFSR}+1)$ vs. $\ln(\chi^2_{addISR}+1)$ for the signal and main background contributions, obtained from the available MC samples (Fig. 2.26, 2.27 and 2.28), properly normalized.

We indicate by continuous black lines (see Fig. 2.26) the cuts used in this plane to separate signal from background. We define the corresponding χ^2 cuts:

- "tight" keeps events with $\ln(\chi^2_{addISR}+1) < 3$;
- "loose" excludes the polygonal area (called background region);
- "intermediate" is the region between loose and tight (it is inside the loose cut, while removed by tight);
- "moderate" (keeps more events than tight but less than loose) is indicated with a dashed red line in the background plots.

The "intermediate" region is used for background and efficiency studies. The "tight", "loose" and "moderate" cuts are designed to remove most of the dominant background coming from $K^+K^-\eta\gamma$, $K^+K^-\pi^0\gamma$ and $q\bar{q}$ events. These cuts also remove the smaller background from the channels $\pi^+\pi^-\pi^0\gamma$, $\pi^+\pi^-2\pi^0\gamma$, $K_SK_L\gamma$ and $\tau^+\tau^-(\gamma)$.

While the tight χ^2 cut can in principle be used at any KK mass, the loose cut would suffer from too much background at high mass, and it could only be used in the [0.95;1.1] GeV interval. However, in view of the spectrum unfolding (which must be done before a comparison of the loose and tight results in the ϕ mass region (see Section 2.10)), the loose cut is also studied up to 5 GeV.

The "moderate" cut has been studied for the [1.1;3] and [3;5] GeV regions. It is more adapted than loose for removing background, but we will explain latter which are the motivations for not keeping this cut and prefering the tight cut for the high mass region.

These χ^2 cuts have essentially no effect on the background from $\pi^+\pi^-\gamma$ and $\mu^+\mu^-\gamma$ which, in this plane, are localized in the same region as most of the signal events. These two backgrounds are significantly reduced only at the level of particle identification.

Whatever the χ^2 cut, studies of its efficiency necessitate the understanding of the various event populations in the χ^2 plane. For these studies, we distinguish some other (sub-)regions of the χ^2 plane. In the signal plots we indicate two red lines which are used to divide the intermediate χ^2 region into three: (additional) ISR (on the top), diagonal (middle) and (additional) FSR or large angle ISR (bottom). They will be especially useful in the studies for the data/MC corrections of the χ^2-cut efficiency. For the other studies it will be enough (if not stated otherwise) to distinguish ISR and FSR halves, on the top and respectively the bottom of the diagonal of the χ^2-plane.

For the final physics results, the choice of χ^2 cut will be "tight". We will explain in turn why we prefer it to the "moderate" and to the "loose" cuts.

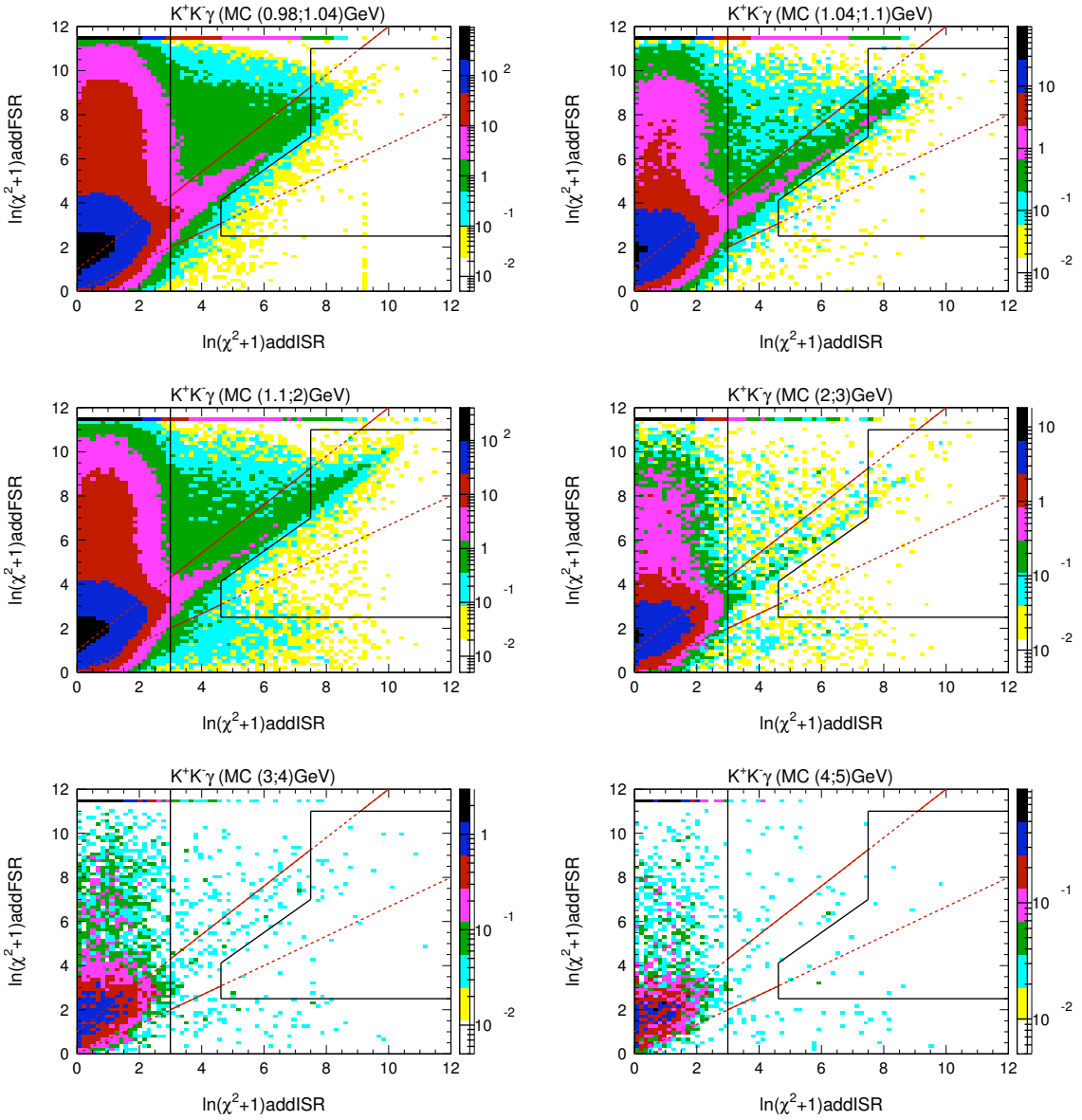

Figure 2.26: χ^2 plane for the $K^+K^-\gamma$ MC sample. The plots correspond to the KK mass regions (from top to bottom and left to right): [0.98;1.04], [1.04;1.1], [1.1;2], [2;3], [3;4] and [4;5] GeV. The black lines indicate the limit of the tight (straight line at $\ln(\chi^2_{addISR}+1) = 3$) and the loose (kinky line) regions respectively. The red lines divide the intermediate region (between loose and tight) into three: ISR(top), diagonal(middle) and FSR(bottom).

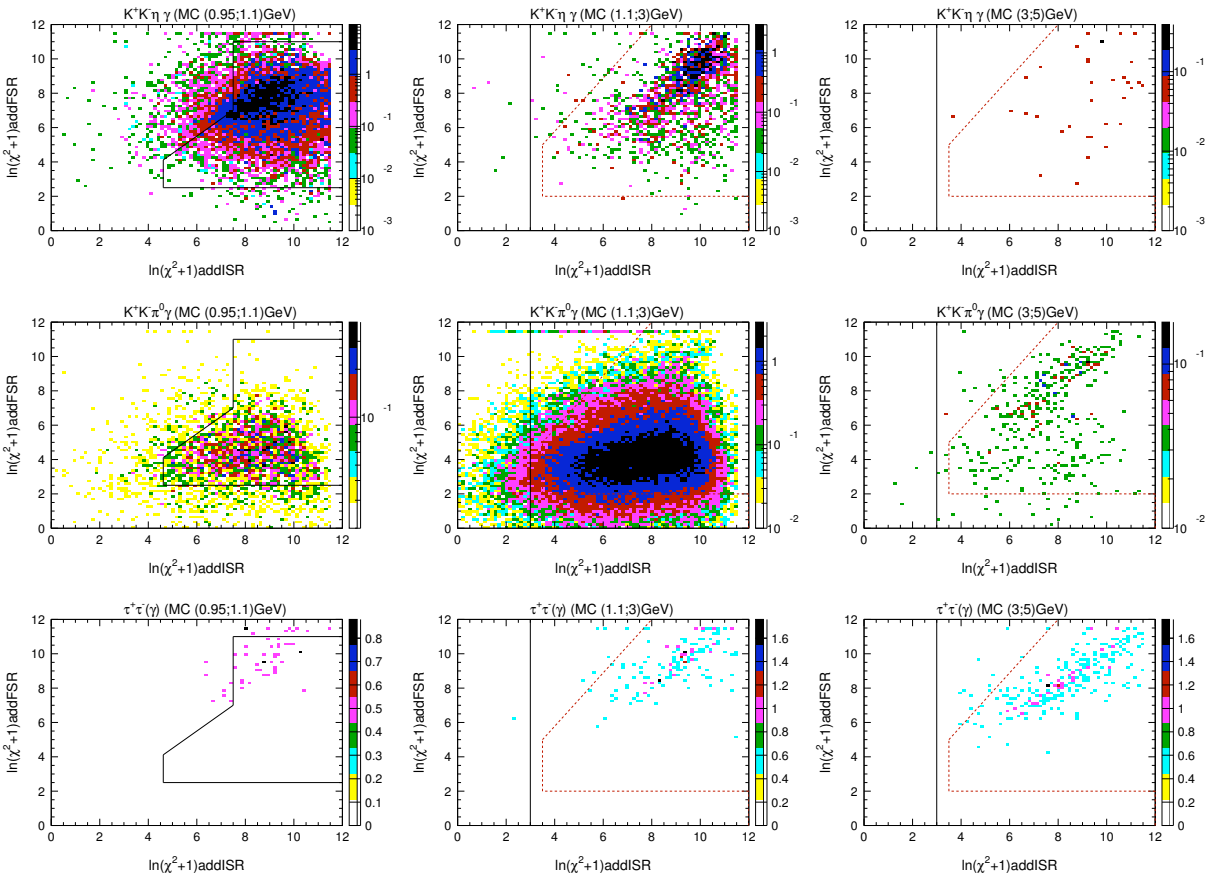

Figure 2.27: χ^2 plane for the $K^+K^-\eta\gamma$ (top), $K^+K^-\pi^0\gamma$ (middle) and $\tau^+\tau^-(\gamma)$ (bottom) MC samples . The plots correspond to the KK mass regions: [0.95;1.1] GeV (left), [1.1;3] GeV (middle) and [3;5] GeV (right). We also indicate by black lines the loose χ^2 cut (left) and the tight χ^2 cut (middle and right), while the red line indicates the moderate cut.

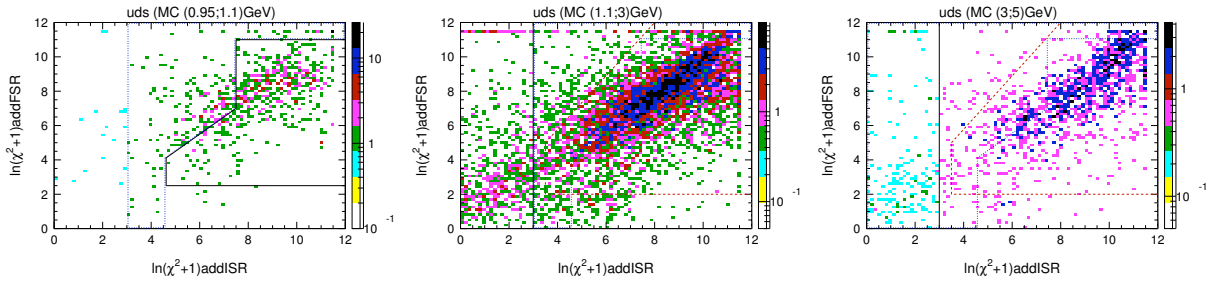

Figure 2.28: χ^2 plane for the $q\bar{q}$ MC sample(normalized to the data). The plots correspond to the KK mass regions: [0.95;1.1] GeV (left), [1.1;3] GeV (middle) and [3;5] GeV (right). We also indicate with a blue dotted line the domain that is used for the normalization (see text).

2.8.3 Normalizing the $q\bar{q}$ MC sample

The $q\bar{q}$ MC sample was generated using JETSET [19], that includes ISR radiation. Fragmentation is needed in order to proceed from the quarks to the final state and one could question the model which is used, especially for the low multiplicity final states that we consider. Therefore we cannot rely on the normalization with the luminosity, but rather on a direct data/MC comparison for this background.

From the $q\bar{q}$ MC sample we keep only events which do not contain primary ISR candidates, as these events are better simulated in the ISR MC samples.

The normalization of the $q\bar{q}$ sample is studied in three mass intervals: [threshold;1.1], [1.1;3] GeV and [3;5] GeV. From the first interval we remove a 20 MeV band around the ϕ mass, to reduce the number of KK signal events. The separation of the last two intervals is motivated by the fact that simulation differences could arise between strongly different kinematical configurations. This normalization is done in a region of the χ^2 plane overlapping with the intermediate region (the corresponding χ^2 region is indicated in Fig. 2.28). From the χ^2-plane, we actually use a domain that contains most of the $q\bar{q}$ events in the loose region (basically the intermediate χ^2-region) and that has a reduced number of $K^+K^-\gamma$ events (see Fig. 2.28 and 2.26). We also remove the so-called additional FSR region, which in data includes a significant amount of events (with an additional large angle ISR) to increase the π^0 signal significance (the $q\bar{q}$ signal is very weak in that region). In the third mass region we also perform the study for the tight χ^2 region as at that mass we do not suffer from the strong KK signal in data.

The background from non-ISR $q\bar{q}$ events is essentially due to the fact that an energetic photon from $\pi^0 \to \gamma\gamma$ could be identified as ISR. To display this background and use the π^0 signal to normalize the MC to data, we plot the invariant mass $\gamma_{ISR}\gamma$ and we search for a $\pi^0 \to \gamma\gamma$ peak, in the data, $q\bar{q}$ MC and ISR plus $\tau\tau(\gamma)$ MC. If several photons are detected, besides the ISR candidate, the retained pair is chosen on the basis of the best kinematic fit for two charged tracks plus two detected photons (add. FSR fit). We fit all the histograms by a second-order polynomial plus a gaussian. We constrain the central value of the gaussian to be equal to the π^0 mass. In Fig. 2.29, 2.30 and 2.31 we show the fits of the π^0 peak in the data, the $q\bar{q}$ MC and the background identified in other MC

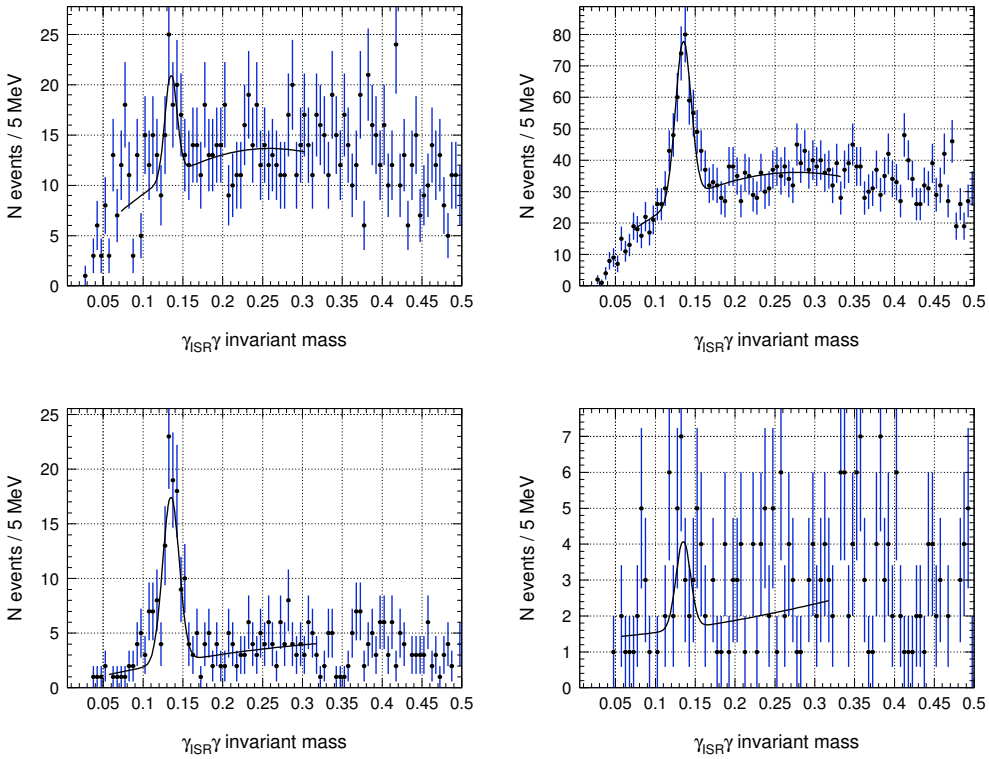

Figure 2.29: Invariant mass of the $\gamma_{ISR}\gamma$ system for the data, on three regions of fitted KK mass: [0.98;1.01] and [1.03;1.1] GeV(top left), [1.1;3] GeV(top right), [3;5] GeV with an intermediate χ^2-cut (bottom left) and [3;5] GeV with tight χ^2-cut (bottom right). A $E_\gamma > 0.025$ GeV cut is used for the second photon. The fit for the normalization of the $q\bar{q}$ MC sample is also shown.

samples (the $K^+K^-\gamma$ and $\tau^+\tau^-(\gamma)$ are dominating). For the data and the background fits, the width of the peak is fixed at the value found in the MC.

The small peak in the KK MC is an artefact caused by splitting of the ISR γ shower (creating a satellite cluster). The granularity of the EMC is such that it produces a peak near the π^0 mass (see Fig. 2.32). This justifies the ϕ mass veto used in order to reject fake π^0's from KK events.

Figure 2.33 shows the number of events in the π^0 signal and background, as a function of the energy cut made for the second photon, in the [1.1;3] GeV mass region. The signal exhibits a slow decrease when increasing the cut energy, whereas the background initially drops rather fast. If one does not fix the width of the fitted π^0 peak, one gets slightly larger and less well determined values for the corresponding number of events. This is due to the fact that the peak observed in the $KK\gamma$ MC sample does not correspond to a real π^0 signal and it is slightly wider than the peak in the $q\bar{q}$ MC. However, for the subtraction of fake π^0 peak from data, in view of the normalization, the result of the fit with fixed width will be used. We choose to apply a cut $E_{\gamma_2} > 0.025$ GeV in the following, as it corresponds to the event selection in the $q\bar{q}$ background subtracted from data. Other cuts on the energy of the second photon, providing a lower background without reducing too

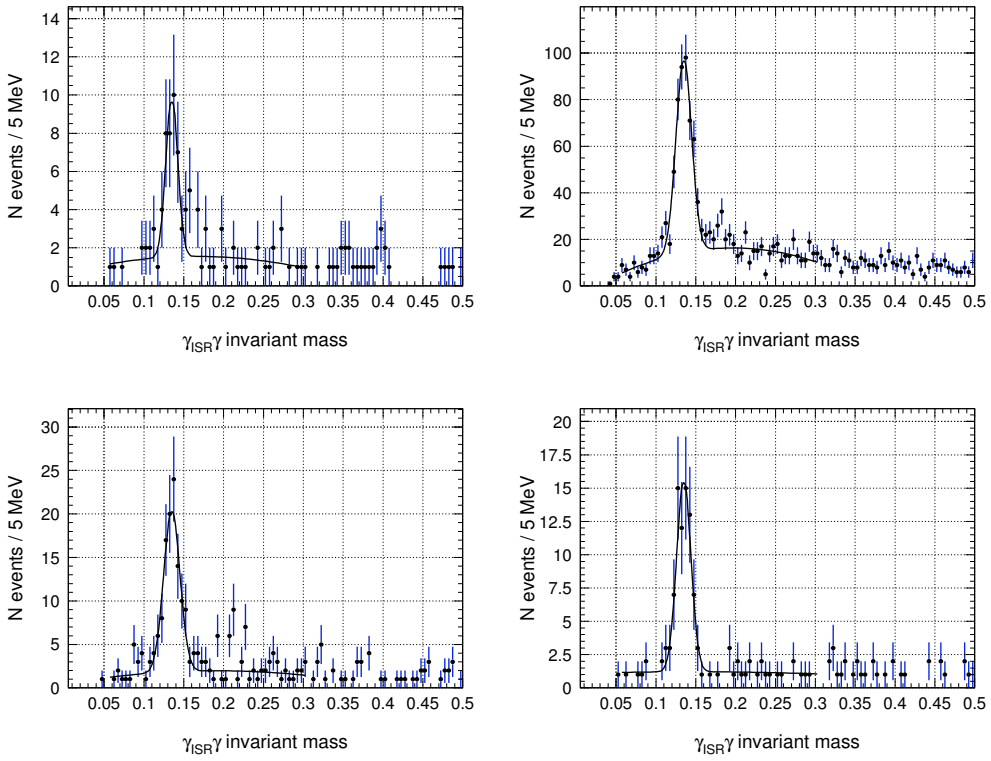

Figure 2.30: Invariant mass of the $\gamma_{ISR}\gamma$ system for the $q\bar{q}$ MC, on three regions of fitted KK mass: [0.98;1.01] and [1.03;1.1] GeV(top left), [1.1;3] GeV(top right), [3;5] GeV with an intermediate χ^2-cut (bottom left) and [3;5] GeV with tight χ^2-cut (bottom right). A $E_\gamma > 0.025$ GeV cut is used for the second photon. The fit for the normalization of the $q\bar{q}$ MC sample is also shown.

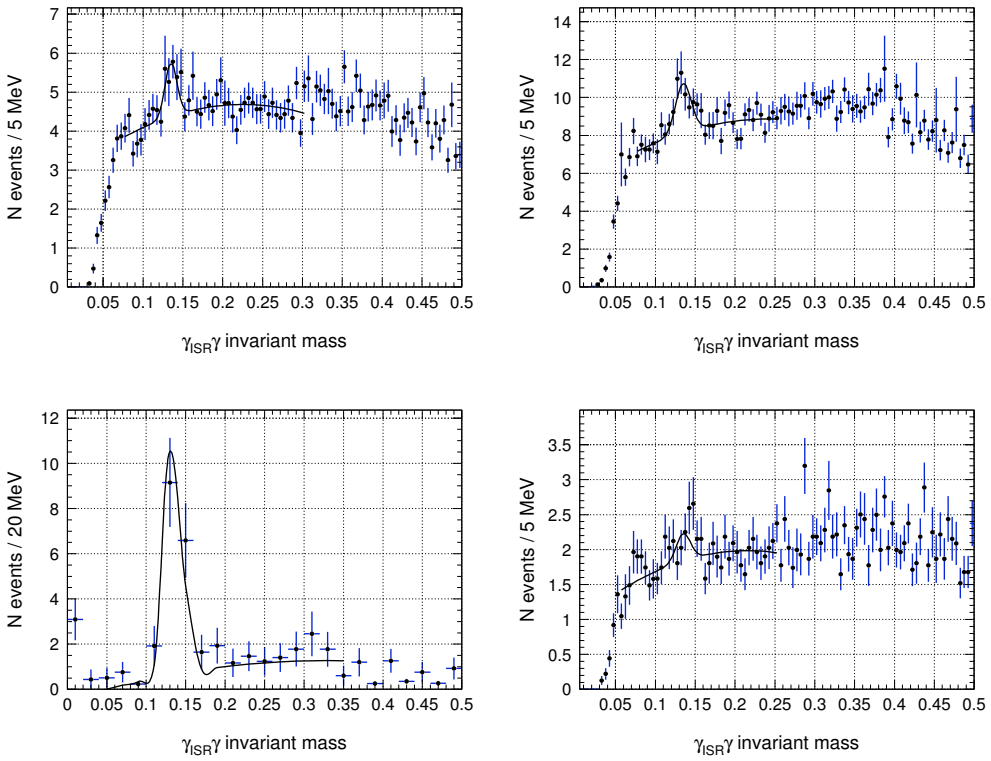

Figure 2.31: Invariant mass of the $\gamma_{ISR}\gamma$ system for the background MC(other than $q\bar{q}$), on three regions of fitted KK mass: [0.98;1.01] and [1.03;1.1] GeV(top left), [1.1;3] GeV(top right), [3;5] GeV with an intermediate χ^2-cut (bottom left) and [3;5] GeV with tight χ^2-cut (bottom right). A $E_\gamma > 0.025$ GeV cut is used for the second photon. The fit for the normalization of the $q\bar{q}$ MC sample is also shown. The contribution shown in the bottom left plot, as well as the apparently large fluctuations of a few points (mainly in the region of the π^0 peak), is due to the $\tau^+\tau^-(\gamma)$ MC sample. Actually, a "true" π^0 can be produced in a τ desintegration, which explains the accumulation of events in this region of $\gamma_{ISR}\gamma$ invariant mass.

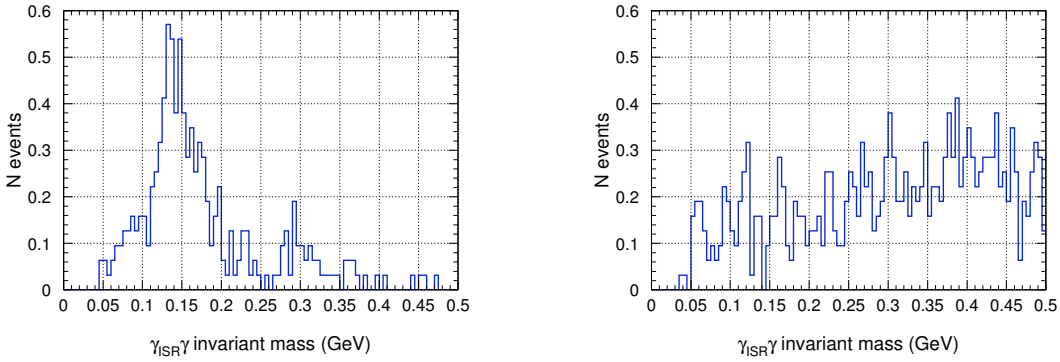

Figure 2.32: The mass of the ISR-second photon system, for events with an angle with the closest kaon higher than 110°(left), and smaller than 110°(right), for the MC. The plots correspond to the [0.95;5] GeV region, for events in the loose χ^2 region, with $\ln(\chi^2_{addFSR}+1) < \ln(\chi^2_{addISR}+1)$ and an additional photon of more than 200 MeV in the lab frame.

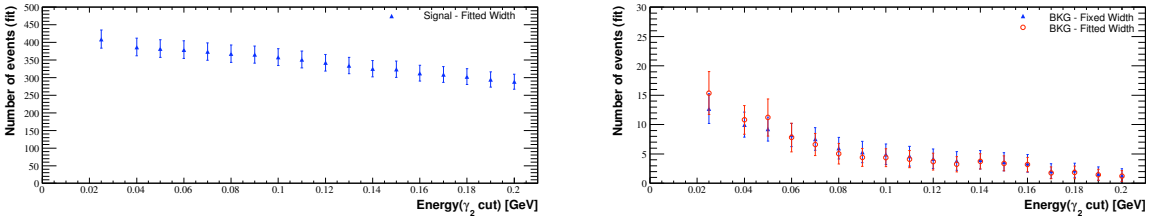

Figure 2.33: Number of π^0 signal (left) and background (right) events for the $\gamma_{ISR}\gamma$ system, in the [1.1;3] GeV region, as a function of the energy at which the cut is made for the second photon. The number of events obtained for the background if the width of the peak is fitted is also shown. These plots are obtained with MC simulation.

Table 2.5: Number of $\pi^0 \to \gamma\gamma$ events in the $q\bar{q}$ MC, other MC samples, and in the data, for three fitted K^+K^- mass regions. Here, a $E_\gamma > 0.025$ GeV cut is used for the second photon. The first error on the normalisation factors is statistical whereas the second is systematic (from the cut on the energy of the second photon).

K^+K^- mass interval (GeV)	$q\bar{q}MC$	$otherMC$	$data-otherMC$	normalization factor
$[0.95; 1.1]$ interm. χ^2 cut	31.2 ± 7.2	5.1 ± 1.3	33.1 ± 11.0	$1.14 \pm 0.60 \pm 0.38$
$[1.1; 3]$ interm. χ^2 cut	409.3 ± 26.0	12.7 ± 2.5	236.9 ± 23.2	$0.58 \pm 0.09 \pm 0.07$
$[3; 5]$ interm. χ^2 cut	95.3 ± 11.5	14.3 ± 2.6	64.1 ± 10.8	$0.69 \pm 0.19 \pm 0.07$
$[3; 5]$ tight χ^2 cut	64.7 ± 9.5	1.7 ± 0.8	9.3 ± 5.2	$0.16 \pm 0.10 \pm 0.14$

much the π^0 signal, are used to estimate a systematic error on the normalization.

The ratio of the π^0 yields in $q\bar{q}$ MC and data, after subtraction of the estimated contributions from samples other than $q\bar{q}$, provides the normalization (see Table 2.5) [2].

The normalization in the tight χ^2 region is possible only in the high mass region, where we benefit from the relatively low KK background for the π^0 peak. The normalization factors in the two other regions are obtained from the one determined at high mass (from events with different kinematical configuration), averaged with the ones at low mass but intermediate χ^2 (from events with higher multiplicity). They account for: 0.65 ± 0.5 in the ϕ mass region and 0.37 ± 0.21 between 1.1 and 3 GeV.

[2]There is a possible overestimation of the error on the normalization factor, due to the implicit inclusion of an error from the free width of the gaussian in the $q\bar{q}$ MC fit. Actually, the systematic effect from the width is expected to essentially cancel in the ratio.

2.8.4 Data χ^2 Distributions

The χ^2 distributions for the data are shown in Fig. 2.34. We can clearly identify the regions containing essentially signal events, as well as the one containing the $q\bar{q}$ and $K^+K^-\eta\gamma$ backgrounds. For all the mass regions, the tails of events with small angle additional ISR photons is clearly visible (along the $\ln(\chi^2_{addFSR}+1)$ axis), as in simulation. On the contrary, we see a tail along the $\ln(\chi^2_{addISR}+1)$ axis due to large-angle additional ISR photons, which is not present in simulation (where only the FSR contribution is seen). The contribution of large angle ISR is indeed dominant in that χ^2 region, since FSR is suppressed by the large mass of the kaons.

2.8.5 Mass spectra for backgrounds

The mass spectra of the main backgrounds (except $\mu\mu\gamma$ and $\pi\pi\gamma$) from the MC samples are shown in Fig.: 2.35 to 2.37. These plots were obtained with the tight χ^2 cut in the high mass region (this is the cut which will be used for the final result) and the loose cut below 1.1 GeV (for the tight cut, the background is very small in this mass region). For all these plots, the MC samples are normalized to the data, as explained before.

There is no background left from the $\pi^+\pi^-2\pi^0$ and K_SK_L channels, once the χ^2 cuts are applied.

The total background (notwithstanding the $\mu^+\mu^-\gamma$ and $\pi^+\pi^-\gamma$ channels) left after the various χ^2 cuts is indicated in Fig. 2.38 and its fraction with respect to data is shown in Fig. 2.39. In the ϕ mass region, this background is dominated by the $K^+K^-\eta\gamma$ events, peaking in the same region. However, this background with many additional photons in the final state is situated in the bad-χ^2 region (the ISR fit, with the additional photon supposed along the beam, is worse than the FSR fit of these events) and hence efficiently removed by the χ^2 cut. A very small ϕ peak is also observed in the $q\bar{q}$ background. Actually, this fraction of background (together with the efficiency of the χ^2-cut extimated from MC) are used to optimize the shape of the χ^2-cut.

The $\mu\mu \to\ 'KK'$ and $\pi\pi \to\ 'KK'$ backgrounds corrected for data/MC differences in mis-ID, as a function of the invariant KK mass are shown in Fig. 2.40. They are subtracted from data, together with the other backgrounds estimated before. The $\pi\pi \to\ 'KK'$ from the ρ (here showing up at $m_{KK} \approx 1.2$ GeV) represents about 20% of the data, while the $\mu\mu \to\ 'KK'$ background is relatively important only at large KK mass.

2.8.6 Mass spectra for signal

The mass spectra of the K^+K^- signal in the MC is shown in Fig. 2.41.

In Fig. 2.42 we plot the K^+K^- mass spectrum in the data, with two different χ^2 cuts. Besides the strong ϕ signal, other structures are visible in the $1.6-2.5$ GeV mass region, as well as a signal at the J/ψ and ψ' resonances.

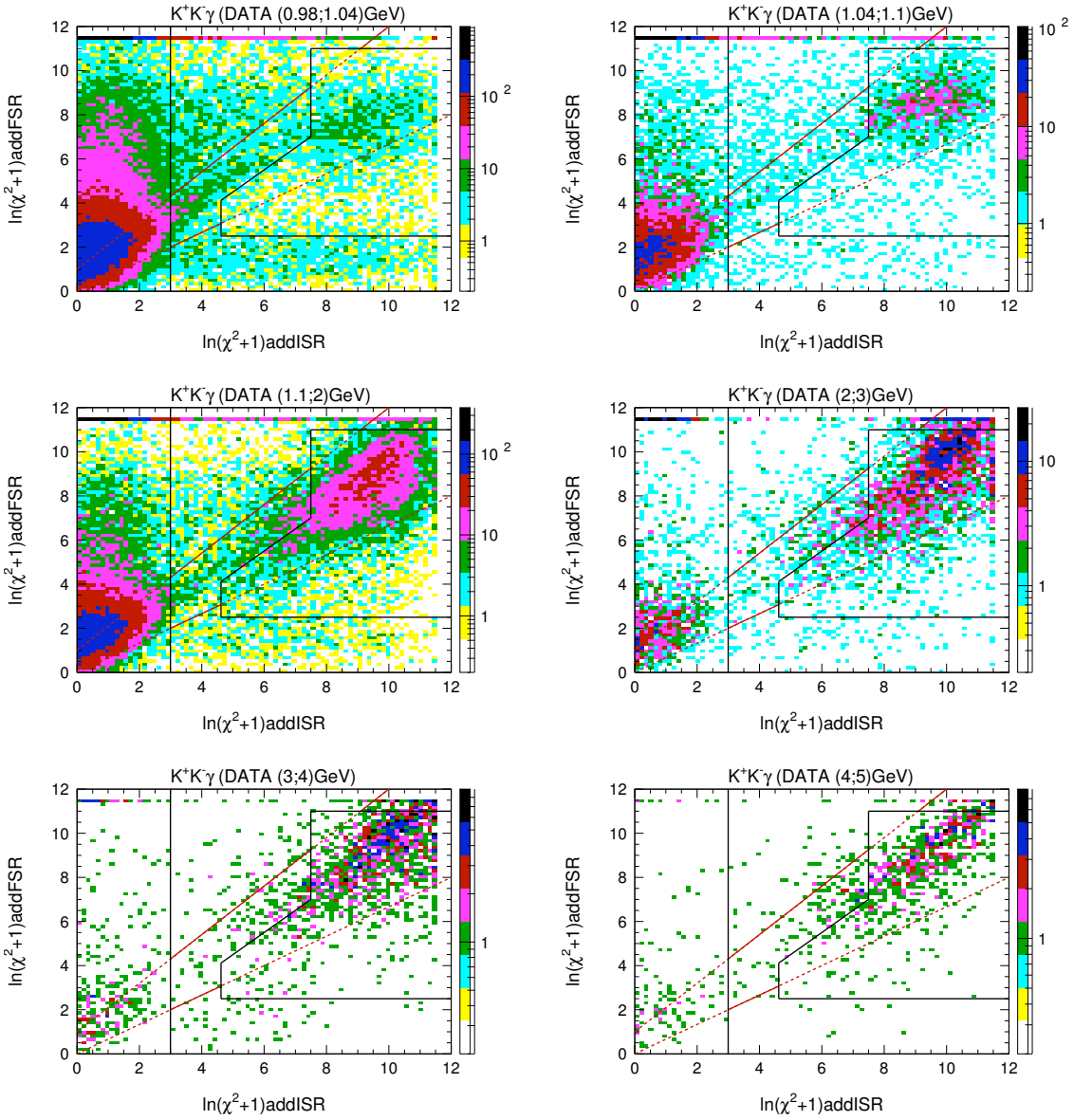

Figure 2.34: χ^2 plane for the data sample. The plots correspond to the KK mass regions (from top to bottom and left to right): [0.98;1.04], [1.04;1.1], [1.1;2], [2;3], [3;4] and [4;5] GeV. The black lines indicate the limits of the loose and tight region respectively. The red lines divide the intermediate region (between loose and tight) into three: (additional) ISR (top), diagonal (middle) and (additional) FSR (bottom).

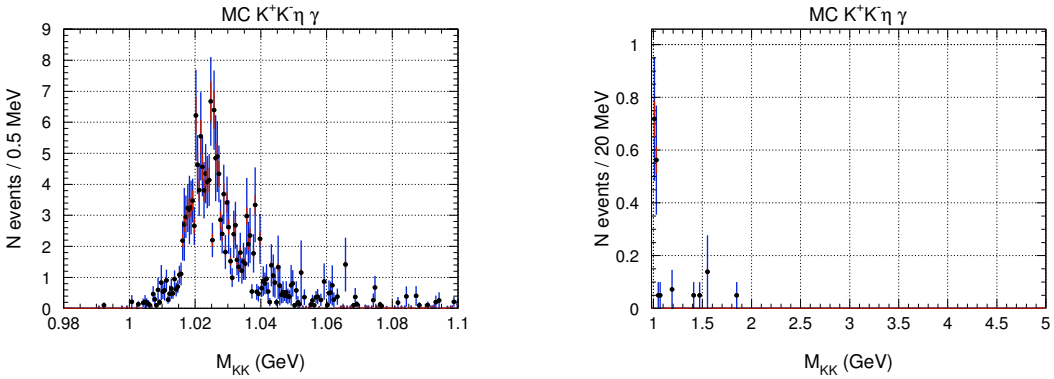

Figure 2.35: Mass spectrum for the $K^+K^-\eta\gamma$ background on the MC sample, after the loose χ^2 cut(left) and tight χ^2 cut(right). The red error bars indicate the systematic error from the normalization (published cross section plus uncertainties at high generated mass), while the blue ones indicate the total error.

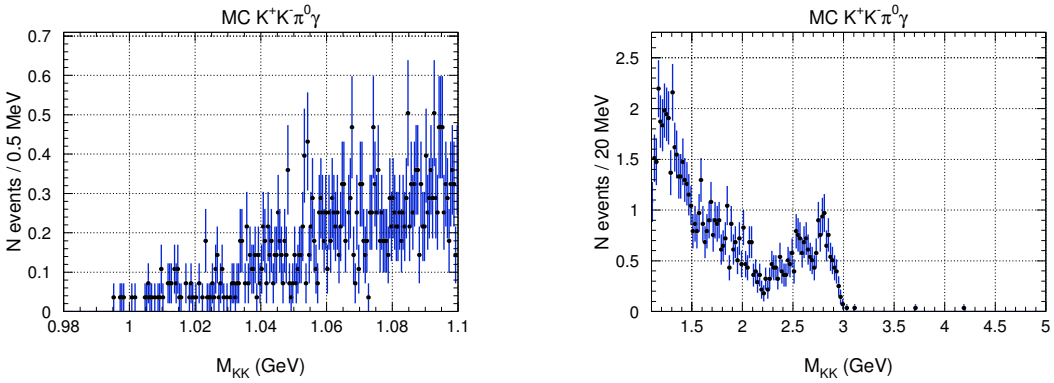

Figure 2.36: Mass spectrum for the $K^+K^-\pi^0\gamma$ background on the MC sample, after the loose χ^2 cut(left) and tight χ^2 cut(right).

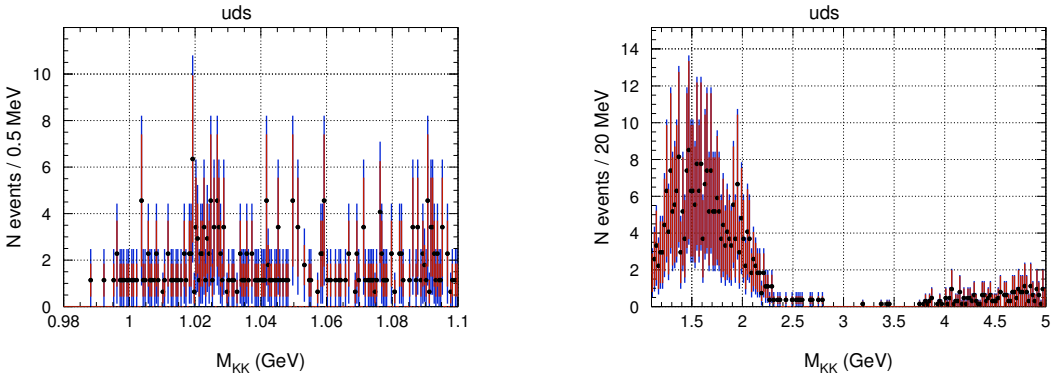

Figure 2.37: Mass spectrum for the $q\bar{q}$ MC sample, after the loose χ^2 cut(left) and tight χ^2 cut(right). The red error bars indicate the correlated (by mass region) systematic errors due to the normalization factors, while the blue error bars correspond to the total errors.

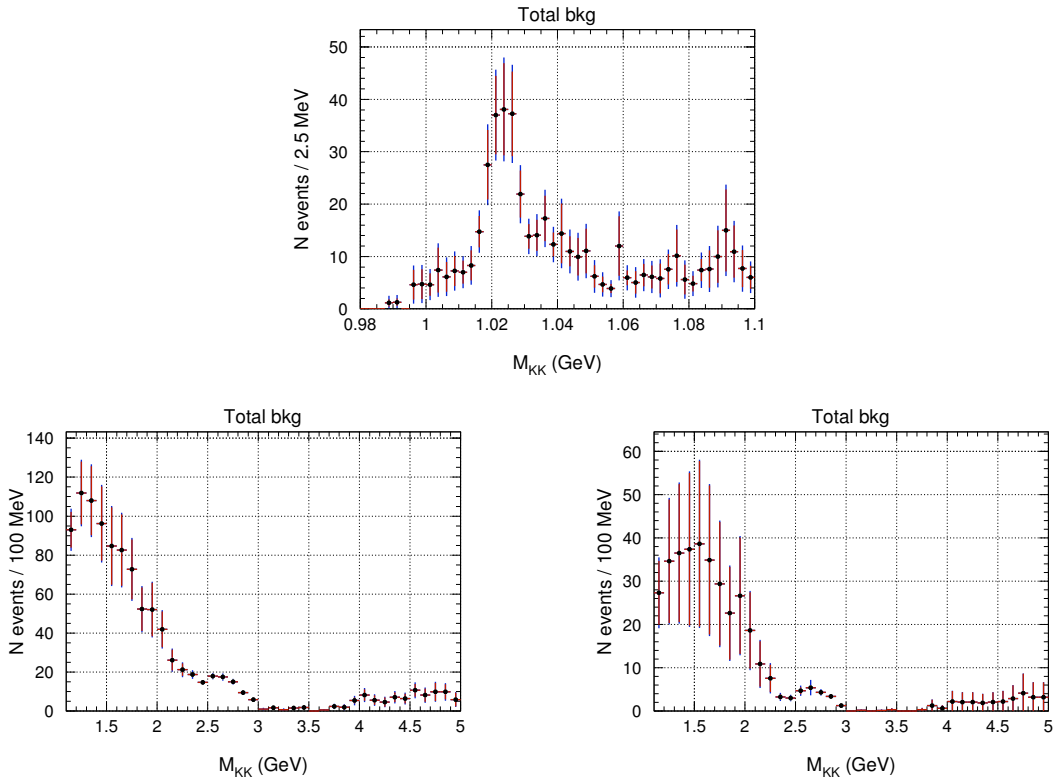

Figure 2.38: Total background computed on the MC ($\mu^+\mu^-\gamma$ and $\pi^+\pi^-\gamma$ backgrounds are not included here). The plots correspond to the [0.95;1.1] GeV region with loose χ^2 cut (top), and to the [1.1;5.] GeV region with the moderate χ^2 cut (bottom left) and with the tight(final) χ^2 cut (bottom right). The red error bars include the correlated (by mass region) systematic errors due to the normalization factors of the $q\bar{q}$ MC and also the one for the $K^+K^-\eta\gamma$, while the blue error bars correspond to the total errors.

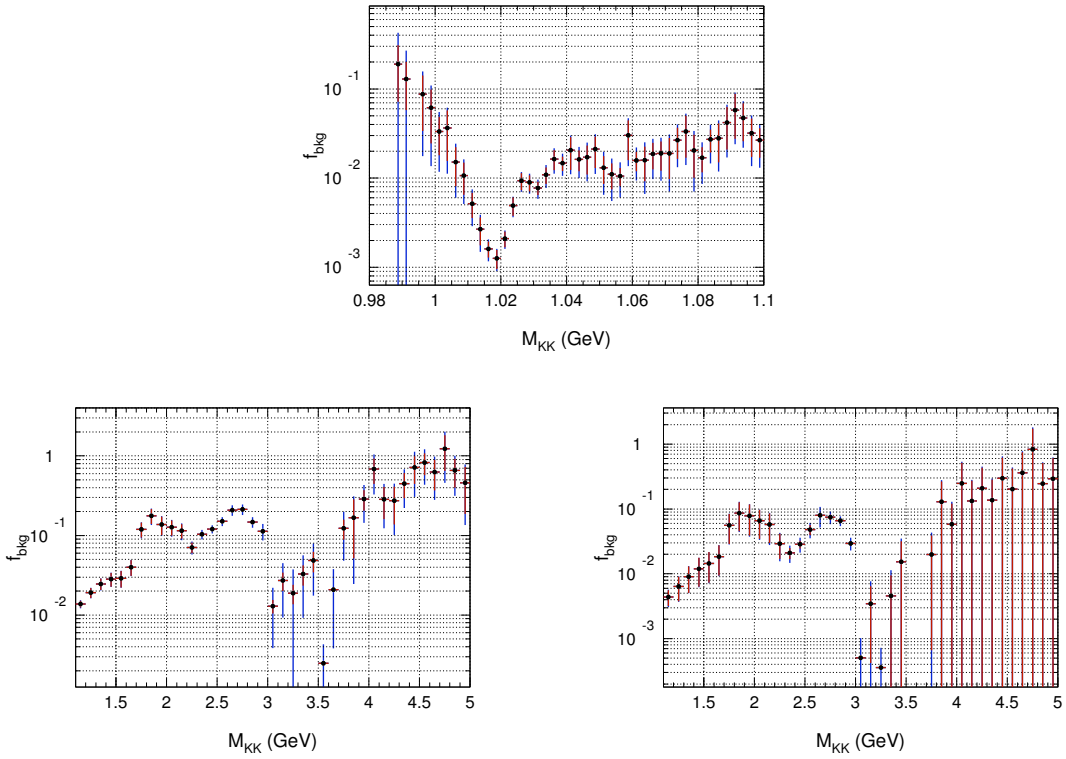

Figure 2.39: Fraction of background in the data ($\mu^+\mu^-\gamma$ and $\pi^+\pi^-\gamma$ backgrounds are not included here). The plots correspond to the [0.95;1.1] GeV region with loose χ^2 cut (top), and to the [1.1;5.] GeV region with the moderate χ^2 cut(bottom left) and with the tight(final) $\chi 2$ cut(bottom right). The red error bars include the correlated (by mass region) systematic errors due to the normalization factors of the $q\bar{q}$ MC and also the one for the $K^+K^-\eta\gamma$, while the blue error bars correspond to the total errors (including statistical errors from data and MC).

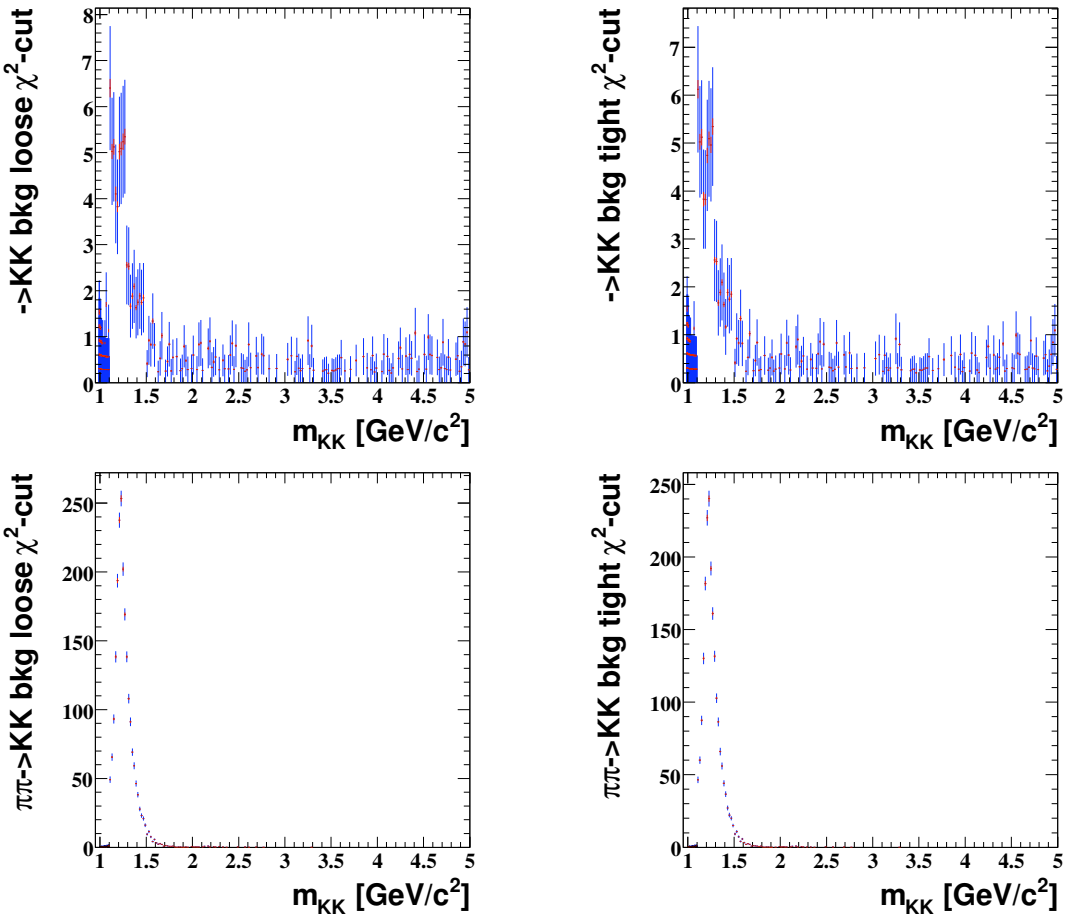

Figure 2.40: The $\mu\mu \rightarrow$ $'KK'$ (top) and $\pi\pi \rightarrow$ $'KK'$ (bottom) backgrounds corrected for data/MC differences in mis-ID, as a function of the invariant KK mass. The plots correspond to the loose χ^2-cut (left) and to the tight χ^2-cut (right). The red error bars indicate the strongly correlated errors from the data/MC corrections for mis-ID, whereas the blue ones are obtained from the diagonal of the covariance matrix once the statistical errors of the MC are included. The systematic error on the data/MC correction for the muons (see text) is not included here.

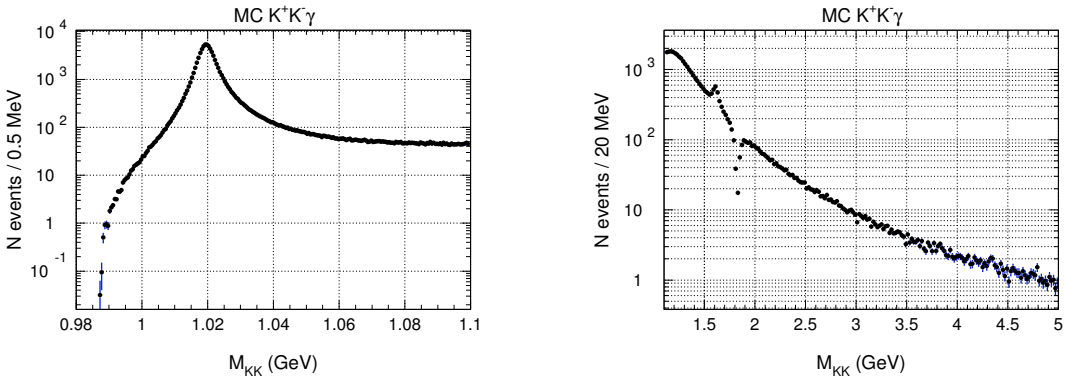

Figure 2.41: Mass spectrum for the $K^+K^-\gamma$ signal on the MC sample, after the loose χ^2 cut(left) and tight χ^2 cut(right).

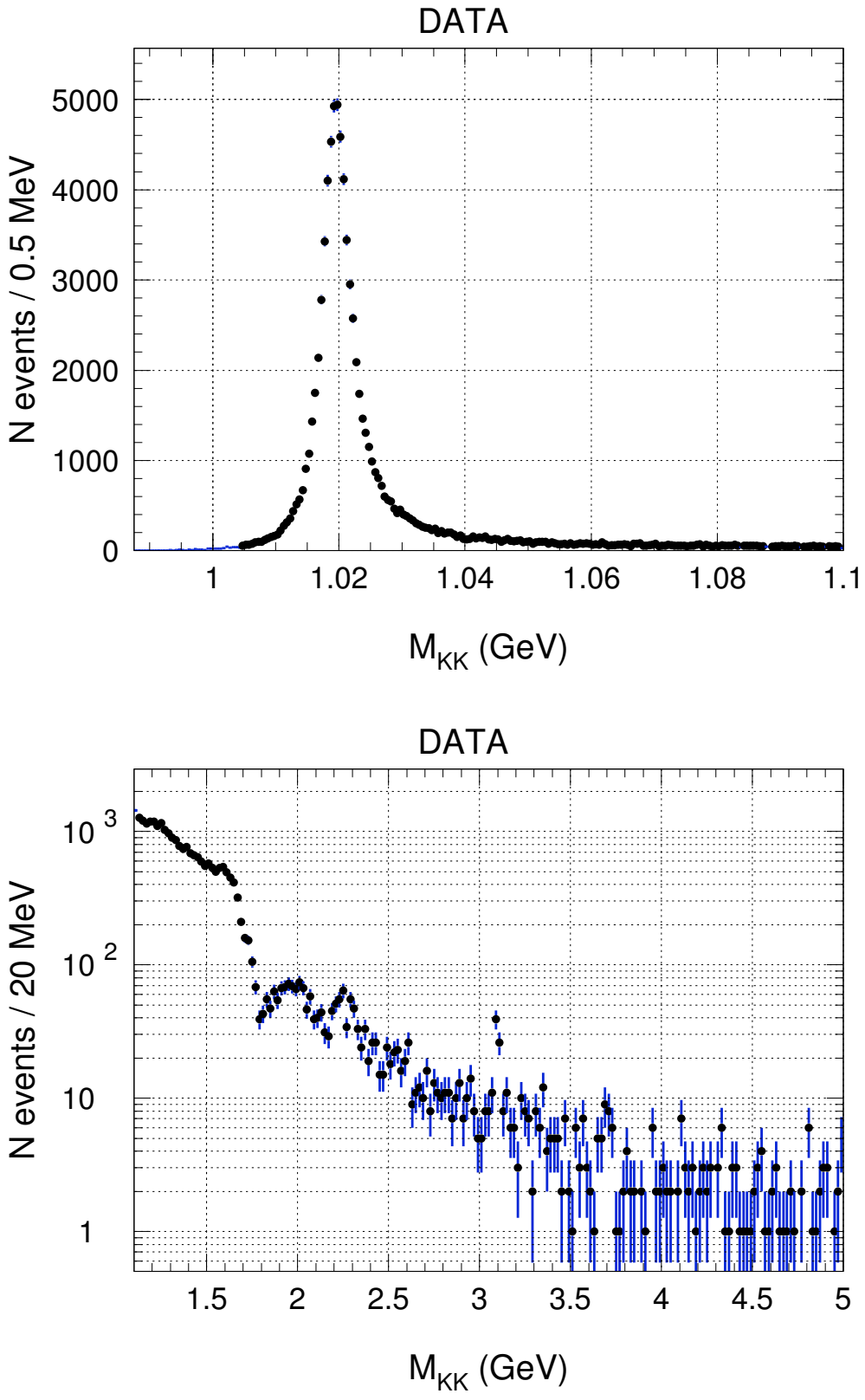

Figure 2.42: K^+K^- mass spectrum for the data sample, after the loose χ^2 cut (top) and tight χ^2 cut (bottom).

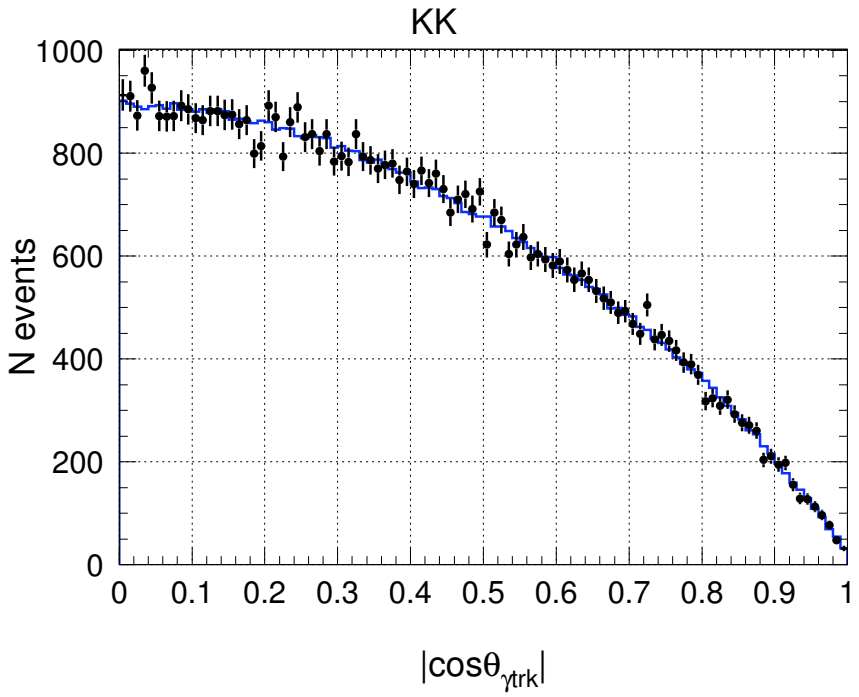

Figure 2.43: Distributions of the absolute value of the cosine of the angle between the ISR photon and the charged tracks in the KK center-of-mass, for data (black points) and MC (blue histogram). The MC distribution was normalized to the number of events in data.

2.8.7 Angular distribution of the ISR photon

Fig. 2.43 shows the distributions of the cosine of the angle between the ISR photon and the charged tracks in the KK center-of-mass frame, for data and MC. The two distributions are compatible, following the expected $\sin^2\theta$ shape.

2.9 Study of the Efficiency of the χ^2 Cut

2.9.1 Strategy

The χ^2 cut applied to remove the background in the KK sample also produces a loss of signal events. Therefore, just as for the other cuts, its efficiency must be measured, i.e. data/MC corrections must be applied to the total acceptance from simulation.

The rejected signal events with large χ^2 are of several types:

- problems in the reconstruction of the direction of the ISR photon,
- problems in track reconstruction,
- tails of the χ^2 distribution of events with additional ISR and FSR,
- more than one additional photon (mostly ISR),
- secondary interactions.

The last type is specific to kaons, but all the other sources are common to kaons and muons. So the $\mu\mu\gamma(\gamma)$ sample, with its very small background, will be used to determine the common χ^2-cut efficiency. However, differences between KK and $\mu\mu$ samples must be handled. In particular the tail of the FSR-fit χ^2 is different for kaons and muons, following the different FSR level. Kaon decays are not expected to contribute much at this level of the analysis, due to particle ID. Indeed, if one of the kaons decays in flight, a mis-ID must occur for one of the decay products (a muon or pion), in order for the event to be kept in our physics sample. Furthermore, decays are expected to be well simulated and, as they produce a change in the track direction, possible differences (in reconstruction) with respect to data are treated together with those due to secondary interactions.

So at the first order, one can follow the method used in the $\pi\pi$ analysis [29], i.e. study the data/MC correction for χ^2-cut efficiency with the $\mu\mu$ sample, and add the effects of secondary interactions and differences in the amount of FSR. The last two corrections are important mainly in the intermediate diagonal and FSR regions respectively. However, further differences between kaons and muons were observed in the intermediate ISR (and diagonal) region, for data, while good agreement was observed when comparing MC simulations in this region. This discrepancy is related to the dominant contribution in the χ^2_{addISR} tail of additional large angle ISR in data, not present in simulation. Due to the mass difference, the effect on kinematics, hence the χ^2_{addISR} fit, is different in $KK\gamma$ and $\mu\mu\gamma$ channels. Therefore, at the second order, one must correct for this effect which is present and can be measured only in data.

In fact, the data/MC correction for the efficiency of the χ^2 cut can be studied directly at the ϕ resonance, where the background in the intermediate χ^2 region is small and at a manageable level. The strategy is to use the efficiency obtained with kaons (on data) at the ϕ , and to rely on the muon studies for the extrapolation of the data/MC correction

to higher masses, assuming the $KK/\mu\mu$ data/MC effect to be independent of the KK mass. Therefore, the data/MC correction for the χ^2-cut efficiency, outside the ϕ mass region, will be derived from the following expression:

$$\frac{\epsilon_{\chi^2}^{KK\gamma(\gamma)\text{data}}}{\epsilon_{\chi^2}^{KK\gamma(\gamma)\text{MC}}}(m) = \frac{\epsilon_{\chi^2}^{\mu\mu\gamma(\gamma)\text{data}}}{\epsilon_{\chi^2}^{\mu\mu\gamma(\gamma)\text{MC}}}(m) \cdot \left(\frac{\epsilon_{\chi^2}^{KK\gamma(\gamma)\text{data}}}{\epsilon_{\chi^2}^{KK\gamma(\gamma)\text{MC}}}\right)^{\text{sec.int.}}(m) \cdot \left[\frac{\left(\epsilon_{\chi^2}^{KK\gamma(\gamma)\text{data}}/\epsilon_{\chi^2}^{KK\gamma(\gamma)\text{MC}}\right)^{\text{sec.int.rem.}}}{\epsilon_{\chi^2}^{\mu\mu\gamma(\gamma)\text{data}}/\epsilon_{\chi^2}^{\mu\mu\gamma(\gamma)\text{MC}}}\right]_{\phi}, \quad (2.13)$$

where the first term on the right side provides the data/MC correction for muons, the second one gives the correction for kaon secondary interactions, while the last term, evaluated at the ϕ peak, accounts for the kaon to muon difference in data/MC correction (excluding the correction due to interactions, specific to kaons). Another implicit assumption here (but tested in the following studies) is that FSR is well simulated for muons, while it is very small and also (sufficiently) well simulated for kaons. The contributions of the FSR and secondary interactions components, measured with simulation, are separated and the second one is corrected for data/MC discrepancies.

As they are applied before the unfolding, data/MC corrections should be expressed as a function of m_{KK}. However, since the mass resolution strongly varies across the χ^2 plane, we prefer to express it as a function of $\sqrt{s'}$ (in any case, the χ^2 efficiency only makes sense as a function of $\sqrt{s'}$). The inefficiency of the χ^2 cut predicted by simulation is shown in Fig. 2.44.

Now we already have all the needed elements to make a choice between the tight and moderate χ^2 cuts, for the high mass region. Indeed, the moderate cut has only a sligtly larger efficiency (by about 1.5%), but it also keeps significantly more non mis-ID background in data (according to Fig. 2.39, it is at least twice as large comparing to the one with the tight cut). It is for these reasons that we prefer the tight χ^2 cut at masses larger than 1.1 GeV.

Following the guideline described by Eq. 2.13, we proceed to study (1) the additional radiation for $\mu\mu$ and KK to control this common part with its differences, (2) the χ^2-cut efficiency for muons, (3) the effect of secondary interactions for kaons, and finally (4) the full study of the K/μ χ^2-cut efficiency using the pure ϕ sample.

2.9.2 Study of additional radiation

Additional small-angle ISR

For the study of additional ISR photons at small angles to the beam, the cuts $\ln(\chi^2_{addFSR}+1) > \ln(\chi^2_{addISR}+1)$ and $E^*_{\gamma addISR} > 200$ MeV are used, where $E^*_{\gamma addISR}$ is the energy of the additional ISR photon in the e^+e^- CM frame (derived from the additional ISR fit).

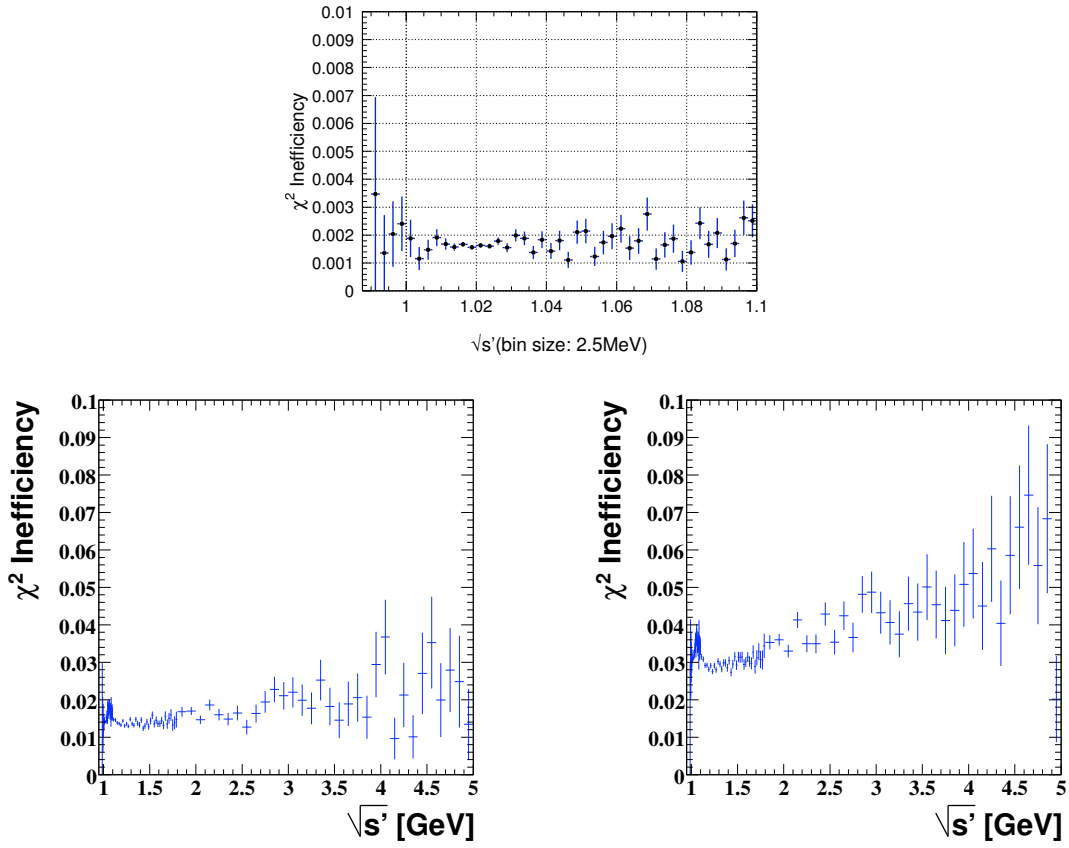

Figure 2.44: Inefficiency of the χ^2 cuts, as predicted by MC simulation. The plots correspond to the regions of generated $K^+K^-(\gamma_{FSR})$ ($\sqrt{s'}$) mass: [0.95;1.1] GeV with a loose χ^2 cut (top), and [0.95;5.] GeV with a moderate χ^2 cut (bottom left) and a tight χ^2 cut (bottom right).

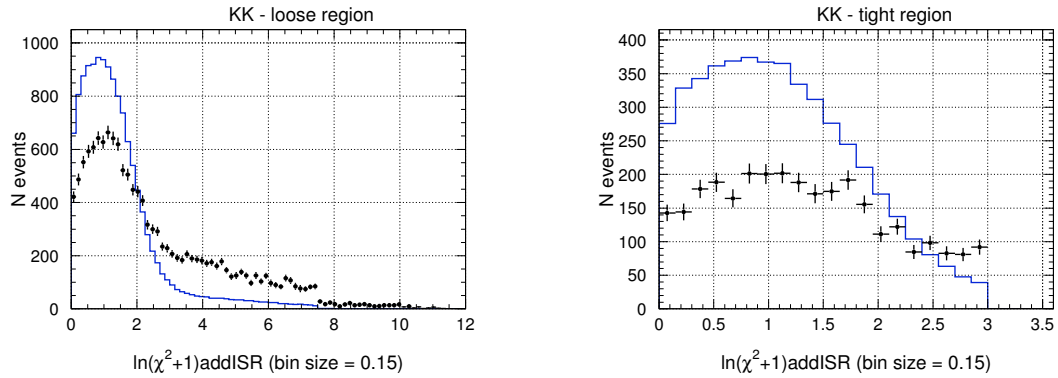

Figure 2.45: χ^2_{addISR} distribution for KK data after background subtraction (black) and MC (blue). The plots correspond to the [0.95;1.1] GeV mass region with a loose χ^2 cut (left), and to the [1.1;5.] GeV region with a tight χ^2 cut (right).

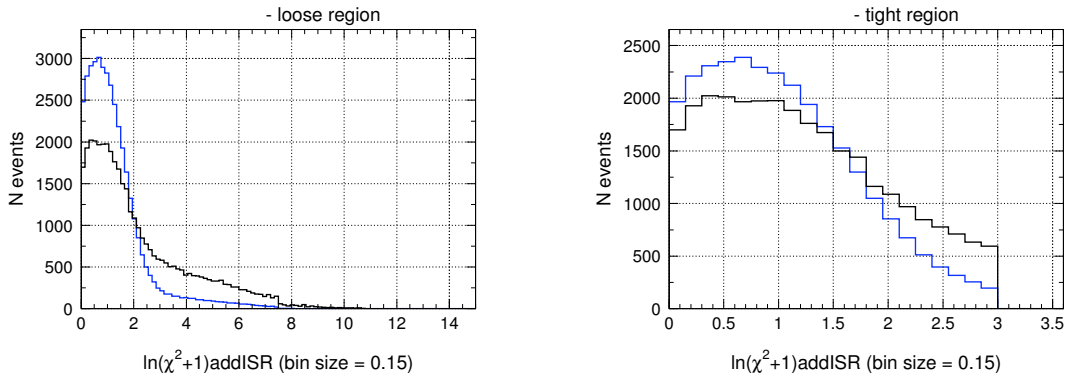

Figure 2.46: χ^2_{addISR} distribution for $\mu\mu$ data(black) and MC (blue). The plots correspond to masses lower than 1 GeV, with a loose χ^2 cut (left) and a tight χ^2 cut (right). In each plot, the MC was normalized to the number of events in data.

Fig. 2.45 shows the χ^2_{addISR} distribution for these events. Just as it is observed for muons (see Fig. 2.46), the agreement is poor for the $KK\gamma$ channel because of the additional ISR photons in AfkQed are generated through the structure function method and exclusively along the beams. As the fit supposes the additional ISR along the beam, it is rather good for the MC. This is not the case for the data, where we can have large angle ISR, producing a very significant tail for the χ^2 distribution.

Fig. 2.47 shows the CM energy distribution of the additional ISR photons as determined by the fit. The distributions drop in simulation around 2.3 GeV as a result of the $m_{KK\gamma(\gamma FSR)} > 8$ GeV cut used at generation level. Below that γ energy, good agreement between data and MC simulation is observed for the ϕ region, while a systematic discrepancy is observed at higher masses. Actually, even at high mass, these distributions have a good agreement in shape, but the normalization is off. This effect, as well as the difference between ratios of amplitudes on the peak in the two comparisons in Fig. 2.45, can be explained by a significant difference for the kaon form factor in data and simulation,

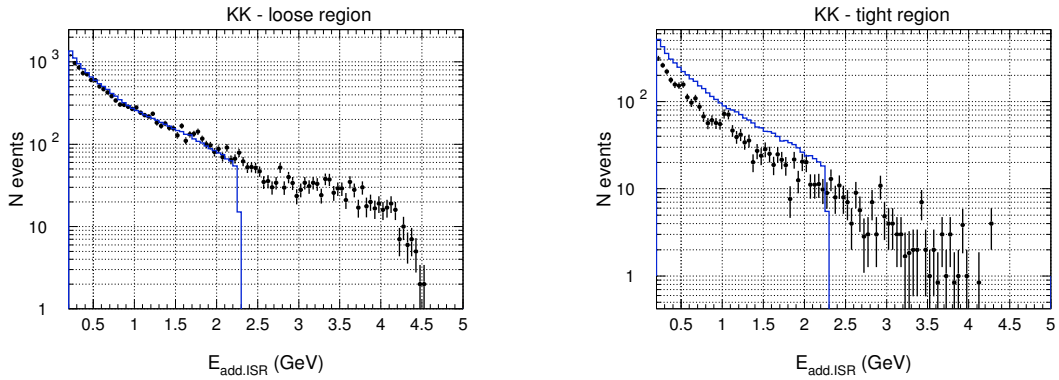

Figure 2.47: Energy distribution of the additional ISR photon in the center-of-mass, for KK data after background subtraction (black) and MC (blue). The plots correspond correspond to the [0.95;1.1] GeV mass region with a loose χ^2 cut (left), and to the [1.1;5.] GeV region with a tight χ^2 cut (right).

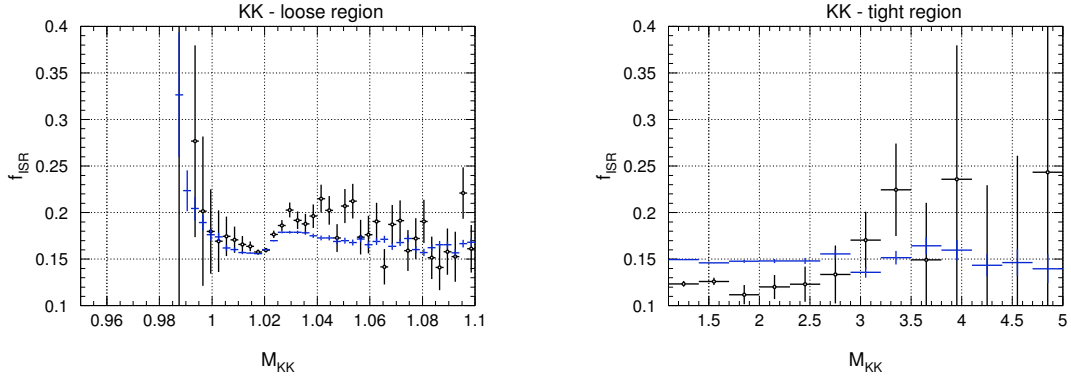

Figure 2.48: Fraction of events with ($\ln(\chi^2_{addFSR}+1) > \ln(\chi^2_{addISR}+1)$ and $E^*_{\gamma addISR} > 200$ MeV) as a function of the fitted K^+K^- mass, for data(black) and MC(blue). The plots correspond correspond to the loose χ^2 cut (left), and to the tight χ^2 cut (right).

in the high mass region. The distribution in data can also be reduced with respect to MC because of the fraction of events with a detected large angle additional ISR photon. These events have a good χ^2_{addFSR} and are not included in the sample considered in this section.

The fraction of selected events in the loose and respectively tight χ^2 regions are indicated in Fig. 2.48. It is higher in the MC because in the data the ISR photons have an angular distribution, and events with a large angle ISR should have a good FSR fit. While the plots in Fig. 2.48 show some variation across the ϕ region (due to FSR), this dependence is removed when plotting the same quantities as a function of $\sqrt{s'}$ in the MC (see Fig. 2.49), which is the relevant variable for ISR photon emission.

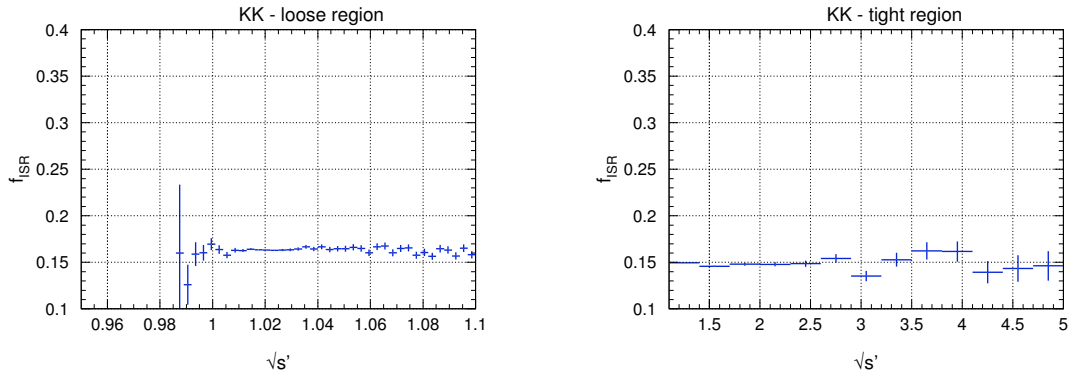

Figure 2.49: Fraction of events with ($\ln(\chi^2_{addFSR}+1) > \ln(\chi^2_{addISR}+1)$ and $E^*_{\gamma addISR} > 200$ MeV) as a function of $\sqrt{s'}$, in the MC. The plots correspond correspond to the loose χ^2 cut (left), and to the tight χ^2 cut (right).

Additional FSR and large-angle ISR, for kaons and muons

For the study of additional FSR and large angle ISR photons, we select events passing the cuts $\ln(\chi^2_{addFSR}+1) < \ln(\chi^2_{addISR}+1)$ and $E_{\gamma 2} > 200$ MeV in the lab frame. FSR photons are emitted preferentially in the direction of the final-state charged particles. Fig. 2.50 shows the distribution of the angle between the 'FSR' photon and the closest muon. The FSR peak is clearly visible at low angle, in data and MC. The contribution of large angle ISR (not simulated in AfkQed) is visible only in data. For kaons (see Fig. 2.51) the data is dominated by the large ISR signal, with some evidence for FSR as predicted by the MC. At large KK masses there is still a weak evidence for FSR, also consistent with the MC. The accumulation of events in the region between 110° and 150° is from fake photons corresponding to a satellite of the large ISR photon shower. Actually, it is the same effect that creates the fake π^0 peak in the non-$q\bar{q}$ backgrounds, as explained in Section 2.8.3. This accumulation of events at large angle is also present for muons and pions, but since there is more FSR radiation (due to the smaller muon and pion masses) their relative effect is smaller.

In order to compare the amount of FSR events in data and MC (generated with PHOTOS in AfkQED) we fit the data angular distribution in Fig. 2.51, for angles smaller than 40°, with the shape from the MC (histogram), plus a first order polynomial for the large angle ISR contribution. We find a data/MC ratio for the amount of FSR events of 1.44 ± 0.95, consistent with unity within a large error. Furthermore, it should be pointed out that the corresponding fraction of events is very small ($5 \cdot 10^{-4}$ level, according to Fig. 2.55).

Fig. 2.52 shows the χ^2_{addFSR} distribution for data and MC, for events in the loose and respectively tight χ^2 region. A large discrepancy is observed for the amount of events, due to the lack of large angle ISR photons in the MC. However, as the events containing such a photon in data generally have a good χ^2_{addFSR}, there is a fair agreement in shape (given the effect of the loose cut at 2.5 and the absence of large angle ISR in MC).

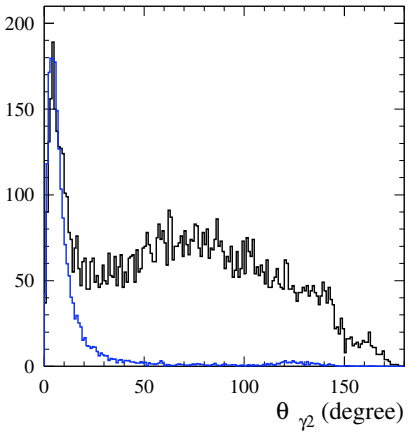

Figure 2.50: The additional 'FSR' photon angular distribution with respect to the closer outgoing muon for the $\mu\mu\gamma(\gamma)$ events with $\ln(\chi^2_{addFSR}+1) < \ln(\chi^2_{addISR}+1)$, $E_{\gamma_{add\ FSR}} > 200$ MeV and $m_{\mu\mu} < 1$ GeV (data: black, MC: blue). MC is normalized to data according to the luminosity.

A better data - MC agreement is observed in Fig. 2.53 where we show the energy distribution of the additional FSR photons in the lab frame, for events with an additional photon making an angle with the closest charged track smaller than 20°. However the 'background' from large angle ISR photons is still large ($\sim 50\%$) preventing an accurate comparison of the E_γ distributions.

In Fig. 2.54 we show the fraction of selected events in the loose and respectively tight χ^2 region as a function of m_{KK} We observe again a large discrepancy between data and simulation for the same reason. While the MC plots in Fig. 2.54 show some variation across the ϕ resonance [3], this dependence is removed when plotting the same quantities as a function of $\sqrt{s'}$ (see Fig. 2.55).

In order to get closer to a selection of FSR events we ask $E_{\gamma addFSR} > 200$ MeV and the angle between the direction of the FSR photon (taken from the FSR fit) and the closest charged track to be smaller than 20°, and we also remove events close to the diagonal in the χ^2 plane (see Fig. 2.56). Actually, even if they are on the FSR side of the χ^2 plane, they more likely originate from problems in track reconstruction, the existence of more than one additional photon, or secondary interactions (for kaons). In Fig. 2.56 we can also appreciate the effect of the cut on the energy of the second photon, removing events in the low χ^2 region.

In order to compute the effect of secondary interactions on the efficiency of the χ^2 cut, we will need to compare the fraction of the FSR events for the kaons and muons (see Fig. 2.57 for the plot of this fraction for the muons). As we perform an average over all the mass spectrum and the FSR emission is mass dependent, the $\mu\mu$ distributions must first be reweighted using the KK mass distribution. We measure the χ^2 efficiency on the

[3]This effect is observed only for events with additional FSR photons (MC). It is not observed for data, where they are dominated by large angle ISR.

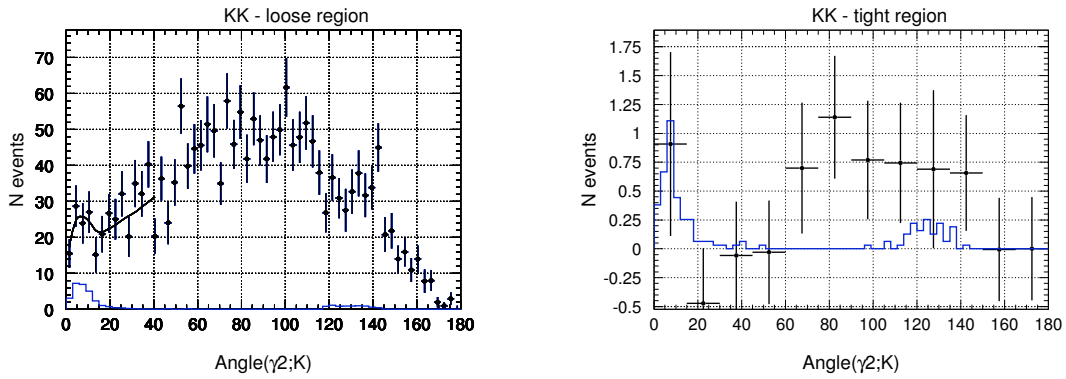

Figure 2.51: Second photon angle (degrees) with the closest kaon for data after background subtraction (black) and KK MC (blue). The plots correspond to the [0.95;1.1] GeV region (left), and to the [1.1;5.] GeV region (right). The MC has been normalized to the luminosity. The fit for the data/MC comparison for the amount of FSR events(see text) is also shown in the left plot.

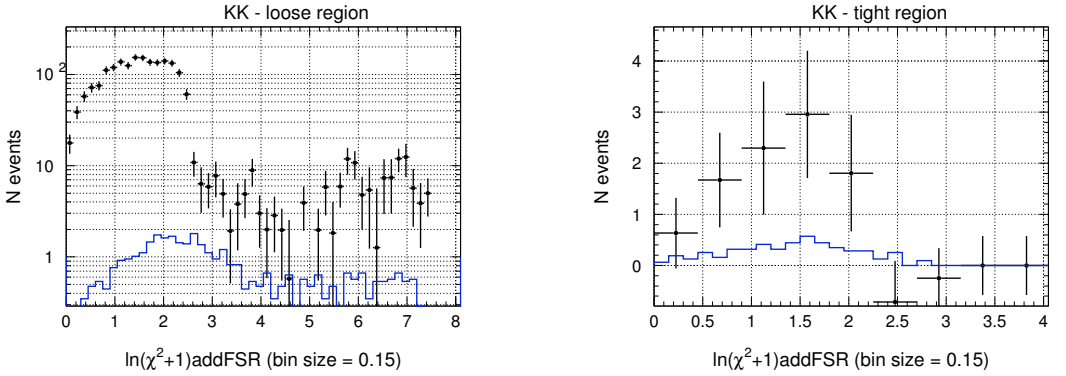

Figure 2.52: χ^2_{addFSR} distribution, for data after background subtraction (black) and MC (blue). The plots correspond to the [0.95;1.1] GeV mass region with a loose χ^2 cut (left), and to the [1.1;5.] GeV region with a tight χ^2 cut (right).

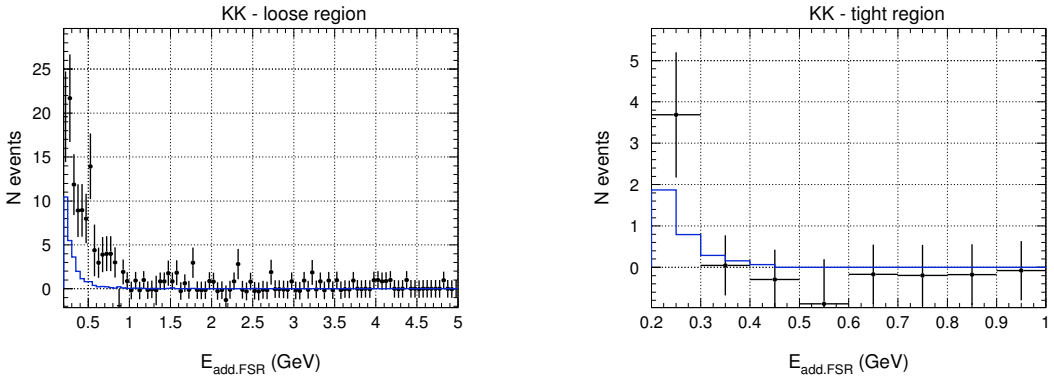

Figure 2.53: Energy distribution of the additional FSR photon in the lab frame, for events where the angle between the FSR photon and the closest kaon trace is smaller than 20°. The plots show data after background subtraction(black) and MC(blue). They correspond to the [0.95;1.1] GeV mass region with a loose χ^2 cut (left), and to the [1.1;5.] GeV region with a tight χ^2 cut (right).

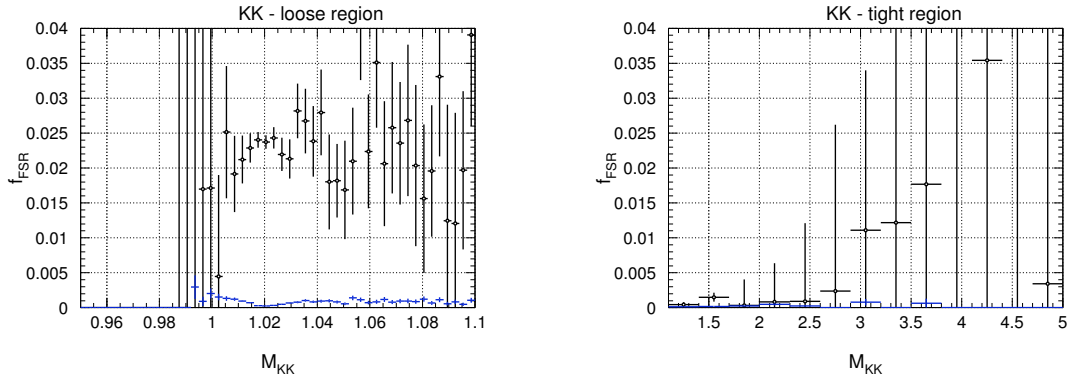

Figure 2.54: Fraction of events with $(\ln(\chi^2_{addFSR}+1) < \ln(\chi^2_{addISR}+1)$ and $E_{\gamma addFSR} >$ 200 MeV), as a function of the reconstructed K^+K^- mass, for data after background subtraction (black) and MC (blue). The plots correspond to the loose χ^2 cut (left), and to the tight χ^2 cut (right).

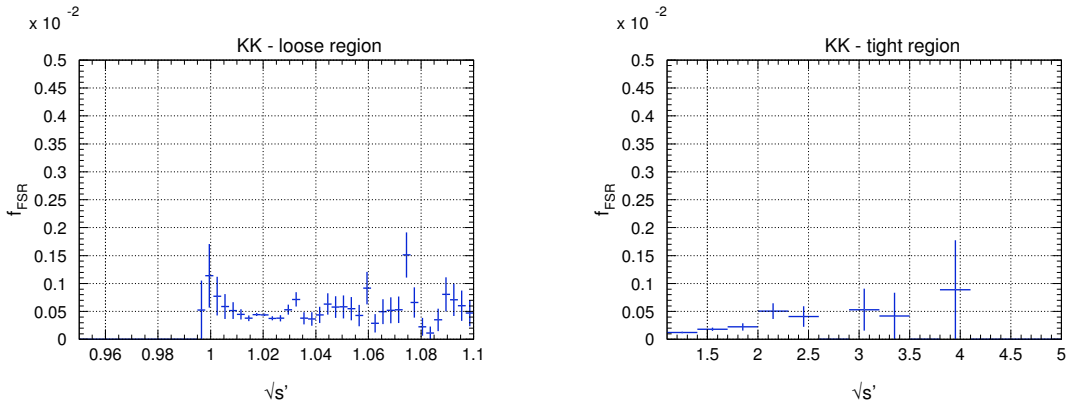

Figure 2.55: Fraction of events with $(\ln(\chi^2_{addFSR}+1) < \ln(\chi^2_{addISR}+1)$ and $E_{\gamma addFSR} > 200$ MeV), as a function of $\sqrt{s'}$, in the MC. The plots correspond to the loose χ^2 cut (left), and to the tight χ^2 cut (right).

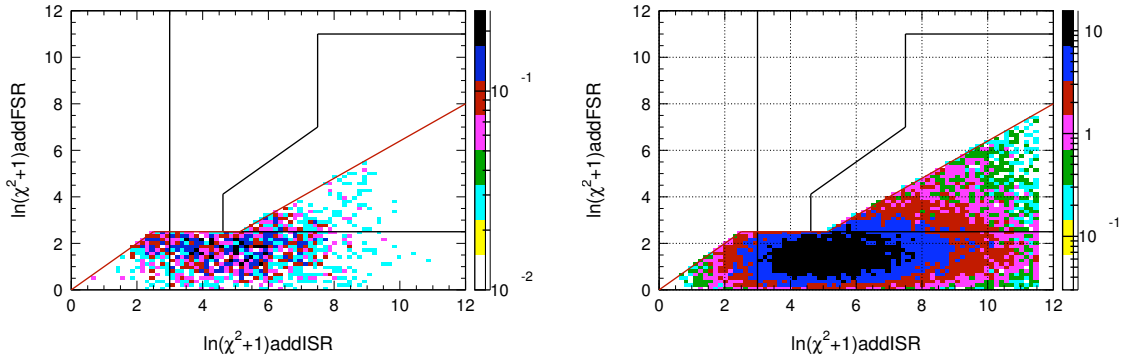

Figure 2.56: χ^2 distribution of events in a tight FSR cut (red curve), with an FSR photon at an angle with the closest muon smaller than 20° and $E_{\gamma addFSR} > 200$ MeV. The plots are done for KK(left) and $\mu\mu$(right) MC, for $\sqrt{s'} \in [0.95; 5]$GeV.

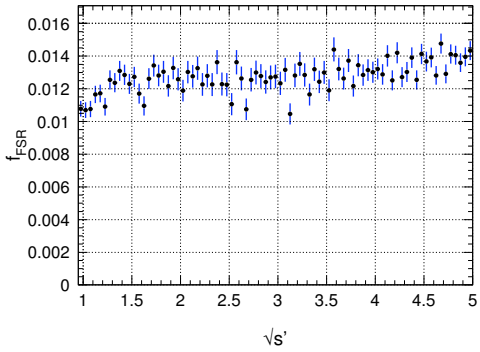

Figure 2.57: Fraction of events in the tight FSR region of Fig. 2.56, with an additional FSR photon at an angle smaller than 20° with the closest muon and $E_{\gamma addFSR} > 200$ MeV, as a function of $\sqrt{s'}$, in the $\mu\mu$ MC. This distribution is independent of the reweighting with the KK lineshape.

Table 2.6: Fraction of FSR events, and efficiencies of the χ^2 cuts for the corresponding sample. The quantities are computed for KK, $\mu\mu$ and "reweighted" $\mu\mu$ MC samples (see text).

channel	$f_{FSR}(\times 10^{-3})$	$\epsilon(\chi^2_{loose})\|_{FSR}$	$\epsilon(\chi^2_{tight})\|_{FSR}$
$\mu\mu$	12.76 ± 0.07	0.847 ± 0.002	0.0595 ± 0.0013
$\mu\mu$ reweighted	11.02 ± 0.35	0.833 ± 0.012	0.0646 ± 0.0078
KK	0.45 ± 0.01	0.865 ± 0.009	0.1165 ± 0.0080

sample of FSR events as defined above (see Table 2.6). While the inefficiencies on that sample are of the same order of magnitude for kaons and muons, the relative fraction of FSR is much smaller for kaons, as expected from the rough estimate:
$f^{KK}_{FSR} \sim f^{\mu\mu}_{FSR} \times \left(\frac{m_\mu}{m_K}\right)^2 = 0.51 \pm 0.02$.

As we saw before, we find no significant difference between the number KK events with additional FSR, in MC with respect to the data. As a conclusion, using the results from Table 2.6 and the previous data/MC ratio, the possible bias (due to FSR) on the efficiency of the χ^2 cut estimated with the MC is negligible: $(0.03 \pm 0.06) \times 10^{-3}$ for the loose cut, and $(0.18 \pm 0.38) \times 10^{-3}$ for the tight cut.

For comparable mass regions (around the ϕ mass for kaons, and up to 2 GeV for muons), about $(4.04 \pm 0.06)\%$ of the events in the loose χ^2 region are situated in the FSR intermediate region for $\mu\mu$ data events, whereas the same fraction for kaons yields $(2.68 \pm 0.06)\%$. The difference is in relatively good agreement with the (well simulated) fraction of events with additional FSR for the muons, which, for the same mass region, is $(1.21 \pm 0.01)\%$. This test shows that (within the approximation of the $\mu\mu$ mass interval used) there is the same fraction of events with additional large angle ISR for kaons and muons (as expected from factorization of additional ISR in the two processes).

2.9.3 Study of the χ^2 cut efficiency for muons

As we explained in the beginning of this section, in order to obtain the total data/MC correction of the χ^2 efficiency for kaons, we first need to perform the corresponding study with the $\mu\mu$ data and MC samples. This will yield the correction (as a function of mass) for the effects common to kaons and muons. Actually, the muons are much less affected by background than kaons, in the loose as well as in the background χ^2 region (see Fig. 2.58). This is the reason why we can perform this complete study (on data and MC, up to 5 GeV) for muons, but not for kaons.

The main backgrounds for the $\mu\mu\gamma$ sample originate from pions and kaons. Their distributions, after data/MC corrections for mis-ID, are shown in Fig. 2.59. As expected, these backgrounds are enhanced in the ρ and ϕ mass regions ("seen" as a function of the fitted $\mu\mu$ mass). The $\pi\pi$ background is significantly larger for the runs 3-4 due to the degradation of the IFR, while KK background is less enhanced, due to the positive kaon identification in the DIRC. Concerning the other backgrounds, the main component

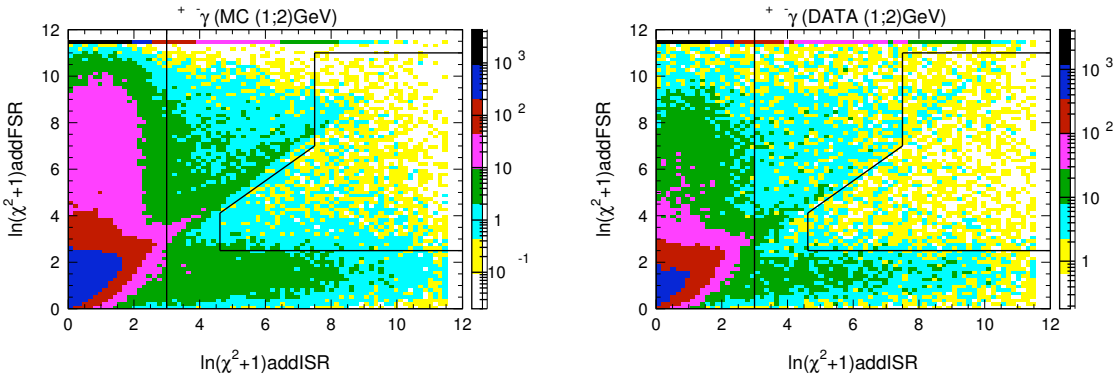

Figure 2.58: The χ^2 plane for $\mu^+\mu^-$ events with a fitted mass between 1 and 2 GeV/c^2 for MC simulation (left) and data (right).

comes from $\tau^+\tau^-(\gamma)$ events (through $\mu\mu$, $\mu\pi$ and fully hadronic final states) followed by $q\bar{q}$ and $\pi^+\pi^-\pi^0\gamma$. Small backgrounds from $p\bar{p}\gamma$, $\pi^+\pi^-\pi^0\pi^0\gamma$, $\pi^+\pi^-\pi^+\pi^-\gamma$, $\pi^+\pi^-\pi^+\pi^-\pi^0\pi^0\gamma$ and $K_SK_L\gamma$ are obtained directly from MC, normalized and/or reweighted as explained before.

One must still consider background to the $\mu\mu$ sample from processes producing real muons. ISR-produced J/ψ decay to $\mu\mu$ is considered as a background since the determination of the ISR luminosity only involves the QED contribution to $ee \to \mu\mu$. The ψ' case is different as it contributes to the studied reaction as a background through its decay to J/ψ, either following the $\pi^0\pi^0 J/\psi$ transition or radiative decays through charmonium states. Evidence for direct and indirect J/ψ production is given in Fig. 2.60. Both contributions are removed excluding events where the measured $\mu\mu$ mass is in the $3.0 - 3.2$ GeV/c^2 window. Since for the analysis we use the fitted $\mu\mu$ mass, this cut does not produce a sharp hole in the final mass spectrum. For this reason, together with an asymmetric effect introduced by this cut in the fitted mass (related to FSR) , we remove a larger ($2.95 - 3.3$ GeV/c^2) mass interval when computing the efficiencies and the final corrections.

Another hidden background from J/ψ comes from the radiative decay $J/\psi \to \mu^+\mu^-\gamma$. This contribution is found to be of the order of 1 10^{-3} (see [28]) and neglected.

The efficiencies of the loose and tight χ^2 cuts for the muons, for data and MC are shown in Fig. 2.61, separately for runs 1-2 and 3-4. We observe a decrease of efficiency in data and MC, when going from threshold to higher masses, due to the increase of the amount of additional FSR. There is also a small increase of efficiency between 4 and 5 GeV, which is absent in the efficiency distribution as a function of $\sqrt{s'}$ (see Fig. 2.63). It is due to the fact that events with strong additional FSR photons (hence a bad ISR fit) have a fitted KK mass significantly lower than $\sqrt{s'}$. The loss of efficiency at the threshold is due to additional ISR radiation, while it adds to the FSR effect at higher masses. It is different in data and MC due to the angular distribution of additional ISR photons in data, not reproduced by the simulation. The corresponding data/MC corrections are plotted as a function of mass in Fig. 2.62. They account for about 1% in the case of the

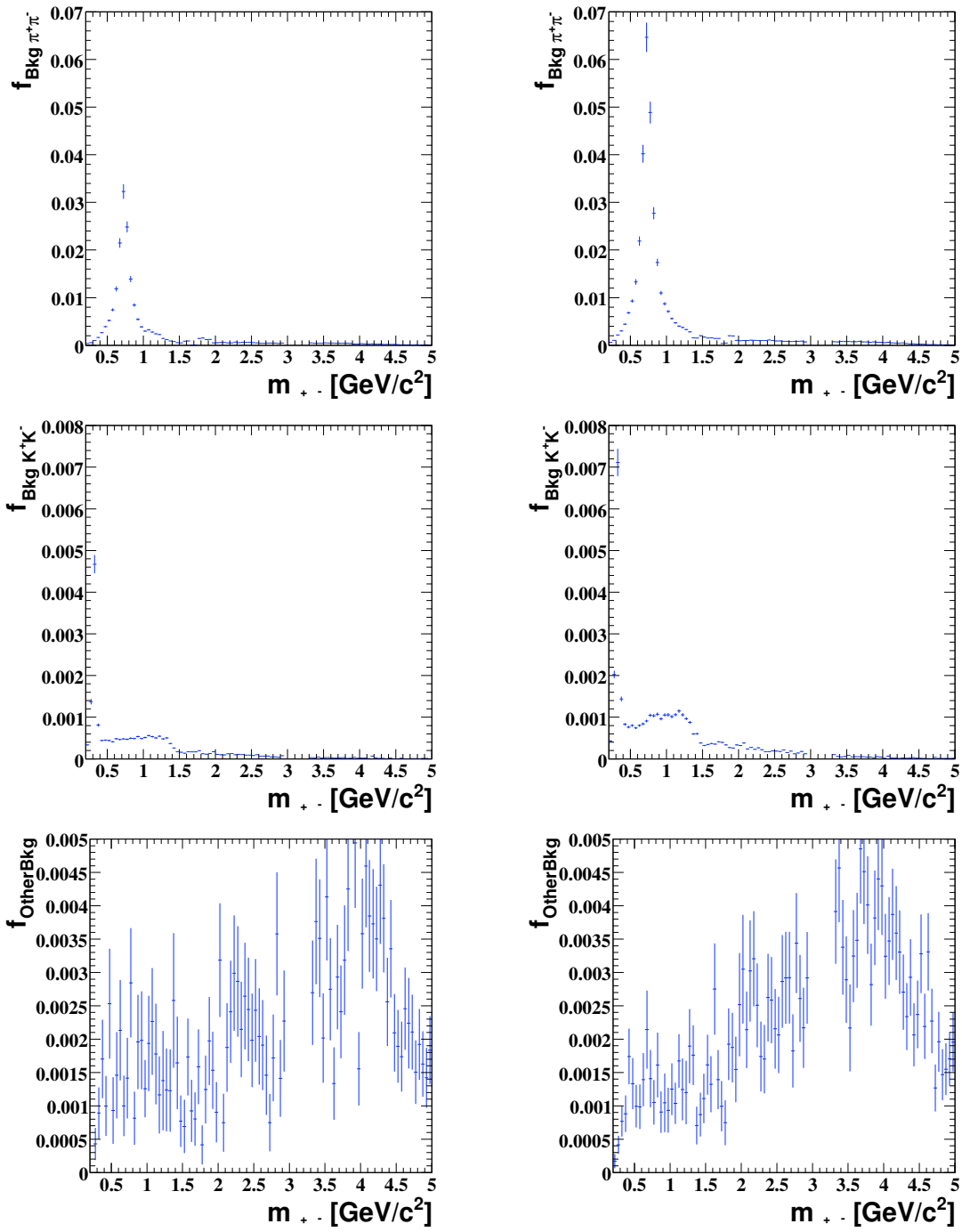

Figure 2.59: The fractional background in the $\mu^+\mu^-\gamma$ spectrum, from $\pi^+\pi^-\gamma$ (top), $K^+K^-\gamma$ (middle) and other sources (mainly $\tau^+\tau^-$)(bottom). The plots correspond to the runs 1-2 (left) and 3-4 (right), for events in all the χ^2 plane. Only the errors coming from the background are plotted here. While $\pi^+\pi^-\gamma$ and $K^+K^-\gamma$ are obtained from particle-ID, the other backgrounds are subtracted statistically, using MC with data/MC normalization and mis-ID corrections.

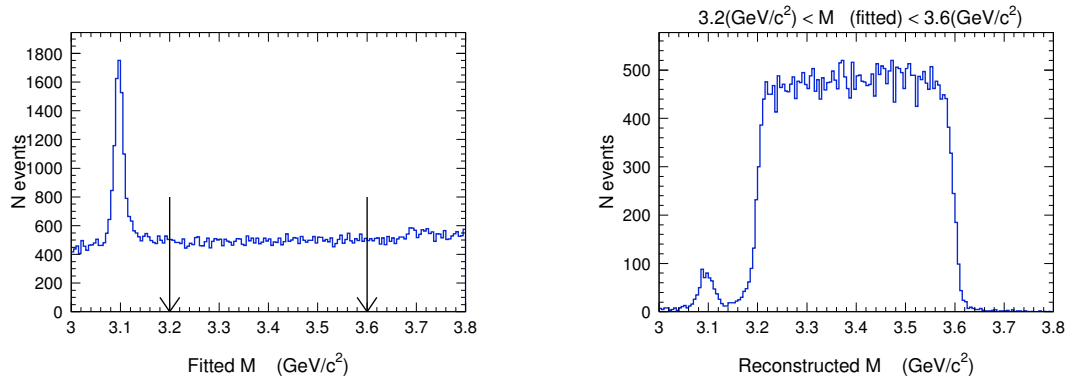

Figure 2.60: The $\mu^+\mu^-$ mass spectrum obtained from the result of the kinematic fit (left) and directly computed from reconstructed tracks for the events with fitted $\mu^+\mu^-$ mass between 3.2 and 3.6 GeV/c^2 (right), for data events in all the χ^2 plane.

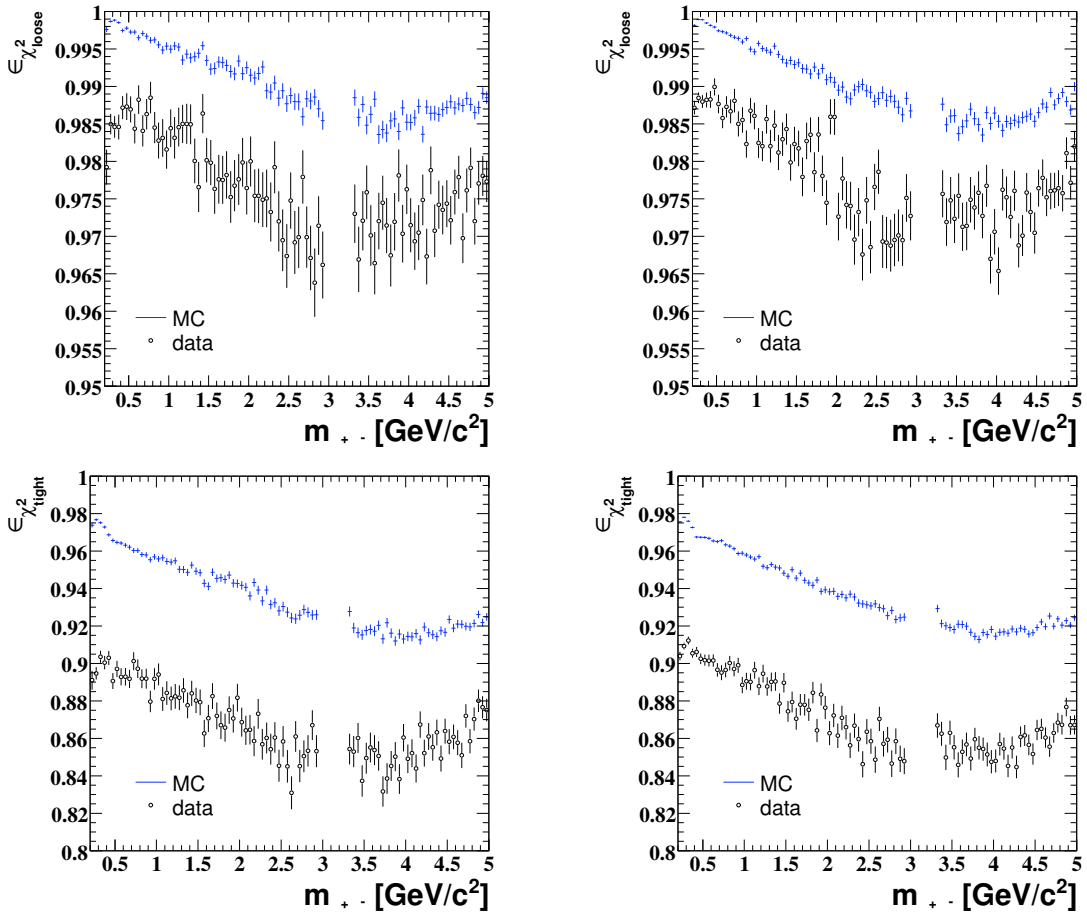

Figure 2.61: Efficiency of the loose χ^2 cut (top) and tight χ^2 cut (bottom), for the runs 1-2 (left) and 3-4 (right), as estimated from the $\mu^+\mu^-$ distributions. We show the MC in blue and the data in black, as a functions of the fitted $\mu^+\mu^-$ mass .

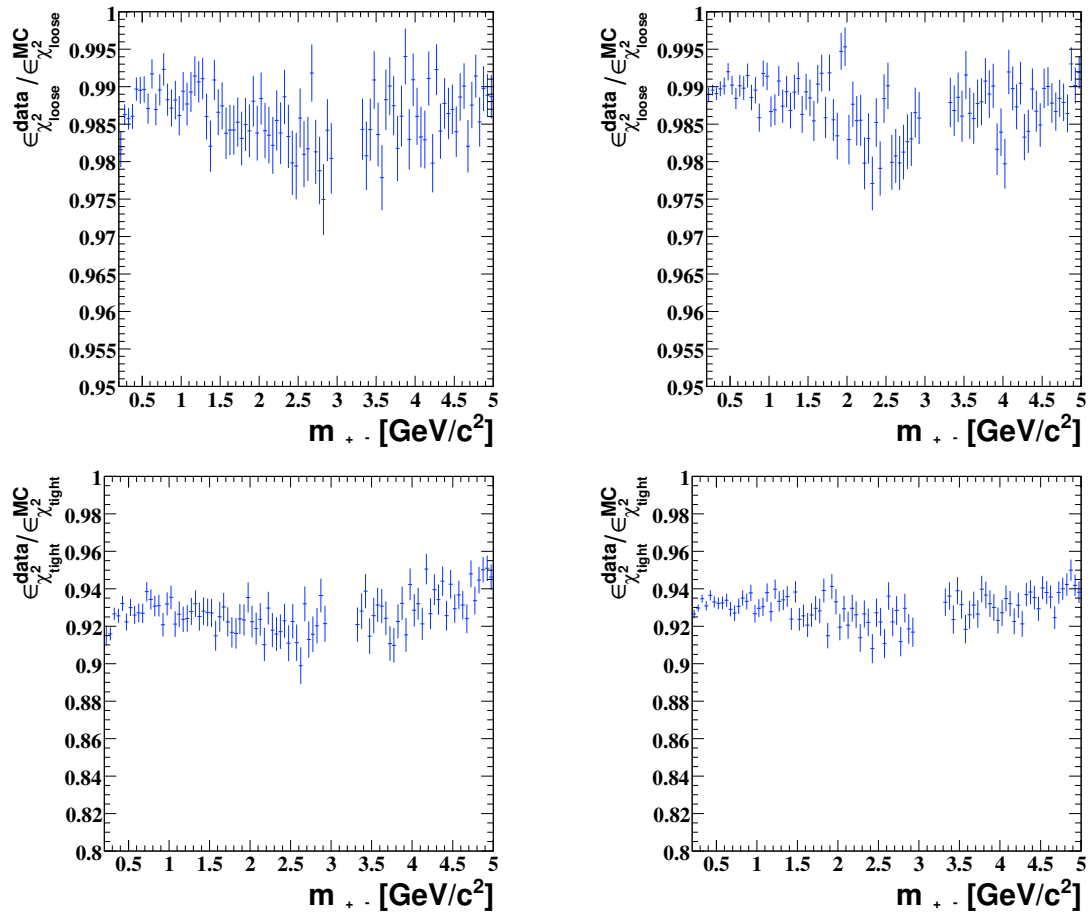

Figure 2.62: Data/MC correction for the efficiency of the loose χ^2 cut (top) and tight χ^2 cut (bottom), for the runs 1-2 (left) and 3-4 (right), as a functions of the fitted $\mu^+\mu^-$ mass .

loose cut and $7-8\%$ for tight.

The bins of the MC distributions are statistically independent, whereas correlations from the uncertainties on the normalization of the subtracted background generate small (anti-)correlations for the data. These (anti-)correlations are propagated through covariance matrices and the error corresponding to their diagonal elements are shown in Fig. 2.61 and Fig. 2.62.

A fit of the data/MC correction by a constant, in the [1;2.9] GeV mass interval, indicates a small but significant difference between the runs 1-2 and 3-4 (1.8 σ for the loose χ^2 cut and 3.0 σ for tight). It is for this reason that we distinguish the corrections for the two data sets and apply them to the corresponding spectra, before merging.

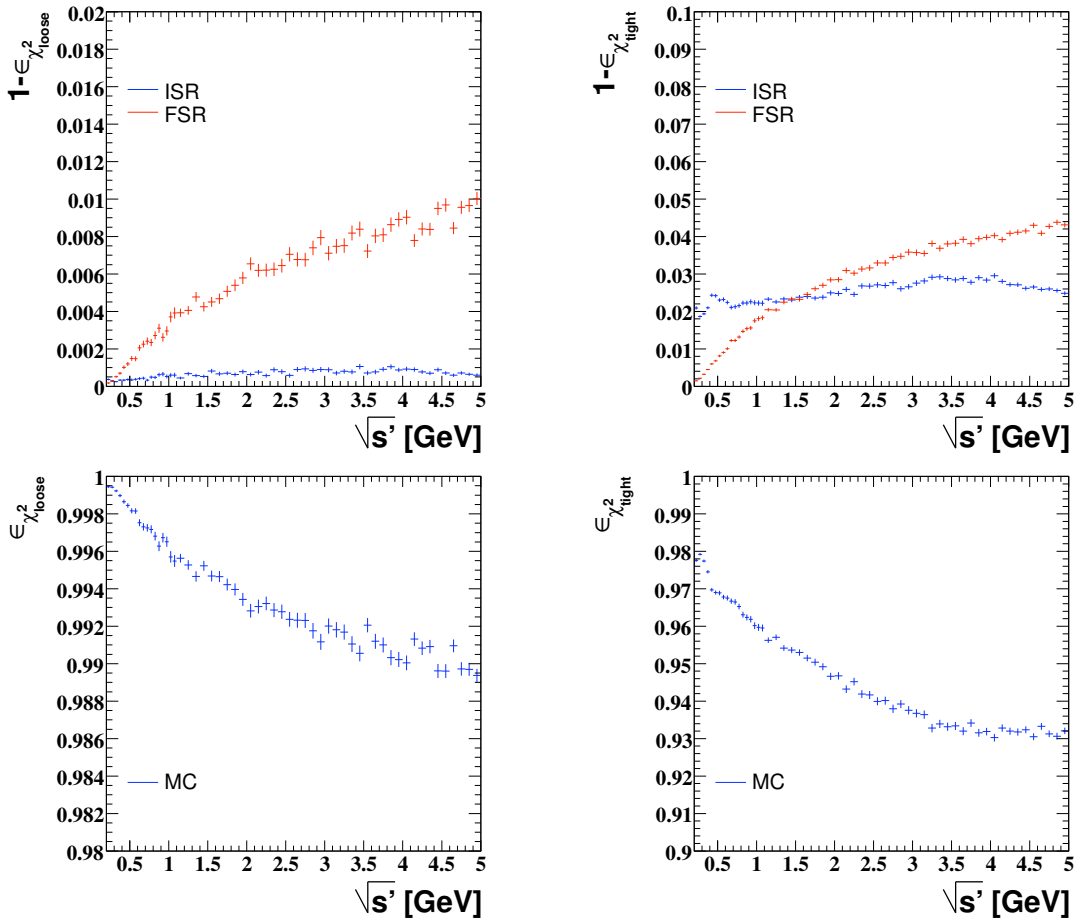

Figure 2.63: Top: fraction of events lost due to the loose(left) and tight(right) χ^2 cut, in the ISR(blue) and FSR(red) half of the χ^2 plane. Bottom: efficiency of the loose(left) and tight(right) χ^2 cut. These plots are done for the $\mu^+\mu^-$ MC and are shown as a function of $\sqrt{s'}$.

2.9.4 Effects of secondary interactions for kaons

Level of secondary interactions in the simulation

The effects of secondary interactions are mostly seen in the tracking efficiency because of the tight cuts imposed on the track pointing to the interaction region. The residual effect in the kinematic fit χ^2-cut efficiency is smaller. It is possible to estimate it using the simulation, by comparing the behaviour of muons and kaons events.

As one can see in Fig. 2.44, 2.61 and 2.63, at threshold, the efficiency of the χ^2-cut is larger for muons than for kaons, in spite of the larger fraction of FSR for muons (see Table 2.6). The lower efficiency for kaons is ascribed to interactions.

The additional FSR contribution can be derived from the χ^2-cut (in-)efficiency as a function of $\sqrt{s'}$, due to the loss of events in the corresponding half of the χ^2 plane (see Fig. 2.63). The loss of additional ISR events through the loose χ^2 cut is small in simulation since in AfkQed additional ISR is collinear to the beam, hence results in good χ^2. The

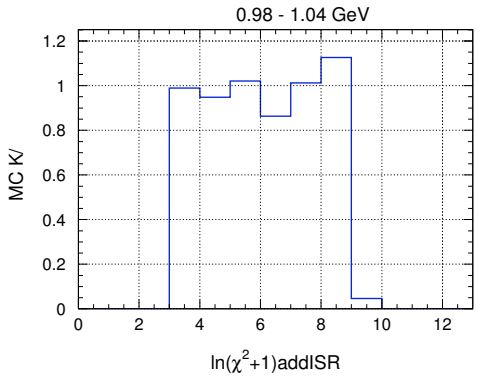

Figure 2.64: Ratio of the fractions of events in the intermediate ISR region of the χ^2-plane (diagonal region excluded), for kaons and muons, as a function of $\ln(\chi^2_{addISR}+1)$. This plot is obtained for MC simulation.

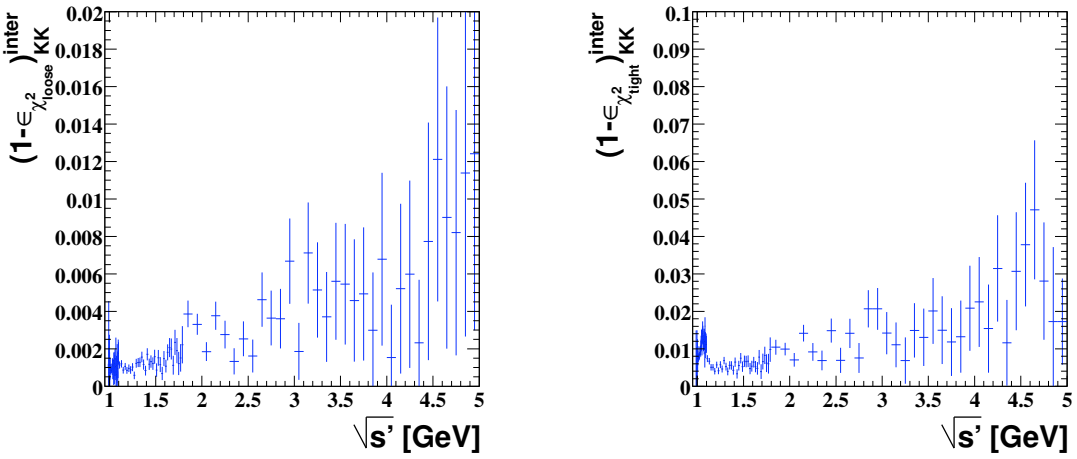

Figure 2.65: χ^2-efficiency loss due to secondary interactions, for the loose(left) and tight(right) χ^2 cut. The diagonal errors are plotted.

same loss with the tight χ^2 cut is however larger. Taking into account the difference of FSR for kaons and muons, one can derive the contribution of secondary interactions to the χ^2-cut efficiency for kaons (inefficiencies are noted $\bar{\epsilon}$):

$$\bar{\epsilon}^{inter}_{KK}(\sqrt{s'}) = \overline{\epsilon_{KK}} - \overline{\epsilon_{\mu\mu}} + \bar{\epsilon}^{FSR}_{\mu\mu} \cdot \left(1 - \frac{f^{FSR}_{KK}}{f^{FSR}_{\mu\mu}}\right) \tag{2.14}$$

It has been tested that kaons and muons have the same behaviour as a function of $\ln(\chi^2_{addISR}+1)$ (see Fig. 2.64) in the intermediate ISR region of the χ^2 plane (where the region next to the diagonal, strongly affected by interactions for kaons, is removed).

The efficiency loss due to interactions, as estimated using the previous formula is shown in Fig. 2.65. The structure around 1.1 GeV, observed in the plot for the tight χ^2-cut, was already present in the KK χ^2 efficiency in the MC (Fig. 2.44). The same type of structure is seen for the muons, close to the $\mu\mu$ threshold (see Fig. 2.63), in data and simulation (cancelling in their ratio). This structure is strongly related to the track overlap in the

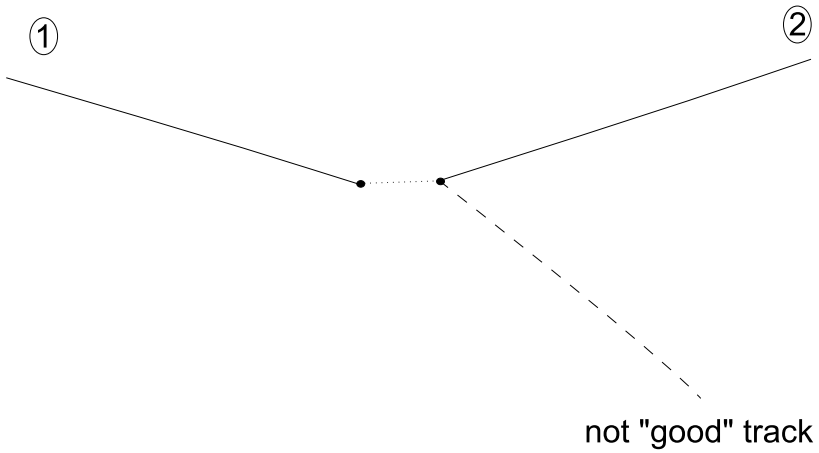

Figure 2.66: A "good" track ((2) in this figure) interacts with the detector or the beam pipe, producing a small scattering and possibly secondary (not identified "good") track.

DCH producing a loss of tracking efficiency (Section 2.6), but also some degradation of the reconstructed tracks, which affects the χ^2 efficiency. A systematic error has been assigned for this effect.

Correlations due to the different (larger) bins of the muon efficiencies, as well as the ones from the correction for the difference in the amount of FSR are propagated through a covariance matrix.

The ISR/FSR separation along the diagonal in the χ^2 plane is however not exact. After a study of the effect of different variations of this cut, a systematic error of the efficiency loss due to interactions is estimated: increasing from 0 (at the $\mu\mu$ threshold) to 0.1% at 5 GeV for the loose χ^2 cut, and from 0.1% to respectively 0.5% in the case of the tight χ^2 cut.

Even if the effect of interactions, as predicted by simulation, is quite small, it is important to check the size of the effect in data. Two methods (described in the next two sections) were developed in order to compare the rates of interacting events in data and MC.

Check of interactions in data: using secondary vertices

Interactions are tagged by the presence of 'bad' tracks (i.e. standard BABAR tracks, but not satisfying the track requirements of the ISR 2-body analysis) in addition to the two good tracks of the selected events, provided a vertex can be found between a bad track and one of the two good tracks (see Fig. 2.66). This is achieved by searching "the best intersection" in space among all possible associations (a cut is applied on the minimal distance between tracks in the z direction(dz_{min}) for the found vertices in the xy plane). The transverse distance to the beam R_{xy} of the secondary vertex, and the $doca_{xy}$ of the main ("interacting") track are used in this analysis.

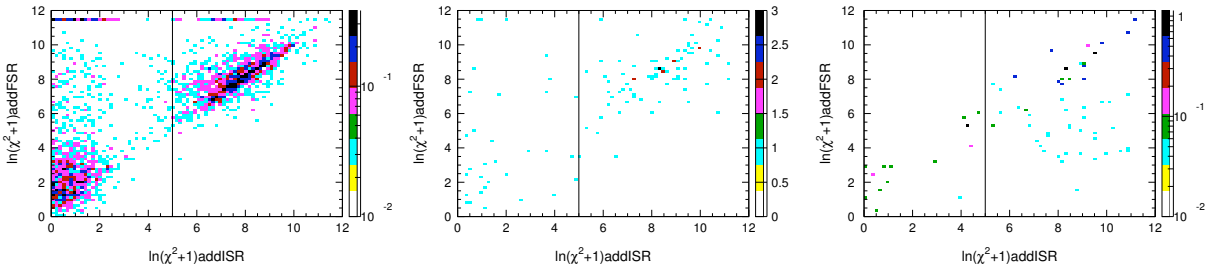

Figure 2.67: χ^2 distribution of events with $R_{xy} \in [2.4; 3]$ cm and $dz_{min} \leq 0.1$ cm for the MC(left), data(middle) and MC background(right). The plots correspond to the region of reconstructed K^+K^- mass: [0.98;5.] GeV .

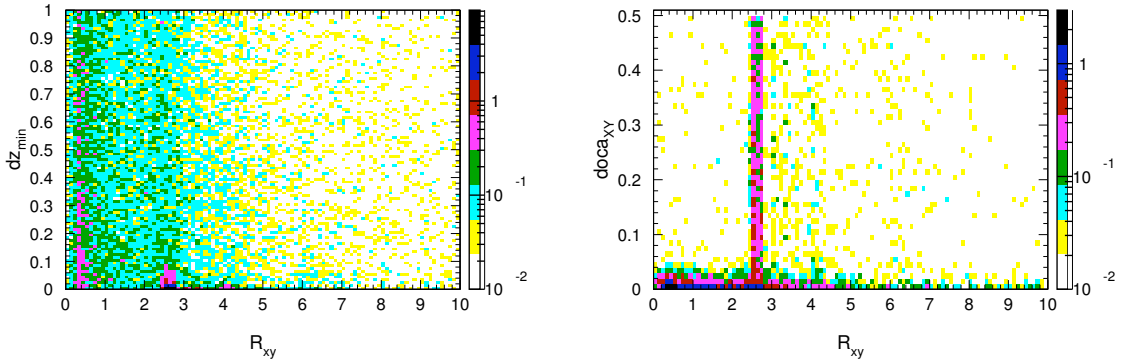

Figure 2.68: dz_{min}, R_{xy} plane(left) and $doca_{xy}$, R_{xy} plane(right) for events with $\ln(\chi^2_{addISR}+1) \geq 5$. In the right plot we also asked $dz_{min} \leq 0.1$ cm, in order to keep only well defined vertices. The plots are obtained from simulation and they correspond to the region of reconstructed K^+K^- mass: [0.98;5.] GeV .

Because of the strict $doca_{xy}$ cut for ISR tracks (0.5 cm), the dominant source of secondary vertices is the beam pipe, with further contributions from the first SVT layers. In Fig. 2.67 we show the χ^2 distribution of events with a secondary vertex in the beam pipe region ($2.4 \leq R_{xy} \leq 3.0$ cm). These events populate the diagonal region, extending through the χ^2-cut boundary. Therefore, they affect the χ^2-cut efficiency. It is found by a simple counting of events with $\ln(\chi^2_{addISR} + 1) \geq 5$, that the MC underestimates the data (after background subtraction) by a factor 1.81 ± 0.24. One needs however to take into account the fact that all these events with a bad-χ^2 are not due to interactions. Accidental vertices may occur and the corresponding events must not be taken into account when normalizing the MC to the data, for interactions.

Fig. 2.68 (left) shows the (dz_{min}, R_{xy}) plane, for events with $\ln(\chi^2_{addISR}+1) \geq 5$. Good vertices are selected by the condition $dz_{min} < 0.1$ cm.

In order to reduce the rate of accidental vertices, we select likely interacting events with the $doca_{xy}$ of the interacting good track to be larger than 0.05 cm (see Fig. 2.68 right). In this way one can determine the expected shape of the R_{xy} distribution for interacting

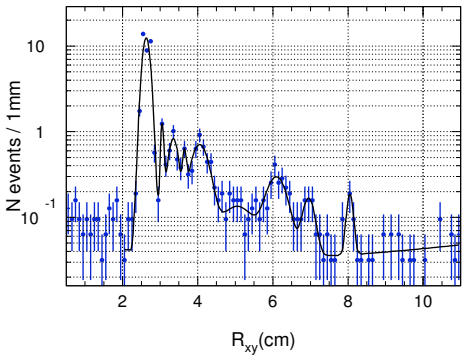

Figure 2.69: R_{xy} distribution for events with $\ln(\chi^2_{addISR}+1) \geq 5$, $dz_{min} \leq 0.1$ cm and $doca_{xy} \geq 0.05$ cm, for the MC. The plot corresponds to the region of reconstructed K^+K^- mass: [0.98;5.] GeV .

events, free of background. The corresponding distribution is shown in Fig. 2.69 for the simulation. It is fitted by a sum of gaussians for the signal, plus a polynomial for the small background of accidental vertices.

Fig. 2.70 presents the fits in MC and data of the R_{xy} distributions without any $doca_{xy}$ in order not to bias the interaction signal and retain a reasonable efficiency. The background of non-interacting events is fitted using a sum of exponentials. The signal is fitted using the expected shape of interaction events, with a free normalisation factor. In order to take into account the difference of resolution effects for the events with $doca_{xy} \geq 0.05$ cm and the others, a gaussian is added to this shape in the region of the main interaction signal from the beam pipe. It is fitted on the MC and fixed for data.

From the two fits, the data/MC ratio of interacting events is found to be 1.53 ± 0.27 with a systematic error of about 4% coming partially from the fit of the shape of the background, partially from the difference in resolution for events with different $doca_{xy}$.

However, this method keeps only about $5-6\%$ of the events with interactions in the KK MC. A method with an enhanced efficiency is described in the following.

Check of interactions in data: using the $doca_{xy}^{max}$ distribution

The quantity $doca_{xy}^{max}$ is defined to be the largest of the $doca_{xy}$ for the two tracks in the event, each limited by the cut at 0.5 cm used in the good track definition. The sensitivity of this variable to secondary interactions can be appreciated in Fig. 2.71, where the events are selected to be in "an intermediate χ^2 region" (with $\ln(\chi^2_{addISR}+1) \geq 3.5$ and a cut to eliminate the background) [4] as indicated in Fig. 2.72. This cut was optimized taking into account its efficiency to keep interaction events as well as the amount of background that has to be subtracted from data. There is a striking difference in the tail of the $doca_{xy}^{max}$ distribution for kaons and muons, as expected from secondary interactions. The

[4] This region is slightly different than the one that is usually called "intermediate" in this analysis.

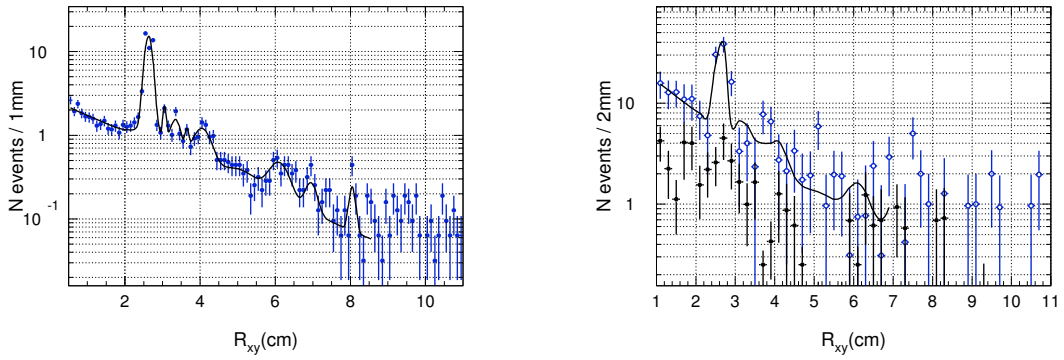

Figure 2.70: R_{xy} distribution for events with $\ln(\chi^2_{addISR}+1) \geq 5$ and $dz_{min} \leq 0.1$ cm for the MC(left) and data(right). The plots correspond to the region of reconstructed K^+K^- mass: [0.98;5.] GeV . The subtracted background is indicated for the data (black points), while the signal is indicated in blue.

muon distribution is therefore used as an estimator of the amount of kaon non-interacting events.

In order to obtain the data/MC correction for the amount of interacting events, we compare the corresponding differences between the number of events in the kaons and muons distributions, for values of $doca_{xy}^{max}$ between 0.15 and 0.5 cm [5]. This method keeps about 51% of the events with secondary interactions in the KK simulation, which represents an important improvement with respect to the previous one. Here again we find that the simulation underestimates the level of secondary interactions by a factor $1.51 \pm 0.07 \pm 0.09$, where the first error is statistical and the second is systematic (from the shape difference of the distributions in data and MC [6]). The bin to bin correlations, coming from the normalization errors of the $q\overline{q}$ MC and from the data/MC corrections for the various mis-ID backgrounds, are taken into account when computing this ratio.

It has been observed that the momentum distributions of muons and kaons have somewhat different shapes, due to their different masses and spins, and this effect could bias the subtraction of non-interacting events in the kaons, using the muons. In order to estimate the size of this possible bias, we have studied the dependence of the $doca_{xy}^{max}$ on the momentum of the charged track with the largest $doca_{xy}$, for muons and kaons. Actually, the estimator can still be further refined, as one should not simply sum the muon distributions for different momenta, normalized to the luminosity (this would produce the spectrum shown with black points in Fig. 2.71). Instead, one should first reweight these distributions using the ones for kaons (the weights being themselves functions of $doca_{xy}^{max}$) and then sum them up. The reweighted distribution of the $\mu^+\mu^-$ events corresponds to

[5] This interval takes into account the difference in the distribution tail at low $doca_{xy}^{max}$ values, for data and simulation. The comparison with the result obtained for $doca_{xy}^{max} \in [0.1; 0.5]$ cm provides an estimation of a systematic error.

[6] An additional systematic error of the data/MC correction for the amount of interacting events, from the normalization of the $\mu^+\mu^-$ distribution with respect to the K^+K^- is estimated to be about 0.3% for data and 0.1% for MC.

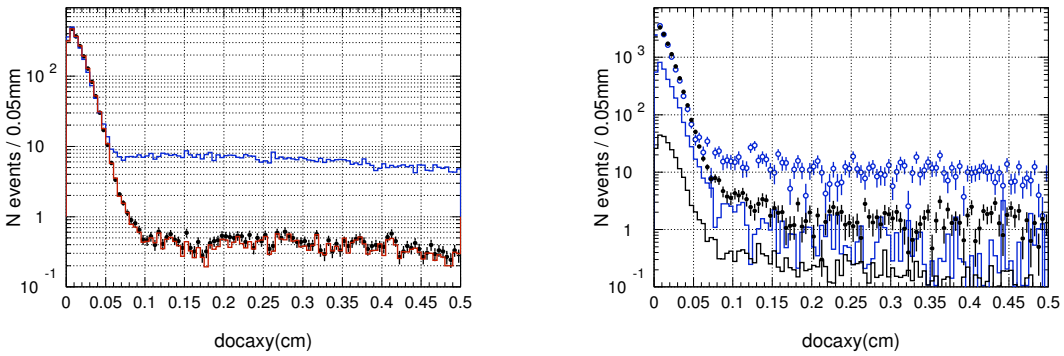

Figure 2.71: Distributions of the largest of the two transverse distances of closest approach to the interaction point ($doca_{xy}^{max}$), for muons(black filled circles) and kaons(blue histogram(left), empty circles(right)), for events in the intermediate χ^2 region. The red histogram in the left plot shows an improved (reweighted) $\mu^+\mu^-$ distribution (see text). The plots correspond to the regions of reconstructed invariant mass(K^+K^- or $\mu^+\mu^-$) smaller than 5 GeV, for the MC(left) and data(right). In the right plot, the histograms indicate the subtracted background (in black for muons and blue for kaons). The $\mu^+\mu^-$ plots are rescaled to the K^+K^- ones, in the region of $doca_{xy}^{max}$ smaller than 0.05 cm.

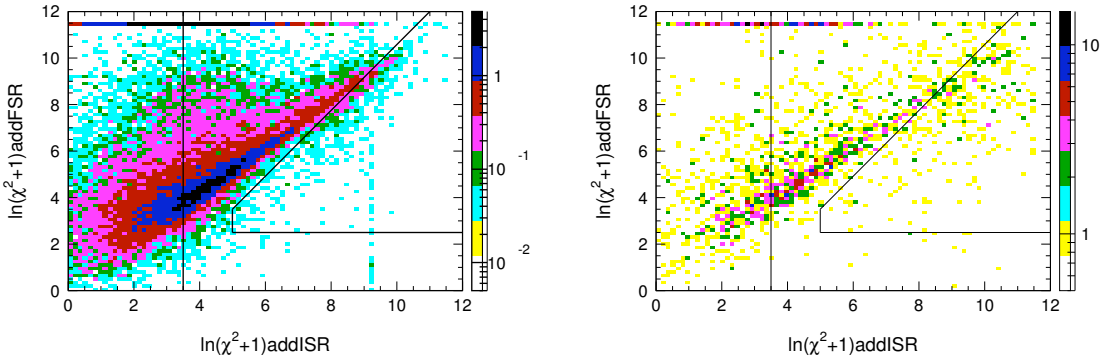

Figure 2.72: χ^2 distribution of K^+K^- events with the largest of the two transverse distances of closest approach to the interaction point ($doca_{xy}^{max}$) larger than 0.1 cm. The plots correspond to the regions of reconstructed K^+K^- mass: [0.98;5.] GeV, for the MC(left) normalized to the luminosity and data(right).

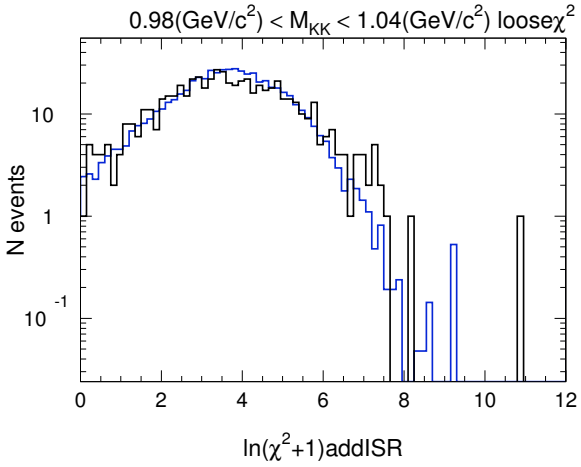

Figure 2.73: χ^2_{addISR} distribution of K^+K^- events in the loose region, with the largest of the two transverse distances of closest approach to the interaction point ($doca^{max}_{xy}$) larger than 0.15 cm. The plot correspond to the regions of reconstructed K^+K^- mass [0.98;1.04] GeV, for the MC(blue) normalized to the luminosity and corrected for data/MC differences for secondary interactions, and data(black).

the red histogram in the left plot of Fig. 2.71. Its comparison with the first distribution (black points on the same plot) for values of $doca^{max}_{xy}$ larger than 0.1 cm allows us to estimate a systematic error on the number of interacting kaon events in simulation. This error is estimated to be about 0.8% of the data/MC correction for the amount of interacting events. Thus the expected $doca^{max}_{xy}$ tail from non-interacting events, as obtained from muon events, is very insensitive to the differences in their respective momentum distributions.

Conclusion for the secondary interactions

The two previous (essentially independent) methods yield very compatible results. Some correlations exist between the two samples used to determine the ratio (the secondary vertices and the $doca^{max}_{xy}$ tail), but they are not large, as the first method keeps events at small $doca_{xy}$ and the second does not require a reconstructed secondary vertex. Combining them yields a data/MC ratio for secondary interactions of 1.51 ± 0.11. As this value was determined essentially in an intermediate χ^2 region, a conservative 100% error will be assigned to it when used in the background region.

Fig. 2.73 shows the χ^2_{addISR} distributions for data and MC events (in the loose region, at the ϕ mass) with $doca^{max}_{xy}$ larger than 0.15 cm, once the MC is corrected with the data/MC ratio for secondary interactions obtained before. A good agreement is observed over the whole range, this being a non-trivial test of our result.

2.9.5 Evaluating K/μ differences with the ϕ sample

Differences between kaons and muons (beyond the effects of FSR and secondary interactions) exist in the tails of χ^2 distributions. In simulation the distributions are consistent (see Fig. 2.64), as both the fit hypotheses (additional ISR colinear to the beams) and the event generation match. This is not the case in data (angular distribution for additional ISR), creating tails in the χ^2_{addISR} distributions, which are found to differ between KK and $\mu\mu$ fits, presumably because of the large K/μ mass difference. Indeed, such an effect was not found for pions [29]. In order to correct for this effect we measure the efficiency of the χ^2-cut on data, for kaons, using the ϕ signal, for which the background in the intermediate χ^2 region is small and under control. Even then, an extrapolation must be done to obtain the number of ϕ events in the background region of the χ^2 plane (where the amount of background prevents a precise direct measurement of this signal) for a complete evaluation of the χ^2 cut efficiency.

This study is done in the three different parts of the intermediate χ^2 region (ISR, diagonal and FSR) due to the various characteristics of the corresponding events. The FSR region, has been studied in Sec. 2.9.2. On one hand, there is good agreement for the large angle additional ISR fractions for $\mu\mu$ and KK (only seen in data). On the other hand, the true FSR fractions agree between data and MC both for muons and kaons. In the following we will concentrate on the study of the ISR and diagonal χ^2 regions, the results being then extrapolated to the background region.

The data/MC comparison for kaons in the ISR and diagonal χ^2 regions is performed in a small mass band ([0.98;1.04] GeV) in the ϕ region, in order to limit the amount of background in data. The amount of FSR events is very small for kaons, and this is also the case for muons in this region of the χ^2 plane. Therefore, data/MC ratios of the number of events in these two regions, for kaons and muons, can be directly compared. A larger mass band is used for muons (after checking the compatibility of the muon correction in the additional mass region and in the one used for kaons), in order to increase statistics. Fig. 2.74 shows the double ratios of the data/MC corrections for kaons and muons in the ISR and diagonal regions, as a function of χ^2_{addISR}. The contribution due to secondary interactions in the diagonal region (see Fig. 2.73) is well reproduced by the simulation after correcting for the absolute interaction yield following Section 2.9.4. It is subtracted accordingly. This subtraction, and the subtraction of the background for kaons, produce the enhancement of the correction error bars in a few bins of the diagonal region.

The double ratios in the ISR and diagonal regions measure essentially the same physical effect, and are consistent. They are combined (at the level of event distributions) and yield the correction shown in the bottom plot of Fig. 2.74. An additional systematic error of 3% on this correction comes from the choice of the KK mass interval for this study. The double ratio is extrapolated to the background region using the average of two linear fits (on all and respectively the four last bins of the distribution). We add an error of 0.04, coming from the $\ln(\chi^2_{addISR}+1)$ value to which the extrapolation is done, in the range $9-9.5$. The main error comes from the difference between the two fits, and it yields 0.26. Finally we get a value of the double ratio, extrapolated to the background region,

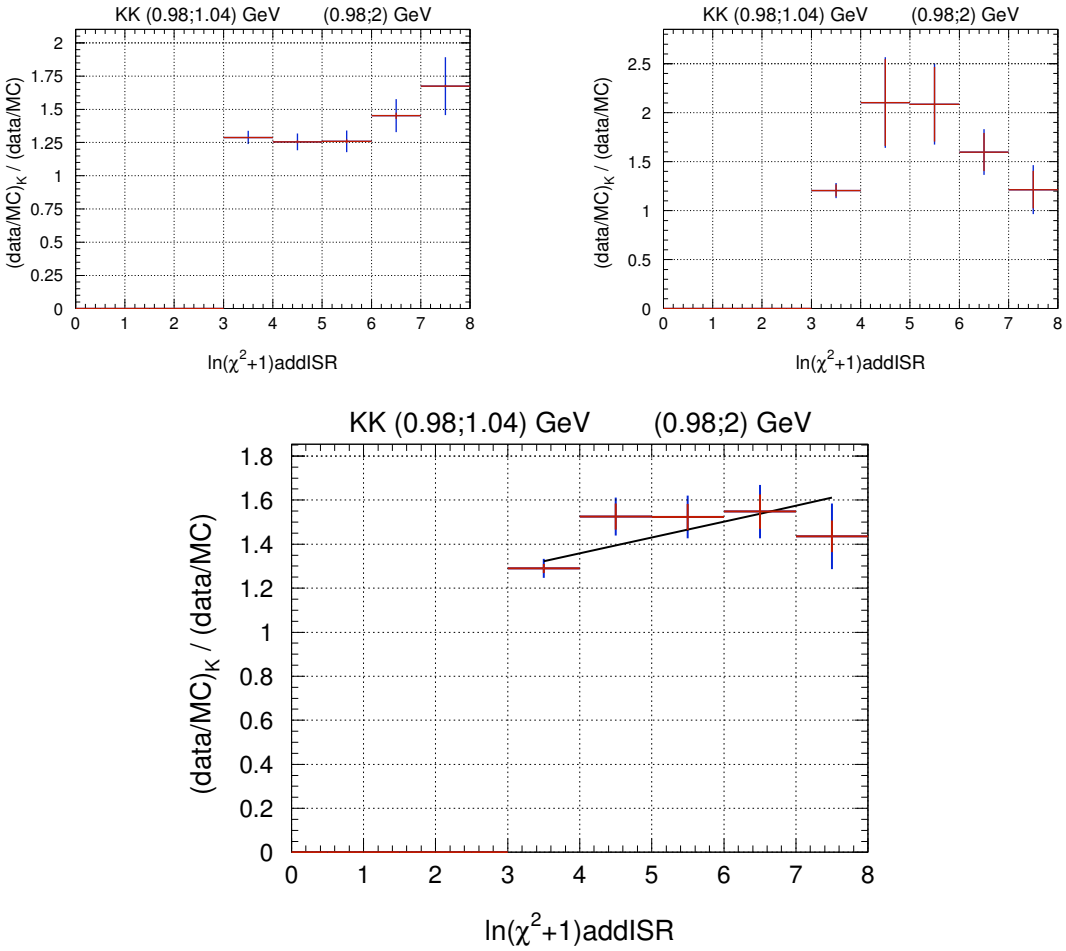

Figure 2.74: *Data/MC* ratio of the number of events for kaons and muons, as a function of χ^2_{addISR}. The plots correspond to the ISR region (top left), the diagonal region (top right) and their combination (bottom). The red error bars indicate the sum of the correlated errors from the efficiency of the $doca^{max}_{xy}$ cut, from the data/MC correction of secondary interactions and the ones from the background subtraction for the kaons (mainly $K^+K^-\eta\gamma$ and $q\bar{q}$), whereas the blue error bars indicate the total errors.

of 1.59 ± 0.31 .

In the background region for the KK simulation, we find 121.8 ± 1.96 events, in the ϕ mass range. A fraction of 0.58 ± 0.06 are due to secondary interactions, and are corrected with the corresponding data/MC ratio, while the comparison with muons is used for the others. Using the data/MC ratio for the number of $\mu\mu$ events (7.62 ± 0.35) in the same region of the χ^2-plane and for masses in the $0.2 - 0.5$ GeV range (to keep FSR down), we get an estimation of the number of K^+K^- events without secondary interactions, we expect in the background region: 622.9 ± 151.5. Including events affected by secondary interactions, we expect 729.2 ± 152.1 events loss by the loose χ^2 cut in KK.

Using the number of KK events in the tight, intermediate and background χ^2 regions, in MC and in data (after the subtraction of background and interactions), in the [0.98;1.04] GeV mass region, we compute the efficiencies of the tight and loose χ^2 cuts, for data and MC. We obtain the ratio between the data/MC corrections for kaons and muons (to be used in Eq. 2.13): 1.0042 ± 0.0022 for the loose χ^2-cut and 0.9931 ± 0.0028 for tight. The data/MC correction for kaons alone, and without subtracting the interactions, is directly applied for masses lower than 1.04 GeV. It accounts for 0.9918 ± 0.0020 for the loose χ^2-cut and 0.9185 ± 0.0022 for tight. For all the values cited in this paragraph, only statistical errors are quoted (which are propagated through the covariance matrix). Systematic errors are propagated directly to the cross section.

2.9.6 Conclusions on the data/MC corrections for the χ^2 cut efficiency

The total data/MC correction for the χ^2 cut efficiency has been measured directly with kaons, at the ϕ and it is applied to the spectrum up to 1.04 GeV.

The correction is then extended to higher masses (according to Eq. 2.13), using the results of studies with muons, as well as the mass dependence of the data/MC correction for secondary interactions, together with the double ratio correction obtained with the ϕ sample.

2.10 Unfolding the Data Distribution

Since the $KK(\gamma)$ cross section has to be established as a function of $\sqrt{s'}$, the measured spectrum, as a function of m_{KK}, must be unfolded to account for resolution and FSR distorsions.

The unfolding must be performed separately for the spectra of events passing the loose and respectively tight χ^2-cuts, corrected for the corresponding data/MC differences (obtained following Eq. 2.12). The following procedure is used:

- the data spectrum of the fitted mass m_{KK} is subtracted for backgrounds and the data/MC corrections for efficiencies are applied;
- the mass-transfer matrix records the probability that an event generated in a $\sqrt{s'}$ bin i is reconstructed in a m_{KK} bin j. It is obtained from the simulation and corrected for differences with data;
- the unfolding procedure is applied to the m_{KK} spectrum, yielding the $\sqrt{s'}$ spectrum, and systematic tests of the unfolding procedure are performed;
- the overall acceptance correction from the simulation is applied.

As the amount of events with additional FSR radiation is very small for kaons, the unfolding corrects mainly resolution effects. The size of the resolution effects can be seen in MC, by plotting the distribution of the difference between $\sqrt{s'}$ and the reconstructed mass (see Fig. 2.75 for the plot corresponding to events in the tight χ^2-region). A fit in the central region of this distribution ($[-0.85; 0.85]$ MeV) shows that the mass resolution predicted by the MC is of 0.808 ± 0.016 MeV, the uncertainty being dominated by the choice of the energy interval used for the fit.

2.10.1 Corrections of the Transfer Matrix

Events in the intermediate χ^2-region are affected by stronger resolution effects than the ones in the tight χ^2-region. The amount of these events is also significantly different in data and MC. In order to minimize/test possible biases in the correction of the resolution effects, one must:
1) compare the size of the resolution effects in data and MC, for events in different regions of the χ^2-plane;
2) reweight events in different regions of the χ^2-plane according to data, in the transfer matrix corresponding to the (composite) loose χ^2-region.

The data vs. reconstructed MC comparison is done in the ϕ region, after background subtraction and data/MC corrections for the efficiencies. This correction is different for the tight and loose χ^2-regions, being larger for the first one (see Section 2.9 above), as expected. The comparison in view of the reweighting of the loose transfer matrix is done separately for four independent χ^2-regions: tight, ISR, diagonal and FSR (see Fig. 2.76).

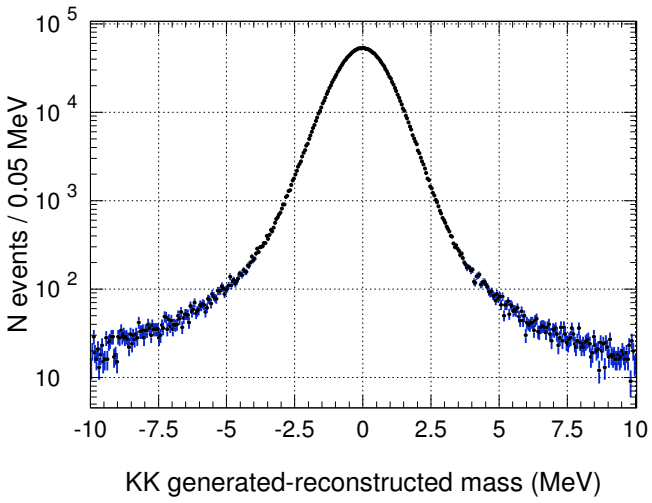

Figure 2.75: Distribution of the difference between the generated and reconstructed mass for KK MC events in the tight χ^2-region.

The last three are restricted to the intermediate χ^2-region, covering it completely (see Section 2.8 above). An identical (loose) data/MC correction for the efficiencies is used for the four regions, in view of the reweighting.

The ratio of the number of events in data and MC normalized to the luminosity, is very close to one for tight-χ^2, 3.75 ± 0.07 in the intermediate ISR region, 1.92 ± 0.10 in the intermediate diagonal region. The latter value is larger than the one coming just from interactions (1.51 ± 0.11) due to a contribution of events with additional ISR. Indeed, the χ^2_{addISR} distribution of MC is much sharper compared to data (which exhibit a strong tail because of the angular distribution of additional ISR). A large factor is observed in the intermediate FSR region (due to the lack of large angle additional ISR in the simulation). However, in this last region, the additional events in data (with large angle additional ISR) have a good χ^2_{addFSR} and are expected to be affected by resolution effects in a way comparable to the events in the tight χ^2 region. Therefore one single rescaling factor is computed for the contributions of the FSR and tight regions to the transfer matrix for the loose χ^2-region.

A fair agreement is observed between data and MC, once the simulation is (re)normalized to the number of events in data (see Fig. 2.77). In the tight χ^2-region, the resolution for data and simulation are expected to be very close. The difference between the two distributions on the ϕ tail is very likely associated to a bad simulation of the K^+K^- form factor. This is even more obvious for reconstructed masses between 1.1 and 2 GeV (see Section 2.8 above), where new structures are seen in data.

The data/MC ratios after the normalization correction for the simulation are shown in Fig. 2.78. Fig. 2.79 shows the double ratios at the reconstructed level, between data and MC, and between the various parts of the intermediate region and tight. If the plots shown in Fig. 2.78 were sensitive to the form factor differences between data and MC, these

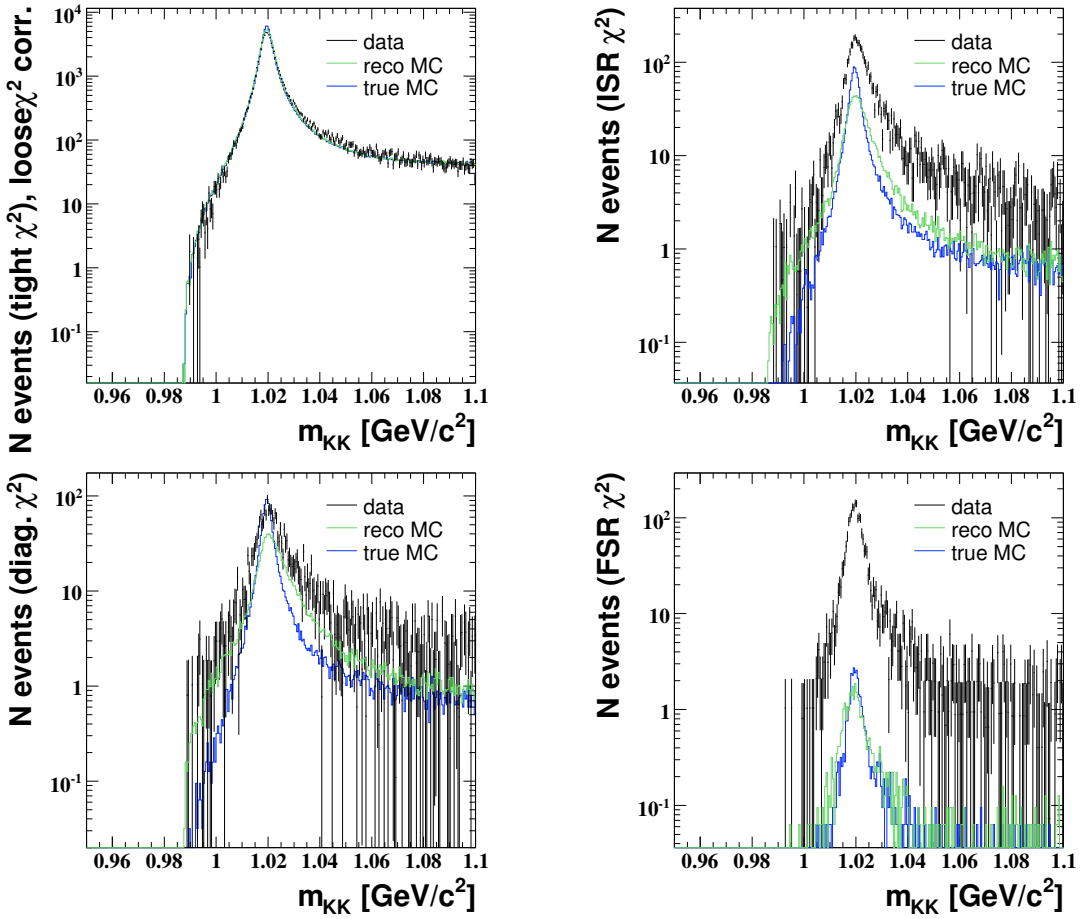

Figure 2.76: Mass distribution for data (black points), reconstructed (green histogram) and true (blue histogram) MC. For all the plots the MC is normalized to the luminosity. A loose data/MC correction for efficiencies was used. The plots correspond to the tight (top left), ISR (top right), diagonal (bottom left) and FSR (bottom right) χ^2-regions. Comparing the true and reconstructed MC, one can see the resolution effects are larger in the intermediate χ^2-region than in the tight one.

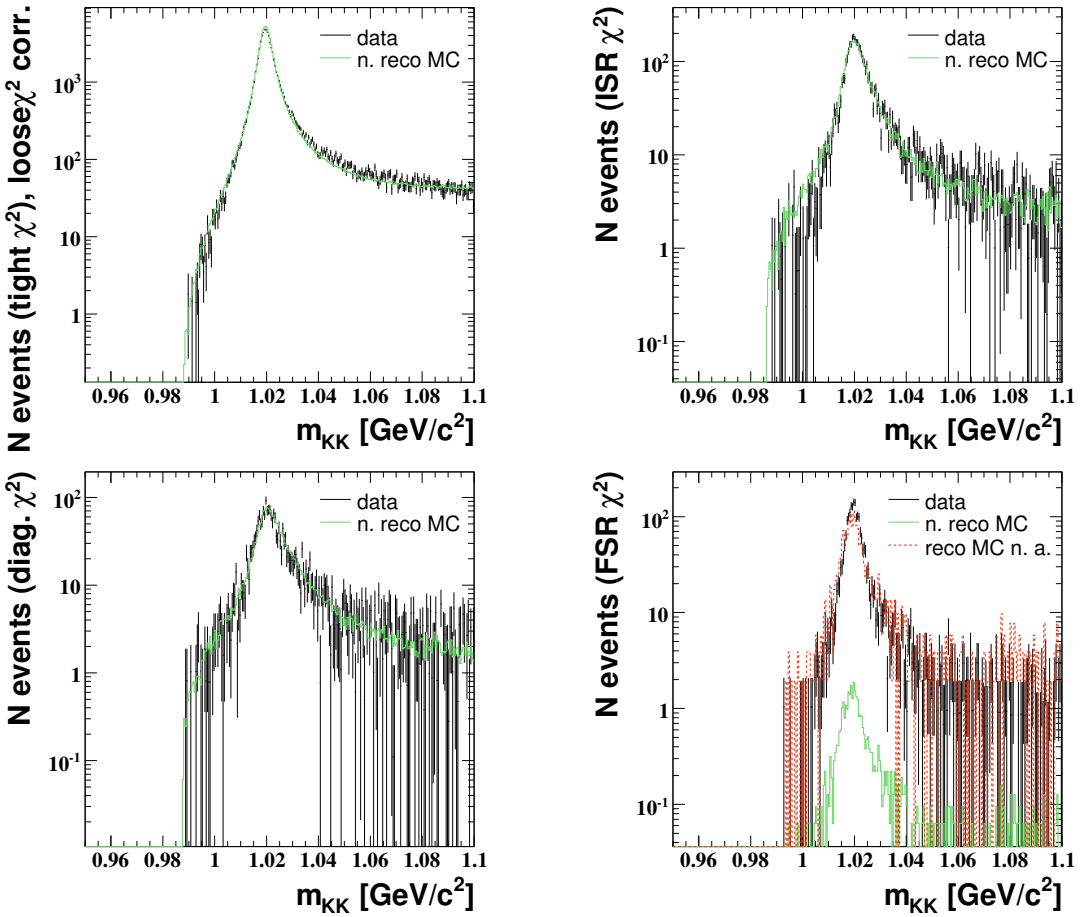

Figure 2.77: Mass distribution for data (black points) and reconstructed MC (green histogram). For all the plots the MC is (re)normalized to the number of events in data. A loose data/MC correction for efficiencies was used. The plots correspond to the tight (top left), ISR (top right), diagonal (bottom left) and FSR (bottom right) χ^2-regions. The red histogram in the right bottom plot indicates the reconstructed MC if it is normalized in the FSR region alone.

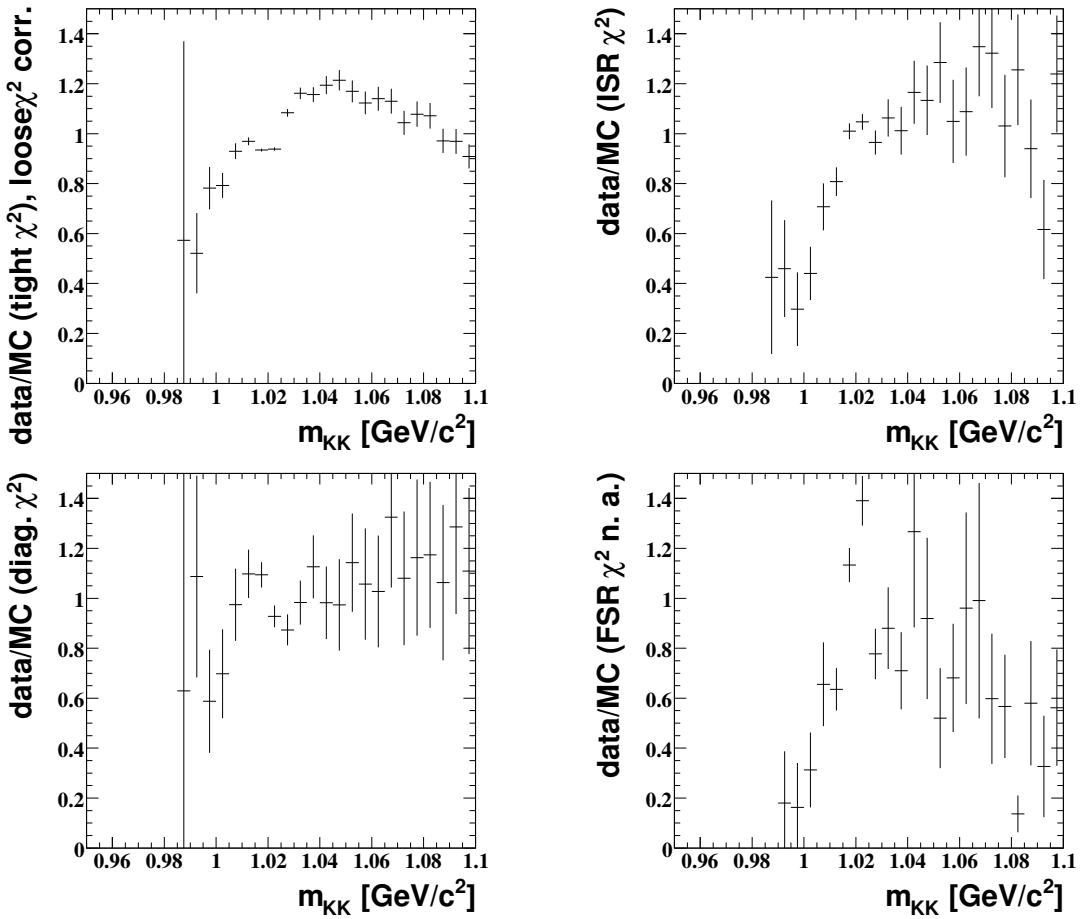

Figure 2.78: Data/MC ratio of the reconstructed spectra, as a function of the m_{KK}. A loose data/MC correction for efficiencies was used. The plots correspond to the tight (top left), ISR (top right), diagonal (bottom left) and FSR (bottom right) χ^2-regions.

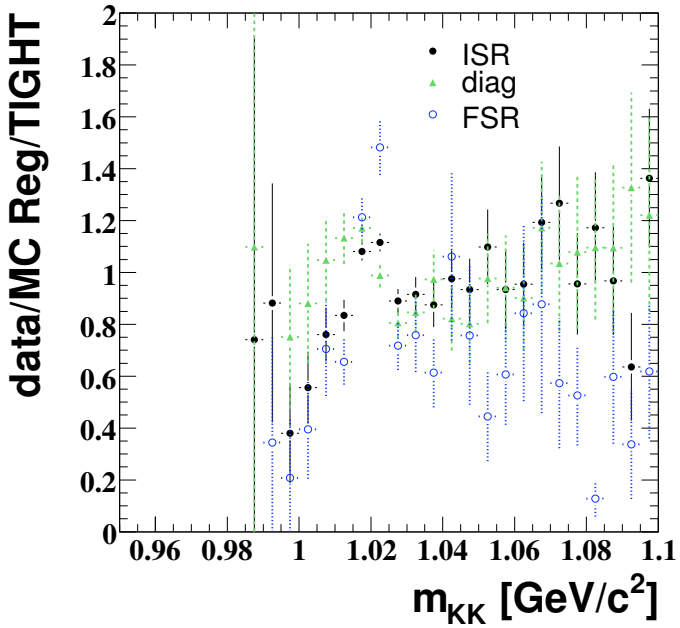

Figure 2.79: Double ratio of the spectra at reconstructed level, between data and MC, and for various intermediate regions and tight.

effects factorize (at the first order) in the double ratios in Fig. 2.79. Therefore, the double ratios show explicitly that there are remnant data/MC differences for detector effects, to which only the spectrum obtained with the loose cut is sensitive. These differences correspond to a mass shift in the diagonal region and to resolution differences in the ISR and FSR regions. These effects need to be taken into account as systematic uncertainties in the loose vs. tight comparison, and they justify the choice of the tight cut for the final Physics results.

The same normalization factors as for spectra are used to reweight the various contributions to the transfer matrices. This clearly corrects the main differences between data and simulation for resolution effects. The corrected transfer matrices are shown in Fig. 2.80 and 2.81 for the loose and tight χ^2 cuts respectively. The longer tails for the loose χ^2 cut are clearly visible.

2.10.2 Calibration and Resolution Studies using K^0_s from ϕ Decays

Relevance of the K^0_s sample

In the previous subsection we described a procedure which corrects data-MC differences for resolution effects, mainly for events in the intermediate χ^2 region (the change in normalization for the transfer matrix of the tight region alone will have basically no implication on the corresponding unfolding result). The simulation of resolution effects for events in the tight χ^2 region is expected to be good, but one should have a quantitative test of this assumption.

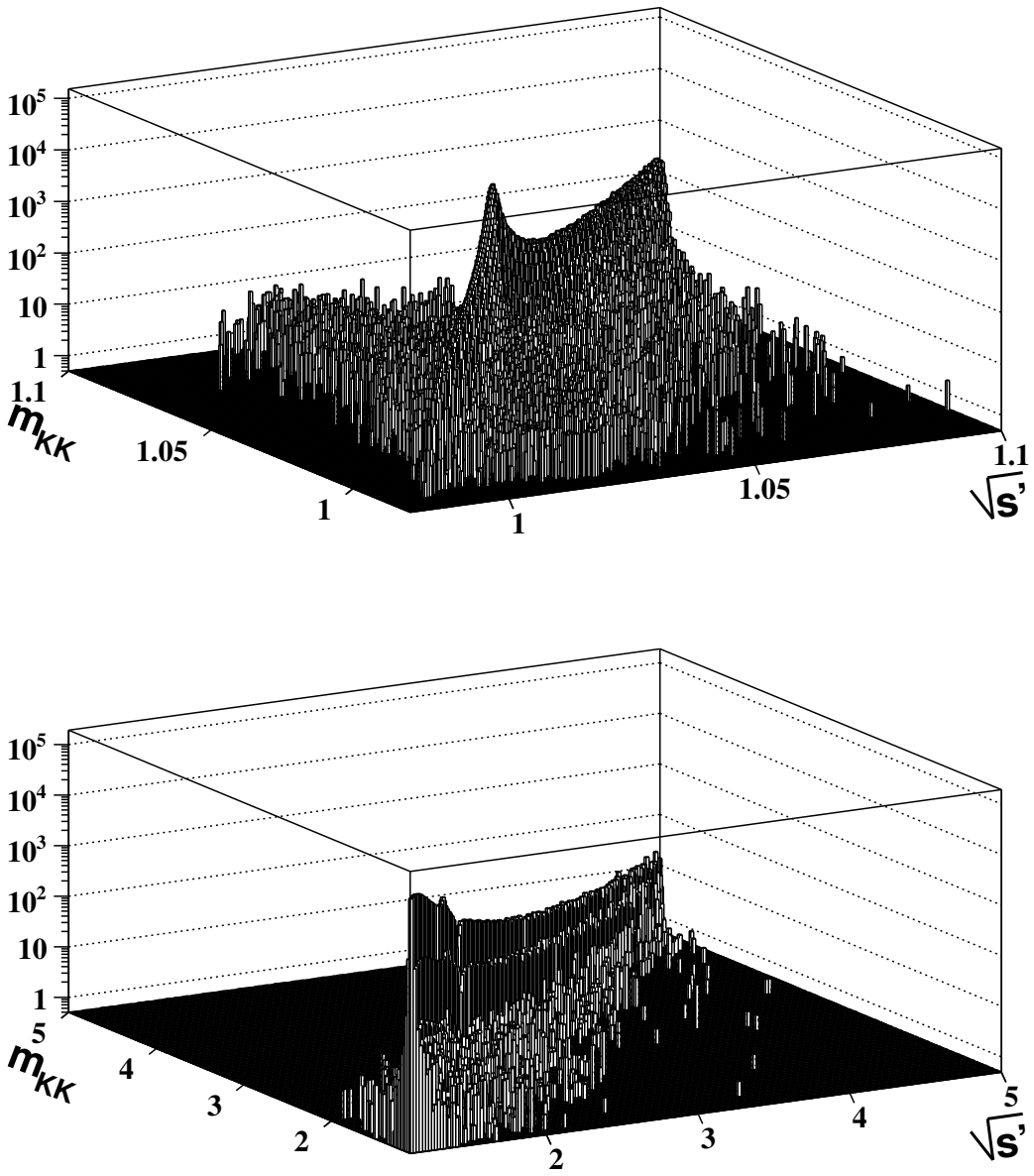

Figure 2.80: Transfer matrix (corrected) for events in the loose χ^2 region.

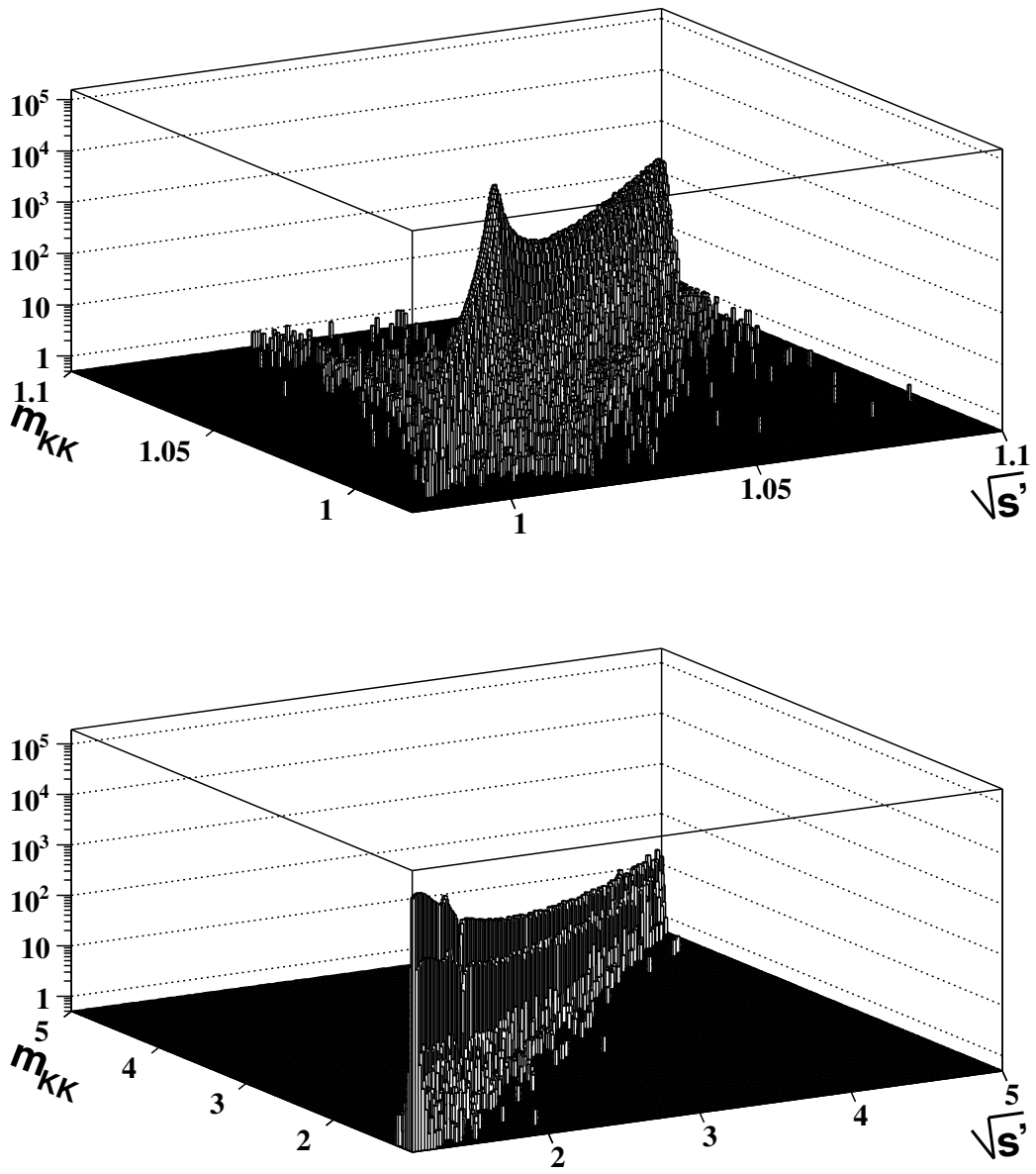

Figure 2.81: Transfer matrix for events in the tight χ^2 region.

This test is provided through a study of the decays $K^0_S \to \pi^+\pi^-$, from a sample of ISR-produced ϕ mesons decaying into $K^0_s K^0_l$. In this case resolution effects can be directly measured on data and MC. In both $\phi \to K^+K^-$ and $K^0_s \to \pi^+\pi^-$ decays the mass calibration and resolution are dominated by the measurement of the opening angle. The momentum measurement plays a minor role, especially in ϕ decays, because of the proximity to the K^+K^- threshold.

On the contrary the decays $J/\psi \to \mu^+\mu^-$ are almost completely controled by the momentum measurement. The J/ψ sample has in fact been used to check the momentum scale calibration in the $e^+e^- \to \pi^+\pi^-\gamma$ analysis, with the result:

$$\frac{\Delta p}{p} = \frac{p_{measured} - p_{true}}{p_{measured}} \tag{2.15}$$

$$= -(2.0 \pm 0.4)\ 10^{-4}. \tag{2.16}$$

The corresponding mass shifts are -0.62 MeV for $J/\psi \to \mu^+\mu^-$, -0.068 MeV for $K^0_s \to \pi^+\pi^-$ and -0.013 MeV for $\phi \to K^+K^-$.

So the K^0_s sample is particularly relevant to the understanding of the ϕ resonance parameters.

Noting α the opening angle in the BaBar frame (for simplicity we take the value for symmetric decays), we get the two components for the mass calibration and the mass resolution in the decay $M \to mm$:

$$\Delta M = (\Delta M)_p + (\Delta M)_\alpha, \tag{2.17}$$

$$\sigma^2_M = (\sigma_M)^2_p + (\sigma_M)^2_\alpha, \tag{2.18}$$

$$(\Delta M)_p = \frac{(M^2 - 4m^2)}{M}\frac{\Delta p}{p}, \tag{2.19}$$

$$(\Delta M)_\alpha = \frac{(M^2 - 4m^2)}{2M}\frac{\sin\alpha}{(1-\cos\alpha)}\Delta\alpha. \tag{2.20}$$

Selection of Events

Events are pre-selected by the ISR filter (the same preselection cuts as for $e^+e^- \to KK\gamma(\gamma)$ events) and the following conditions are used for data and MC:

- L1-L3 triggers and BGFilter satisfied
- ISR photon in the polar range 0.35-2.40 rad and with $E^*_\gamma > 3$ GeV
- 2 standard tracks with $P > 0.5$ GeV and in the polar range 0.40-2.45 rad
- 1 K^0_s candidate (K^0_s bank) with $\chi^2_{vertex} < 10$.

No attempt was made to select K^0_l interactions in the EMC (no information on IFR neutral clusters is available in the ntuples), the K^0_s signal being clearly visible over a

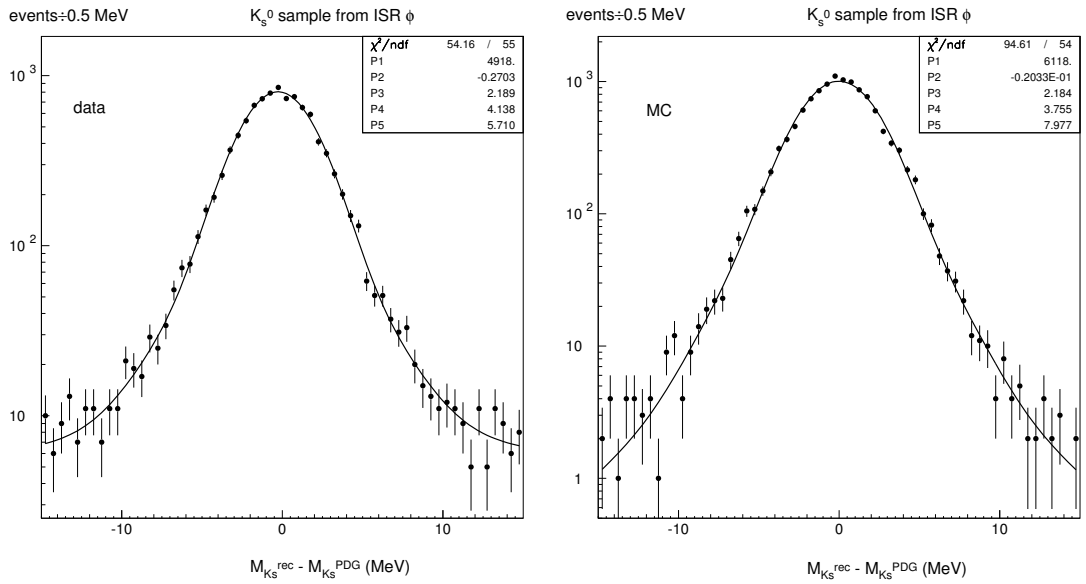

Figure 2.82: Distributions of the difference between the reconstructed K^0 mass in $K^0_s \to \pi^+\pi^-$ decays and the PDG mass for data (left) and MC (right) from samples of $e^+e^- \to K^0_s K^0_l \gamma$ events. The resolution function is fitted using three gaussians and a constant background, for data.

reasonably small background. The selected events are dominated by the process $e^+e^- \to K^0_s K^0_l \gamma$, itself dominated by $\phi\gamma$.

The K^0_s selected have a mean momentum of 1.6 GeV, smaller than the mean ϕ momentum of 2.7 GeV in the ISR K^+K^- process. This is taken into account in the corresponding contributions to the mass calibration and resolution. The average opening angle in the K^0_s sample is 16°, compared to 5.5° for our $\phi \to K^+K^-$ events.

Mass fits

We compare the reconstructed value of the K^0 mass and the PDG value [9], by performing fits of the distributions of the mass difference $M^{rec}_{Ks} - M_K s^{PDG}$ in data and MC. The fit to the MC distribution sample requires three gaussians with respective fractions of 0.78, 0.20, and 0.02. The central value and the three gaussian widths are adjusted. Because of the background, the fit to the data distribution is not sensitive to the width of the widest gaussian which is taken from simulation. Thus only the central value, the first two gaussian widths, and the constant background level are fitted. In this way we are able to compare data and simulation over almost the full resolution function, down to the 1% level on the tails. For vertices beyond L_T =10 cm we expect the quality of the tracks to be somewhat degraded and therefore not comparable to the prompt tracks in $\phi \to K^+K^-$ decays, so we limit the L_T range to this value. The distributions of the mass difference and the corresponding fits are given in Fig. 2.82.

The results for the central value of the gaussian are shown, for data and MC, in Fig. 2.83. The procedure works well as the central values in the MC are independent of

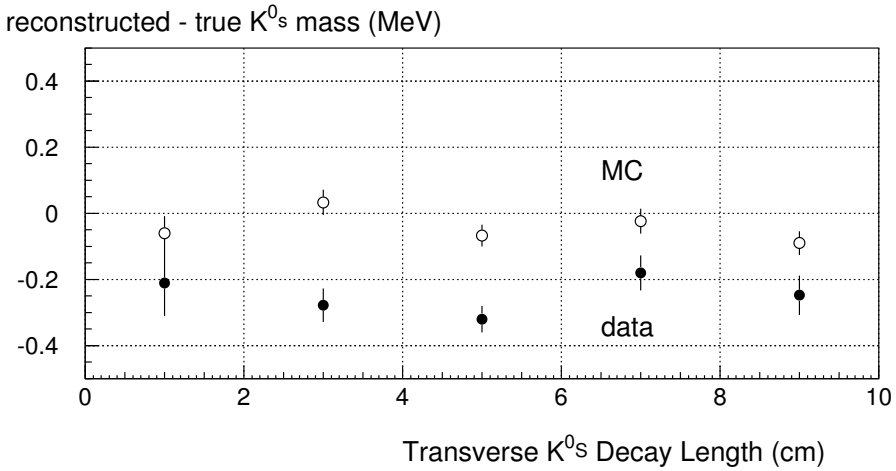

Figure 2.83: The mean of difference between the reconstructed K^0 mass in $K^0_s \to \pi^+\pi^-$ decays and the PDG mass for data (filled circles) and MC (open circles), as a function of the transverse decay length (cm).

the vertex location and consistent with the true mass. For data there is also no dependence on L_T, however a distinct overall shift of -0.25 MeV is observed.

From the reconstructed to the fitted K^+K^- mass

The K^0_s mass used in this study is at the reconstruction level. In the K^+K^- sample we perform kinematic fits and therefore we expect some improvement in resolution and possibly calibration. This has been studied on data and MC looking at the distributions of the difference between the fitted and reconstructed K^+K^- masses in the ϕ sample, $M^{fit}_\phi - M^{rec}_\phi$. We obtained average shifts of 0.027 ± 0.002 MeV in data and 0.008 ± 0.001 MeV in simulation. Thus a small improvement of the mass shift in data is achieved through the kinematic fits. As expected the effect is more significant for the resolution, as the rms of the $M^{fit}_\phi - M^{rec}_\phi$ distributions are 0.540 ± 0.002 MeV in data and 0.437 ± 0.001 MeV in simulation.

These factors have to be taken into account for the final evaluation of the calibration and resolution systematic uncertainties.

Mass calibration

From the J/ψ study we expect a K^0_s mass shift of -0.07 MeV, so the remaining bias of -0.18 MeV has to originate from the measurement of the opening angle. From Eq. (2.17), this corresponds to a bias on the opening angle of $-(1.66 \pm 0.22)\ 10^{-4}$ rad.

Applying this bias to the $\phi \to K^+K^-$ case, we obtain:

$$(\Delta M_\phi)_p^{rec} = -0.013 \pm 0.003 \text{ MeV} \quad (2.21)$$
$$(\Delta M_\phi)_\alpha^{rec} = -0.110 \pm 0.015 \text{ MeV} \quad (2.22)$$

for a total calibration bias of -0.123 ± 0.015 MeV on the reconstructed K^+K^- mass and -0.096 ± 0.015 MeV on the fitted mass.

However, in the absence of a realistic model for this bias, and noting that the obtained opening angle is in fact the result of measurements of θ and ϕ angles, we prefer to be conservative and ascribe the full bias to a systematic error. Thus no correction is applied and the systematic uncertainty is estimated to be

$$(\Delta M_\phi)_{syst}^{fit} = 0.11 \text{ MeV} \quad (2.23)$$

Mass resolution

The K_s^0 study also provides interesting information relevant to the mass resolution of the ϕ resonance in the K^+K^- analysis. Since we perform an unfolding of the mass distribution using the mass transfer matrix from simulation it is important to check that the simulated mass resolution agrees well enough with data. An estimate of the comparative MC-data mass resolution can be achieved with the $K_s^0 \to \pi^+\pi^-$ sample.

From the three-gaussian fits of the K_s^0 mass-difference distributions for $0.3 < L_T < 10$ cm in data and MC and by weighting the fitted widths, one obtains effective resolution values which are close: (2.629 ± 0.047) MeV in data and (2.579 ± 0.031) MeV in MC. These values translate into the corresponding resolutions on the opening angle α, $\sigma_\alpha^{data} = (2.006 \pm 0.042)$ mrad and $\sigma_\alpha^{MC} = (1.934 \pm 0.029)$ mrad.

Adding quadratically the small contribution from momentum measurement (0.2 MeV) these values can be translated into $\phi \to K^+K^-$ decays, yielding

$$\sigma_{M_\phi}^{data-rec} = (1.347 \pm 0.028) \text{ MeV} \quad (2.24)$$
$$\sigma_{M_\phi}^{MC-rec} = (1.302 \pm 0.019) \text{ MeV} \quad (2.25)$$

Here again we take into account the improvement from the kinematic fits evaluated above, and express the data-MC resolution difference as a bias on the resulting ϕ width after unfolding:

$$(\Delta\Gamma_\phi)^{fit} = 0.013 \pm 0.059 \text{ MeV}. \quad (2.26)$$

As for the calibration, no correction is applied and a systematic uncertainty of 0.07 MeV is assigned to the fitted ϕ width.

2.10.3 The Unfolding Procedure

The unfolding procedure used here is a simplified version of the method described in Chapter 1. As in data there is no new structure containing enough events to signifi-

cantly affect the global normalization of the MC, we drop the normalization improving procedure (it has been tested that its use would have no implication on the result of the unfolding). Furthermore, we make no estimation of possible background fluctuations, as in general they are relatively small (except for the high mass regions which are basically not connected to the ϕ region by the transfer matrix).

A little improvement of the data/MC comparison in a couple of bins on the ϕ peak is due to the reweighting of the transfer matrix. However, important differences occur in this comparison when beginning the unfolding procedure, close to threshold, as well as at large masses (see Fig. 2.84). It is for this reason that, in order to avoid biases, the first unfolding step is performed with a large value of its parameter (see [29] and [10]) so that only the correction predicted by the input transfer matrix is performed at this level. Nevertheless, this corrects the main resolution effects on the spectrum (see Fig. 2.85 and 2.86). The result is compared to the true MC and used to perform a maximal improvement of the transfer matrix, by (bin-to-bin) reweighting. After this reweighting, almost all the systematic differences between data and reconstructed MC are removed. Therefore, the next unfolding (using the improved matrix) produces only small changes in the result, except around 1.8 GeV, where we initially had the largest data-MC differences and the effect of this iteration is slightly larger. The effect of a second iteration would be small, proving the convergence of the procedure. The corrected spectrum after the first iteration provides the result we keep from the unfolding procedure, whereas the effect of the second iteration is used to estimate a systematic uncertainty (see next sub-section). The overall unfolding correction on the ϕ peak is of about 15% for the spectrum obtained in the tight χ^2-region and 20% for loose.

2.10.4 Tests of the Unfolding Procedure

A test of the unfolding procedure is performed following the method described in Sec. 1.9.3. A model of "true data" is built using the initial true MC plus a "perturbation" given by the difference between data and the initial reconstructed MC [7]. The model of the reconstructed data is obtained by folding the "true data" with the transfer matrix A. They are then unfolded, with the same procedure as for the real data, using a transfer matrix A' obtained after statistically fluctuating A. The difference between the result of this unfolding and the "true data" measures the bias due to the unfolding procedure. The reconstructed data before the unfolding are either statistically fluctuated, in which case we test the stability of the method (which is good), or used without additional fluctuations, in which case we have a more precise test of possible biases. The result of the test for such possible biases is shown in Fig. 2.87.

This comparison shows essentially local statistical fluctuations and biases at larger scales must be measured in larger bins. Doing so, we obtain a systematic error of 0.32% in the mass interval $[0.98; 1.01]$ GeV, 0.12% for $[1.03; 1.1]$ GeV, 0.07% for $[1.1; 1.5]$ GeV, and negligible elsewhere.

[7] Tests have also been made with this perturbation changed by $\pm 50\%$, proving the reliability of this study.

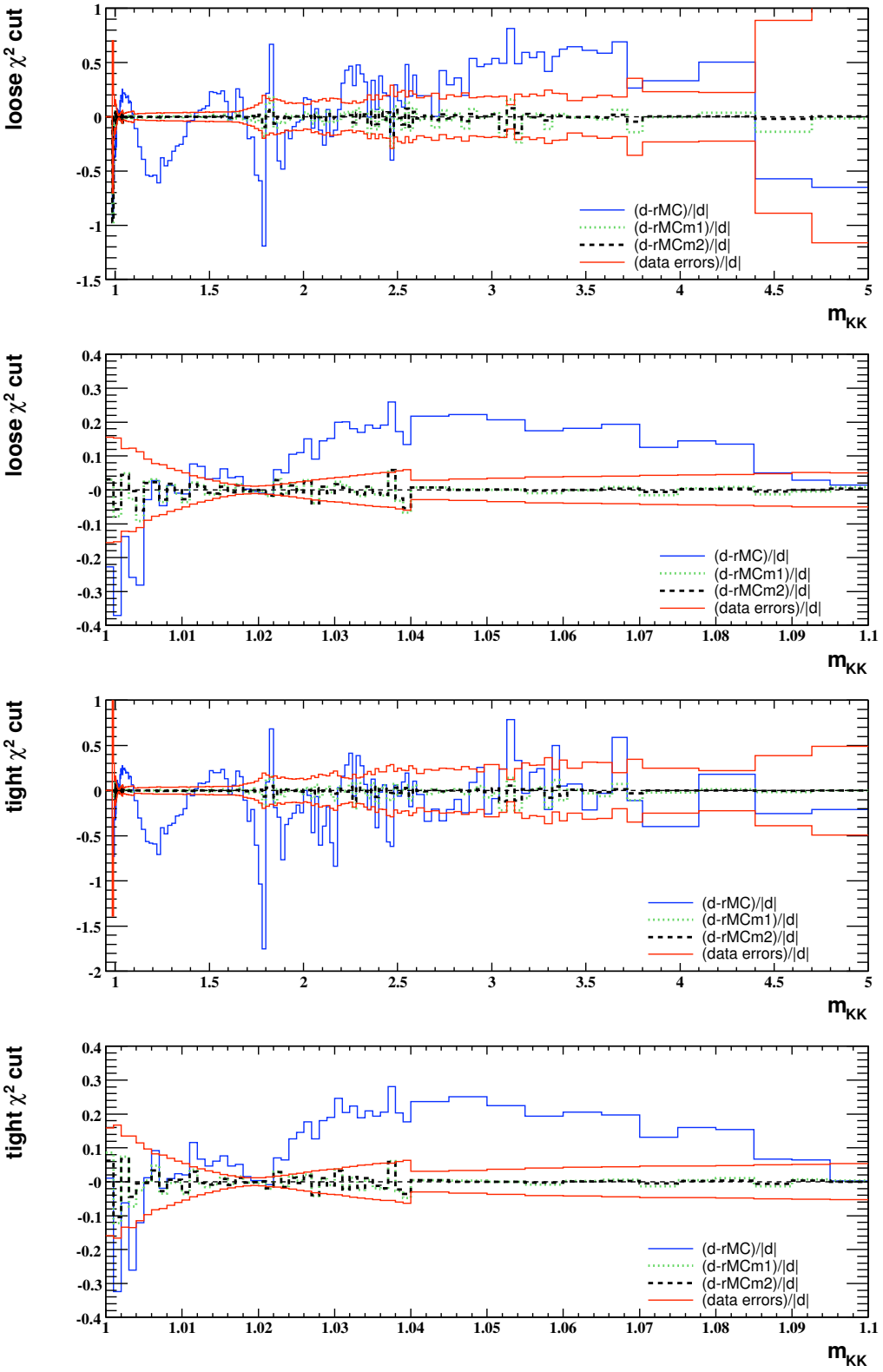

Figure 2.84: Relative values of the difference between data and reconstructed MC spectra in the loose and tight χ^2 region, at the first step (blue), after one iteration (dotted green) and after a second iteration (dashed black line). The diagonal errors are indicated by the red histograms.

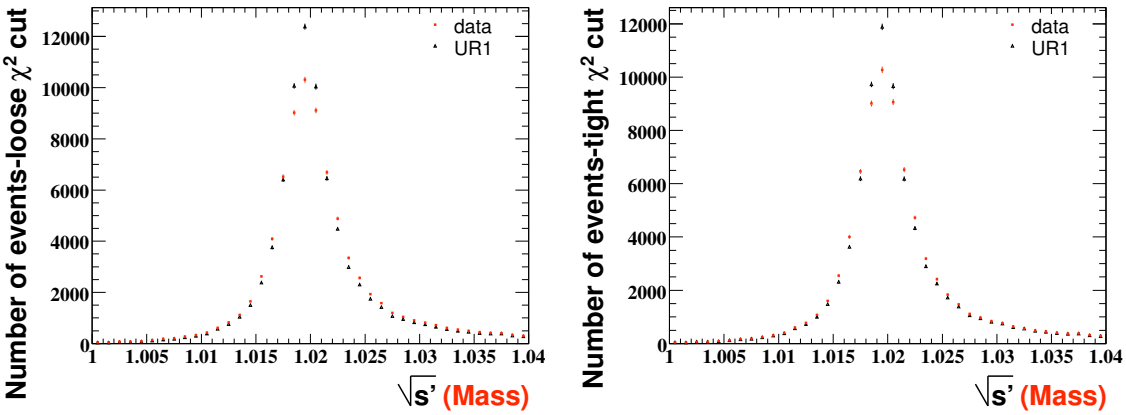

Figure 2.85: Distributions of number of events for data before unfolding (red) and after the first unfolding step (black). The plots correspond to events passing the loose χ^2-cut (left) and the tight χ^2-cut (right).

2.10.5 Comparison of the Unfolded Loose and Tight Spectra

Fig. 2.88 shows the relative comparison of the spectra obtained with the tight and respectively loose χ^2 cuts, after applying all the corrections described above, in a mass region where the loose spectrum is not too affected by possible biases in background subtraction. We observe some systematic differences at the level of one percent. Actually, the spectrum obtained with the loose χ^2 cut is more sensitive to the corrections of resolution effects. Indeed, the differences observed at the mass of the ϕ peak are of the same order of magnitude as the effect of correcting the transfer matrix for events in the loose region. Hence, these differences are compatible with the corresponding systematic errors, which apply to the loose spectrum only. While the tight χ^2 selection makes the statistical errors larger, this is balanced by the larger systematic uncertainties in the loose χ^2 selection. Therefore, we decide to keep the more precise tight spectrum for the computation of the cross section in the following.

2.11 Geometrical Acceptance

The overall efficiency $\epsilon_{KK\gamma}$ is calculated using the AfkQed generator and full simulation, in the same way as the overall efficiency $\epsilon_{\mu\mu\gamma}$ that enters the effective luminosity calculation. Both are corrected for differences between data and detector simulation. This section deals with acceptance corrections that apply to the $KK\gamma$ cross-section measured from the ratio of the kaon spectrum to the effective luminosity. Despite the large data/MC discrepancies related to the AfkQed limitations, as studied for the absolute measurement of the $\mu\mu\gamma$ cross-section to be compared with QED, most of the data/MC acceptance corrections cancel in the $KK\gamma$ to $\mu\mu\gamma$ ratio, but for the second-order effects studied below.

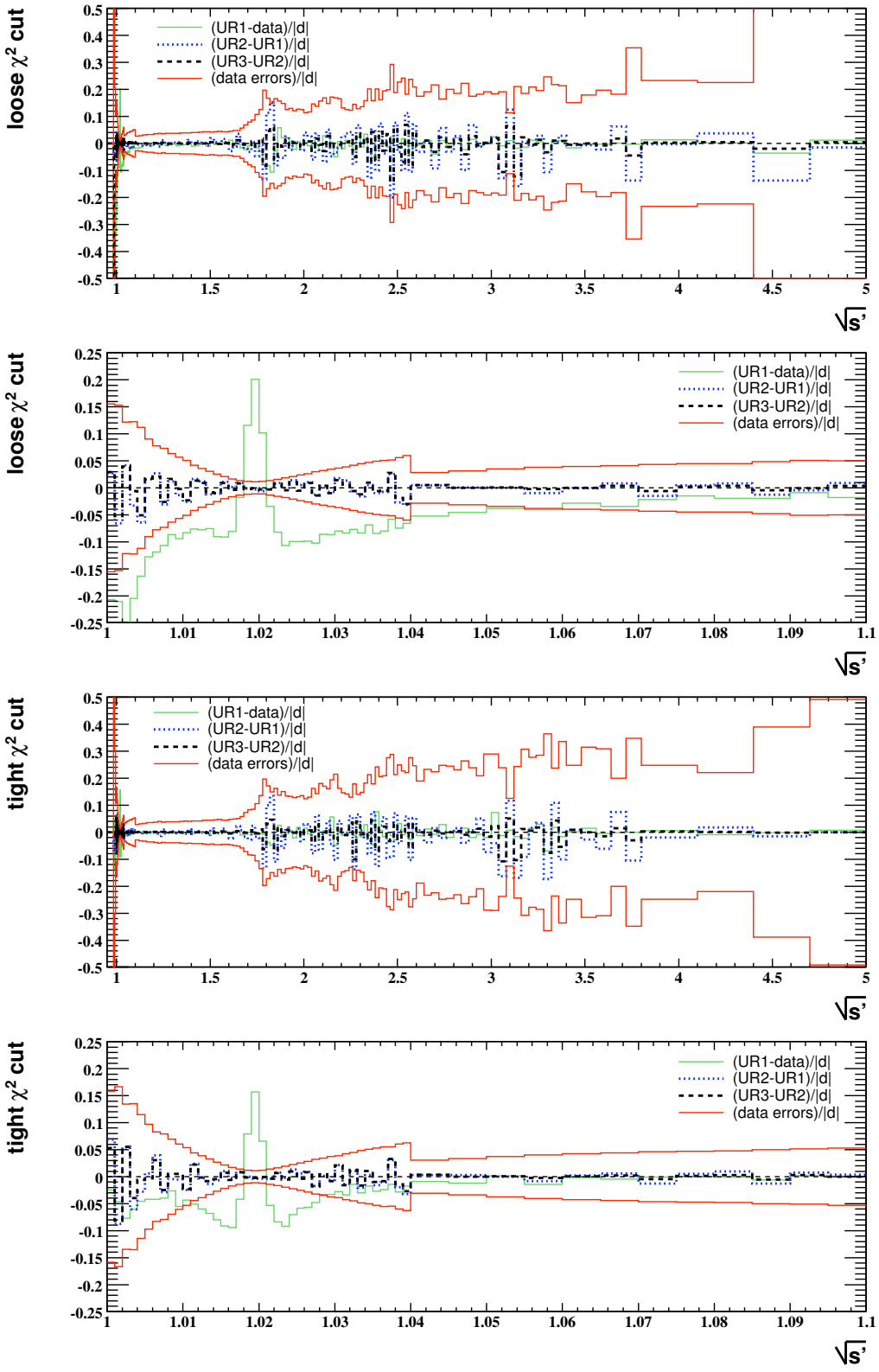

Figure 2.86: Relative correction done by the first step of the unfolding (green histogram), by one iteration (dotted blue line) and by a second iteration (dashed black line), for events in the loose and respectively tight χ^2 regions. The diagonal errors are indicated by the red histograms.

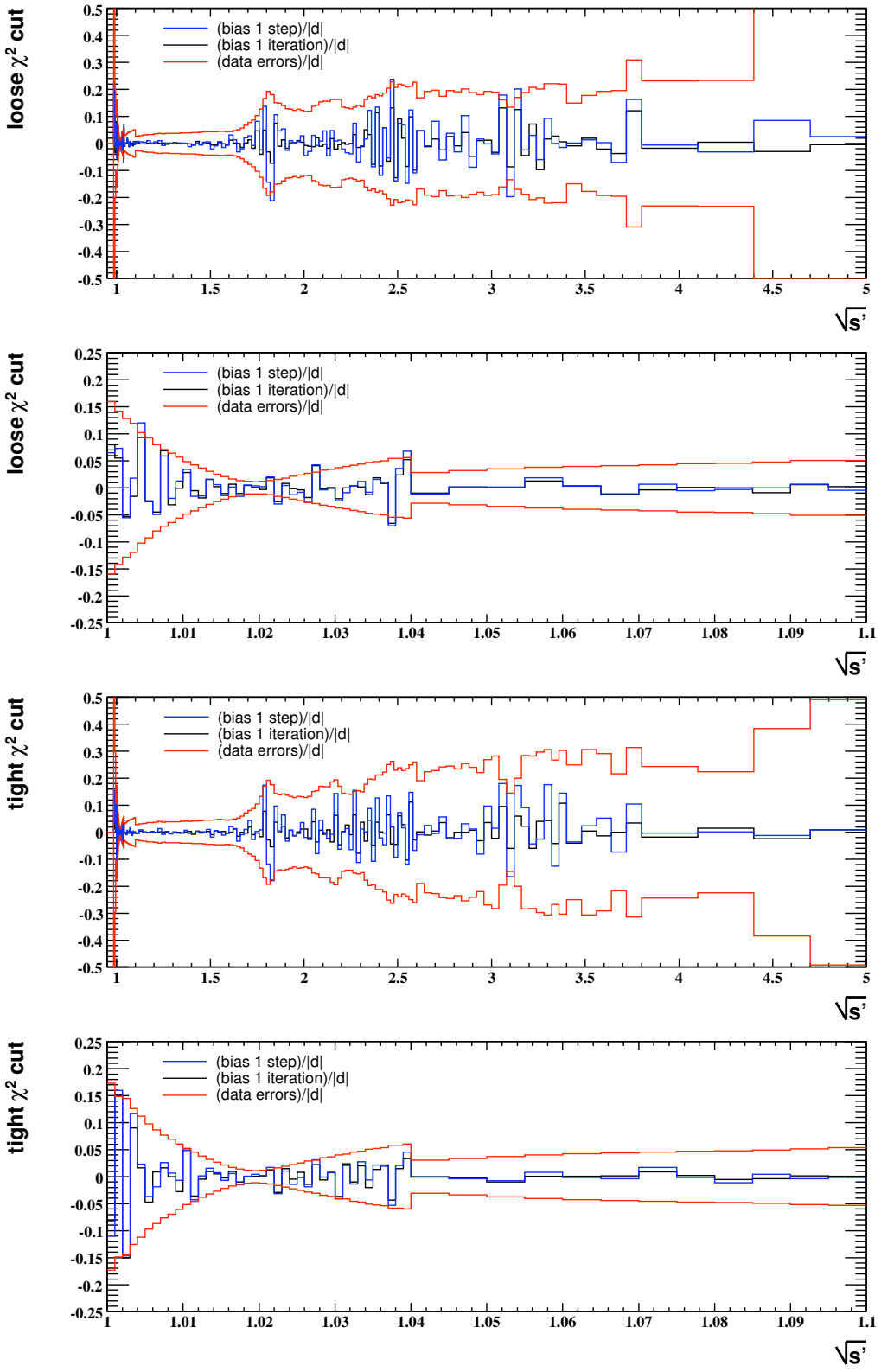

Figure 2.87: Relative bias of the unfolding result, after the first step (blue) and afer one iteration (black), for the loose and tight χ^2 region. The diagonal errors are indicated by the red histograms. These plots were obtained without additional fluctuations of the data after folding.

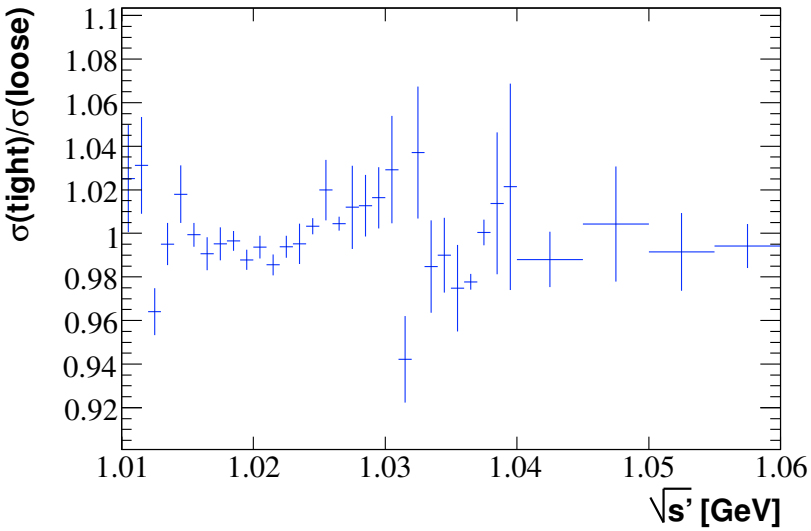

Figure 2.88: Ratio of the tight and loose spectra after unfolding, and after applying all the data/MC and acceptance corrections. The statistical errors are indicated.

2.11.1 Effects of the different acceptance cuts

The main criteria affecting the geometrical acceptance are: both charged tracks in the polar angle range $0.4 < \theta_{tr} < 2.45$ (rad), with momenta larger than 1 GeV/c, the most energetic photon in the CM in the polar angle range $0.35 < \theta_{\gamma} < 2.4$ (rad) (ISR candidate) [8] with $E^*_{\gamma} > 3$ GeV, and from the pre-selection cut (as described in Sec. 2.4.2). Other factors come from the definition of the active areas for the DIRC (z_{DIRC} cut and veto on cracks). The DIRC z cut actually limits the polar angle of tracks to about 0.45 rad.

In Fig. 2.89 we show the effect of the various (acceptance and pre-selection) cuts, at quadrivector level, for kaons and muons, on the efficiency with the AfkQed and Phokhara generators. The efficiency of the cut on the ISR photon (the most energetic photon in the CM among the ones in the angular acceptance) energy in the CM (> 3 GeV) is about 72% at the ϕ mass, slowly increasing with mass. The cut for the charged tracks in the angular acceptance of the detector has a larger efficiency at threshold and at 5 GeV, than at intermediate masses where it exhibits a minimum. Actually, in the e^+e^- CM frame, at threshold both charged tracks are in the direction opposite to the ISR photon, whereas at high x^+x^- masses one track is close to the ISR photon and the second track is in the opposite direction. As the efficiency of this cut is measured on a sample where the ISR photon is (by definition) in the angular acceptance of the detector, the events at low and high mass have their efficiency no further reduced. Events at intermediate masses have more distributed angles between the charged tracks, hence their lower efficiency. Additional radiation and the difference between the acceptance cuts of the ISR photon and charged tracks make the efficiency of the cut for the charged tracks in the angular acceptance more difficult to understand analytically. However, these effects explain the loss of events by this cut at the threshold as well as at high masses. The same effects of

[8] All the previous cuts are defined in the lab frame.

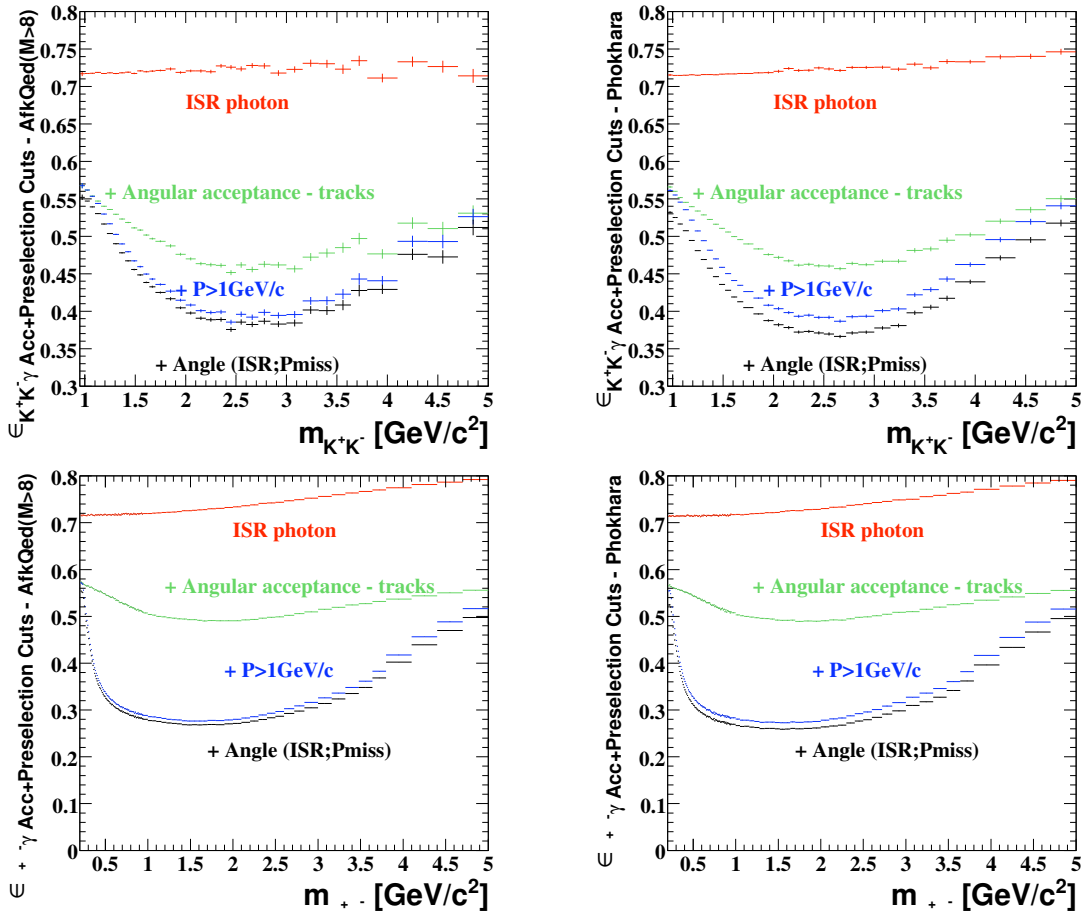

Figure 2.89: Efficiency of the various cuts tested at the quadrivector level for AfkQed (left), Phokhara (right), for K^+K^- (top) and $\mu^+\mu^-$ (bottom). For the two generators we measure the efficiencies of the following cuts applied sequentially: (1) the acceptance cuts: the most energetic photon (in the center-of-mass) in the angular acceptance of the detector has more than 3 GeV (red), plus each of the charged tracks is in the angular acceptance of the detector (green), plus the momentum of each of the charged tracks in the lab frame is larger than 1GeV/c (blue); (2) plus the pre-selection cut: the angle between the ISR photon and the missing momentum is smaller than 0.3 rad (black).

the geometry of the final state, together with the energy momentum conservation explain the high efficiency of the cut on the tracks momenta at the threshold and at high masses. At intermediate masses, the lower efficiency of the P > 1 GeV/c cut is due to asymmetric configurations. The effect of the cut on the momentum is stronger for muons than for kaons. This is due to the polar angle distribution of the ISR photon in the x^+x^- center-of-mass frame. Indeed, the $\cos\theta^*$ distribution goes like $(1+\cos^2\theta^*)$ for muons, peaking for asymmetric momenta of the charged tracks in the e^+e^- center-of-mass, while the distribution for kaons goes like $\sin^2\theta^*$, which peaks for equal momenta.

2.11.2 Common issues to $KK\gamma$ and $\mu\mu\gamma$ acceptance calculations

Acceptance is calculated using full simulation with the AfkQed generator. Apart from the kaon form factor, the leading order (LO) $KK\gamma$ process follows QED, as does $\mu\mu\gamma$, and therefore we do not expect any problem at this level [9]. The situation is different at the NLO level, where approximations are made in AfkQed: additional ISR photons are generated with the structure function method in the collinear approximation and additional FSR photons by PHOTOS. The FSR prescription is found to agree reasonably well with data (within a precision that is good enough, given the small fraction of FSR for kaons). This is not the case for additional ISR (see Section 2.9 above) for which large data/MC discrepancies were found related to (1) the assumption of collinear radiation instead of the QED angular distribution, sharply peaked along the beams, but with long tails, and (2) the lack of hard photon radiation because of a cut at generation level, $m_{KK\gamma ISR(\gamma addFSR)} > 8$ GeV. These two problems affect the event acceptance. They have been studied in detail in [28], as they have an effect on the absolute measurement of the $\mu\mu\gamma$ cross-section and the comparison with QED.

However the additional ISR issues are common to the $KK\gamma$ and $\mu\mu\gamma$ channels and first order cancel in the $KK\gamma/\mu\mu\gamma$ ratio. The acceptance corrections are studied in the next section and found to be larger than the ones that are obtained for the $\pi\pi\gamma/\mu\mu\gamma$ ratio [29], but still within acceptable limits (a few per mil on the ϕ resonance, increasing to the percent level when going up to 4 GeV, and larger, but with higher statistical errors, between 4 and 5 GeV). This difference is understood as being due to the different kinematic conditions (see below). As the full correction to the $KK\gamma/\mu\mu\gamma$ acceptance ratio is found to be considerably smaller (and better known) than the precision one can get on the measurement of the $KK\gamma$ spectrum alone, the KK cross section measurement does not rely on the accurate description of NLO effects by the MC generator. This feature is considered to be a strength of this analysis method.

[9] The data/simulation difference concerning the form factor in the high mass region only affects the statistics which is available, but not the estimation of the acceptance itself.

2.11.3 Effects not cancelling in the $KK\gamma/\mu\mu\gamma$ ratio

With a perfect generator, the acceptances calculated from simulation would accurately reproduce the ones in data and would fully account for the differences between the KK and $\mu\mu$ channels due to their different angular and momentum distributions. However, due to the approximate generation of additional ISR in AfkQed, acceptance from simulation has been found to differ from data. The nearly-exact NLO Phokhara generator has been used to estimate the necessary corrections for the measurement of the $\mu\mu$ cross section in Ref. [28]. One therefore has to worry whether the data/MC correction is different for the KK and $\mu\mu$ channels, since it would spoil the cancellation of the additional ISR effects in the acceptance ratios.

Another effect on acceptance originating from additional ISR (i.e. precisely where AfkQED cannot be trusted) comes through the efficiency of the pre-selection described in Section 2.4: that requires that the angle between the ISR photon and the missing momentum from the two charged particles (plus additional photons, if any) be less than 0.3 rad. As the cut is applied on data at an early stage, a direct study of the different behaviour of this cut in data and simulation can not be made and the correction is not readily available. Here again we will benefit from important cancelations of systematic effects, when taking the ratio of kaon to muon spectra, while Phokhara will be used to estimate second order differences. Furthermore, one then should investigate whether the pre-selection cut could produce a different data/MC correction for muons and kaons, when reconstructed quantities are involved. Possible causes of deviations include the effect of secondary interactions of kaons.

Finally, the fact that $\mu\mu\gamma$ process proceeds at lowest-order by ISR and FSR, unlike $KK\gamma$ which has negligible FSR, could also produce some difference. The $|FSR|^2/|ISR|^2$ contribution for muons is about 1.4% at the ϕ mass, and larger at higher masses.

Most of these effects can be studied at generator level because they involve essentially kinematics, due to the strong Lorentz boost along the beams when hard additional ISR photons are emitted. This boost affects the event acceptance in a way that could introduce a kaon/muon difference in acceptance. It also has an effect on the efficiency of the kinematics-dependent pre-selection cut. A comparison between the Phokhara and AfkQed generators with events at quadrivector level is used to provide realistic estimates of data/MC corrections and $KK/\mu\mu$ ratio. On the contrary the study of the effect of secondary interactions of kaons requires full simulation to compare with data. It must be stressed again that all these effects are second-order effects as they only involve KK to $\mu\mu$ differences on the data/MC acceptance corrections.

Residual effects of additional ISR radiation

The main kinematic effect resulting from the additional ISR photon is taken into account at generator level, both for its change in $KK\gamma$ and $\mu\mu\gamma$ acceptances and in the pre-selection cut efficiencies. For this study large samples of events have been generated: 8 10^7 for the muons with AfkQed and 5 10^7 with Phokhara, 1.6 10^7 for the kaons with

AfkQed and 11.9 10^7 with Phokhara. For the kaons some 0.9 10^7 additional events were generated with Phokhara at masses larger than 1.5 GeV in order to compensate for the faster form factor fall off, comparing to AfkQed.

We obtain the acceptances (with pre-selection cut) with Phokhara and AfkQed, and compute their ratios for the same generated mass ($\mu^+\mu^-$ or K^+K^-), because we are interested in R (see Fig. 2.90). This can produce larger differences than in the case of the comparison between $\mu^+\mu^-$ and $\pi^+\pi^-$, due to the larger mass difference between kaons and muons. At least in the low mass region, relatively large differences (of the order of 4%) between the efficiencies obtained with AfkQed and Phokhara, are observed for kaons as well as for muons. This is mainly due to the different treatment of additional radiation in the two generators. The final effect on the double ratio (bottom plot in Fig. 2.90):

$$C1 = \left(\frac{\epsilon^{K^+K^-\gamma}_{Phokhara,gen}}{\epsilon^{K^+K^-\gamma}_{AfkQed,gen}} \right)_{acc+presel} \Big/ \left(\frac{\epsilon^{\mu^+\mu^-\gamma}_{Phokhara,gen}}{\epsilon^{\mu^+\mu^-\gamma}_{AfkQed,gen}} \right)_{acc+presel}, \tag{2.27}$$

is however very much reduced, due to the cancelation of generator effects in the two channels, as already observed for pions/muons. In the previous formula 'gen' stands for generator level, while 'acc' and 'presel' for acceptance and pre-selection cut efficiencies, respectively. Here however the residual effect in the $K^+K^-/\mu^+\mu^-$ ratio is larger as the result of more different kinematic conditions affecting the K^+K^- and $\mu^+\mu^-$ acceptances for hard additional ISR photons. The correction is of a few per mil in the ϕ region, increasing to 1-2 percent in the 1.5-4 GeV interval and to 3-4 percent (but with larger errors) at higher masses.

This global test also includes the effect of lowest order FSR in the muon channel.

Effect of secondary interactions in the pre-selection cut

A second source of bias on the pre-selection cut efficiency could arise from the kaon secondary interactions which can affect the event kinematics, hence the acceptance. In order to measure this effect we use AfkQed. In the top part of Fig. 2.91 we show the ratio of the pre-selection cut efficiencies for kaons and muons, at the generated level and with full simulation. At generator level we see only differences due to kinematics (mass difference between kaons and muons), while at reconstructed level the interactions introduce additional differences. We indicate in black the errors coming from the K^+K^- efficiencies and in green the total errors. The errors of the K^+K^- efficiencies are partially correlated because it is a part of the generated events (the ones that are reconstructed) that are used to compute the efficiency in the full simulation. This correlation factor is indicated in the bottom left part of the figure. It is of about 40% (or slightly larger on the ϕ tails). There $\mu^+\mu^-$ efficiencies are not correlated because independent samples are used at the generated (with more statistics) and reconstructed level. We finally compute the double ratio (Fig. 2.91, bottom right) :

$$C_2 = \left(\frac{\epsilon^{AfkQed,full}_{K^+K^-\gamma}}{\epsilon^{AfkQed,full}_{\mu^+\mu^-\gamma}} \right)_{presel} \Big/ \left(\frac{\epsilon^{AfkQed,gen}_{K^+K^-\gamma}}{\epsilon^{AfkQed,gen}_{\mu^+\mu^-\gamma}} \right)_{presel}, \tag{2.28}$$

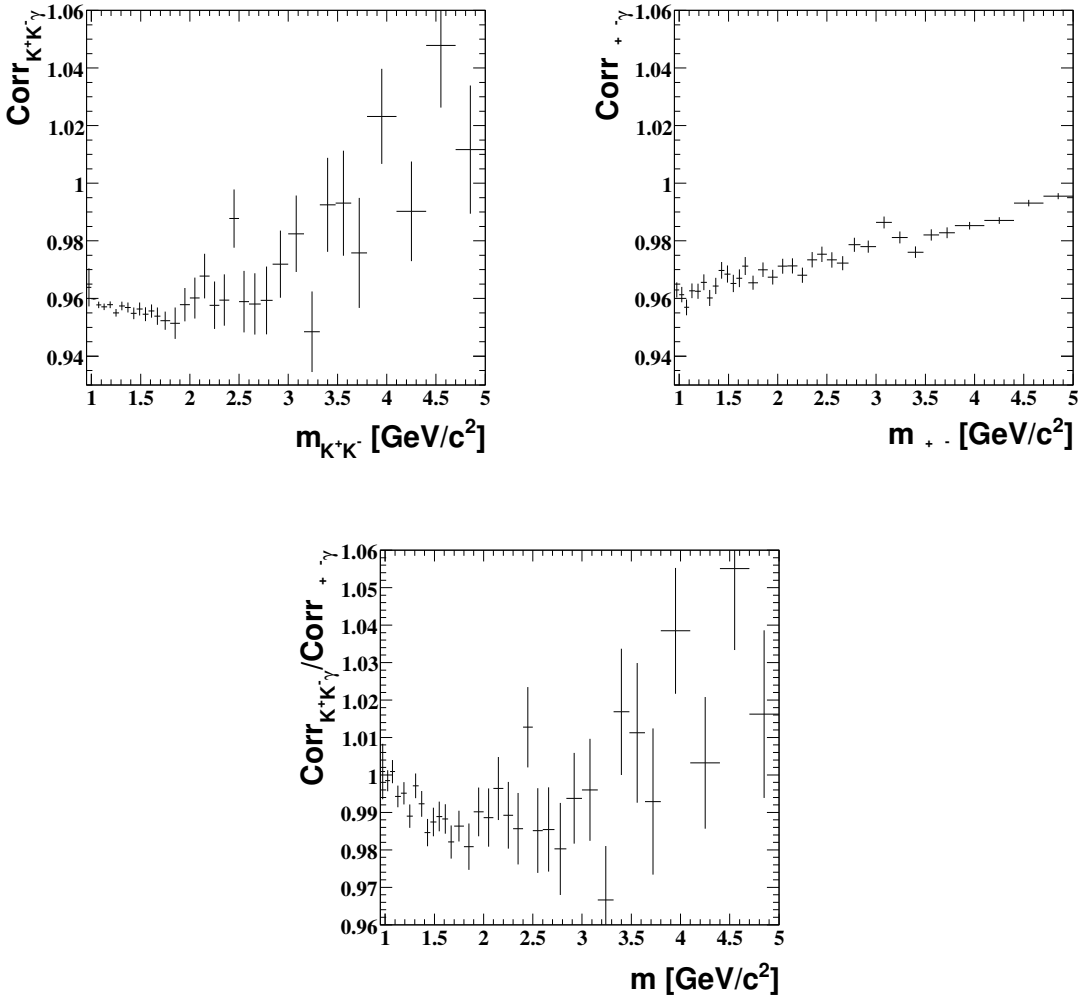

Figure 2.90: The ratios of acceptances (including the pre-selection cut) $\epsilon_{KK\gamma}^{Phokhara}/\epsilon_{KK\gamma}^{AfkQed}$ (top left) and $\epsilon_{\mu\mu\gamma}^{Phokhara}/\epsilon_{\mu\mu\gamma}^{AfkQed}$ (top right), as well as the double ratio $\left(\epsilon_{KK\gamma}^{Phokhara}/\epsilon_{KK\gamma}^{AfkQed}\right) / \left(\epsilon_{\mu\mu\gamma}^{Phokhara}/\epsilon_{\mu\mu\gamma}^{AfkQed}\right)$ (bottom), at generator level.

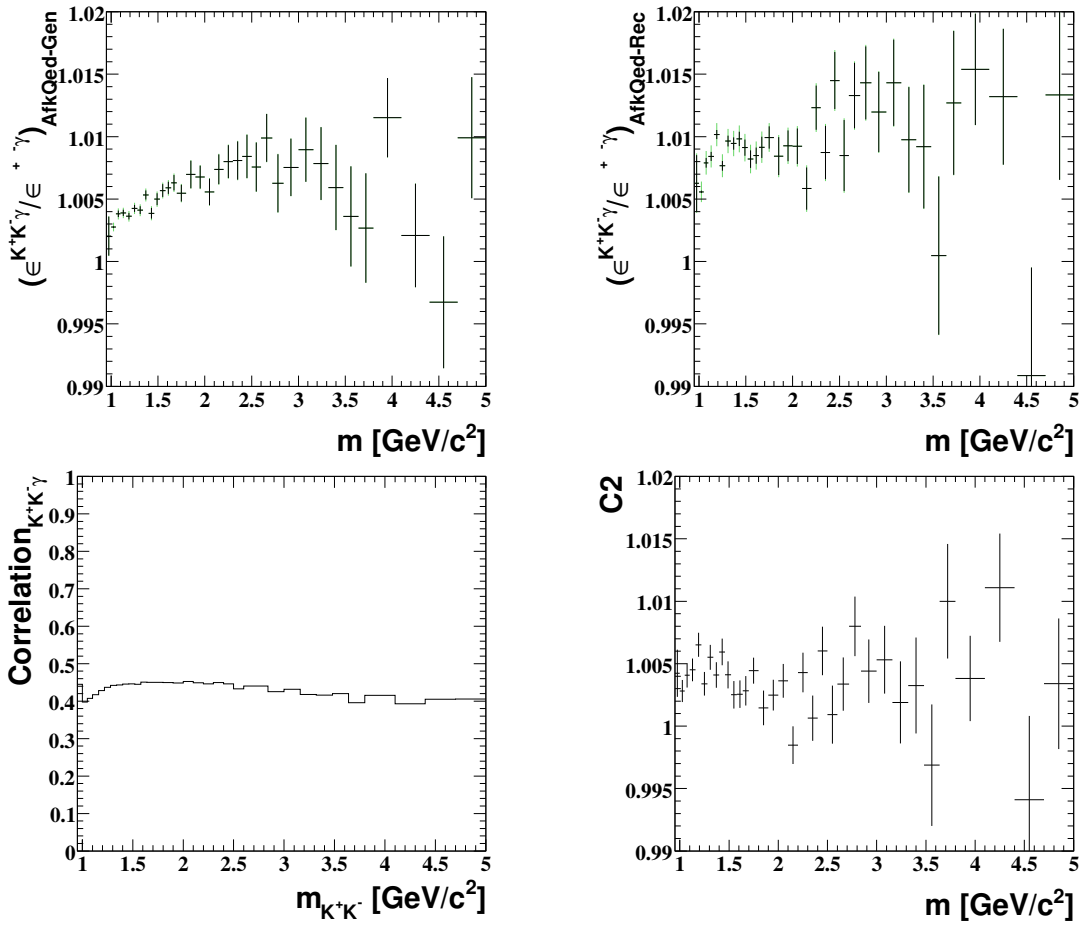

Figure 2.91: Top left: the ratio of the pre-selection cut efficiencies for kaons and muons, for AfkQed at the generator level. Top right: the ratio of the pre-selection cut efficiencies for kaons and muons, for AfkQed with full simulation. The errors from the K^+K^- efficiencies (partially correlated between the generated and the reconstructed level) are indicated in black while the total errors are in green. Bottom left: the correlation factor between the K^+K^- events at the generated and reconstructed level. Bottom right: C_2 = the ratio of the right and left histograms in the top part of this figure (see text).

where 'full' stands for full simulation level. This ratio measures the effect of interactions on the pre-selection cut efficiency. It is rather flat as a function of mass, at the level of a few per mil.

We have seen (Section 2.9.4) that the measured ratio of interactions between data and MC is 1.51 ± 0.11. Therefore, the deviation from one observed in C_2 should be scaled by this factor to obtain the data/MC correction from secondary interactions to the $KK/\mu\mu$ acceptance ratio.

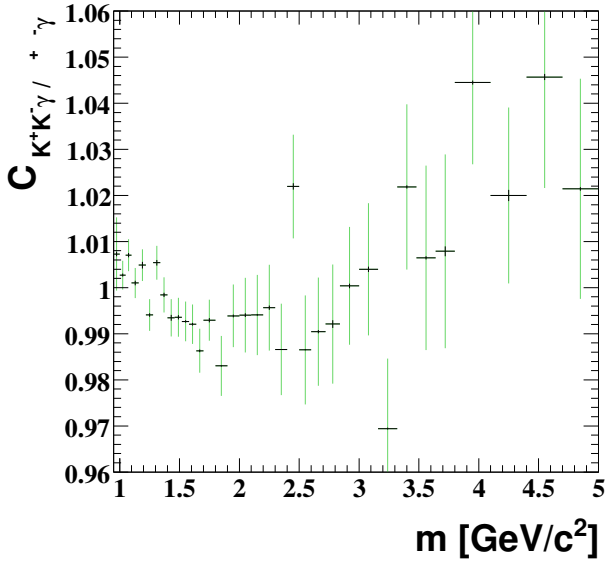

Figure 2.92: The full correction to the $K^+K^-\gamma/\mu^+\mu^-\gamma$ acceptance ratio from differences for additional ISR between AfkQed and Phokhara and data/MC differences for the ISR pre-selections cut. The vertical black error bars show the small but fully correlated errors coming from the data/MC correction of secondary interactions. The green error bars show the total error in each bin.

Overall $KK/\mu\mu$ acceptance correction

The global test at generated level and the correction from secondary interactions are combined into an overall mass-dependent correction factor to be applied to the $K^+K^-\gamma$ acceptance when using the muon ISR luminosity for the K^+K^- cross section. The overall correction $C_{K^+K^-\gamma/\mu^+\mu^-\gamma}$ given by

$$C_{K^+K^-\gamma/\mu^+\mu^-\gamma} = C_1 \cdot [1 + (1.51 \pm 0.11) \cdot (C_2 - 1)], \tag{2.29}$$

is shown as a function of mass in Fig. 2.92. As for the other corrections, the statistical uncertainties (with their correlations) are included in the final cross section.

ISR photon efficiency in the effective ISR luminosity

The effective ISR luminosity includes the ISR photon efficiency which in principle factorizes in the $KK\gamma/\mu\mu\gamma$ ratio at fixed mass. However this is only true in the limit where the photon angular distribution remains the same after selection cuts for kaons and muons. If that was not the case, the events distribution would sample different photon efficiencies, introducing a violation of the factorization rule. Since the photon efficiency and the ratio of data to MC efficiencies have been measured (see Section 9 of Ref. [28]) in bins of gamma CM-energies and lab angles $(E^*_\gamma, \theta_\gamma)$, one can actually perform the sampling for kaon and muon events using MC. The resulting data/MC corrections are given in Fig. 2.93. No correction is applied to the KK cross section, but a systematic error of 1.2 10^{-3} is assigned in order to cover the small difference between the two corrections.

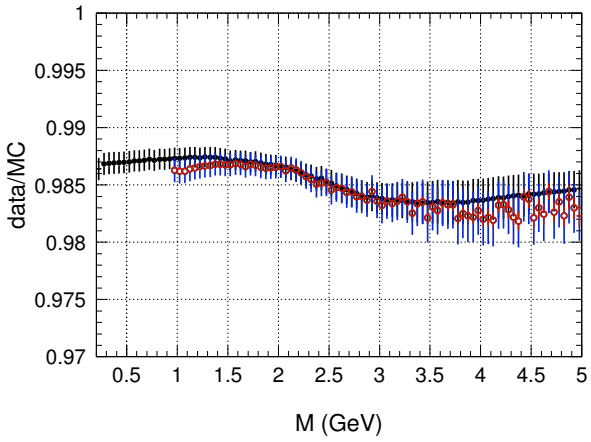

Figure 2.93: The data/MC correction of ISR photon efficiency for $KK\gamma$ (red open circles) and $\mu\mu\gamma$ (black filled circles) processes obtained by sampling the measured correction as a function of photon angle and energy for each mass bin. The total errors are shown in blue for kaons and in black for the muons. The error bars are dominated by the errors propagated from the measurement over almost all the spectrum, hence their correlation. It is only in the high mass region that the statistical errors of the kaons are not negligible (they are shown in red).

2.12 The Effective ISR Luminosity

The effective ISR luminosity (Eq. 2.2) is obtained directly from the analysis of $\mu\mu(\gamma)$ events, with methods very similar to the ones described in the previous sections for kaons. Details can be found in Ref. [28].

2.12.1 Comparison of the measured cross section for $e^+e^- \to \mu^+\mu^-(\gamma_{FSR})$ to QED

To asses the method, a direct comparison of the $\mu\mu(\gamma)$ cross section with QED was performed and a summary of this important test is given here. This comparison is made through the ratio (as a function of $m_{\mu\mu}$) of the distributions of data, subtracted from background, and of the simulation based on AfkQed, corrected from all data/MC detector and reconstruction effects and from the NLO generator problems using the Phokhara/AfkQed comparison with fast simulation, and normalized to the data luminosity. Because of the latter adjustments, this ratio is equivalent to a direct comparison of data to QED.

The QED prediction for the $m = m_{\mu\mu}$ distribution is obtained in the following way:

$$\frac{dN_{QED}}{dm} = L_{ee}\ \sigma^{NLO}_{Phokhara}\ \left(\frac{1}{N_0}\frac{dN}{dm}\right)^{AfkQed,M>8}_{fullsim} \frac{\left(\frac{1}{N_0}\frac{dN}{dm}\right)^{Phokhara}_{fastsim}}{\left(\frac{1}{N_0}\frac{dN}{dm}\right)^{AfkQed,M>8}_{fastsim}}\ C_{data/MC}\ , \qquad (2.30)$$

where for each case N_0 is the generated number of events, dN/dm the mass spectrum of

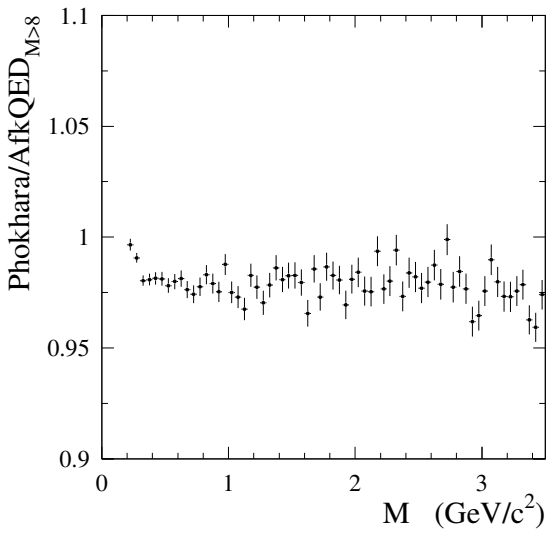

Figure 2.94: The ratio of the $\mu\mu$ mass spectra within acceptance cuts in Phokhara and AfkQed at generator level with fast simulation.

events satisfying all criteria. The ratio of spectra at generator level with fast simulation are labelled '$fastsim$', while '$fullsim$' denotes the spectrum of events with full detector simulation. AfkQed was run with a cut limiting hard additional ISR, noted '$M > 8$', namely $m_{\mu\mu\gamma_{ISR}(\gamma_{addFSR})} > 8$ GeV. Finally the $C_{data/MC}$ factor incorporates all corrections from data to the simulation for detector efficiencies, such as trigger, tracking, muon ID, χ^2 cut.

The ratio of spectra Phokhara/AfkQed at fast-simulation level is given in Fig. 2.94 for events satisfying the geometrical acceptance and the muon momentum cut. It is rather flat with a sharp increase at threshold, caused by the expected change of cross section in Phokhara for NLO FSR, which is not present in AfkQed. This contribution is small everywhere in the spectrum (see Section 2.12.2). The $C_{data/MC}$ correction is given in Fig. 2.95, the largest effect being from muon ID.

The ratio data/QED is shown in Fig. 2.96 separately for runs 1-2 and runs 3-4. Both distributions are flat from threshold to 3.5 GeV and consistent with unity within errors with satisfactory χ^2 values. Fits with a constant value give

$$\frac{\sigma^{data}_{\mu\mu\gamma(\gamma)}}{\sigma^{NLO\ QED}_{\mu\mu\gamma(\gamma)}} = 1 + (7.8 \pm 3.1 \pm 6.5 \pm 9.4)\ 10^{-3} \quad \text{runs } 1-2 \quad 0.2-3.5\ \text{GeV} \quad (2.31)$$

$$= 1 + (1.8 \pm 2.4 \pm 5.3 \pm 9.4)\ 10^{-3} \quad \text{runs } 3-4 \quad 0.2-3.5\ \text{GeV} \quad (2.32)$$

where the errors are statistical (data, MC, efficiencies), systematic from our measurements, and systematic from the BaBar luminosity, respectively. The BaBar luminosity L_{ee} is obtained from analyses of Bhabha and $\gamma\gamma$ samples [31, 32].

Both groups of runs are consistent within errors: the difference of the ratios for runs

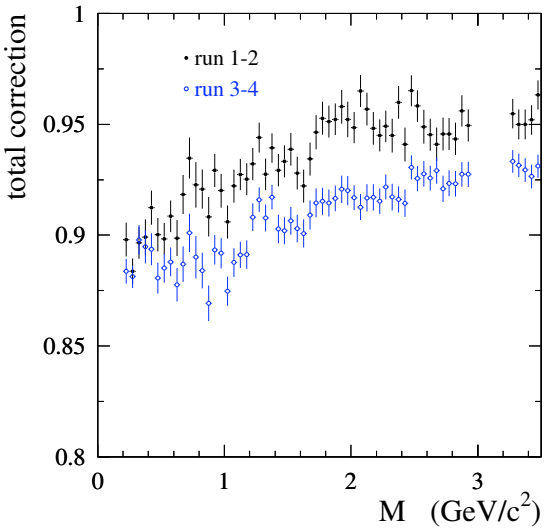

Figure 2.95: The total correction data/MC for the detector simulation as a function of $m_{\mu\mu}$ for runs 1-2 and 3-4.

1-2 and runs 3-4 in the 0.2-3.5 GeV range is $(6.0 \pm 4.0 \pm 3.5 \pm 4.4)\ 10^{-3}$, where the first error is statistical, the second from uncommon systematics (photon efficiency ratio for run 1, uncorrelated parts of the μ-ID systematic uncertainties), and the third from the BaBar luminosity (an estimate of the relative error on the BaBar luminosity is found in Ref. [29]). The two results can thus be combined (see Fig. 2.97), yielding

$$\frac{\sigma^{data}_{\mu\mu\gamma(\gamma)}}{\sigma^{NLO\ QED}_{\mu\mu\gamma(\gamma)}} = 1 + (4.0 \pm 1.9 \pm 5.5 \pm 9.4)\ 10^{-3} \quad \text{runs } 1-4 \quad 0.2 - 3.5\ \text{GeV} \quad (2.33)$$

The values found for the $\mu\mu$ data/QED ratio are consistent with 1 over the full mass range explored in this analysis. We conclude that our measurement of the $ee \to \mu\mu\gamma(\gamma)$ cross section using the BaBar luminosity agrees with NLO QED in the $\mu\mu$ mass range from threshold to 3.5 GeV within the overall accuracy of 1.1%. This test is limited by the accuracy of L_{ee}, but requires the full understanding of the global absolute efficiency for the $\mu\mu\gamma$ sample. Nevertheless, this test is more demanding than the $KK\gamma$ cross section measurement from the $KK\gamma/\mu\mu\gamma$ ratio, where systematic uncertainties are smaller.

2.12.2 Determination of the effective ISR Luminosity

In this section we express the results obtained on the $\mu\mu\gamma(\gamma)$ sample in terms of the effective ISR luminosity, following Eqs. (2.1) and (2.2). This quantity can be used together with any measurement of a hadronic process with the ISR method, such as $\pi^+\pi^-(\gamma_{FSR})$, $K^+K^-(\gamma_{FSR})$, or $X(\gamma_{FSR})$ where X is a multihadronic final state. In order to facilitate its use we will give results as a function of $\sqrt{s'}$ with $\sqrt{s'} = m_{X(\gamma_{FSR})}$, rather than s', since ISR results on cross sections have been given so far in this way.

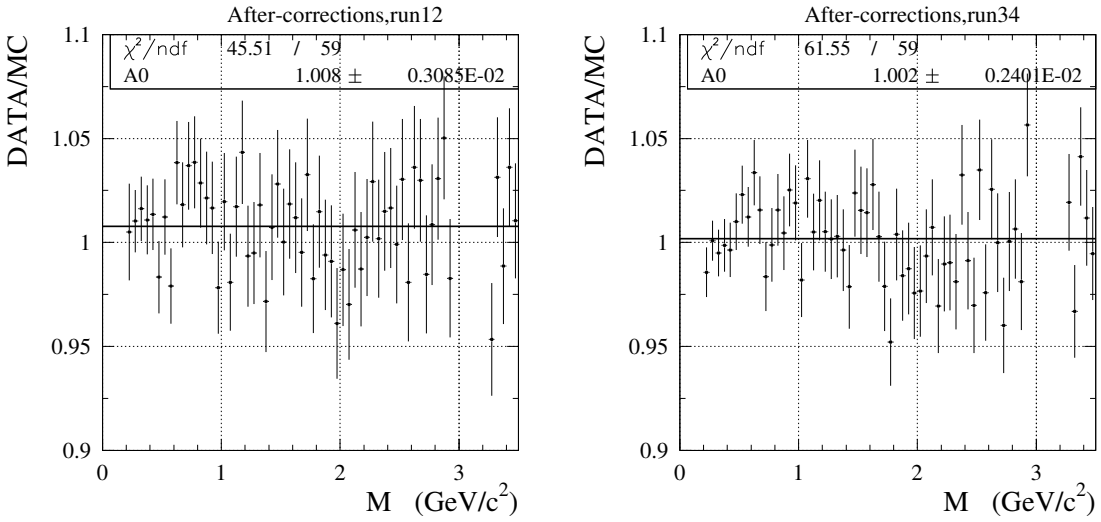

Figure 2.96: The ratio of the $\mu\mu$ mass spectrum in data over the absolute prediction from QED using the BaBar luminosity: runs 1-2 (left), runs 3-4 (right). The NLO QED prediction is obtained from the data-corrected (for detector simulation) and Phokhara-corrected (for NLO effects) AfkQed mass spectrum. The solid line is a fit of the 0.2-3.5 GeV with a free constant.

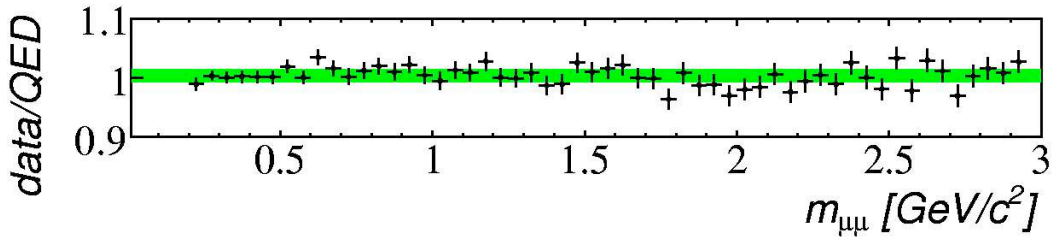

Figure 2.97: The ratio of the $\mu\mu$ mass spectrum in data over the absolute prediction from QED using the BaBar luminosity: runs 1-4. The NLO QED prediction is obtained from the data-corrected (for detector simulation) and Phokhara-corrected (for NLO effects) AfkQed mass spectrum. The band is drawn around the fit of the 0.2-3.5 GeV to a free constant, with a width given by $\pm$ the total expected systematic uncertainty (from this analysis and from the BaBar ee luminosity).

As discussed in [28], the $\mu\mu\gamma(\gamma)$ event acceptance appearing in Eq. (2.1) is obtained from a large simulated sample generated with AfkQed. Corrections have been applied at the simulation level for detector and reconstruction effects.

Several effects need to be considered in addition: (1) the LO FSR correction from Eq. (2.7), (2) the unfolding of the data from $m_{\mu\mu}$ to $\sqrt{s'}$, thus including the possible emission of an additional FSR photon, and (3) the QED cross section $\sigma_0(ee \to \mu\mu(\gamma_{FSR})\ (s')$ at the Born level concerning ISR, but including FSR. We take these points in turn before giving the final results.

Lowest-order FSR correction

The most energetic detected photon is assumed to be emitted by the initial state. This is largely true at low mass, but there is an increasing probability at larger s' values that this photon originates from muon radiation. Thus the observed $\mu\mu$ mass spectrum has to be corrected in order to keep only ISR production, since for all practical purposes at BaBar, where $\sqrt{s} \sim 10.58$ GeV and $\sqrt{s'} < 5$ GeV, main FSR production ('main' as opposed to 'additional' FSR) is completely negligible for hadronic processes.

Fig. 2.98 shows the quantity δ_{FSR} obtained with AfkQed at the generator level, since at this level the final mass spectrum is already corrected for acceptance and efficiencies. The correction is defined as

$$\delta_{FSR} = \frac{|FSR + (FSR + addISR, FSR)|^2}{|ISR + (ISR + addISR, FSR)|^2} \tag{2.34}$$

as a function of $\sqrt{s'}$. It would have been preferable to use Phokhara instead, as we know additional ISR is approximate in AfkQed, but by construction the labels FSR or ISR for photons are not available in Phokhara, hence s' is not accessible on an event-by-event basis. However the difference is expected to be at a negligible level, about 10^{-4} and $2\ 10^{-3}$ at 1 and 3 GeV, respectively.

In fact the importance of main FSR production can be experimentally determined in the case of 2-body processes $x^+x^-\gamma$ using the measurement of a charge asymmetry which projects the interference between ISR and FSR amplitudes. The charge asymmetry, being dependent on the relative FSR and ISR amplitudes, is a sensitive test of an FSR contribution. Such a measurement has been already carried out in preliminary form for the $\mu^+\mu^-\gamma$ and $\pi^+\pi^-\gamma$ processes [33]. The results obtained show a good agreement within a few % for muons with the large asymmetry predicted by AfkQed (QED) at large mass with its characteristic shape. Final results from this ISR-FSR interference analysis are not yet officially available, and we rely here safely on the AfkQed prediction for the FSR fraction as a function of mass.

Unfolding the Mass Distribution

As the ISR luminosity should be expressed as a function of $\sqrt{s'}$ which is the relevant variable for the process $ee \to \mu\mu(\gamma_{FSR})$, the $\sqrt{s'}$ distribution must be unfolded from the

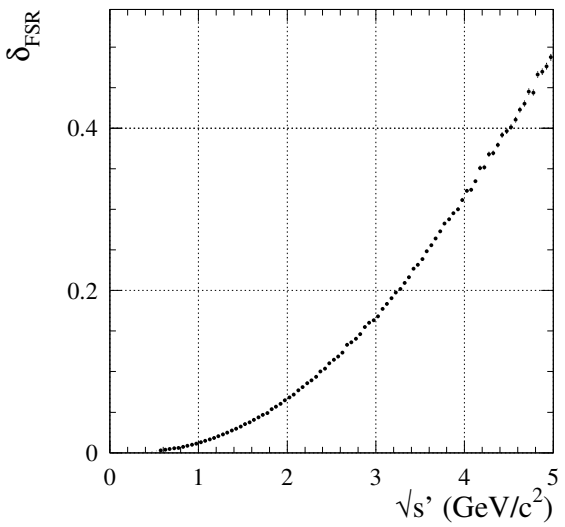

Figure 2.98: The FSR correction $\delta^{\mu\mu}_{FSR} = \frac{|FSR|^2}{|ISR|^2}$ obtained with AfkQed.

background-subtracted and data/MC-corrected $m_{\mu\mu}$ spectrum. This procedure should take into account mass resolution effects and additional FSR which shifts from $\sqrt{s'}$ to $m_{\mu\mu}$). Both sources produce small distortions of the spectrum.

We have used the unfolding technique, described in some detail in Chapter 1 and already exploited for the KK spectrum in section 2.10. The method is based on a MC-generated mass-transfer matrix to perform the deconvolution of the spectrum. The ($\sqrt{s'_{true}}$, $m_{\mu\mu\ reconstructed}$) mass matrix, where the reconstructed mass is obtained from the kinematic fit, has the structure of a sharp ridge along the diagonal with a width resulting from resolution effects and a low-level tail from FSR, as seen in Fig. 2.99. Compared to the KK and $\pi\pi$ analysis with the prominent ϕ and respectively ρ resonances, the $\mu\mu$ unfolding is uncritical. The mass spectrum has a smooth shape and resolution effects play a very small role. In fact the larger effect to correct is the FSR event shift.

The method delivers the unfolded distribution in the same 50-MeV mass bins as for the input spectrum. A large mass range 0-6 GeV is considered, although we need only a smaller region of the spectrum for luminosity purposes. A covariance matrix containing the statistical correlations between the bin contents is obtained with toy simulations, where both the data and the transfer matrix are statistically fluctuated.

Inadequacies in the detector simulation, essentially μ-ID, are corrected by comparing the distributions for data and reconstructed MC, thus modifying the transfer matrix. Only one unfolding step is necessary, but one can use an iteration (improving the transfer matrix) to check the stability of the unfolded spectrum. Fig. 2.100 shows the data - reconstructed MC difference before and after the first unfolding step, with a clear improvement, while Fig. 2.101 demonstrates that one iteration does not bring further improvement to the unfolded spectrum.

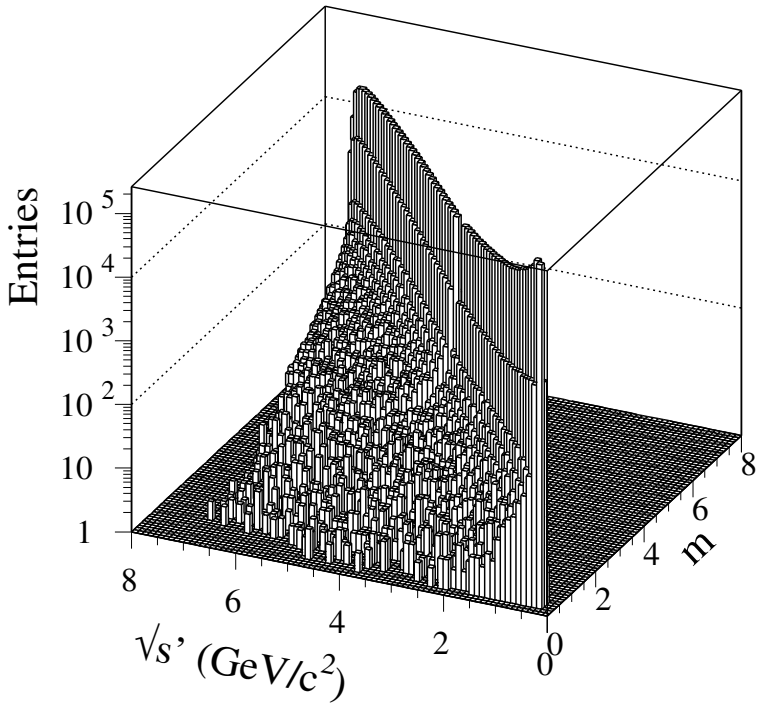

Figure 2.99: The mass transfer matrix from $\sqrt{s'}$ to $m_{\mu\mu}$ from the AfkQed simulation.

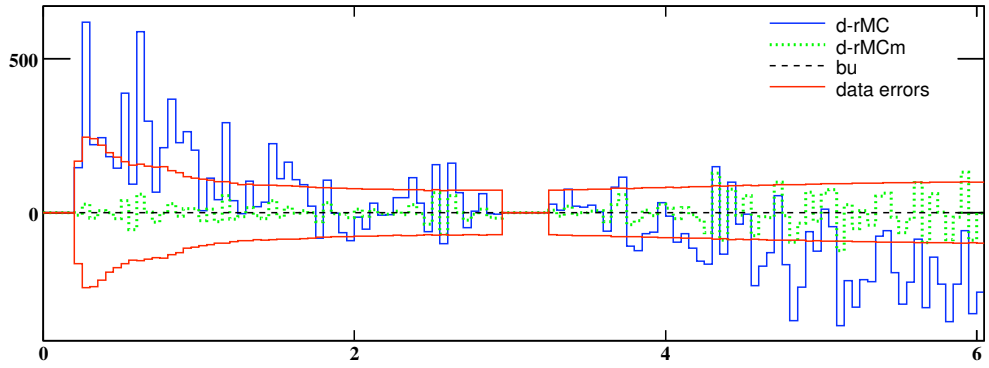

Figure 2.100: Data - reconstructed MC difference for the $\mu\mu$ spectrum, before($d - rMC$) and after ($d - rMCm$) one iteration. These values are compared to the statistical data errors.

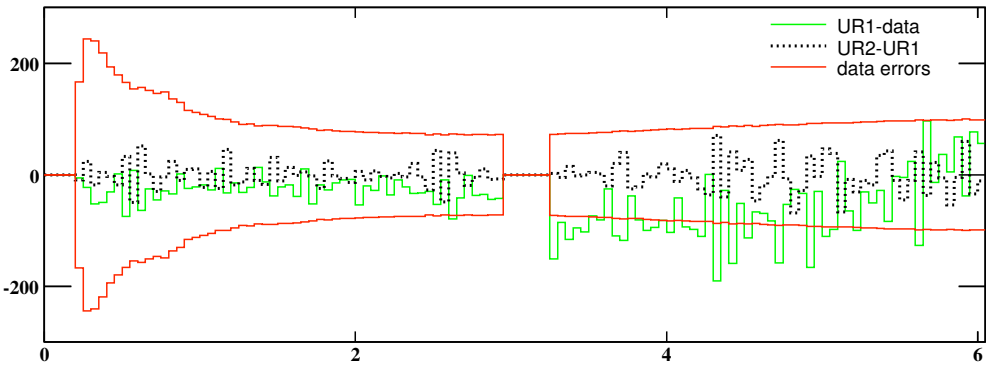

Figure 2.101: Correction of the $\mu\mu$ spectrum by the first unfolding(UR1-data) and by one iteration(UR2-UR1). These values are compared to the statistical data errors.

As for the KK unfolding, extensive toy studies with MC samples have been used to study the robustness and the accuracy of the unfolding method. These tests show that the systematic uncertainty from the unfolding method is within 10^{-3}.

Born QED cross section with additional FSR

The cross section for $e^+e^- \to \mu^+\mu^-(\gamma_{FSR})$, at Born level for the initial state and without vacuum polarization, can be calculated exactly in QED at NLO. It has the form:

$$\sigma_0^{\mu\mu(\gamma)}(s') = \sigma_{pt}(s') \left[1 + \frac{\alpha}{\pi}\eta(s')\right] \tag{2.35}$$

with

$$\sigma_{pt}(s') = \frac{4\pi\alpha^2}{3s'} \frac{\beta(3-\beta^2)}{2} \tag{2.36}$$

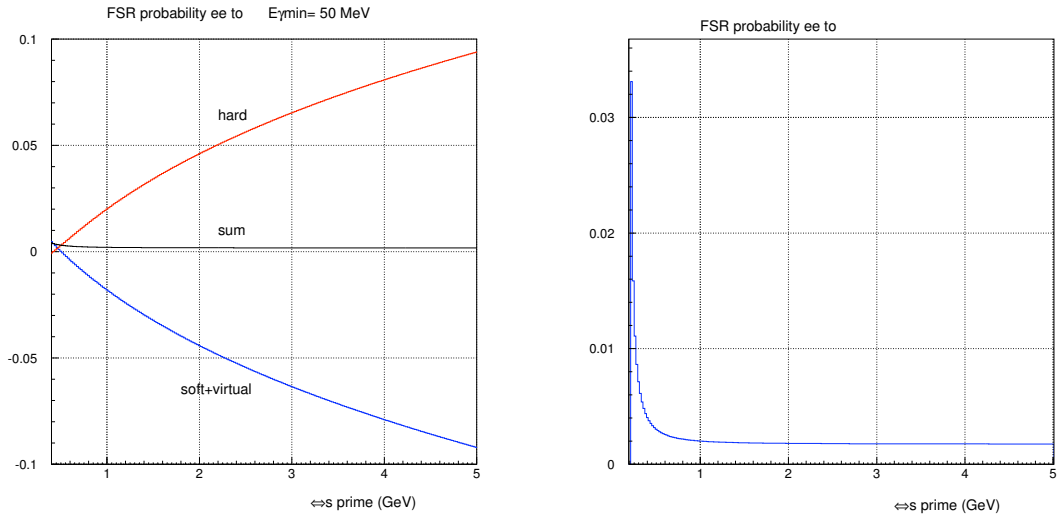

Figure 2.102: The relative FSR contributions as a function of $\sqrt{s'}$ in the process $e^+e^- \to \mu^+\mu^-(\gamma_{FSR})$, $\frac{\alpha}{\pi}\eta_{h,v+s}$ at NLO (left), and their sum (right). The separation between hard and soft radiation has been chosen at 50 MeV in the $\mu\mu\gamma$ center-of-mass.

$$\beta = \sqrt{1 - \frac{4m_\mu^2}{s'}} \tag{2.37}$$

$$\eta(s') = \eta_h(s') + \eta_s(s') + \eta_v(s') \tag{2.38}$$

where $\eta_{h,s,v}$ are the $O(\alpha)$ contributions (in the final state) from hard and soft bremsstrahlung, and the one-loop/Born interference. The sum of η_v and η_s is IR-finite, while the total sum is independent of the choice of the energy used to separate soft and hard photons (within reasonable limits). Expressions for all 3 components can be found in many papers, for ex. in Refs. [18, 36].

By virtue of the Kinoshita-Lee-Nauenberg (KLN) theorem [35], the dominant logarithmic terms cancel between the (soft+virtual) and hard contributions. As seen in Fig. 2.102, although each term reaches a level of a few % with opposite signs, the sum stays in the few 10^{-3} range. This explains why we see a sizeable additional-FSR signal in data, despite the fact that the total additional-FSR contribution is very small.

Effective ISR luminosity for the $KK/\pi\pi$ analysis

For the KK and $\pi\pi$ analysis, the luminosity L_{eff}^{full} integrates all configurations up to 2 ISR photons with at least one with $E_\gamma^* > 3$ GeV and $20° < \theta_\gamma^* < 160°$. To obtain the measured full effective ISR luminosity $dL_{eff}^{full}/d\sqrt{s'}$ according to (Eq.2.1) the event acceptance is taken from AfkQed, in spite of its limitations, since data/MC correction estimates from Phokhara are strongly reduced in the ratios $\pi\pi/\mu\mu$ and $KK/\mu\mu$ (see Sec. 2.11). The results are given for runs 1-4 in Fig. 2.103 for 50 MeV bins.

The obtained luminosity can be compared to the standard estimate using LO QED,

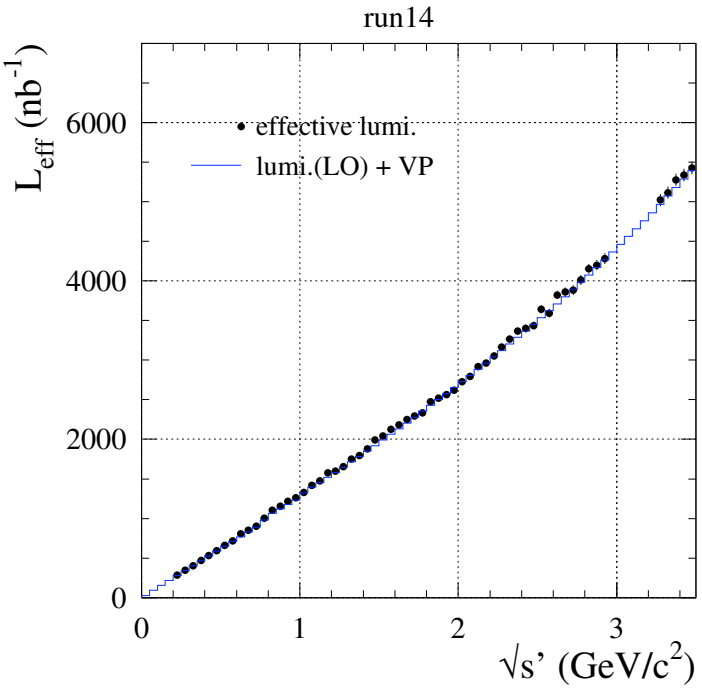

Figure 2.103: The effective ISR luminosity in runs 1-4 for the $\pi\pi$ and KK analyses: the data points give ΔL_{eff}^{full} in $\Delta\sqrt{s'} = 50$ MeV bins. Conditions for the detected/identified ISR photon are $E_\gamma^* > 3$ GeV and $20^\circ < \theta_\gamma^* < 160^\circ$ in the ee CM frame, while one additional ISR photon is allowed without any restriction. The superimposed histogram is the lowest-order ISR prediction following Eq. (2.39). The J/ψ mass region is cut out for the data.

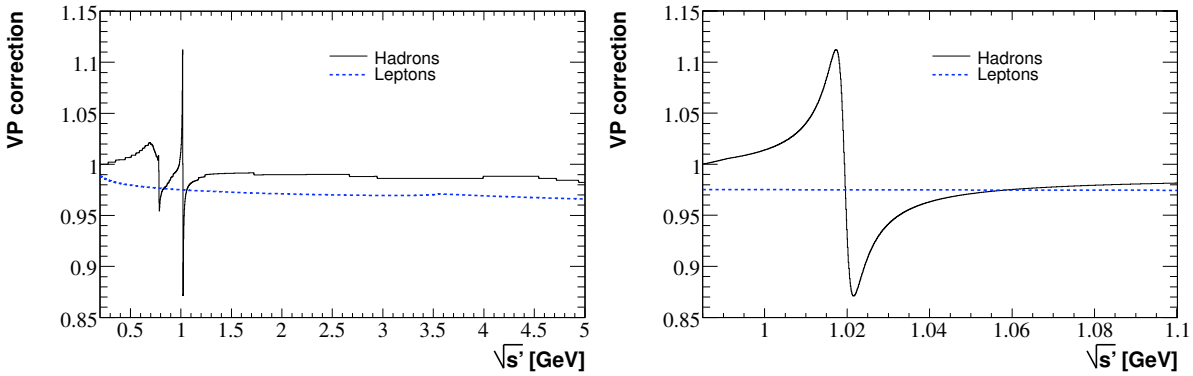

Figure 2.104: Hadronic (black line) and leptonic (blue dashed line) vacuum polarization corrections. The contributions from the J/ψ and the ψ' were not included (see text).

given by

$$\frac{dL_{LO}}{d\sqrt{s'}} = \frac{\alpha}{\pi x}\left[(2-2x+x^2)\ln\frac{1+c}{1-c} - x^2 c\right]\frac{2\sqrt{s'}}{s}\left(\frac{\alpha(s')}{\alpha(0)}\right)^2 L_{ee} \tag{2.39}$$

where $x = 1 - s'/s$ and $c = \cos\theta^*_{\gamma\ min}$ with $\theta^*_{\gamma\ min} = 180^\circ - \theta^*_{\gamma\ max} = 20^\circ$. We have left the vacuum polarization factor in Eq. (2.39) for a convenient comparison. The LO prediction is superimposed to the measured luminosity in Fig. 2.103. The agreement is fair, with some deterioration at large mass. The vacuum polarization factor includes both leptonic and hadronic contributions (see Fig. 2.104), but without the J/ψ and the ψ'. The hadronic contribution is taken from the parametrization used in AfkQed and it has been checked that it agrees well with independent determinations [37]. The systematic uncertainties on this correction are mainly due to the parameters of the narrow ϕ resonance, with an additional contribution from the continuum. The first contribution is included in the total uncertainty of the bare cross section, while the second cancels in the $KK/\mu\mu$ ratio.

The effective ISR luminosity as a function of $\sqrt{s'}$ is determined in 50-MeV bins which is insufficient near narrow resonances (ω and ϕ) because of the rapid variation of hadronic vacuum polarization. Therefore we consider in each 50-MeV bin the ratio between the measured luminosity and the product of the lowest-order QED luminosity function times the vacuum polarization factor (see Eq. (2.39)). In this way the detailed local features of the vacuum polarization are incorporated, while preserving the measured effective luminosity as a function of mass. This ratio is expected to be slowly varying with mass, the only sources of variation being the difference between the LO and full luminosity functions, the ratio of data to MC of the ISR photon efficiencies, and any residual effect in the detection efficiency. The latter contribution should be small, owing to the successful QED test performed with the $\mu\mu\gamma(\gamma)$ cross section. Finally, in order to compute the cross section, we use the theoretical luminosity multiplied by the binned ratio mentioned above.

Since the statistical error on the KK cross section on the ϕ resonance (and $\pi\pi$ cross section on the ρ resonance) is limited by the statistics on the ISR luminosity, we have tried to reduce statistical fluctuations by suitable averages of the ISR luminosity ratio. Three methods have been considered for the ratio.

1. The most straightforward method is to use the distribution of the ratio in 50-MeV bins. Certainly the assumption of slow variation is very conservatively fulfilled within the bins. Luminosity errors are then taken fully correlated in the $\pi\pi$ cross section bins (2 or 10 MeV) inside a 50-MeV luminosity bin, and incorporated in the full covariance matrix. We have explicitely checked that the statistical error on the dispersion integral used in the $g-2$ determination does not depend on the chosen luminosity bin size, from 50 down to 2 MeV. The disadvantage here comes from statistical fluctuations in groups of cross section values.

2. The ratio distribution in 50-MeV bins is smoothed by averaging n consecutive bins (sliding bins). The value $n = 5$ is chosen as a compromise between smoothing and validity of the assumption of slow variation. This method does not improve in principle on the ISR luminosity statistical error because the reduced local error is compensated by the correlation between neighbouring bins. In practice a slight improvement in the dispersion integral is observed due to the weighting in different mass regions. Statistical fluctuations are efficiently distributed.

3. The ratio is fitted over the full mass range between 0 and 3 GeV with polynomials. The statistical uncertainty is greatly improved in the important region below 1 GeV, at the expense of a systematic error, estimated by varying the fitting function. The difficulty here is the reliability of the systematic error estimate, because of the large mass range used in the fit.

We have discarded method (3), at least with a small systematic uncertainty. The other two methods are statistically equivalent for the KK ($\pi\pi$) cross section since we handle in both cases all the bin-to-bin correlations. The latter are larger in method (2), but we need anyway a covariance matrix for both. The advantage of the sliding bins is the re-distribution of the statistical fluctuations from the muons, so that the KK (and $\pi\pi$) cross section is better behaved. This is particularly apparent when doing mass-dependent fits and looking at the residuals as a function of mass. Therefore we have chosen method (2) for the final results.

Fig. 2.105 shows the effective luminosity in 50-MeV bins, divided by the LO formula. Up to 3 GeV, it is on average about 2% above one, weakly dependent on mass. A slightly stronger mass dependence is observed between 3 and 5 GeV. With this binning, we also observe statistical bin to bin fluctuations while a slow variation is expected. The result from the 250 MeV-wide sliding-bin method (2) is superimposed. This smoothing method is used for the region between the threshold and 2.95 GeV. A linear interpolation is performed for the region between 2.95 and 3.25 GeV, where the data events were removed, whereas an average in bins of variable size is performed at higher mass.

The statistical errors on the ISR effective luminosity from the measurement of efficiencies are included in the statistical covariance matrix, while the systematic errors from the different procedures are accounted for separately as systematic uncertainties. These errors are 1.3 10^{-3} for tracking, 2.9 10^{-3} for μ-ID, and 1.0 10^{-3} for acceptance. The uncertainty from correlated loss of μ-ID for both tracks is not included for $\pi\pi$, giving a total systematic uncertainty of 3.4 10^{-3}, since it is anticorrelated with the pion rate

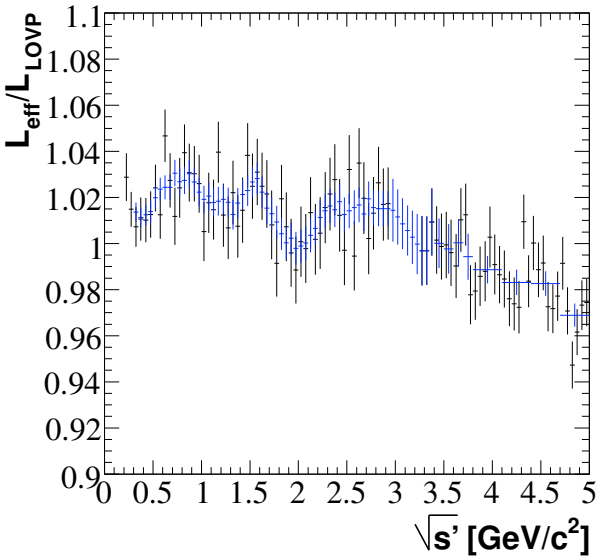

Figure 2.105: Ratio between the effective ISR luminosity measured with the $\mu\mu\gamma$ sample and the LO formula with vacuum polarization, as a function of $\sqrt{s'}$, in 50 MeV bins (black) and in bins of variable size, after a smoothing procedure -see text- (blue). The data correspond to the runs 1-4.

and counted in the $\pi\pi$ systematic errors. For kaons however it is included in the μ-ID uncertainty and the luminosity error becomes 3.7 10^{-3}. The systematic error on the ISR luminosity was conservatively increased in the 3-5 GeV interval (up to $1-2\%$), in order to account for the fact that the QED test is done only at lower masses, and for the increase of the $|FSR|^2$ correction.

2.13 Results on the $e^+e^- \to K^+K^-(\gamma)$ Cross Section

2.13.1 Computing the K^+K^- cross section

The $KK(\gamma)$ cross section is computed from the unfolded spectrum corrected for the global acceptance obtained with AfkQED (see Fig. 2.106) and for differences between Phokhara and AfkQED, together with the effective ISR luminosity obtained as explained above.

All the correlations (from the various corrections) are fully propagated to the final covariance matrix of the cross section.

The systematic uncertainties affecting the bare $KK(\gamma)$ cross section are summarized in Table 2.7. Each source of systematic error is treated as fully correlated in all mass bins, except for the ones on the unfolding and on the vacuum polarization correction which have important anti-correlations (and hence a negligible effect on the dispersion integral). The error on the vacuum polarization correction does not affect the dressed form factor.

Table 2.7: Systematic uncertainties (in 10^{-3}) on the bare cross section for $e^+e^- \to KK(\gamma_{FSR})$ from the determination of the various efficiencies in different KK mass ranges (in GeV) for runs 1-4. The statistical part of the efficiency measurements is included in the total statistical error in each mass bin. The last line gives the total systematic uncertainty on the KK cross section, including the systematic error on the ISR luminosity from muons.

sources	0.98-0.99	0.99-1	1-1.01	1.01-1.03	1.03-1.04	1.04-1.05	1.05-1.1
filter	11.2	3.2	1.8	1.8	1.8	2.7	2.7
tracking	1.3	1.3	1.3	1.3	1.3	1.3	6.2
K-ID	2.8	2.8	2.8	2.8	2.8	2.8	2.8
background	22.0	22.0	1.6	0.1	0.5	0.5	0.5
acceptance	1.6	1.6	1.6	1.6	1.6	1.6	1.6
kinematic fit (χ^2)	3.1	3.1	3.1	3.1	3.1	6.0	6.0
ISR luminosity	3.7	3.7	3.7	3.7	3.7	3.7	3.7
unfolding	3.2	3.2	3.2	-	1.2	1.2	1.2
VP correction	-	-	0.4	2.5	0.5	-	-
sum (cross section)	25.6	23.2	7.2	6.7	6.4	8.4	10.4

sources	1.1-1.2	1.2-1.3	1.3-1.5	1.5-1.7	1.7-2.3	2.3-3	3-3.8	3.8-5
filter	2.3	20.0	10.0	3.2	1.1	1.5	2.3	17.7
tracking	6.2	6.2	6.2	6.2	6.2	6.2	6.2	6.2
K-ID	2.8	2.8	2.8	2.8	2.8	2.8	2.8	2.8
background	4.5	4.5	4.5	4.5	32.4	5.5	8.0	391.0
acceptance	1.6	1.6	1.6	1.6	1.6	1.6	1.6	1.6
kinematic fit (χ^2)	5.6	5.7	6.1	6.5	7.2	9.4	11.7	14.9
ISR luminosity	3.7	3.7	3.7	3.7	3.7	3.7	10.7	20.3
unfolding	0.7	0.7	0.7	-	-	-	-	-
VP correction	-	-	-	-	-	-	-	-
sum (cross section)	11.0	22.7	14.9	11.6	34.1	13.6	19.2	392.3

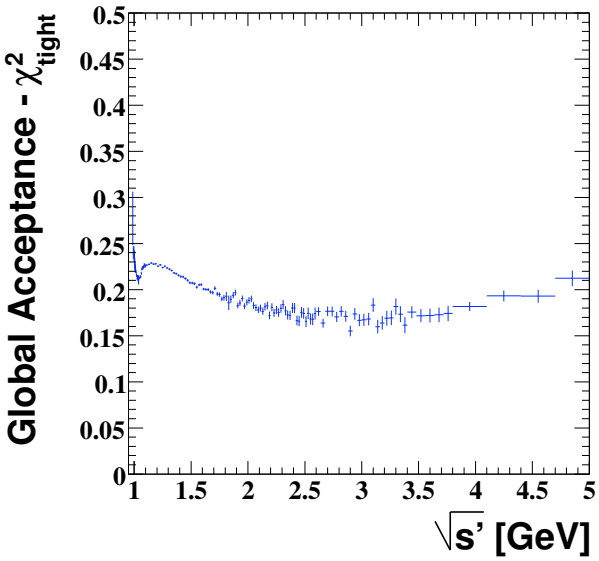

Figure 2.106: Global acceptance of the KK MC computed with AfkQED, for events passing the tight χ^2-cut.

The overall systematic uncertainty on the bare KK cross section is 6.7 10^{-3} in the $[1.01; 1.03]$ GeV mass range, but significantly larger outside the ϕ region.

2.13.2 The Born cross section and the charged kaon form factor

The $e^+e^- \to K^+K^-$ bare cross section is shown in Fig. 2.107, on the full mass range from the threshold up to 5 GeV. It exhibits a very large dynamical range (over more than six orders of magnitude), being dominated by the ϕ resonance close to the threshold, while other structures are clearly visible at higher mass. No vacuum polarization (VP) correction was applied for the J/ψ and the ψ', as for narrow resonances it would significantly shift their masses and it is customary to work with dresses quantities.

Fig. 2.108 shows three enlargements in the $[1; 2.1]$ GeV mass interval. Data from previous measurements are also shown. There is a fair agreement between BABAR and previous measurements, but the BABAR data are more precise and they cover the full energy range of interest. In particular, the dip around 1.8 GeV is mapped with much increased precision.

The square of the kaon form factor is defined as usual by the ratio of the dressed cross section without FSR, and the lowest-order cross section for point-like spin 0 charged particles. Thus,

$$|F_K|^2(s') = \frac{3s'}{\pi\alpha^2(0)\beta_K^3}\,\sigma_{KK}(s') \tag{2.40}$$

with

$$\sigma_{KK}(s') = \frac{\sigma^0_{KK(\gamma)}(s')}{1+\frac{\alpha}{\pi}\eta_K(s')}\,\left(\frac{\alpha(s')}{\alpha(0)}\right)^2\,, \tag{2.41}$$

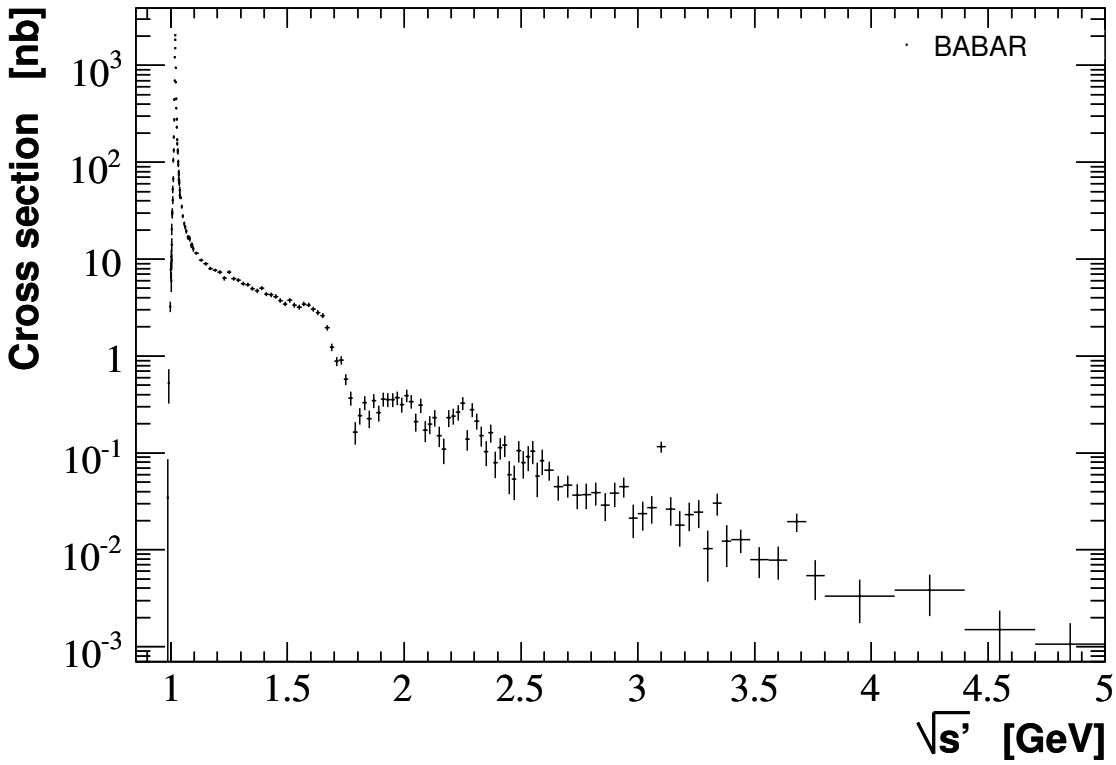

Figure 2.107: The measured $e^+e^- \to K^+K^-\gamma$ bare cross section. Systematic and statistical uncertainties are shown, i.e. the diagonal elements of the total covariance matrix.

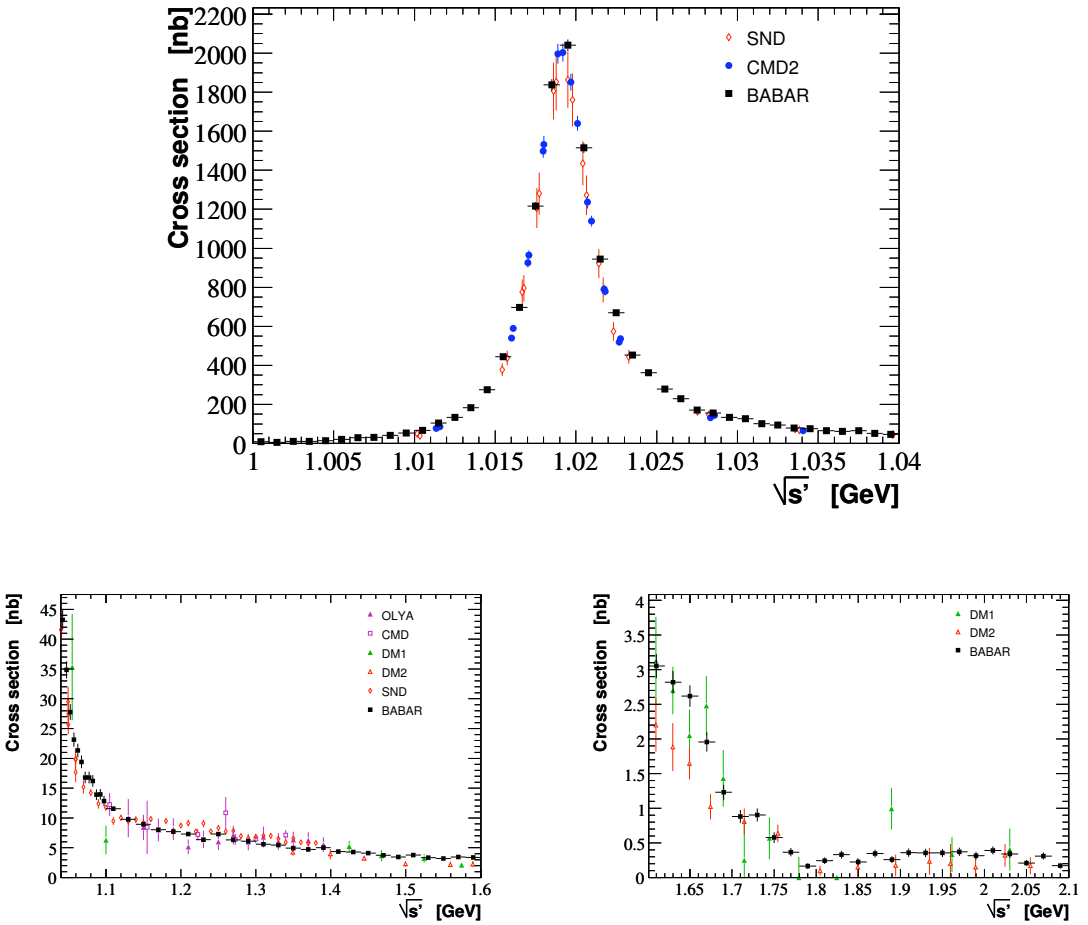

Figure 2.108: The measured $e^+e^- \to K^+K^-$ cross section in the $[1; 1.04]$ GeV (top), $[1.04; 1.6]$ GeV (bottom left) and $[1.6; 2.1]$ GeV (bottom right) mass intervals, together with results published by previous experiments. Systematic and statistical uncertainties are shown, i.e. the diagonal elements of the total covariance matrices.

and $\beta_K = \sqrt{1-4m_K^2/s'}$. The FSR correction [18,36] $\alpha/\pi\ \eta_K(s')$ amounts to 4% at the ϕ mass, 1% at 1.7 GeV, slowly decreassing at higher masses.

2.13.3 A phenomenological fit to the kaon form factor

We fit the BABAR kaon form factor with a model based on a sum of resonances, given by :

$$F_K(s) = \frac{\sum_r \alpha_r\ BW_r}{\sum_r \alpha_r}, \tag{2.42}$$

which, due to the fact that $BW_r(0) = 1$, satisfies the constraint $F_K(0) = 1$. K^+K^- being not an eigenstate of isospin, both I = 0 and I = 1 resonances must be considered. Eight resonances are enough to fit the form factor up to about 1.8 GeV. They correspond to the well known $\phi,\ \phi',\ \rho,\ \rho',\ \rho'',\ \omega,\ \omega'$ and ω'' states. Two additional resonances are needed in order to fit the structures seen between 1.8 and 2.4 GeV. If one follows the ansatz proposed in [34] for the masses of higher excitations of $\phi,\ \rho$ and ω, these two resonances would correspond to ρ''' or ω''' (which are almost degenerate) and ϕ'' respectively. We will call them $(\rho/\omega)'''$ and ϕ''.

The amplitude of the ϕ is taken with a complex phase ($\alpha_\phi = |\alpha_\phi|\ e^{i\ \theta_\phi}$), while the others are supposed real. We fix the amplitudes of the ρ and ω to:

$$\alpha_{\rho,\omega} = \sqrt{\frac{B(\rho,\omega \to ee)\ \Gamma_{\rho,\omega}\ m_\phi}{2\ B(\phi \to ee)\ \Gamma_\phi\ m_{\rho,\omega}}}\ . \tag{2.43}$$

Actually, if the $SU(3)$ symmetry was exact, $|\alpha_\phi|$ should be equal to unity, and the ratio of the amplitudes for ϕ, ρ and ω should be fixed (up to a phase).

The BW of the resonances is described by:

$$BW(s,m,\Gamma) = \frac{m^2}{m^2 - s - i\ m\Gamma(s)}, \tag{2.44}$$

where the width is, in general, energy dependent. For the ρ we use the Kuhn-Santamaria model, where this dependence is given by:

$$\Gamma_\rho(s) = \Gamma_\rho \frac{s}{m_\rho^2}\left(\frac{\beta(s,2m_\pi)}{\beta(m_\rho^2,2m_\pi)}\right)^3, \tag{2.45}$$

where $\beta(s,m) = \sqrt{1-m^2/s}$. For the ϕ one has separate contributions from different decay modes, approximated as

$$\begin{aligned}\Gamma_\phi(s) = \ \Gamma_\phi \Big[& B(\phi \to K^+K^-)\ \frac{\Gamma_{\phi\to K^+K^-}(s,m_\phi,\Gamma_\phi)}{\Gamma_{\phi\to K^+K^-}(m_\phi^2,m_\phi,\Gamma_\phi)} + B(\phi \to K^0\bar{K}^0)\ \frac{\Gamma_{\phi\to K^0\bar{K}^0}(s,m_\phi,\Gamma_\phi)}{\Gamma_{\phi\to K^0\bar{K}^0}(m_\phi^2,m_\phi,\Gamma_\phi)} \\ & +1 - B(\phi \to K^+K^-) - B(\phi \to K^0\bar{K}^0)\Big]\ ,\end{aligned}$$

with $\Gamma_{\phi\to K\bar{K}}(s,m_\phi,\Gamma_\phi)$ given by Eq. 2.45 with suitable replacements. Thus a fixed width is used for the ϕ decay modes other than K^+K^- and $K^0\bar{K}^0$, as well as for resonances other than ϕ and ρ.

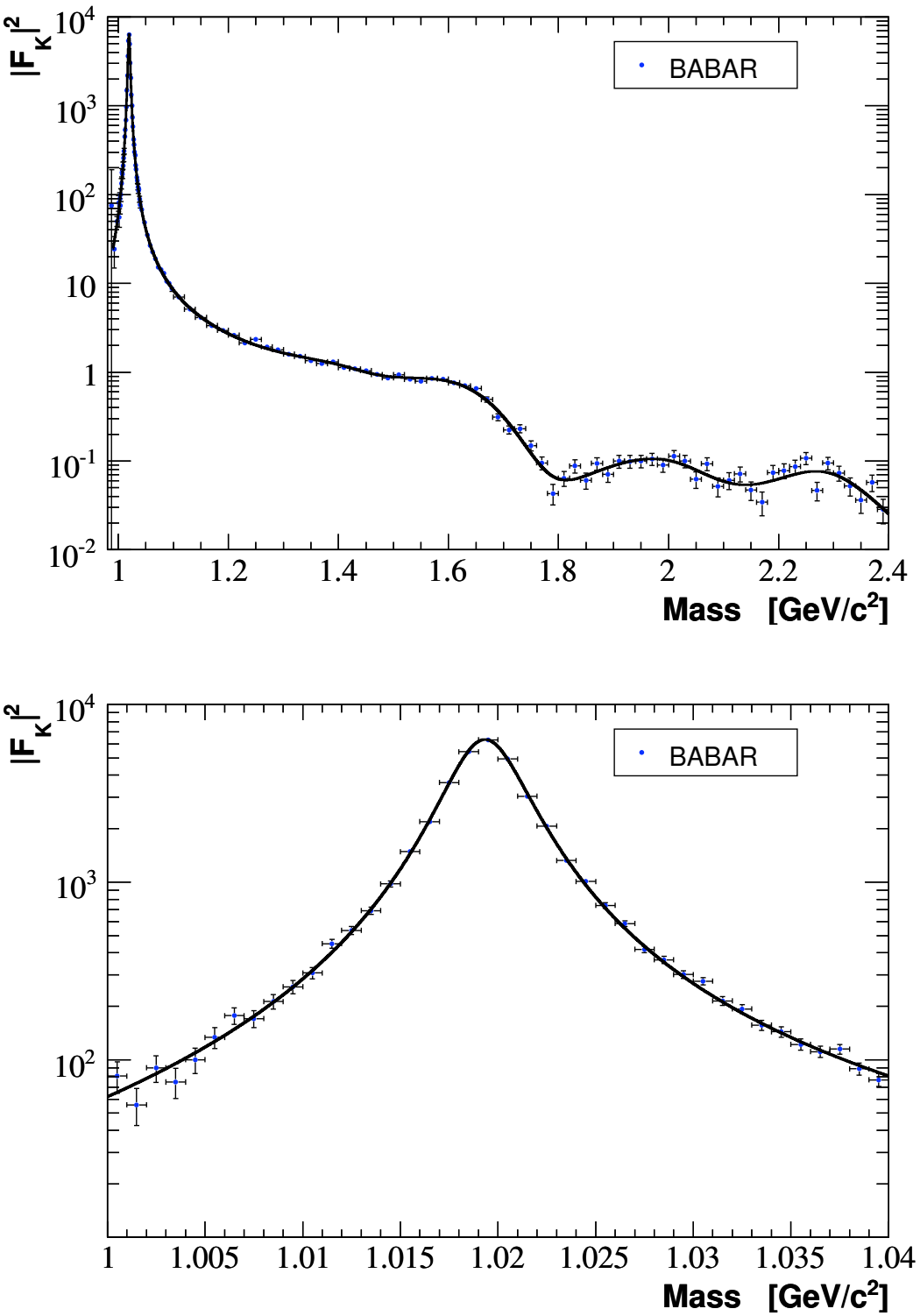

Figure 2.109: Fit of the squared BABAR charged kaon form factor, with a model based on a sum of resonances (see text), in the energy interval from thereshold up to 2.4 GeV (top) and [1; 1.04] GeV (bottom). Systematic and statistical uncertainties are shown for data points, i.e. the diagonal elements of the total covariance matrices.

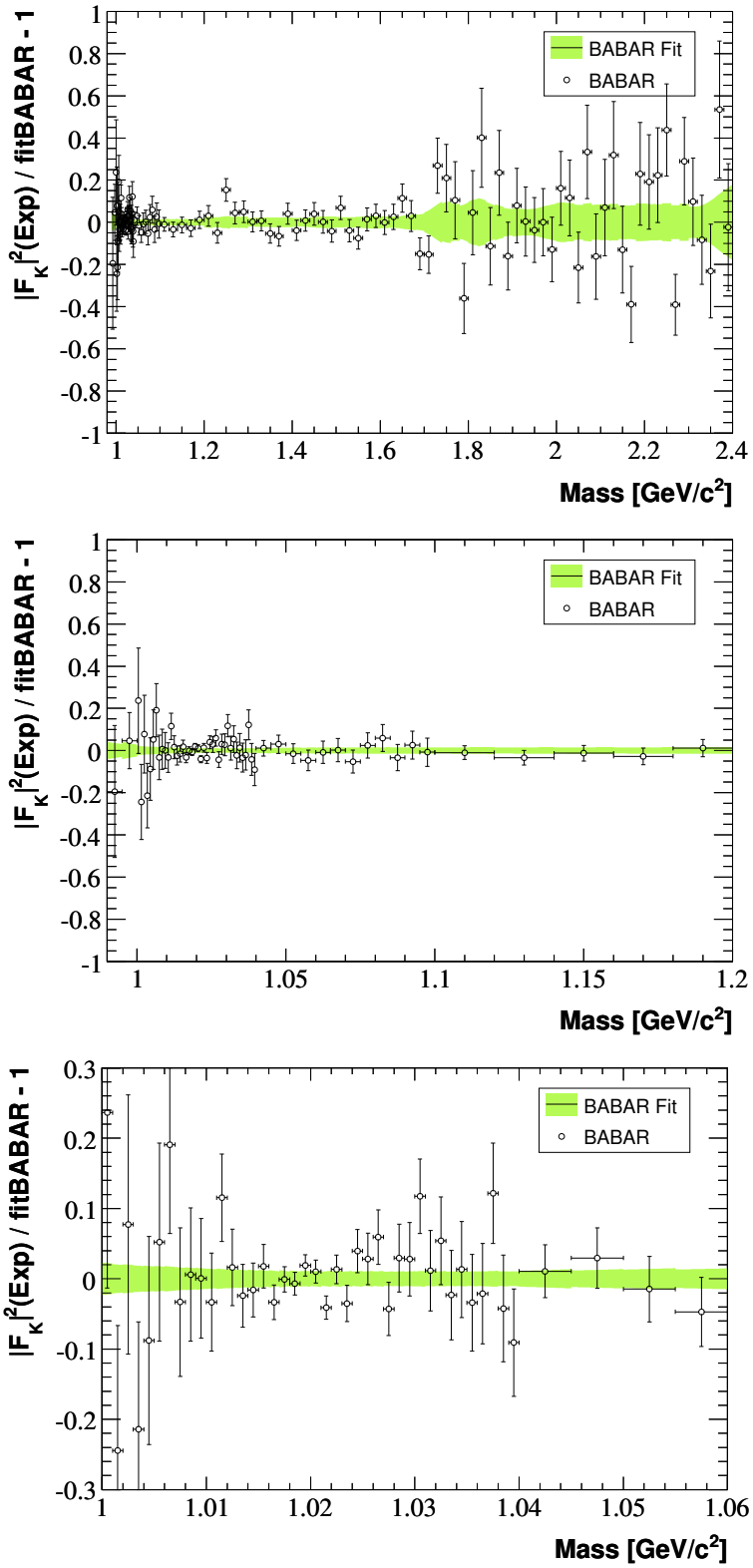

Figure 2.110: Relative difference between the charged kaon squared form factor from BABAR data and the 16-parameter phenomenological fit in three mass regions. Systematic and statistical uncertainties are included for data (diagonal errors). The width of the band shows the propagation of statistical errors in the fit and the quoted systematic uncertainties, added quadratically.

The fit described previously provides a good description of BABAR data (see Fig. 2.109) from the threshold up to 2.4 GeV. We get a closer look by plotting the relative ratio (data/fit -1) in Fig.2.110. While the agreement is very good in general, some oscillations are observed at 1.25 and 1.7 GeV. They correspond to regions where the data-MC difference between spectra, at the beginning of the unfolding procedure, is relatively large. While the unfolding correction is almost negligible for the first oscillation, one iteration slightly enhances the oscillation at 1.7 GeV. Thus, the latter effect is probably real.

The χ^2 of the fit is 131.3 for 103 degrees of freedom. About 31 units from the total χ^2 come from the 18 bins in the region between 2.04 and 2.4 GeV. Although the main goal here was to get a good smooth representation of the BABAR data, to be used for the comparison with other experiments, it is interesting to have a look at the parameters obtained from this fit (shown in Table 2.8). The masses and widths of resonances which are not fitted were fixed to the ones given by PDG. More information on the parameters of the $I = 0$ and $I = 1$ contributions to the form factor could be obtained using data on the $K^0\bar{K}^0$ mode.

We find a fitted mass and a width of the ϕ resonance which are in very good agreement with the PDG values. Our error on this mass is dominated by the calibration untertainty. The fitted value of $|\alpha_\phi|$ is compatible with one, hence agrees with the $SU(3)$ prediction. The phase of this amplitude is however different from zero. The poor information on ϕ' the amplitude is due to the nearby presence of ω'' and ρ'', and their parameters are strongly (anti-)correlated ($75 - 90\%$). The fitted width of the ρ'' is also in very good agreement with the PDG value (250 ± 100 MeV).

Fig. 2.111 shows the various contributions to the form factor model in the ϕ mass region. The total contribution is clearly dominated by the ϕ resonance with an important correction from the interference with ρ plus ω. An uncertainty on the ρ plus ω in the interference term would directly affect the ϕ mass determination, but the corresponding effect would be well below the quoted systematic uncertainty. The contribution from the ρ plus ω alone is relatively small, and this is also true for the effect from higher mass resonances.

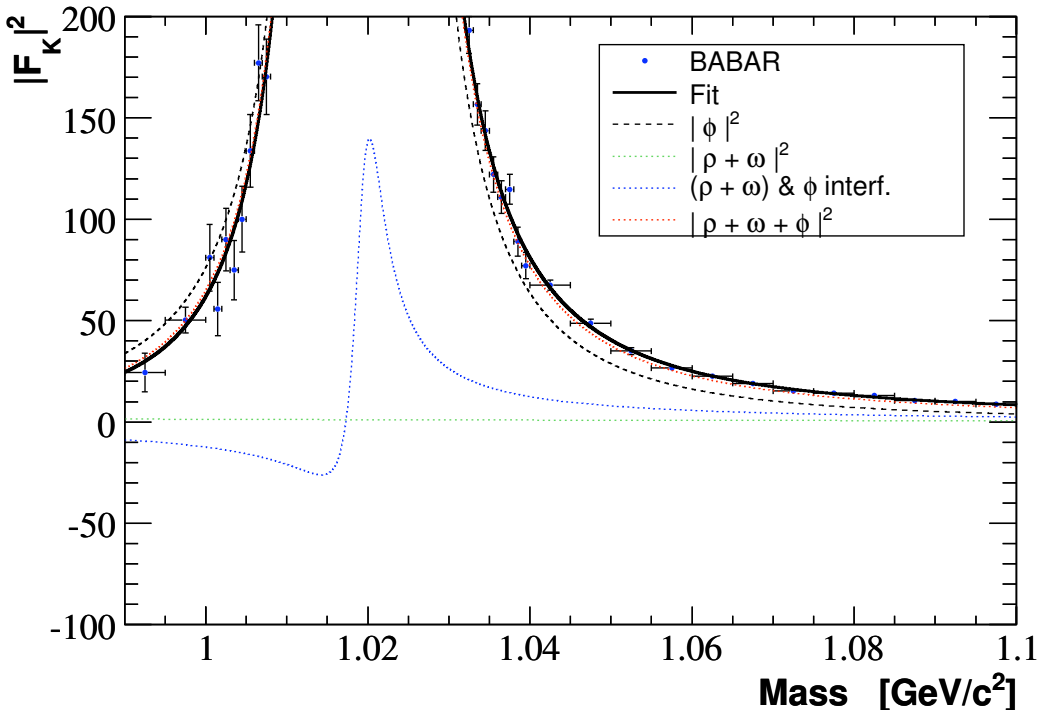

Figure 2.111: Fit of the squared BABAR charged kaon form factor (black line), with a model based on a sum of resonances (see text), shown in the energy interval $[0.99; 1.1]$ GeV. The contributions from the various resonances in that mass region are also shown, namely from: the ϕ alone, the ρ plus ω, the interference term between the ϕ and ρ plus ω, the total contribution from the ϕ plus ρ plus ω. Systematic and statistical uncertainties are shown for data points, i.e. the diagonal elements of the total covariance matrices.

Table 2.8: Fitted and fixed parameters for the fit (described in the text) to the BABAR kaon form factor data. The errors include both statistical and systematic uncertainties. The second error quoted for the ϕ mass (width) is due to the calibration (resolution) uncertainty.

Parameter	Fixed Value	Value ± Error
m_ϕ (MeV)	–	1019.51 ± 0.02 (± 0.11)
Γ_ϕ (MeV)	–	4.29 ± 0.04 (± 0.07)
$\lvert\alpha_\phi\rvert$	–	0.967 ± 0.019
θ_ϕ (rad)	–	0.500 ± 0.089
m_ρ (MeV)	775.5	–
Γ_ρ (MeV)	149.4	–
α_ρ	1.902	–
m_ω (MeV)	782.65	–
Γ_ω (MeV)	8.49	–
α_ω	0.558	–
$m_{\rho'}$ (MeV)	1465.0	–
$\Gamma_{\rho'}$ (MeV)	400.0	–
$\alpha_{\rho'}$	–	0.133 ± 0.083
$m_{\omega'}$ (MeV)	1425.0	–
$\Gamma_{\omega'}$ (MeV)	215.0	–
$\alpha_{\omega'}$	–	−0.101 ± 0.032
$m_{\rho''}$ (MeV)	1720.0	–
$\Gamma_{\rho''}$ (MeV)	–	326.21 ± 36.37
$\alpha_{\rho''}$	–	0.430 ± 0.091
$m_{\omega''}$ (MeV)	1670.0	–
$\Gamma_{\omega''}$ (MeV)	315.0	–
$\alpha_{\omega''}$	–	−0.754 ± 0.098
$m_{\phi'}$ (MeV)	1680.0	–
$\Gamma_{\phi'}$ (MeV)	150.0	–
α'_ϕ	–	0.009 ± 0.024
$m_{(\rho/\omega)'''}$ (MeV)	–	2009.80 ± 16.64
$\Gamma_{(\rho/\omega)'''}$ (MeV)	–	262.63 ± 75.87
$\alpha_{(\rho/\omega)'''}$	–	−0.072 ± 0.032
$m_{\phi''}$ (MeV)	–	2287.15 ± 10.82
$\Gamma_{\phi''}$ (MeV)	–	229.27 ± 43.03
$\alpha_{\phi''}$	–	−0.067 ± 0.014

2.13.4 Comparison to other e^+e^- results

The measured form factor can be compared in some mass regions to data published by previous experiments. In practice, we compare the published data to the smooth BABAR phenomenological fit, by plotting their relative difference.

Fig. 2.112 shows the relative difference between the CMD2 [38] and SND [39] data, and the BABAR fit, in the ϕ mass region. The two Novosibirsk experiments have normalization systematic uncertainties of 2.2% and respectively 7.1%. The BABAR result as well as the Novosibirsk measurements, are affected by systematic uncertainties on mass calibration, which were not included in the previous plot. In order to test the compatibility of the observed differences with the systematic uncertainties, we have performed a fit of the relative difference with the lineshape obtained from the difference of two non-relativistic Breit-Wigner distributions, with different normalizations and ϕ masses. For this fit we use the following parametrisation:

$$\frac{F_K^2(\mathrm{CMD2})}{F_K^2(\mathrm{BABAR})} - 1 = \frac{(m-m_\phi)^2 + \frac{\Gamma_\phi^2}{4}}{(1+\lambda)\left[(m-m_\phi+\Delta m)^2 + \frac{\Gamma_\phi^2}{4}\right]} - 1 \quad (2.46)$$

$$\approx -\lambda + \frac{2\,\Delta m\,(m_\phi - m)}{(m-m_\phi)^2 + \frac{\Gamma_\phi^2}{4}} \quad (2.47)$$

where $\Delta m = m_\phi(\mathrm{BABAR}) - \mathrm{m}_\phi(\mathrm{CMD2})$ and $\lambda = \frac{\mathrm{norm(BABAR)}}{\mathrm{norm(CMD2)}} - 1$ parametrise the mass and respectively normalization differences. A similar parametrisation is used for the comparison between BABAR and SND.

The result of the fit for the comparison between BABAR and CMD2 is $\Delta m = 0.092 \pm 0.008\,(\mathrm{CMD2}) \pm 0.016\,(\mathrm{BABAR})$ MeV and $\lambda = 0.053 \pm 0.003\,(\mathrm{CMD2}) \pm 0.007\,(\mathrm{BABAR})$, where only the statistical uncertainties were included. The observed mass difference is compatible with the BABAR and CMD2 calibration uncertainties, but the normalization difference would imply scaling up the corresponding systematic error by a factor 2.4 for CMD2 and 7.9 for BABAR.

The result of the fit for the comparison between BABAR and SND is $\Delta m = 0.065 \pm 0.026\,(\mathrm{SND}) \pm 0.016\,(\mathrm{BABAR})$ MeV and $\lambda = 0.098 \pm 0.009\,(\mathrm{SND}) \pm 0.007\,(\mathrm{BABAR})$, where only the statistical uncertainties were included. The observed mass difference is compatible with the BABAR and SND calibration uncertainties, but the normalization difference would imply scaling up the corresponding systematic error by a factor 1.4 for SND and 14.6 for BABAR. It should be pointed out that the uncertainties on the mass calibration for the two Novosibirsk measurements are fully correlated.

The comparisons with the SND, CMD, OLYA, DM1 and DM2 measurements, at higher masses, are shown in Fig. 2.114. The systematic difference between BABAR and SND continues up to about 1.15 GeV, where a crossover produces, and at higher masses SND has values which are larger than the ones from BABAR. Indeed, the BABAR data stand somewhere between the SND results and the preliminary CMD2 data [42] in that region, probably in better agreement with the second one. The BABAR data are in rather

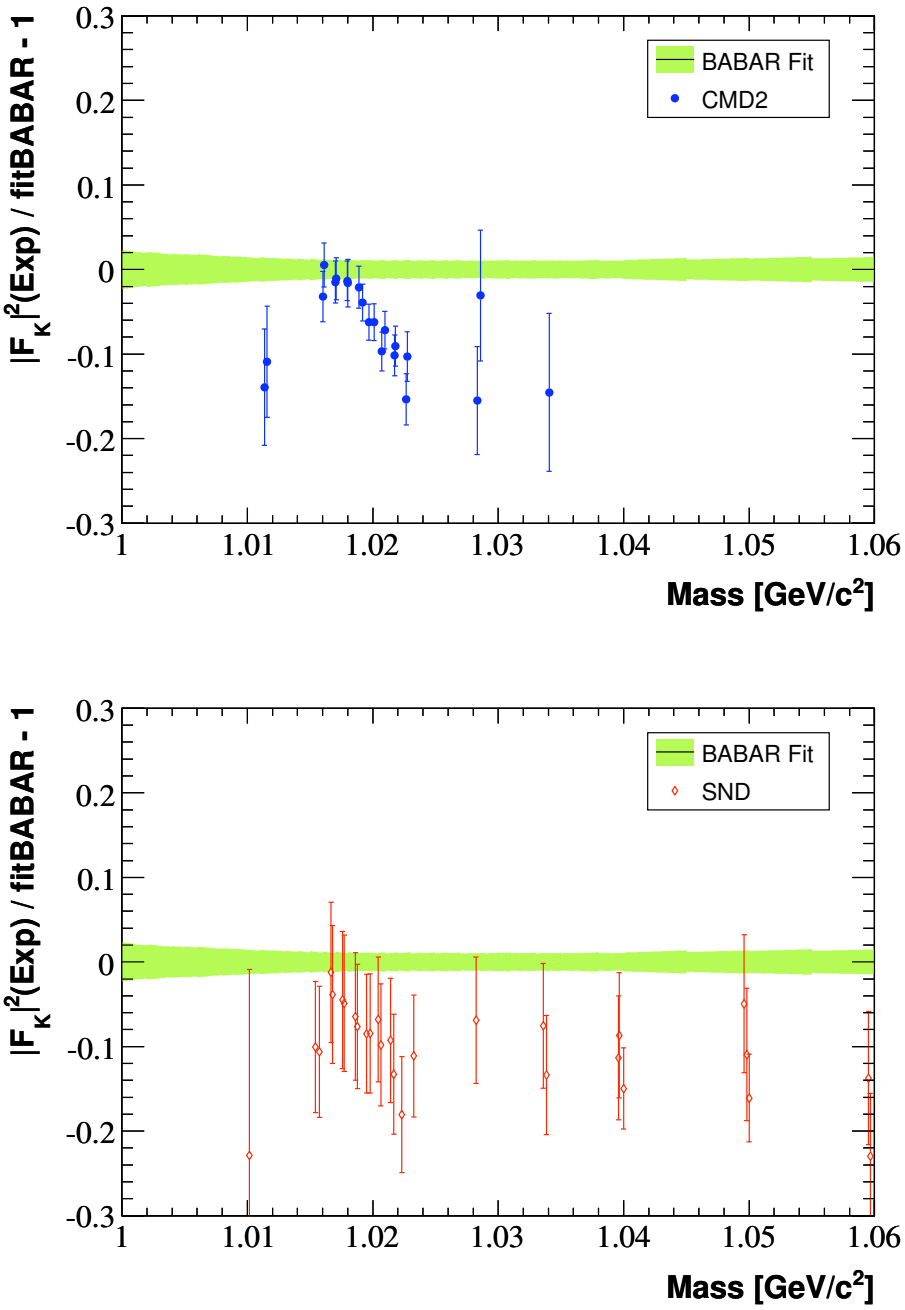

Figure 2.112: Relative difference between the charged kaon squared form factor from CMD2 (top) and SND (bottom) data, and the BABAR phenomenological fit in the ϕ mass region. Systematic and statistical uncertainties are included for data (diagonal errors). The width of the band shows the propagation of statistical errors in the fit and the quoted systematic uncertainties, added quadratically.

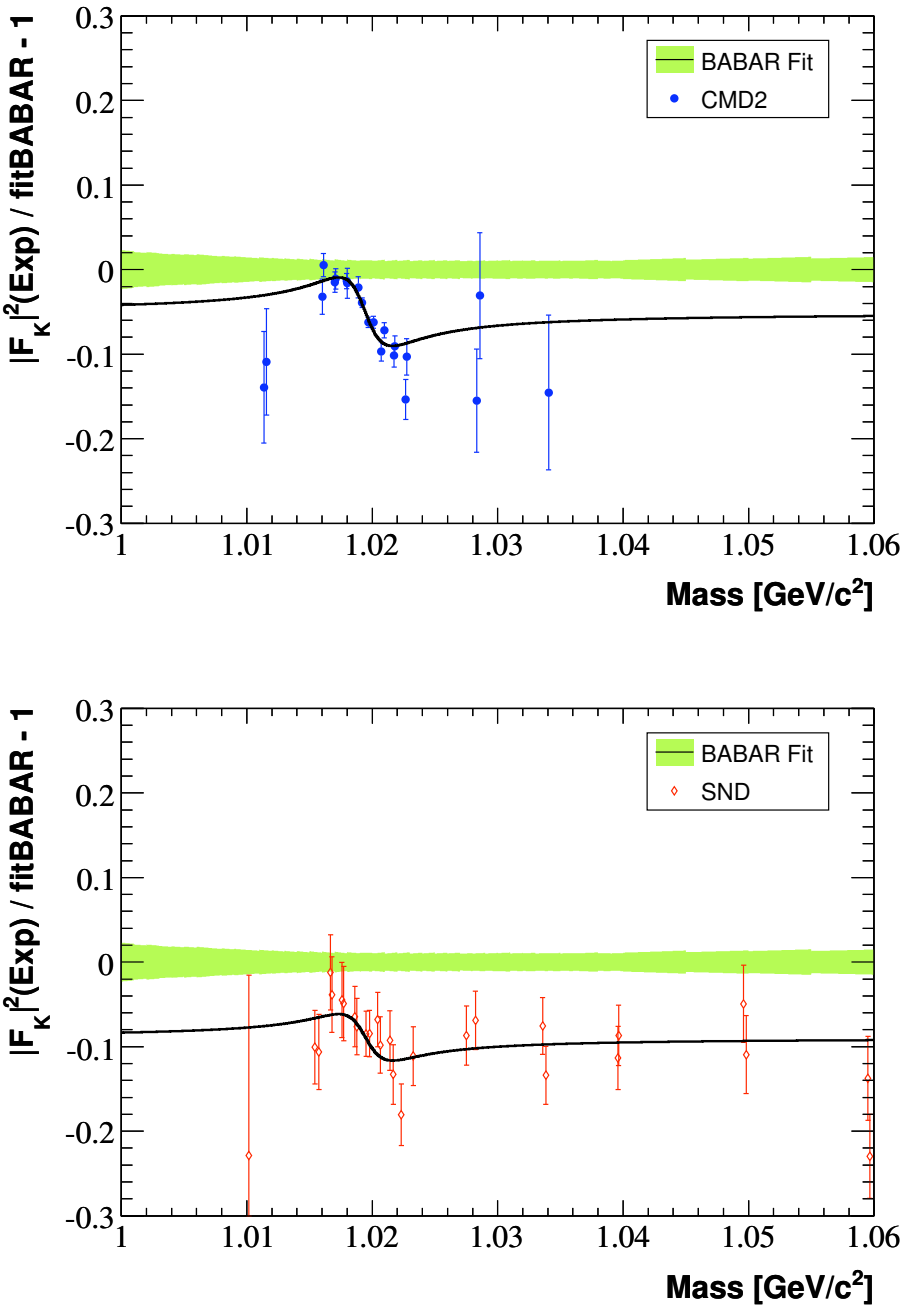

Figure 2.113: Relative difference between the charged kaon squared form factor from CMD2 (top) and SND (bottom) data, and the BABAR phenomenological fit in the ϕ mass region. Only the statistical uncertainties are included for data (diagonal errors). The width of the band shows the propagation of statistical errors in the fit and the quoted systematic uncertainties, added quadratically. A fit of the relative difference is performed with a shape obtained from two non-relativistic Breit-Wigner distributions, with ϕ masses different by Δm (see text).

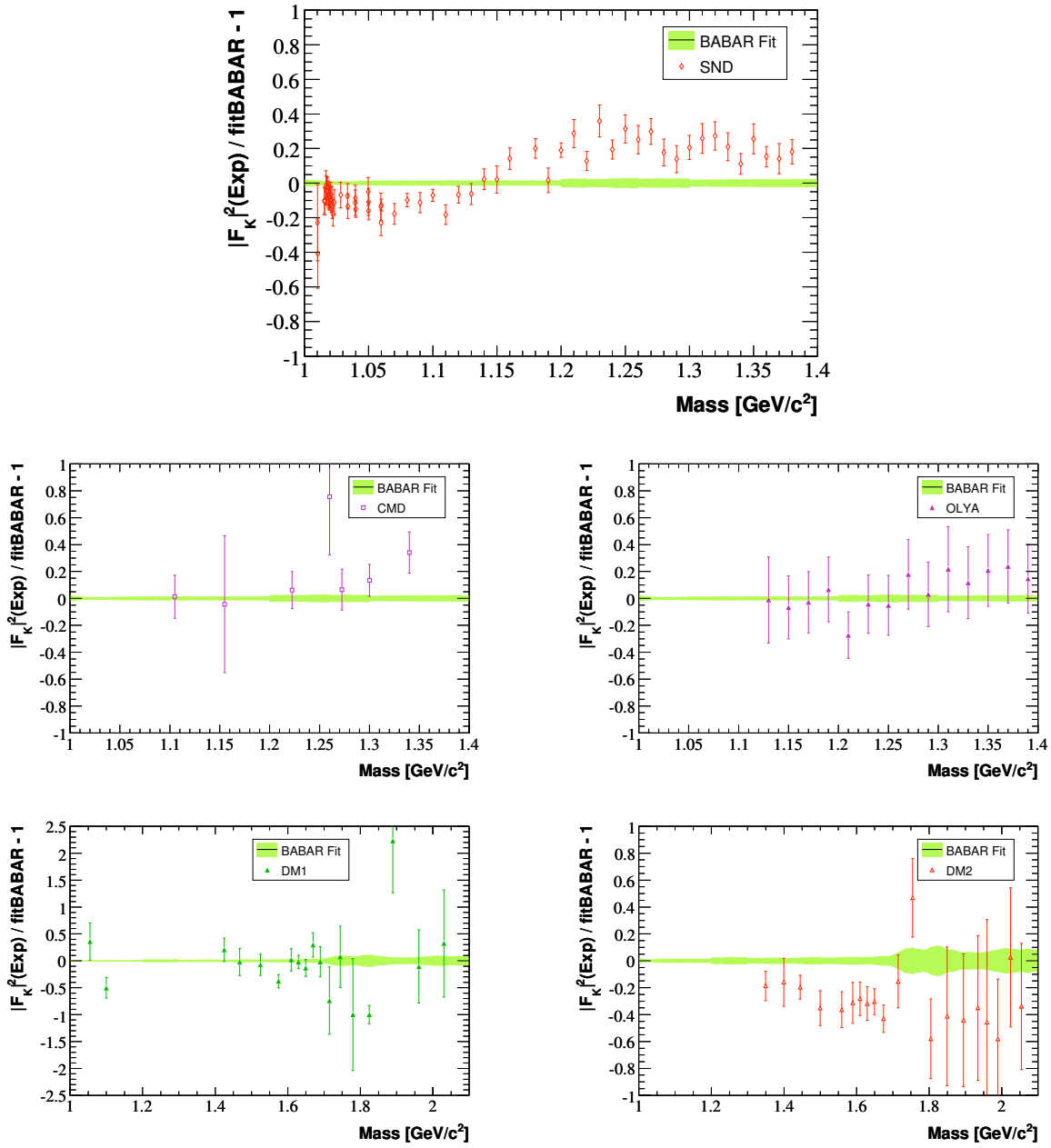

Figure 2.114: Relative difference between the charged kaon squared form factor from SND (top), CMD and OLYA (middle), DM1 and DM2 (bottom) data, and the BABAR phenomenological fit in different mass regions. Systematic and statistical uncertainties are included for data (diagonal errors). The width of the band shows the propagation of statistical errors in the fit and the quoted systematic uncertainties, added quadratically.

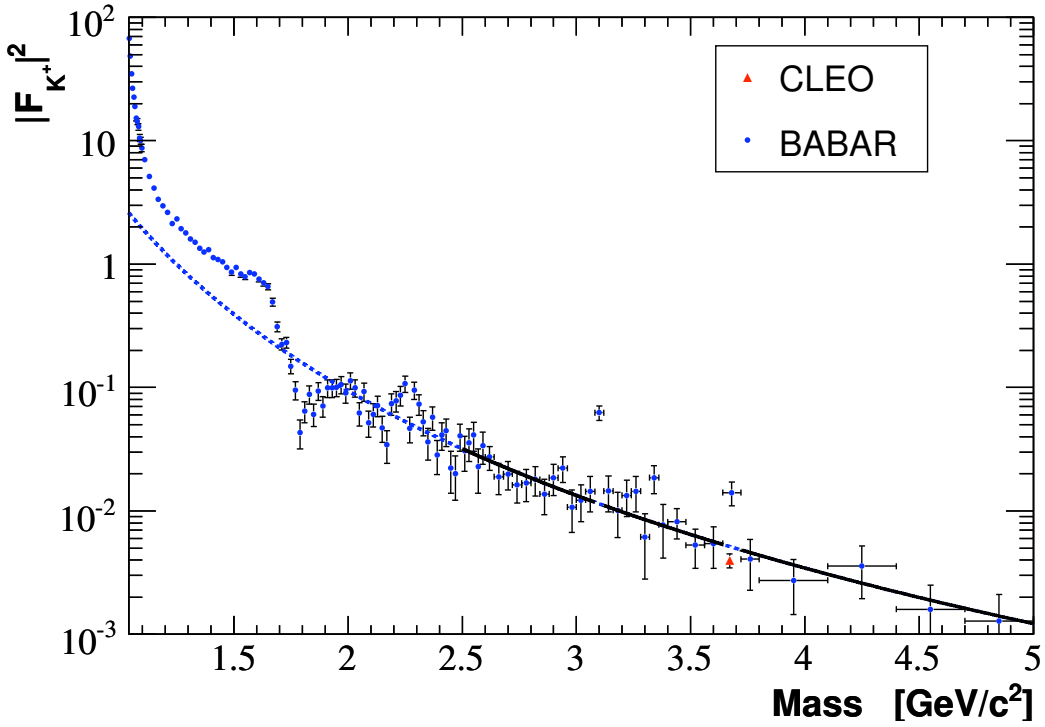

Figure 2.115: Fit (black histogram) of the squared BABAR charged kaon form factor, in the high mass region, using a function which has the shape of the QCD prediction (see text). The two bins at the J/ψ and respectively ψ' mass were ignored in the fit. The extrapolation of the fit is indicated by the blue dotted histogram. We also indicate a measurement from CLEO (red triangle), close to the ψ' mass. Systematic and statistical uncertainties are shown for data points, i.e. the diagonal elements of the total covariance matrices.

good agreement with data from CMD, OLYA and DM1, while a systematic difference is obtained when comparing to DM2.

2.13.5 A fit to the BABAR form factor in the high mass region

In the previous sections we described a phenomenological fit to the BABAR form factor, based on a sum of resonances. This fit works reasonably well up to 2.4 GeV. At higher masses however, one expects the asymptotic behaviour to set in, i.e. the form factor to be described by the QCD prediction [41] which, in the asymptotic limit, yields:

$$F_K(|Q|^2) = 16\pi\,\alpha_s\left(|Q|^2\right)\,\frac{f_{K^+}^2}{|Q|^2}. \tag{2.48}$$

We test this description by making a fit of the squared form factor, between 2.5 and 5 GeV, with a function $C\alpha_s^2(s)/s^n$. Both C and n are fitted. The result of the fit between 2.5 and 5 GeV (but ignoring the two bins at the J/ψ and respectively ψ' mass) is shown in Fig. 2.115. The fit describes very well the data (the χ^2 is of 20.9 for 30 degrees of freedom). We find $n = 1.98 \pm 0.20$, which is in very good agreement with the QCD prediction

$n = 2$. This result confirms the shape of the QCD prediction. This fit, extrapolated at lower masses, follows the average shape of the spectrum down to about 1.7 GeV.

It is instructive to compare the BABAR result with the previous measurement from CLEO [40], which was done at a fixed mass, close to the ψ'. We observe a good agreement with the neighbouring BABAR points and with the BABAR fit. Our result confirms the disagreement observed between the CLEO measurement and the absolute perturbative QCD prediction in Eq.2.48 (which is about a factor of 4 smaller). We obtain a shape of the form factor which is compatible with the asymptotic QCD prediction, but the measured amplitude is significantly larger. Given these results, one could question the asymptotic approximation (2.48). The higher order contributions to $F_K(|Q|^2)$ could help in getting a better understanding of these problems.

2.14 Summary

The $e^+e^- \to K^+K^-(\gamma)$ cross section has been measured using ISR events gathered with the BABAR detector, in the mass range from the threshold up to 5 GeV. The background subtraction was performed, and data/MC corrections were determined and applied to the spectrum before unfolding. In particular, data/MC differences for additional radiation have been studied with care. The cross section was obtained from the spectrum unfolded for resolution effects and corrected for the global acceptance (taken from simulation). The overall systematic uncertainty on the ϕ peak is of 6.7 per mil. This is the most precise measurement of the $e^+e^- \to K^+K^-(\gamma)$ cross section up to date.

Two phenomenological fits of the form factor were performed, one based on a sum of resonances for the mass interval between threshold and 2.4 GeV, and a second based on the asymptotic QCD prediction, between 2.5 and 5 GeV. The two provide a good description of the data, the second proving the good agreement with the shape predicted by QCD. The absolute value of the form factor in the high mass region agrees with a measurement done by CLEO, but the two are significantly larger than the asymptotic QCD prediction.

Chapter 3

Results on the $\pi^+\pi^-$ BABAR Cross Section

An analysis similar to the one described for the K^+K^- channel, in the previous chapter, was performed for the ISR $\pi^+\pi^-$ events. The background was subtracted, the efficiency was measured with simulation and data/MC corrections were applied before the unfolding. I contributed to this study by exploiting the unfolding method described in Chapter 1, doing the full propagation of uncertainties and their correlations, as well as by performing a series of phenomenological studies. In fact, as we will see later, the $\pi^+\pi^-$ cross section allows one to compute an important contribution to the anomalous magnetic moment of the muon. I will also show some other phenomenological applications.

Part of the results presented in the following were published in Ref. [60] and a more detailed publication is in preparation.

3.1 Application of the Unfolding to the $\pi^+\pi^-$ Mass Spectrum

Just as for kaons and muons, the distribution of the fitted $\pi\pi$ mass is altered by several effects: reconstruction, resolution, kinematic fit, FSR, all resulting in transfers of events between different mass regions. All these effects are included in the Monte Carlo simulation of the detector response, but it needs to be corrected to take into account differences between data and MC. The same procedure as for muons and kaons was applied here too.

3.1.1 Implementation

The same energy range 0-3 GeV is chosen for data and the MC transfer matrix. The $'\pi\pi'$ (central ρ region conditions, optimizing statistics) and $'\pi\pi'_h$ (ρ tails conditions, optimized to reduce the background) spectra are unfolded separately over the full mass range,

and the unfolded spectra are combined afterwards, each being used in its respective mass region. Different bin sizes are used: 10 MeV for the 'tails' condition (300×300 matrix) and 2 MeV for the 'central' condition (1500×1500 matrix). The method delivers the unfolded distribution in the same mass bins as for the input spectrum, and a covariance matrix containing the statistical correlations between the bin contents. The covariance matrix is obtained with toy simulations, where both the data and the transfer matrix are statistically fluctuated. The significant covariance matrix elements lie near the diagonal over a width of typically 6-8 MeV for 2 MeV bins, corresponding to the mass resolution of 6 MeV. Thus the diagonal element alone yields a statistical uncertainty in a given bin which is roughly a factor of two smaller than the original error. As a result of the unfolding, by the transfer of events mainly between neighbouring bins, the mass spectrum becomes smoother.

Fig. 3.1 shows the initial mass-transfer matrix from the AfkQed simulation that uses a model of the pion form factor. It is seen that the matrix is reasonably diagonal, with small tails from resolution effects and FSR. More details on the mass resolution and the FSR mass transfer are given in Fig. 3.2.

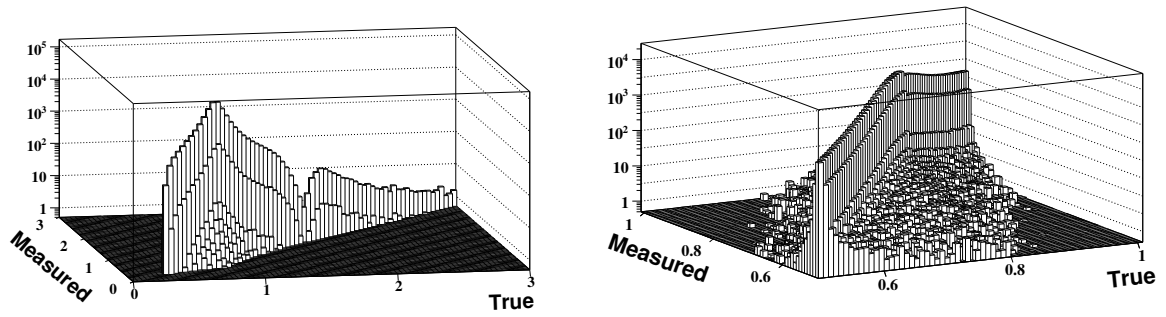

Figure 3.1: The initial mass-transfer matrix from the simulation giving the number of events generated with a (true) mass $\sqrt{s'}$ in a bin i and reconstructed with a (measured) mass $m_{\mu\mu}$ in a bin j, both masses in GeV. The $\sqrt{s'}$ dependence comes from a model of the pion form factor used in the generator. Left: outside ρ conditions. Right: central ρ conditions (the full mass matrix is used in the unfolding, but only the range 0.5-1.0 GeV is shown).

As seen in Fig. 3.3 (top plot) the most significant data − reconstructed MC difference in relative terms corresponds to the region 1.7-2 GeV, where the pion form factor is not well simulated. This difference is much larger than the data statistical errors in this region. Some other smaller differences are observed in the ρ lineshape, but not exceeding the statistical errors. This is also true in the $\rho - \omega$ interference region where a bipolar glitch is observed. These differences can be corrected in an iterative way, but it is observed that already at the first step the difference is reduced to a negligible level.

In fact these systematic differences have no effect on the result of the unfolding, as proven in Fig. 3.3 (bottom plot). The first unfolding result is very close to the initial data (well within the statistical error), except in the $\rho - \omega$ interference region, as expected since the interference pattern which is controlled by the ω width (8.4 MeV) is comparable

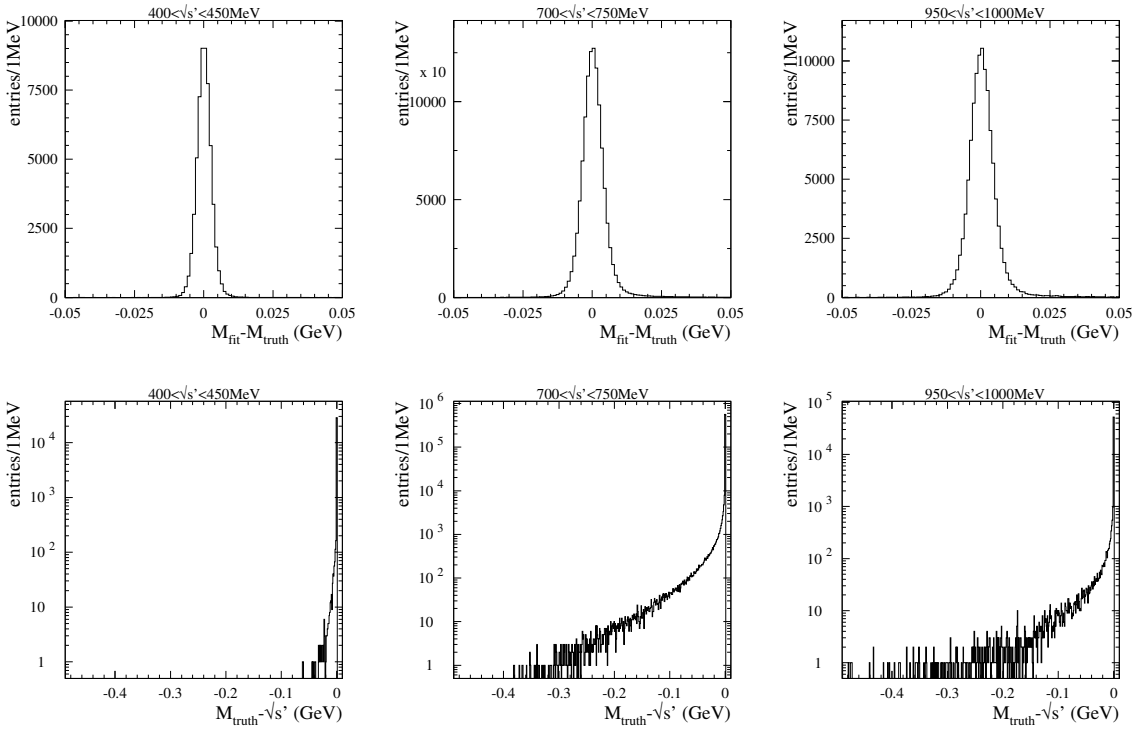

Figure 3.2: Top: the distributions of the difference between the fitted and true $\pi\pi$ masses for 3 $\sqrt{s'}$ ranges (from left to right: 0.40-0.45 GeV, 0.70-0.75 GeV, 0.95-1.00 GeV) show the effect of mass resolution in full simulation. Bottom: the distributions of the difference between the true $\pi\pi$ mass and $\sqrt{s'}$ for 3 $\sqrt{s'}$ ranges (from left to right: 0.40-0.45 GeV, 0.70-0.75 GeV, 0.95-1.00 GeV) show the effect of FSR mass transfer in AfkQed (PHOTOS).

to the mass resolution. Adding one iteration in the unfolding does not show any further improvement.

3.1.2 Tests of the unfolding technique

A direct test of the unfolding procedure has been performed, investigating potential systematic biases introduced by the method. The test uses toy distributions of true and reconstructed data, the latter produced with a transfer matrix A identical to the real one. The toy reconstructed data are then unfolded with a transfer matrix (A') obtained after statistically fluctuating A. The unfolding result is then compared to the true toy data.

The true data distribution is constructed from the true MC with a bias added. In order to build a test as close as possible to the real situation, the bias is taken as the difference between data and the normalized initial reconstructed MC. Two variations of the test have been considered, where the reconstructed data are additionally fluctuated statistically or not. The first situation is closer to the real unfolding operation and could reveal spurious effects due to the limited statistics in the data (and MC). The second test allows one to search for potential systematic effects of the method.

The results of the tests are given in Fig. 3.4. No systematic bias is observed already in the first step, and also after one iteration. This result still stands after additional fluctuation of the input data. By averaging over wider bins to reduce statistical fluctuations we find that the systematic bias from the unfolding technique is below the 10^{-3} level, except in the bins 0.5-0.6 GeV ($1.9\ 10^{-3}$) and 0.9-1.0 GeV ($1.2\ 10^{-3}$). The latter two values are anti-correlated with the rest of the spectrum, hence the systematic uncertainty on the dispersion integral remains smaller than 10^{-3}.

Combining the effects from the knowledge of the transfer matrix and the robustness of the unfolding technique, the total systematic uncertainty of the unfolding procedure is estimated to be 1.0×10^{-3}.

The spectra of corrected $\pi\pi\gamma$ events are compared in Fig. 3.5 before and after unfolding. The main change is in the $\rho - \omega$ interference region, but also the correcting effect of tails. It amounts to about 3% at 0.5 GeV and 2% at 1.0 GeV for the loose χ^2 cut. If the tighter χ^2 cut is used instead ($\ln(\chi^2_{ISR} + 1) < 3.$), the unfolding correction is significantly reduced ($\sim$1%) in the tails, corresponding to a better mass resolution due to the removal of most secondary interactions and effects from a bad reconstruction.

3.1.3 Systematic uncertainty from the mass-matrix

The resolution effects are relatively small, except in the $\rho - \omega$ interference region. However, events in the intermediate χ^2 region have longer resolution tails which need to be understood in view of the unfolding. These tails are mostly due to bad additional-ISR fits and also to secondary interactions. We know from the χ^2 efficiency studies that additional ISR in AfkQed is only generated along the beams, unlike in data. Thus there are much

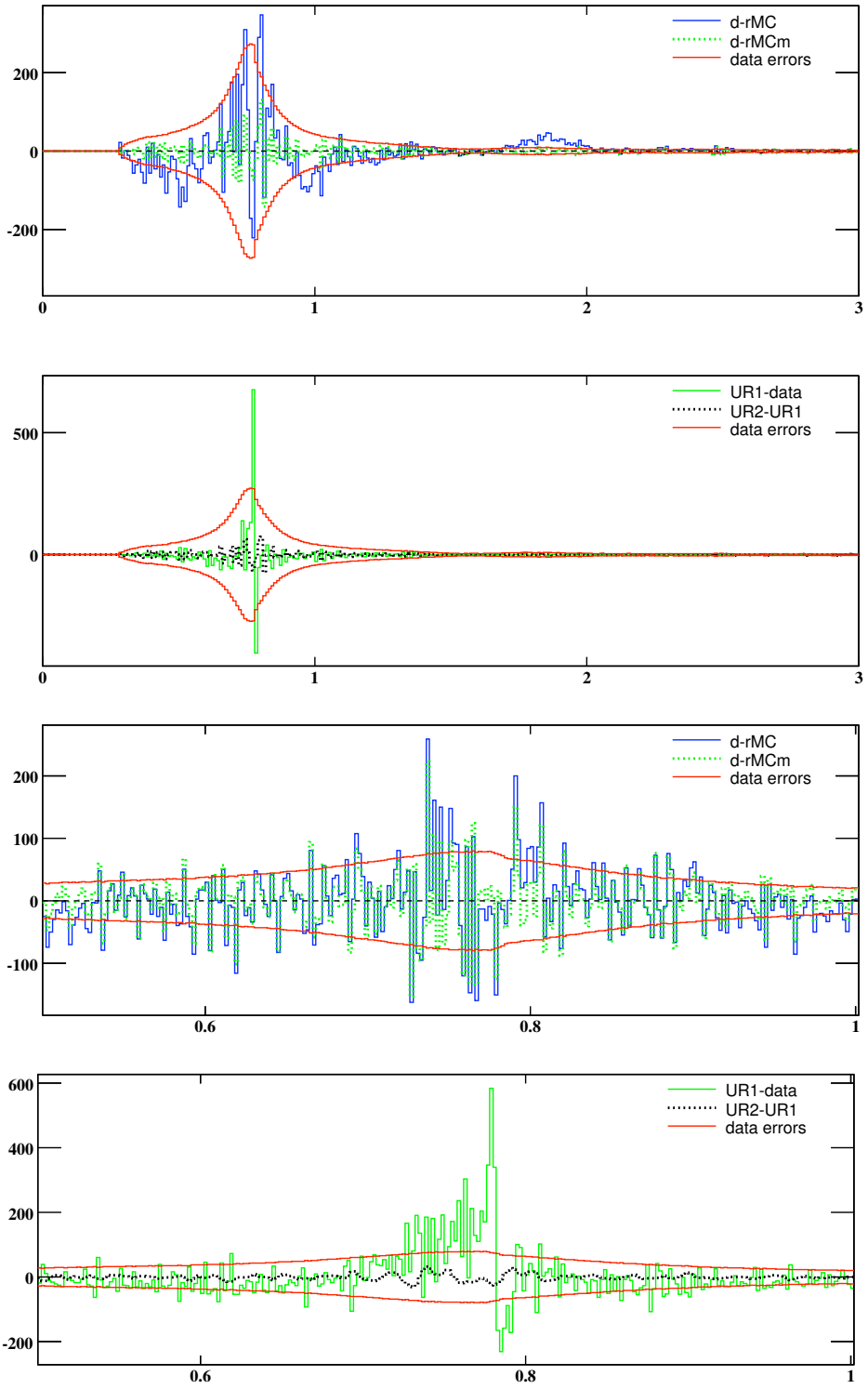

Figure 3.3: From top to bottom: (1) The difference between the mass distributions (outside ρ conditions) of data and reconstructed MC at the first step (d-rMC) and after one iteration (d-rMCm). The data statistical errors ($\pm$ data errors) are shown for comparison. (2) The difference between the result of the first unfolding (UR1) and the initial data exceeds the data statistical error only in the $\rho - \omega$ interference region. No significant improvement is observed between the first (UR1) and second (UR2) unfolding results. (3) and (4) Same plots for the central ρ conditions with longer resolution tails.

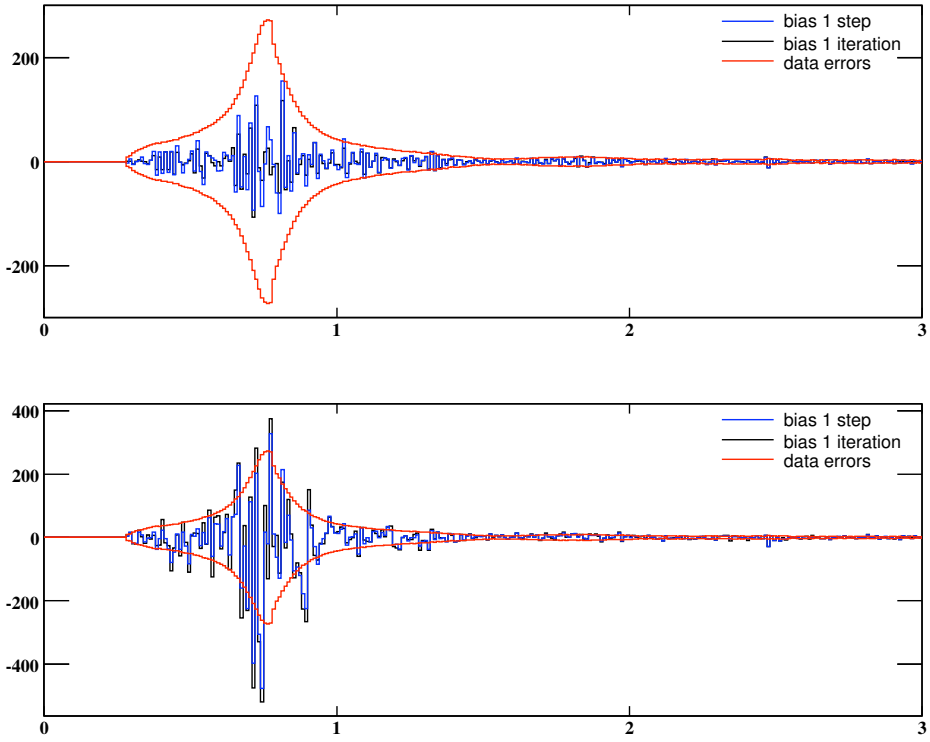

Figure 3.4: Systematic test of the unfolding technique using toy data obtained from the MC distribution distorted by a known bias (outside ρ conditions). The plots show the difference with the true data of the first unfolding result and the result after one iteration step. These values are compared to the statistical data errors. For the top plot there were no data fluctuations, whereas statistical fluctuations were introduced for the bottom plot.

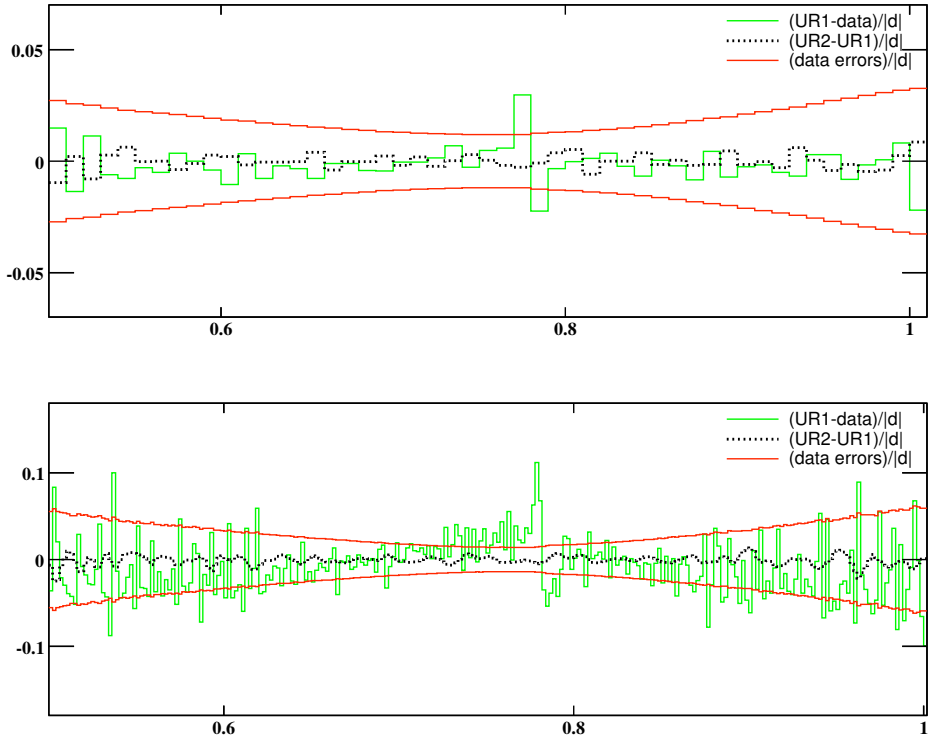

Figure 3.5: The relative difference of the mass distributions before ($m_{\pi\pi}$ in GeV) and after ($\sqrt{s'}$ in GeV) unfolding for the 'ρ central' conditions, but imposing either the tight (top), or the loose (bottom) χ^2 cut. The unfolding of the increased resolution tails is verified in the latter case.

more data events in the χ^2_{ISR} tail than MC. This effect has been studied in detail with muon pairs [28]. Also events with secondary interactions will produce a distorted mass spectrum. In both cases it is important to compare these effects in data and simulation in order to apply corrections to the MC mass matrix.

We recall that the intermediate region of the (χ^2_{ISR}, χ^2_{FSR}) plane is defined to lie between the tight cut ($\ln(\chi^2_{ISR}+1) < 3$) and the loose cut, identical to the ones used for the studies with kaons (see Section 2.8). Events in this region have different origins and we split this region into three parts: additional 'FSR', diagonal and additional ISR. For each region the data mass distribution is compared to the simulation.

In practice for additional ISR and diagonal we fit the data with two components, the signal and the background shapes from MC, and adjust their normalizations. It has been tested that the fitted backgrounds are consistent within errors with the independently estimated rates. The situation is different for the signal which is found too small in MC and must be scaled up. However, after rescaling, the fits are good within the precision of data, as shown in Fig. 3.6. This means that the resolution worsening in these regions is well described by the simulation, but that it fails to predict the true fraction of events. To achieve a good fit the MC contributions have to be re-normalized by factors of 3.20 in the additional ISR region and 1.65 in the diagonal. These scale factors are close to the ones that we obtained for kaons (see Section 2.10.1).

In the additional 'FSR' region (which is a good-χ^2_{FSR} region), the situation is a bit more complicated, as three contributions are present: background, additional FSR signal, and large-angle additional ISR signal. The last contribution is not present in the MC. So three free components are fitted from MC, the last one taken from the tight χ^2 region (also well reconstructed events). Again the fit is good (Fig. 3.6) and the ratio FSR/ISR found is consistent with the independent value obtained from the distribution of the angle between the additional photon and the nearest pion.

The line shapes in additional ISR and diagonal regions are compared to the distribution for good-χ^2 events from the tight region in the last plot in Fig. 3.6. For convenience they are normalized at 0.775 MeV, so that the increase in the tails is clear.

Of course several effects are expected to contribute to differences in mass resolution, distortions, and tails between data and MC: different angular distributions of additional ISR, reconstruction effects, background photons, secondary interactions,... But we have shown that the rescaling with only two factors in each of the two bad-χ^2 regions is in agreement with data within the precision of data.

To estimate the systematic uncertainty from the imperfect knowledge of the true mass matrix, we compare the relative distortion of the unfolded mass spectra for the central ρ region (the only one using the loose χ^2 cut) produced with the raw MC matrix and the matrix corrected with the two scale factors in the relevant regions. The result in Fig. 3.7 shows that the full effect of the correction has the expected shape and is typically well below 1%, except near 1 GeV. Since the agreement between data and MC (after rescaling) is good, one can estimate that the possible deviations are a small fraction ($\sim$10%) of the correction, corresponding to a systematic uncertainty smaller than 0.1%. The uncertainty

on the a_μ integral coming from this effect is even smaller due to anti-correlations in the unfolded spectrum.

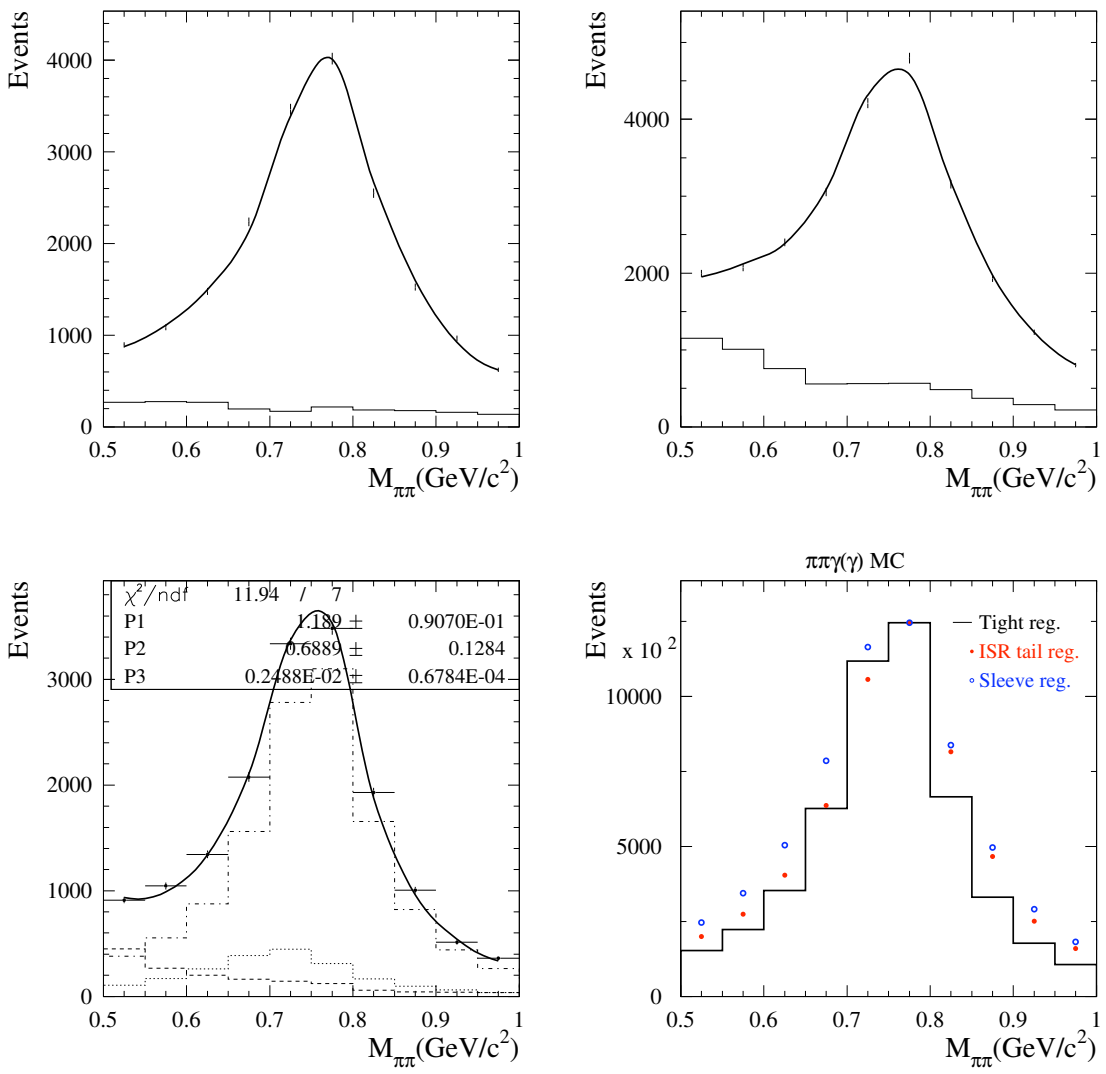

Figure 3.6: Fits of the data $\pi\pi$ mass spectra in the intermediate χ^2 region with background and signal MC distributions freely adjusted: additional ISR (top left), diagonal (top right), additional 'FSR' (bottom left) (see text for definitions). Bottom right: comparison of the MC signal line shapes in different regions (normalized at 0.775 GeV).

The small excess of events with additional FSR in data compared to the simulation produces a distortion of the mass spectrum not taken into account in the mass-transfer matrix. By appropriately reweighting the energy distribution of FSR photons by the energy-dependent excess fraction one can obtain the resulting systematic uncertainty on the mass distribution. The maximum deviation in the rho region occurs at 0.5-0.6 GeV at the 2 10^{-3} level, while it decreases to -0.8 10^{-3} at the rho peak and -0.5 10^{-3} at 1

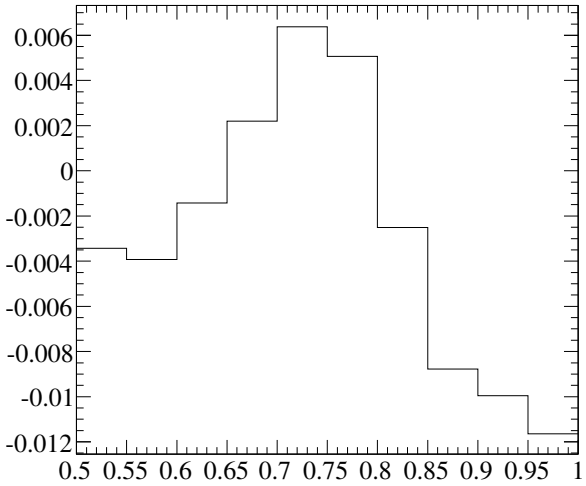

Figure 3.7: Total relative effect of the mass-transfer matrix correction on the unfolded spectrum.

GeV. These values are taken as systematic uncertainties on the cross section. Because of the anti-correlation occuring below and above the peak, this effect produces a systematic uncertainty on the dispersion integral well below 10^{-3}.

3.1.4 Consistency check with tight and loose χ^2 selection

The loose χ^2-cut is used in the ρ central region, while the tight one is used in the tails where backgrounds are larger. However it is possible to compare the results obtained with both methods in the central region. This provides a test of the χ^2-cut efficiency and of the multihadronic background. It is also sensitive to the unfolding, as the mass resolutions are different in the different 2D-χ^2 regions. In order to keep the test at these levels only, the same $'\pi\pi'$-ID is used for both, namely the $'\pi_h\pi'$-ID, and an additional V_{xy}-cut, initially applied for the tight χ^2 condition, is removed.

The result of the test, expressed as the ratio of the corrected and unfolded spectra for loose/tight, is shown in Fig. 3.8. The ratio is consistent with 1 for the full central mass range, 0.5-1.0 GeV within errors, being equal to 0.9983 ± 0.0049 with a χ^2/DF of 53.6/49. Fits in 100-MeV intervals, given in Fig. 3.9, do not show any significant trend for a resolution mismatch between data and corrected-MC. They are also within the range of estimated uncertainties between the two χ^2 conditions (background and χ^2-cut efficiencies) and within the estimated systematic uncertainties for the χ^2-cut efficiencies. We thus conclude that the procedure used for correcting the MC mass-transfer matrix is consistent within the quoted systematic uncertainties.

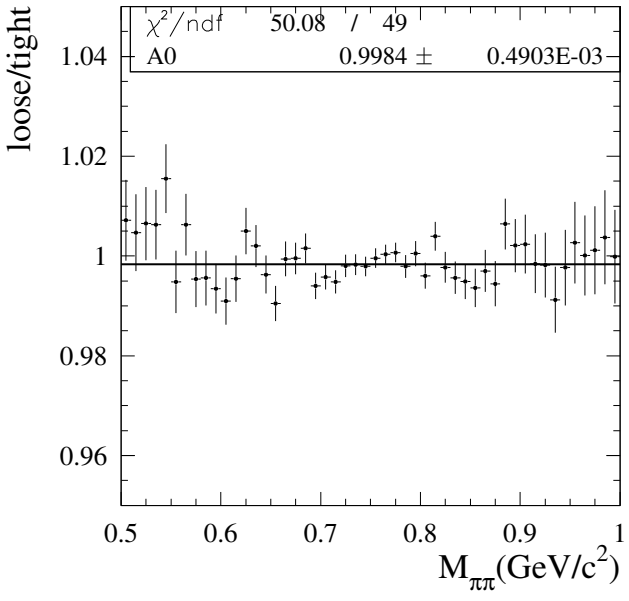

Figure 3.8: The ratio of the corrected and unfolded mass spectra for loose over tight 2D-χ^2 cuts in the central ρ region.

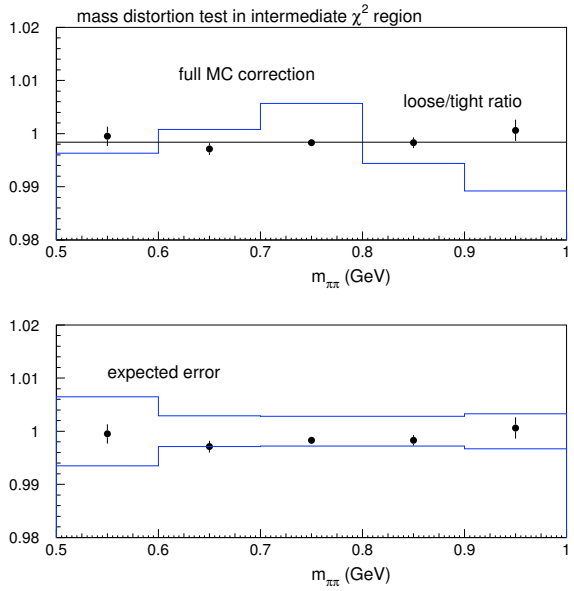

Figure 3.9: The ratio of the corrected and unfolded mass spectra for loose over tight 2D-χ^2 cuts in the central ρ region fitted in 100-MeV bins, compared to the effect of the MC mass-matrix resolution correction (top) and to the band of independently estimated uncertainties.

3.2 Treatment of the Uncertainties

3.2.1 Summary on the treatment of statistical uncertainties

The statistical covariance matrix of the cross section includes the correlations coming from the $\pi\pi$ spectrum and from the luminosity.

The statistical covariance matrix of the $\pi\pi$ spectrum is not trivial (diagonal), due to correlations introduced by the transfers of events in the unfolding, but already before since the corrections were initially computed in 50MeV bins, but applied to spectra with 2- or 10-MeV bins. The reduction of the bin size for these corrections was achieved using linear splines passing through the initial uncorrelated points. The values in the final bins, computed with the splines, are thus correlated through the sharing of values in the initial bins.

The total background was also initially computed in 50-MeV bins. The background in the final bins is determined using second order splines, conserving the number of events in each initial bin. Since the initial splines go through all the points, the procedure introduces some small discontinuities between the splines. The covariance matrix of the background histogram obtained in this way is obtained by a series of 10^4 toys.

The ratio of the measured luminosity to the LO luminosity including vacuum polarisation is initially computed in (almost) uncorrelated bins of 50MeV. The procedure of sliding bins, used for the smoothing of this distribution, introduces correlations between the final values. The luminosity errors for the final cross-section (2- or 10-MeV) bins are 100% correlated within a 50-MeV bin, whereas additional correlations occur between the 50MeV bins because of the bin-sliding procedure. Finally, the correlation effect from the $\mu\mu$ spectrum unfolding is rather weak, but it is however propagated to the final correlation matrix.

3.2.2 Summary of systematic uncertainties for the $\pi\pi$ sample

Here we summarize all systematic uncertainties affecting the $\pi\pi$ sample in different mass regions. The statistical errors of the measured efficiencies are included with the main statistical uncertainty on the $\pi\pi$ mass spectrum. However, in some cases, remaining systematic uncertainties are attached to the efficiency measurement process. They have been considered and listed in the relevant supporting BADs [20–22]. The results on all systematic uncertainties are listed in Table 3.1.

The overall relative systematic uncertainty on the $\pi\pi(\gamma_{FSR})$ cross section is 5.0 10^{-3} in the 0.6-0.9 GeV mass range, but significantly larger below and above the central region.

In fact, a fuller treatment of the systematic uncertainties is implemented, using a full covariance matrix. This is very important for the computation of the dispersion integral, To achieve this we consider the individual systematic errors (for each source, as given in Table 3.1) to be 100% correlated in all the mass bins. Then the total systematic

Table 3.1: Systematic uncertainties (in 10^{-3}) on the cross section for $e^+e^- \to \pi\pi(\gamma_{FSR})$ from the determination of the various efficiencies in different $\pi\pi$ mass ranges (in GeV) for runs 1-4. The statistical part of the efficiency measurements is included in the total statistical error in each mass bin. The last line gives the total systematic uncertainty on the $\pi\pi$ cross section, including the systematic error on the ISR luminosity from muons.

sources	0.3-0.4	0.4-0.5	0.5-0.6	0.6-0.9	0.9-1.2	1.2-1.4	1.4-2.0	2.0-3.0
trigger/ filter	5.3	2.7	1.9	1.0	0.5	0.4	0.3	0.3
tracking	3.8	2.1	2.1	1.1	1.7	3.1	3.1	3.1
π-ID	10.1	2.5	6.2	2.4	4.2	10.1	10.1	10.1
background	3.5	4.3	5.2	1.0	3.0	7.0	12.0	50.0
acceptance	1.6	1.6	1.0	1.0	1.6	1.6	1.6	1.6
kinematic fit (χ^2)	0.9	0.9	0.3	0.3	0.9	0.9	0.9	0.9
correl $\mu\mu$ ID loss	3.0	2.0	3.0	1.3	2.0	3.0	10.0	10.0
$\pi\pi/\mu\mu$ cancel.	2.7	1.4	1.6	1.1	1.3	2.7	5.1	5.1
unfolding	1.0	2.7	2.7	1.0	1.3	1.0	1.0	1.0
ISR luminosity	3.4	3.4	3.4	3.4	3.4	3.4	3.4	3.4
sum (cross section)	13.8	8.1	10.2	5.0	6.5	13.9	19.8	52.4

covariance matrix is built as the sum of the covariance matrices corresponding to each individual systematic source.

3.3 Results on the $e^+e^- \to \pi^+\pi^-(\gamma)$ Cross Section

3.3.1 The Born cross section with additional FSR

The results for the $e^+e^- \to \pi^+\pi^-(\gamma)$ bare cross section including FSR, $\sigma^0_{\pi\pi(\gamma)}$, are given after unfolding in Figs. 3.10,3.11,3.12. It is dominated by the ρ resonance, with structures at larger masses. The dip region near 1.6 GeV, usually interpreted as resulting from interference between the ρ' and ρ'' amplitudes, is mapped with much increased precision, compared to previous experiments. There is also an indication for more structure in the 2.2-2.25 GeV region which could be due to a still higher-mass ρ''' vector meson.

3.3.2 The pion form factor

As for the kaons, the square of the pion form factor is defined by the ratio of the dressed cross section without FSR, divided by the lowest-order cross section for point-like spin 0

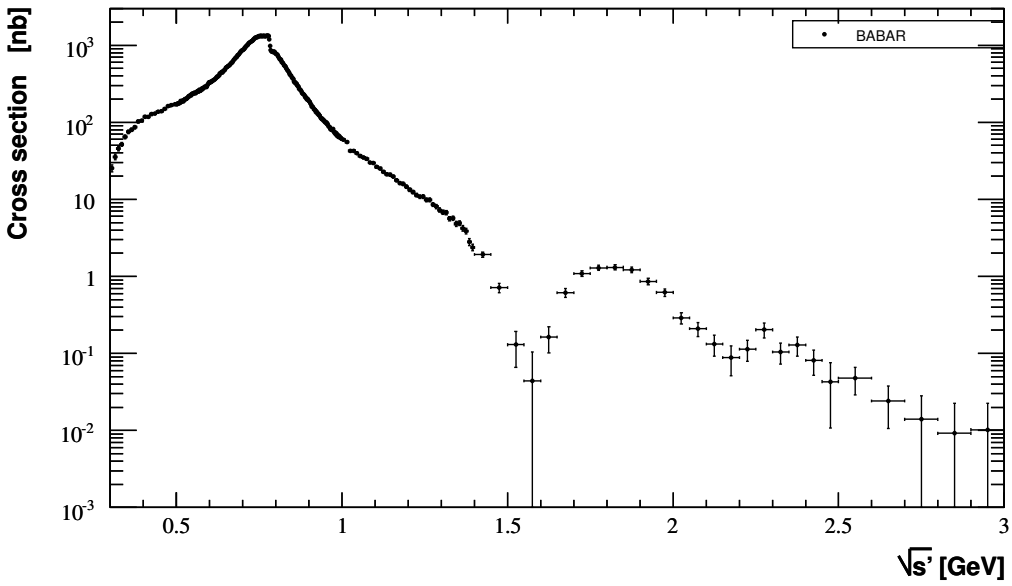

Figure 3.10: The measured cross section for $e^+e^- \to \pi^+\pi^-(\gamma)$ over the full mass range. Systematic and statistical uncertainties are shown, but only the diagonal elements of the covariance matrix.

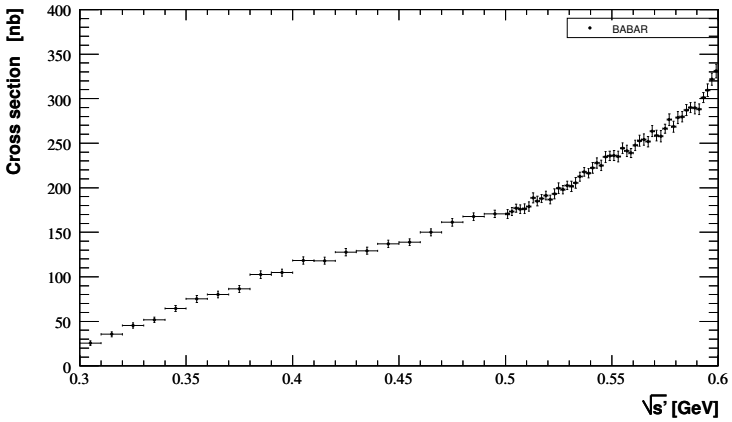

Figure 3.11: The measured cross section for $e^+e^- \to \pi^+\pi^-(\gamma)$ in the lower mass range. Systematic and statistical uncertainties are shown, but only the diagonal elements of the covariance matrix.

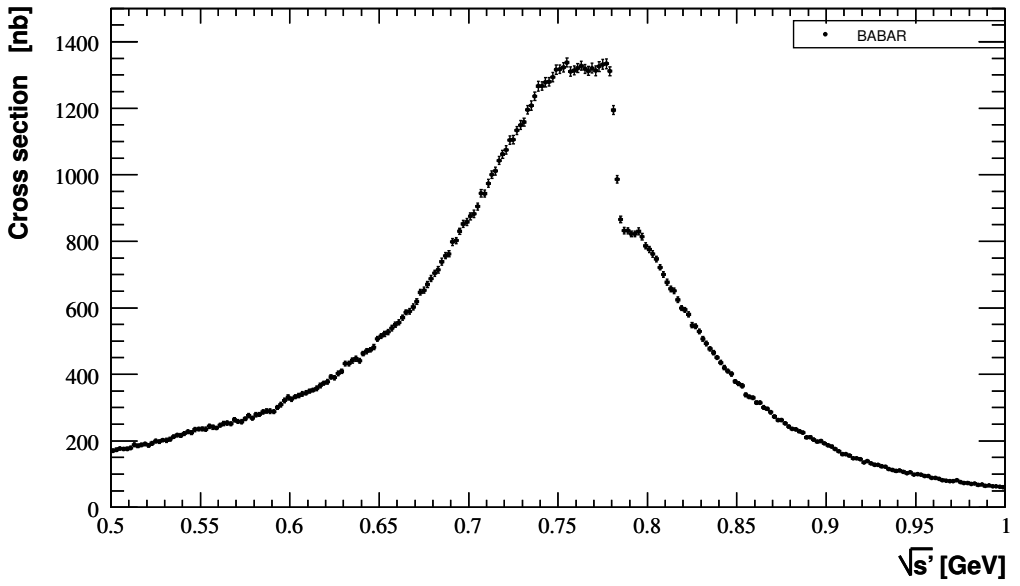

Figure 3.12: The measured cross section for $e^+e^- \to \pi^+\pi^-(\gamma)$ in the central ρ region. Systematic and statistical uncertainties are shown, but only the diagonal elements of the covariance matrix.

charged particles. Thus,

$$|F_\pi|^2(s') = \frac{3s'}{\pi\alpha^2(0)\beta_\pi^3}\,\sigma_{\pi\pi}(s') \tag{3.1}$$

with

$$\sigma_{\pi\pi}(s') = \frac{\sigma^0_{\pi\pi(\gamma)}(s')}{1+\frac{\alpha}{\pi}\eta_\pi(s')}\,\left(\frac{\alpha(s')}{\alpha(0)}\right)^2\,, \tag{3.2}$$

and $\beta_\pi = \sqrt{1-4m_\pi^2/s'}$. The FSR correction [18,36] $\alpha/\pi\ \eta_\pi(s')$ is slowly decreasing with s' and amounts to 8.0 10^{-3} at the ρ mass.

3.3.3 Phenomenological fits to the pion form factor

We use a standard vector-dominance model (VDM) to fit the BABAR pion form factor, given by:

$$F_\pi(s) = \frac{BW_\rho^{GS}(s,m_\rho,\Gamma_\rho)\frac{1+\alpha BW_\omega^{KS}(s,m_\omega,\Gamma_\omega)}{1+\alpha} + \beta BW_{\rho'}^{GS}(s,m_{\rho'},\Gamma_{\rho'}) + \gamma BW_{\rho''}^{GS}(s,m_{\rho''},\Gamma_{\rho''})}{1+\beta+\gamma} \tag{3.3}$$

The BW functions, for all the four resonances considered here, are given by models which take into account the variation of their width with energy. Their amplitudes are complex: $\alpha = |\alpha|e^{i\phi_\omega}$, $\beta = |\beta|e^{i\phi_{\rho'}}$ and $\gamma = |\gamma|e^{i\phi_{\rho''}}$. The BW of the ω is described by:

$$BW(s,m,\Gamma) = \frac{m^2}{m^2 - s - im\Gamma(s,m,\Gamma)}. \tag{3.4}$$

The wide ρ, ρ' and ρ'' resonances are described by the Gounaris-Sakurai (GS) model [86]:

$$BW^{GS}(s,m,\Gamma) = \frac{m^2(1+d(m)\Gamma/m)}{m^2 - s + f(s,m,\Gamma) - im\Gamma(s,m,\Gamma)}. \tag{3.5}$$

In these two models, the energy dependent width is given by:

$$\Gamma(s,m,\Gamma) = \Gamma\frac{s}{m^2}\left(\frac{\beta(s,2m_\pi)}{\beta(m^2,2m_\pi)}\right)^3, \tag{3.6}$$

where $\beta(s,m) = \sqrt{1-m^2/s}$.

The other auxiliary functions used in the GS model are:

$$d(m) = \frac{3}{\pi}\frac{m_\pi^2}{k(m^2)^2}ln\left(\frac{m+2k(m^2)}{2m_\pi}\right) + \frac{m}{2\pi k(m^2)} - \frac{m_\pi^2 m}{\pi k(m^2)^3}, \tag{3.7}$$

with $k(s) = \frac{1}{2}\sqrt{s}\beta(s,2m_\pi)$, and

$$f(s,m,\Gamma) = \frac{\Gamma m^2}{k(m^2)^3}\left[k(s)^2(h(s)-h(m^2)) + (m^2-s)k(m^2)^2h'(m^2)\right], \tag{3.8}$$

where

$$h(s) = \frac{2}{\pi}\frac{k(s)}{\sqrt{s}}ln\left(\frac{\sqrt{s}+2k(s)}{2m_\pi}\right). \tag{3.9}$$

Actually, $d(m)$ arises when one builds an analytic representation of the form factor with a cut on the real axis, starting at the 2π threshold. It is the dispersion relation that imposes a constraint between the real and imaginary parts of the denominator in Eq. (3.5). So, if one wants to use an energy dependent width $\Gamma(s)$, it determines the (complicated) expressions of d and f.

We fit the form factor data from 0.3 to 3.0 GeV. All together 14 parameters are fitted: the mass and width of the ρ, and for each other resonance (ω, ρ', ρ'') the amplitude (modulus and phase) with respect to the ρ, and their mass and width. The full statistical and systematic covariance matrix is used. Because of the correlations of both origins, but mostly from systematic errors and ISR luminosity 50-MeV sliding bins, the χ^2 minimization when using the full covariance matrix yield a fit which is systematically shifted with respect to the data points. This is a well-known effect [44], the solution of which is not straightforward. Here we have used the fit with only diagonal errors to obtain the central values for the fitted parameters, while the errors on the parameters are obtained from the fit with the full covariance matrix of the data distribution [1]. As shown in Fig. 3.13 the VDM fit provides a good description of the BABAR data over the full mass range ($\chi^2/DF = 334/323$).

The quality of the fit can be checked in more detail in the low-mass range and the ρ peak region with the $\rho-\omega$ interference in Fig. 3.14. A closer look is obtained by plotting

[1] In fact we conservatively used the largest of the errors obtained with the diagonal-error and full-covariance fits, the latter one being usually the largest.

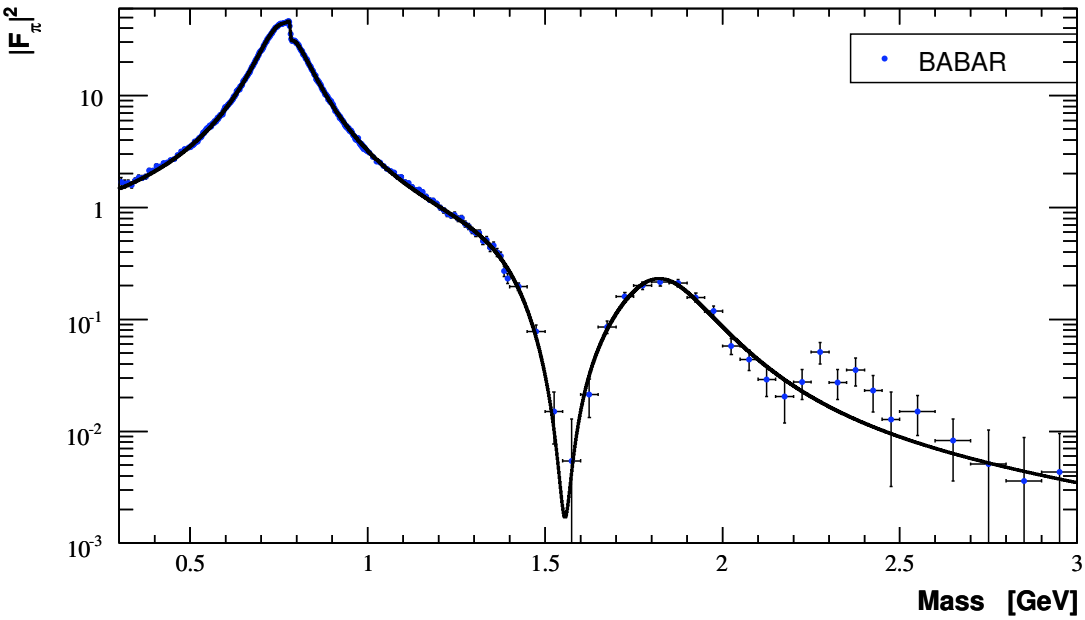

Figure 3.13: The pion form factor squared measured by BABAR as a function of the $\pi\pi$ mass from 0.3 to 3 GeV and the VDM fit described in the text.

the relative ratio $(data/fit - 1)$ in Fig. 3.15. While the agreement is satisfactory in the 0.5-1.0 GeV mass region, some differences are observed in the low-mass region where the fit underestimates the data. Some oscillation is also observed berwteen 0.9 and 1.2 GeV. However it is hard to assess the reliability of the VDM description, involving the parametrization of very broad resonances with large inelasticity.

It is not easy to compare the fitted resonance parameters to those obtained by other experiments if the mass range and the parametrizations are different. The corresponding values from CMD-2 and SND for the ρ mass are (776.0 ± 0.8) MeV and (774.6 ± 0.6) MeV, and for the ρ width (146.0 ± 0.9) MeV and (146.1 ± 1.7) MeV, respectively.

The phase of the $\rho-\omega$ interference is not in good agreement with CMD-2 (0.182 ± 0.067; SND uses a different parametrization). However in the CMD-2 fit, the ω mass is fixed to the PDG value. If we do the same in the BABAR fit ($m_\omega = 782.65$ MeV) the phase comes out to be 0.137 ± 0.023, in agreement with CMD-2. In fact in the 14-parameter fit the fitted values for m_ω, ϕ_ω, and α are strongly correlated (80%). The fitted ω width is found to be a bit smaller (7.84 ± 0.36 MeV) than the PDG value (8.49 ± 0.08 MeV), but not really inconsistent.

The goodness of the fit over the 0.3-2 GeV mass range shows that the GS parametrization of the wide dominant ρ resonance adequately describes the data, as well as the contributions from the higher ρ' and ρ'' resonances. In particular the strong interference dip near 1.6 GeV is well reproduced. Beyond 2 GeV the fit fails to describe the structure seen in the data. This feature needs at least another higher vector resonance, but the statistics of the data does not allow for a quantitative description, unless one reduces the number of extra parameters.

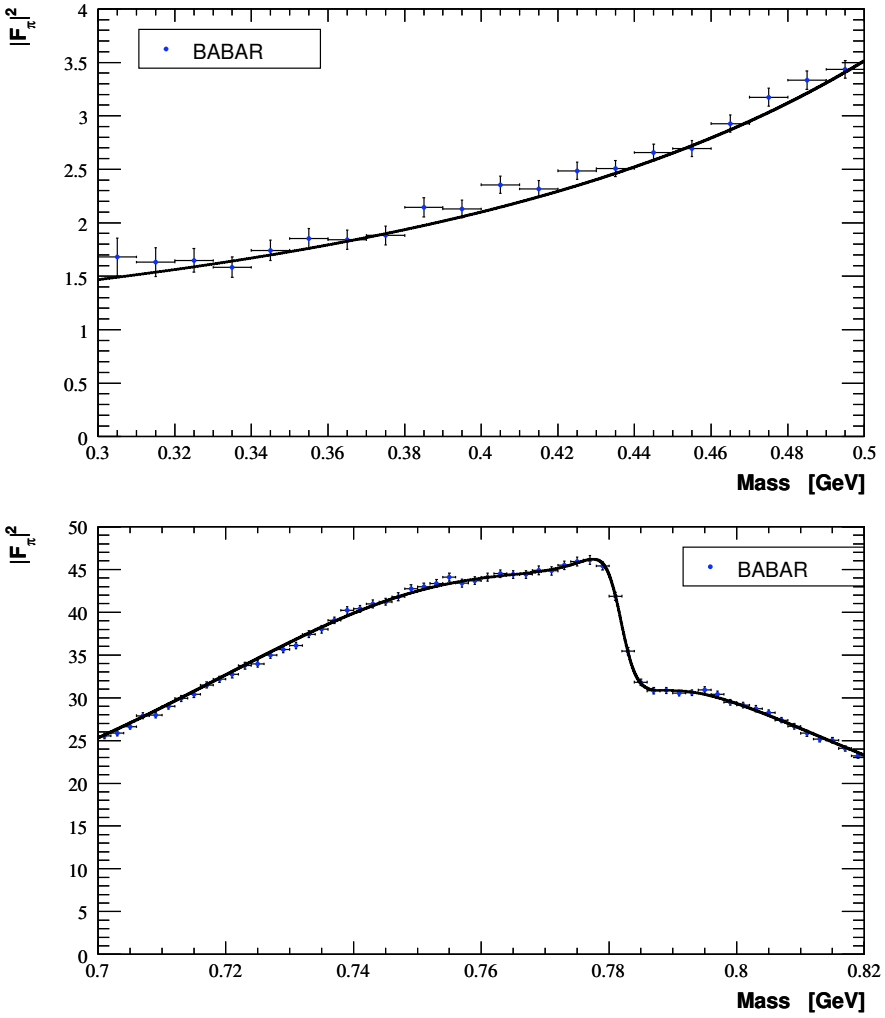

Figure 3.14: The pion form factor squared measured by BABAR as a function of the $\pi\pi$ mass and the VDM fit from 0.3 to 3 GeV described in the text. Top: low-mass region (0.3-0.5 GeV). Bottom: ρ peak region with $\rho - \omega$ interference (0.70-0.82 GeV).

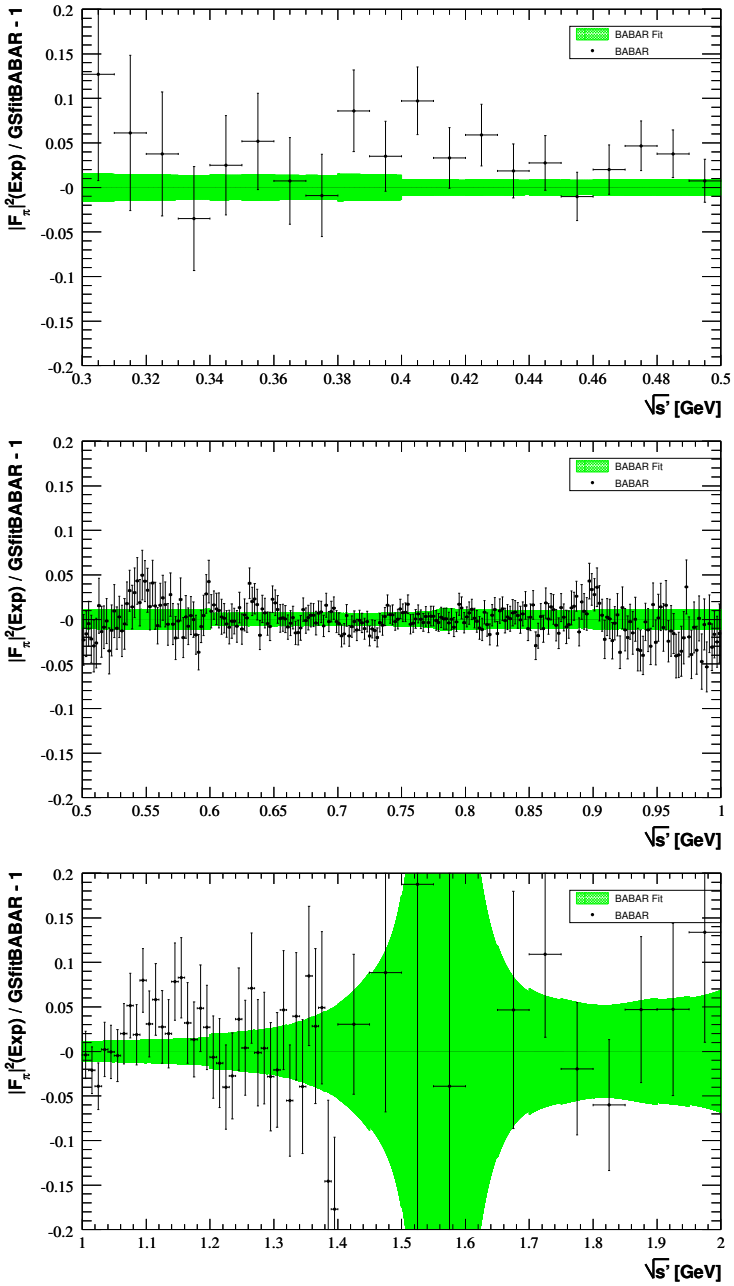

Figure 3.15: The relative difference between the pion form factor squared from BABAR data and the 14-parameter phenomenological fit in three mass regions. Systematic and statistical uncertainties are included for data (diagonal errors). The width of the band shows the propagation of statistical errors in the fit and the quoted systematic uncertainties, added quadratically.

Table 3.2: Parameters obtained for the VDM fit (described in the text) to the BABAR pion form factor data. The errors include both statistical and systematic uncertainties. The error shown in parentheses for m_ρ is the mass calibration uncertainty (see text).

Parameter	Value ± Error
$\|\alpha\|$	$(1.656 \pm 0.061)\ 10^{-3}$
$\|\beta\|$	0.160 ± 0.011
$\|\gamma\|$	0.068 ± 0.006
m_ρ (MeV)	$774.77 \pm 0.28 \quad (\pm 0.16)$
Γ_ρ (MeV)	149.42 ± 0.64
$m_{\rho'}$ (MeV)	1487 ± 14
$\Gamma_{\rho'}$ (MeV)	440 ± 29
$m_{\rho''}$ (MeV)	1841 ± 14
$\Gamma_{\rho''}$ (MeV)	306 ± 23
m_ω (MeV)	781.83 ± 0.19
Γ_ω (MeV)	7.84 ± 0.36
ϕ_ω (rad)	0.006 ± 0.039
$\phi_{\rho'}$ (rad)	3.71 ± 0.07
$\phi_{\rho''}$ (rad)	1.22 ± 0.18

The Gounaris Sakurai representation has good analytic properties and should hold not only in the physical region, but also around t=0. Therefore, taking the derivative of the form factor modulus at zero using the parameters of the global fit provides a value for the quadratic charge radius of the pion:

$$< r_\pi^2 >= (0.4319 \pm 0.0016)\ \text{fm}^2\ , \tag{3.10}$$

to be compared with the value given by CMD-2, (0.4219 ± 0.0016) fm^2. The BABAR value is in better agreement with the direct measurement in the space-like region by NA7, (0.439 ± 0.008) fm^2.

One can use the VDM fit to check the mass calibration by leaving the ω mass free, and using the CMD2 result for the $\rho - \omega$ phase (the Novosibirsk experiments are well calibrated in energy, thanks to the resonant depolarization method). One obtains:

$$m_\omega = (782.53 \pm 0.11 \pm 0.27)\ \text{MeV}\ , \tag{3.11}$$

where the first error is from the fit to the data and the second from the uncertainty on the CMD-2 value for ϕ_ω. The absolute difference with the world average ω mass is

$$m_\omega^{fit} - m_\omega^{PDG} = (-0.12 \pm 0.29)\ \text{MeV}\ , \tag{3.12}$$

consistent with our calibration from the $J/\psi \to \mu\mu$ study, (-0.16 ± 0.16) MeV. The calibration error is added to the fit error for m_ρ in Table 3.2.

3.3.4 Comparison to other e^+e^- results

The measured form factor can be compared to published data from the CMD-2 [55, 56] and SND [57] experiments in Novosibirsk, KLOE in Frascati, in the mass range between 0.5 and 1 GeV. We use the new KLOE [59] data released in Dec. 2008 which are claimed to supersede the older published ones [58].

For this comparison the data of the other experiments are compared with the result from the BABAR form factor fit. Each plot shows the relative difference between the form factor squared of the other experiment and BABAR as data points, while the width of the band around zero is the result of the propagation of statistical errors in the BABAR fit with systematic uncertainties in each mass region (Table 3.1) added quadratically.

The comparisons with other experiments are shown in Figs. 3.16, 3.17, and 3.20. The agreement looks rather reasonable with Novosibirsk within systematic errors, the BABAR results lying generally above, especially on the lower side of the ρ resonance. The discrepancy is larger with KLOE above the ρ peak, although it is much reduced compared to the previous published KLOE results.

The region of the $\rho - \omega$ interference is examined in more detail in Figs. 3.18 and 3.19. No evidence is found for a significant variation in the steep part of the interference pattern around the ω mass, showing that the BABAR mass calibration is not shifted with respect to Novosibirsk by more than 0.3 MeV.

The comparison for the form factor squared in the low mass region is made in Fig. 3.21. The agreement is reasonable, except with the NA7 experiment at CERN.

A direct cross section comparison is made in the large mass region in Fig. 3.22. The BABAR results agree with CMD-2 up to 1.4 GeV, while the DM2 cross section [134] appears larger by about 30-40%.

The comparison in relative terms of BABAR to other experiments is presented in Figs.3.23 and 3.24 for masses lower than 0.5 GeV and between 1.0 and 1.4 GeV, respectively. It is worth noting that the small discrepancy between the 'babar' fit and CMD-2 is in fact also observed in Fig.3.15 where BABAR data are compared to the fit. So it looks more like a problem in the parametrization rather than in the data.

3.4 Summary

The unfolding method described in Chapter 1 has been applied to the sample corresponding to the process $e^+e^- \to \pi^+\pi^-(\gamma)$, in the energy range from 0.3 to 3 GeV, obtained with the radiative return method at BABAR. A precise result was obtained when performing the unfolding of detector effects on a large dynamical range. In particular, a good

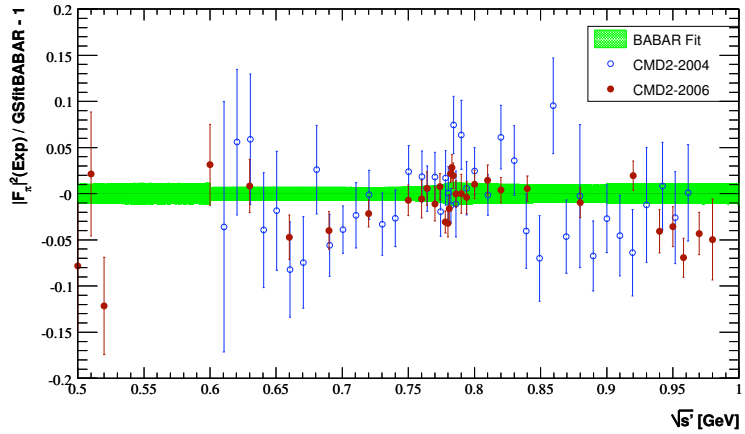

Figure 3.16: The relative difference of pion form factor squared from CMD-2 and the BABAR fit in the 0.5-1 GeV mass region. Systematic and statistical uncertainties are included in the data points. The width of the BABAR band shows the propagation of statistical errors in the fit and the quoted systematic uncertainties, added quadratically.

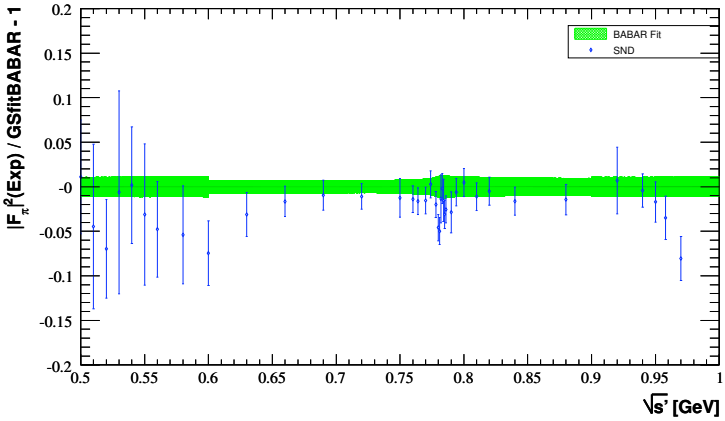

Figure 3.17: The relative difference of pion form factor squared from SND and the BABAR fit in the 0.5-1 GeV mass region. Systematic and statistical uncertainties are included in the data points. The width of the BABAR band shows the propagation of statistical errors in the fit and the quoted systematic uncertainties, added quadratically.

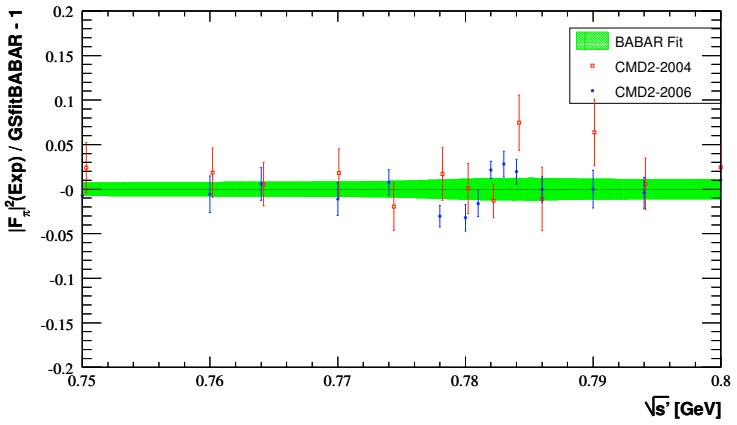

Figure 3.18: The relative difference of pion form factor squared from CMD-2 and the BABAR fit in the $\rho - \omega$ mass region. Systematic and statistical uncertainties are included in the data points. The width of the BABAR band shows the propagation of statistical errors in the fit and the quoted systematic uncertainties, added quadratically.

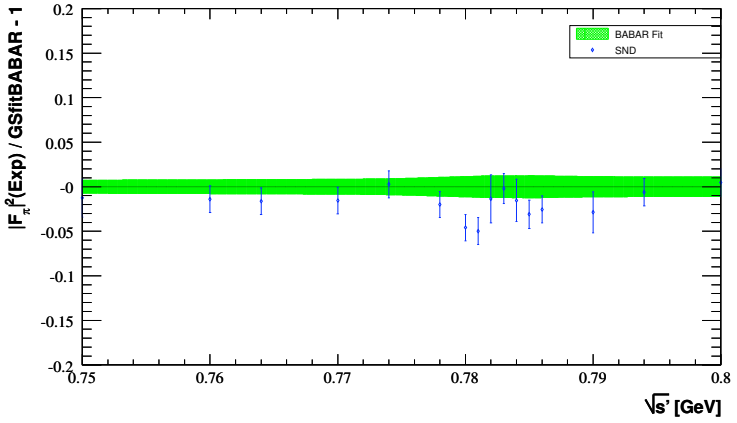

Figure 3.19: The relative difference of pion form factor squared from SND and the BABAR fit in the $\rho - \omega$ mass region. Systematic and statistical uncertainties are included in the data points. The width of the BABAR band shows the propagation of statistical errors in the fit and the quoted systematic uncertainties, added quadratically.

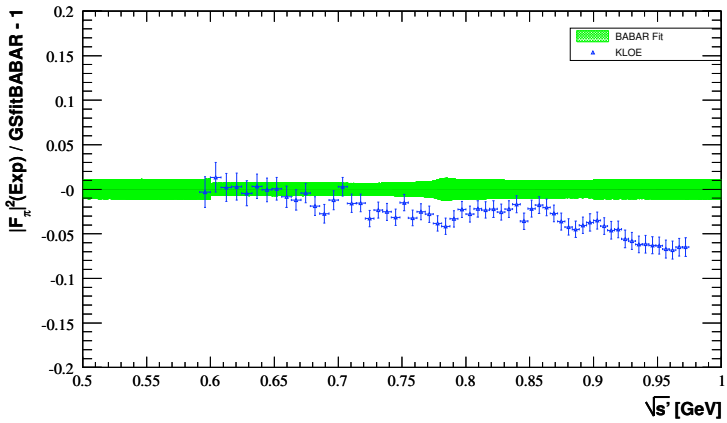

Figure 3.20: The relative difference of pion form factor squared from KLOE and the BABAR fit in the 0.5-1 GeV mass region. Systematic and statistical uncertainties are included in the data points. The width of the BABAR band shows the propagation of statistical errors in the fit and the quoted systematic uncertainties, added quadratically.

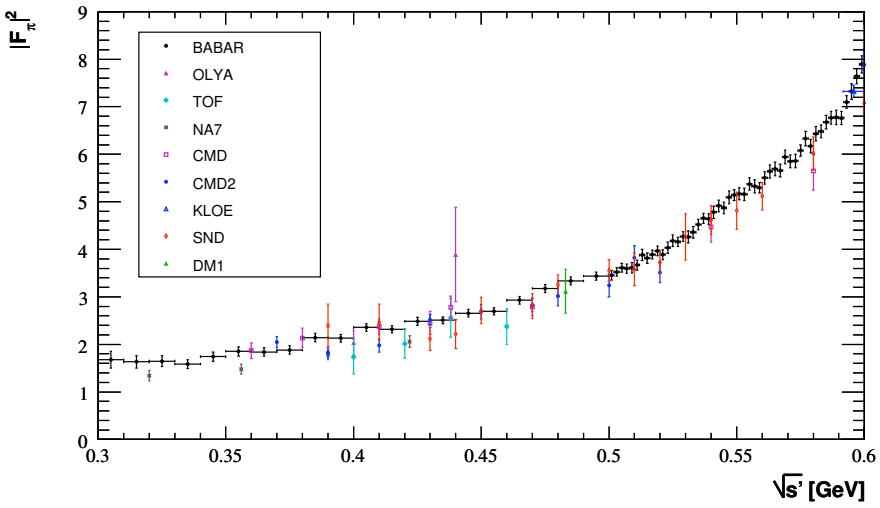

Figure 3.21: The measured pion form factor squared compared to published results from other experiments. Systematic and statistical uncertainties are shown for all results, with the diagonal elements of the BABAR covariance matrix.

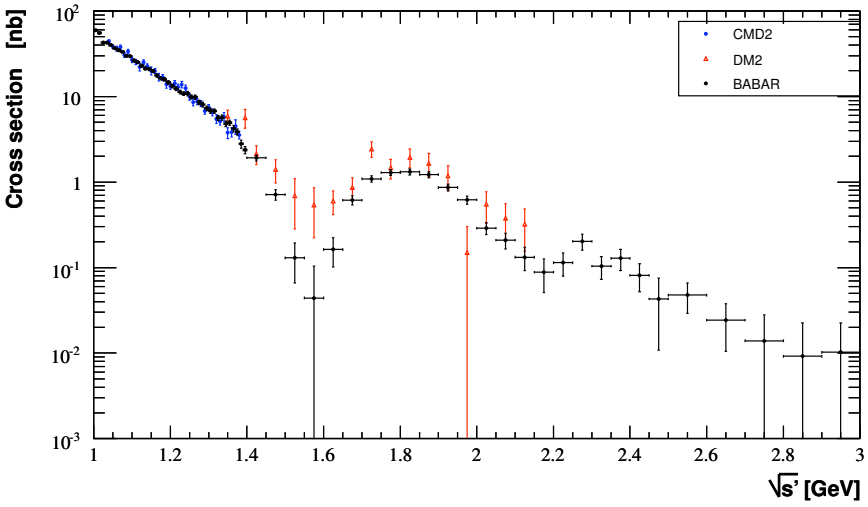

Figure 3.22: The measured cross section for $e^+e^- \to \pi^+\pi^-(\gamma)$ compared to published results from CMD-2 up to 1.4 GeV and DM2 above. Systematic and statistical uncertainties are shown for all results, with the diagonal elements of the BABAR covariance matrix.

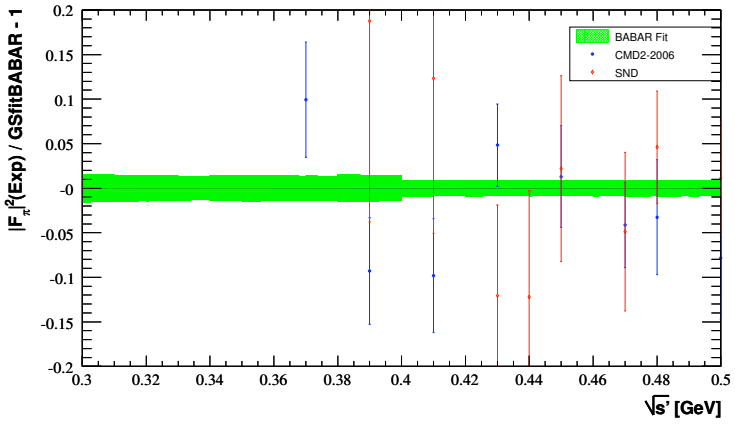

Figure 3.23: The relative difference of pion form factor squared from CMD-2 and SND and the BABAR fit in the mass region below 0.5 GeV. Systematic and statistical uncertainties are included in the data points. The width of the BABAR band shows the propagation of statistical errors in the fit and the quoted systematic uncertainties, added quadratically.

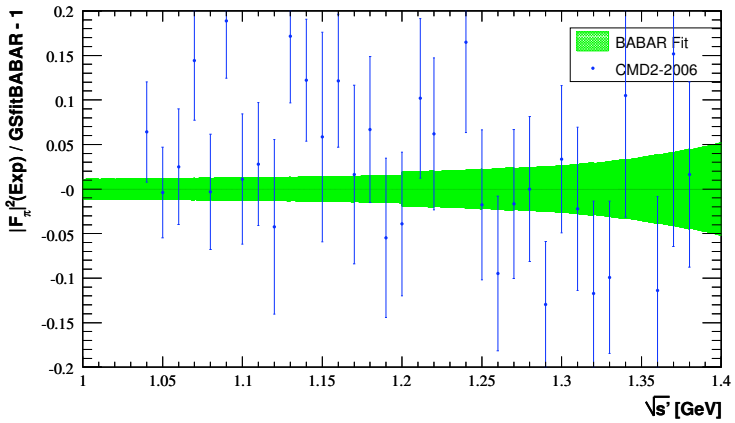

Figure 3.24: The relative difference of pion form factor squared from CMD-2 and the BABAR fit in the mass region above 1 GeV. Systematic and statistical uncertainties are included in the data points. The width of the BABAR band shows the propagation of statistical errors in the fit and the quoted systematic uncertainties, added quadratically.

accuracy is obtained in the $\rho - \omega$ interference region, which is particularly sensitive to resolution effects.

The cross section and formfactor were computed from the unfolded spectrum, using the ISR effective luminosity. The systematic uncertainty in the main ρ resonance region of 5.0 10^{-3} permits a precise evaluation of the hadronic vacuum polarization contribution to the muon magnetic anomaly. A fit of the formfactor was performed, using a model with four resonances, providing a good description of the data. The data from other experiment were compared to that fit. We found a good agreement when comparing with CMD2 and SND data, but a slope is observed in the comparison with KLOE.

Chapter 4

The Anomalous Magnetic Moment of the Muon

4.1 The lepton magnetic anomaly in the Standard Model

The magnetic dipole moment of a charged lepton $\vec{\mu}$ is related to its spin $\vec{s}$ through the formula

$$\vec{\mu} = g\frac{e}{2m}\vec{s}, \tag{4.1}$$

where g is the gyromagnetic ratio, e is the elementary charge and m is the mass of the lepton. A great success of Dirac's theory was the prediction $g_e = 2$ for the electron, explaining thus earlier observations in atomic spectroscopy. Given this result, the magnetic anomaly is defined as $a = \frac{g-2}{2}$, so that Dirac's prediction corresponds to $a_e = 0$.

Tventy years later, an anomaly was discovered for the electron [51] and then explained by Schwinger [52], showing that a is sensitive to quantum fluctuations of the fields. Schwinger computed the first-order QED correction to Dirac's prediction (equivalent to the lowest order diagram contribution), both shown in Fig. 4.1.

With the increase in precision of the experimental measurements, it became obvious that additional contributions must be considered. Hence, the SM prediction for the anomalous magnetic moment of any lepton l is given by

$$a_l^{\mathrm{SM}} = a_l^{\mathrm{QED}} + a_l^{\mathrm{had}} + a_l^{\mathrm{weak}}, \tag{4.2}$$

with the QED, hadronic (Fig. 4.2) and weak (Fig. 4.3) contributions respectively.

4.2 The electron anomaly

Because of the small electron mass, only a_e^{QED} plays a role in practice, although the present experiments are just sensitive to the hadronic contribution. The latest result [45]:

$$a_e^{exp} = 0.001\,159\,652\,180\,73(28) \qquad (0.24\text{ ppb}) \tag{4.3}$$

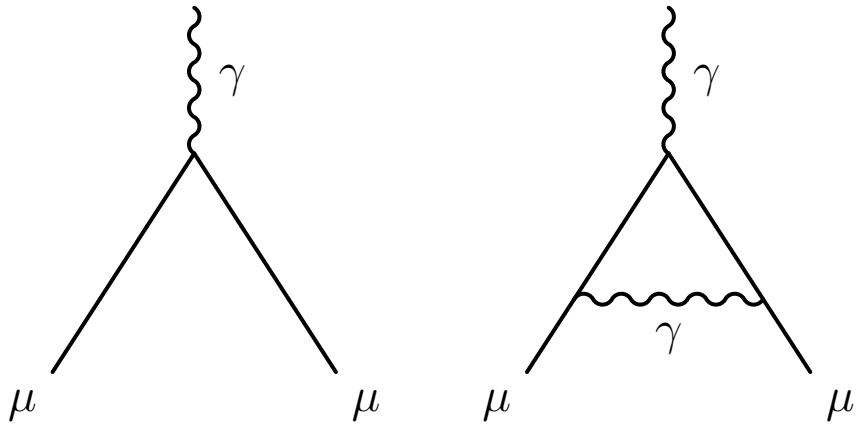

Figure 4.1: Lowest order diagram (left) and first-order QED correction (right) to a_μ. Similar diagrams hold for other leptons.

can be compared to the QED prediction at $O(\alpha^4)$ with $O(\alpha^5)$ estimates [46]. Using the independently determined value of α, a good agreement with QED is observed:

$$a_e^{exp} - a_e^{th} = (3.1 \pm 5.2_\alpha \pm 0.3)\ 10^{-12}. \tag{4.4}$$

Assuming QED to be valid, the a_e measurement provides by far the currently best determination of α.

4.3 The muon anomaly

The muon being 200 times heavier than the electron, its magnetic anomaly is sensitive to quantum fluctuations at much larger energy scales. In this case the hadronic contribution plays an important role and the current experimental accuracy even requires the consideration of weak contributions (a_μ^{weak}).

In Eq. (4.2) for muons, the QED contribution dominates (by far), but its uncertainty is very small (one order of magnitude smaller than the one for a_μ^{weak}, and two orders of magnitude smaller than the uncertainty of a_μ^{had}). The a_μ^{had} term can be further decomposed into

$$a_\mu^{had} = a_\mu^{\mathrm{had,LO}} + a_\mu^{had,HO} + a_\mu^{had,LBL}, \tag{4.5}$$

where $a_\mu^{\mathrm{had,LO}}$ is the lowest-order contribution from hadronic vacuum polarization and $a_\mu^{had,HO}$ is the corresponding higher order part. The third contribution is the so-called hadronic light-by-light (LBL) and nowadays it can only be evaluated in a model-dependent approach. Its value is comparable with $|a_\mu^{had,HO}|$ and about 70 times smaller than $a_\mu^{had,LO}$. However, while $|a_\mu^{had,HO}|$ is relatively well known, the absolute uncertainty on $a_\mu^{had,LBL}$ is only twice smaller than the one for $a_\mu^{\mathrm{had,LO}}$ (which dominates in the sum). The values of these various contributions are given in Table 4.1.

The hadronic contribution cannot be computed using QCD as a quark loop in the hadronic insertion would be a good approximation only at large q^2 values of the photon

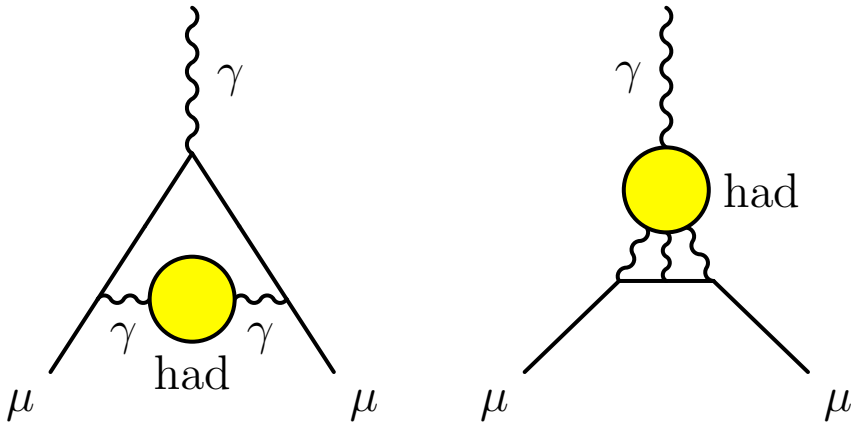

Figure 4.2: Lowest order hadronic vacuum polarization contribution to a_μ (left) and light-by-light scattering (right).

QED	$11\,658\,471.809 \pm 0.015$
LO had	~ 700
HO had	$-9.79 \pm 0.08_{\rm exp} \pm 0.03_{\rm rad}$
LBL	10.5 ± 2.6
EW	$15.4 \pm 0.1_{\rm had} \pm 0.2_{\rm Higgs}$

Table 4.1: Contributions to a_μ from QED [115], lowest order (LO) hadronic vacuum polarization (see later), higher order (HO) hadronic loops [101], hadronic light-by-light (LBL) scattering [98] and respectively electroweak (EW) effects [116,117]. All the values are given in units of 10^{-10}.

propagator. Instead, low energies are emphasized (less virtuality) in the loop diagram of Fig. 4.2 (left) and perturbative QCD cannot be applied at this scale. Fortunately a solution using a dispersion relation can be used instead [47].

Indeed, owing to unitarity and to the analyticity of the two point correlator, using the optical theorem, the lowest order hadronic vacuum polarisation contribution to the anomalous magnetic moment of the muon ($a_\mu^{\rm had,LO}$) can be computed through an energy-squared dispersion integral (ranging from the $\pi^0\gamma$ threshold to infinity):

$$a_\mu^{\rm had,LO} = \frac{1}{4\pi^3}\int_{m_{\pi^0}^2} ds K(s)\sigma_{e^+e^-\to{\rm hadrons}}(s)\,, \tag{4.6}$$

where $K(s)$ is a QED kernel function [94] (Fig. 4.4),

$$K(s) \;=\; x^2\left(1-\frac{x^2}{2}\right) \;+\; (1+x)^2\left(1+\frac{1}{x^2}\right)\left[\ln(1+x)-x+\frac{x^2}{2}\right] \;+\; x^2\ln x\frac{1+x}{1-x}\;, \tag{4.7}$$

with $x = (1-\beta_\mu)/(1+\beta_\mu)$ and $\beta_\mu = (1-4m_\mu^2/s)^{1/2}$. The computation of this contribution will be in the center of the following studies.

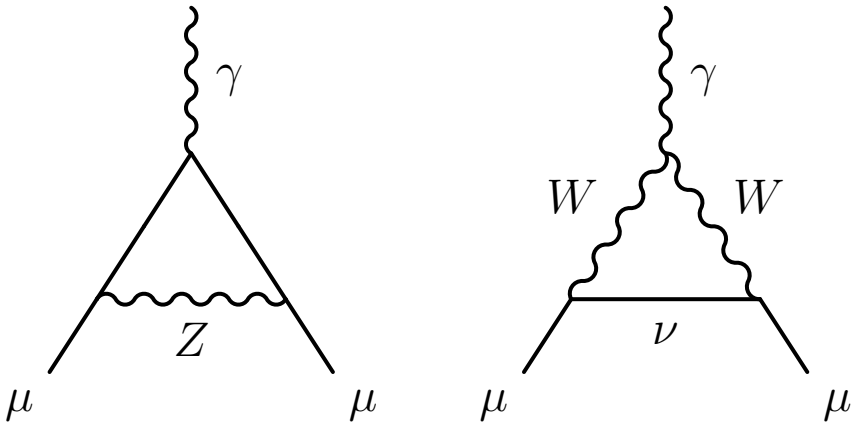

Figure 4.3: Weak interaction diagrams contributing to a_μ.

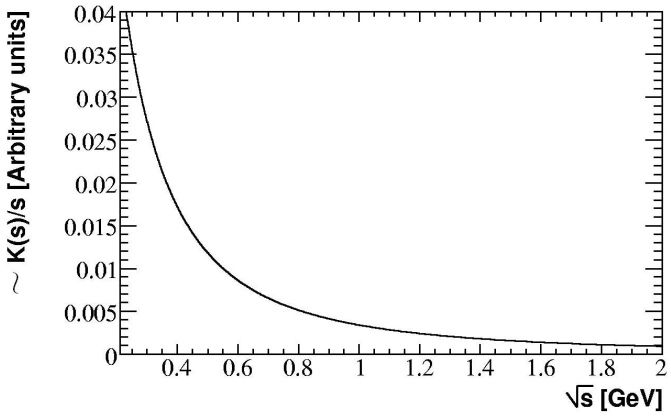

Figure 4.4: Energy dependence for $K(s)/s$.

4.4 Sensitivity to New Physics

Eventually, one could also get contributions to a_μ from diagrams envolving Physics beyond the SM (see for example Fig. 4.5). It has been noticed that the sensitivity of the anomalous magnetic moment to New Physics contributions goes like the square of the mass of the lepton [53]. Therefore, although less precisely measured, a_μ is much more sensitive to these effects compared to a_e and hence prefered in the searches for Physics beyond the SM.

For example, the leading effect in supersymmetry (Fig. 4.5) is approximately given by [48]

$$a_\mu^{\rm SUSY} \simeq \frac{\alpha(\mathrm{M_Z})}{8\pi \sin^2\theta_{\rm w}} \frac{\mathrm{M}_\mu^{\,2}}{\mathrm{M}} \tan\beta \simeq 13\ 10^{-10} \left(\frac{100\ \mathrm{GeV}}{\mathrm{M}}\right)^2 \tan\beta\ , \qquad (4.8)$$

where $\tan\beta$ is the ratio of the vacuum expectation values of the two Higgs field doublets and M a typical SUSY mass. For $\tan\beta \sim 10$, the present situation of experiment and theory is sensitive to $\mathrm{M} \sim 400$ GeV, comparable to the range accessible at LHC for direct searches.

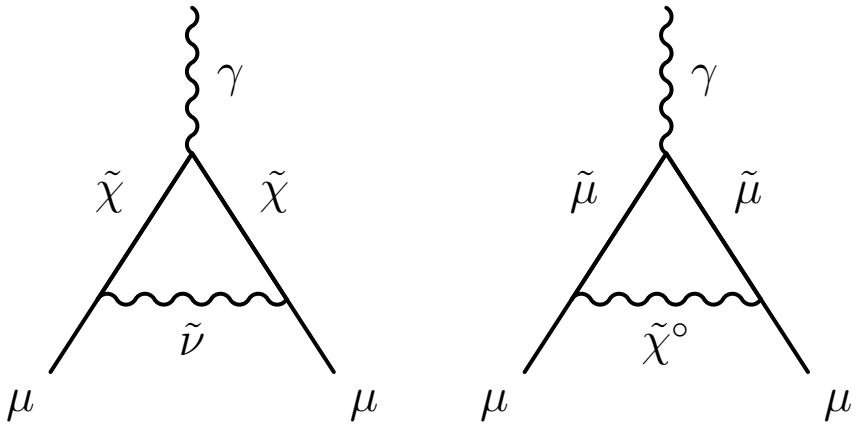

Figure 4.5: Possible contributions to a_μ, coming from lowest-order supersymmetry.

4.5 Experimental measurement

The experimental measurement of a_μ is based on the storage ring technique pioneered at CERN in the 1970s. It exploits the angular dependence of the muon weak decay probability (see Fig. 4.6) to infer the direction of the spin of the muon as a function of time, and hence the difference of the rotation and precession frequencies. A precise measurement of the magnetic field allows the measurement of a_μ through a ratio of frequencies.

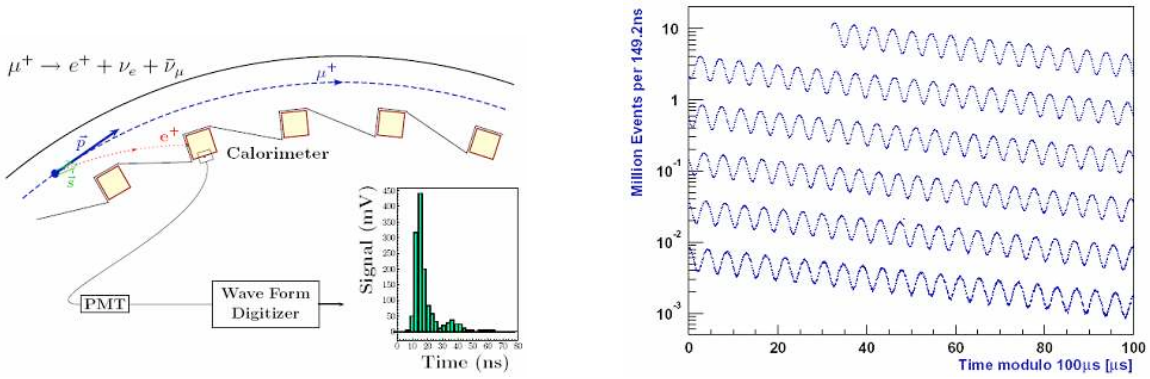

Figure 4.6: Experimental measurement of a_μ. Left: muon weak decay in the storage ring. Right: number of registered events as a function of the elapsed time.

The most recent measurement of a_μ was performed at BNL [99] with a precision of 0.54 ppm:

$$a_\mu^{\text{exp}} = 0.001\,165\,920\,89(54)_{\text{stat}}(3.3)_{\text{syst}}. \tag{4.9}$$

New projects for measuring a_μ with increased accuracy ($\times 4$) are being considered at FNAL [49] and KEK [50]. Its comparison with the theoretical prediction allows a precise test of the SM.

Chapter 5

The Hadronic Contribution to the Anomalous Magnetic Moment of the Muon

The Standard Model (SM) prediction of the anomalous magnetic moment of the muon, a_μ, is limited in precision by contributions from hadronic vacuum polarization (VP) loops. These contributions can be conveniently separated into a dominant lowest order ($a_\mu^{\mathrm{had,LO}}$) and higher order ($a_\mu^{\mathrm{had,HO}}$) parts.

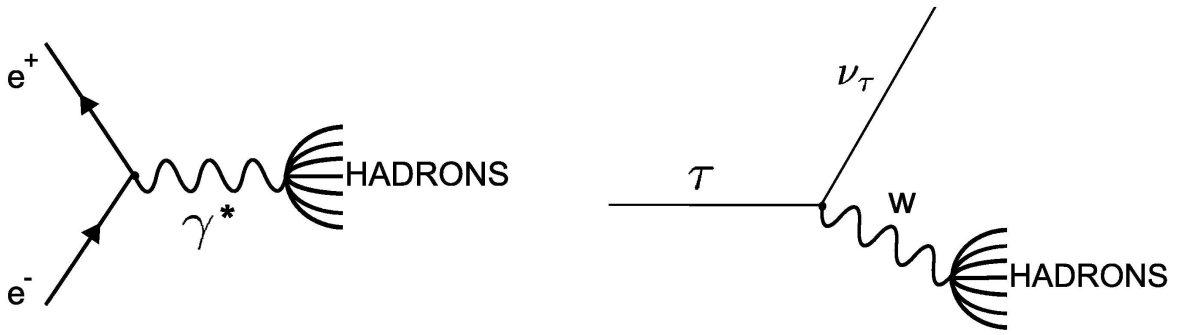

Figure 5.1: e^+e^- annihilation to hadrons (left) and hadronic τ decay (right).

Spectral functions determined from the cross sections of e^+e^- annihilation to hadrons or from hadronic τ decays mass spectra (see Fig. 5.1) are fundamental quantities, especially useful at low energy where perturbative QCD alone fails to describe the data. They play a crucial role in calculations of $a_\mu^{\mathrm{had,LO}}$, which is obtained through an energy-squared dispersion integral (Eq. (4.6)). The integration kernel strongly emphasises the low-energy part of the spectrum (see Fig. 4.4), therefore a good knowledge of the spectral function is required in this region. About 73% of the lowest order hadronic contribution is provided by the $\pi\pi\gamma$ final state [1]. More importantly, 62% of its total *quadratic* error stems from the $\pi\pi$ mode, stressing the need for ever more precise experimental data in this channel.

[1]Throughout this chapter, final state photon radiation is implied for the $\pi\pi$ final state.

5.1 The Discrepancy Between τ and e^+e^- Spectral Functions Revisited and the Consequences for the Muon Magnetic Anomaly

During the last decade, measurements of the $\pi^+\pi^-$ spectral function with percent accuracy became available [55–57, 59], superseding older and less precise data. The former lack of precision data inspired the search for an alternative. It was found [62] in form of accurate $\tau^- \to \pi^-\pi^0\nu_\tau$ spectral functions [2] [63, 146, 158, 180] transferred from the charged to the neutral state using isospin symmetry. With the increasing $e^+e^- \to \pi^+\pi^-$ experimental precision, which today is on a level with the τ data, systematic discrepancies in shape and normalisation of the spectral functions were observed between the two systems [64, 65]. It was found that, when computing the hadronic VP contribution to the muon magnetic anomaly using the τ instead of the e^+e^- data for the 2π and 4π channels, the observed deviation with the experimental value [66] would reduce from 3.3 times the combined experimental and estimated theoretical error to less than 1 [67].

In this section we obtain a combined τ spectral function, including recent $\tau^- \to \pi^-\pi^0\nu_\tau$ data from the Belle experiment [68], and revisit all isospin-breaking corrections in this channel taking advantage of more accurate data and new theoretical investigations. We recompute the lowest order hadronic contributions to the muon $g-2$ using e^+e^- and τ data with the new corrections, and compare the outcome. The results presented here were published in [54].

5.1.1 Tau data

The τ-based a_μ evaluation in [64, 65] used the τ spectral functions measured by the ALEPH [180], CLEO [63] and OPAL [146] experiments for the dominant hadronic decay mode $\tau^- \to \pi^-\pi^0\nu_\tau$. We include here a high-statistics measurement of the same decay mode performed by Belle [68]. Rather different experimental conditions are met at the Z centre-of-mass energy (ALEPH, OPAL) and at the $\Upsilon(4S)$ resonance (CLEO, Belle). At LEP the $\tau^+\tau^-$ events can be selected with high efficiency ($> 90\%$) and small non-τ background ($< 1\%$), thus ensuring little bias in the efficiency determination. The situation is not as favourable at low energy: because the dominant hadronic cross section has a smaller particle multiplicity, it is more likely to pollute the τ sample and strong cuts must be applied, resulting in smaller selection efficiency with larger relative uncertainty. On the other hand, the $\Upsilon(4S)$ machines outperform LEP in statistics for τ-pair production: Belle's analysis contains 5.4 million $\tau^- \to h^-\pi^0\nu_\tau$ candidates ($72.2\,\mathrm{fb}^{-1}$ integrated luminosity), compared to 81 thousand candidates used by ALEPH (including the full LEP statistics accumulated on the Z pole). Moreover, CLEO and Belle have an advantage for the τ final state reconstruction since particles are more separated in space. The LEP detectors have to cope with collimated τ decay products and the granularity

[2] In order to compute the contribution corresponding to different hadronic e^+e^- annihilation channels, the $\tau \to \nu_\tau + 2\pi^-\pi^+\pi^0$, $\pi^-3\pi^0$ were also used.

of the detectors, particularly the calorimeters, plays a crucial role. One can therefore consider ALEPH/OPAL and CLEO/Belle data to be approximately uncorrelated as far as experimental procedures are concerned.[3] These four data sets are combined to provide the most precise τ spectral function, using the newly developed software package HVP-Tools. The methods used in this package will be discussed in Section 5.4.2. It transforms the original τ data and associated statistical and systematic covariance matrices into fine-grained energy bins (1 MeV). In the combination, when the χ^2 value of a bin-wise average exceeds the number of degrees of freedom ($n_{\rm dof}$), the error in the averaged bin is rescaled by $\sqrt{\chi^2/n_{\rm dof}}$ to account for inconsistencies, which occur because most experiments are dominated by systematic uncertainties. Figure 5.2 shows the relative comparison of the combined data with those of each experiment.[4]

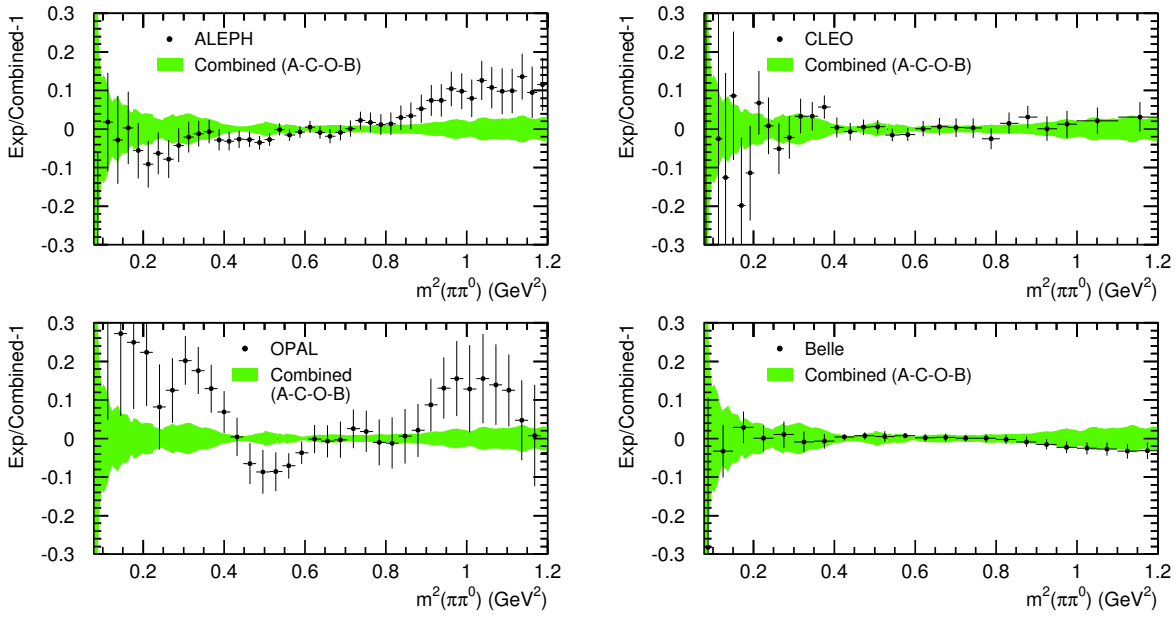

Figure 5.2: Relative comparison between the $\tau^- \to \pi^-\pi^0\nu_\tau$ invariant mass-squared measurements from ALEPH, CLEO, OPAL, Belle (data points) and the combined result (shaded band).

The branching fraction $\mathcal{B}_{\pi\pi^0}$ for $\tau^- \to \pi^-\pi^0\nu_\tau$ is obtained from the measured decay channel $\tau^- \to h^-\pi^0\nu_\tau$ ($\mathcal{B}_{h\pi^0}$) by subtracting the non-π contribution from the generic charged hadron mode (h^-). The average $\mathcal{B}_{h\pi^0}$ value from these experiments and the two other LEP experiments L3 [71] and DELPHI [72] is $(25.847 \pm 0.101)\%$. Subtracting from this the current world average value $(0.428 \pm 0.015)\%$ for $\tau^- \to K^-\pi^0\nu_\tau$ [9], gives

[3]Experimental correlations are introduced by common systematic errors in the Monte Carlo simulation used. All experiments employ the same tau decay and radiative corrections libraries, which are used for the correction of feed-through from non-$h^-\pi^0$ final states, as well as for the determination of the acceptance and efficiency after applying the selection requirements. ALEPH and OPAL use however data-driven spectral functions for the feed-through corrections, so that the resulting correlations should be small. They are hence neglected in the average.

[4]The total systematic uncertainty from Belle is derived from the correlated mass spectra containing revised information with respect to Table V of Ref. [68], which has been provided to us by Belle [70]. They differ mostly at the low mass region below the ρ mass peak.

$\mathcal{B}_{\pi\pi^0} = (25.42 \pm 0.10)\%$, which is the result used in the following.

5.1.2 Isospin-breaking corrections

Historically, the conserved vector current (CVC) relation between τ and e^+e^- data was considered even before the discovery of the τ lepton [73, 74]. In the limit of isospin invariance, the spectral function of the vector current decay $\tau \to X^-\nu_\tau$ is related to the $e^+e^- \to X^0$ cross section of the corresponding isovector final state X^0,

$$\sigma^{I=1}_{X^0}(s) = \frac{4\pi\alpha^2}{s}\, v_{1,\,X^-}(s) \;, \tag{5.1}$$

where s is the centre-of-mass energy-squared or equivalently the invariant mass-squared of the τ final state X, α is the electromagnetic fine structure constant, and $v_{1,\,X^-}$ is the non-strange, isospin-one vector spectral function. In practice, one must apply isospin-breaking (IB) corrections, and $v_{1,\,X^-}$ is substituted by the useful spectral function, given by

$$v^{IC}_{1,\,X^-}(s) = \frac{m_\tau^2}{6\,|V_{ud}|^2}\,\frac{\mathcal{B}_{X^-}}{\mathcal{B}_e}\,\frac{1}{N_X}\frac{dN_X}{ds}\left(1-\frac{s}{m_\tau^2}\right)^{-2}\left(1+\frac{2s}{m_\tau^2}\right)^{-1}\frac{R_{\rm IB}(s)}{S_{\rm EW}}\,, \tag{5.2}$$

with

$$R_{\rm IB}(s) = \frac{{\rm FSR}(s)}{G_{\rm EM}(s)}\frac{\beta_0^3(s)}{\beta_-^3(s)}\left|\frac{F_0(s)}{F_-(s)}\right|^2 \;. \tag{5.3}$$

In Eq. (5.2), $(1/N_X)dN_X/ds$ is the normalised invariant mass spectrum of the hadronic final state, and $\mathcal{B}_{X^-}$ denotes the branching fraction of $\tau \to X^-(\gamma)\nu_\tau$ (throughout this section, final state photon radiation is implied for τ branching fractions). We use for the τ mass the value $m_\tau = (1776.84 \pm 0.17)\,{\rm MeV}$ [9], and for the CKM matrix element $|V_{ud}| = 0.97418 \pm 0.00019$ [130], which assumes CKM unitarity. For the electron branching fraction we use $\mathcal{B}_e = (17.818 \pm 0.032)\%$, obtained [122] supposing lepton universality. Short-distance electroweak radiative effects lead to the correction $S_{\rm EW} = 1.0235 \pm 0.0003$ [64,75–78]. All the s-dependent isospin-breaking corrections are included in $R_{\rm IB}$, and discussed in the following for the dominant $\pi\pi$ decay channel.

The first term in Eq. (5.3) is the ratio ${\rm FSR}(s)/G_{\rm EM}(s)$, where ${\rm FSR}(s)$ refers to the final state radiative corrections [79] in the $\pi^+\pi^-$ channel, and $G_{\rm EM}(s)$ denotes the long-distance radiative corrections of order α to the photon inclusive $\tau^- \to \pi^-\pi^0\nu_\tau$ spectrum. $G_{\rm EM}(s)$ includes the virtual and real photonic corrections and was calculated originally in [80] in the framework of the Resonance Chiral Theory [81]. In that work the small axial contributions to real photon emission were fixed using the axial anomalous terms [82]. A recalculation of $G_{\rm EM}(s)$ was presented in [83], where the real photon corrections were incorporated via a meson dominance model. Since these corrections diverge in the soft-energy limit, a small mass must be given to the photon as regularisation. Consistency however requires that the real photon corrections are calculated by summing over all three polarization states of the massive photon [85]. If we include the longitudinal polarization

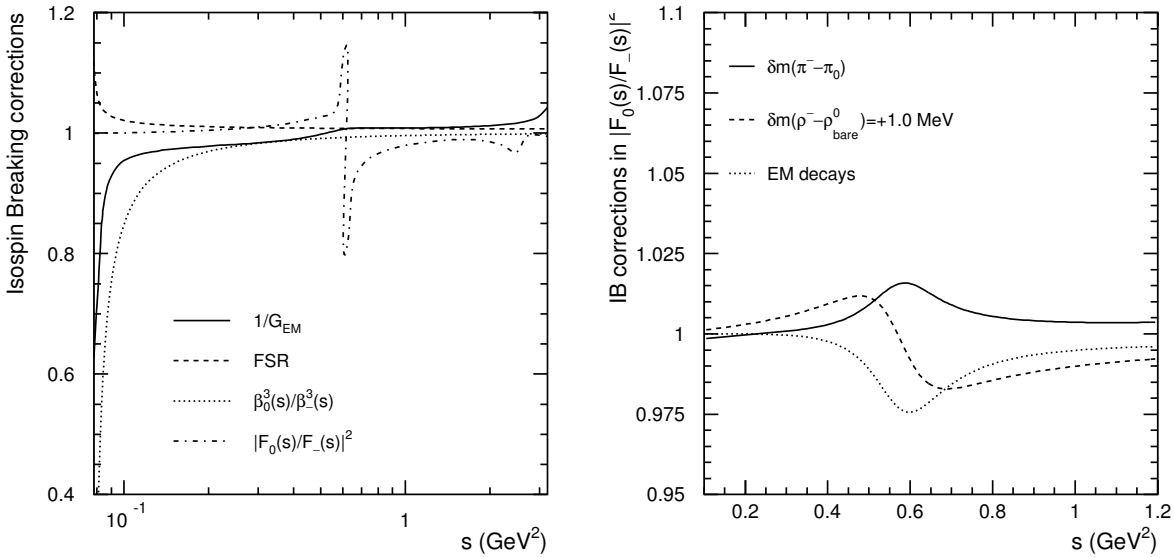

Figure 5.3: Left: Isospin-breaking corrections from $G_{\rm EM}$, FSR, $\beta_0^3(s)/\beta_-^3(s)$ and $|F_0(s)/F_-(s)|^2$. Right: Isospin-breaking corrections in the ratio of $I = 1$ components of the form factors $|F_0(s)/F_-(s)|^2$ due to the π mass splitting $\delta m_\pi = m_{\pi^\pm} - m_{\pi^0}$, the ρ mass splitting $\delta m_\rho = m_{\rho^\pm} - m_{\rho^0_{\rm bare}}$, and the difference $\delta\Gamma_\rho$ in the ρ meson widths.

according to Ref. [85], the model-independent piece of the radiative corrections changes by at most 0.3% close to threshold and rapidly vanishes with increasing s.

The $G_{\rm EM}(s)$ correction used in this analysis is based on Ref. [83]. We do not apply, however, any correction for the contribution from the square of the $\pi(\omega \to \pi^0\gamma)$ amplitude, since it is considered as a background by all experiments and hence subtracted from the measured spectral functions. On the other hand, we do keep the interference between bremsstrahlung and ω amplitudes. The resulting $G_{\rm EM}(s)$ function is shown by the solid curve in the left-hand plot of Fig. 5.3. The main numerical difference between this correction and that of [80] lies below the ρ peak. Since the origin of the difference is presently only partly understood, we assign the full effect as systematic uncertainty to the $G_{\rm EM}$ correction.

The second correction term in Eq. (5.3), $\beta_0^3(s)/\beta_-^3(s)$, arises from the $\pi^\pm$–π^0 mass splitting (hence the phase space difference) and is important close to the threshold (dotted curve in Fig. 5.3 (left)).

The third IB correction term involves the ratio of the electromagnetic to weak form factors $|F_0(s)/F_-(s)|$ and is the most delicate one. Below 1 GeV, the pion form factors are dominated by the ρ meson resonance, such that IB effects mainly stem from the mass and width differences between the $\rho^\pm$ and ρ^0 mesons, and from ρ^0–ω mixing. The overall effect of this correction is shown by the dash-dotted curve in Fig. 5.3 (left).

Let us analyse in more detail the IB effects in the form factors. A direct calculation of the 2π production amplitudes in e^+e^- annihilation and τ decays using vector meson

dominance leads to

$$F_0(s) = f_{\rho^0}(s)\left[1+\delta_{\rho\omega}\frac{s}{m_\omega^2 - s - i m_\omega \Gamma_\omega(s)}\right], \quad (5.4)$$

$$F_-(s) = f_{\rho^-}(s), \quad (5.5)$$

where f_ρ gives the ρ lineshape (if no interference was present) and $\delta_{\rho\omega}$ is a complex ρ–ω mixing parameter. Following [180], two phenomenological fits to the e^+e^- form factor data have been performed using the Gounaris-Sakurai (GS) [86] and Kühn-Santamaria (KS) [87] parametrisations[5]. For the corresponding mixing strengths and phases of the fits we find $|\delta_{\rho\omega}^{\rm GS}| = (2.00 \pm 0.06)\times 10^{-3}$, $\arg(\delta_{\rho\omega}^{\rm GS}) = (11.6 \pm 1.8)^\circ$, and $|\delta_{\rho\omega}^{\rm KS}| = (1.87 \pm 0.06)\times 10^{-3}$, $\arg(\delta_{\rho\omega}^{\rm KS}) = (13.2 \pm 1.7)^\circ$, respectively. In both parametrisations, the absorptive parts of the ρ propagators have an explicit energy-dependence of the form $-i\sqrt{s}\Gamma_{\rho^{0,-}}(s)$.

One of the IB effects is associated with the ρ meson width difference. Within an accuracy of 0.1%, the decay widths of the ρ mesons below $\sqrt{s} = 1\,\text{GeV}$ are given by their photon inclusive rates into $\pi\pi$ modes [91]. A direct calculation of the $\rho \to \pi\pi(\gamma)$ and $\pi\pi\gamma$ decay rates shows that the width difference, $\delta\Gamma_\rho = \Gamma_{\rho^0} - \Gamma_{\rho^-}$, is given by [91]

$$\delta\Gamma_\rho(s) = \frac{g_{\rho\pi\pi}^2\sqrt{s}}{48\pi}\left[\beta_0^3(s)(1+\delta_0) - \beta_-^3(s)(1+\delta_-)\right], \quad (5.6)$$

where $g_{\rho\pi\pi}$ is the strong coupling of the isospin-invariant $\rho\pi\pi$ vertex and $\delta_{0,-}$ denote radiative corrections for photon-inclusive $\rho \to \pi\pi$ decays, which include $\rho \to \pi\pi\gamma$. Contrary to expressions used in previous approaches the ρ meson decay widths in Eq. (5.6) are independent of the photon energy cut-off used to separate the $\rho \to \pi\pi(\gamma)$ and $\rho \to \pi\pi\gamma$ rates. In addition to the IB arising from the $\pi^\pm$–π^0 mass difference, the radiative corrections to $\rho \to \pi\pi$ and their corresponding radiative rates produce a splitting in the ρ meson widths. For instance, at $\sqrt{s} = m_\rho = 775\,\text{MeV}$, the width difference of Eq. (5.6) is $\delta\Gamma_\rho \approx +0.76\,\text{MeV}$, compared to the value $\delta\Gamma_\rho \approx (-0.42 \pm 0.58)\,\text{MeV}$ used in [62]. The difference between the two results is mainly due to the effects from radiative corrections (the $\delta_{0,-}$ terms in Eq. (5.6)). Our results can also be compared to the one used in [80], $\delta\Gamma_\rho = (m_\rho s/96\pi F_\pi^2)[\beta_0^3(s) - \beta_-^3(s)] + (0.45 \pm 0.45)\,\text{MeV}$, which at $\sqrt{s} = 775\,\text{MeV}$ gives $\delta\Gamma_\rho = (-0.61 \pm 0.45)\,\text{MeV}$. Note that if electromagnetic effects were ignored ($\delta_{0,-} = 0$) in Eq. (5.6), we would have $\delta\Gamma = -1.06\,\text{MeV}$, which is very similar to the cases considered in [62, 80].

The second input required to assess the IB effects in the form factors is the mass splitting between neutral and charged ρ mesons. Using the expected difference $m_{\rho^0} - m_{\rho^0_{\rm bare}} \approx 3\Gamma(\rho^0 \to e^+e^-)/(2\alpha) = 1.45\,\text{MeV}$, between dressed and bare ρ^0 mass [92], together with the experimental value $m_{\rho^\pm} - m_{\rho^0} = (-0.4 \pm 0.9)\,\text{MeV}$, obtained by KLOE from a fit to the $\phi \to \pi^+\pi^-\pi^0$ Dalitz plot [93], one finds $\delta m_\rho = m_{\rho^\pm} - m_{\rho^0_{\rm bare}} = (1.0 \pm$

[5]The fits are performed in the full mass range where the e^+e^- data are available. This differs from those fits performed in Ref. [88] in which the fits were limited to a given single e^+e^- experiment (with data available only below 1 GeV) with fewer number of free parameters. We do not use the Hidden Local Symmetry effective model [89] and the effective field theory model [90] as these models do not include contributions from the high mass resonances such as ρ' and therefore can only be valid for the mass range below about 1 GeV.

0.9) MeV, which we use here instead of the degeneracy assumed in previous analyses [64, 80].

The IB effects in the ratio of $I = 1$ components of the pion form factors (except for ρ–ω mixing) are drawn in the right-hand plot of Fig. 5.3. It is noticeable that the effects of photonic corrections and of the $\pi^{\pm}$–π^0 mass difference in the ρ meson widths largely cancel each other.

Figure 5.4 shows the relative difference between the e^+e^- and the isospin-breaking-corrected τ spectral functions versus s. The relative normalisation is consistent within the respective errors and the shape is found in better agreement than before [65], despite a remaining deviation above the ρ-mass-squared. The discrepancy with the KLOE data, although reduced, persists.

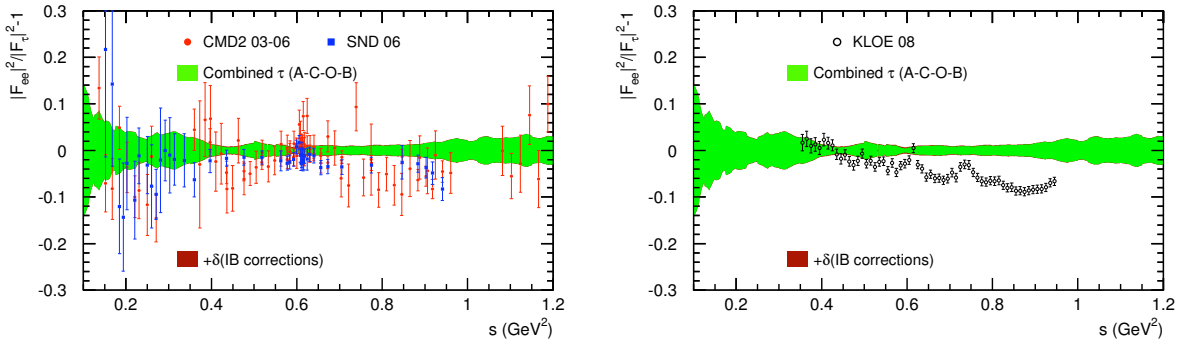

Figure 5.4: Relative comparison between e^+e^- and τ spectral functions, expressed in terms of the difference between neutral and charged pion form factors. Isospin-breaking (IB) corrections are applied to τ data with its uncertainties, although hardly visible, included in the error band.

5.1.3 Update of $a_\mu^{\rm had,LO}[\pi\pi,\tau]$

The IB corrections applied to the lowest order hadronic contribution to the muon $g-2$ using τ data in the same, dominant, $\pi\pi$ channel can be evaluated with

$$\Delta^{\rm IB} a_\mu^{\rm LO,had}[\pi\pi,\tau] = \frac{\alpha^2 m_\tau^2}{6\,|V_{ud}|^2\pi^2}\,\frac{\mathcal{B}_{\pi\pi^0}}{\mathcal{B}_e}\int_{4m_\pi^2}^{m_\tau^2} ds\,\frac{K(s)}{s} \times \frac{dN_X}{N_X\,ds}\left(1-\frac{s}{m_\tau^2}\right)^{-2}\left(1+\frac{2s}{m_\tau^2}\right)^{-1}\left[\frac{R_{\rm IB}(s)}{S_{\rm EW}}-1\right]. \quad (5.7)$$

The numerical values for the various corrections are given in Table 5.1 for the energy range between the 2π mass threshold and 1.8 GeV. The present estimate of the IB effect from long-distance corrections is smaller than the previous one [67,83], because we now use a $G_{\rm EM}(s)$ correction in which the contributions involving the $\rho\omega\pi$ vertex are explicitly excluded (except for its interference with the QED amplitude). Its uncertainty corresponds to the difference between the correction used in this analysis and that from Ref. [80]. The quoted 10% uncertainty on the FSR and $\pi\pi\gamma$ electromagnetic corrections is an estimate of the structure-dependent effects (pion form factor) in virtual corrections and of

Table 5.1: Contributions to $a_\mu^{\rm had,LO}$ $[\pi\pi,\tau]$ ($\times 10^{-10}$) from the isospin-breaking corrections discussed in Sec. 5.1.2. Corrections shown in two separate columns correspond to the Gounaris-Sakurai (GS) and Kühn-Santamaria (KS) parametrisations, respectively.

Source	$\Delta a_\mu^{\rm had,LO}[\pi\pi,\tau]$ (10^{-10})		
	GS model		KS model
$S_{\rm EW}$		-12.21 ± 0.15	
$G_{\rm EM}$		-1.92 ± 0.90	
FSR		$+4.67 \pm 0.47$	
ρ–ω interference	$+2.80 \pm 0.19$		$+2.80 \pm 0.15$
$m_{\pi^\pm} - m_{\pi^0}$ effect on σ		-7.88	
$m_{\pi^\pm} - m_{\pi^0}$ effect on Γ_ρ	$+4.09$		$+4.02$
$m_{\rho^\pm} - m_{\rho^0_{\rm bare}}$	$0.20^{+0.27}_{-0.19}$		$0.11^{+0.19}_{-0.11}$
$\pi\pi\gamma$, electrom. decays	-5.91 ± 0.59		-6.39 ± 0.64
Total	-16.07 ± 1.22		-16.70 ± 1.23
		-16.07 ± 1.85	

intermediate resonance contributions to real photon emission [91, 95, 96]. The systematic uncertainty assigned to the ρ–ω interference contribution accounts for the difference in $a_\mu^{\rm had,LO}$ between two phenomenological fits, where the mass and width of the ω resonance are either left free to vary or fixed to their world average values.

Some of the corrections in Table 5.1 are parametrisation dependent. We choose to take the final corrections from the Gounaris-Sakurai parametrisation and assign the full difference with respect to the KS results[6] as systematic error. The total correction for isospin breaking amounts to $(-16.07 \pm 1.85) \cdot 10^{-10}$ for $a_\mu^{\rm had,LO}[\pi\pi,\tau]$, where all systematic errors have been added in quadrature except for the GS and KS difference which has been added linearly. This correction is to be compared to the value $(-13.8 \pm 2.4) \cdot 10^{-10}$ obtained previously [64]. Since the FSR correction was previously included, but not counted in the IB corrections, the net change amounts to -6.9×10^{-10}, dominated by the electromagnetic decay correction.

The corresponding IB-corrected $a_\mu^{\rm had,LO}[\pi\pi,\tau]$ in the dominant $\pi^+\pi^-$ channel below 1.8 GeV is given in Table 5.2 for ALEPH, CLEO, OPAL, Belle, and for the combined mass spectrum from these experiments. The evaluation at energy below 0.36 GeV is obtained by fitting an (Chiral Perturbation Theory (ChPT) - inspired) expansion in s

$$F_\pi^{ChPT} \simeq 1 + \frac{1}{6} \left\langle r^2 \right\rangle_\pi s + c_\pi s^2 + O(s^3) \tag{5.8}$$

[6] We do not confirm the significant IB correction difference of the KS parametrisation on the $\rho - \omega$ interference with respect to the GS parametrisation observed in Ref. [88].

Table 5.2: The IB-corrected $a_\mu^{\rm had,LO}$ $[\pi\pi,\tau]$ ($\times 10^{-10}$) from the measured mass spectrum by ALEPH, CLEO, OPAL and Belle, and the combined spectrum using the corresponding branching fraction values. The results are shown separately in two different energy ranges. The first errors are due to the shapes of the mass spectra, which also include a small contribution of 0.11 from the τ mass and $|V_{ud}|$. The second errors are due to $\mathcal{B}_{\pi\pi^0}$ and $\mathcal{B}_e$, and the third errors from the isospin-breaking corrections, which are partially anti-correlated between the two energy ranges. The last line gives the world average branching fraction and also the evaluations of the combined spectra (which are not equivalent to the arithmetic averages of the individual evaluations – see text).

Experiment	$a_\mu^{\rm had,LO}[\pi\pi,\tau]$ (10^{-10})		$\mathcal{B}_{\pi\pi^0}$ (%)
	$2m_{\pi^\pm} - 0.36\,\text{GeV}$	$0.36 - 1.8\,\text{GeV}$	
ALEPH	$9.46 \pm 0.33_{\rm exp} \pm 0.05_{\mathcal{B}} \pm 0.07_{\rm IB}$	$499.19 \pm 5.20_{\rm exp} \pm 2.70_{\mathcal{B}} \pm 1.87_{\rm IB}$	$25.49 \pm 0.10_{\rm stat} \pm 0.09_{\rm syst}$
CLEO	$9.65 \pm 0.42_{\rm exp} \pm 0.17_{\mathcal{B}} \pm 0.07_{\rm IB}$	$504.51 \pm 5.36_{\rm exp} \pm 8.77_{\mathcal{B}} \pm 1.87_{\rm IB}$	$25.44 \pm 0.12_{\rm stat} \pm 0.42_{\rm syst}$
OPAL	$11.31 \pm 0.76_{\rm exp} \pm 0.15_{\mathcal{B}} \pm 0.07_{\rm IB}$	$515.56 \pm 9.98_{\rm exp} \pm 6.95_{\mathcal{B}} \pm 1.87_{\rm IB}$	$25.46 \pm 0.17_{\rm stat} \pm 0.29_{\rm syst}$
Belle	$9.74 \pm 0.28_{\rm exp} \pm 0.15_{\mathcal{B}} \pm 0.07_{\rm IB}$	$503.95 \pm 1.90_{\rm exp} \pm 7.84_{\mathcal{B}} \pm 1.87_{\rm IB}$	$25.24 \pm 0.01_{\rm stat} \pm 0.39_{\rm syst}$
Combined	$9.76 \pm 0.14_{\rm exp} \pm 0.04_{\mathcal{B}} \pm 0.07_{\rm IB}$	$505.46 \pm 1.97_{\rm exp} \pm 2.19_{\mathcal{B}} \pm 1.87_{\rm IB}$	25.42 ± 0.10

to the corresponding mass spectrum, following the method introduced in [64]. The comparison of the fit with the τ data at low energy is shown in Fig. 5.5 (left). Good agreement is observed. Indeed, a direct determination using data gives $(10.18 \pm 0.98_{\rm exp}) \times 10^{-10}$ in agreement with the fit-based result of $(9.76 \pm 0.14_{\rm exp}) \times 10^{-10}$, which is more precise because of the constraint $F(0) = 1$. The evaluation in the remaining energy region is performed directly from a finely (1 MeV) binned mass spectrum obtained using HVPTools by interpolating the original measurements with second order polynomials (conserving by means of renormalisation the integral in each bin before and after interpolation). The consistent propagation of all errors is ensured by generating large samples of pseudo Monte Carlo experiments. The uncertainty due to the interpolation procedure is estimated from a test with a known model to be at most 0.2×10^{-10}, which is negligible compared to the other systematic uncertainties. It is interesting to compare the first and second errors between the experiments. The first errors are mainly experimental, but also include small contributions from the uncertainties in τ mass and $|V_{ud}|$. The second errors are due to $\mathcal{B}_{\pi\pi^0}$, as measured by each experiment, and – to a lesser extent – to $\mathcal{B}_e$, for which a common value has been used everywhere. Belle has the most precise experimental precision on the measurement of the mass spectrum, whereas ALEPH dominates the $\mathcal{B}_{\pi\pi^0}$ measurement. The result $a_\mu^{\rm had,LO}[\pi\pi,\tau] = 515.2 \pm 2.0_{\rm exp} \pm 2.2_{\mathcal{B}} \pm 1.9_{\rm IB}$ (if not stated otherwise, this and the following numbers for a_μ are given in units of 10^{-10}) is obtained from the combined $\pi^-\pi^0$ mass spectrum of ALEPH, CLEO, OPAL and Belle using the world average $\mathcal{B}_{\pi\pi^0} = (25.42 \pm 0.10)\%$. This result is consistent with the direct average $516.1 \pm 1.8_{\rm exp} \pm 2.2_{\mathcal{B}} \pm 1.9_{\rm IB}$, obtained from the four individual a_μ calculations. The experimental error from the combined spectrum is slightly less precise as it accounts for the incompatibility between experiments in certain region of the mass spectrum.

The contributions to $a_\mu^{\rm had,LO}$ from the $\pi^+\pi^-2\pi^0$ and $2\pi^+2\pi^-$ channels below 1.8 GeV

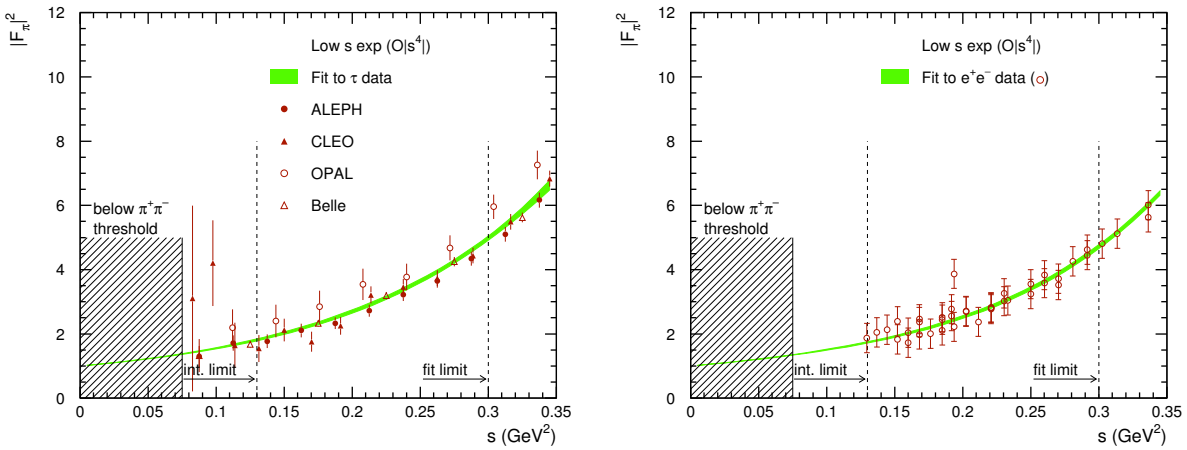

Figure 5.5: Fit of the pion form factor from $4m_\pi^2$ to $0.3\,\mathrm{GeV}^2$ using a third order expansion with the constraints $F(0) = 1$ and using the measured pion charge radius-squared from space-like data [97]. The result of the fit to the τ data (left) and to e^+e^- data (right) is integrated only up to $0.13\,\mathrm{GeV}^2$, beyond which we directly integrate over the data points.

are $21.4 \pm 1.3_{\mathrm{exp}} \pm 0.6_{\mathrm{IB}}$ and $12.3 \pm 1.0_{\mathrm{exp}} \pm 0.4_{\mathrm{IB}}$, respectively. This leads to the complete τ-based lowest order hadronic contribution

$$\begin{aligned} a_\mu^{\mathrm{had,LO}}[\tau] &= 705.3 \pm 3.9_{\mathrm{exp}} \pm 0.7_{\mathrm{rad}} \pm 0.7_{\mathrm{QCD}} \pm 2.1_{\mathrm{IB}}\,, \\ &= 705.3 \pm 4.5\,, \end{aligned} \tag{5.9}$$

where the second error is due to our treatment of (potentially) missing radiative corrections in old data included in the calculation of the dispersion integral [65], and the third error stems from the uncertainty in the perturbative evaluation of the inclusive hadronic cross section in the energy ranges 1.8–3.7 GeV and beyond 5 GeV. The central value decreases from previously 710.3, obtained using incomplete isospin corrections [67] and the superseded combined τ spectral function from ALEPH, CLEO and OPAL.

We also re-evaluate the lowest order hadronic contribution to the muon $g-2$ using e^+e^- data, updating our most recent preliminary result [67] with published CMD-2 [56] and KLOE [59] data. The results are given in Table 5.3. We have separated the evaluation into four distinct energy ranges. The most recent e^+e^- data from CMD2, SND and KLOE overlap in the range 0.63–0.958 GeV so that the corresponding $a_\mu^{\mathrm{had,LO}}[\pi\pi, e^+e^-]$ values can be compared. Agreement is observed between CMD2 and SND, while KLOE lies somewhat lower. To account for this, we consider two combinations of the e^+e^- data, distinguished by either including or excluding the KLOE data. The combination of the data is performed also using HVPTools, to transform the original e^+e^- bare cross sections and associated statistical and systematic covariance matrices into fine-grained energy bins (1 MeV), taking into account to our best knowledge the correlation within each experiment as well as between the experiments. The evaluation in the low energy range $2m_{\pi^\pm}$–0.36 GeV is performed as for the τ data by fitting an expansion in s to the combined e^+e^- data [64] (right-hand plot of Fig. 5.5), benefiting from additional space-like precision data [97]. The evaluations in the other three energy ranges are obtained by integrating directly the combined e^+e^- cross sections (*cf.* Table 5.3).

Table 5.3: Evaluated $a_\mu^{\rm had,LO}$ $[\pi\pi, e^+e^-]$ ($\times 10^{-10}$) contribution from the e^+e^- data, including and excluding KLOE data. The errors correspond to the experimental uncertainties with the statistical and systematical errors added in quadrature (but shown separately for individual experiments).

Energy range (GeV)	Experiment	$a_\mu^{\rm had,LO}[\pi\pi, e^+e^-]$ (10^{-10})	
		Incl. KLOE	Excl. KLOE
$2m_{\pi^\pm} - 0.36$	Combined e^+e^- (fit)	$9.71 \pm 0.12_{\rm exp}$	
$0.36 - 0.63$	Combined e^+e^-	$120.27 \pm 1.67_{\rm exp}$	$119.63 \pm 1.88_{\rm exp}$
$0.63 - 0.958$	CMD2 03	$361.82 \pm 2.43_{\rm stat} \pm 2.10_{\rm syst}$	
	CMD2 06	$360.17 \pm 1.75_{\rm stat} \pm 2.83_{\rm syst}$	
	SND 06	$360.68 \pm 1.38_{\rm stat} \pm 4.67_{\rm syst}$	
	KLOE 08	$356.82 \pm 0.39_{\rm stat} \pm 3.08_{\rm syst}$	
	Combined e^+e^-	$358.51 \pm 2.41_{\rm exp}$	$360.24 \pm 3.02_{\rm exp}$
$0.958 - 1.8$	Combined e^+e^-	$15.02 \pm 0.36_{\rm exp}$	$15.02 \pm 0.39_{\rm exp}$
Total	Combined e^+e^-	$503.51 \pm 3.47_{\rm exp}$	$504.60 \pm 4.33_{\rm exp}$

We find for the difference, $\delta a_\mu^{\rm had,LO}[\pi\pi]$, between the τ and e^+e^--based evaluations in the dominant $\pi^+\pi^-$ channel

$$\delta a_\mu^{\rm had,LO}[\pi\pi] = \begin{cases} 11.7 \pm 3.5_{ee} \pm 3.5_{\tau+\rm IB}\,, \\ 10.6 \pm 4.3_{ee} \pm 3.5_{\tau+\rm IB}\,, \end{cases} \tag{5.10}$$

where the upper (lower) value is for KLOE data included (excluded). The discrepancies amount to 2.4 and 1.9 times the overall errors, respectively.

Including the contributions from the other hadronic channels [67], we find for the total e^+e^--based lowest order hadronic evaluation

$$a_\mu^{\rm had,LO}[e^+e^-] = \begin{cases} 689.8 \pm 4.3_{\rm exp+rad} \pm 0.7_{\rm QCD}\,, \\ 690.9 \pm 5.2_{\rm exp+rad} \pm 0.7_{\rm QCD}\,, \end{cases}$$

with total errors of 4.4(5.2) when including (excluding) KLOE. Adding the other contributions [67] including the latest estimate of the light-by-light scattering (LBLS) contribution of 10.5 ± 2.6 [98], we obtain the Standard Model predictions (still in 10^{-10} units)

$$\begin{aligned} a_\mu^{\rm SM}[\tau] &= 11\,659\,193.2 \pm 4.5 \pm 2.6 \pm 0.2\,, \\ a_\mu^{\rm SM}[e^+e^-] &= \begin{cases} 11\,659\,177.7 \pm 4.4 \pm 2.6 \pm 0.2\,, \\ 11\,659\,178.8 \pm 5.2 \pm 2.6 \pm 0.2\,, \end{cases} \end{aligned}$$

where the first errors are due to the lowest order hadronic contributions, the second error includes higher hadronic orders, dominated by the uncertainty in the LBLS contribution, and the third error accounts for the uncertainties in the electromagnetic and weak contributions. The predictions deviate from the experimental average, $a_\mu^{\rm exp} = 11\,659\,208.9(5.4)(3.3)$ [99,100], by 15.7±8.2 (τ), 31.2±8.1 (e^+e^- with KLOE) and 30.1±8.6 (e^+e^- without KLOE), respectively.

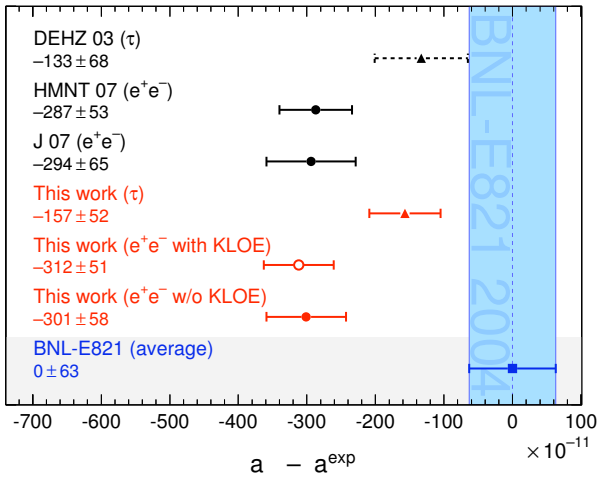

Figure 5.6: Compilation of recently published results for $a_\mu^{\rm SM}$ (in units of 10^{-11}), subtracted by the central value of the experimental average [99, 100]. The shaded band indicates the experimental error. The SM predictions are taken from: DEHZ 03 [65], HMNT 07 [101], J 07 [102,103], and the present τ- and e^+e^--based predictions using τ and e^+e^- spectral functions.

The lowest order hadronic contribution now reaches an uncertainty that is smaller than the measurement error and comparable in size with the LBLS uncertainty. Further progress in this field thus requires, apart from continuously improved low-energy e^+e^- cross section measurements, a more accurate muon $g-2$ measurement and LBLS calculation. A compilation of this and other recent $a_\mu^{\rm SM}$ predictions, compared to the experimental value, is shown in Fig. 5.6.

5.1.4 CVC prediction of $\mathcal{B}_{\pi\pi^0}$

The CVC relation (5.1) allows one to predict the branching fraction of a heavy lepton decaying into a G-parity even hadronic final state, X^-, via the vector current

$$\mathcal{B}_X^{\rm CVC} = \frac{3}{2}\frac{\mathcal{B}_e|V_{ud}|^2}{\pi\alpha^2 m_\tau^2}\int_{s_{\rm min}}^{m_\tau^2} ds\, s\, \sigma_{X^0}^I \left(1-\frac{s}{m_\tau^2}\right)^2\left(1+\frac{2s}{m_\tau^2}\right),$$

with $s_{\rm min}$ being the threshold of the invariant mass-squared of the final state X^0 in e^+e^- annihilation. This relation was tested ever since the discovery of the τ lepton. In the best known vector channel, the $\pi^-\pi^0$ final state, it has attained a precision of better than

Table 5.4: Contributions to $\mathcal{B}^{\rm CVC}_{\pi^-\pi^0}$ ($\times 10^{-2}$) from the isospin-breaking corrections discussed in Sec. 5.1.2. For those corrections shown in two separated columns, they correspond to the Gounaris-Sakurai and Kühn-Santamaria parametrisations, respectively.

Source	$\Delta\mathcal{B}^{\rm CVC}_{\pi^-\pi^0}$ (10^{-2})		
	GS model		KS model
$S_{\rm EW}$		$+0.57 \pm 0.01$	
$G_{\rm EM}$		-0.07 ± 0.17	
FSR		-0.19 ± 0.02	
ρ–ω interference	-0.01 ± 0.01		-0.02 ± 0.01
$m_{\pi^\pm} - m_{\pi^0}$ effect on σ		$+0.19$	
$m_{\pi^\pm} - m_{\pi^0}$ effect on Γ_ρ		-0.22	
$m_{\rho^\pm} - m_{\rho^0_{\rm bare}}$	$+0.08 \pm 0.08$		$+0.09 \pm 0.08$
$\pi\pi\gamma$, electrom. decays	$+0.34 \pm 0.03$		$+0.37 \pm 0.04$
Total	$+0.69 \pm 0.19$		$+0.72 \pm 0.19$
		$+0.69 \pm 0.22$	

1% [67], and a discrepancy between $\mathcal{B}^{\rm CVC}_{\pi^-\pi^0}$ and $\mathcal{B}_{\pi^-\pi^0}$ at a level of 4.5σ was observed.[7] CVC comparisons of τ branching fractions are of special interest because they are essentially insensitive to the shape of the τ spectral function, hence avoiding experimental difficulties, such as the mass dependence of the π^0 detection efficiency and feed-through, and biases from the unfolding of the raw mass distribution from acceptance and resolution effects.

Similar to $\Delta a_\mu^{\rm had,LO}[\pi\pi,\tau]$, we have evaluated the IB corrections to

$$\begin{aligned}\Delta\mathcal{B}^{\rm CVC}_{\pi^-\pi^0} &= \frac{3}{2}\frac{\mathcal{B}_e|V_{ud}|^2}{\pi\alpha^2 m_\tau^2}\int_{s_{\rm min}}^{m_\tau^2} ds\, s\, \sigma^0_{\pi^+\pi^-}(s) \\ &\quad\times \left(1-\frac{s}{m_\tau^2}\right)^2\left(1+\frac{2s}{m_\tau^2}\right)\left[\frac{S_{\rm EW}}{R_{\rm IB}}-1\right],\end{aligned} \tag{5.11}$$

where $s_{\rm min} = (m_{\pi^-} + m_{\pi^0})^2$. The results are summarised in Table 5.4. The corresponding $\mathcal{B}^{\rm CVC}_{\pi^-\pi^0}$ (Table 5.5) is $(24.78 \pm 0.17_{\rm exp} \pm 0.22_{\rm IB})\%$ and $(24.92 \pm 0.21_{\rm exp} \pm 0.22_{\rm IB})\%$, based on the combined e^+e^- data, including and excluding the KLOE data, respectively. The first error quoted corresponds to the experimental error and the second error due to uncertainties in the isospin-breaking corrections. It differs from the τ measurement by $(0.64 \pm 0.10_\tau \pm 0.28_{ee})\%$ and $(0.50 \pm 0.10_\tau \pm 0.30_{ee})\%$, respectively, which is still substantial,

[7] The use of the term standard deviation (σ) in this context requires caution because the results discussed in this section are mostly dominated by systematic uncertainties with questionable statistical properties.

Table 5.5: Evaluated $\mathcal{B}^{\rm CVC}_{\pi^-\pi^0}$ ($\times 10^{-2}$) from the e^+e^- data including and excluding KLOE data, respectively. The errors correspond to the experimental uncertainties with the statistical and systematical errors added in quadrature (but shown separately for individual experiments). The IB uncertainty of 0.22 is not explicitly quoted for the subcontributions.

Energy range (GeV)	Experiment	$\mathcal{B}^{\rm CVC}_{\pi^-\pi^0}$ (%)	
		Incl. KLOE	Excl. KLOE
$m_{\pi^-}+m_{\pi^0}-0.36$	Combined e^+e^- (fit)	$0.03 \pm 0.00_{\rm exp}$	
$0.36-0.63$	Combined e^+e^-	$1.96 \pm 0.03_{\rm exp}$	$1.94 \pm 0.03_{\rm exp}$
$0.63-0.958$	CMD2 03	$20.67 \pm 0.13_{\rm stat} \pm 0.12_{\rm syst}$	
	CMD2 06	$20.58 \pm 0.08_{\rm stat} \pm 0.16_{\rm syst}$	
	SND 06	$20.54 \pm 0.07_{\rm stat} \pm 0.27_{\rm syst}$	
	KLOE 08	$20.26 \pm 0.02_{\rm stat} \pm 0.17_{\rm syst}$	
	Combined e^+e^-	$20.40 \pm 0.14_{\rm exp}$	$20.56 \pm 0.17_{\rm exp}$
$0.958-m_\tau$	Combined e^+e^-	$2.39 \pm 0.06_{\rm exp}$	
Total	Combined e^+e^-	$24.78 \pm 0.17_{\rm exp} \pm 0.22_{\rm IB}$	$24.92 \pm 0.21_{\rm exp} \pm 0.22_{\rm IB}$

but less significant than the previous result [65, 67]. A graphical comparison between the IB-corrected $\mathcal{B}^{\rm CVC}_{\pi\pi^0}$ and the measured branching fractions $\tau^- \to \pi^-\pi^0\nu_\tau$ [63, 68, 146, 180] is shown in Fig. 5.7. The $\mathcal{B}^{\rm CVC}_{\pi\pi^0}$ results are obtained using the e^+e^- data from CMD2, SND and KLOE in 0.63–0.958 GeV and the combined e^+e^- data in the other energy regions.

5.1.5 Summary

In this section, we have revisited and updated the isospin-breaking corrections to τ data in the 2π mode, incorporating new ingredients in the long-distance radiative corrections and in the mass and width splittings of mesons that enter the pion form factors. We find that the τ and e^+e^- spectral functions from CMD-2 and SND are now marginally consistent, while a disagreement with the KLOE measurement remains. The corrected τ-based result for the Standard Model prediction of the muon $g-2$ is now 1.9 standard deviations lower than the direct measurement, coming closer to the e^+e^- value. Similarly, the prediction of the $\tau^- \to \pi^-\pi^0\nu_\tau$ branching fraction with e^+e^- annihilation data exhibits a reduced discrepancy with the τ measurement.

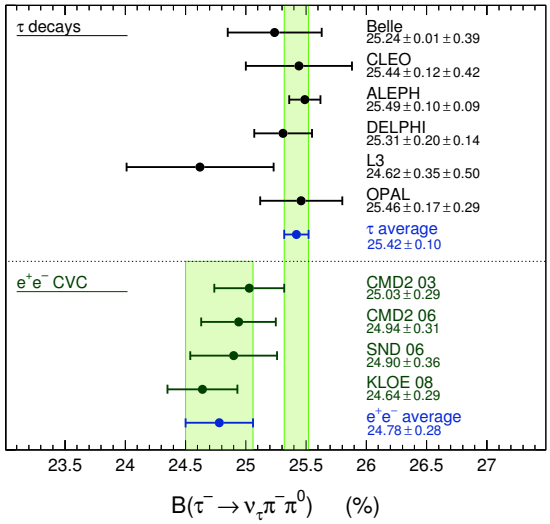

Figure 5.7: The measured branching fractions for $\tau^- \to \pi^-\pi^0\nu_\tau$ [63,68,71,72,146,180] compared to the predictions from the $e^+e^- \to \pi^+\pi^-$ spectral functions, applying the isospin-breaking corrections discussed in Sec. 5.1.2. For the e^+e^- results, we have used only the data from the indicated experiments in $0.63 - 0.958\,\text{GeV}$ and the combined e^+e^- data in the remaining energy domains below m_τ. The long and short vertical error bands correspond to the τ and e^+e^- averages of $(25.42 \pm 0.10)\%$ and $(24.78 \pm 0.28)\%$, respectively.

5.2 Comparison of the 2π Spectra from τ Decays and the BABAR ISR Measurement

It is interesting to compare the BABAR e^+e^- result to the $\tau \to \nu_\tau\pi\pi^0$ spectral function, corrected for IB effects as explained in the previous section. This is done in Fig. 5.8, for the ALEPH [180], Belle [68], CLEO [63], and OPAL [146] experiments, in a manner similar to the e^+e^- comparisons shown before. Here there is another uncertainty resulting from the IB theoretical corrections, corresponding roughly to a scale uncertainty of 0.3%. For this comparison the spectral functions are normalized by the $B_{\pi\pi} \equiv B(\tau \to \pi\pi^0\nu_\tau)$ value measured by each experiment, rather than using the world average as usually done. In this way the spectral functions are really independent. The error bars on the τ data points include all sources of uncertainty, statistical and systematic, $B_{\pi\pi}$ and IB corrections.

The comparison with ALEPH shows agreement up to the ρ peak and some slope above, keeping in mind that the ALEPH points are strongly correlated. Agreement is also observed within errors with the results of CLEO and Belle. Some systematics effects are observed in the comparison with the less precise OPAL data, but there also the correlations of the point by point uncertainties must be taken into account in the comparison. However, similar effects were observed in the comparison between OPAL and combined τ data (Fig. 5.2).

We conclude that the general agreement with data from τ decays is good, being even excellent when comparing with the most recent Belle results.

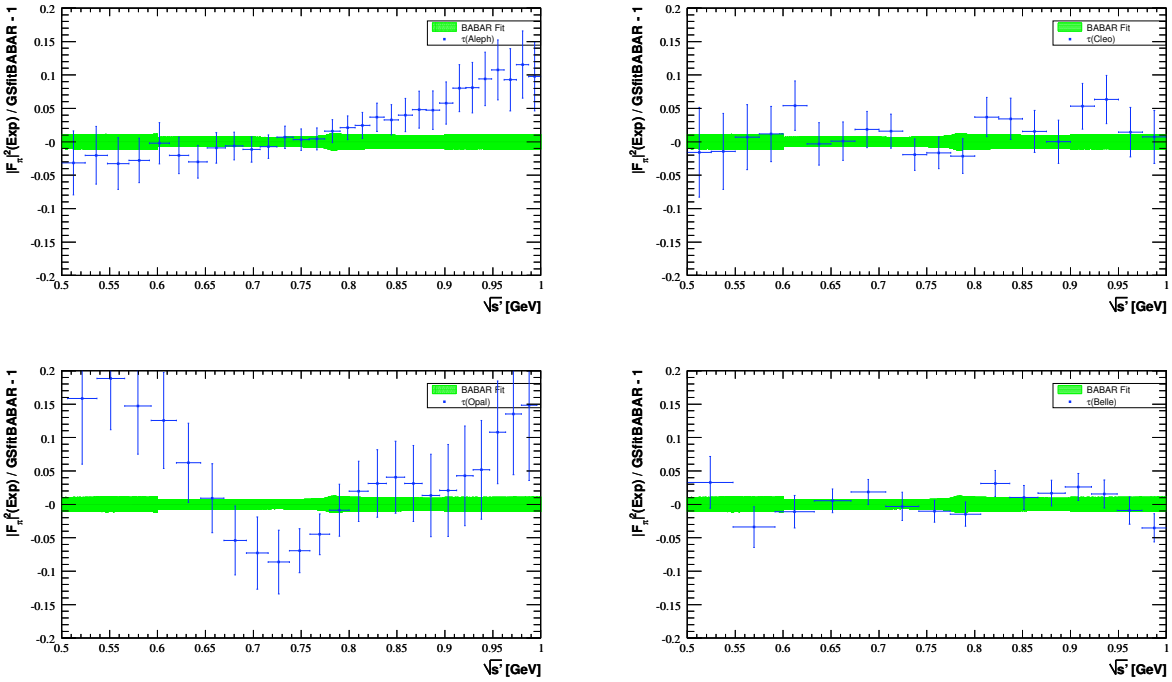

Figure 5.8: The relative difference of the form factor squared from the τ data of ALEPH (top left), CLEO (top right), OPAL (botton left) and Belle (bottom right), with respect to the $e^+e^- \to \pi^+\pi^-$ BABAR measurements (fit) in the 0.5-1 GeV mass region. Systematic and statistical uncertainties are included in the data points. The width of the BABAR band shows the propagation of statistical errors in the fit and the quoted systematic uncertainties, added quadratically.

5.3 The BABAR $\pi\pi$ Contribution to the Anomalous Muon Magnetic Moment

For the BABAR data, the integration 4.6 is carried out directly over the measured cross section bins. The statistical and systematic errors are computed using the corresponding covariance matrices described in Sections 3.2.1 and 3.2.2. When not specified, all results on $a_\mu^{\pi\pi(\gamma),LO}$ are given in units of 10^{-10}, with statistical and systematic errors in that order.

Several tests are performed.

- When the integral is done with the original 50-MeV ISR luminosity bins the result is $514.40 \pm 2.54 \pm 3.11$ in the range 0.3-1.8 GeV, while the value $513.54 \pm 2.22 \pm 3.11$ is obtained with the chosen sliding-bin method. The difference is consistent with the statistical fluctuations of the luminosity in the 50-MeV bins (Fig. 2.105) and the a_μ kernel weighting effect.

- In the 0.5-1.0 GeV mass range one can compare the 'ρ central' and the 'ρ tails' conditions. The main difference is the χ^2 cut, which affects the background level, the χ^2 efficiency, the mass resolution, hence the performance of the unfolding. For the range 0.5-1.0 GeV the result of the integration with the 'central' conditions is 445.94 10^{-10} in 2-MeV bins, and 446.56 10^{-10} in 10-MeV bins with the 'tails' conditions. Thus the effect of different resolution and efficiencies has little effect on the integral. The difference of 0.62 10^{-10} between the two analyses is consistent with their estimated uncommon systematic error and uncommon statistical error, giving an uncertainty on the integral of 1.8 10^{-10}.

The evaluation of the integral in the threshold region was made in previous estimates using a polynomial expansion in s' for the pion form factor, incorporating the constraint of the normalization of $F_\pi(0) = 1$ and the known slope in s' given by the quadratic charge radius of the pion. This procedure also compensated for the relatively poorer quality of data in this region. The BABAR continuous low-mass data permit a direct evaluation, consistent with the constrained method. The very small contribution ((0.55 ± 0.01) 10^{-10}) between the 2π threshold and 0.3 GeV is evaluated using the extrapolation of the constrained fit between 0.3-0.5 GeV.

The BABAR results are given in Table 5.6 in different mass ranges. The upper range (1.8 GeV) is chosen in accordance with previous evaluations in which the contribution of the higher energy region was computed using QCD. The contribution from threshold to 1.8 GeV is obtained for the first time from a single experiment:

$$a_\mu^{\pi\pi(\gamma),LO} \;=\; (514.09 \pm 2.22 \pm 3.11)\ 10^{-10}\ , \tag{5.12}$$

where the first error is statistical and the second systematic. The total uncertainty is 3.82, so that the precision of the measurement is 0.74%.

A direct comparison to the results from other experiments can only be made over a restricted mass range, between 0.630 and 0.958 GeV, where CMD-2, SND, and KLOE

Table 5.6: Evaluation of $a_\mu^{\pi\pi(\gamma),LO}$ using the BABAR data (in units of 10^{-10}) in different mass regions (see text for details). The first error is statistical and the second systematic.

$m_{\pi\pi}$ range (GeV)	$a_\mu^{\pi\pi(\gamma),LO}$ BABAR
0.28−0.30	$0.55 \pm 0.01 \pm 0.01$
0.30−0.50	$57.62 \pm 0.63 \pm 0.55$
0.50−1.00	$445.94 \pm 2.10 \pm 2.51$
1.00−1.80	$9.97 \pm 0.10 \pm 0.09$
0.28−1.80	$514.09 \pm 2.22 \pm 3.11$

,

Table 5.7: Evaluation of $a_\mu^{\pi\pi(\gamma),LO}$ from the dispersion integral between threshold and 1.8 GeV using the BABAR data (in units of 10^{-10}). Updated evaluations using published e^+e^- data [54], dominated by the CMD-2, SND, and KLOE results, and using the combined $\tau \to \pi\pi^0\nu_\tau$ spectral function [54] from ALEPH-Belle-CLEO-OPAL. Errors include statistical, systematic and IB corrections untertainties (for the τ result).

data	$a_\mu^{\pi\pi(\gamma),LO}$ $[0.28 - 1.8]$ GeV
BABAR	514.1 ± 3.8
previous e^+e^- combined	503.5 ± 3.5
τ combined	515.2 ± 3.5

data overlap (see table 5.3). The BABAR measurement for the same interval yields $365.2 \pm 1.9 \pm 1.9$ (± 2.7), where the first error is statistical and the second systematic (their quadratic sum is given in parentheses). It is seen that the BABAR result is the most precise, in addition from covering the full mass range. This direct, but partial, comparison, involving about 71% of the total 2π contribution, is shown in Fig. 5.9. The disagreement between KLOE and BABAR is in contrast with the overconsistency of CMD-2 and SND, but overall the picture is acceptable: $\chi^2 = 4.2/4\ DF$, ignoring the correlations between the two CMD-2 results, and also between CMD-2 and SND for radiative corrections. The corresponding value for the average of the τ data with updated IB corrections is $366.7 \pm 1.7 \pm 1.4_{IB}$ (± 2.2), in good agreement with the BABAR result and somewhat higher than the other e^+e^- results. It is important to note that the four inputs (CMD-2/SND, KLOE, BABAR, τ) have completely independent systematic uncertainties.

In Table 5.7 the BABAR result in the full mass range from threshold to 1.8 GeV is compared to the corresponding values taking the combined spectral functions using all previous e^+e^- experiments on one hand and τ results on the other hand, following the update in Sec. 5.1.

Including the BABAR results will reduce the observed 3.8σ discrepancy between the BNL measurement [99] of the muon magnetic anomaly and the Standard Model prediction

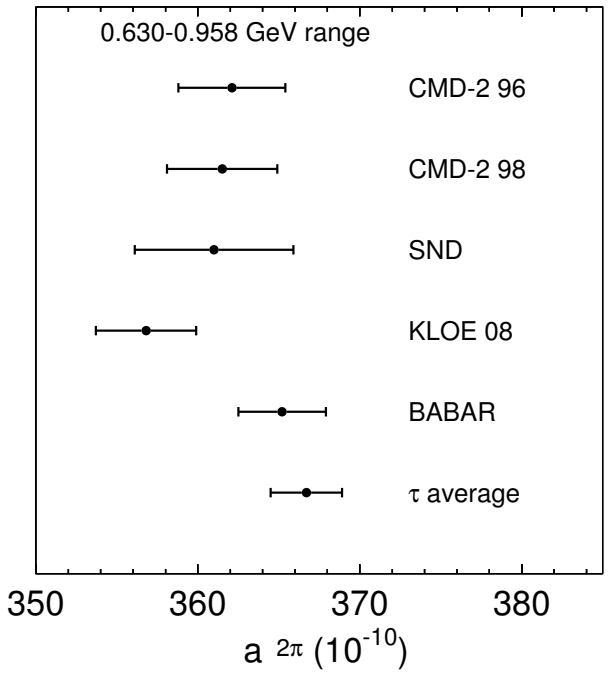

Figure 5.9: The LO hadronic VP 2π contributions to the muon magnetic anomaly, evaluated in the 0.630-0.958 GeV mass range where CMD-2, SND, and KLOE data overlap, are compared to the BABAR result and the average τ result from ALEPH, Belle, CLEO, and OPAL.

which was estimated in Sec. 5.1 using previous e^+e^- data. In fact the deviation decreases to $(18.0 \pm 8.6)\ 10^{-10}$ (2.1 σ), if only the BABAR result is used for the 2π contribution. Of course all available experimental information should be used, taking into account the internal discrepancies in the estimate of the final uncertainty. This will be studied into some detail in the next section.

5.4 Reevaluation of the hadronic contribution to the muon magnetic anomaly including $e^+e^- \to \pi^+\pi^-$ cross section data from BABAR

The discrepancy between the evaluations of $a_\mu^{\rm had,LO}$ using e^+e^- and respectively τ spectral functions decreased, after the inclusion of new τ data from the Belle experiment [68], published e^+e^- data from CMD2 [56] and KLOE [59] (superseding earlier data [58]), and a reevaluation of isospin-breaking corrections affecting the τ-based evaluation (Section 5.1).[8] In terms of $a_\mu^{\rm had,LO}$, the difference between the τ and e^+e^--based evaluations in the dominant $\pi^+\pi^-$ channel was found to be $11.7 \pm 3.5_{ee} \pm 3.5_{\tau+\rm IB}$ [54] (if not otherwise stated, this and all following a_μ numbers are given in units of 10^{-10}), where KLOE exhibits the strongest discrepancy with the τ data (without the KLOE data the discrepancy reduces from 2.4σ to 1.9σ). Another quantity for comparison, which is more sensitive to the higher-energy $\pi^+\pi^-$ spectrum, is the $\tau^- \to \pi^-\pi^0\nu$ branching fraction showing a difference between measurement and e^+e^- prediction of $(0.64 \pm 0.10_\tau \pm 0.28_{ee})\%$ [54].[9]

Recently, the BABAR Collaboration has published [60] a $\pi^+\pi^-(\gamma)$ spectral function measurement based on half a million selected $e^+e^- \to \pi^+\pi^-\gamma(\gamma)$ events, where the hard photon is dominantly radiated in the initial state (ISR). It benefits from a large cancellation of systematic effects in the ratio $\pi^+\pi^-\gamma(\gamma)$ to $\mu^+\mu^-\gamma(\gamma)$ employed for the measurement. In this section, we present a reevaluation of the lowest order hadronic contribution to a_μ including the new BABAR data. We deploy the new software package HVPTools, featuring a more accurate data interpolation, averaging and integration method, better systematic tests, and an improved statistical analysis based on the generation of large samples of pseudo experiments. The results presented here were first published in [61].

5.4.1 $e^+e^- \to \pi^+\pi^-$ cross section data

The contribution to $a_\mu^{\rm had,LO}$ coming from the light u, d, s quark states is evaluated using exclusive experimental cross section data up to an energy of 1.8 GeV, where resonances dominate, and perturbative QCD to predict the quark continuum beyond that energy. In this work we only reevaluate the contributions from the $e^+e^- \to \pi^+\pi^-$ and $\pi^+\pi^-2\pi^0$

[8] The total size of the isospin-breaking correction to $a_\mu^{\rm had,LO}$ has been estimated to $(-16.1 \pm 1.9) \cdot 10^{-10}$, which is dominated by the short-distance contribution of $(-12.2 \pm 0.2) \cdot 10^{-10}$ [54].

[9] A total isospin-breaking correction of $(+0.69 \pm 0.22)\%$ has been added to the e^+e^- prediction of the $\tau^- \to \pi^-\pi^0\nu$ branching fraction [54].

channels. For all the others we refer to Refs. [64, 65, 67].

A large number of $e^+e^- \to \pi^+\pi^-$ cross section measurements are available. Older measurements stem from OLYA [105,132], TOF [106], CMD [132], DM1 [107] and DM2 [108].[10] They are affected by an incomplete or undocumented application of radiative corrections. Equation (4.6) and the treatment of higher order hadronic contributions require initial state radiation as well as leptonic and hadronic VP contributions to be subtracted from the measured cross section data, while final state radiation should be included. Because of lack of documentation, the latter contribution of approximately 0.9% in the $\pi^+\pi^-$ channel has been added to the data, accompanied by a 100% systematic error [64]. Initial state radiation and leptonic VP effects are corrected by all experiments, however hadronic VP effects are not. They are strongly energy dependent, and in average amount to approximately 0.6%. We apply this correction accompanied by a 50% systematic error [64]. These FSR and hadronic VP systematic errors are treated as fully correlated between all measurements of one experiment, and also among different experiments.

More recent precision data, where all required radiative corrections have been applied by the experiments, stem from the CMD2 [56] and SND [57] experiments at the VEPP-2M collider (Novosibirsk, Russia). They achieve comparable statistical errors, and energy-dependent systematic uncertainties down to 0.8% and 1.3%, respectively.

These measurements have been complemented by results from KLOE [59] at DAΦNE (Frascati, Italy) running at the ϕ resonance centre-of-mass energy. KLOE applied for the first time a hard-photon ISR technique to precisely determine the $\pi^+\pi^-$ cross section between 0.592 and 0.975 GeV. The cross section data are obtained from a binned distribution, corrected for detector resolution and acceptance effects. The analysed data sample corresponds to 240 pb^{-1} integrated luminosity providing a 0.2% relative statistical error on the $\pi^+\pi^-$ contribution to $a_\mu^{\rm had,LO}$. KLOE does not normalise the $\pi^+\pi^-\gamma$ cross section to $e^+e^- \to \mu^+\mu^-\gamma$ so that the ISR radiator function must be taken from Monte Carlo simulation (*cf.* [110] and references therein). The systematic error assigned to this correction varies between 0.5% and 0.9% (closer to the ϕ peak). The total assigned systematic error lies between 0.8% and 1.2%.

In a recent publication [60] the BABAR Collaboration reported measurements of the processes $e^+e^- \to \pi^+\pi^-(\gamma), \mu^+\mu^-(\gamma)$ using the ISR method at 10.6 GeV centre-of-mass energy. The detection of the hard ISR photon allows BABAR to cover a large energy range from threshold up to 3 GeV for the two processes. The $\pi^+\pi^-(\gamma)$ cross section is obtained from the $\pi^+\pi^-\gamma(\gamma)$ to $\mu^+\mu^-\gamma(\gamma)$ ratio, so that the ISR radiation function cancels, as well as additional ISR radiative effects. Since FSR photons are also detected, there is no additional uncertainty from radiative corrections at NLO level. Experimental systematic uncertainties are kept to 0.5% in the ρ peak region (0.6–0.9 GeV), increasing to 1% outside.

[10] We do not use the data from NA7 [109].

5.4.2 Combining cross section data

The requirements for averaging and integrating cross section data are: (*i*) properly propagate all the uncertainties in the data to the final integral error, (*ii*) minimise biases, *i.e.*, reproduce the true integral as closely as possible in average and measure the remaining systematic error, and (*iii*) optimise the integral error after averaging while respecting the two previous requirements. The first item practically requires the use of pseudo-Monte Carlo (MC) simulation, which needs to be a faithful representation of the measurement ensemble and to contain the full data treatment chain (interpolation, averaging, integration). The second item requires a flexible data interpolation method. The trapezoidal rule is not sufficient, as shown below, and a (local) second order polynomial interpolation provides a better description of the spectrum shape. A realistic truth model is used to test the accuracy of the integral computation with pseudo-MC experiments. Finally, the third item requires optimal data averaging taking into account all known correlations to minimise the spread in the integral measured from the pseudo-MC sample.

The combination and integration of the $e^+e^- \to \pi^+\pi^-$ cross section data is performed using the newly developed software package HVPTools [69].[11] It transforms the bare cross section data and associated statistical and systematic covariance matrices into fine-grained energy bins, taking into account to our best knowledge the correlations within each experiment as well as between the experiments (such as uncertainties in radiative corrections). The covariance matrices are obtained by assuming common systematic error sources to be fully correlated. To these matrices are added statistical covariances, present for example in binned measurements as provided by KLOE, BABAR or the τ data, which are subject to bin-to-bin migration that has been unfolded by the experiments, thus introducing correlations.

The interpolation between adjacent measurements of a given experiment uses second order polynomials. This is an improvement with respect to the previously applied trapezoidal rule, corresponding to a linear interpolation, which leads to systematic biases in the integral (see below, and also Fig. 5.10). In the case of binned data, the interpolation function within a bin is renormalised to keep the integral in that bin invariant after the interpolation. This may lead to small discontinuities in the interpolation function across bin boundaries. The final interpolation function per experiment within its applicable energy domain is discretised into small (1 MeV) bins for the purpose of averaging and numerical integration.

The averaging of the interpolated measurements from different experiments contributing to a given energy bin is the most delicate step in the analysis chain. Correlations between measurements and experiments must be taken into account. Moreover, the ex-

[11] HVPTools is written in object-oriented C++ and relies on ROOT functionality [111]. The cross section database is provided in XML format and can be made available to users – please contact the authors. The systematic errors are introduced component by component as an algebraic function of mass or as a numerical value for each data point (or bin). Systematic errors belonging to the same identifier (name) are taken to be fully correlated throughout all measurements affected. So far, HVPTools has been employed for the numerical evaluation of the most important $\pi^+\pi^-$ (and $\pi^+\pi^-2\pi^0$) parts of the dispersion integral (4.6), as well as for combining the $\pi\pi^0$ mass spectra from τ decays.

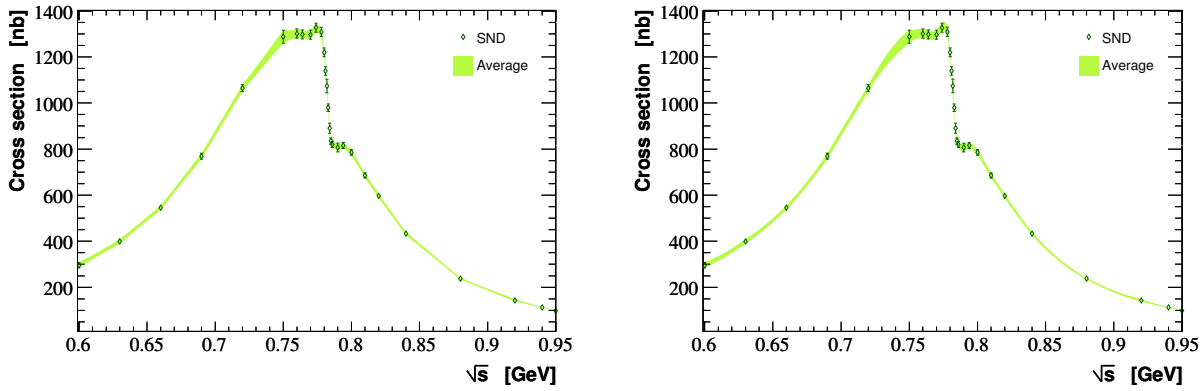

Figure 5.10: Linear (left) and quadratic (right) interpolation of SND data points for the 2π channel.

periments have different measurement densities or bin widths within a given energy interval and one must avoid that missing information in case of a lower measurement density is substituted by extrapolated information from the polynomial interpolation. To derive proper *averaging weights* given to each experiment, wider *averaging regions*[12] are defined to ensure that all locally available experiments contribute to the averaging region, and that in case of binned measurements (KLOE, BABAR, τ data) at least one full bin is contained in it. The averaging regions are used to compute weights for each experiment, which are applied in the bin-wise average of the original finely binned interpolation functions.

The averaging weights for each experiment are computed as follows:

1. pseudo-MC generation fluctuates the data points (or bins) along the original measurements taking into account all known correlations; the polynomial interpolation is redone for each generated pseudo MC;

2. the averaging regions are filled for each experiment and each pseudo-MC generation and interpolated with second order polynomials;

3. small (1 MeV) bins are filled for each experiment, in the energy intervals covered by that experiment, using the interpolation of the averaging regions;

4. in each small bin a correlation matrix between the experiments is computed from which the averaging weights are obtained by χ^2 minimisation.

The bin-wise average between experiments is computed as follows:

1. pseudo-MC generation fluctuates the data points (or bins) along the original measurements taking into account all known correlations; the polynomial interpolation is redone for each generated MC;

[12]For example, when averaging two binned measurements with unequal bin widths, a useful averaging region would be defined by the experiment with the larger bin width, and the bins of the other experiments would be statistically merged before computing the averaging weights.

2. for each generated pseudo-MC, small (1 MeV) bins are filled for each experiment, in the energy intervals covered by that experiment, using the polynomial interpolation;

3. the average and its error are computed in each small bin using the weights previously obtained;

4. the covariance matrix among the experiments is computed in each small bin;

5. χ^2 rescaling corrections are computed for each bin.

If the χ^2 value of a bin-wise average exceeds the number of degrees of freedom ($n_{\rm dof}$), the error in this averaged bin is rescaled by $\sqrt{\chi^2/n_{\rm dof}}$ to account for inconsistencies (*cf.* Fig. 5.11). Such inconsistencies frequently occur because most experiments are dominated by systematic uncertainties, which are difficult to estimate.

The consistent propagation of all errors into the evaluation of $a_\mu^{\rm had,LO}$ is ensured by generating large samples of pseudo experiments, representing the full list of available measurements and taking into account all known correlations. With this method, it is straightforward to identify the various contributions to the total untertainty on the result. For each generated set of pseudo measurements, the identical interpolation and averaging treatment leading to the computation of Eq. (4.6) as for real data is performed, hence resulting in a probability density distribution for $a_\mu^{\rm had,LO}$ ($\pi^+\pi^-$), the mean and RMS of which define the 1σ allowed interval (and which – by construction – has a proper pull behaviour). The procedure yielding the weights of the experiments can be optimised with respect to the resulting error on $a_\mu^{\rm had,LO}$, exploiting the freedom left for the choice of the size of the averaging regions.

We have tested the fidelity of the full analysis chain (polynomial interpolation, averaging, integration) by using as truth representation a Gounaris-Sakurai [86] vector-meson resonance model faithfully describing the $\pi^+\pi^-$ data. The central values for each of the available measurements are shifted to agree with the Breit-Wigner model, leaving their statistical and systematic errors unchanged. The so created set of measurements is then analysed akin to the original data sets. The difference between true and estimated $a_\mu^{\rm had,LO}$ values is a measure for the systematic uncertainty due to the data treatment. We find negligible bias below 0.1 (remember the 10^{-10} unit), increasing to 0.5 (1.2 without the high-density BABAR data) when using the trapezoidal rule for interpolation instead of second order polynomials.

The individual $e^+e^- \to \pi^+\pi^-$ cross section measurements (dots) and their average (shaded/green band) are plotted in Fig. 5.12. The error bars contain statistical and systematic errors. For better comparison we also plot in Fig. 5.13 the relative differences between BABAR, KLOE, CMD2, SND, and the average. Fair agreement is observed, though with a tendency to larger (smaller) cross sections above $\sim$0.8 GeV for BABAR (KLOE). These inconsistencies (among others) lead to the error rescaling shown versus $\sqrt{s}$ in Fig. 5.11.

The left hand plot of Fig. 5.14 shows the weights versus $\sqrt{s}$ the different experiments carry in the average. BABAR and KLOE dominate over the entire energy range. Owing

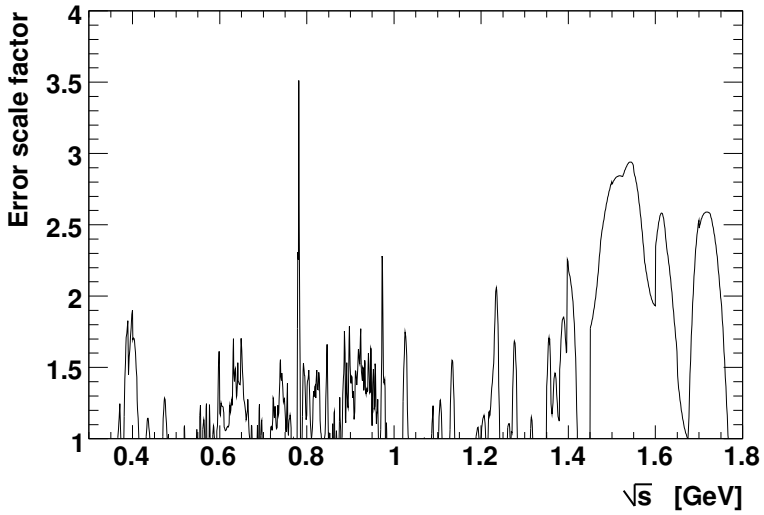

Figure 5.11: Rescaling factor accounting for inconsistencies among experiments versus $\sqrt{s}$ (see text). The peak around 0.4 GeV is introduced by a discrepancy between CMD2 and TOF measurements versus BABAR. The peaks around 0.65 and 0.74 GeV are introduced by outlier from CMD. The sharp peak at 0.78 GeV is due to local discrepancies along the ρ–ω interference. The bump between 0.85 and 0.95 GeV is due to a discrepancy between KLOE and BABAR. Finally, between 1.45 and 1.65 GeV measurements from MEA and DM2 significantly exceed the BABAR cross sections.

to the sharp radiator function, the available statistics for KLOE increases towards the ϕ mass, hence outperforming BABAR above $\sim$0.8 GeV. For example, at 0.9 GeV KLOE data have statistical errors of 0.5%, which is twice smaller than for BABAR (renormalising BABAR to the 2.75 times larger KLOE bins at that energy). Conversely, at 0.6 GeV the comparison reads 1.2% (KLOE) versus 0.5% (BABAR, again given in KLOE bins which are about 4.2 times larger than BABAR at that energy). The experiments labelled "other exp" in the figure correspond to older data with incomplete radiative corrections. Their weights are small throughout the entire energy domain.

Figure 5.14 (right) shows versus $\sqrt{s}$ the combined $e^+e^- \to \pi^+\pi^-$ cross section multiplied by the kernel function $K(s)$ occurring in the dispersion integral (4.6). The kernel strongly emphasises the low-energy spectrum. The dashed (red) curve belonging to the right axis in the plot gives the corresponding error contribution (diagonal errors only, statistical and systematic errors have been added in quadrature). The peaks are introduced by the error rescaling and indicate inconsistencies between the measurements. The uncertainty in the integral is dominated by the measurements below 0.8 GeV.

5.4.3 Results

A compilation of results for $a_\mu^{\rm had,LO}[\pi\pi]$ for the various sets of experiments and energy regions is given in Table 5.8. The comparison with our previous result [54], $a_\mu^{\rm had,LO}[\pi\pi] = 503.5 \pm 3.5_{\rm tot}$, shows that the inclusion of the new BABAR data significantly increases the central value of the integral, without however providing a large error reduction. This

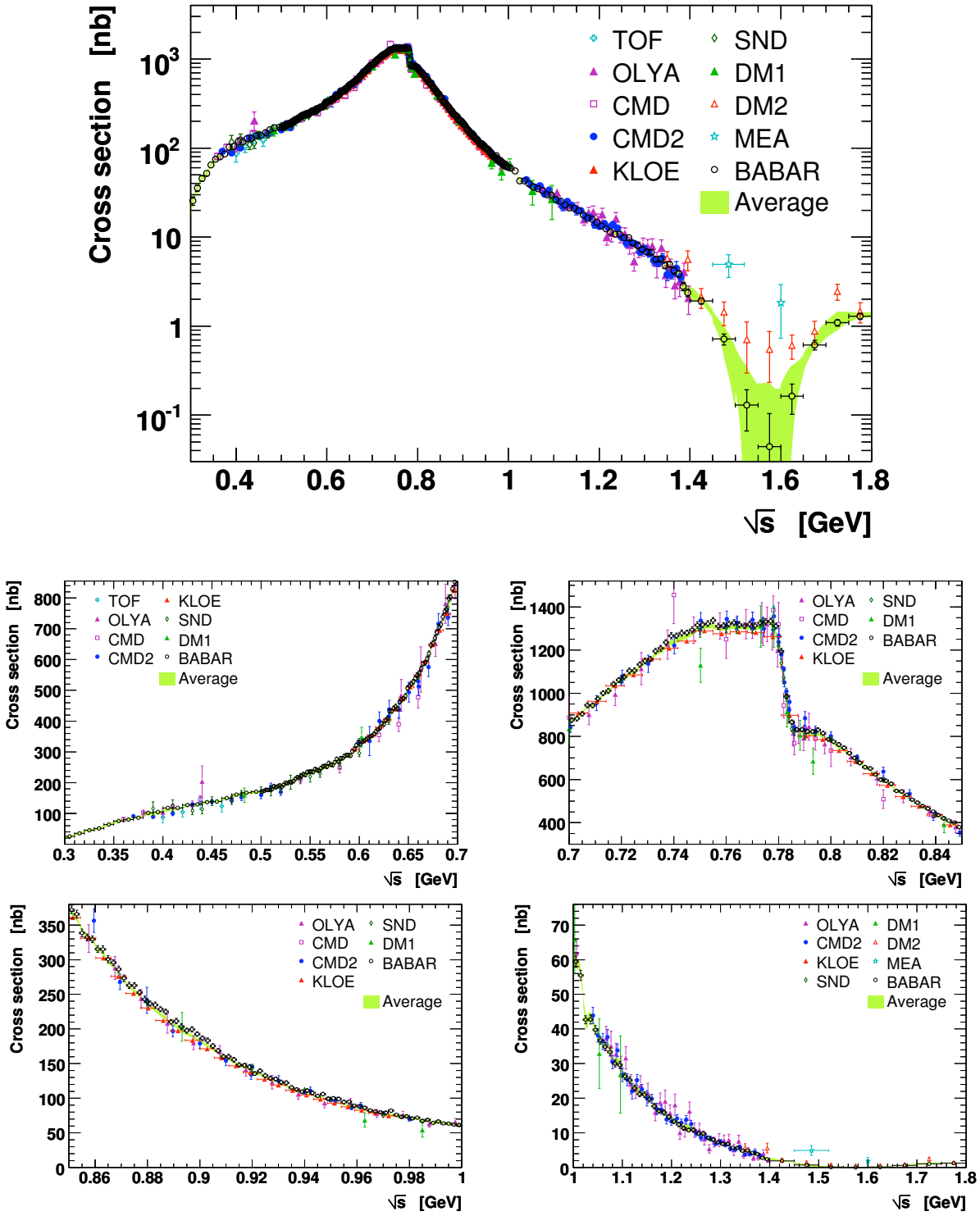

Figure 5.12: Cross section for $e^+e^- \to \pi^+\pi^-$ annihilation measured by the different experiments for the entire energy range (top), and zoomed energy intervals (all other plots). The errors bars contain both statistical and systematic errors, added in quadrature. The shaded (green) band represents the average of all the measurements obtained by HVPTools, which is used for the numerical integration following the procedure discussed in Sec. 5.4.2.

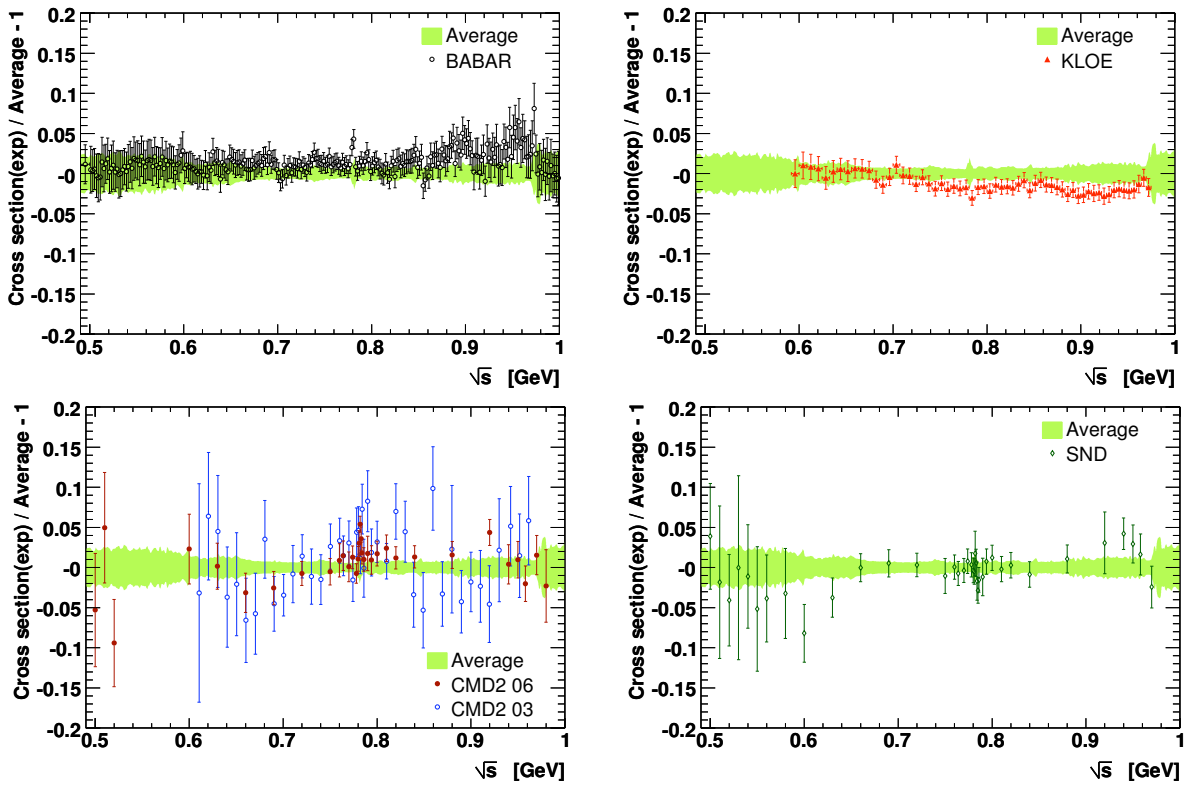

Figure 5.13: Relative cross section comparison between individual experiments (symbols) and the HVPTools average (shaded band) computed from all measurements considered. Shown are BABAR (top left), KLOE (top right), CMD2 (bottom left) and SND (bottom right).

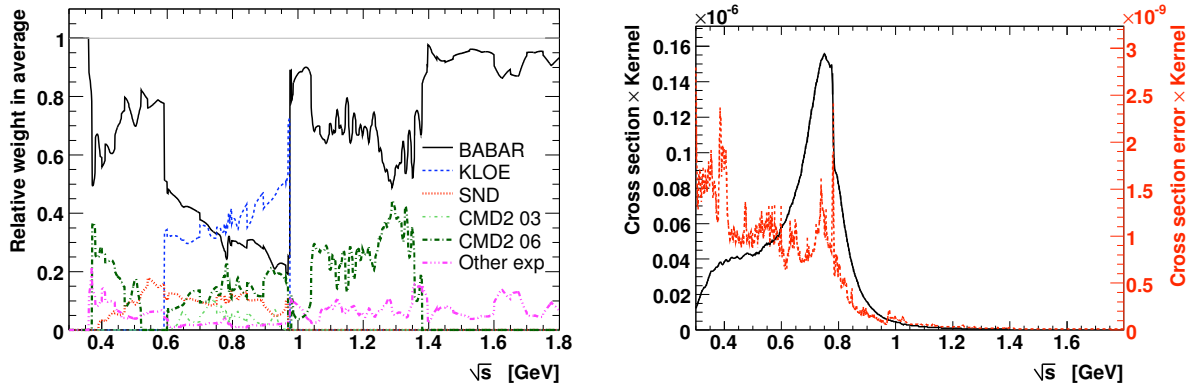

Figure 5.14: Left: relative averaging weights per experiment versus $\sqrt{s}$. Right: contribution to the dispersion integral (4.6) for the combined e^+e^- data obtained by multiplying the $\pi^+\pi^-$ cross section by the kernel function $K(s)$ (solid line). The dashed (red) curve belonging to the right axis shows the corresponding error contribution, where statistical and systematic errors have been added in quadrature. Note that the information conveyed by this curve is incomplete because only diagonal errors are shown, disregarding correlations between the cross section measurements which have significant influence on the integral error.

Table 5.8: Evaluated $a_\mu^{\rm had,LO}[\pi\pi]$ contributions from the e^+e^- data for different energy intervals and experiments. Where two errors are given, the first is statistical and the second systematic. We also recall the τ-based result combining all available τ data. The combined error has been rescaled to account for the inconsistency between the two evaluations.

Energy range (GeV)	Experiment	$a_\mu^{\rm had,LO}[\pi\pi]$ (10^{-10})
$2m_{\pi^\pm} - 0.3$	Combined e^+e^- (fit)	0.55 ± 0.01
$0.30 - 0.63$	Combined e^+e^-	$132.6 \pm 0.8 \pm 1.0$ $(1.3_{\rm tot})$
$0.63 - 0.958$	CMD2 03	$361.8 \pm 2.4 \pm 2.1$ $(3.2_{\rm tot})$
	CMD2 06	$360.2 \pm 1.8 \pm 2.8$ $(3.3_{\rm tot})$
	SND 06	$360.7 \pm 1.4 \pm 4.7$ $(4.9_{\rm tot})$
	KLOE 08	$356.8 \pm 0.4 \pm 3.1$ $(3.1_{\rm tot})$
	BABAR 09	$365.2 \pm 1.9 \pm 1.9$ $(2.7_{\rm tot})$
	Combined e^+e^-	$360.8 \pm 0.9 \pm 1.8$ $(2.0_{\rm tot})$
$0.958 - 1.8$	Combined e^+e^-	$14.4 \pm 0.1 \pm 0.1$ $(0.2_{\rm tot})$
Total	Combined e^+e^-	$508.4 \pm 1.3 \pm 2.6$ $(2.9_{\rm tot})$
Total	Combined τ	$515.2 \pm 2.0_{\rm exp} \pm 2.2_{\mathcal{B}} \pm 1.9_{\rm IB}$ $(3.5_{\rm tot})$

is due to the incompatibility between mainly BABAR and KLOE, causing an increase of the combined error. In the energy interval between 0.63 and 0.958 GeV, the discrepancy between the $a_\mu^{\rm had,LO}[\pi\pi]$ evaluations from KLOE and BABAR amounts to 2.0σ. BABAR is the only experiment covering the entire energy region between $2m_\pi$ and 1.8 GeV. Using only the BABAR data to evaluate $a_\mu^{\rm had,LO}[\pi\pi]$ one finds [60] $514.1 \pm 2.2_{\rm stat} \pm 3.1_{\rm syst}$.

Also given in Table 5.8 is the combined τ-based result from Ref. [54]. The difference between the τ and e^+e^--based evaluations of $a_\mu^{\rm had,LO}[\pi\pi]$ now reads $6.8 \pm 3.5_{\tau+\rm IB} \pm 2.9_{ee}$, thus reducing to 1.5σ compared to 2.4σ without BABAR [54] (the BABAR-only result is in excellent agreement with the τ data).[13] A comparison between the combined e^+e^- and τ two-pion cross sections relative to the e^+e^- result is shown in Fig. 5.15. Significant local discrepancies arise in particular above the ρ peak.

We also reevaluate the $e^+e^- \to \pi^+\pi^-2\pi^0$ contribution to $a_\mu^{\rm had,LO}$. The CMD2 data used previously [112] have been superseded by modified or more recent, but yet unpublished data [113], recovering agreement with the published SND cross sections [114]. Since the new data are unavailable, we discard the obsolete CMD2 data from the $\pi^+\pi^-2\pi^0$ average, finding $a_\mu^{\rm had,LO}[\pi\pi2\pi^0] = 17.6 \pm 0.4_{\rm stat} \pm 1.7_{\rm syst}$ (compared to $17.0 \pm 0.4_{\rm stat} \pm 1.6_{\rm syst}$ when including the obsolete CMD2 data). The corresponding cross section measurements and

[13] Combining the e^+e^- and τ-based evaluations would lead to an error rescaling by a factor of 1.5 to account for the inconsistency in the integrated data. This would approximately cancel the expected precision gain from the combination.

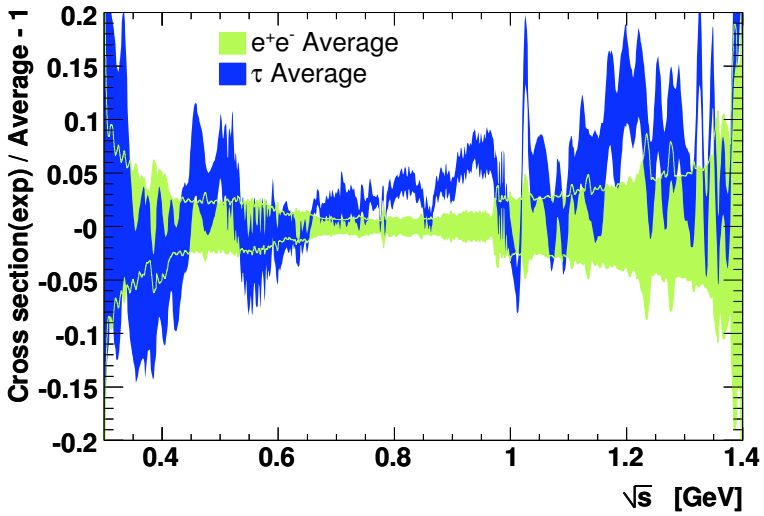

Figure 5.15: Relative comparison between the combined τ (dark shaded) and e^+e^- spectral functions (light shaded), normalised to the e^+e^- result. The apparently oscillating structure around 0.5 GeV is due to two Belle measurements fluctuating to large cross section values. Clearly visible is the interference due to ρ–ϕ mixing around 1 GeV, which is not included in the isospin-breaking corrections applied to the τ data. It is also visible in the upper, and lower right hand plots of Fig. 5.12. The deviation between 0.8 and 0.95 GeV is due to the discrepancy between τ and KLOE data, which dominate in this region (cf. Fig. 5.14 left). Comparing the τ data with the combined e^+e^- data instead of a fit to a single experiment CMD-2 limited to 1 GeV as it was done for Fig. 4 in Ref. [103] and Fig. 28 in Ref. [104], we observe a reduced discrepancy, in particular between 1.0GeV and 1.4GeV. We therefore disagree with the conclusion reached in these references, where the difference goes up to a factor 4, and is even in the opposite direction with respect to the one we observe.

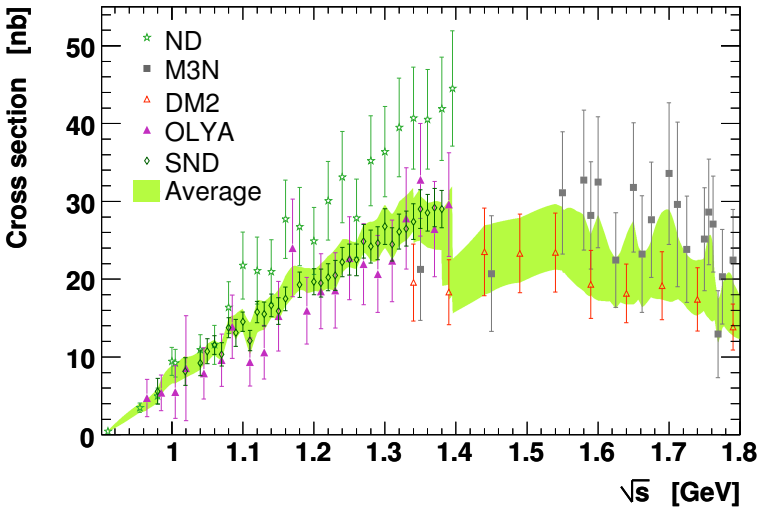

Figure 5.16: Cross section measurements $e^+e^- \to \pi^+\pi^-2\pi^0$ used in the calculation of $a_\mu^{\rm had,LO}[\pi\pi2\pi^0]$. The shaded band depicts the HVPTools interpolated average within 1σ errors. The individual measurements are referenced in [64].

HVPTools average are shown in Fig. 5.16.

Adding to the e^+e^--based $a_\mu^{\rm had,LO}[\pi\pi]$ and $a_\mu^{\rm had,LO}[\pi\pi2\pi^0]$ results the remaining exclusive multi-hadron channels as well as perturbative QCD [67], we find for the complete lowest order hadronic term

$$a_\mu^{\rm had,LO}[e^+e^-] = 695.5 \pm 4.0_{\rm exp} \pm 0.7_{\rm QCD}\ (4.1_{\rm tot})\,.$$

It is noticeable that the error from the $\pi^+\pi^-$ channel now equals the one from all other contributions to $a_\mu^{\rm had,LO}$.

Adding further the contributions from higher order hadronic loops, $-9.79 \pm 0.08_{\rm exp} \pm 0.03_{\rm rad}$ [101], hadronic light-by-light scattering (LBLS), 10.5 ± 2.6 [98], as well as QED, $11\,658\,471.809 \pm 0.015$ [115] (see also [100] and references therein), and electroweak effects, $15.4 \pm 0.1_{\rm had} \pm 0.2_{\rm Higgs}$ [116, 117], we obtain the SM prediction (still in 10^{-10} units)

$$a_\mu^{\rm SM}[e^+e^-] \;=\; 11\,659\,183.4 \pm 4.1 \pm 2.6 \pm 0.2\ (4.9_{\rm tot})\,,$$

where the errors have been split into lowest and higher order hadronic, and other contributions, respectively. The $a_\mu^{\rm SM}[e^+e^-]$ value deviates from the experimental average, $a_\mu^{\rm exp} = 11\,659\,208.9 \pm 5.4 \pm 3.3$ [99, 100], by 25.5 ± 8.0 (3.2σ).

A compilation of recent SM predictions for a_μ compared with the experimental result is given in Fig. 5.17. The BABAR results are not yet contained in evaluations preceding the present one. The result by HMNT [101] contains older KLOE data [58], which have been superseded by more recent results [59], leading to a slightly larger value for $a_\mu^{\rm had,LO}$.

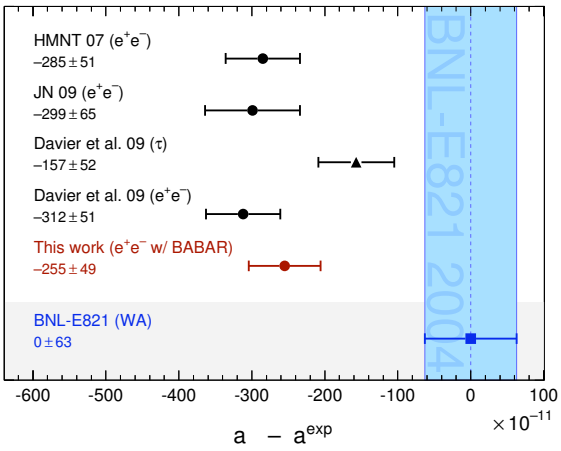

Figure 5.17: Compilation of recent results for $a_\mu^{\rm SM}$, subtracted by the central value of the experimental average [99]. The shaded vertical band indicates the experimental error. The SM predictions are taken from: HMNT 07 [101], JN 09 [104], Davier *et al.* 09 [54] (τ-based and e^+e^- including KLOE), and the e^+e^--based value from this work.

5.4.4 Work in progress: other than 2π hadronic contributions to the anomalous magnetic moment of the muon

The KK channel

The bare KK cross section obtained in the analysis described in Chapter 2 can be used to compute the $g-2$ dispersion integral. The contribution of the KK mode to the theoretical prediction of the anomalous magnetic moment of the muon is:

$$a_\mu^{KK,\ LO} = (23.03 \pm 0.13\ (\text{stat}) \pm 0.17\ (\text{syst}))\ \ 10^{-10}, \tag{5.13}$$

for the energy interval between the threshold and 1.8 GeV. The achieved precision is $9.3\ 10^{-3}$, the total error being slightly dominated by systematics. This is the most precise result for the KK channel, and the only one covering the full energy range of interest.

The quoted result is dominated by the ϕ region. Indeed, we get a contribution of $(19.57 \pm 0.13\ (\text{stat}) \pm 0.13\ (\text{syst}))\ \ 10^{-10}$, when integrating up to 1.1 GeV. The contribution up to 1.06 GeV is $(18.71 \pm 0.12\ (\text{stat}) \pm 0.12\ (\text{syst}))\ \ 10^{-10}$.

The last compilation of the various data for this channel was done in Ref. [64], and the average presented therein is dominated by SND [39] with a precision of about 7.1 %. Our result is much more precise, and the central value is about one unit larger than the previous average. Hence we expect the discrepancy between the SM prediction and the experimental measurement to be reduced, once the new BABAR data will be included in the average for this channel. Since the last compilation was performed, new data from CMD2 [38] became available. Their uncertainty is dominated by systematics, accounting for about 2.2 %. A value for the contribution to a_μ is quoted in that paper, but our preliminary studies using their published cross section lead to a significantly larger value.

Further results are expected from BABAR for the channel $e^+e^- \to \pi^+\pi^-2\pi^0$. They should help in the understanding of the present difference between τ and e^+e^- results for that channel.

The channels $K\bar{K}\pi\pi$ with a K_S will also be measured by BABAR. The contribution to a_μ coming from these channels was previously evaluated using isospin relations [64], accounting for $(2.2 \pm 1.0)\ 10^{-10}$.

5.4.5 Summary

We have reevaluated the lowest order hadronic contribution to the muon magnetic anomaly in the dominant $\pi^+\pi^-$ channel, using new precision data published by the BABAR Collaboration. After combination with the other e^+e^- data a 1.5σ difference with the τ data remains for the dominant $\pi^+\pi^-$ contribution. For the full e^+e^--based Standard Model prediction, including also a reevaluated $\pi^+\pi^-2\pi^0$ contribution, we find a deviation of 3.2σ from experiment (reduced from 3.7σ without BABAR). The deviation reduces to 2.9σ when excluding KLOE data, and further decreases to 2.4σ when using only the BABAR data in the $\pi^+\pi^-$ channel. As a reminder, the τ-based result deviates by 1.9σ from the Standard Model.

5.5 Conclusions Concerning $g-2$

The present situation for the evaluation of $a_\mu^{\rm had,LO}[\pi\pi]$ is improved compared to that of recent years, as more input data from quite different experimental facilities and conditions have become available (e^+e^- energy scan, e^+e^- ISR from low and high energies, τ decays) and isospin-breaking corrections for τ spectra have been improved. Our attitude has been to combine all the data and include in the uncertainty the effects from differences in the spectra. At the moment the ideal accuracy cannot be reached as a consequence of the existing discrepancies due to uncorrected or unaccounted systematic effects in the data. A critical look must be given to the different analyses in order to identify their weak points and to improve on them or to assign larger systematic errors.

It is thereby not sufficient to concentrate on improving the $\pi^+\pi^-$ channel alone. Problems also persist in the $\pi^+\pi^-2\pi^0$ mode, where the τ and e^+e^--based evaluations differ by $(3.8 \pm 2.2) \cdot 10^{-10}$, but also the e^+e^- data among themselves exhibit discrepancies. Fortunately, new precision data from BABAR should soon help to clarify the situation in that channel.

The observed difference between the SM prediction and the experimental measurement of a_μ does not allow one to claim a discovery. However, it puts important constraints on possible contributions from New Physics, and hence on the corresponding "acceptable" models. For example, in the scenario where supersymmetry is discovered at the LHC,

few constraints on its parameters (ex: tanβ) would be available from the direct measurement. In that scenario, the a_μ constraint would bring important knowledge on the allowed values of these parameters (see Fig. 5.18) [118]. With the increased accuracy of the proposed experimental measurements of a_μ, as well as with an improved precision on the theoretical prediction, these constraints would be significantly stronger, hence the better determination of the SUSY parameters.

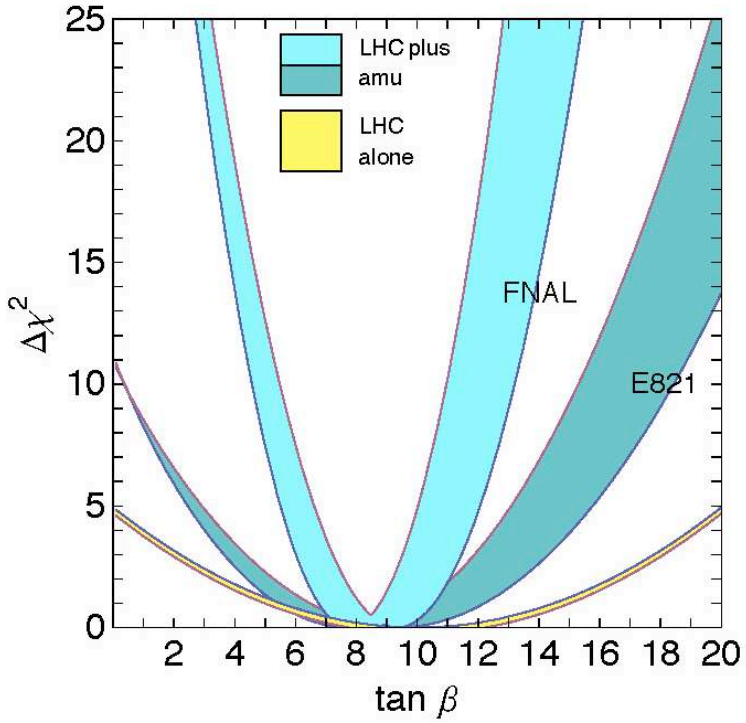

Figure 5.18: Constraints on the parameter tanβ, from the LHC alone or respectively with present and future a_μ constraints, in the scenario where supersymetry is discovered at the LHC and it corresponds to the MSSM.

Chapter 6

The Determination of α_S from τ Decays

The relatively large mass of the τ lepton, its leptonic nature and its decay through weak interaction promotes it to a particular status for probing the Standard Model (see [122] for a detailed review, and references therein). In the previous chapter, we already saw how the τ hadronic spectral functions can be exploited in the theoretical computation of the anomalous magnetic moment of the muon. Inclusive hadronic quantities, obtained after integrating over the spectral functions (or directly via the measurement of hadronic or leptonic τ branching fractions), have been found to be dominated by perturbative contributions at energies above $\sim$1 GeV. They can be exploited to precisely determine the strong coupling constant at the τ-mass scale, $\alpha_s(m_\tau^2)$ ([123–126], reassessed more recently [122] in the light of the existing data on τ decays and e^+e^- annihilation). The comparison of $\alpha_s(m_\tau^2)$ with the values obtained at different energies, in particular at the Z-scale, provides an important test of the running of QCD.

In this chapter we update the determination of $\alpha_s(m_\tau^2)$ from hadronic τ decays, motivated by progress performed in two different areas: on the theoretical side, the perturbative expression of the relevant correlator has been computed up to fourth order [127], and on the experimental side, new precision measurements from BABAR of τ branching fractions involving kaons [128] decrease the uncertainty in the separation of vector and axial-vector spectral functions. We utilise this opportunity to analyse several features of the theoretical frameworks commonly used to determine $\alpha_s(m_\tau^2)$ in more detail. This concerns the treatments of the perturbative series, the convergence of the expansions, and the impact of nonperturbative effects.

In Sec. 6.1 we describe recent experimental improvement on the measurements of $K\overline{K}\pi$ decays, the spectral functions and the τ branching fractions. This is followed in Sec. 6.2 by a summary of the various theoretical prescriptions used to extract $\alpha_s(m_\tau^2)$ from a fit to data, and a discussion of their advantages and shortcomings. We also analyse the role played by nonperturbative contributions in this determination. In Sec. 6.3 we exploit the normalisation and shape of the spectral functions to constrain the relevant nonperturbative contributions and to provide an improved determination of $\alpha_s(m_\tau^2)$.

The determination of $\alpha_s(m_\tau^2)$ and a series of studies on the various perturbative meth-

ods, presented in this chapter, were published in [119]. Some complements to these studies were given in [120], and the analysis of the renormalons models, relevant for these topics, was published in [121].

6.1 Tau Hadronic Spectral Functions

For vector (axial-vector) hadronic τ decay channels $V^-\nu_\tau$ ($A^-\nu_\tau$), the nonstrange vector (axial-vector) spectral function v_1 (a_1, a_0), where the subscript refers to the spin J of the hadronic system, is derived from the invariant mass-squared hadronic distribution $(1/N_{V/A})(dN_{V/A}/ds)$, divided by the appropriate kinematic factor, and normalised to the hadronic branching fraction

$$v_1(s)/a_1(s) = \frac{m_\tau^2}{6\,|V_{ud}|^2\,S_{\rm EW}}\,\frac{\mathcal{B}_{V^-/A^-\nu_\tau}}{\mathcal{B}_e}\,\frac{dN_{V/A}}{N_{V/A}\,ds}\,\left[\left(1-\frac{s}{m_\tau^2}\right)^2\left(1+\frac{2s}{m_\tau^2}\right)\right]^{-1}. \tag{6.1}$$

For $a_0(s)$, the same expression holds if the term $(1+2s/m_\tau^2)$ is removed. Here $S_{\rm EW} = 1.0198 \pm 0.0006$ is a short-distance electroweak correction [64, 76], $\mathcal{B}_{V^-/A^-\nu_\tau}$ ($\mathcal{B}_e$) denotes the inclusive $\tau \to V^-/A^-(\gamma)\nu_\tau$ ($\tau \to e^-\overline{\nu}_e\nu_\tau(\gamma)$) branching fraction (throughout this letter, final state photon radiation is accounted for in the τ branching fractions). We use universality in the leptonic weak charged currents and the measurements of $\mathcal{B}_e$, $\mathcal{B}_\mu$ and the τ lifetime, to obtain the improved branching fraction $\mathcal{B}_e = \mathcal{B}_e^{\rm uni} = (17.818 \pm 0.032)\%$ [122]. We also use $m_\tau = (1776.90 \pm 0.20)$ MeV [129] and $|V_{ud}| = 0.97418 \pm 0.00019$ [130] (assuming CKM unitarity). Integration of the spectral function over the τ phase space leads to the inclusive τ hadronic width, expressed through the ratio

$$R_{\tau,V/A} = \frac{\mathcal{B}_{V^-/A^-\nu_\tau}}{\mathcal{B}_e}\,. \tag{6.2}$$

By unitarity and analyticity the spectral functions are connected to the imaginary part of the two-point correlation function, $\Pi^{\mu\nu}_{ij,U}(q)$, for time-like momenta-squared $q^2 > 0$,

$$\begin{aligned}\Pi^{\mu\nu}_{ij,U}(q) &\equiv i\int d^4x\, e^{iqx}\langle 0|T(U^\mu_{ij}(x)U^\nu_{ij}(0)^\dagger)|0\rangle \\ &= \left(-g^{\mu\nu}q^2 + q^\mu q^\nu\right)\,\Pi^{(1)}_{ij,U}(q^2) + q^\mu q^\nu\,\Pi^{(0)}_{ij,U}(q^2)\,,\end{aligned} \tag{6.3}$$

where $U = A, V$ denotes the nature of the relevant currents, either vector ($U^\mu_{ij} = V^\mu_{ij} = \overline{q}_j\gamma^\mu q_i$) or axial-vector ($U^\mu_{ij} = A^\mu_{ij} = \overline{q}_j\gamma^\mu\gamma_5 q_i$) charged colour-singlet quark currents. By Lorentz decomposition, the correlation functions can be split into their $J = 1$ and $J = 0$ parts.

In the complex $s = q^2$ plane, the polarization functions $\Pi^{\mu\nu}_{ij,U}(s)$ are expected to exhibit a very simple analytic structure, the only non-analytic features being along the real axis: a branch cut for all polarization functions, and a pole at the pion (kaon) mass for a_0. The

imaginary part of the polarization functions on the branch cut is linked to the spectral functions defined in Eq. (6.1), for nonstrange (strange) quark currents

$$\mathrm{Im}\Pi^{(1,0)}_{\overline{u}d(s),V/A}(s) = \frac{1}{2\pi} v_1/a_{1,0}(s)\,, \tag{6.4}$$

which provide the basis for comparing a theoretical description of strong interaction with hadronic data.

Experimentally, the total hadronic observable R_τ,

$$R_\tau = R_{\tau,V} + R_{\tau,A} + R_{\tau,S}\,, \tag{6.5}$$

where $R_{\tau,S}$ denotes the hadronic width to final states with net strangeness, is obtained from the measured leptonic branching ratios,

$$R_\tau = \frac{1-\mathcal{B}_e-\mathcal{B}_\mu}{\mathcal{B}_e} = \frac{1}{\mathcal{B}_e^{\rm uni}} - 1.9726 = 3.640 \pm 0.010\,. \tag{6.6}$$

6.1.1 New Input to the Vector/Axial-Vector Separation

The separation of vector and axial-vector components is straightforward in the case of hadronic final states with only pions using G-parity [1], provided that isospin symmetry holds. An even number of pions has $G = 1$ corresponding to vector states, while an odd number of pions has $G = -1$, which tags axial-vector states. Modes with a $K\overline{K}$ pair are not in general eigenstates of G-parity and contribute to both V and A channels. While the decay to K^-K^0 is pure vector, additional information is required to separate the $K\overline{K}\pi$ and the rarer $K\overline{K}\pi\pi$ modes. For the latter channel an axial-vector fraction of 0.5 ± 0.5 is used [122].

Until recently, there was some confusion on this issue for the $K\overline{K}\pi$ modes:

1. In the ALEPH analysis of τ decay modes with kaons [131], an estimate of the vector contribution was obtained using the e^+e^- annihilation data from DM1 [133] and DM2 [134] in the $K\overline{K}\pi$ channel, extracted in the $I = 1$ state. This contribution was found to be small, and, using the conserved vector current (CVC), a branching fraction of $\mathcal{B}_{\rm CVC}(\tau \to \nu_\tau (K\overline{K}\pi)_V) = (0.26 \pm 0.39) \cdot 10^{-3}$, was found, corresponding to an axial fraction of $f_{A,{\rm CVC}}(K\overline{K}\pi) = 0.94^{+0.06}_{-0.08}$.

2. The ALEPH CVC result was corroborated by a partial-wave and lineshape analysis of the a_1 resonance from τ decays in the $\nu_\tau\pi^-2\pi^0$ mode performed by CLEO [135]. The effect of the $K^\star K$ decay mode of the a_1 was seen through unitarity and a branching fraction of $\mathcal{B}(a_1 \to K^\star K) = (3.3 \pm 0.5)\%$ was derived. With the known $\tau^- \to \nu_\tau a_1^-$ branching fraction, this value more than saturates the total branching fraction available for the $K\overline{K}\pi$ channel, yielding an axial fraction of $f_{A,a_1}(K\overline{K}\pi) = 1.30 \pm 0.24$.

[1] G-parity combines charge conjugation and a rotation of π rad around de second axis of the isospin space.

3. Another piece of information, also contributed by CLEO [136], but conflicting with the two previous results, is based on a partial-wave analysis in the $K^-K^+\pi^-$ channel using two-body resonance production and including many possible contributing channels. A much smaller axial fraction of $f_{A,K\overline{K}\pi}(K\overline{K}\pi) = 0.56 \pm 0.10$ was found here.

Since the three determinations are inconsistent, the value $f_A = 0.75 \pm 0.25$ has been used previously to account for the discrepancy [122]. This led to a systematic uncertainty in the V, A spectral functions that competed with the purely experimental uncertainties.

Precise cross section measurements for e^+e^- annihilation to $K^+K^-\pi^0$ and to $K^0K^\pm\pi^\mp$ have been recently published by the BABAR Collaboration [128], using the method of radiative return. In the mass range of interest for τ physics they show strong dominance of $K^\star(890)K$ dynamics and a fit of the Dalitz plot yields a clean separation of the $I = 0, 1$ contributions. Assuming CVC, the mass distribution of the vector final state in the decays $\tau \to \nu_\tau K\overline{K}\pi$ can be obtained. The result is shown in Fig. 6.1 and compared with the full τ spectrum from ALEPH [131] summing up the contributions from the $K^-K^+\pi^-$, $\overline{K}^0K^0\pi^-$, and $K^-K^0\pi^0$ modes. The BABAR results reveal a small vector component. After integration, one obtains

$$f_{A,\mathrm{CVC}}(K\overline{K}\pi) = 0.833 \pm 0.024, \tag{6.7}$$

which is about 1.3σ lower than the ALEPH determination using the same method (but with much poorer e^+e^- input data) and 2.7σ higher than the CLEO partial-wave-analysis result. The new determination has a precision that exceeds the previously used value by an order of magnitude, thus effectively reducing the uncertainties in the vector and axial-vector spectral functions to the experimental errors only.

One notices from Fig. 6.1 that the axial fraction varies versus the $K\overline{K}\pi$ mass, with lower masses being further axial-enhanced. The observed axial-vector dominance is at variance with several estimates such as $f_A \sim 0.10$ [137], 0.37 [138], obtained within the Resonance Chiral Theory, which attempts at incorporating massive vector and axial resonances decaying into light mesons into a framework inspired by chiral and large-N_c arguments. On the other hand, this axial-vector dominance is closer to the prediction $f_A \sim 0.71$, based on a model combining axial-vector and vector resonances of finite widths with a leading-order chiral Lagrangian [140].

In deriving Eq. (6.7) care was taken to include a small contribution from the $\phi\pi$ final state, observed by BABAR in the same analysis [128]. Since BABAR also published a $\tau^- \to \nu_\tau\phi\pi^-$ branching fraction measurement [141], it is possible to perform a test of CVC in this channel with

$$\mathcal{B}_{\mathrm{CVC}}(\tau \to \nu_\tau\phi\pi^-) = (3.8 \pm 0.9 \pm 0.2) \cdot 10^{-5}, \tag{6.8}$$

$$\mathcal{B}_\tau(\tau \to \nu_\tau\phi\pi^-) = (3.42 \pm 0.55 \pm 0.25) \cdot 10^{-5}, \tag{6.9}$$

for which we find agreement within the quoted statistical and systematic errors. For comparison the dominant CVC $\tau \to \nu_\tau K^\star(890)K$ branching fraction is $(7.3 \pm 0.6 \pm 0.4) \cdot 10^{-4}$.

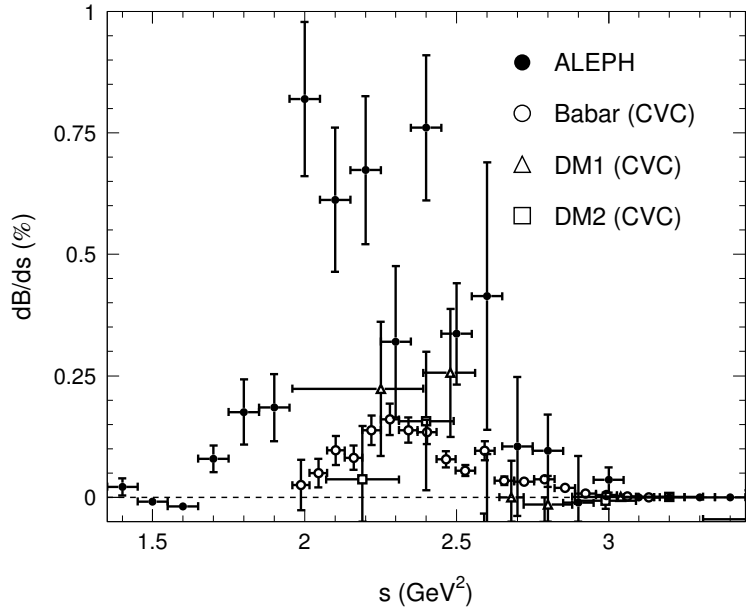

Figure 6.1: The mass-squared distribution for $\tau \to \nu_\tau K\overline{K}\pi$ decay modes from ALEPH and the predictions for the vector component obtained by CVC using DM1, DM2 and BABAR e^+e^- data.

Since this study was performed, a new analysis [139] based on Chiral Perturbation Theory was published, predicting a dominance of the vector component in this channel. They also point out that an important systematic error for the study we have described could originate from the neglected interference between two production chains passing through different intermediate states. Indeed, the error on the individual V and A components of the spectral functions should probably be increased, but our final result obtained from the $V + A$ spectral functions is not be affected.

6.1.2 Update on the Branching Fraction for Strange Decays

New measurements of τ strange decays have been published since our last compilation [122]. This is the case for the hadronic channels $K\pi^0$ [142], $K_S\pi^-$ [143], and $K^-\pi^+\pi^-$ [128]. Also using the more precise estimate from universality for the K^- channel [122], the updated value of $R_{\tau,S}$ becomes

$$R_{\tau,S} = 0.1615 \pm 0.0040\,, \tag{6.10}$$

replacing the previous value of 0.1666 ± 0.0048 [122].

Using the new $f_A(K\overline{K}\pi)$ value (6.7), the updated hadronic widths $R_{\tau,V/A}$ from ALEPH, slightly renormalised so that their sum agrees with the new average for $R_{\tau,V+A}$ obtained

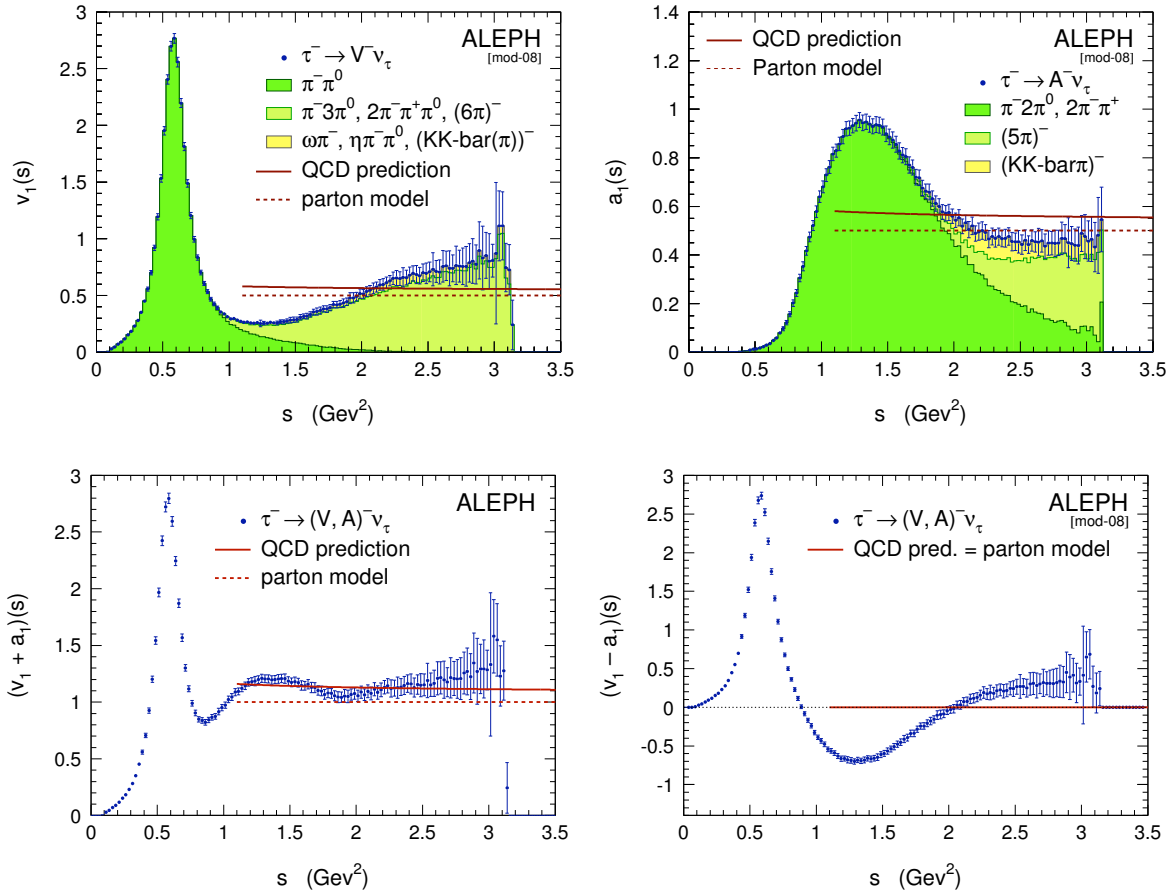

Figure 6.2: Vector (V), axial-vector (A), $V+A$ and $V-A$ τ hadronic spectral functions measured by ALEPH, and updated using the new V, A separation in the $K\overline{K}\pi$ channels discussed in the text. The shaded areas indicate the main contributing exclusive τ decay channels. The curves show the predictions from the parton model (dotted) and from massless perturbative QCD using $\alpha_S(M_Z^2) = 0.120$ (solid).

from (6.6) and (6.10) read

$$R_{\tau,V} = 1.783 \pm 0.011 \pm 0.002\,, \tag{6.11}$$
$$R_{\tau,A} = 1.695 \pm 0.011 \pm 0.002\,, \tag{6.12}$$
$$R_{\tau,V+A} = 3.479 \pm 0.011\,, \tag{6.13}$$
$$R_{\tau,V-A} = 0.087 \pm 0.018 \pm 0.003\,, \tag{6.14}$$

where the first errors are experimental and the second due to the V/A separation, now dominated by the $K\overline{K}\pi\pi$ channel.

The ALEPH spectral functions are updated accordingly and shown in Fig. 6.2 for respectively vector, axial-vector, $V + A$ and $V - A$.

6.2 Theoretical Prediction of R_τ

Tests of QCD and the precise measurement of the strong coupling constant α_s at the τ mass scale [123–126], carried out first by the ALEPH [144] and CLEO [145] collaborations, have triggered many theoretical developments. They concern primarily the perturbative expansion for which different optimised rules have been suggested. Among these are contour-improved (resummed) fixed-order perturbation theory [147, 148], effective charge and minimal sensitivity schemes [149–153], the large-β_0 expansion [154, 156, 157], as well as combinations of these approaches. Their main differences lie in how they deal with the fact that the perturbative series is truncated at an order where the missing part is not expected to be small. While a review and discussion of the various approaches can be found in [122], we only recall some of their salient features in the following.

With the publication of the full vector and axial-vector spectral functions by ALEPH [158, 159] and OPAL [146] it became possible to directly study the nonperturbative properties of QCD through $V - A$ sum rules and through fits to spectral moments computed from weighted integrals over the spectral functions (we refer again to the discussions in [122]). Inclusive observables like R_τ can be accurately predicted in terms of $\alpha_s(m_\tau^2)$ using perturbative QCD, and including small nonperturbative contributions within the framework of the Operator Product Expansion (OPE) [160].

6.2.1 Operator Product Expansion

According to Eq. (6.4), the absorptive (imaginary) parts of the vector and axial-vector two-point correlation functions $\Pi^{(J)}_{\overline{u}d,V/A}(s)$, with the spin J of the hadronic system, are proportional to the τ hadronic spectral functions with corresponding quantum numbers. The nonstrange ratio $R_{\tau,V+A}$ can be written as an integral of these spectral functions over the invariant mass-squared s of the final state hadrons [125]

$$R_{\tau,V+A}(s_0) = 12\pi S_{\rm EW}|V_{ud}|^2 \int\limits_0^{s_0} \frac{ds}{s_0}\left(1-\frac{s}{s_0}\right)^2 \Big[{\rm Im}\Pi^{(0)}(s+i\varepsilon) + \left(1+2\frac{s}{s_0}\right){\rm Im}\Pi^{(1)}(s+i\varepsilon)\Big], \tag{6.15}$$

where $\Pi^{(J)}$ can be decomposed as $\Pi^{(J)} = \Pi^{(J)}_{ud,V} + \Pi^{(J)}_{ud,A}$. We work in the chiral limit[2] to study the perturbative contribution, so that the lower integration limit is zero because of the pion pole at zero mass. The correlation function $\Pi^{(J)}$ is analytic in the complex s plane everywhere except on the positive real axis where singularities exist. Hence by Cauchy's theorem, and using the fact that the imaginary part of $\Pi^{(J)}$ is proportional to

[2]Vector and axial-vector currents are conserved in the chiral limit, so that $s\Pi^{(0)}_V = s\Pi^{(0)}_A = 0$.

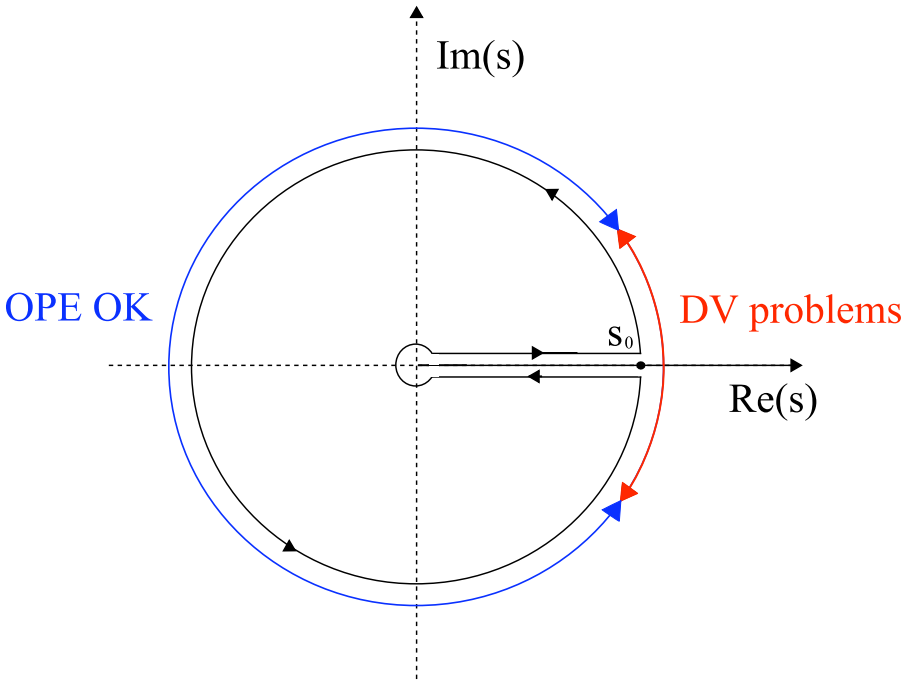

Figure 6.3: Integration contour used for Eq. 6.16. We also indicate the region where OPE is expected to provide a good description of QCD (blue), and the region where DV effects are expected to be rather large (red): see text.

the discontinuity across the positive real axis, one has

$$\frac{1}{\pi}\int_0^{s_0} ds\; w(s)\;\mathrm{Im}\Pi(s) = -\frac{1}{2\pi}\oint_{|s|=s_0} ds\; w(s)\;\Pi(s)\;, \tag{6.16}$$

and the integral (6.15) can be replaced by a contour integral over $\Pi(s)$ running counter-clockwise around the circle from $s = s_0 + i\varepsilon$ to $s = s_0 - i\varepsilon$ (see Fig. 6.3).

The energy scale $s_0 = m_\tau^2$ is large enough that contributions from nonperturbative effects are expected to be subdominant and the use of the Operator Product Expansion is appropriate. The latter is expected to yield relevant results in the deep Euclidean region ($Q^2 \equiv -q^2 = -s \gg 0$) where s is large and negative, whereas the extension to other regions in the complex plane is questionable. Fortunately, in the case of R_τ, the kinematic factor $(1 - s/s_0)^2$ suppresses the contribution from the region near the positive real axis where $\Pi^{(J)}(s)$ has a branch cut and the validity of the OPE is doubtful due to large quark-hadron duality violations (DV) [161, 162].

The OPE of the vector and axial-vector ratio $R_{\tau,V/A}$ can be written as

$$R_{\tau,V/A} = \frac{3}{2} S_{\rm EW} |V_{ud}|^2 \left(1 + \delta^{(0)} + \delta'_{\rm EW} + \delta^{(2,m_q)}_{ud,V/A} + \sum_{D=4,6,\ldots} \delta^{(D)}_{ud,V/A}\right), \tag{6.17}$$

with the massless universal[3] perturbative contribution $\delta^{(0)}$, the residual non-logarithmic electroweak correction $\delta'_{\rm EW} = 0.0010$ [77] (*cf.* the discussion on radiative corrections in [122]), and the dimension $D = 2$ perturbative contribution $\delta^{(2,m_q)}_{ud,V/A}$ from massive quarks. The term $\delta^{(D)}$ denotes the OPE contributions of mass dimension D [126]

$$\delta^{(D)}_{ud,V/A} = \sum_{\dim\mathcal{O}=D} C'_{V/A}(s_0,\mu)\frac{\langle\mathcal{O}_D(\mu)\rangle_{V/A}}{s_0^{D/2}}\,, \tag{6.18}$$

where $\delta^{(D)}_{ud,V+A} = \frac{1}{2}\big(\delta^{(D)}_{ud,V} + \delta^{(D)}_{ud,A}\big)$. In practice, the OPE provides a separation between short and long distances by following the flow of a large incoming momentum. The scale parameter μ separates the long-distance nonperturbative effects, absorbed into the vacuum expectation value of the operators $\langle\mathcal{O}_D(\mu)\rangle$, from the short-distance effects that are included in the coefficients $C_{V/A}(s,\mu)$, which become $C'_{V/A}(s_0,\mu)$ after performing the integration (6.15). The vacuum expectation values $\langle\mathcal{O}_D(\mu)\rangle$ encode information on the nonperturbative features of QCD vacuum and its effects on the propagation of quarks: they cannot be computed from first principles and have to be extracted from data. The short-distance coefficients $C_{V/A}(s,\mu)$ can be determined within perturbative QCD.

6.2.2 Perturbative Contribution to Fourth Order in α_S

R_τ is a doubly inclusive observable since it is the result of an integration over all hadronic final states at a given invariant mass and further over all masses between m_π and m_τ. The scale m_τ lies in a compromise region where $\alpha_S(m_\tau^2)$ is large enough so that R_τ is sensitive to its value, yet still small enough so that the perturbative expansion converges safely and nonperturbative power terms are small. The prediction for R_τ is thus found to be dominated by the lowest-dimension term in Eq. (6.18), *i.e.*, the term obtained from a perturbative computation of the correlator Π. To state this another way, it is the perturbative contribution that will provide the main sensitivity to α_s.

For the evaluation of the perturbative series, it is convenient to introduce the analytic Adler function [166] $D(s) \equiv -s\cdot d\Pi_{V/A}(s)/ds$, which avoids extra subtractions that are unrelated to QCD dynamics. The function $D(s)$ calculated in perturbative QCD within the $\overline{\rm MS}$ renormalisation scheme is a function of α_S and depends on the renormalisation scale μ, occurring through $\ln(\mu^2/s)$. Since $D(s)$ is connected to a physical quantity, the spectral function ${\rm Im}\Pi(s)$, it cannot depend on the choice of the renormalisation scale μ. This is achieved through the cancellation of the μ-dependence of α_S and of the explicit occurrences of μ in D. Nevertheless, in the realistic case of a series truncated at a given order in α_S our knowledge of the renormalisation scale dependence is imperfect, *i.e.*, D depends on μ, thus inducing a systematic uncertainty.

[3] In the chiral limit of vanishing quark masses the contributions from vector and axial-vector currents coincide to any given order of perturbation theory and the results are flavour independent.

To introduce the Adler function in Eq. (6.15), one uses partial integration, giving

$$1 + \delta^{(0)} = -2\pi i \oint\limits_{|s|=s_0} \frac{ds}{s} w(s) D(s) \,, \tag{6.19}$$

where $w(s) = 1 - 2s/s_0 + 2(s/s_0)^3 - (s/s_0)^4$. The perturbative expansion of $D(s)$ reads

$$D(s) = \frac{1}{4\pi^2} \sum_{n=0}^{\infty} \tilde{K}_n(\xi) a_s^n(-\xi s) \,, \tag{6.20}$$

with $a_s \equiv \alpha_s/\pi$, and where the dimensionless factor ξ parametrises the renormalisation scale ambiguity. While the coefficients $K_{0,1} = \tilde{K}_{0,1} = 1$ are universal (we use the notation $K_n = \tilde{K}_n(\xi = 1)$ in the following), the $\tilde{K}_{n\geq 2}$ depend on the renormalisation scheme and scale used. Powerful computational techniques have recently allowed to determine K_4. The authors of [127] exploited the dependence of the four-loop master integrals (used to express all relevant four-loop integrals with massless propagators) on the space-time dimension to compute the integrals to the required accuracy. For $n_f = 3$ quark flavours and $\xi = 1$ one has[4] $K_2 \simeq 1.640$, $K_3 \simeq 6.371$ and $K_4 \simeq 49.08$ [127, 167–171]. The full expressions for the functions $\tilde{K}_n(\xi)$ for arbitrary ξ up to order $n = 5$ can be found in [122].

With the series (6.20), inserted into the r.h.s. of Eq. (6.19), one obtains the perturbative expansion

$$\delta^{(0)} = \sum_{n=1}^{\infty} \tilde{K}_n(\xi) A^{(n)}(a_s) \,, \tag{6.21}$$

with the functions [147]

$$A^{(n)}(a_s) = \frac{1}{2\pi i} \oint\limits_{|s|=s_0} \frac{ds}{s} w(s) a_s^n(-\xi s) = \frac{1}{2\pi} \int\limits_{-\pi}^{\pi} d\varphi \, w(-s_0 e^{i\varphi}) a_s^n(\xi s_0 e^{i\varphi}) \,. \tag{6.22}$$

Similarly, the Adler function also serves to obtain the perturbative expansion of the inclusive e^+e^- annihilation cross section ratio

$$R_{e^+e^-}(s) = \frac{\sigma(e^+e^- \to \text{hadrons}\,(\gamma))}{\sigma(e^+e^- \to \mu^+\mu^-)} = -6\pi i \sum_f Q_f^2 \oint_{|s'|=|s|} ds' \cdot \frac{D(s')}{s'} . \tag{6.23}$$

Evaluating the contour integral in fixed-order perturbation theory (*cf.* Sec. 6.2.2) with

[4]The numerical expressions for an arbitrary number of quark flavours (n_f) in the $\overline{\text{MS}}$ renormalisation scheme for $\xi = 1$ are: $K_0 = 1$, $K_1 = 1$, $K_2 \simeq 1.9857 - 0.1153\, n_f$, $K_3 \simeq 18.2428 - 4.2158\, n_f + 0.0862\, n_f^2$, and $K_4 \simeq 135.7916 - 34.4402\, n_f + 1.8753\, n_f^2 - 0.0101\, n_f^3$.

$n_f = 5$ active quark flavours, and inserting all known coefficients, gives[5]

$$R^{(5)}_{e^+e^-}(s) = 3\sum\nolimits_f Q_f^2 \big[1 + a_s(s) + 1.4092\, a_s^2(s) - 12.7673\, a_s^3(s) - 79.9795\, a_s^4(s) + (K_5 + 79.7306)\, a_s^5(s) + (K_6 + 2202.78)\, a_s^6(s) + \ldots\big] . \quad (6.24)$$

Fixed-Order and Contour-Improved Perturbation Theory

The standard perturbative method to compute the contour integral consists of expanding all the quantities up to a given power of $a_s(s_0)$. The starting point is the solution of the renormalisation group equation (RGE) for $a_s(s)$, which is expanded in a Taylor series of $\eta \equiv \ln(s/s_0)$ around the reference scale s_0 [122]

$$\begin{aligned} a_s(s) &= a_s - \beta_0\eta a_s^2 + \left(-\beta_1\eta + \beta_0^2\eta^2\right) a_s^3 + \left(- \beta_2\eta + \frac{5}{2}\beta_0\beta_1\eta^2 - \beta_0^3\eta^3\right) a_s^4 \\ &+ \left(-\beta_3\eta + \frac{3}{2}\beta_1^2\eta^2 + 3\beta_0\beta_2\eta^2 - \frac{13}{3}\beta_0^2\beta_1\eta^3 + \beta_0^4\eta^4\right) a_s^5 \\ &+ \left(- \beta_4\eta + \frac{7}{2}\beta_1\beta_2\eta^2 + \frac{7}{2}\beta_0\beta_3\eta^2 - \frac{35}{6}\beta_0\beta_1^2\eta^3 - 6\beta_0^2\beta_2\eta^3 + \frac{77}{12}\beta_0^3\beta_1\eta^4 - \beta_0^5\eta^5\right) a_s^6 \\ &+ \mathcal{O}(\eta^6; a_s^7) \, . \end{aligned} \quad (6.25)$$

Here the series has been reordered in powers of $a_s \equiv a_s(s_0)$ and we use the RGE β-function[6] as defined in [172].

Computing the contour integral (6.22), and ordering the contributions according to their powers in a_s, leads to the familiar expression for fixed-order perturbation theory (FOPT) [147]

$$\delta^{(0)} = \sum_{n=1}^{\infty} \Big[\tilde{K}_n(\xi) + g_n(\xi)\Big]\, a_s^n(\xi s_0) \, , \quad (6.26)$$

where the g_n are functions of $\tilde{K}_{m<n}$ and $\beta_{m<n-1}$, and of elementary integrals with logarithms of power $m < n$ in the integrand. Setting $\xi = 1$ and replacing all known β_i

[5]The explicit formula reads:

$$R_{e^+e^-}(s) = 3\sum_f Q_f^2 \bigg[1 + a_s(s) + K_2\, a_s^2(s) + \left(K_3 - \frac{1}{3}\pi^2\beta_0^2\right) a_s^3(s) + \left(K_4 - \frac{5}{6}\pi^2\beta_0\beta_1 - K_2\pi^2\beta_0^2\right) a_s^4(s) + \left(K_5 - \frac{1}{2}\pi^2\beta_1^2 - \pi^2\beta_0\beta_2 - \frac{7}{3}\pi^2\beta_0\beta_1 K_2 - 2\pi^2\beta_0^2 K_3 + \frac{1}{5}\pi^4\beta_0^4\right) a_s^5(s) + \ldots\bigg] .$$

[6]The full expressions for an arbitrary number of quark flavours (n_f) are:
$\beta_0 = \frac{1}{4}\left(11 - \frac{2}{3}n_f\right)$, $\beta_1 = \frac{1}{16}\left(102 - \frac{38}{3}n_f\right)$, $\beta_2 = \frac{1}{64}\left(\frac{2857}{2} - \frac{5033}{18}n_f + \frac{325}{54}n_f^2\right)$, and $\beta_3 = \frac{1}{256}\left[\frac{149753}{6} + 3564\,\zeta_3 - \left(\frac{1078361}{162} + \frac{6508}{27}\,\zeta_3\right) n_f + \left(\frac{50065}{162} + \frac{6472}{81}\,\zeta_3\right) n_f^2 + \frac{1093}{729}n_f^3\right]$, where the $\zeta_{i=\{3,4,5\}} = \{1.2020569, \pi^4/90, 1.0369278\}$ are the Riemann ζ-functions. The $\beta_{n\geq 4}$ are unknown.

coefficients by their numerical values for $n_f = 3$ gives [122, 173]

$$\begin{aligned}\delta^{(0)} &= a_s(s_0) + (K_2 + 3.5625)\, a_s^2(s_0) + (K_3 + 19.995)\, a_s^3(s_0) \\ &\quad + (K_4 + 78.003)\, a_s^4(s_0) + (K_5 + 307.787)\, a_s^5(s_0) \\ &\quad + (K_6 + 17.813\, K_5 + 1.5833\, \beta_4 - 5848.19)\, a_s^6(s_0)\,,\end{aligned} \tag{6.27}$$

where for the purpose of later studies we have kept terms up to sixth order.

The FOPT series is truncated at a given order despite the fact that parts of the higher coefficients $g_{n>4}(\xi)$ are known and could be resummed: these are the higher order terms of the $a_s(s)$ expansion that are functions of $\beta_{n\leq 3}$ and $K_{n\leq 4}$ only. Moreover, at each integration step, the expansion (6.25) with respect to the physical value $a_s(s_0)$ is used to predict $a_s(s)$ on the entire $|s| = s_0$ contour. This might not always be justified, and leads to systematic errors as discussed in Sec. 6.2.2.

A more accurate approach to the solution of the contour integral (6.22) is to perform a direct numerical evaluation by step-wise integration. At each integration step, it takes as input for the running $a_s(s)$ the solution of the RGE to four loops, computed using the value from the previous step [147, 148]. It implicitly provides a partial resummation of the (known) higher order logarithmic contributions, and does not require the validity of the $a_s(s)$ Taylor series for large absolute values of the expansion parameter η. This numerical solution of Eq. (6.21) is referred to as *contour-improved* perturbation theory (CIPT).

Alternative Perturbative Expansions

Inspired by the pioneering work in [149–153] the *effective charge approach* to the perturbative prediction of R_τ (ECPT) has triggered many studies [174–176]. The advocated advantage of this technique is that the perturbative prediction of the effective charge is renormalisation scheme and scale invariant since it is a physical observable. The effective τ charge is defined by $a_\tau = \delta^{(0)}$. The ECPT scheme has been used in the past to estimate the unknown higher-order perturbative coefficient K_4, by exploiting the mediocre convergence of the series (because $a_\tau(m_\tau^2) \simeq 1.8 \cdot a_s(m_\tau^2)$). As pointed out in [127], these estimates missed the actual value of K_4 by approximately a factor of two. One reason for this disagreement may come from the fact that these methods neglected the contributions from the next higher and also unknown orders. Owing to the insufficient convergence, the uncertainty on the coefficient estimate introduced by this neglect is significant and exceeds the errors quoted [122].

For completeness we also mention the *large-β_0 expansion*, which is an approximation to the full FOPT result assuming the dominance of the $[\beta_0 a_s(-s)]^n$ term. It is thus possible to derive estimates for the FOPT coefficients of a given perturbative series at all orders by neglecting higher order terms in the β-function. The large-β_0 expansion corresponds to inserting chains of fermion loops into the gluon propagators and to determining the impact on the quark-antiquark vacuum polarization. The procedure provides hence a *naive non-abelianisation* of the theory, because the lowest-order radiative corrections do not include gluon self-coupling. As an illustration, the R_τ FOPT series (6.26) can be

expanded as $\delta^{(0)}(s) = a_s \sum_{n=0} a_s^n \, (d_n \beta_0^n + \delta_n)$, where $d_n \beta_0^n + \delta_n = K_{n+1} + g_{n+1}$ (setting $\xi = 1$). The coefficients d_n are computed in terms of fermion bubble diagrams [177], where they are identified with their leading-n_f pieces $d_n^{[n]}$ in the expression $d_n = d_n^{[n]} n_f^k + \cdots + d_k^{[0]}$. Neglecting the corrections δ_n, the above series leads to the large-β_0 expansion of $\delta^{(0)}$. The first elements of the series are [178]: $d_0 = 1$, $d_1\beta_0 = 5.119$, $d_2\beta_0^2 = 28.78$, $d_3\beta_0^3 = 156.6$, $d_4\beta_0^4 = 900.9$, $d_5\beta_0^5 = 4867$. They compare reasonably well with the FOPT terms (6.27) where these are known, in particular the large size of the fourth-order term has been anticipated ($K_4 \sim 79$). However, it turns out that the estimated coefficients of the Adler series itself (before integration on the contour) do not compare well with the exact solutions, which emphasises the uncontrolled theoretical uncertainties associated with this method [122].

Comparing Perturbative Methods

This section updates and completes the discussion given in Secs. 3 and 8 of [122], including here the known value of the fourth-order perturbative coefficient in the Adler function, K_4 [127]. We perform a numerical study of the FOPT and CIPT approaches to expose the differences between these two methods. Both use the Taylor series (6.25), and they assume that one can perform an analytic continuation of the solution of the RGE for complex values of s,[7] namely along the circular contour of integration in Eq. (6.22). One should thus make sure that the series is used only inside the domain of good convergence. As one approaches the limit of this domain, the error induced by the finite Taylor series increases. For CIPT the convergence is guaranteed because the integration proceeds along infinitesimal steps such that $|\eta| \ll 1$ everywhere. The situation is more complicated for FOPT as the absolute value of η in Eq. (6.25) approaches π close to the branch cut.

The tests carried out here use the expansion (6.25) to sixth order in $a_s(s_0)$ (hence fifth order in $\eta = \ln(s/s_0)$) — if not stated otherwise, with estimates for $K_{5,6}$ and β_4 assuming a geometric growth of the corresponding series (*i.e.*, $K_{5(6)} = K_{4(5)}(K_{4(5)}/K_{3(4)})$ and $\beta_4 = \beta_3(\beta_3/\beta_2)$), and setting all coefficients at higher-orders than these to zero.

Taylor Series

To check the stability of the results obtained with FOPT, we consider a variant (denoted FOPT^{++}) where all known or estimated terms of order $\eta^{n \leq 5}$ are kept (*i.e.*, including the known expressions with powers $a_s^{n=7}(s_0)$ and beyond), which should reduce the error associated with the use of the Taylor expansion in FOPT. Figure 6.4 shows the evolution of the real part of $\alpha_s(s)$ along the integration circle as found for CIPT, FOPT and FOPT^{++}. As expected, the values for CIPT and FOPT$^{(++)}$ agree in the region around $\phi = 0$ (the fix-point of the expansion in FOPT$^{(++)}$), but significant discrepancies occur elsewhere. For FOPT^{++} we find large values for $\mathrm{Re}(\alpha_s)$ close to the branch cut. Estimating the convergence speed of the η series (6.25) reveals that it is slower for FOPT^{++}, where larger powers of a_s are kept, than for FOPT, for which the series is truncated at a_s^6.

[7] One of the first limits of this hypothesis shows up in the discontinuity of the imaginary part of α_s at $\phi = \pm\pi$, which is due to the cut of the logarithm in the complex plane.

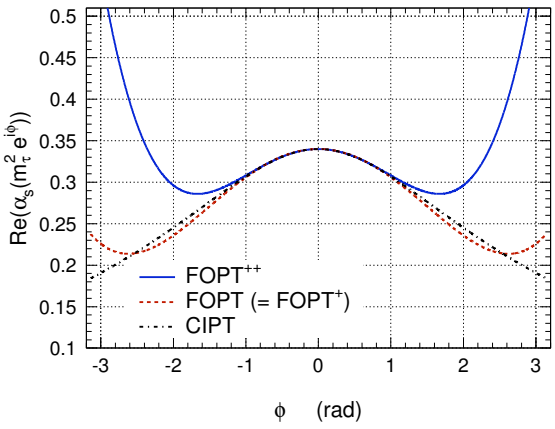

Figure 6.4: Real part of $\alpha_s(s)$ computed along the $|s| = s_0$ contour for $\xi = 1$, using respectively FOPT^{++} (solid line, see text), FOPT and FOPT$^+$ (dashed, see text) and CIPT (dashed-dotted).

Including higher orders $\eta^{n>5}$ in FOPT^{++} we find that these terms dominate the value of Re(α_s) near the branch cut, leading to large deviations from the correct evolution, which rise with the order n. On the contrary, for CIPT performed with infinitesimal integration steps, the full five-loop RGE solution is equivalent to Eq. (6.25), *i.e.*, CIPT = CIPT^{++}.[8]

Although the values of α_s differ significantly on half of the integration domain, the standard FOPT and CIPT methods give similar results for the integral. This is because the integration kernel (6.19) vanishes for $s = -s_0$ ($\phi = \pm\pi$), suppressing the contributions to the integral coming from the region near the branch cut.[9] The main difference between the two results stems from the regions $\phi \approx \pm 2.1$ and $\phi \approx \pm 1$ (*cf.* right-hand plot of Fig. 6.5). In the region $|\phi| < 1$, the values of $\alpha_s(s)$ estimated by the two methods are close, and the difference between the two integrands can be ascribed to the truncation at the sixth order in $a_s(s_0)$ for the integrand of FOPT.

Fixed-order Truncation

In addition to employing a Taylor series in a region with questionable convergence properties, FOPT truncates the full expression of the contour integral in Eq. (6.26). To disentangle the impact of these two approximations, we have tested another variant of FOPT (denoted FOPT$^+$), where Eq. (6.25) is used as is, but without truncating the Adler function (or equivalently $\delta^{(0)}$) at the sixth order in $a_s(s_0)$. This method leads to a similar integrand as in CIPT, with however the usual difference in the evolution. The

[8]To understand this feature, one can compare the errors induced by the Taylor approximation for the FOPT and CIPT numerical procedures along the circular contour. To compute the contour integral, $N \gg 1$ equidistant integration points along the contour are added. At the j^{th} point, the error on the value of α_s is given directly by Eq. (6.25) for FOPT, whereas one can easily show that it is reduced by the factor j/N^{n+1} for CIPT, where $n = 5$ is the expansion order in η. Therefore, the error on the contour integral coming from the determination of α_s is suppressed by $1/N^n$ in the case of CIPT compared to FOPT.

[9]In addition, a significant cancellation takes place in this region: for FOPT, the contribution of the contour integral vanishes on the intervals $[-\pi; -1.73]$ and $[1.73; \pi]$, whereas for CIPT a vanishing contribution comes from $[-\pi; -1.57]$ and $[1.57; \pi]$.

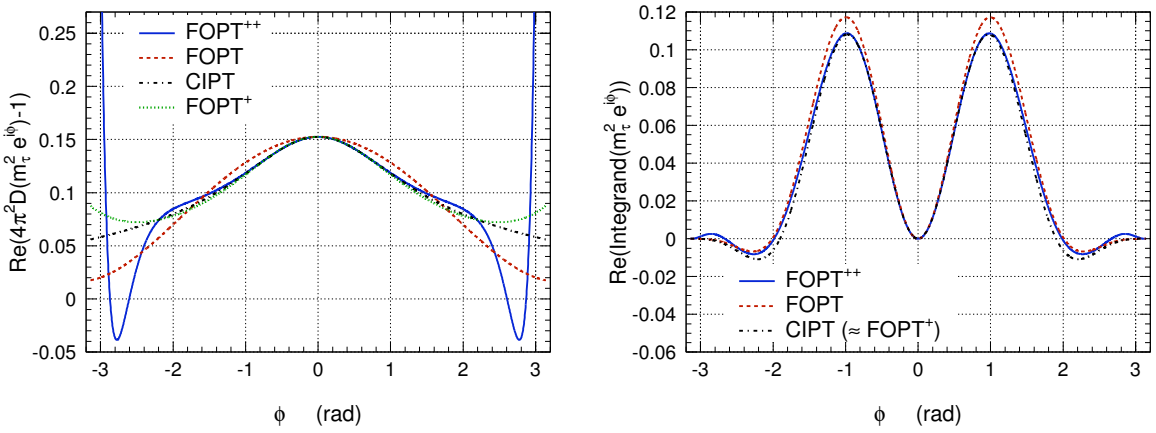

Figure 6.5: Real part of $(4\pi^2 D(s) - 1)$ (left) and of the integrand in Eqs. (6.22) and (6.21) (right), computed along the integration contour for $\xi = 1$, using respectively FOPT^{++} (solid line), FOPT (dashed), CIPT (dashed-dotted) and FOPT^{+} (dotted, not shown on the right hand plot because it is almost indistinguishable from CIPT).

left-hand plot of Fig. 6.5 shows the evolution of the real part of $(4\pi^2 D(s) - 1)$ along the contour for all methods. FOPT^{+} and CIPT differ close to the branch cut as a consequence of the deficient Taylor approximation, with however little difference in the integration result [122] due to the suppression by the integration kernel. The FOPT^{++} approach without truncating the Adler function leads to a $\delta^{(0)}$ that lies between CIPT and FOPT, with however unstable numerical dependence on the largest power in η kept in the Taylor series.

One can analytically prove that the FOPT result can also be obtained by making small steps, with a fixed order cut of the result at each step. However, in that case the effective RGE is modified at every single step. This is another way to see the problems of the FOPT method.

Numerical Comparisons

Table 6.1 summarises the contributions of the orders $n \leq 6$ in PT to $\delta^{(0)}$ for FOPT, CIPT and the large-β_0 expansion,[10] using as benchmark value $\alpha_s(m_\tau^2) = 0.34$, and $\xi = 1$. For systematic studies we vary ξ in the range $\xi \cdot m_\tau^2 = m_\tau^2 \pm 2\,\text{GeV}^2$, and the maximum observed deviations with respect to $\xi = 1$ are reported in the corresponding lines of Table 6.1. We assume a geometric growth of the perturbative terms for all unknown PT and RGE coefficients, with 100% uncertainty assigned to each of them for the purpose of illustration. We recall that the n-th contributions to the FOPT and CIPT series should be compared with care. Whereas the FOPT contributions can be directly obtained from Eq. (6.26), the entanglement of the different perturbative orders generated by CIPT prevents us from separating the contributions in powers of $a_s(s_0)$. Instead, the columns given for CIPT in Table 6.1 correspond to the terms in Eq. (6.21). If the two methods were

[10] We do not include ECPT into the present study, because — as concluded in [122] — the convergence of the perturbative series is insufficient for a precision determination of $\alpha_s(m_\tau^2)$.

Table 6.1: Massless perturbative contribution $\delta^{(0)}$ in R_τ using FOPT, CIPT and the large-β_0 expansion, respectively, and computed for $\alpha_s(m_\tau^2) = 0.34$. The unknown higher-order $K_{5,6}$ and β_4 coefficients are estimated by assuming a geometric growth (see text), while the remaining ones are set to zero. The quoted uncertainties δ correspond to the indicated error ranges.

Pert. Method	$n=1$	$n=2$	$n=3$	$n=4$	$(n=5)$	$(n=6)$	$\sum_{n=1}^{4}$	$\sum_{n=1}^{5}$	$\sum_{n=1}^{6}$
FOPT ($\xi=1$)	0.1082	0.0609	0.0334	0.0174	0.0101	0.0067	0.2200	0.2302	0.2369
$\delta(\beta_4 \pm 100\%)$	0	0	0	0	0	$\pm$0.0006	0	0	$\pm$0.0006
$\delta(K_5 \pm 100\%)$	0	0	0	0	$\pm$0.0056	$\pm$0.0108	0	$\pm$0.0056	$\pm$0.0164
$\delta(K_6 \pm 100\%)$	0	0	0	0	0	$\pm$0.0047	0	0	$\pm$0.0047
$\delta(\xi \pm 0.63)$	–	–	–	–	–	–	$^{+0.0317}_{-0.0151}$	$^{+0.0209}_{-0.0119}$	$^{+0.0152}_{-0.0095}$
CIPT ($\xi=1$)	0.1476	0.0295	0.0121	0.0085	0.0049	0.0020	0.1977	0.2027	0.2047
$\delta(\beta_4 \pm 100\%)$	$\mp$0.0003	$\mp$0.0001	$\mp$0.0001	$\mp$0.0001	$\mp$0.0001	$\mp$0.0001	$\mp$0.0006	$\mp$0.0007	$\mp$0.0008
$\delta(K_5 \pm 100\%)$	0	0	0	0	$\pm$0.0049	0	0	$\pm$0.0049	$\pm$0.0049
$\delta(K_6 \pm 100\%)$	0	0	0	0	0	$\pm$0.0020	0	0	$\pm$0.0020
$\delta(\xi \pm 0.63)$	–	–	–	–	–	–	$^{+0.0032}_{-0.0051}$	$^{+0.0005}_{-0.0044}$	$^{+0.0001}_{-0.0079}$
Large-β_0 expansion	0.1082	0.0600	0.0364	0.0215	0.0134	0.0078	0.2261	0.2395	0.2473

equally well suited for the integration, their column sums should converge to the same value. However, differences of about 10% (or more) subsist between the two estimations, computed at the order known up to day. This difference could have been much larger if not for the properties of the kernel in the integral (6.22) which has small absolute values in the region where the $\alpha_s(s)$ predictions of the two methods are rather different.

The variations of $\delta^{(0)}$ with the scale parameter ξ are strongly non-linear (*cf.* the asymmetric errors in Table 6.1 and the functional forms plotted for FOPT (left) and CIPT (right) in Fig. 6.7). CIPT exhibits significantly less renormalisation scale dependence than FOPT at order $n = 4$, while the interpretation of the subsequent orders strongly depends on the values used for the unknown coefficients $K_{n\geq 5}$.

Comparison on the Real Axis

The problems observed for the FOPT philosophy when used to perform a transformation on the circle in the complex plane, also exist for a scale transformation on the real axis. Indeed, this is another ground where the two methods can be compared.

At the order β_0 one can analytically compute the solution of the RGE,

$$a_s^{an}(s) = \frac{a_s(s_0)}{1 + \beta_0 \cdot a_s(s_0) \cdot ln\left(\frac{s}{s_0}\right)} \tag{6.28}$$

$$\approx a_s(s_0) - \beta_0 \cdot (a_s(s_0))^2 \cdot ln\left(\frac{s}{s_0}\right) . \tag{6.29}$$

On the real axis, as well as on the circle in the complex plane, CIPT reproduces the

analytical solution(6.28), whereas FOPT its approximation(6.29).

At higher orders, one can analytically compute the integral of the inverse beta function, yielding at the order β_1

$$\int_{a_s(s_0)}^{a_s(s)} \frac{da}{\beta(a)} = \left[\frac{1}{a\beta_0} + \frac{\beta_1}{\beta_0^2} ln\left(\frac{a}{\beta_0 + a\beta_1}\right)\right]_{a_s(s_0)}^{a_s(s)}, \tag{6.30}$$

and then relate it to $ln(s/s_0)$ using the RGE. Solving the resulting equation one gets a solution that we will call $\alpha_S^{an}(s)$. It is also instructive to compare the results of the two methods with a solution proposed for example in [155], consisting of an expansion in inverse powers of logarithms

$$a_s^{PDG}(s) = \frac{1}{\beta_0 \cdot ln\left(\frac{s}{\Lambda^2}\right)}\left[1 - \frac{\beta_1}{\beta_0^2} \cdot \frac{ln\left(ln\left(\frac{s}{\Lambda^2}\right)\right)}{ln\left(\frac{s}{\Lambda^2}\right)} + O\left(\frac{1}{ln^2\left(\frac{s}{\Lambda^2}\right)}\right)\right]. \tag{6.31}$$

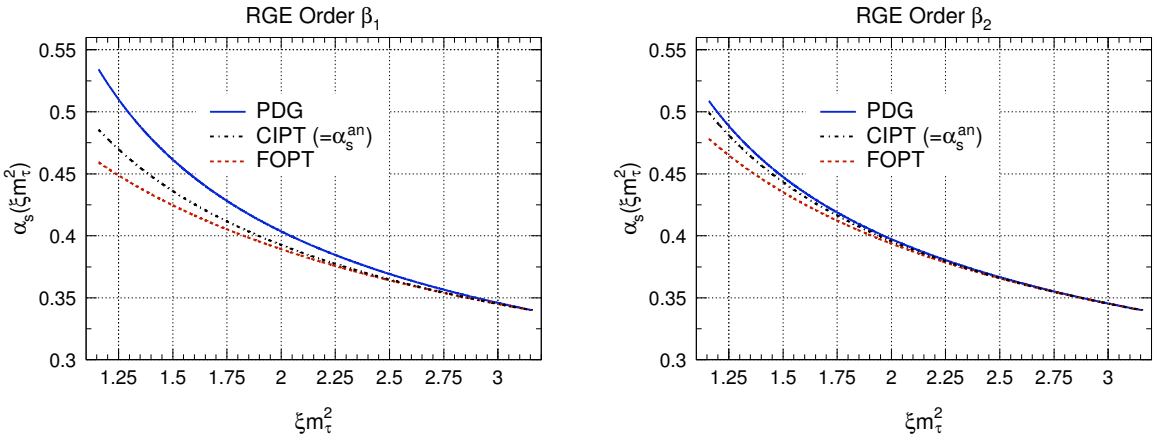

Figure 6.6: The evolution of $\alpha_S(s)$ to lower scales ξm_τ^2 using CIPT, FOPT, the analytical solution of the RGE ($\alpha_S^{an}(s)$) and the expansion in inverse powers of logarithms ($\alpha_S^{PDG}(s)$). These solutions were computed up to the order β_1 of the RGE (left), and β_2 (right).

In Fig. 6.6 we show a comparison of scale transformations performed with CIPT, FOPT and the two other RGE solutions described above. CIPT yields to the same result as the analytical solution, and the expansion in inverse powers of logarithms is closer to it than to FOPT. We should emphasize the fact that, on the contrary to CIPT, the FOPT solution is problematic even on the real axis, generally not satisfying to the RGE (it satisfies it only up to the degree of truncation, which numerically becomes an important issue).

Conclusions

The CIPT series is found to be better behaved than FOPT and is therefore to be preferred for the numerical analysis of the τ hadronic width. This preference is also

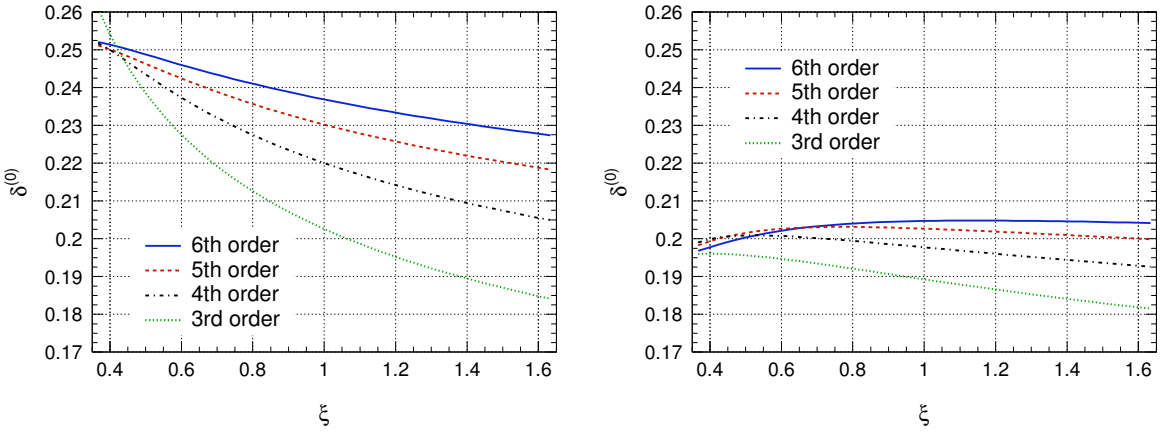

Figure 6.7: Scale dependence of $\delta^{(0)}$ in R_τ computed at the third to the estimated sixth order with FOPT (left) and CIPT (right).

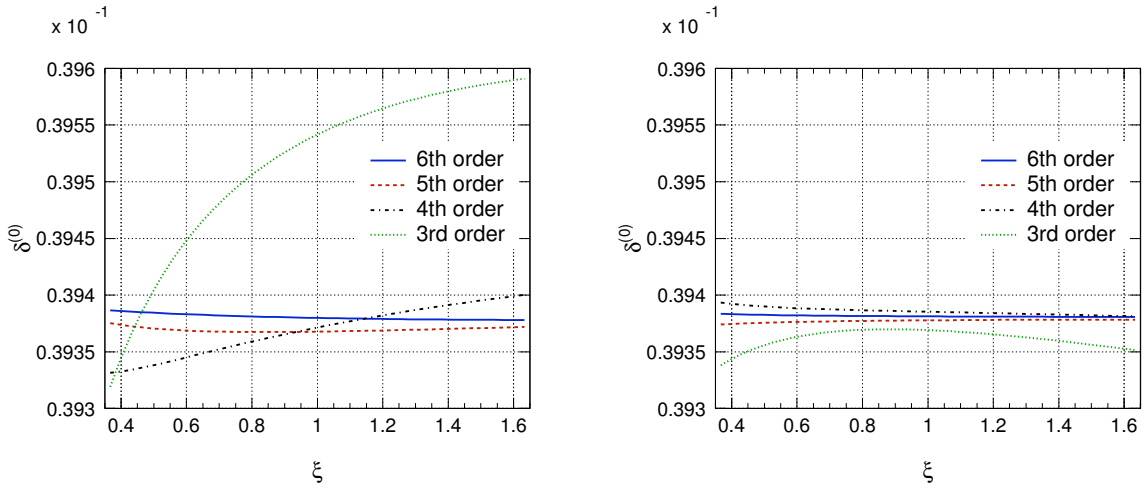

Figure 6.8: Scale dependence of $\delta^{(0)}$ in $R^{(5)}_{e^+e^-}(M_Z^2)$ computed at the third to the estimated sixth order with FOPT (left) and CIPT (right).

supported by the analysis of the integrand in the previous section, suggesting a pathological behaviour of FOPT for a_s near the branch cut. Our coarse extrapolation of the higher-order coefficients could indicate that minimal sensitivity is reached at $n \sim 5$ for FOPT, while the series further converges for CIPT. The uncertainties due to K_5 and K_6 are smaller for CIPT whereas the one due to the unknown value of β_4 is similar in both approaches. The difference in the result observed when using a Taylor expansion and truncating the perturbative series after integrating along the contour (FOPT) with the exact result at given order (CIPT) exemplifies the incompleteness of the perturbative series. The situation is even worse since, not only large known contributions are neglected in FOPT, but the series is also used in a domain where its convergence is not guaranteed: taking the difference between CIPT and FOPT as an estimate of the related systematic error overestimates the uncertainty due to the truncation of the perturbative series. In the line of this discussion, and following [122], we will not use this prescription to estimate

Table 6.2: Massless perturbative contributions to $\delta^{(0)}$ in $R^{(5)}_{e^+e^-}(M_Z^2)$ using FOPT and CIPT, respectively, and computed for $\alpha_S(M_Z^2) = 0.12$. The unknown higher-order $K_{5,6}$ and β_4 coefficients are estimated by assuming a geometric growth, while the others are set to 0. The quoted uncertainties δ stem from the indicated range of values for the unknown parameters and from the renormalisation scale.

Pert. Method	$n=1$	$n=2$	$n=3$	$n=4$	$(n=5)$	$(n=6)$	$\sum_{n=1}^{4}$	$\sum_{n=1}^{5}$	$\sum_{n=1}^{6}$
FOPT ($\xi=1$)	0.038197	0.002056	-0.000712	-0.000170	-0.000004	0.000012	0.039372	0.039368	0.039380
$\delta(\beta_4 \pm 100\%)$	0	0	0	0	0	0	0	0	0
$\delta(K_5 \pm 100\%)$	0	0	0	0	$\mp 10^{-5}$	0	0	$\mp 10^{-5}$	$\mp 10^{-5}$
$\delta(K_6 \pm 100\%)$	0	0	0	0	0	$\pm 5 \cdot 10^{-6}$	0	0	$\pm 5 \cdot 10^{-6}$
$\delta(\xi \pm 0.63)$	–	–	–	–	–	–	$^{+29}_{-40} \cdot 10^{-6}$	$^{+7.4}_{-0.3} \cdot 10^{-6}$	$^{+6.7}_{-1.9} \cdot 10^{-6}$
CIPT ($\xi=1$)	0.037462	0.001941	-0.000034	0.000016	-0.000008	0.000003	0.039385	0.039378	0.039381
$\delta(\beta_4 \pm 100\%)$	$< 10^{-6}$	≈ 0	≈ 0	≈ 0	≈ 0	≈ 0	$< 10^{-6}$	$< 10^{-6}$	$< 10^{-6}$
$\delta(K_5 \pm 100\%)$	0	0	0	0	$\mp 8 \cdot 10^{-6}$	0	0	$\mp 8 \cdot 10^{-6}$	$\mp 8 \cdot 10^{-6}$
$\delta(K_6 \pm 100\%)$	0	0	0	0	0	$\pm 3 \cdot 10^{-6}$	0	0	$\pm 3 \cdot 10^{-6}$
$\delta(\xi \pm 0.63)$	–	–	–	–	–	–	$^{+8.2}_{-4.1} \cdot 10^{-6}$	$^{+0.6}_{-3.7} \cdot 10^{-6}$	$^{+2.3}_{-0.5} \cdot 10^{-6}$

the systematic error on the truncation of the series, and we will limit the analysis to the uncertainties coming from the study of CIPT only.

The discrepancies found between FOPT and CIPT at $|s| = m_\tau^2$ are reduced drastically when computing $R^{(5)}_{e^+e^-}(M_Z^2)$ (see Fig. 6.8 and Table 6.2). The small value of $\alpha_S(M_Z^2)$ ensures a much better convergence of the perturbative series. The better convergence also leads to a tiny scale dependence, which is even smaller for CIPT than for FOPT, and hence to small theoretical uncertainties.

6.2.3 Quark-Mass and Nonperturbative Contributions

Following SVZ [160], the first contribution to R_τ beyond the $D=0$ perturbative expansion is the non-dynamical quark-mass correction of dimension $D=2$, *i.e.*, corrections scaling like $1/m_\tau^2$. The leading $D=2$ corrections induced by the light-quark masses are computed using the running quark masses evaluated at the two-loop level (denoted $\overline{m}$ in the following). The evaluation of the contour integral in FOPT [125] leads to terms $\delta^{(2,m_q)}_{ud,V/A} \propto \overline{m}^2_{u,d}(m_\tau^2)/m_\tau^2$, $\overline{m}_u(m_\tau^2)\overline{m}_d(m_\tau^2)/m_\tau^2$, which are small.

The dimension $D=4$ operators have dynamical contributions from the gluon condensate $\langle a_s GG\rangle$ and the light u,d quark condensates $\langle m_i q_i q_i\rangle$ (see Fig. 6.9, left and middle), which are the vacuum expectation values of the gluon field strength-squared and of the scalar quark densities, respectively. The remaining $D=4$ operators involve the running quark masses to the fourth power. Solving the contour integral [125] results in terms $\delta^{(4)}_{ud,V/A} \propto \alpha_S^2(m_\tau^2)\langle a_s GG\rangle/m_\tau^4$, $\langle m_q\overline{q}q\rangle/m_\tau^4$, $\mathcal{O}_4(\overline{m}_q^4/m_\tau^4)$, where remarkably the contribution from the gluon condensate vanishes at the first order in $\alpha_S(m_\tau^2)$.

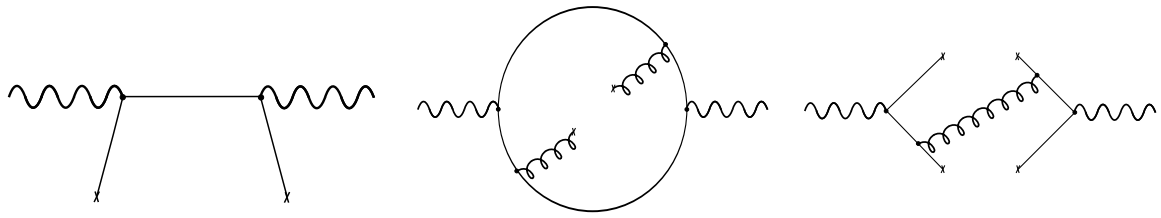

Figure 6.9: Examples of lowest order graphs giving rise to the operators: $m\overline{q}q$ (left), GG (middle) and $\overline{q}\Gamma q\overline{q}\Gamma q$ (right).

The contributions from dimension $D = 6$ operators are more delicate to analyse. The most important operators arise from four-quark terms of the form $\overline{q}_i\Gamma_1 q_j\overline{q}_k\Gamma_2 q_l$ (see Fig. 6.9, right). We neglect other operators, such as the triple gluon condensate whose Wilson coefficient vanishes at order α_s, or those which are suppressed by powers of quark masses, in the evaluation of the contour integrals performed in [125]. The large number of independent operators of the four-quark type occurring in the $D = 6$ term can be reduced by means of the *vacuum saturation* assumption [160]. The operators are then expressed as products of (two-)quark condensates $\alpha_s(\mu)\langle\overline{q}_i q_i(\mu)\rangle\langle\overline{q}_j q_j(\mu)\rangle$. Since the scale dependence of the four-quark and two-quark operators are different, such factorisation can hold for a specific value of the renormalisation scale (at best, as it is not even clear that the scale should be the same for all the different 4-quark operators). To take into account this problem as well as likely deviations from the vacuum saturation assumption, one can introduce an effective parameter ρ (in principle scale-dependent) to replace the four-quark contribution by $\rho\alpha_s\langle\overline{q}q\rangle^2$. The effective $D = 6$ term obtained in this way is [125] $\delta^{(6)}_{ud,V/A} \propto \rho\alpha_s\langle\overline{q}q\rangle^2/m_\tau^6$, with a relative factor of $-7/11$ between vector and axial vector contributions.

The $D = 8$ contribution has a structure of non-trivial quark-quark, quark-gluon and four-gluon condensates whose explicit form is given in [179]. For the theoretical prediction of R_τ it is customary to absorb the whole long- and short-distance parts into the scale invariant phenomenological $D = 8$ operator $\langle\mathcal{O}_8\rangle$, which is fit simultaneously with α_s and the other unknown nonperturbative operators. Higher-order contributions from $D \geq 10$ operators to R_τ are expected to be small since, like in the case of the gluon condensate, constant terms and terms in leading order in α_s vanish after integrating over the contour. We will not consider these terms in the following.

6.2.4 Impact of Quark-Hadron Duality Violation

A matter of concern for the QCD analysis at the τ mass scale is the reliability of the theoretical description, *i.e.*, the use of the OPE to organise the perturbative and nonperturbative expansions, and the control of unknown higher-order terms in these series. A reasonable stability test consists in varying m_τ continuously to lower values $\sqrt{s_0} \leq m_\tau$ for both theoretical prediction and measurement, which is possible since the shape of the full τ spectral function is available. This test was successfully carried out [122, 146, 159] and

confirmed the validity of the approach down to $s_0 \sim 1$ GeV^2 with an accuracy of 1–2%. In this section, we consider a different test of the sensitivity of the analysis to possible OPE violations.

The SVZ expansion provides a description of the correlator Π (or of the Adler function D) for values of the incoming momentum in the deep Euclidean region, based on the separation between large and soft momenta flowing through the diagrams associated to this correlator. If the OPE description were accurate, we could check the cogency of this description by performing an analytic continuation of the OPE to any value of the momentum in the physical region and comparing it with the spectral functions in Fig. 6.2. As seen from these figures, perturbative QCD describes the asymptotic behaviour of the functions, but fails to reproduce their details.

The OPE suffers from a similar failure as can be expected from the intrinsic nature of the OPE procedure [160–164]: it only yields a truncated expansion in the first powers of $1/Q$, *i.e.*, the singularities near $x = 0$ of $\Pi^{\mu\nu}$ (*cf.* Eq. (6.3)). Therefore, it misses singularities for finite x^2 or $x^2 \to \infty$ related to long-distance effects. Even a large momentum q flowing through the vacuum polarization diagrams may be split into a soft quark-antiquark pair and soft gluons: this physical possibility cannot be properly described by OPE, since no separation can be performed between hard and soft physics in such a situation. One expects for some of these effects to yield terms proportional to $\exp(-\lambda Q)/Q^k$ or $\exp(-\lambda^2 Q^2)/Q^\ell$ (where k, ℓ are positive and λ is a typical hadronic distance), which are exponentially suppressed in the deep Euclidean region and thus absent in the truncated OPE series. But once these terms are continued analytically along the branch cut, they generate a (power suppressed or exponentially suppressed) oscillatory behaviour of the spectral function, which is similar to the one in Fig. 6.2. Such a behaviour is generally called "violation of local quark-hadron duality".

To determine R_τ, we compute the convolution of the OPE expression of the Adler function with a kernel along the circle of radius s_0. We know that duality violation will have a small impact for the two regions close to the real axis (these terms are exponentially suppressed in the Euclidean region, and the kernel vanishes for $s = s_0$). But to assess the systematic uncertainties related to the use of OPE, it is instructive — even if very approximate — to simulate the contributions of duality violating terms on the rest of the circle. For this purpose, we use two different models proposed in [163], which provide a coarse and rather qualitative description of such effects (one of these models has been very recently reconsidered in [165] to investigate duality-violating effects on the determination of nonperturbative condensates from ALEPH data in the vector channel). In both cases, one does not aim at a complete description of the correlator Π, but focuses on the deviation between the full description and its truncated OPE expansion $\Delta\Pi = \Pi - \Pi^{\rm OPE}$. In the first model ($I$) the quarks propagate in an instanton background field with a fixed size ρ, leading to the duality violation

$$\Delta\Pi^{(I)}(Q) = \frac{C_I}{Q^2} K_1(Q\rho) K_{-1}(Q\rho)\,, \tag{6.32}$$

where the $K_{(-)1}$ are modified Bessel functions of the second kind. The second model (II) mimics a comb of resonances with a width that grows with the energy, so that they

overlap progressively when the energy increases

$$\Pi^{(II)}(Q) = -\frac{1}{4\pi^2}\frac{1}{1-B/3\pi}\left(\psi(z)+\frac{1}{z}\right). \tag{6.33}$$

Here $\psi(z)$ is the di-gamma function, and $z = (Q^2/\sigma^2)^{1-B/3\pi}$, where σ parametrises the offset between the resonances, and B their (growing) widths. In this model, one can define $\Pi^{\rm OPE}$ as the expansion in powers of $1/z$ (up to z^4 here, since we neglect operators of $D = 10$ and beyond). Duality violations are encoded in $\Delta\Pi^{(II)} = C_{II}(\Pi - \Pi^{\rm OPE})^{(II)}$. The factors $C_{I,II}$ are normalisation constants.

One can check that the two models share the same features: they are exponentially suppressed in the Euclidean region, and exhibit a branch cut for time-like values of s, such that they contribute to the spectral functions with oscillations decreasing in amplitude when the energy increases. They differ by the dependence of their oscillation frequency on the energy: the instanton model oscillates like $\sin(\sqrt{s}\rho)$, while the resonance model varies like $\sin(s/\sigma)$.

To investigate the numerical impact of quark-duality violation on our results, we vary for each model the parameters and fix the normalisation such that the imaginary part of sum of the perturbative QCD computation and of the duality-violating terms match smoothly the $V+A$ spectral function near $s = m_\tau^2$. We then compute the contribution of the duality-violating part to $\delta^{(0)}$ by performing the contour integral (6.19). For the instanton model we asymptotically reproduce the data for ρ values between 2.4 and 4.4 GeV^{-1}, leading to a contribution to $\delta^{(0)}$ below $4.5\cdot10^{-3}$. For the resonance model we find values for σ^2 between 1.65 and 2 GeV^2, and B between 0.3 and 0.6, leading to a contribution to $\delta^{(0)}$ below $7\cdot10^{-4}$. These limits are however quite conservative because the models used exhibit significant oscillations in the $V+A$ spectral function. Although allowed by the ALEPH data because of the larger error bars close to the m_τ^2 endpoint, such oscillations are disfavored by the overall pattern of the spectral function, with oscillation amplitudes that are strongly suppressed above 1 GeV. Even though these two models could be improved in many ways, it is hard to see how their contributions to $\delta^{(0)}$ could be enhanced by an order of magnitude such that they would invalidate the OPE approach. At least in the case of the $V+A$ spectral function, we therefore expect the violation of quark-hadron duality to have a negligible impact on our results. In the next section, we will see that the induced error on $\delta^{(0)}$ remains well within the systematic uncertainties coming from other sources.

In Ref. [165], larger contributions from DV were estimated, using a model inspired by resonance saturation and fitting it to data. However, the result of that fit shows a possible pathology, as it has almost no exponential damping at large s. Actually, one must choose a specific mass window when performing the fit on the τ data, and e^+e^- data at higher s are not enough precise to improve the accuracy.

6.3 Combined Fit

Apart from the perturbative term, the full OPE contains contributions of nonperturbative nature parametrised by higher-dimensional operators, whose value cannot be computed from first principles. It was shown in [126] that one can exploit the shape of the spectral functions via weighted integrals to obtain additional constraints on $\alpha_s(m_\tau^2)$ and — more importantly — on the nonperturbative power terms.

6.3.1 Spectral Moments

The τ *spectral moments* at $s_0 = m_\tau^2$ are defined by

$$R_{\tau,V/A}^{k\ell} = \int_0^{m_\tau^2} ds \, \left(1 - \frac{s}{m_\tau^2}\right)^k \left(\frac{s}{m_\tau^2}\right)^\ell \frac{dR_{\tau,V/A}}{ds} \,, \tag{6.34}$$

where $R_{\tau,V/A}^{00} = R_{\tau,V/A}$. Using the same argument of analyticity as for R_τ, one can reexpress (6.34) as a contour integral along the circle $|s| = s_0$. The factor $(1 - s/m_\tau^2)^k$ suppresses the integrand at $s = m_\tau^2$ where the validity of the OPE is less certain and the experimental accuracy is statistically limited. Its counterpart $(s/m_\tau^2)^\ell$ projects upon higher energies. The spectral information is used to fit simultaneously $\alpha_s(m_\tau^2)$ and the leading $D = 4, 6, 8$ nonperturbative contributions. Due to the intrinsic experimental correlations (all spectral moments rely on the same spectral function) only four moments are used as input to the fit.

In analogy to R_τ (6.17), the contributions to the moments originating from perturbative QCD and nonperturbative OPE terms are separated. The prediction of the perturbative contribution takes the form

$$\delta^{(0,k\ell)} = \sum_{n=1}^{\infty} \tilde{K}_n(\xi) A^{(n,k\ell)}(a_s) \,, \tag{6.35}$$

with the functions [122]

$$\begin{aligned} A^{(n,k\ell)}(a_s) \;=\; & \frac{1}{2\pi i} \oint\limits_{|s|=m_\tau^2} \frac{ds}{s} \Bigg[2\Gamma(3+k) \left(\frac{\Gamma(1+\ell)}{\Gamma(4+k+\ell)} + 2 \frac{\Gamma(2+\ell)}{\Gamma(5+k+\ell)} \right) \\ & - I\left(\frac{s}{s_0}, 1+\ell, 3+k\right) - 2I\left(\frac{s}{s_0}, 2+\ell, 3+k\right) \Bigg] a_s^n(-\xi s) \,, \end{aligned} \tag{6.36}$$

which make use of the elementary integrals $I(\gamma, a, b) = \int_0^\gamma t^{a-1}(1-t)^{b-1} dt$. The contour integrals are numerically solved for the running $a_s(-\xi s)$ using the CIPT prescription.

In the chiral limit and neglecting the small logarithmic s dependence of the Wilson coefficients, the dimension D nonperturbative contributions $\delta_{ud,V/A}^{(D,k\ell)}$ to the spectral

moments simplify greatly (*cf.* matrix (133) in [122]). One finds that with increasing weight ℓ the contributions from low dimensional operators vanish. For example, the only nonperturbative contribution to the moment $R^{13}_{\tau,V/A}$ stems from dimension $D = 8$ and beyond (neglected). In Ref. [199] it was pointed out that, when using these weights, the determination of α_s could be sensitive to higher order contributions (in particular for the last moment). Other weights could indeed improve the situations here, by taming those contributions and thus reducing the uncertainty from higher dimension condensates neglected in the fit. We will come back later to the discussion of the particular weights proposed in Ref. [199].

For practical purpose it is more convenient to define moments that are normalised to the corresponding $R_{\tau,V/A}$ to decouple the normalisation from the shape of the τ spectral functions,

$$D^{k\ell}_{\tau,V/A} = \frac{R^{k\ell}_{\tau,V/A}}{R_{\tau,V/A}} \; . \tag{6.37}$$

The two sets of experimentally almost uncorrelated observables — $R_{\tau,V/A}$ on one hand, and the moments $D^{k\ell}_{\tau,V/A}$ on the other hand — yield independent constraints on $\alpha_s(m^2_\tau)$ and thus provide an important test of consistency. The correlation between these observables is negligible in the $V + A$ case where $R_{\tau,V+A}$ is calculated from the difference $R_\tau - R_{\tau,S}$, which is independent of the hadronic invariant mass spectrum. One experimentally obtains the $D^{k\ell}_{\tau,V/A}$ by integrating weighted normalised invariant mass-squared spectra. The corresponding theoretical predictions are easily adapted.

The measured V, A and $(V+A)$ spectral moments and their linear correlations matrices are given in Tables 6.3 and 6.4, respectively. Also shown are the central values of the theory prediction after fit convergence (*cf.* Sec. 6.3.2). The correlations between the moments are computed analytically from the contraction of the derivatives of two involved moments with the covariance matrices of the respective normalised invariant mass-squared spectra. In all cases, the negative sign for the correlations between the $k = 1, \ell = 0$ and the $k = 1, \ell \geq 1$ moments is due to the ρ (V) and the π, a_1 (A) peaks, which determine the major part of the $k = 1, \ell = 0$ moments. They are less prominent for higher moments and consequently the amount of negative correlation increases with $\ell = 1, 2, 3$. This also explains the large and increasing positive correlations between the $k = 1, \ell \geq 1$ moments, in which, with growing ℓ, the high energy tail is emphasised more than the low energy peaks. The total errors for the $(V + A)$ case are dominated by the uncertainties on the hadronic branching fractions.

6.3.2 Fit Results

Along the line of the previous analyses from ALEPH [122, 144, 159, 180], CLEO [145], and OPAL [146], we simultaneously determine $\alpha_s(m^2_\tau)$, the gluon condensate, and the effective $D = 6, 8$ nonperturbative operators from a combined fit to R_τ and the spectral moments $D^{k\ell}_{\tau,V/A}$ with $k = 1$, $\ell = 0, 1, 2, 3$, taking into account the strong experimental and theoretical correlations between them.

The fit minimises the χ^2 of the differences between measured and predicted quantities contracted with the inverse of the sum of the experimental and theoretical covariance matrices. The theoretical uncertainties include separate variations of the unknown higher-order coefficient K_5, for which the value/error $K_5 = K_4(K_4/K_3) \approx 378 \pm 378$ has been used, and of the renormalisation scale. The latter quantity has been varied within the range $m_\tau^2 \pm 2$ GeV^2 (corresponding to $\xi = 1 \pm 0.63$), and the maximum variations of the observables found within this interval are assigned as systematic uncertainties (*cf.* Sec. 6.2.2). To avoid double counting of errors the estimated K_5 term has been fixed when varying ξ. The corresponding systematic errors for $\alpha_s(m_\tau^2)$ are 0.0062 (K_5) and $^{+0.0007}_{-0.0040}$ (ξ). The errors induced by the uncertainties on $S_{\rm EW}$ and $|V_{ud}|$ amount to 0.0007 and 0.0005, respectively. With these inputs, the massless perturbative contribution $\delta^{(0)}$ is fully defined, and the parameter $\alpha_s(m_\tau^2)$ can be determined by the fit.

Table 6.5 summarises the results for the V, A and $V+A$ combined fits using CIPT. The $\delta^{(2)}$ term is not determined by the fit, but is fixed from a theoretical input on the light quark masses varied within their errors [122]. The quark condensates in the $\delta^{(4)}$ term are obtained from partial conservation of the axial-vector current (PCAC), while the gluon condensate is determined by the fit, as are the higher-dimensional operators $\langle\mathcal{O}_6\rangle_{V/A}$and $\langle\mathcal{O}_8\rangle_{V/A}$.

The advantage of separating the vector and axial-vector channels and comparing to the inclusive $V+A$ fit becomes obvious in the adjustment of the leading nonperturbative contributions of $D=6$ and $D=8$, which have different signs for V and A and are thus suppressed in the inclusive sum. The total nonperturbative contribution, $\delta_{\rm NP} = \delta^{(4)} + \delta^{(6)} + \delta^{(8)}$, from the $V+A$ fit, although non-zero, is significantly smaller than the corresponding values from the V and A fits, hence increasing the confidence in the $\alpha_s(m_\tau^2)$ determination from inclusive $V+A$ observables.

There is a remarkable agreement within statistical errors between the $\alpha_s(m_\tau^2)$ determinations using the vector and axial-vector data, with $\alpha_s^{(V)}(m_\tau^2) - \alpha_s^{(A)}(m_\tau^2) = 0.013 \pm 0.013$, where the error takes into account the anticorrelation in the experimental separation of the V and A modes. This result provides an important consistency check since the two corresponding spectral functions are experimentally almost independent, they manifest a quite different resonant behaviour, and their fits yield relatively large nonperturbative contributions compared to the $V+A$ case. Contrary to the vector case, the axial-vector fit has a poor χ^2 value originating from a discrepancy between data and theory for the $\ell = 0, 1$ normalised moments (*cf.* Table 6.3). Although the origin of this discrepancy is unclear, it may indicate a shortcoming of the OPE in form of noticeable inclusive duality violation in this channel. The observed systematic effect on the $\alpha_s(m_\tau^2)$ determination in this mode appears however to be within errors. From the fit to the $V+A$ τ spectral function, we obtain

$$\alpha_s(m_\tau^2) \;=\; 0.344 \pm 0.005 \pm 0.007 \;, \tag{6.38}$$

where the two errors are experimental and theoretical. The values of the gluon condensate obtained in the V, A, and $V+A$ fits are not very stable. Despite the apparent significance of the result for $V+A$, we prefer to enlarge the error taking into account the discrepancies

between the V/A results. We find for the combined value $\langle a_s GG\rangle = (-1.5 \pm 0.8) \cdot 10^{-2}$ GeV^4, which is at variance with the usual values quoted in the applications of SVZ sum rules. We note however that not much is known from theoretical grounds about the value of the gluon condensate [178].

The result (6.38) can be compared with the recent determination [127], $\alpha_s(m_\tau^2) = 0.332 \pm 0.005 \pm 0.015$, also at N^{3}LO, but using as experimental input only $R_{\tau,V+A}$, and not including the new information given in Sec. 6.1. Another major difference with our analysis is that both perturbative procedures, FOPT and CIPT, are considered on equal footing, and their results are averaged. This leads to the lower value for $\alpha_s(m_\tau^2)$ and to an inflated theoretical error including half of the discrepancy between the two prescriptions.

The evolution of the value (6.38) to M_Z^2, using Runge-Kutta integration of the four-loop β-function [172], and using three-loop quark-flavour matching [183, 185–187], gives

$$\begin{aligned} \alpha_s^{(\tau)}(M_Z^2) &= 0.1212 \pm 0.0005 \pm 0.0008 \pm 0.0005\,, \\ &= 0.1212 \pm 0.0011\,. \end{aligned} \tag{6.39}$$

The first two errors in the upper line are propagated from the $\alpha_s(m_\tau^2)$ determination, and the last error summarises uncertainties in the evolution.[11] All errors have been added in quadrature for the second line. The result (6.39) is a determination of the strong coupling at the Z-mass scale with a precision of 0.9%, unattained by any other $\alpha_s(M_Z^2)$ measurement. The evolution path of $\alpha_s(m_\tau^2)$ is shown in the upper plot of Fig. 6.10 (the two discontinuities are due to the chosen quark-flavour matching scale of $\mu = 2\overline{m}_q$). The evolution is compared in this plot with other α_s determinations compiled in [181] (we also included [184]), and with new NNLO measurements based on hadronic event shapes from e^+e^- annihilation covering the energy range between 91.2 and 206 GeV [182].

The theoretically most robust precision determination of α_s stems from the global fit to electroweak data at the Z-mass scale. As for $\alpha_s(m_\tau^2)$, this determination benefits from the computation of the N^{3}LO coefficient K_4 occurring in the radiator functions that predict the vector and axial-vector hadronic widths of the Z (and also in the prediction of the total W width). We use the newly developed *Gfitter* package [188] for the fit, and obtain

$$\alpha_s^{(Z)}(M_Z^2) = 0.1191 \pm 0.0027 \pm 0.0001\,. \tag{6.40}$$

The value and first error represents the fit result, and the second error is due to the truncation of the perturbative series. It is estimated similarly to the τ case by adding a fifth-order term proportional to K_5, estimated by $K_4(K_4/K_3)$, to the massless part, and a fourth-order term (estimated accordingly), containing large logarithms $\ln(\overline{m}_t/M_Z)$, to the massive part. We also vary the renormalisation scale of the massless contribution

[11] The evolution error [122] receives contributions from the uncertainties in the c-quark mass (0.00020, $\overline{m}_c$ varied by ± 0.1 GeV) and the b-quark mass (0.00005, $\overline{m}_b$ varied by ± 0.1 GeV), the matching scale (0.00023, μ varied between $0.7\,\overline{m}_q$ and $3.0\,\overline{m}_q$), the three-loop truncation in the matching expansion (0.00026) and the four-loop truncation in the RGE equation (0.00031), where we used for the last two errors the size of the highest known perturbative term as systematic uncertainty. These errors have been added in quadrature.

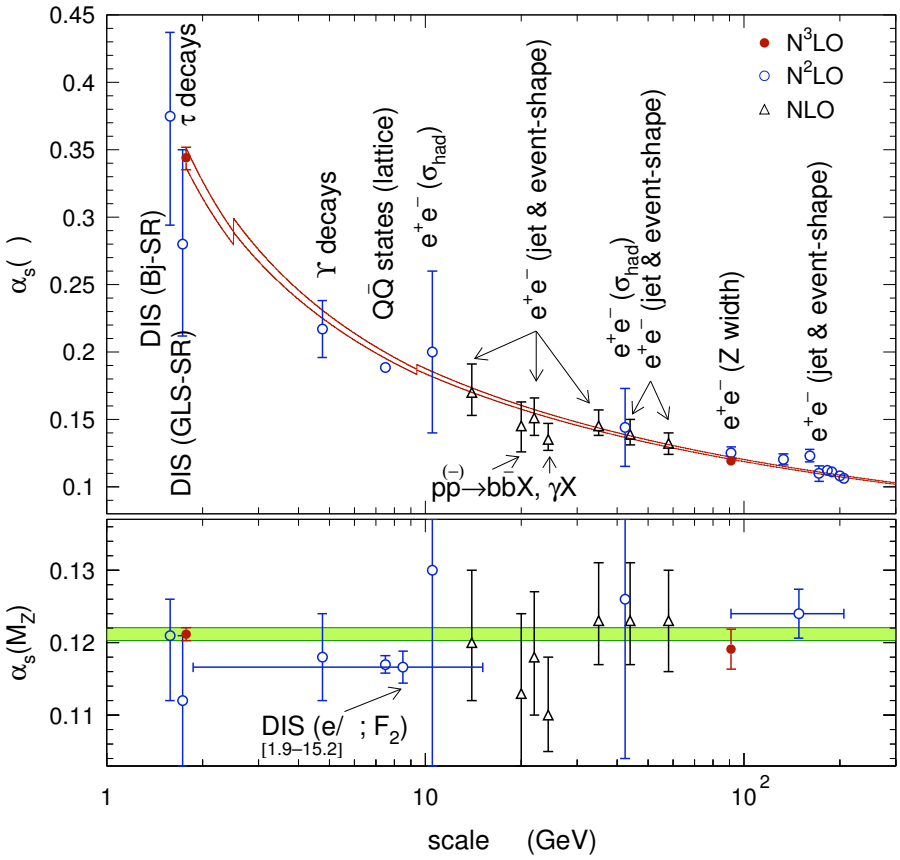

Figure 6.10: Top: The evolution of $\alpha_S(m_\tau^2)$ to higher scales μ using the four-loop RGE and the three-loop matching conditions applied at the heavy quark-pair thresholds (hence the discontinuities at $2\overline{m}_c$ and $2\overline{m}_b$). The evolution is compared with independent measurements (taken from the compilation [181], and including the recent measurements [182, 184]) covering μ scales that vary over more than two orders magnitude. Bottom: The corresponding α_S values evolved to M_Z. The shaded band displays the τ decay result within errors.

within the interval $\xi = 1 \pm 0.63$, assuming the fifth order coefficient to be known. The result (6.40) agrees with the finding of Ref. [127].

The τ-based result (6.39) appears now twice more accurate than the determination from the Z width. Yet the errors are very different in nature with a τ value dominated by theoretical uncertainties, whereas the determination at the Z resonance, benefiting from the much larger energy scale and the correspondingly small uncertainties from the truncated perturbative expansion, is limited by the experimental precision of the electroweak observables. The consistency between the two results, $\alpha_S^{(\tau)}(M_Z^2) - \alpha_S^{(Z)}(M_Z^2) = 0.0021 \pm 0.0029$, provides the most powerful present test of the evolution of the strong interaction coupling as it is predicted by the nonabelian nature of QCD over a range of s spanning more than three orders of magnitude. The $\alpha_S^{(\tau)}(M_Z^2)$ determination agrees with the average of the three currently most precise full NN(N)LO measurements (deep inelastic scattering [181, 189], ALEPH event shapes between 91 and 206 GeV [182], and global electroweak fit at M_Z), yielding an average of 0.1189 ± 0.0015 (0.1204 ± 0.0009)

when not including (including) the τ result, which is justifiably assuming uncorrelated errors. The τ-based result differs at the 2.5σ level from the value 0.1170 ± 0.0012 found in lattice QCD calculations with input from the mass splitting of the Υ resonances [190]. The average of all five values reduces the discrepancy to 2.1σ (χ^2 probability of 0.04).

Table 6.3: Experimental ($D^{1\ell}_{\tau,V/A}$) and theoretical ($D^{1\ell\,(\mathrm{theo})}_{\tau,V/A}$, obtained after fit convergence, *cf.* Sec. 6.3.2) spectral moments of inclusive vector (V), axial-vector (A) and vector plus axial-vector ($V+A$) hadronic τ decays. The errors $\Delta^{\exp} D^{1\ell}_{\tau,V/A}$ summarise statistical and systematic uncertainties.

	$\ell = 0$	$\ell = 1$	$\ell = 2$	$\ell = 3$
$D^{1\ell}_{\tau,V}$	0.71668	0.16930	0.05317	0.02254
$D^{1\ell\,(\mathrm{theo})}_{\tau,V}$	0.71568	0.16971	0.05327	0.02265
$\Delta^{\exp} D^{1\ell}_{\tau,V}$	0.00250	0.00043	0.00054	0.00041
$D^{1\ell}_{\tau,A}$	0.71011	0.14903	0.06586	0.03183
$D^{1\ell\,(\mathrm{theo})}_{\tau,A}$	0.71660	0.14571	0.06574	0.03130
$\Delta^{\exp} D^{1\ell}_{\tau,A}$	0.00182	0.00063	0.00036	0.00025
$D^{1\ell}_{\tau,V+A}$	0.71348	0.15942	0.05936	0.02707
$D^{1\ell\,(\mathrm{theo})}_{\tau,V+A}$	0.71668	0.15767	0.05926	0.02681
$\Delta^{\exp} D^{1\ell}_{\tau,V+A}$	0.00159	0.00037	0.00033	0.00025

Table 6.4: Experimental correlations between the moments $D^{k\ell}_{\tau,V/A/V+A}$. Correlations between $R_{\tau,V+A}$, determined from the leptonic τ branching fractions, and the corresponding moments are negligible.

	$D^{10}_{\tau,V}$	$D^{11}_{\tau,V}$	$D^{12}_{\tau,V}$	$D^{13}_{\tau,V}$
$R_{\tau,V}$	−0.287	0.153	0.274	0.302
$D^{10}_{\tau,V}$	1	−0.821	−0.981	−0.993
$D^{11}_{\tau,V}$	–	1	0.899	0.824
$D^{12}_{\tau,V}$	–	–	1	0.988

	$D^{10}_{\tau,A}$	$D^{11}_{\tau,A}$	$D^{12}_{\tau,A}$	$D^{13}_{\tau,A}$
$R_{\tau,A}$	−0.255	0.013	0.178	0.272
$D^{10}_{\tau,A}$	1	−0.746	−0.963	−0.978
$D^{11}_{\tau,A}$	–	1	0.866	0.646
$D^{12}_{\tau,A}$	–	–	1	0.938

	$D^{11}_{\tau,V+A}$	$D^{12}_{\tau,V+A}$	$D^{13}_{\tau,V+A}$
$D^{10}_{\tau,V+A}$	−0.722	−0.974	−0.987
$D^{11}_{\tau,V+A}$	1	0.801	0.662
$D^{12}_{\tau,V+A}$	–	1	0.975

Table 6.5: Fit results for $\alpha_s(m_\tau^2)$ and the nonperturbative contributions for vector, axial-vector and $V + A$ combined fits using the corresponding experimental hadronic widths and spectral moments as input parameters, and using the CIPT prescription for the perturbative prediction. Where two errors are given the first is experimental and the second theoretical. The $\delta^{(2)}$ term comes from theoretical input on the light quark masses varied within their allowed ranges (see text). The quark condensates in the $\delta^{(4)}$ term are obtained from PCAC, while the gluon condensate is determined by the fit. The total nonperturbative contribution is the sum $\delta_{\rm NP} = \delta^{(4)} + \delta^{(6)} + \delta^{(8)}$.

Parameter	Vector (V)	Axial-Vector (A)	$V + A$
$\alpha_s(m_\tau^2)$	$0.3474 \pm 0.0074^{+0.0063}_{-0.0074}$	$0.3345 \pm 0.0078^{+0.0063}_{-0.0074}$	$0.3440 \pm 0.0046^{+0.0063}_{-0.0074}$
$\delta^{(0)}$	0.2093 ± 0.0080	0.1988 ± 0.0087	0.2066 ± 0.0070
$\delta^{(2)}$	$(-3.2 \pm 3.0) \cdot 10^{-4}$	$(-5.1 \pm 3.0) \cdot 10^{-4}$	$(-4.3 \pm 2.0) \cdot 10^{-4}$
$\langle a_s GG \rangle$ (GeV^4)	$(-0.8 \pm 0.4) \cdot 10^{-2}$	$(-2.2 \pm 0.4) \cdot 10^{-2}$	$(-1.5 \pm 0.3) \cdot 10^{-2}$
$\delta^{(4)}$	$(0.1 \pm 1.5) \cdot 10^{-4}$	$(-5.9 \pm 0.1) \cdot 10^{-3}$	$(-3.0 \pm 0.1) \cdot 10^{-3}$
$\delta^{(6)}$	$(2.68 \pm 0.20) \cdot 10^{-2}$	$(-3.46 \pm 0.21) \cdot 10^{-2}$	$(-3.7 \pm 1.7) \cdot 10^{-3}$
$\delta^{(8)}$	$(-8.0 \pm 0.5) \cdot 10^{-3}$	$(9.5 \pm 0.5) \cdot 10^{-3}$	$(8.1 \pm 3.6) \cdot 10^{-4}$
Total $\delta_{\rm NP}$	$(1.89 \pm 0.25) \cdot 10^{-2}$	$(-3.11 \pm 0.16) \cdot 10^{-2}$	$(-5.9 \pm 1.4) \cdot 10^{-3}$
χ^2/DF	0.07	3.57	0.90

6.4 A Study on Renormalon Models for the Determination of $\alpha_s(M_\tau)$

Several studies have been performed to determine which of the two perturbative methods, CIPT or FOPT, (if any) is to be preferred. A first ("internal") way of dealing with this issue consists in comparing the two methods to determine if one has a more regular and stable behaviour than the other, proving thus its robustness. For instance, in Sec. 6.2.2, our current knowledge of the perturbative series for the Adler function led us to conclude that CIPT showed a much better stability than FOPT as far as the dependence of the scale defining the integration contour is concerned, and that the FOPT integrand showed a pathological behaviour once one gets close to the end of the integration circle $s = M_\tau^2$. In Ref. [191], a similar study was performed, where the reference point for the Taylor expansion of the coupling constant used in FOPT was varied on a circle of radius M_τ in the complex energy plane, hinting at a strong dependence of the FOPT value due to a large impact of logarithmic corrections in the Taylor expansion. However, let us stress that these conclusions rely on the determination of α_s at a reference point in the complex plane by iterating the RGE step by step along the contour of integration (in a similar way to the CIPT method), and thus use a "non-canonical" version of FOPT including elements of the CIPT philosophy. A model for higher orders in the perturbative expansion of the Adler function [192] suggested that FOPT could actually oscillate towards the (more stable) CIPT value once higher-order are included.

One can also opt for a different ("external") approach, where the true value of the Adler function and its perturbative expansion are assumed to be known. One can then determine if the true value of the integral is approached by one of the two methods when one starts increasing the accuracy of the perturbative expansion (before the series becomes asymptotic). A particular model was proposed more recently in Ref. [193], based on renormalon calculus [154,157,194,195]. Renormalons are higher order contributions to the perturbative series, obtained for example by the insertion of fermion-loop chains into a fermion-antifermion vacuum-polarization diagram (see Fig. 6.11). The first observation

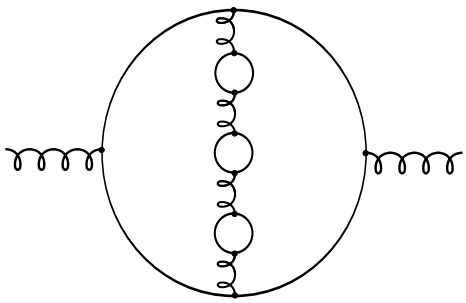

Figure 6.11: Multifermion loop insertion (renormalons) into a fermion-antifermion vacuum-polarization diagram.

consists in the fact that perturbative series like

$$D(Q^2) = \frac{N_c}{12\pi^2}\left(1 + \sum_{n=1}^{\infty} c_{n,1} a_Q^n\right) = \frac{N_c}{12\pi^2}\left(1 + \hat{D}(a_Q)\right), \qquad a_Q = \alpha_s(Q)/\pi \tag{6.41}$$

are at best asymptotic ones, with a zero convergence radius in a_Q. Actually, the number of Feynman graphs increases at each order and one expects a factorial growth of the perturbative coefficients $c_{n,1}$. Furthermore, the divergent behaviour of the perturbative expansion has physical significance, being related to the nonperturbative structure of the vacuum and its excitations.

A convenient way to deal with divergences of the Adler function is to consider its Borel transform, defined as

$$B[D](t) = \sum_{n=0}^{\infty} c_{n+1,1} \frac{t^n}{\pi^{n+1} n!} \tag{6.42}$$

with improved convergence properties (due to the explicit $n!$ factor in the denominator), and in particular a non-vanishing convergence radius. If $B[D](t)$ has no singularity for t real and positive, and does not increase too quickly at infinity, one can define the Borel sum:

$$\tilde{D}(a) = \int_0^{\infty} dt\ e^{-t/a} B[D](t) \tag{6.43}$$

$\tilde{D}(a)$ defined in this way has the same perturbative expansion in powers of a as $\hat{D}(a_Q)$ in the expansion of $D(Q^2)$ in $\alpha_s(Q)$. Actually, the Borel transform is expected to have singularities along the real axis (encoding the divergent behaviour of the original series [12] [194]), for both positive and negative values of t (see Fig. 6.12). The former are called infrared renormalons, and are related to power corrections and condensates in the Operator Product Expansion of the Adler function (cf. Sec. 6.2.1), whereas the latter are called ultraviolet renormalons and are related to the large-order (and often oscillatory) behaviour of the series. Actually, one can recover the result of OPE from renormalon calculus applying factorization, since there are two different scales: Q (fixed by external momenta) and Λ (fixed by QCD dynamics, $\Lambda < Q$). One can then separate contributions below and above Λ, the former can be absorbed into dimensionful quantities equivalent to the OPE condensates, whereas the latter yield the Wilson coefficients. It is remarkable that the power corrections introduced in this way, for small-momentum expansion in the internal gluon momentum, scale in the same way as the OPE contributions. This connection between IR renormalons and nonperturbative parameters of power corrections justifies the lack of an IR renormalon at $t = 1$, as one would not be able to write any operator matrix element of dimension two for it.

The presence of infrared renormalons requires to give a prescription to avoid the singularities in eq.6.43 (most often the principal value). In that case, the Borel integral may still

[12] If $c_{n,1} \sim a^n\, n!\, n^{\gamma}$ for large n, and unless γ is a negative integer, the Borel transform is given by $B[D](t) \sim (1 - at)^{-1-\gamma}$. Hence, if γ is positive, we have a singularity at $t = 1/a$. Just as a, t can have both positive or negative values. The larger a, the faster diverging the series is and the singularity is closer to zero.

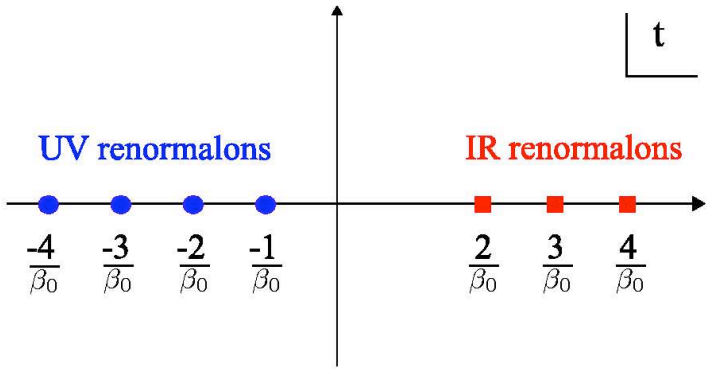

Figure 6.12: Ultraviolet (UV) and infrared (IR) singularities in the Borel plane of the Adler function. The UV renormalons correspond to t = $-$m/β_0, for m = 1, 2 ,3 ... The IR renormalons correspond to t = m/β_0, for m = 2 ,3 ...

be defined by moving the contour above or below the singularities. The so-defined Borel integral (6.43) acquires an imaginary part with a sign ambiguity depending on whether the integration is taken in the upper or lower half of the complex plane. The difference of the two definitions is often identified to an "ambiguity of the Borel integral" [194]. We will get back to this point, in the context of a particular model, in Sec. 6.4.2.

In Ref. [193], a particular ansatz $B[D]$ was proposed to describe the first singularities close to the edge of the domain of convergence as a sum of "poles" with fractional powers (actually cuts). The free parameters were determined from the first orders of the perturbative expansion and the known properties of the Operator Product Expansion. This ansatz was used to compute $\tilde{D}$ at arbitrary orders in perturbation theory, and then the integral $\delta^{(0)}$ using either FOPT or CIPT. In this case, when one increases the order, the evolution of the FOPT value of $\delta^{(0)}$ exhibits a plateau in agreement with the value obtained from the Borel sum $\tilde{D}$.

This analysis is based on several assumptions. Because D and $\tilde{D}$ share the same perturbative expansion for real positive values of the coupling constant, the latter is expected to yield the "true" value of the Adler function for arbitrary (complex) values of the strong coupling constant in its convergence radius. One could then determine the "true" value of δ^0 by integrating the Borel sum $D(\alpha(s))$ over a circle in the complex s-plane, i.e. for complex values of α_s. The ansatz for $B[D]$ contains the three singularities that are relevant not only at high orders (where they are dominated by the first ultraviolet renormalons), but also at intermediate orders (where they are dominated by the first infrared renormalons), and even at low orders (since the first five orders of the perturbative expansion of D are used to determine the free parameters in $B[D]$).

In Refs. [196–198], some aspects of this ansatz were discussed to map the Borel parameter t into another parameter w so that the cut plane along the real axis would be mapped into a disc of unit radius. It was argued that the series eq. (6.42) has optimal convergence properties once expressed in w, which would select this variable as the appropriate one to discuss renormalon models. Even though the main ingredients are the same (structure

of the singularities, first orders of the perturbative series), the choice of w rather than t modifies the (non-singular) structure of the series eq. (6.42) and it was enough to alter significantly the outcome of the analysis.

This section aims at investigating other aspects of this ansatz.

6.4.1 Model of renormalons

In Ref. [193], a renormalon model was presented to describe higher orders for the Adler function $\hat{D}$ eq. (6.41), and thus to compare different integration methods once higher order are taken into account. The ansatz consisted in one ultraviolet renormalon, corresponding to the sign-alternating divergence expected at higher orders in the perturbative series of D, and two infrared renormalons, mirroring the presence of condensates of dimension 4 (gluon condensate) and 6 (higher order quark and gluon condensates) in the OPE of the Adler function taken in the chiral limit [154, 157, 194, 195].

In the Borel plane, the ansatz for the Adler function has the following representation

$$B[\hat{D}](u) = B[\hat{D}_1^{UV}](u) + B[\hat{D}_2^{IR}](u) + B[\hat{D}_3^{IR}](u) + d_0^{PO} + d_1^{PO} u \tag{6.44}$$

where each renormalon "pole" has a cut singularity of the form

$$B[\hat{D}_p^X](u) = \frac{d_p^X}{(p \mp u)^{1+\gamma}}[1 + b_1(p \mp u) + b_2(p \mp u)^2 + \ldots] \tag{6.45}$$

where the negative sign corresponds to an infrared (IR) renormalon, and the positive one to an ultraviolet (UV) renormalon.

The corresponding model for the Adler function is given by

$$\hat{D}(\alpha) = \int_0^\infty dt e^{-t/\alpha} B[\hat{D}](t(u)) \tag{6.46}$$

with $t = \pi u/\beta_0$. The real part of this integral is expected to yield the "true" value of the perturbative series, whereas its imaginary part (divided by π) should provide an estimate of the uncertainty, attached to the way one treats the singularities related to IR renormalons.

The corresponding perturbative series can be worked out as outlined in sec.5 of Ref. [193]

$$\begin{aligned} \hat{D}_p^X(a_Q) &= \frac{\pi d_p^X}{p^{1+\gamma}\Gamma(1+\gamma)} \sum_{n=0}^{\infty} \Gamma(n+1+\gamma) \left(\pm\frac{\beta_0}{p}\right)^n a_Q^{n+1} \\ &\quad \times \left[1 + \frac{p}{\beta_0}\frac{(b_1+c_1)}{n+\gamma} + \left(\frac{p}{\beta_0}\right)^2 \frac{(b_2+b_1c_1+c_2)}{(n+\gamma)(n+\gamma-1)} + O\left(\frac{1}{n^3}\right)\right] \end{aligned} \tag{6.47}$$

where $a_Q = \alpha_s(Q)/\pi$. The values of the coefficients can be determined in the case of IR renormalons because their structure is connected with the contributions of the non-perturbative condensates occurring in the Operator Product Expansion of the correlator:

p is related to the naive dimension of the condensate, γ to its anomalous dimension, the b coefficients to the running of the strong coupling constant and the c coefficients to the perturbative series multiplying the condensate in the OPE. An analytic continuation can then be performed to assume a similar connection between UV renormalons and higher-dimension operators.

The relative weight of the three renormalon contributions (indicated by $d_1^{UV}, d_2^{IR}, d_3^{IR}$) was fixed using the 3rd, 4th and 5th orders in the expansion of the Adler function ($c_{3,1}, c_{4,1}, c_{5,1}$, the latter being set assuming a geometrical growth of the coefficients). All the coefficients c in eq. (6.47), related to the Wilson coefficients in the OPE, were set to zero apart from the coefficient c_1 for the d_2^{IR} pole. The first two terms ($c_{1,1}, c_{2,1}$) were not considered and are reproduced by adding an ad hoc term in the model (constant and linear terms in u).

6.4.2 Uncertainty on the Borel integral

One can use eq. (6.46) in order to derive a "resummed value" of the perturbative expansion. The presence of IR poles on the positive real axis means that we have to give a prescription for the integral, depending on whether we take the contour integral above or below the real axis, which yields:

$$\hat{D}(s) = \hat{D}_{PV}(s) \pm i\hat{D}_{pole}(s) \tag{6.48}$$

corresponding to the principal value and the pole contribution of the integral in eq. (6.46). When s is along the real axis, both $\hat{D}_{PV}$ and $\hat{D}_{pole}$ are real, but this does not remain the case in the complex plane.

We perform the contour integral in the complex plane eq. (6.19) in order to compute $\delta^{(0)}$:

$$\delta^{(0)} = \frac{1}{2\pi}\int_{-\pi}^{\pi} d\phi\ w(s)\ \hat{D}(s) = \frac{1}{2\pi}\int_{-\pi}^{\pi} d\phi\ w(s)\ [\hat{D}_{PV}(s) \pm i\hat{D}_{pole}(s)] \tag{6.49}$$

where $s = -s_0 \exp[i\phi]$. $Re\ \hat{D}_{PV}(s)$, $Re\ \hat{D}_{pole}(s)$ and $Re\ w(s)$ are even functions of ϕ, whereas the imaginary parts are odd functions of the same variable. Therefore the value of $\delta^{(0)}$ is obtained from

$$\delta^{(0)} = \frac{1}{2\pi}\int_{-\pi}^{\pi} d\phi\ w(s)\ \hat{D}_{PV}(s) = \frac{1}{2\pi}\int_{-\pi}^{\pi} d\phi\ [Re\ w\ Re\ \hat{D}_{PV} - Im\ w\ Im\ \hat{D}_{PV}](s) \tag{6.50}$$

The imaginary part of the integral evaluated with the principal value prescription (and divided by π) is sometimes taken as an estimate of the uncertainty on the value of the Borel integral [193]:

$$Err\ \delta^{(0)} = \frac{1}{2\pi^2}\int_{-\pi}^{\pi} d\phi\ w(s)\ \hat{D}_{pole}(s) = \frac{1}{2\pi}\int_{-\pi}^{\pi} d\phi\ [Re\ w\ Re\ \hat{D}_{pole} - Im\ w\ Im\ \hat{D}_{pole}](s) \tag{6.51}$$

Once several IR poles are included in the model, one must decide how to combine the contributions from $\hat{D}_{pole}^{IR2}$ and $\hat{D}_{pole}^{IR3}$ in $Err\ \delta^{(0)}$. Ref. [193] takes the sum of the two

contributions with a relative sign maximising the error, i.e.

$$Err\ \delta^{(0)} = \frac{1}{2\pi^2}\int_{-\pi}^{\pi} d\phi\ w(s)\ \left|[\hat{D}^{IR2}_{pole}(s) \pm \hat{D}^{IR3}_{pole}(s)]\right| \tag{6.52}$$

This amounts to assuming correlations for the variation of the uncertainty when one moves along the circle in the complex plane (the relative sign is assumed to be the same for any position along the circle). It seems more conservative to assume an absence of correlations, taking:

$$Err\ \delta^{(0)} = \frac{1}{2\pi^2}\int_{-\pi}^{\pi} d\phi\ w(s)\ [|\hat{D}^{IR2}_{pole}(s)| + |\hat{D}^{IR3}_{pole}(s)|] \tag{6.53}$$

This prescription tends to increase the error bar on the Borel integral in a significant way.

6.4.3 A Different Presentation of CIPT and FOPT

Two different methods of treating perturbation theory (CIPT and FOPT) were introduced and studied in Sec. 6.2.2. In Ref. [193], a different angle was chosen to present the methods. The starting point consisted not in inserting the solution of the RGE (6.25) into the perturbative expansion of the Adler function eq. (6.41), but rather in exploiting the fact that the Adler function is independent of the renormalisation scale. Indeed if we start from the perturbative expression for Π:

$$\Pi^{(1+0)}_{V/A}(s) = -\frac{N_c}{12\pi^2}\sum_{n=0}^{\infty} a_\mu^n \sum_{k=0}^{n+1} c_{n,k}\tilde{\eta}^k \qquad \tilde{\eta} = \log\frac{-s}{\mu^2} \tag{6.54}$$

with $a_\mu = \alpha_s(\mu)/\pi$, we get the following expansion for the Adler function

$$D^{(1+0)}_{V/A}(s) = \frac{N_c}{12\pi^2}\sum_{n=0}^{\infty} a_\mu^n \sum_{k=1}^{n+1} k c_{n,k}\tilde{\eta}^{k-1} \tag{6.55}$$

In the language of Ref. [126, 147], we obtain for the function arising in eq. (6.26)

$$\tilde{K}_n(\xi) = \sum_{k=1}^{n+1} k c_{n,k}(-\log\xi)^{k-1} \tag{6.56}$$

But since the Adler function is independent of the renormalisation scale, as implemented in eq. (6.41), we can take the derivative of eq. (6.55) with respect to $\log\mu$ and exploit the RGE to reexpress the derivative of a_μ in terms of a_μ itself. We obtain an expansion in powers of a_μ and η which is identical to zero. This yields expressions for $c_{n,k\geq 2}$ from $c_{n,1}$. Since the values of $\beta_{n\geq 4}$ and $c_{n\geq 5,1}$ are unknown, the reconstruction of of $c_{n,k\geq 2}$ based on the RGE is only partial: the coefficients $c_{n,k}$ with $n \geq 6$ and $1 \leq k \leq n-4$ cannot be computed fully because their equations involve some of these unknown coefficients.

One can then perform the computation of the perturbative contribution to the tau width:

$$\delta^{(0)} = \sum_{n=1}^{\infty} \sum_{k=1}^{n} k c_{n,k} \frac{1}{2i\pi} \oint_{|x|=1} \frac{dx}{x} (1-x)^3 (1+x) \log^{k-1} \left(\frac{-M_\tau^2 x}{\mu^2} \right) a_\mu^n \tag{6.57}$$

in two different ways, either by performing FOPT or CIPT. In FOPT, we set $\mu = M_\tau$, leading to

$$\delta_{FOPT}^{(0)} = \sum_{n=1}^{\infty} a_{M_\tau}^n \sum_{k=1}^{n} k c_{n,k} J_{k-1} \tag{6.58}$$

with

$$J_k = \frac{1}{2i\pi} \oint_{|x|=1} \frac{dx}{x} (1-x)^3 (1+x) \log^k(-x) \tag{6.59}$$

In CIPT, we take $\mu^2 = -M_\tau^2 x$ to get

$$\delta_{CIPT}^{(0)} = \sum_{n=1}^{\infty} c_{n,1} J_n^a \tag{6.60}$$

with

$$J_n^a = \frac{1}{2i\pi} \oint_{|x|=1} \frac{dx}{x} (1-x)^3 (1+x) a^n(-M_\tau^2 x) \tag{6.61}$$

Since the two presentations are not obviously identical, it is interesting to determine if they are fully equivalent. In the case of CIPT, only the coefficients $c_{n,1}$ coefficients from eq.(6.41) are involved, so that the definitions are easily recognised as identical. In the case of FOPT, the situation is rather different, since we use the RGE at all orders to derive the coefficients $c_{n,k\geq 2}$ according to Ref. [193], whereas it is only exploited to up to a given order in the other references (α_s^5 in Ref. [122]). The two results differ from each other through the higher-order terms that are kept or not. Indeed, the FOPT expression contains terms up to a certain order in $\alpha_s(M_\tau)$ coming from:

- the perturbative expansion of $\hat{D}$, known up to an arbitrary order through the renormalon model
- the RGE of α_s, used to reexpress the integral in terms of a series in $\alpha_s(M_\tau)$, with coefficients known only up to β_3.

The two previous definitions of FOPT can be rephrased in the following way:

- In Ref. [193], the RGE is used to expand $\alpha_s^n(s)$ for n arbitrary, in powers of $\alpha_s(s_0)$ up to the required order in perturbation theory, setting all $\beta_{k\geq 4} = 0$. Then these expansions are put in eq. (6.41) to compute the FOPT value of $\delta^{(0)}$ at a given order in perturbation theory. This method is denoted FOPT(BJ) in the following.

- In Ref. [122], the expansion of α_s, eq. (6.25) up to $O(\alpha_s^5)$ is plugged directly into the series for the Adler function, eq. (6.41). This expansion is used to compute the FOPT value of $\delta^{(0)}$ at a given order of perturbation theory. We denote FOPT this way of dealing with higher orders.

The difference between the two methods comes from a different use of the RGE for orders above the known terms (i.e., once $\beta_{n\geq 4}$ is involved). For instance, for the $n = 6$ contribution to $\delta^{(0)}$, we should use eq. (6.25) up to α_s^6, involving β_4. This difference was already discussed in Sec. 6.2.2, where only low orders were known and included. In Sec. 6.2.2, we also discussed a method called FOPT$^+$, which corresponds to the prescription denoted FOPT here, up to high-order coefficients in the perturbative expansion of D (modeled here, but set to zero in FOPT$^+$). A second method, called FOPT^{++} in Sec. 6.2.2, is related to the prescription denoted FOPT(BJ) here (in FOPT^{++}, we stopped the Taylor expansion at $\eta^{n\leq 5}$).

Following the methods presented in Ref. [193], we obtain the plot in Fig. 6.13 (in this section, we will always use the illustrative value of the strong coupling constant $\alpha_s(M_\tau) = 0.34$). Let us emphasize that neither FOPT nor FOPT(BJ) is "the true" FOPT as soon as we look for contributions from orders higher than $n = 5$, and they are both different from the complete value that would be derived by applying FOPT if the full RGE series were known: a piece is missing.

One can see that the exploitation of the RGE at higher orders has a significant impact on $\delta^{(0)}$. The difference between the two methods remains within our (conservative) error bars, but which exceeds the limited error bars chosen by Ref. [193]. In the case of CIPT, one has also to decide up to which order of perturbation theory one should write eq. (6.25). However, the integration of RGE is performed by small-step integration, and thus it is much less dependent on the exact cut on the power of η placed on eq. (6.25).

6.4.4 Extension of the renormalon model

Based on the renormalon model presented in sec. 6.4.1, Ref. [193] fixed the renormalon residues d_i in eq. (6.44) by requiring the model to reproduce the first orders of the perturbative series $c_{3,1}, c_{4,1}, c_{5,1}$ (the latter being set to $c_{5,1} = 283$ following an ansatz concerning the geometrical growth of this coefficients). The argument stated in Ref. [193] is that only a constant term d_0^{PO} is actually needed to reproduce $c_{1,1}$ and $c_{2,1}$ (even though a linear term d_1^{PO} is included, but turned out to be very small in the ansatz of Ref. [193]).

With this assumption, Ref. [193] shows that the balance between the two IR renormalons has a direct consequence on the discussion of CIPT/FOPT in their model:

- A dominance of the $d = 6$ renormalon favours CIPT (in the sense that it yields a value close to the Borel sum of the series)
- A dominance of the $d = 4$ renormalon favours FOPT (in the sense that it yields a value close to the Borel sum of the series)

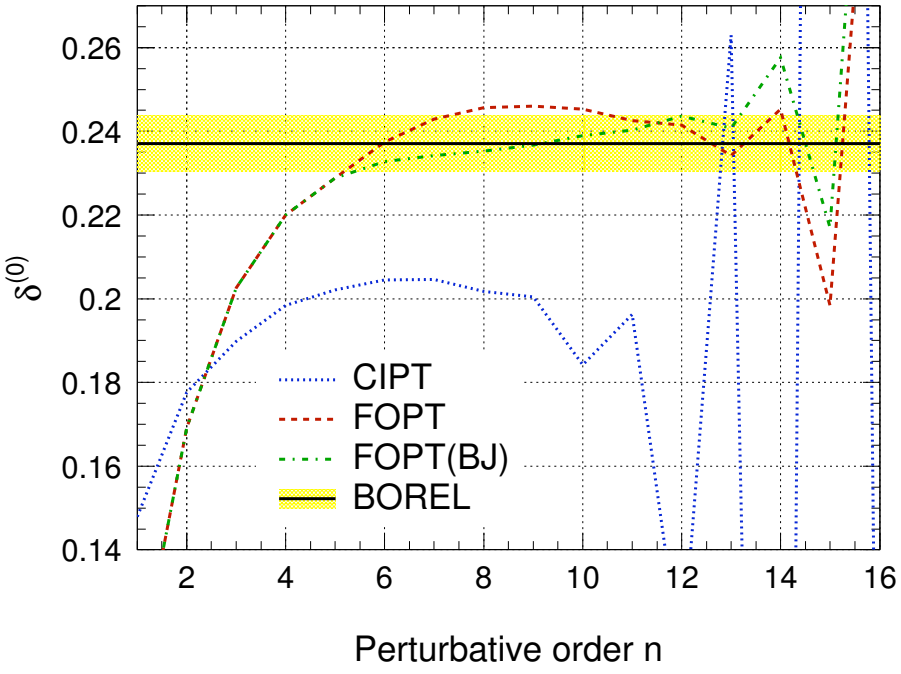

Figure 6.13: Value of $\delta^{(0)}$ as a function of the order and type of perturbation theory, corresponding to Fig. 7 from Ref. [193]. FOPT and FOPT(BJ) indicate two different ways of dealing with Fixed-Order Perturbation Theory as one goes to higher orders in perturbation theory.

However, this procedure to fix the residues d_i *assumes* that the perturbative expansion eq. (6.47) is valid exactly when one neglects the contributions coming from the coefficient c_2 and from $1/n^3$ remainders (since they are set to 0 in Ref. [193]). Actually, these contributions can be quite significant, compared to other contributions that are explictly included in the renormalon model in ref [193]. Indeed, Tables 6.6 and 6.7 collect the relative contribution from $1/n^3$ and c_2 terms:

$$E_p^{n,X}(a_Q) = \frac{\pi d_p^X}{p^{1+\gamma}\Gamma(1+\gamma)}\Gamma(n+1+\gamma)\left(\pm\frac{\beta_0}{p}\right)^n a_Q^{n+1}\frac{1}{n^3} \tag{6.62}$$

$$F_p^{n,X}(a_Q) = \frac{\pi d_p^X}{p^{1+\gamma}\Gamma(1+\gamma)}\Gamma(n+1+\gamma)\left(\pm\frac{\beta_0}{p}\right)^n a_Q^{n+1}\left(\frac{p}{\beta_0}\right)^2 \times\frac{1}{(n+\gamma)(n+\gamma-1)} \tag{6.63}$$

compared to the total contribution of a pole for a given order in perturbation theory as

Pole	1	2	3	4	5	6	7	8	9	10	11	12
UV	36.1	11.7	3.7	1.6	0.8	0.5	0.3	0.2	0.1	0.1	0.1	0.1
IR2	-377.4	46.2	7.5	2.5	1.2	0.6	0.4	0.2	0.2	0.1	0.1	0.1
IR3	-106.3	-59.3	26.3	4.6	1.7	0.8	0.5	0.3	0.2	0.1	0.1	0.1

Table 6.6: Relative contribution (in percent) $E_p^{n,X}/D_p^{n,X}$ from $1/n^3$ to a given order of perturbation theory for each pole of the renormalon model. The correction cannot be estimated for $n = 0$.

Pole	0	1	2	3	4	5	6	7	8	9	10	11	12
UV	36.4	28.1	6.7	2.8	1.5	0.9	0.6	0.4	0.3	0.3	0.2	0.2	0.1
IR2	-29.7	-73.1	31.6	9.8	5.0	3.1	2.1	1.6	1.2	0.9	0.8	0.6	0.5
IR3	-17.9	-23.7	-57.3	53.8	15.2	8.0	5.1	3.6	2.7	2.1	1.7	1.4	1.2

Table 6.7: Relative contribution (in percent) $F_p^{n,X}/D_p^{n,X}$ from c_2 to a given order of perturbation theory for each pole of the renormalon mode.

computed in ref [193]:

$$D_p^{n,X}(a_Q) = \frac{\pi d_p^X}{p^{1+\gamma}\Gamma(1+\gamma)}\Gamma(n+1+\gamma)\left(\pm\frac{\beta_0}{p}\right)^n a_Q^{n+1} \times\left[1+\frac{p}{\beta_0}\frac{(b_1+c_1)}{n+\gamma}+\left(\frac{p}{\beta_0}\right)^2\frac{(b_2+b_1c_1)}{(n+\gamma)(n+\gamma-1)}\right] \tag{6.64}$$

In other words, the actual contribution to the perturbative expansion of the Adler series from a given pole at a given order would be

$$a_Q^{n+1}[D_p^{n,X}+zE_p^{n,X}+c_2F_p^{n,X}] \tag{6.65}$$

z and c_2 are unknown coefficients, in principle of order 1. One could neglect their presence at a given order a_s^{n+1} of perturbation theory if $E_p^{n,X}/D_p^{n,X}$ and $F_p^{n,X}/D_p^{n,X}$ are small numbers (this is in particular assumed in ref [193] for $n = 2, 3, 4$).

One notices that the perturbative coefficient for $n \leq 3$ is significantly affected by both kinds of contribution (E and F), and that the IR_3 pole is more affected by such corrections than IR_2. In addition, the value of c_2 can affect significantly the situation for IR_3 even for higher orders. Therefore, the model discussed in Ref. [193] is likely to have its perturbative expansion affected by significant corrections at low orders – where the term "low orders" includes the $O(a_s^3)$ term (i.e., $n = 2$), which is used to determine the residues of the poles.

One can take into account the possibility of such large corrections at the lower orders by adding a quadratic term in u to the polynomial part, which will contribute to the

Table 6.8: Coefficients of the ansatz for different values of d_2^{PO}.

d_0^{PO}	d_1^{PO}	d_2^{PO}	d_1^{UV}	d_2^{IR}	d_3^{IR}
-9.116	-3.834	-1	0.028	7.82	-176.8
-4.167	-1.913	-0.5	0.006	5.49	-95.16
0.781	0.008	0	-0.0160	3.16	-13.53
3.255	0.968	0.25	-0.026	1.99	27.29
5.729	1.929	0.5	-0.037	0.83	68.10
10.68	3.850	1	-0.059	-1.50	149.7

perturbative expansion of the Adler function at $O(a_s^3)$:

$$B[\hat{D}](u) = B[\hat{D}_1^{UV}](u) + B[\hat{D}_2^{IR}](u) + B[\hat{D}_3^{IR}](u) + d_0^{PO} + d_1^{PO}u + d_2^{PO}u^2 \tag{6.66}$$

The choice of d_2^{PO} can be seen converted into a guess on the value of $c_{6,1}$, with the corresponding equivalence:

d_2^{PO}	-1	-0.5	0	0.25	0.5	1
c_6	1291	2283	3275	3771	4267	5259

The dependence of all results on d_2^{PO} is linear, and one can perform exactly the same analysis as before, with the corresponding plots in Fig. 6.14. As expected, $O(1)$ values of d_2^{PO} are enough to change the balance between the IR renormalon poles, as shown in Table 6.8.

One recovers the model in Ref. [193] in the case where $d_2^{PO} = 0$. The discussion of CIPT vs FOPT can be converted into a discussion on the value of d_2^{PO}. The cases where d_2^{IR} vanishes (for d_2^{PO} approximately between 0.5 and 1) correspond to cases where CIPT is preferred to FOPT if one wants an agreement with the value of $\delta^{(0)}$ from the Borel resummation. The cases where d_3^{IR} vanishes (approximately d_2^{PO} between 0 and 0.5) correspond to cases where FOPT is preferred to CIPT.

Larger (positive or negative) values of d_2^{PO} correspond to values where neither FOPT nor CIPT yield a plateau with a value in agreement with the Borel resummation. CIPT yields a result that is stable, but in disagreement with the value obtained by Borel resummation, whereas FOPT yields an unstable result which sometimes crosses the Borel result. We see that the value of the Borel resummation depends significantly on the value of d_2^{PO}, as well as the uncertainty attached to it.

Table 6.9: Relative contribution (in %) to the coefficients of the perturbative expansion of the Adler function for different values of $d_2^{PO} = -0.5, 0, 0.25, 0.5$

d_2^{PO}	Pole	$c_{4,1}$	$c_{5,1}$	$c_{6,1}$	$c_{7,1}$	$c_{8,1}$	$c_{9,1}$	$c_{10,1}$	$c_{11,1}$	$c_{12,1}$	$c_{13,1}$
	UV_1	-3.8	6.1	-8.9	9.2	-15.9	16.7	-45.5	33.7	-576.4	59.4
-0.5	IR_2	174.4	236.1	243.0	164.8	177.7	112.6	180.1	77.1	752.1	43.7
	IR_3	-70.6	-142.2	-134.1	-74.1	-61.7	-29.4	-34.6	-10.8	-75.7	-3.1
	UV_1	9.7	-15.6	15.8	-38.6	30.3	-236.7	54.0	200.0	77.6	119.5
0	IR_2	100.4	135.9	97.5	155.9	76.3	360	48.3	-103.6	22.9	-19.9
	IR_3	-10.0	-20.2	-13.3	-17.3	-6.5	-23.2	-2.3	3.6	-0.6	0.3
	UV_1	16.4	-26.5	23.3	-96.5	45.6	314.6	72.3	127.2	89.4	107.0
0.25	IR_2	63.3	85.7	53.4	145.0	42.7	-178	24.1	-24.5	9.8	-6.6
	IR_3	20.2	40.8	23.3	51.4	11.7	-36.7	3.6	-2.7	0.8	-0.4
	UV_1	3.1	-37.4	29.0	-258.7	57.8	159.4	84.2	110.4	95.4	102.5
0.5	IR_2	26.3	35.6	19.6	114.6	15.9	-26.6	8.3	-6.3	3.1	-1.9
	IR_3	50.5	101.8	51.3	244.1	26.3	-32.9	7.5	-4.1	1.5	-0.6

6.4.5 Definition of pole dominance

From the previous section, one can see that a seemingly small change in d_2^{PO} has an important impact on higher orders and on the value obtained from the Borel resummation. It seems difficult to determine a priori which model is more relevant, and different criteria can be imagined. A rather usual approach consists in assuming that the first IR pole should "dominate" over the following ones for the model to be reasonable. Let us remark first that such a requirement is by no means mandatory in the framework of the renormalon approach, in which the relative contributions form different poles is free, at least in principle. For the time being, let us assume that such a dominance is indeed the sign of a good model. The next question is: what is the definition of this dominance in practice ?

Table 6.10: Order-by-order results for $\delta^{(0)}$ FOPT(BJ) (top) and CIPT (bottom), for d_2^{PO} = -0.5

Order	1	2	3	4	5	6
UV_1	-0.00682	-0.01114	-0.01277	-0.01281	-0.01219	-0.01161
IR_2	-0.90568	-1.28083	-1.37745	-1.33435	-1.25036	-1.17583
IR_3	2.43770	3.58286	3.99478	3.99000	3.82183	3.64055
Pol	-1.41698	-2.12173	-2.40198	-2.42283	-2.33050	-2.22195
Sum FOPT(BJ)	0.10822	0.16916	0.20258	0.22001	0.22878	0.23116
UV_1	-0.00932	-0.01194	-0.01141	-0.01174	-0.01150	-0.01165
IR_2	-1.23768	-1.27781	-1.26035	-1.24537	-1.23643	-1.23238
IR_3	3.33131	3.64857	3.67319	3.66712	3.66174	3.65950
Pol	-1.93642	-2.18124	-2.21166	-2.21166	-2.21166	-2.21166
Sum (CIPT)	0.14790	0.17758	0.18977	0.19836	0.20214	0.20381
Borel sum	0.26036					

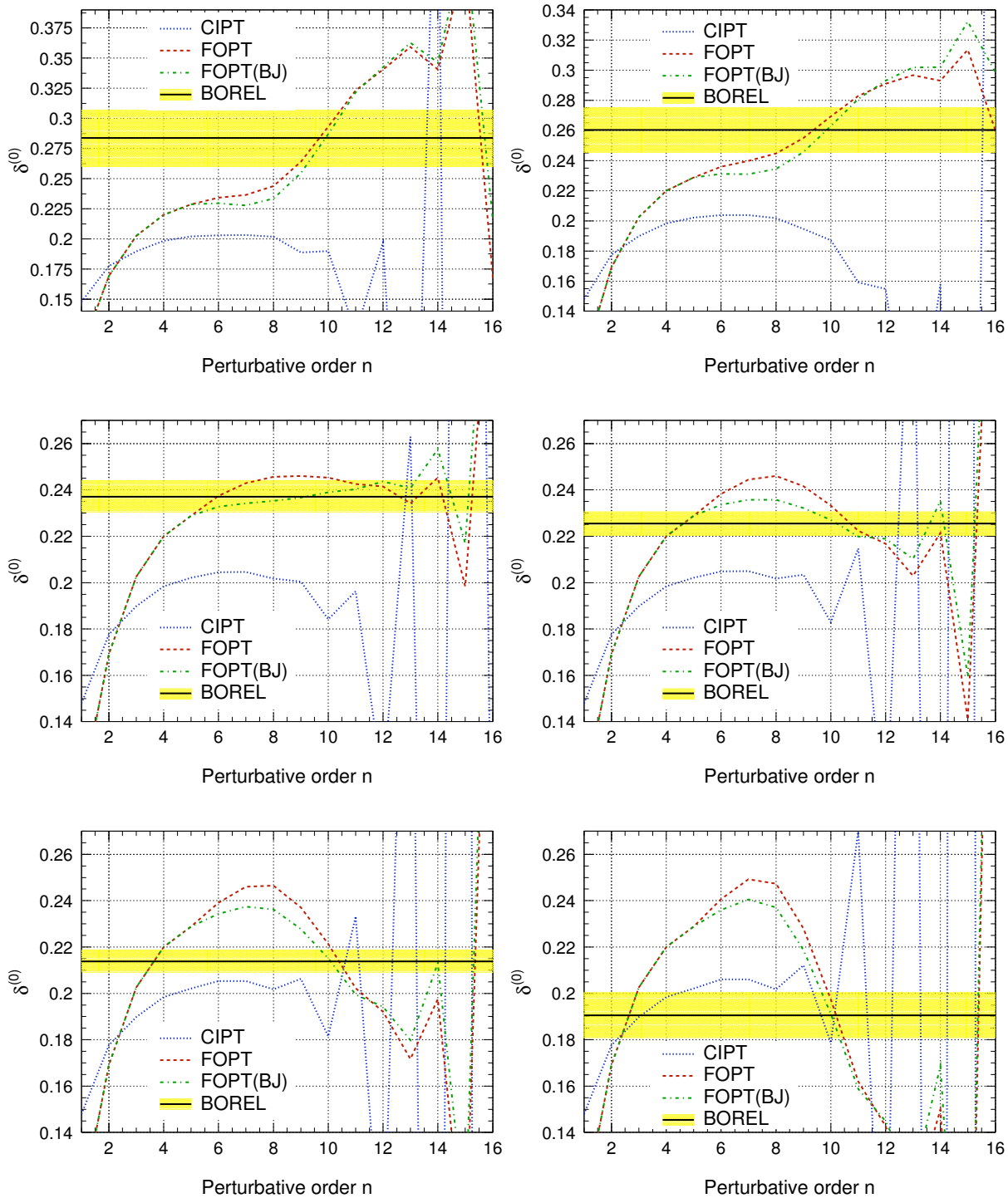

Figure 6.14: Value of $\delta^{(0)}$ as a function of the order and type of perturbation theory, corresponding to Fig. 7 from Ref. [193]. FOPT and FOPT(BJ) indicate two different ways of dealing with Fixed-Order Perturbation Theory as one goes to higher orders in perturbation theory. The figures correspond to different values of the quadratic coefficient $d_2^{PO} = -1, -0.5, 0, 0.25, 0.5, 1$ (from left to right and top to bottom)

Table 6.11: Order-by-order results for $\delta^{(0)}$ FOPT(BJ) (top) and CIPT (bottom), for $d_2^{PO} = 0$.

Order	1	2	3	4	5	6
UV_1	0.01734	0.02836	0.03248	0.032583	0.031007	0.029536
IR_2	-0.52120	-0.73709	-0.79269	-0.767886	-0.719556	-0.676666
IR_3	0.34660	0.50942	0.56798	0.567304	0.543394	0.517619
Pol	0.26548	0.36847	0.39480	0.388012	0.373940	0.362262
Sum FOPT(BJ)	0.10822	0.16916	0.20258	0.22001	0.22878	0.23275
UV_1	0.02370	0.03039	0.02903	0.02986	0.02927	0.02965
IR_2	-0.71226	-0.73534	-0.72530	-0.71668	-0.71154	-0.70920
IR_3	0.47365	0.51876	0.52226	0.52140	0.52063	0.52031
Pol	0.36280	0.36378	0.36378	0.36378	0.36378	0.36378
Sum (CIPT)	0.14790	0.17758	0.18977	0.19836	0.20214	0.20453
Borel sum	0.23709					

A first definition, chosen in Ref. [193], consists in considering the contribution of the different poles to the expansion of the Adler function at intermediate orders (for n between 4 and 8). A dominant pole gives the largest contribution to each coefficient of the perturbative series for intermediate orders. In Ref. [193], the case $d_2^{PO} = 0$ is considered as interesting because the relative contribution to a given $c_n, 1$ from IR_2 is larger than IR_3. This is recalled in Table 6.9. Let us remark that already for $n = 7$, large cancellations occur between the UV pole and the first IR pole. If one now considers different values of d_2^{PO}, one notices that $d_2^{P0} = 0.25$ is also in good agreement with this criterion. In this case, there is no plateau for FOPT at intermediate orders in perturbation theory, and the outcome of the Borel resummation lies between FOPT and CIPT. Larger positive values of d_2^{PO} would be disfavoured according to this definition of dominance. On the other hand, negative values of d_2^{PO}, in particular large ones, fulfill this definition, as can be seen for instance from Table. 6.9.

But one may wonder whether the relative contribution to intermediate orders of D the best way of determining whether one element of the model or another yields the most significant contribution to $\delta^{(0)}$. Indeed, the intermediate orders contribute only mildly to the actual value of $\delta^{(0)}$, since they are multiplied by higher and higher powers of α_s. It seems rather natural to break down the contribution to $\delta^{(0)}$ into the contributions from the UV pole, the two IR poles and the polynomial term.

An alternative definition of the dominance from one pole would correspond to providing most of the contribution to $\delta^{(0)}$. Looking at Table 6.11, we see that in the case of

Table 6.12: Order-by-order results for $\delta^{(0)}$ FOPT(BJ) (top) and CIPT (bottom), for $d_2^{PO} = 0.25$

Order	1	2	3	4	5	6
UV_1	0.02943	0.04811	0.05511	0.05528	0.05260	0.05011
IR_2	-0.32896	-0.46522	-0.50031	-0.48466	-0.45415	-0.42708
IR_3	-0.69896	-1.02730	-1.14541	-1.14404	-1.09582	-1.04385
Pol	1.10671	1.61357	1.78311	1.77170	1.70077	1.63356
Sum	0.10822	0.16916	0.20258	0.22001	0.22878	0.23355
UV_1	0.04021	0.05156	0.04925	0.05066	0.04966	0.05030
IR_2	-0.44954	-0.46412	-0.45778	-0.45234	-0.44909	-0.44762
IR_3	-0.95518	-1.04615	-1.05320	-1.05146	-1.04992	-1.04928
Pol	1.51241	1.63629	1.65150	1.65150	1.65150	1.65150
Sum	0.147898	0.17758	0.189766	0.198358	0.202144	0.204897
Borel sum	0.22546					

$\delta^{(0)}$ for $d_2^{PO} = 0$, and contrary to our intuition, the so-called dominant IR_2 pole yields a contribution that is almost canceled by the so-called subdominant IR_3 pole – the contributions from the two IR poles and the polynomial part being of the same order of magnitude. When one increases d_2^{PO} (see Tables 6.12 and 6.13), one can notice that the contribution from the IR_3 pole grows and is canceled by the polynomial part. The value $d_2^{PO} \simeq 0.08$ corresponds to the extreme situation where the residue of the IR_3 pole vanishes (and thus this pole does not contribute) and the IR_2 pole saturates the contribution from IR renormalons. It seems fair to require all the various contributions (individual "poles" and polynomial term) to yield contributions of the same size, which is the case for $-0.5 \leq d_2^{PO} \leq 0.25$ (see Tables 6.10-6.12), corresponding to a rather wide range of behaviours of FOPT/CIPT/Borel sum.

6.4.6 Anomalous dimension for the operator of dimension 6

As can be seen from eq. (6.45), the term of renormalon "pole" is slightly misleading, since one expects radiative corrections to turn these poles into cuts in the Borel plane. One can relate both types of renormalons to QCD operators. In particular, the presence of IR renormalons mirrors the existence of condensates in the OPE of the correlator under scrutiny [194]. In particular, the anomalous dimensions of the latter are used to fix some unknown parameters of the model. Ref. [193] considers:

Table 6.13: Order-by-order results for $\delta^{(0)}$ FOPT(BJ) (top) and CIPT (bottom), for $d_2^{PO} = 0.5$

Order	1	2	3	4	5	6
UV_1	0.04151	0.06787	0.07774	0.07797	0.07420	0.07068
IR_2	-0.13672	-0.19335	-0.20793	-0.20143	-0.18875	-0.17750
IR_3	-1.74451	-2.56403	-2.85881	-2.85539	-2.73504	-2.60531
Pol	1.94795	2.85867	3.17143	3.15538	3.02761	2.90485
Sum FOPT(BJ)	0.10822	0.16916	0.20258	0.22001	0.22878	0.23435
UV_1	0.05672	0.07273	0.06947	0.07146	0.07004	0.07095
IR_2	-0.18683	-0.19289	-0.19026	-0.18799	-0.18664	-0.18603
IR_3	-2.38401	-2.61105	-2.62867	-2.62433	-2.62047	-2.61887
Pol	2.66202	2.90880	2.93922	2.93922	2.93922	2.93922
Sum CIPT	0.14790	0.17758	0.18977	0.19836	0.20214	0.20526
Borel sum	0.21382					

- for UV_1, a vanishing anomalous dimension for a single "effective" condensate
- for IR_2, the anomalous dimension corresponding to the gluon condensate [eq. (5.13) in this reference]
- for IR_3, a vanishing anomalous dimension for a single "effective" condensate

As explained in Ref. [194], the structure of the cuts becomes rather involved once the full set of operators are considered. IR_2 is rather simple since only one operator is involved by dimensional arguments: this renormalon is linked to $d = 4$ operators, and only the gluon condensate is involved (neither the identity operator nor the quark condensate since we work in the massless limit). On the other hand, both UV_1 and IR_3 are related to dimension-6 operators, namely:

$$(\bar{\psi}\gamma_\mu\psi)(\bar{\psi}\gamma^\mu\psi) \qquad (\bar{\psi}\gamma_\mu\gamma_5\psi)(\bar{\psi}\gamma^\mu\gamma_5\psi) \tag{6.67}$$

$$(\bar{\psi}\gamma_\mu T^A\psi)(\bar{\psi}\gamma^\mu T^A\psi) \qquad (\bar{\psi}\gamma_\mu\gamma_5 T^A\psi)(\bar{\psi}\gamma^\mu\gamma_5 T^A\psi) \qquad f_{ABC}G^A_{\mu\nu}G^\nu_\rho\ {}^B G^{\rho\mu C} \tag{6.68}$$

In Ref. [194], the anomalous dimensions of $d = 6$ operators were reconsidered. After diagonalising the RG mixing matrix, the diagonal operators were shown to have anomalous dimensions at one loop of the form

$$\gamma^{(1)}_{O_6^i} = \beta_1\lambda_i \qquad \lambda_i = \{0.379, 0.126, -0.332, -0.753, 0\} \tag{6.69}$$

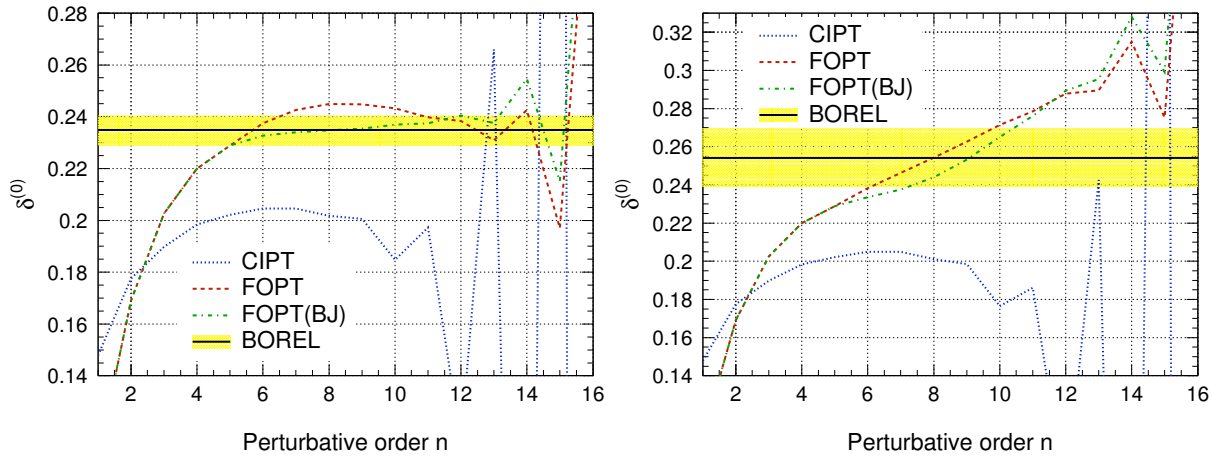

Figure 6.15: Figures for different values of the anomalous dimension of the effective $d = 6$ condensate: $\gamma_{O_6}^{(1)} = \beta_1 \lambda$ with $\lambda = 0.379$ (left) and -0.753 (right).

These five contributions should a priori be included individually in the renormalon model, rather than through a single "effective" condensate of unclear anomalous dimension, and actually set to zero. Since the $d = 4$ operator is described with its correct anomalous dimension and since we compare $d = 4$ and $d = 6$ renormalons, it seems fair to treat both renormalons on the same footing.

As can be seen from the perturbative expansion eq. (6.47), the large-order behaviour of a "pole" is:

$$D_{V/A}^{(1+0)}(Q^2) = \frac{1}{4\pi^2} \sum_{n=0}^{\infty} r_n a_Q^n \qquad r_n \sim_{n\to\infty} \left(\frac{\beta_0}{p}\right)^n n!\; n^{\gamma} \tag{6.70}$$

We see that the larger the anomalous dimension γ, the more dominant the pole at large n. But conversely, at smaller n, the operators with smaller anomalous dimensions compete (and can even be more significant) than the pole with the largest γ. Therefore, once the proper cut structure of the second IR pole is taken into account, it becomes necessary but difficult to fix the relative "strengths" of the cuts from the different operators from the lowest orders of perturbation theory.

As an illustration of the role of anomalous dimensions in the discussion, we set $\gamma_{O_6}^{(1)} = \beta_1 \lambda$ with $\lambda = -0.753$ and 0.379 (rather than 0 in the original model), and follow the same procedure as in Ref. [193] to obtain the two plots in Fig. 6.15, indicating a rather wide range of behaviours for FOPT, depending on the choice of anomalous dimensions (CIPT on the other hand remains very stable). In addition, the resummed values for $\delta^{(0)}$ can vary from 0.23455 to 0.25553 if one changes this single parameter.

We can extend the model of Ref. [193] by assuming a value for $c_{6,1}$ and splitting the second IR pole into two different poles, with different anomalous dimensions:

$$B[\hat{D}](u) = B[\hat{D}_1^{UV}](u) + B[\hat{D}_2^{IR}](u) + B[\hat{D}_{3a}^{IR}](u) + B[\hat{D}_{3b}^{IR}](u) + d_0^{PO} + d_1^{PO} u \tag{6.71}$$

Table 6.14: Relative contribution (in %) to the coefficients of the perturbative expansion of the Adler function for different values of $c_{6,1}$, for a model with two IR poles for $u = 3$.

$c_{6,1}$	Pole	$c_{4,1}$	$c_{5,1}$	$c_{6,1}$	$c_{7,1}$	$c_{8,1}$	$c_{9,1}$	$c_{10,1}$	$c_{11,1}$	$c_{12,1}$	$c_{13,1}$
3275	UV_1	9.7	-15.7	15.9	-38.9	30.4	-241.3	54.1	199.1	77.7	119.4
	IR_2	100.	136.6	98.0	157.3	76.7	367.5	48.5	-103.3	23.0	-19.8
	IR_{3a}	-9.4	-12.8	-8.2	-11.1	-4.4	-16.7	-1.7	2.8	-0.5	0.3
	IR_{3b}	-1.2	-8.0	-5.6	-7.3	-2.7	-9.4	-0.9	1.3	-0.2	0.1
2283	UV_1	5.8	-9.4	13.6	-59.6	56.9	95.6	139.3	77.8	128.0	87.1
	IR_2	-81.4	-110.3	-113.5	-324.6	-193.3	-196.0	-168.2	54.3	-50.9	19.5
	IR_{3a}	179.4	244.9	225.2	542.9	262.9	-211.3	140.9	-34.9	24.7	-7.1
	IR_{3b}	-3.8	-25.3	-25.4	-58.7	-26.4	19.6	-12.1	2.8	-1.8	0.5
4267	UV_1	13.6	-22.0	17.0	-33.8	25.3	-96.2	42.9	599.3	66.5	142.0
	IR_2	283.1	383.2	211.0	274.4	128.2	293.7	77.1	-623.0	39.4	-47.4
	IR_{3a}	-198.0	-270.4	-133.0	-145.8	-55.4	-100.5	-20.5	127.0	-6.1	5.5
	IR_{3b}	1.4	9.1	4.9	5.2	1.8	3.1	0.6	-3.3	0.1	-0.1

We denote IR_{3a} for the cut with $\lambda_a = 0.379$ and IR_{3b} with $\lambda_b = -0.753$. If we vary $c_{6,1}$ between 2283 and 4267 (values corresponding $d_2^{PO} = \pm 0.5$ in the previous model) and look at the relative contribution of each pole to a given order of D (Table 6.14), we see that for values above 3000, one has a dominance of IR_2, with a significant cancellation of IR_{3a} and a growing contribution from IR_{3b}. On the other hand, below 3000, IR_{3a} takes over IR_2, whereas IR_{3b} remains small. If we now consider the contributions to $\delta^{(0)}$ (Tables 6.15-6.17) and if we require them to be of similar order, values of $c_{6,1}$ above 3000 are acceptable. In this case, it is quite interesting to notice that the breakdown in terms of the contributions from different poles is very different, as well as the relative contributions to given orders of perturbation theory. Even though the value of $\delta^{(0)}$ is quite similar *in fine*, the agreement with FOPT and CIPT depends quite strongly on the value chosen for $c_{6,1}$.

6.4.7 Other moments

One can use the same machinery to analyse further moments, for instance some higher moments used to determine the condensates from a fit to τ spectral data as shown in

Table 6.15: Results for the FOPT(BJ) integral, for $c_{6,1} = 3275$ in a model with two IR poles for $u = 3$.

Order	1	2	3	4	5	6
UV_1	0.01740	0.02846	0.03259	0.03269	0.03111	0.02964
IR_2	-0.52346	-0.74029	-0.79613	-0.77122	-0.72268	-0.67960
IR_{3a}	0.03761	0.05553	0.06153	0.06031	0.05618	0.05208
IR_{3b}	0.41127	0.59763	0.66170	0.65995	0.63438	0.60771
Pol	0.16540	0.22783	0.24289	0.23829	0.22979	0.22293
Sum FOPT(BJ)	0.10822	0.16916	0.20258	0.22001	0.22878	0.23275
Borel sum	0.23655					

Sec. 6.3 and Ref. [122,126,147] (Fig. 6.16), and moments proposed in Ref. [199] (Fig. 6.17):

$$R^{k=1,l}_{\tau,V+A} = \frac{6\,|V_{ud}|^2\,S_{\rm EW}}{m_\tau^2}\int_0^{m_\tau^2} ds\left(1-\frac{s}{m_\tau^2}\right)^3\left(\frac{s}{m_\tau^2}\right)^l\left(1+\frac{2s}{m_\tau^2}\right)(v_1(s)+a_1(s))$$

$$R^{N}_{\tau,V+A} = \frac{6\,|V_{ud}|^2\,S_{\rm EW}}{m_\tau^2}\int_0^{m_\tau^2} ds\left[1-\frac{N}{N-1}\frac{s}{m_\tau^2}+\frac{1}{N-1}\left(\frac{s}{m_\tau^2}\right)^N\right]$$

As in the case of the τ width, we can use OPE to expand these moments. If we focus on the perturbative contribution ($D = 0$), we can reexpress it as an integral over the circle using integration by part:

$$\begin{aligned} 1+\delta_w^{(0)} &= -2\pi i\oint_{|s|=s_0}\frac{ds}{s}w(s)[D(s)]_{D=0} \\ &= -2\pi i\oint_{|s|=s_0} ds u(s)[\Pi^{(1+0)}]_{D=0}(s) = -4\pi\int_0^{s_0} u(s)[\text{Im }\Pi^{(1+0)}(s)]_{D=0} \end{aligned} \tag{6.72}$$

where $w(s) = \int_{s_0}^s ds'\,u(s')$, so that we have

$$u_{0l}(s) = -\frac{2}{s_0}\left(1-\frac{s}{s_0}\right)^2\left(1+2\frac{s}{s_0}\right)\left(\frac{s}{s_0}\right)^l \tag{6.73}$$

$$w_{0l}(s) = \frac{12}{(l+1)(l+3)(l+4)} - \frac{2}{l+1}\left(\frac{s}{s_0}\right)^{l+1} + \frac{6}{l+3}\left(\frac{s}{s_0}\right)^{l+3} - \frac{4}{l+4}\left(\frac{s}{s_0}\right)^{l+4} \tag{6.74}$$

Table 6.16: Results for the FOPT(BJ) integral, for $c_{6,1} = 2283$ in a model with two IR poles for $u = 3$.

Order	1	2	3	4	5	6
UV_1	0.01044	0.01707	0.01955	0.01961	0.01866	0.01778
IR_2	0.42298	0.59818	0.64330	0.62317	0.58395	0.54915
IR_{3a}	-0.72479	-1.07018	-1.18572	-1.16230	-1.08269	-1.00363
IR_{3b}	1.29039	1.87510	2.07611	2.07060	1.99040	1.90671
Pol	-0.89078	-1.25101	-1.35066	-1.33107	-1.28154	-1.23885
Sum FOPT(BJ)	0.10822	0.16916	0.20258	0.220014	0.22878	0.23116
Borel sum	0.19598					

$$u_{1l}(s) = -\frac{2}{s_0}\left(1-\frac{s}{s_0}\right)^3\left(1+2\frac{s}{s_0}\right)\left(\frac{s}{s_0}\right)^l \tag{6.75}$$

$$w_{1l}(s) = \frac{12(3l+7)}{(l+1)(l+2)(l+3)(l+4)} - \frac{2}{l+1}\left(\frac{s}{s_0}\right)^{l+1} + \frac{2}{l+2}\left(\frac{s}{s_0}\right)^{l+2} + \frac{6}{l+3}\left(\frac{s}{s_0}\right)^{l+3} - \frac{10}{l+4}\left(\frac{s}{s_0}\right)^{l+4} + \frac{4}{l+5}\left(\frac{s}{s_0}\right)^{l+5} \tag{6.76}$$

$$u_N(s) = \frac{1}{s_0}\left[1 - \frac{N}{N-1}\frac{s}{s_0} + \frac{1}{N-1}\left(\frac{s}{s_0}\right)^N\right] \tag{6.77}$$

$$w_N(s) = -\frac{N}{2(N+1)} + \frac{s}{s_0} - \frac{N}{2(N-1)}\left(\frac{s}{s_0}\right)^2 + \frac{1}{N^2-1}\left(\frac{s}{s_0}\right)^{N+1} \tag{6.78}$$

The moments u_N were introduced in Ref. [199] to suppress the higher dimensional condensates that were noted to affect the analysis of the pinched weight moments in Sec. 6.3 and Refs. [122, 126, 147]. These moments u_N were used to extract the strong coupling constant by fitting the tau data, once the quark and gluon condensate were set to fixed values. The authors extracted the information on two different quantities (the strong coupling constant and a high-dimension condensate) by fitting the integrals $I^N(s_0)$ obtained with the same weight u_N but different radii for the contour of integration s_0 (between 2.3 GeV^2 and m_τ^2). The authors claimed an impressive agreement between the values of the strong coupling constant obtained for different N.

Such an agreement is not particularly surprising. Let us first of all notice that the points from τ data between $s^* = 2.3$ GeV^2 and m_τ^2 are correlated and have significant uncertainties, meaning that the input for the fit is essentially one integral, say $I^N(s^*)$, the integrals for other values of s_0 carrying very little additional information. The fit is

Table 6.17: Results for the FOPT(BJ) integral, for $c_{6,1} = 4267$ in a model with two IR poles for $u = 3$.

Order	1	2	3	4	5	6
UV_1	0.02437	0.03984	0.04563	0.04577	0.04356	0.04149
IR_2	-1.46990	-2.07876	-2.23557	-2.16562	-2.02932	-1.90836
IR_{3a}	0.80001	1.18125	1.30878	1.28293	1.19506	1.10779
IR_{3b}	-0.46784	-0.67983	-0.75271	-0.75071	-0.72163	-0.69129
Pol	1.22158	1.70666	1.83645	1.80764	1.74112	1.68471
Sum FOPT(BJ)	0.10822	0.16916	0.20258	0.22001	0.22878	0.23434
Borel sum	0.27712					

therefore perfect, with one input and two parameters (the strong coupling constant and a high-dimensional condensate). Moreover, the output of the fit is indeed very stable as far as the strong coupling constant is concernend, since these weights can be rewritten as:

$$u_N(s) = \frac{1}{s_0}\left[\left(1 - \frac{s}{s_0}\right) + \frac{1}{N-1}\left(\left(\frac{s}{s_0}\right)^N - \frac{s}{s_0}\right)\right] \tag{6.79}$$

Once inserted in the integral used to computed $\delta^{(0)}$, and taking only power corrections (without logarithms) for the the OPE of Π, one can see that the first bracket provides essentially a correlation between α_s and the dimension-four condensates, and this correlation is identical for all the values of N. The second one fixes the value of the condensate of dimension $2N+2$ in terms of the dimension-4 condensate. Two sum rules for two different values of N provide therefore the same correlation between α_s and the gluon condensate, fixed in the analysis of ref [199].

When we compare the figures 6.16 and 6.17 for the different moments, it is not clear whether CIPT or FOPT should be preferred in such a context. The moments tend to put a different emphasis between the contribution from $d = 4$ and $d = 6$ renormalons, which alter the discussion followed previously for $\delta^{(0)}$. It is quite interesting to notice that the agreement between FOPT and the Borel sum is not automatic, and depends on the structure of the kernel considered. In order to quantify this, one can consider the difference between the contribution of the IR poles in FOPT/CIPT and their Borel resummed values, as shown in Table 6.18 for u_{00}, u_{10}, u_{11} and u_2. The agreement with the Borel resummed version for n around 7 is better for CIPT in the case of u_2, equally bad for FOPT and CIPT in the case of u_{kl} for $k = 1, l = 0$, and better for FOPT in the case of $k = 1, l = 1$.

Table 6.18: Results for the discrepancy between contributions for IR poles in FOPT/CIPT computations and the Borel sum for various weights

	IR	4	5	6	7	8	9	10
$k,l=0,0$	2	-0.028952	-0.013646	-0.000064	0.007366	0.007794	0.003553	-0.001291
FOPT	3	-0.003477	-0.001710	0.000195	0.001334	0.001405	0.000674	-0.000239
$k,l=0,0$	2	-0.012736	-0.011107	-0.010368	-0.010359	-0.011042	-0.012507	-0.014986
CIPT	3	-0.000084	-0.000028	-0.000004	-0.000004	-0.000017	-0.000040	-0.000067
$k,l=1,0$	2	-0.013614	-0.009428	-0.003829	0.001039	0.004036	0.005141	0.005348
FOPT	3	-0.001338	-0.001083	-0.000471	0.000110	0.000423	0.000406	0.000167
$k,l=1,0$	2	-0.006784	-0.005691	-0.005018	-0.004723	-0.004830	-0.005442	-0.006781
CIPT	3	-0.000165	-0.000127	-0.000106	-0.000098	-0.000100	-0.000109	-0.000124
$k,l=1,1$	2	-0.002037	0.000328	0.001658	0.001569	0.000149	-0.002133	-0.004686
FOPT	3	-0.000389	0.000017	0.000317	0.000423	0.000337	0.000131	-0.000076
$k,l=1,1$	2	-0.000323	-0.000647	-0.001017	-0.0014017	-0.001768	-0.002060	-0.002160
CIPT	3	0.000131	0.000120	0.000108	0.000098	0.000090	0.000086	0.000085
$N=2$	2	-0.009792	-0.006531	-0.002007	0.002078	0.004959	0.006847	0.008774
FOPT	3	-0.000934	-0.000814	-0.000391	0.000014	0.000222	0.000206	0.000066
$N=2$	2	-0.004806	-0.003168	-0.001764	-0.000503	0.000692	0.001890	0.003152
CIPT	3	-0.000243	-0.000186	-0.000141	-0.000109	-0.000085	-0.000067	-0.000053

6.4.8 Conclusions from the Studies of Renormalon Models

In this section, we have investigated several aspects of renormalon models for the Adler function, used recently to compare fixed-order and contour-improved perturbation theories (FOPT and CIPT) to treat the contour integral for the theoretical estimate of the τ width [193, 197]. Indeed the difference between the two treatments induce a significant systematics on the extraction of the strong coupling constant at the τ mass. The particular renormalon ansatz for the Adler function in Ref. [193] suggested that FOPT was to be preferred with respect to CIPT, since it converges to the value of the Borel sum (taken as the true value of the integral).

During our study, we have noticed the following points:

- Once several infrared poles are included in the model, one needs to define how one combines the uncertainties estimated from the Borel integral. Depending on the treatment of the RGE for α_s at higher orders (for which the β function is

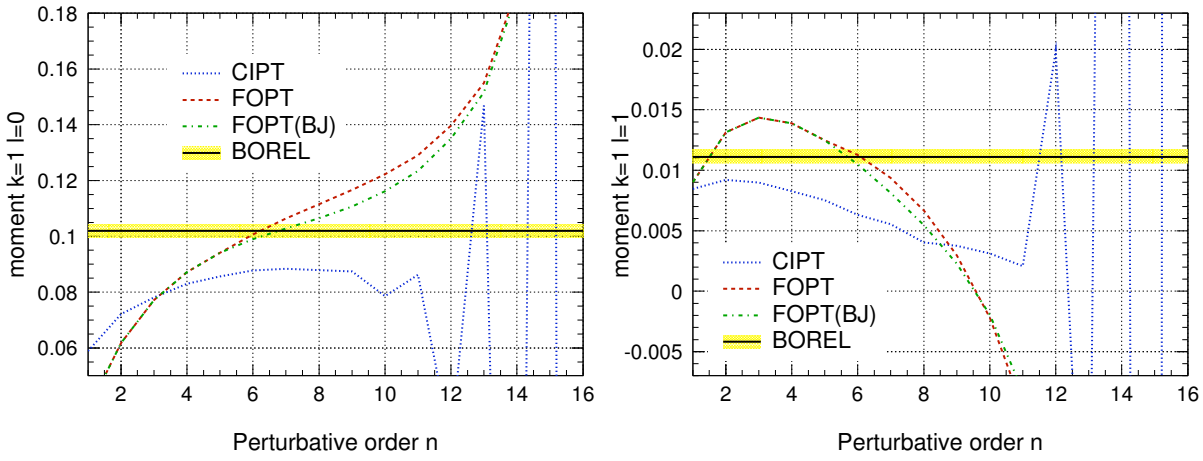

Figure 6.16: Figures for u_{kl} moments with $k = 1, l = 0$ (left) and $k = 1, l = 1$ (right).

not known), the FOPT prescription can yield noticeable differences at intermediate orders, in agreement with more conservative estimates of the uncertainty.

- Ref. [193] sets to zero the contributions from unknown terms in the Wilson coefficients involved in the OPE of the Adler function. Moreover, the perturbative expansion of the ansatz is obtained through an expansion in powers of $1/n$ (where n is the order of perturbation theory) where only the first order are kept. This (truncated) perturbative expression is used to determine the residues of the poles from the first order of the perturbative expansion of D. We noticed that the neglected contributions are not particularly small at the orders of perturbation theory used to determine these residues, which can affected by significant uncertainties.

- We extended the renormalon models by taking into account such potentially large contributions in particular for $n = 3$, and we investigated some cases where FOPT or CIPT are in better agreement with the values obtained from the Borel integral. We discussed two different definitions of the dominance of a pole, in order to determine which cases of these extended models could be considered as acceptable because of the dominance of the first infrared pole.

- We examined the issue of the anomalous dimension of the second infrared pole, which actually corresponds to five operators of different dimensions, and observed rather different behaviours of the perturbative series.

- We discussed other weights, noticing that the better agreement of FOPT with the value of the Borel integral is not a universal feature, and depends on which part of the contour integral is suppressed or enhanced by the weight.

Renormalon models provide very attractive features to discuss qualitative aspects of higher-order perturbation theory. However, in the present discussion, we want to compare

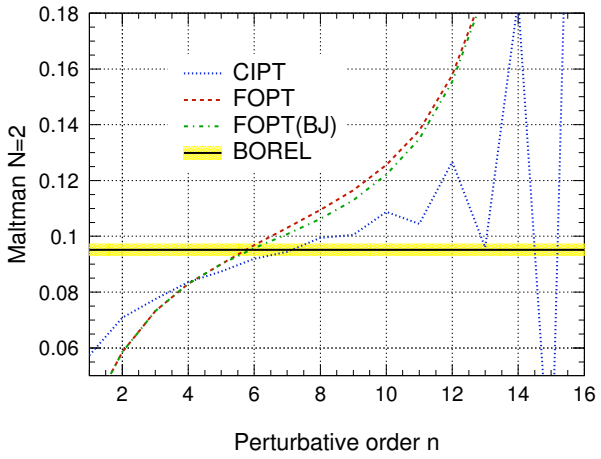

Figure 6.17: Figure for u_N moment with $N = 2$.

small differences between two treatments of perturbation theory, requiring a quantitative model of the higher orders of the Adler function. Any given ansatz based on renormalon calculus involve a large number of unknown coefficients both for the singular terms (residues of the renormalon "poles") and the non-singular terms (polynomial contribution). Only a limited number of these coefficients can be fixed through the first few known terms of the perturbative expansion of the Adler function – the other ones being generally set to zero. It is not clear that the simplified description of the renormalon singularities by an ansatz, assumed to be valid at high orders, is sufficient at such low orders.

The particular ansatz chosen in Ref. [193] does not exhaust the potentialities of model building provided by renormalon calculus, and we have described a few extensions leading to rather varied conclusions concerning the comparison of FOPT versus CIPT. Our study shows that this particular ansatz cannot be taken as part of a reference test to determine whether FOPT, CIPT or yet another method should be adopted to extract α_s from hadronic τ decays. Moreover, significant systematics (as large as the difference between the standard CIPT and FOPT results) ought to be added to the results based on such an ansatz, since it is only one among many different renormalon models for perturbative expansions at high orders.

The previous discussion is essentially based on the fact that we assume the Borel sum eq. (6.43) to provide the "true" value of the asymptotic perturbative series for the Adler function. In particular, its value is used to determine whether FOPT or CIPT should be preferred. Let us mention that the theoretical estimation of the τ decay is rather particular in this respect, since the low value of the τ mass compared to hadronic scales requires one to compute an integral over a contour in the complex energy plane. The assumption that the Borel sum yields the true value of the Adler function should hold not only for real positive values of the coupling constant, but also for values of $\alpha_s(s)$ where s is complex. The theory of asymptotic expansions [200] indicates that there are functions for which this continuation of asymptotic series is not simple and one might encounter

discontinuities when one crosses frontiers in the complex plane (Stokes lines). It would be interesting to determine whether such a situation could occur in renormalons models, and what their impact could be in the issues discussed here.

6.5 Summary of the α_s Studies

We have revisited the determination of $\alpha_s(m_\tau^2)$ from the ALEPH τ spectral functions using recently available results. On the experimental side, new BABAR measurements of the e^+e^- annihilation cross section into $K\overline{K}\pi$ using the radiative return method now permit, through CVC, a much more accurate determination of the vector/axial-vector fractions in the corresponding τ decays. Also, better results are available on τ decays into strange final states from BABAR and Belle. On the theory side, the first unknown term in the perturbative expansion of the Adler function, the fourth-order term K_4, was recently calculated, opening the possibility to further push the accuracy of the theoretical analysis of the hadronic τ decay rate.

Motivated by these improvements we have reexamined the theoretical framework of the analysis. In particular the convergence properties of the perturbative expansions for the τ and Z hadronic widths have been studied, and the ambiguity between the fixed-order (FOPT) and contour-improved (CIPT) approaches for summing up the series has been discussed. The study confirms our earlier findings (at third order) that CIPT is the more reliable treatment. Furthermore we have identified specific consistency problems of FOPT, which do not exist in CIPT.

Recently, models for the Adler function based on renormalon calculus have been proposed to determine which of the two methods is the most accurate, by comparing the resulting asymptotic series with the true value of the integral. We have discussed the assumptions of such ansatz and the determination of their free parameters. We have shown that variations of this renormalon ansatz can yield opposite conclusions concerning the comparison of CIPT versus FOPT, and that such models are not constrained enough to provide a definite answer on this issue or to be exploited for a high-precision determination of $\alpha_s(m_\tau^2)$.

Possible violations of quark-hadron duality at the τ mass scale have been considered using specific models, and their effect has been found to be well within our quoted overall theoretical uncertainty (however, due to the coarseness of the models, we do not introduce additional theoretical errors).

We perform a combined fit of the τ hadronic width and hadronic spectral moments resulting in the value $\alpha_s(m_\tau^2) = 0.344 \pm 0.005_{\rm exp} \pm 0.007_{\rm theo}$, consistent with the previous value obtained for three known orders, and with a 20% reduced theoretical uncertainty. This somewhat moderate improvement is the result of the relatively large value $K_4 \sim 49$, suggesting a slowly converging perturbative series and giving rise to relatively large truncation uncertainties. Nevertheless, the result confirms the excellent accuracy that can be obtained from the analysis of τ decays, albeit indicating that this method may

approach its ultimate accuracy.

The evolved τ result at the M_Z scale, $\alpha_s(M_Z^2) = 0.1212 \pm 0.0005_{\rm exp} \pm 0.0008_{\rm theo} \pm 0.0005_{\rm evol}$, is the most accurate determination available. It agrees with the corresponding value directly obtained from Z decays, which we have reevaluated. Both determinations are so far the only results obtained at $\rm N^3LO$ order. They confirm the running of α_s between 1.8 and 91 GeV as predicted by QCD with an unprecedented precision of 2.4%.

Conclusion and Perspectives

In this thesis, a precise measurement of the cross section $e^+e^- \to K^+K^-(\gamma)$ was performed using ISR events gathered with the BABAR detector. This measurement was done at NLO, specific studies for additional radiation being performed. Background from muons and pions was obtained with data/MC corrections for particle-ID, while background from other channels was obtained with MC and subtracted statistically. All the efficiency measurements are based on data. The unfolding of resolution effects was performed using a simplified version of a newly developed method. In its full generality, this method allows one to treat a series of problems which were not considered before, and some further improvements could be foreseen. Finally, the cross section was obtained from the ratio with the ISR luminosity obtained with a similar study of $\mu\mu$ ISR events. This procedure provides a very good precision of the result, as many systematic uncertainties cancel in the ratio. A systematic uncertainty of 0.7 % has been achieved on the dominant ϕ resonance. The cross section $e^+e^- \to \pi^+\pi^-(\gamma)$ was obtained in a similar way, the systematic uncertainty in the central ρ region being 0.5 %. In both studies, a full propagation of the uncertainties and their correlations was performed. Both cross sections were compared to previous results, and were further exploited for the computation of the hadronic contribution to the anomalous magnetic moment of the muon. A significant improvement of the precision, with respect to the one achieved by previous measurements, was obtained.

A new software was developed in order to combine cross section and mass spectra from different experiments. It takes into account the full statistical and systematic covariance matrices of the measurements from each experiment, as well as the correlations between experiments. It uses a quadratic interpolation between data points or bins, which reduces the systematic uncertainty with respect to a linear interpolation. So far, this software was used to combine mass spectra from hadronic τ decays, as well as cross sections for the channels $e^+e^- \to \pi^+\pi^-$ and $e^+e^- \to \pi^+\pi^-2\pi^0$. Work is in progress to apply this procedure for the other hadronic modes relevant for the computation of $(g-2)_\mu$, and other applications could be foreseen in different contexts. The isospin-breaking corrections, allowing the direct comparison of spectral functions from hadronic τ decays and e^+e^- annihilations, were revisited. This significantly reduced the difference between the corresponding predictions of the hadronic contribution to $(g-2)_\mu$. The discrepancy was further reduced when including the $\pi\pi$ BABAR data in the global average, but some differences between the shapes of the spectral functions still subsist. The Standard Model prediction for $(g-2)_\mu$ was compared to the experimental measurement, and a difference

of 3.2 standard deviations was obtained, which is significantly smaller compared to the previous estimations. This difference is expected to be further reduced when the BABAR results for the KK and the $\pi^+\pi^-2\pi^0$ channels will be included in the global average.

The τ hadronic spectral functions were further exploited for the determination of the strong coupling constant. Special studies were performed, testing the convergence properties of the main perturbative methods used in this determination, in order to choose the most appropriate one. The reliability of a class of renormalon-based models, for the choice between these methods, has been tested and these models were found not to be enough constrained. The value of $\alpha_S(m_\tau^2)$ was obtained and, together with the direct determination at the Z scale, provides the strongest test of the running of α_S, over a large energy range. Further improvements of the weight functions used in the α_S determination are in preparation and this study will be extended to e^+e^- data, once that precise measurements of the full set of relevant hadronic modes will be available.

.1 Notation

In the following we recall the definitions of some quantities which are trequently used in the text [13]:

- n_d = number of bins in the data and in the reconstructed MC distribution
- n_u = number of bins in the unfolding result and in the true MC distribution
- A_{ij} = the number of simulated events which were generated in the bin j and reconstructed in the bin i.
- P_{ij} = the probability for an event generated in the bin j to be reconstructed in the bin i (folding probability matrix, as estimated from the MC simulation)
- $\tilde{P}_{ij}$ = the probability for the "source" of an event reconstructed in the bin i to be situated in the bin j (unfolding probability matrix, as estimated from the MC simulation)
- d_i = number of reconstructed, background subtracted, data events in the bin i
- u_j = number of unfolded events in the bin j
- $\bar{r}$ = spectrum of reconstructed MC events in the transfer matrix model. This spectrum is (almost) exactly known (up to fluctuations in the folding matrix, if is not known analytically) in a "toy test", but only an estimation of it can be computed (up to a change in the normalization factor) when unfolding real data.
- $\bar{t}$ = MC model in the transfer matrix. This distribution can be computed exactly for "toy tests", and it is known up to a change in the normalization factor when unfolding real data.
- r_i = number of reconstructed MC events in the bin i. It is a random realization of $\bar{r}_i$.
- t_j = number of true MC events in the bin j. It is a random realization of $\bar{t}_j$.
- $\sigma(v_i)$ = uncertainty on the element i of the vector v
- $f(\Delta x, \sigma, \lambda)$ = regularization function, depending on Δx, the absolute deviation between two values to be compared, σ, the estimate of the total error to be used for the comparison of the given bin of two spectra, and λ, a positive regularization parameter.
- N_d = number of events in the data and, by preservation, in the unfolding result
- N_{MC} = number of events in the true and reconstructed MC spectra

[13] As the acceptance correction will be performed at the very end, after the unfolding, only events passing all the physical cuts will be implicitly considered when computing these quantities.

- N_d^{MC} = estimate of the number of events in the data, which were simulated in the MC

- $bias_j$ = events corresponding to structures in the data model, which are not simulated in the MC.

- $B^d(B^u)$ = vector of the number of events in the data (unfolded) distribution which are estimated as being potentially due to fluctuations in background subtraction

Bibliography

[1] A. Hocker and V. Kartvelishvili, Nucl. Instrum. Meth. A **372**, 469 (1996) [arXiv:hep-ph/9509307].

[2] V. Blobel, DESY 84-118, [arXiv:hep-ex/0208022].

[3] A. Kondor, JINR-E11-82-853.

[4] L. Lindemann and G. Zech, Nucl. Instrum. Meth. A **354**, 516 (1995).

[5] G. D'Agostini, Nucl. Instrum. Meth. A **362**, 487 (1995).

[6] P. D. Acton *et al.* [OPAL Collaboration], Z. Phys. C **59**, 1 (1993).

[7] H. N. Multhei and B. Schorr, Math. Methods Appl. Sci. **9**, 137 (1987).

[8] H. N. Multhei and B. Schorr, Nucl. Instrum. Meth. A **257**, 371 (1987).

[9] C. Amsler et al., Physics Letters B667, 1 (2008) available on the PDG WWW pages (URL: http://pdg.lbl.gov/)

[10] arxiv:0907.3791, B. Malaescu

[11] V.N. Baier and V.S. Fadin, Phys. Lett. B **27**, 233 (1968).

[12] PEP-II Conceptual Design Report, SLAC-418, LBL-5379 (1993).

[13] B. Aubert *et al.* (BABAR collaboration), Nulc. Instrum. Meth. A **479**, 1-116 (2002).

[14] H. Czyż and J.H. Kühn, Eur. Phys. J. C **18**, 497 (2001).

[15] M. Caffo, H. Czyż and E. Remiddi, Nuovo Cimento A **110**, 515 (1997).

[16] E. Barberio, B. van Eijk, and Z. Was, Comput. Phys. Commun. **66**, 115 (1991).

[17] H. Czyż *et al.*, Eur. Phys. J. C **35**, 527 (2004).

[18] H. Czyż et al., Eur. Phys. J. C **39** (2005) 411.

[19] T. Sjostrand, Comput. Phys. Commun. **82**, 74 (1994).

[20] M. Davier, A.M. Lutz, and W.F. Wang, BABAR Analysis Document (BAD)-1605 (2007).

[21] M. Davier, A.M. Lutz, S. Rodier, and W.F. Wang, BAD-1775 (2007).

[22] M. Davier and W. F. Wang, BAD-1773 (2008).

[23] D. Azzopardi *et al.*, BAD-60 (2000).

[24] R. Gamet and C. Touramanis, BAD-1312 (2005)

[25] R. Gamet and C. Touramanis, BAD-1850 (2007)

[26] M. Davier and W. F. Wang, BAD-1774 (2008).

[27] N. Arnaud, M. Davier, P. Lukin, and W.F. Wang, BAD-1880 and BAD-1504 (2007).

[28] M. Davier, A.M. Lutz, B. Malaescu, L.L. Wang, and W. Wang, BAD-1988 (2008).

[29] M. Davier, A.M. Lutz, B. Malaescu, L.L. Wang, and W. Wang, BAD-1989 .

[30] BABAR Collaboration, B. Aubert *et al.*, Phys. Rev. D **73**: 012005 (2006).

[31] R. Gamet and C. Touramanis, BAD-1312 (2005).

[32] R. Gamet and C. Touramanis, BAD-1850 (2007).

[33] M. Davier, L.L. Wang, W.F. Wang (BAD to come, preliminary)

[34] arxiv:1002.0279, H. Czyż *et al.*

[35] T. Kinoshita, J. Math. Phys. **3** (1962) 650; T.D. Lee and M. Nauenberg, Phys. Rev. **133** (1964) 1549.

[36] Yu.M. Bystritskiy et al., hep-ph/0505236 (2005).

[37] M. Davier, A. Höcker, and Z. Zhang, routine for computing $\Delta\alpha(s)$.

[38] CMD2 Collaboration, R.R.Akhmetshin *et al.*, Phys. Letters B, Vol. 669, 217-222, [arxiv:0804.0178].

[39] SND Collaboration, M.N. Achasov *et al.*, Phys. Rev. D **63**, 072002, 2001.

[40] CLEO Collaboration, T.K. Pedlar *et al.*, Phys. Rev. Lett. **95**, 261803, 2005, [hep-ex/0510005].

[41] S.J. Brodsky and G.P. Lepage, Phys. Lett. B **87**, 359, 1979.

[42] I.B. Logashenko, Talk given at conference TAU '08

[43] S. Bethke, Eur. Phys. J. C **64** (2009) 689 [arXiv:0908.1135 [hep-ph]].

[44] G. D'Agostini, Nucl. Inst. Meth. A **346** (1994) 306.

[45] D. Hanneke, S. Fogwell, G. Gabrielse, Phys. Rev. Lett. **100**, 120801 (2008).

[46] T. Kinoshita in "Lepton Dipole Moments", Advanced Series on Directions in High Energy Physics – Vol. 20.

[47] C. Bouchiat, L. Michel, J. Phys. Radium **22**, 121 (1961).

[48] Czarnecki, A., and W. Marciano in "Lepton Dipole Moments", Advanced Series on Directions in High Energy Physics – Vol. 20.

[49] B. Lee Roberts, Chinese Physics C (HEP & NP), **34** (6), (2010).

[50] Tsumotu Mibe, Chinese Physics C (HEP & NP), **34** (6), (2010).

[51] J. E. Nafe, E. B. Nelson and I. I. Rabi, Phys. Rev. **71**, 914 (1947).

[52] J. S. Schwinger, Phys. Rev. **73**, 416 (1948).

[53] Czarnecki, A., and W. Marciano, Phys. Rev. D 64 (2001), 013014

[54] M. Davier *et al.*, BIHEP-TH-09-01, CERN-OPEN-2009-007, LAL-09-50, Eur. Phys. J. C **66**, 127, (2010) [arXiv:0906.5443[hep-ph]].

[55] CMD-2 Collaboration (R.R. Akhmetshin *et al.*), Phys. Lett. B **578**, 285 (2004) [arXiv:hep-ex/0308008];

[56] CMD-2 Collaboration (V. M. Aulchenko *et al.*), JETP Lett. **82**, 743 (2005) [arXiv:hep-ex/0603021]; CMD-2 Collaboration (R. R. Akhmetshin *et al.*), JETP Lett. **84**, 413 (2006) [arXiv:hep-ex/0610016]; CMD-2 Collaboration (R.R. Akhmetshin *et al.*), Phys. Lett. B **648**, 28 (2007) [arXiv:hep-ex/0610021].

[57] SND Collaboration (M. N. Achasov *et al.*), JETP Lett. **103**, 380 (2006) [arXiv:hep-ex/0605013].

[58] KLOE Collaboration (F. Aloisio *et al.*), Phys. Lett. B **606**, 12 (2005).

[59] KLOE Collaboration (F. Ambrosino *et al.*), Phys. Lett. B **670**, 285 (2009) [arXiv:0809.3950 (hep-ex)].

[60] B. Aubert *et al.* [BABAR Collaboration], Phys. Rev. Lett. **103**, 231801 (2009) [arXiv:0908.3589 [hep-ex]].

[61] M. Davier, A. Hoecker, B. Malaescu, C. Z. Yuan and Z. Zhang, Eur. Phys. J. C **66**, 1 (2010) [arXiv:0908.4300 [hep-ph]].

[62] R. Alemany, M. Davier and A. Hoecker, Eur. Phys. J. C **2**, 123 (1998).

[63] CLEO Collaboration (S. Anderson *et al.*), Phys. Rev. D **61**, 112002 (2000).

[64] M. Davier, S. Eidelman, A. Höcker and Z. Zhang, *Europ. Phys. J.*C **27**, 497 (2003) [hep-ph/0208177].

[65] M. Davier, S. Eidelman, A. Hoecker and Z. Zhang, Eur. Phys. J. C **31**, 503 (2003).

[66] G.W. Bennett *et al.*, Phys. Rev. Lett. **89**, 101804 (2002).

[67] M. Davier, Nucl. Phys. Proc. Suppl. **169**, 288 (2007).

[68] Belle Collaboration (M. Fujikawa *et al.*), Phys. Rev. D **78**, 072006 (2008), arXiv:0805.3773v1 [hep-exp].

[69] The HVPTools source code (C++, relying on ROOT functionality) and database (XML format) can be made publicly available. Please contact the author.

[70] H. Hayashii, private communication.

[71] L3 Collaboration (M. Acciarri *et al.*), Phys. Lett. B **345**, 93 (1995).

[72] DELPHI Collaboration (J. Abdallah *et al.*), Eur. Phys. J. C **46**, 1 (2006).

[73] Y.S. Tsai, Phys. Rev. D **4**, 2821 (1971) [Erratum-ibid. D **13**, 771 (1976)].

[74] H.B. Thacker and J.J. Sakurai, Phys. Lett. **36**, 103 (1971).

[75] A. Sirlin, Rev. Mod. Phys. **50**, 573 (1978) [Erratum-ibid. **50**, 905 (1978)]; A. Sirlin, Nucl. Phys. B **196**, 83 (1982).

[76] W. Marciano and A. Sirlin, *Phys. Rev. Lett.***61**, 1815 (1988).

[77] E. Braaten and C.S. Li, *Phys. Rev.*D **42**, 3888 (1990).

[78] J. Erler, Rev. Mex. Fis. **50**, 200 (2004).

[79] J.S. Schwinger, "Particles, Sources and Fields", Vol. 3, Reading, Massachusetts (1989); see also, M. Drees and K. Hikasa, Phys. Lett. B **252**, 127 (1990)

[80] V. Cirigliano, G. Ecker and H. Neufeld, Phys. Lett. B **513**, 361 (2001); JHEP 0208, 002 (2002).

[81] For a recent review, see *e.g.* J. Portoles, Nucl. Phys. Proc. Suppl. **169**, 3 (2007).

[82] J. Wess and B. Zumino, Phys. Lett. B **37**, 95 (1971); E. Witten, Nucl. Phys. B **223**, 422 (1983).

[83] A. Flores-Tlalpa F. Flores-Baez, G. Lopez Castro and G. Toledo Sanchez, Phys. Rev. D **74**, 071301 (2006); Nucl. Phys. Proc. Suppl. **169**, 250 (2007).

[84] A. Flores-Talpa, G. Lopez Castro, and G. Toledo Sanchez, Phys. Rev. D **76** (2007) 096010.

[85] T. Kinoshita and A. Sirlin, Phys. Rev. **113**, 1652 (1959).

[86] G.J. Gounaris and J.J. Sakurai, Phys. Rev. Lett. **21**, 244 (1968).

[87] J.H. Kühn and A. Santamaria, Z. Phys. C **48** (1990) 445.

[88] K. Maltman and C.E. Wolfe, Phys. Rev. D **73**, 013004 (2006).

[89] M. Benayoun *et al.*, Eur. Phys. J. C **55**, 199 (2008).

[90] F. Guerrero and A. Pich, Phys. Lett. B **412**, 382 (1997).

[91] F. Flores-Baez, G. Lopez Castro and G. Toledo Sanchez, Phys. Rev. D **76**, 096010 (2007).

[92] See e.g. J.J. Sakurai, "Currents and Mesons", The university of Chicago press, 1969.

[93] KLOE Collaboration (A. Aloisio *et al.*), Phys. Lett. B **561**, 55 (2003).

[94] S.J. Brodsky and E. de Rafael, Phys. Rev. **168**, 1620 (1968).

[95] F. Flores-Baez and G. López Castro, Phys. Rev. D **78**, 077301(2008).

[96] S. Dubinsky, A. Korchin, N. Merenkov, G. Pancheri and O. Shekhovtsova, Eur. Phys. J. C **40**, 41 (2005) [arXiv:hep-ph/0411113].

[97] NA7 Collaboration (S.R. Amendolia *et al.*), Nucl. Phys. B **277**, 168 (1986).

[98] J. Prades, E. de Rafael and A. Vainshtein, UG-FT-242-08, CAFPE-112-08, CPT-P092-2008, FTPI-MINN-08-41, UMN-TH-2723-08, [arXiv:0901.0306].

[99] Muon $g-2$ Collaboration (G.W. Bennett *et al.*), Phys. Rev. D **73**, 072003 (2006).

[100] A. Hoecker and W. Marciano, "The Muon Anomalous Magnetic Moment" in [9]; updated (2009) at http://pdglive.lbl.gov.

[101] K. Hagiwara, A.D. Martin, D. Nomura and T. Teubner, Phys. Lett. B **649**, 173 (2007).

[102] F. Jegerlehner, Acta Phys. Polon. B **38**, 3021 (2007) [arXiv:hep-ph/0703125].

[103] F. Jegerlehner, Nucl. Phys. B (Proc. Suppl.) **181**, 26 (2008).

[104] F. Jegerlehner and A. Nyffeler, Phys. Rept. **477**, 1 (2009).

[105] OLYA Collaboration (I.B. Vasserman *et al.*), Sov. J. Nucl. Phys. **30**, 519 (1979).

[106] TOF Collaboration (I.B. Vasserman *et al.*), Sov. J. Nucl. Phys. **33**, 368 (1981).

[107] DM1 Collaboration (A. Quenzer *et al.*), Phys. Lett. B **76**, 512 (1978).

[108] DM2 Collaboration (D. Bisello *et al.*), Phys. Lett. B **220**, 321 (1989).

[109] NA7 Collaboration (S.R. Amendolia *et al.*), Phys. Lett. B **138**, 454 (1984).

[110] H. Czyż, A. Grzelińska, J.H. Kühn, Phys. Rev. D **75**, 074026 (2007).

[111] R. Brun and F. Rademakers, Nucl. Inst. Meth. in Phys. Res. A **389**, 81 (1997).

[112] CMD2 Collaboration (R.R. Akhmetshin *et al.*), Phys. Lett. B **466**, 392 (1999).

[113] I.B. Logashenko, Talk given at conference "e^+e^- Collisions From Phi To Psi" Novosibirsk, Russia, 27 Feb – 2 Mar 2006; I.B. Logashenko, Nucl. Phys. B (Proc. Suppl.) **162**, 13 (2006).

[114] SND Collaboration (M.N. Achasov *et al.*), Budker INP 2001-34, Novosibirsk (2001).

[115] T. Kinoshita and M. Nio, Phys. Rev. D **73**, 013003 (2006).

[116] R. Jackiw and S. Weinberg, Phys. Rev. D **5**, 2396 (1972).

[117] A. Czarnecki *et al.*, Phys. Rev. D **67**, 073006 (2003).

[118] D. St ockinger, private communication.

[119] M. Davier, S. Descotes-Genon, A. Hocker, B. Malaescu and Z. Zhang, Eur. Phys. J. C **56** (2008) 305 [arXiv:0803.0979 [hep-ph]].

[120] B. Malaescu, Nucl. Phys. Proc. Suppl. **186**, 183 (2009) [arXiv:0809.2823 [hep-ph]].

[121] S. Descotes-Genon and B. Malaescu, arXiv:1002.2968 [hep-ph].

[122] M. Davier, A. Hocker and Z. Zhang, Rev. Mod. Phys. **78**, 1043 (2006) [arXiv:hep-ph/0507078].

[123] S. Narison and A. Pich, *Phys. Lett.*B **211**, 183 (1988).

[124] E. Braaten, *Phys. Rev.*D **39**, 1458 (1989).

[125] E. Braaten, S. Narison and A. Pich, *Nucl. Phys.*B **373**, 581 (1992).

[126] F. Le Diberder and A. Pich, Phys. Lett. B **289**, 165 (1992).

[127] P. Baikov, K.G. Chetyrkin and J.H. Kühn, SFB-CPP-08-04, TTP08-01, arXiv:0801.1821 (2008).

[128] BABAR Collaboration (B. Aubert et al.), SLAC-PUB-12968, BABAR-PUB-07-052, arXiv:0710.4451 (2007).

[129] Particle Data Group (W.M. Yao *et al.*), J. Phys. G **33**, 1 (2006) and 2007 partial update for the 2008 edition.

[130] CKMfitter Group (J. Charles *et al.*), *Europ. Phys. J.*C **41**, 1 (2005) [hep-ph/0406184]; updates at http://ckmfitter.in2p3.fr.

[131] ALEPH Collaboration (R. Barate, *et al.*), *Europ. Phys. J.*C **11**, 599 (1999) [hep-ex/9903015].

[132] OLYA, CMD Collaborations (L.M. Barkov *et al.*), Nucl. Phys. B **256**, 365 (1985).

[133] F. Mané et al. (DM1 Collaboration), *Phys. Lett.*B **112**, 178 (1982).

[134] D. Bisello et al. (DM2 Collaboration), Z. Phys. C **52**, 227 (1991).

[135] CLEO Collaboration (D. Asner, et al.), *Phys. Rev.*D **61**, 012002 (2000) [hep-ex/9902022].

[136] CLEO Collaboration (T.E. Coan, et al.), *Phys. Rev. Lett.***92**, 232001 (2004) [hep-ex/0401005].

[137] J.J. Gomez-Cadenas, M.C. Gonzalez-Garcia and A. Pich, *Phys. Rev.*D **42**, 3093 (1990).

[138] P. Roig, AIP Conf. Proc. **964**, 40-46 (2007) [arXiv:0709.3734].

[139] D. G. Dumm, P. Roig, A. Pich and J. Portoles, Phys. Rev. D **81**, 034031 (2010) [arXiv:0911.2640 [hep-ph]].

[140] M. Finkemeier and E. Mirkes, Z. Phys. C **69**, 243 (1996) [hep-ph/9503474].

[141] BABAR Collaboration (B. Aubert et al.), *Phys. Rev. Lett.***100**, 011801 (2008) [arXiv:0707.2981].

[142] BABAR Collaboration (B. Aubert et al.), *Phys. Rev.*D-RC **76**, 051104 (2007).

[143] Belle Collaboration (D. Epifanov et al.), *Phys. Lett.*B **654**, 65 (2007) [arXiv:0706.2231].

[144] ALEPH Collaboration (D. Buskulic, *et al.*), *Phys. Lett.*B **307**, 209 (1993).

[145] CLEO Collaboration (T. Coan, *et al.*), *Phys. Lett.*B **356**, 580 (1995).

[146] OPAL Collaboration (K. Ackerstaff, *et al.*), *Europ. Phys. J.*C **7**, 571 (1999) [hep-ex/9808019].

[147] Le Diberder:1992te F. Le Diberder and A. Pich, Phys. Lett. B **286**, 147 (1992).

[148] A.A. Pivovarov, Sov. J. Nucl. Phys. **54**, 676 (1991); *Z. Phys.*C 53, 461 (1992).

[149] G. Grunberg, *Phys. Lett.*B **95**, 70 (1980), Erratum-ibid. B 110, 501 (1982).

[150] G. Grunberg, *Phys. Rev.*D **29**, 2315 (1984).

[151] A. Dhar, *Phys. Lett.*B **128**, 407 (1983).

[152] A. Dhar and V. Gupta, *Phys. Rev.*D **29**, 2822 (1983).

[153] P.M. Stevenson, *Phys. Rev.*D **23**, 2916 (1981).

[154] P. Ball, M. Beneke and V.M. Braun, *Nucl. Phys.*B **452**, 563 (1995) [hep-ph/9502300].

[155] W. M. Yao *et al.* [Particle Data Group], J. Phys. G **33** (2006) 1.

[156] G. Altarelli, P. Nason and G. Ridolfi, *Z. Phys.*C **68**, 257 (1995) [hep-ph/9501240].

[157] M. Neubert, *Nucl. Phys.*B **463**, 511 (1996) [hep-ph/9509432].

[158] ALEPH Collaboration (R. Barate, *et al.*), *Z. Phys.*C **76**, 15 (1997).

[159] ALEPH Collaboration (R. Barate, *et al.*), *Europ. Phys. J.*C **4**, 409 (1998).

[160] M.A. Shifman, A.L. Vainshtein and V.I. Zakharov, *Nucl. Phys.*B **147**, 385, 448, 519 (1979).

[161] E. Poggio, H. Quinn and S. Weinberg, *Phys. Rev.*D **13**, 1958 (1976).

[162] E. Braaten, *Phys. Rev. Lett.***60**, 1606 (1988).

[163] M.A. Shifman, *Quark-hadron duality*, Boris Ioffe Festschrift *At the Frontier of Particle Physics, Handbook of QCD*, M.A. Shifman (ed.), World Scientific, Singapore, 2001, hep-ph/0009131.

[164] O. Cata, M. Golterman and S. Peris, JHEP **0508**, 076 (2005) [hep-ph/0506004].

[165] O. Cata, M. Golterman and S. Peris, arXiv:0803.0246 (2008).

[166] S. Adler, *Phys. Rev.*D **10**, 3714 (1974).

[167] L.R. Surguladze and M.A. Samuel, *Phys. Rev. Lett.***66**, 560 (1991), Erratum-ibid. **66**, 2416 (1991).

[168] S.G. Gorishnii, K.L. Kataev and S.A. Larin, *Phys. Lett.*B **259**, 144 (1991).

[169] K.G. Chetyrkin, A.L. Kataev and F.V. Tkachov, *Phys. Lett.***85**, 277 (1979).

[170] M. Dine and J.R. Sapirstein, *Phys. Rev. Lett.***43**, 668 (1979).

[171] W. Celmaster and R.J. Gonsalves, *Phys. Rev. Lett.***44**, 560 (1980).

[172] S.A. Larin, T. van Ritbergen and J.A.M. Vermaseren, *Phys. Lett.*B **400**, 379 (1997) [hep-ph/9701390]; *Phys. Lett.*B **404**, 153 (1997) [hep-ph/9702435].

[173] A.L. Kataev and V.V. Starshenko, Mod. Phys. Lett. A **10**, 235 (1995) [hep-ph/9502348].

[174] C.J. Maxwell and D.G. Tonge, *Nucl. Phys.*B **481**, 681 (1996) [hep-ph/9606392]; *Nucl. Phys.*B **535**, 19 (1998) [hep-ph/9705314].

[175] P.A. Raczka, *Phys. Rev.*D **57**, 6862 (1998) [hep-ph/9707366].

[176] J.G. Körner, F. Krajewski and A.A. Pivovarov, *Phys. Rev.*D **63**, 036001 (2001) [hep-ph/0002166].

[177] D.J. Broadhurst, *Z. Phys.*C **58**, 339 (1993).

[178] M. Beneke and V.M. Braun, *Phys. Lett.*B **348**, 513 (1999) [hep-ph/9411229].

[179] D.J. Broadhurst and S.C. Generalis, *Phys. Lett.***165**, 175 (1985).

[180] ALEPH Collaboration (S. Schael, *et al.*), Phys. Rept. **421**, 191 (2005) [hep-ex/0506072].

[181] S. Bethke, Prog. Part. Nucl. Phys. **58**, 351 (2007) [hep-ex/0606035].

[182] G. Dissertori *et al.*, JHEP **0802**, 040 (2008) [arXiv:0712.0327].

[183] K.G. Chetyrkin, B.A. Kniehl and M. Steinhauser, *Phys. Rev. Lett.***79**, 2184 (1997) [hep-ph/9706430]; *Nucl. Phys.*B **510**, 61 (1998) [hep-ph/9708255].

[184] J. Schieck *et al.*, *Europ. Phys. J.*C **48**, 3 (2006), Erratum-ibid. 50, 769 (2007) [arXiv:0707.0392].

[185] W. Bernreuther and W. Wetzel, *Nucl. Phys.*B **197**, 228 (1982); Erratum ibid. B **513**, 758 (1998).

[186] W. Wetzel, *Nucl. Phys.*B **196**, 259 (1982).

[187] G. Rodrigo, A. Pich and A. Santamaria, *Phys. Lett.*B **424**, 367 (1998) [hep-ph/9707474].

[188] Gfitter Group (M. Göbel *et al.*), Programme library for electroweak fits and beyond (publication in preparation); more information at: https://twiki.cern.ch/twiki/bin/view/Gfitter/WebHome.

[189] J. Santiago and F.J. Ynduráin, *Nucl. Phys.*B **611**, 447 (2001).

[190] Q. Mason *et al.*, *Phys. Rev. Lett.***95**, 052002 (2005).

[191] S. Menke, arXiv:0904.1796 [hep-ph].

[192] M. Jamin, JHEP **0509**, 058 (2005) [arXiv:hep-ph/0509001].

[193] M. Beneke and M. Jamin, JHEP **0809** (2008) 044 [arXiv:0806.3156 [hep-ph]].

[194] M. Beneke, Phys. Rept. **317**, 1 (1999) [arXiv:hep-ph/9807443].

[195] M. Beneke and V. M. Braun, arXiv:hep-ph/0010208.

[196] I. Caprini and J. Fischer, Phys. Rev. D **60** (1999) 054014 [arXiv:hep-ph/9811367].

[197] I. Caprini and J. Fischer, Eur. Phys. J. C **64** (2009) 35 [arXiv:0906.5211 [hep-ph]].

[198] I. Caprini, J. Fischer and I. Vrkoc, J. Phys. A **42** (2009) 395403 [arXiv:0909.0110 [hep-th]].

[199] K. Maltman and T. Yavin, arXiv:0812.2457 [hep-ph].

[200] R. B. Dingle, Asymptotic expansions: their derivation and interpretation, Academic Press London and New York (1973).

Remerciements

C'est avec une grande émotion que j'arrive au chapitre destiné aux remerciements. C'est un chapitre qui me tient à coeur car, tout d'abord, je ressens le besoin d'être reconnaissants vis-à-vis des personnes sans lesquels ce travail n'aurait jamais pu être réalisé. En ce sens, je pense tout particulièrement aux deux personnes qui ont encadré mon travail pendent ces trois ans, Michel DAVIER et Sébastien DESCOTES-GENON. Vous m'avez appris beaucoup de choses et c'était toujours un plaisir de travailler avec vous. Je vous remercie beaucoup pour tout votre soutien et je suis sûr que nous aurons l'occasion de travailler ensemble sur d'autres sujets très intéressants. Toute mon activité scientifique à venir sera certainement très marquée par les interactions que nous avons eues.

Je tiens à remercier Guy WORMSER pour l'accueil au LAL, où j'ai pu effectuer ma thèse dans d'excellentes conditions, ainsi que d'avoir accepté de présider mon jury de thèse. Je remercie également les deux rapporteurs, Patrick AURENCHE et Gautier HAMEL de MONCHENAULT pour le fait d'avoir accepté cette tâche ainsi que pour leur lecture détaillée du manuscrit. Merci à Antonio PICH de m'avoir fait l'honneur d'examiner mon travail, ainsi qu'à Denis BERNARD d'avoir accepté l'invitation de faire partie de ce jury.

Je suis très reconnaissant à tous les gens avec lesquels j'ai eu la chance de travailler pendant ma thèse. Je pense bien sûr à Michel et Sébastien, mais aussi à Andreas HOECKER et Zhiqing ZHANG avec lesquels nous avons eu beaucoup de réunions le lundi matin à 9 h, des nombreux échanges de mails, notamment le dimanche soir entre 11 h et minuit (tout ça pour réaliser HVPTools, mais je pense que ça a valu le coup), ainsi que des discussions sur Skype jusqu'à 2-3 h du matin pour la préparation de certaines publications. Concernant le travail sur les analyses ISR, je me suis toujours senti dans une vraie équipe. Il y avait toujours le soutien de Michel, mais j'ai également beaucoup bénéficié de l'apport des autres membres de l'équipe : Nicolas ARNAUD, Anne-Marie LUTZ, Liangliang WANG et Wenfeng WANG.

Je remercie beaucoup Anne-Marie, Michel et Sébastien pour leur lecture et $(\text{re})^{\text{n}}$-lectures des diverses parties de ce manuscrit.

J'ai eu des discussions très intéressantes et utiles avec Volker BLOBEL, au sujet des méthodes d'unfolding, et avec Martin BENEKE, Samuel FRIOT, Matthias JAMIN et Antonio PICH au sujet de modèles de renormalons. Je les en remercie.

Je vais toujours me souvenir avec plaisir de toutes les interactions avec les autres membres des groupes BABAR, Super B et Théorie, que je n'ai pas encore eu l'occasion

de mentionner. Je pense notamment à Achille, Benoît, Emi, Marie-Hélène et Patrick, ainsi qu'aux étudiants, Denis (nous avons partagé le même bureau pendant trois ans), Alejandro, Andrey, Joao, Justine, Leonid et Viola.

Je tiens à remercier Gilbert GROSDIDIER et Christian PASCAUD pour leur aide sur un certain nombre de problèmes " techniques ". J'ai également bénéficié de tout le soutien du service informatique et je leur en remercie.

Je remercie François COUCHOT pour le fait d'avoir accepté de financer mes déplacements à plusieurs conférences et une école d'été. J'ai également bénéficié du financement du réseau FLAVIANET, pour une autre école d'été, et je leur suis reconnaissant. Je remercie également le personnel du service missions pour leur aide dans toutes les démarches de déplacement. Je remercie également Sylvie PRANDT et Catherine ZOMER pour leur aide dans des diverses démarches administratives. Je ne pourrais pas oublier de remercier Françoise MARECHAL pour ses réponses très rapides aux demandes de numéro LAL pour les publications, ainsi que pour son aide dans les recherches de certains articles pas facilement accessibles.

Ma passion pour la Physique date depuis plus d'une douzaine d'années avant le début de ma thèse. Je ne pourrai jamais remercier assez tous les enseignants qui, tout au long de ma formation, ont su m'inspirer l'amour pour ce que je considère être la plus belle des sciences.

Je pense maintenant à tous mes amis, Adrian, Alexandra, Consuela, Dan, David, Diana, Emi, Ioana, Jérôme, Mihai, Simon, Thomas, et à tous ceux que j'aurai oublié de mentionner. Même si nous n'avons pas eu l'occasion ou le temps de nous voir trop souvent pendant ces trois dernières années, j'ai toujours eu le sentiment que vous étiez proche de moi.

Je tiens à remercier chaleureusement ma famille pour tout le soutien qu'ils m'ont offert, ainsi que pour leur compréhension pendant les périodes de " vacances " où j'ai du consacrer une certaine partie de mon temps au travail.